

Appendix 1

Švec, P.; Webre, W.; Richards, G.; Labuta, J.; Wakayama, Y.; Miklík, D.; Karr, P.; Mori, T.; Ariga, K.; D'Souza, F.; Hill Jonathan, P., Phenanthroline-fused Pyrazinacenes: One-pot Synthesis, Tautomerization and a Ru(II)(2,2'-bpy)₂ Derivative. *Eur. J. Inorg. Chem.* **2018**, 2541-2548. **Times Cited: 4; IF = 2.58.**

P. Švec performed the synthesis of pyrazinacene compounds, collected NMR characterization data, assisted with elucidating the isomeric composition of alkylated pyrazinacenes, and helped with writing the manuscript.

Photoactive Ruthenium Complexes

Phenanthroline-Fused Pyrazinacenes: One-Pot Synthesis, Tautomerization and a Ru^{II}(2,2'-bpy)₂ Derivative

Pavel Švec,^[a,b] Whitney A. Webre,^[c] Gary J. Richards,^{*,[a,d]} Jan Labuta,^[a] Yutaka Wakayama,^[a] David Miklík,^[a,e] Paul A. Karr,^[f] Toshiyuki Mori,^[g] Katsuhiko Ariga,^[a,h] Francis D'Souza^{*,[c]} and Jonathan P. Hill^{*,[a]}

Abstract: We report the one-pot synthesis of a phenanthroline-fused pyrazinacene derivative (6,13-dihydrodiprido-[3,2-a:2',3'-c]-5,6,7,8,11,12,13,14-octazaapentacene-9,10-dicarbonitrile) and its behaviour under alkylating conditions used to improve solubility. Tautomerization of the starting pyrazinacene due to the presence of a reduced pyrazine ring contained within an octaazatetracene chromophore led to mixtures of isomers, and factors affecting the relative yields of these isomers were considered. Isomer population can be described by a two-

step reaction model where initial N-alkylation affects the reactivity of the remaining nitrogen atoms available for subsequent alkylation. A discrete soluble non-isomerizable phenanthroline-fused pyrazinacene was also prepared and the activity of its Ru(bpy)₂ complex as a photosensitizer for dye-sensitized solar cell application was investigated. The compounds reported illustrate the unusual reactivity of reduced pyrazinacenes and also their potential as photosensitizers.

Introduction

Heteroacenes^[1–12] have become an increasingly important branch of the acene family due to their diverse properties making them suitable for various applications. These properties include their more usually cited molecular electronic applications as n- or p-type semiconductors.^[13–15] Pyrazinacenes^[16] are a specific type of heteroacene containing linearly-fused 1,4-

pyrazine units exemplified in work by Stöckner and co-workers who prepared pyrazinacenes containing up to six linearly-fused pyrazine groups.^[17] Other examples containing different multiplicities have also been prepared often incorporated in CH-acene derivatives.^[18] Introducing pyrazine units presents distinct advantages for these compounds in presenting points for easy elaboration, oxidation state control, while also adding sites for accommodation of exchangeable protons whose position can affect the electronic structure of the pyrazinacenes through tautomerization.^[19,20] Fluorubine (6,13-dihydro-5,6,7,12,13,14-hexaazapentacene) is a typical example of a pyrazinacene, which possesses such tautomerizable protons and also presents substantial fluorescence quantum yields in its derivatives.^[21] Their optical absorption properties also make these compounds excellent candidates as sensitizing moieties for solar energy conversion. Materials used for such applications commonly contain a transition metal cation such as Ru^{II} or Ir^{III}^[22] although more recent examples have also exploited more available first-row transition metal cations such as Cu^I.^[23] For this reason, it would be practical to introduce a ligating group to the pyrazinacene chromophore in order to couple prospective molecules with a transition metal cation or complex. In this work, we have investigated the synthesis of extended pyrazinacene derivatives with emphasis on introducing a phenanthroline moiety in order to investigate their utility as sensitizing materials for dye-sensitized solar cell (DSSC) applications. During this work we were also presented with a rare opportunity to assess tautomeric processes in extended pyrazinacenes due to the synthesis of an unsymmetrical phenanthrolopyrazinacene.

Here we report the one-pot syntheses of phenanthroline and phenanthrene-appended pyrazinacenes from commercially available reagents. We also report the stepwise synthesis of a

[a] International Center for Materials Nanoarchitectonics (MANA), National Institute for Materials Science (NIMS), 1-1 Namiki, Tsukuba, Ibaraki 305-0044, Japan
E-mail: Jonathan.Hill@nims.go.jp

[b] Institute of Macromolecular Chemistry, Academy of Sciences of the Czech Republic,

Heyrovského nám. 2, 162 06 Prague 6, Czech Republic

[c] Department of Chemistry, University of North Texas, 1155 Union Circle, #305070, Denton, Texas 76203, USA
E-mail: francis.dsouza@unt.edu

[d] Department of Chemistry, Ochanomizu University, Otsuka 2-1-1, Bunkyo-ku, Tokyo 112-8610, Japan
E-mail: Richards.Gary@nims.go.jp

[e] Department of Organic Materials, Institute of Organic Chemistry and Technology, Faculty of Chemical Technology, University of Pardubice, Studentská 573, 532 10 Pardubice, Czech Republic

[f] Department of Physical Sciences and Mathematics, Wayne State College, 111 Main Street, Wayne, Nebraska, 68787, USA

[g] Solid Oxide Fuel Cell Materials Design Group, Center for Green Research on Energy and Environmental Materials, National Institute for Materials Science (NIMS), Namiki 1-1, Tsukuba, Ibaraki 305-0044, Japan

[h] Department of Advanced Materials Science, Graduate School of Frontier Sciences, The University of Tokyo, 5-1-5 Kashiwanoha, Kashiwa, Chiba 277-8561, Japan

Supporting information and ORCID(s) from the author(s) for this article are available on the WWW under <https://doi.org/10.1002/ejic.201800283>.

phenanthroline-appended pyrazinacene, which was chelated, in this case, with bis(2,2'-bipyridine)ruthenium(II) to demonstrate the utility of this approach to prepare materials for DSSCs.

Results and Discussion

In our previous work on the pyrazinacene systems, we have prepared mostly unsymmetrically substituted compounds.^[16,24–26] This was initially as a result of our use of the reaction of 2,3-diamino-5,6-dicyanopyrazine (DADCP) with 1,2-diketones, such as benzil derivatives, where the synthesis naturally provides different groups at the terminal ends of the molecules. In particular, we were interested to study the effect of such unsymmetrically substituted structures on the self-assembly properties of the compounds.

For this purpose, we performed initial scanning tunneling microscopy (STM) studies on 5,12-dihydro-2,3-diphenyl-1,4,6,7,10,11,12-octaazatetraacene-8,9-dicarbonitrile^[16] (Figure 1a, Figure 1b, Figure 1c), which revealed its assembly into paired antiparallel lines of molecules and a potentially unique method for templating the structure of crystalline thin films grown from these materials. The self-assembled structure (Figure 1d) is formed due to several hydrogen bonding interactions between nitrile groups and either dihydropyrazine NH groups or phenyl CH groups suggesting to us that the planarization of the phenyl groups to phenanthrenyl or phenanthrolyl might improve the quality of monolayer films by (a) optimizing supra-molecular interactions between these groups, and (b) providing a larger π electronic surface for interaction with the metal sub-

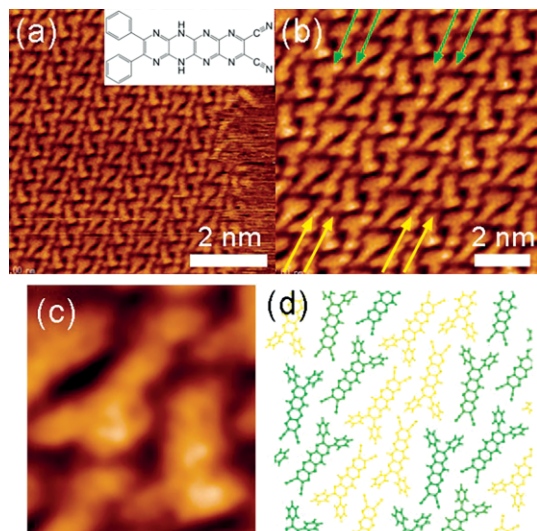


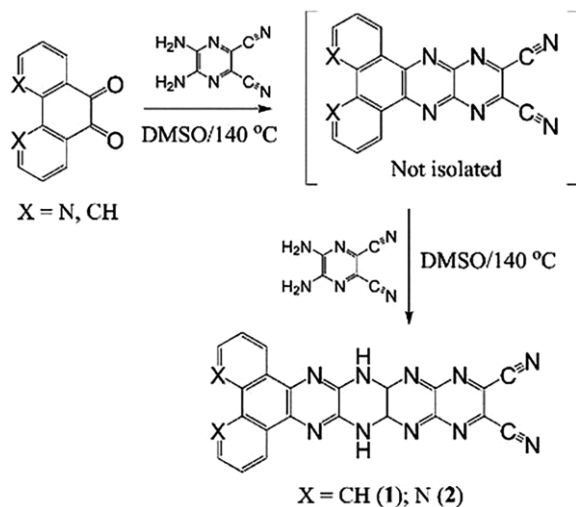
Figure 1. Scanning tunneling microscopy of 5,12-dihydro-2,3-diphenyl-1,4,6,7,10,11,12-octaazatetraacene-8,9-dicarbonitrile.^[16] (a) Chemical structure and monolayer on Cu(111) ($I_t = 60$ pA; $V_t = +1.0$ V). (b) Alternating antiparallel rows of molecules on Cu(111) indicated by the green and yellow arrows ($I_t = 60$ pA; $V_t = +1.0$ V). (c) Detail of (b) showing close approach of nitrile groups to the pyrazinacene backbone (CN...HN H-bonding). (d) Packing model for the molecules indicating the close approaches of nitriles to the phenyl substituents in adjacent molecules. Green and yellow colors denote the rows of molecules in (b).

strate. Some of these observed interactions also give insight into the reasons for the often extreme insolubilities of these compounds and their resulting intractability. Ultimately, however, we have found that introduction of phenanthroline to the structure unexpectedly yields compounds of greater solubility probably due to the part removal of the intermolecular CH...N hydrogen bonding network observed by STM. This has permitted us to proceed with the present work.

During this work, we noted that the initial condensation of a 1,2-phenylenediamine with phenanthrene-9,10-quinone, although normally promoted by acid catalysis, can also proceed at elevated temperature in polar solvents,^[27] being as it is a simple dehydration reaction. This reaction yields a 1,4,5,8-tetraazanaphthalo-2,3-nitrile derivative that is sufficiently electron deficient that nitrile groups are capable of acting as effective leaving groups in nucleophilic substitution reactions. With these points in mind, we investigated the reaction of phenanthroline-9,10-quinone with DADCP in dimethylsulfoxide at different temperatures. To our satisfaction, the main product obtained from reactions performed at 140 °C was 6,13-dihydrodipyrido[3,2-a:2',3'-c]-5,6,7,8,11,12,13,14-octaazapentacene-9,10-dicarbonitrile (**2**), if two equivalents of DADCP were applied in the presence of 2 equiv. of sodium carbonate to neutralize HCN generated in the 2nd phase of the reaction. The reaction is summarized in Scheme 1. It represents a facile method for preparing a rather unusual pyrazinacene, which incidentally possesses attributes suitable for utilization in the aforementioned applications. We also undertook the preparation of the corresponding bis(benzo) derivative **1**. Both compounds are quite intractable and, for this reason, difficult to purify. However, **1** could be partly purified using column chromatography although it is subsequently so insoluble that it was not possible to obtain reasonable NMR spectra – the compound can just be observed by ¹H NMR in neat [D₁]TFA. On the other hand, ¹H and ¹³C NMR spectra of **2** could be obtained after purification either by Soxhlet extraction or column chromatography followed by precipitation. **1** and **2** could also not be purified by sublimation even in ultrahigh vacuum.

Compounds **1** and **2** are relatively insoluble in common solvents so that we considered their modification by N-alkylation in order to improve solubility. However, protic tautomerization^[19,20] is a significant process occurring in these compounds so that N-alkylation generally yields complex mixtures of isomeric products although these are generally restricted to isomers with one N-alkyl group per side with N-alkylation not favoured at end pyrazine groups of the pyrazinacene unit even if there is a further fused benzo group present. We attempted to N-alkylate **2** using simple *n*-alkyl bromides or 3,4,5-tris(dodecyloxy)benzyl chloride but either solubility was not increased sufficiently (for *n*-C₁₂H₂₅) or separation of the resulting isomer mixture remained unfeasible despite improved solubility. Regardless, the higher solubility of the 3,4,5-tris(dodecyloxy)benzyl derivatives **3** presented the possibility of studying the isomeric identities of the products.

Figure 2 shows the ¹H NMR spectra of the isomeric mixture of bis[3,4,5-tris(dodecyloxy)benzyl] derivatives obtained by gel permeation chromatography. The spectrum can be decom-



Scheme 1. One-pot synthesis of unsymmetrically substituted octaazapentacene derivatives **1** and **2**.

posed according to the magenta fitted spectrum. We have assigned the isomer structures based on the expected position of the NH protons in **2**. Based on the synthesis, the NH protons ought to exist on the second pyrazine ring (counting from the nitrile groups). However, the extension of donor–acceptor

(D–A) interaction over another pyrazine ring ought to further stabilize the molecule although existence of the protons on a terminal pyrazinacene ring (i.e. one that does not have two adjacent fused pyrazine groups) is not favoured.^[19,20] Therefore, the protons reside with highest probability on the third pyrazine ring remote from the nitrile groups. This assignment is supported by an X-ray crystallographic study of a similar compound, which indicates that this shift occurs.^[16] Under this assignment of the isomer structure, **3a**, **3b**, and **3c** exist in a percentage ratio of 37:22:41. Initial N-alkylation is favoured at the third pyrazine ring, due to the aforementioned D–A interaction. Subsequent N-alkylation is subject to an apparent preference for N-alkylation on the adjacent non-terminal pyrazine perhaps due to the steric effects of the bulky dendritic substituent.

The populations of resulting isomers obtained in reaction can be modelled using a two-step reactivity model (see Figure 3a). The fitting procedure yields values of populations for **3a**, **3b** and **3c** isomers $p_{AA} = 0.37$, $p_{BB} = 0.22$ and $p_{AB+BA} = 0.41$, respectively (see Figure 3b). The subscript indicates the order in which the corresponding nitrogens react in the two-step model; ($p_{AA} + p_{BB} + p_{AB+BA} = 1$). The populations deviate from the expected statistical distribution where $p_{AA} / p_{BB} / p_{AB+BA} = 0.25:0.25:0.5$. The basis of the model consists of the two parameters α and β . The probability α corresponds to the intrinsic reactivity of nitrogen A over nitrogen B. $+\beta$ and $-\beta$ correspond

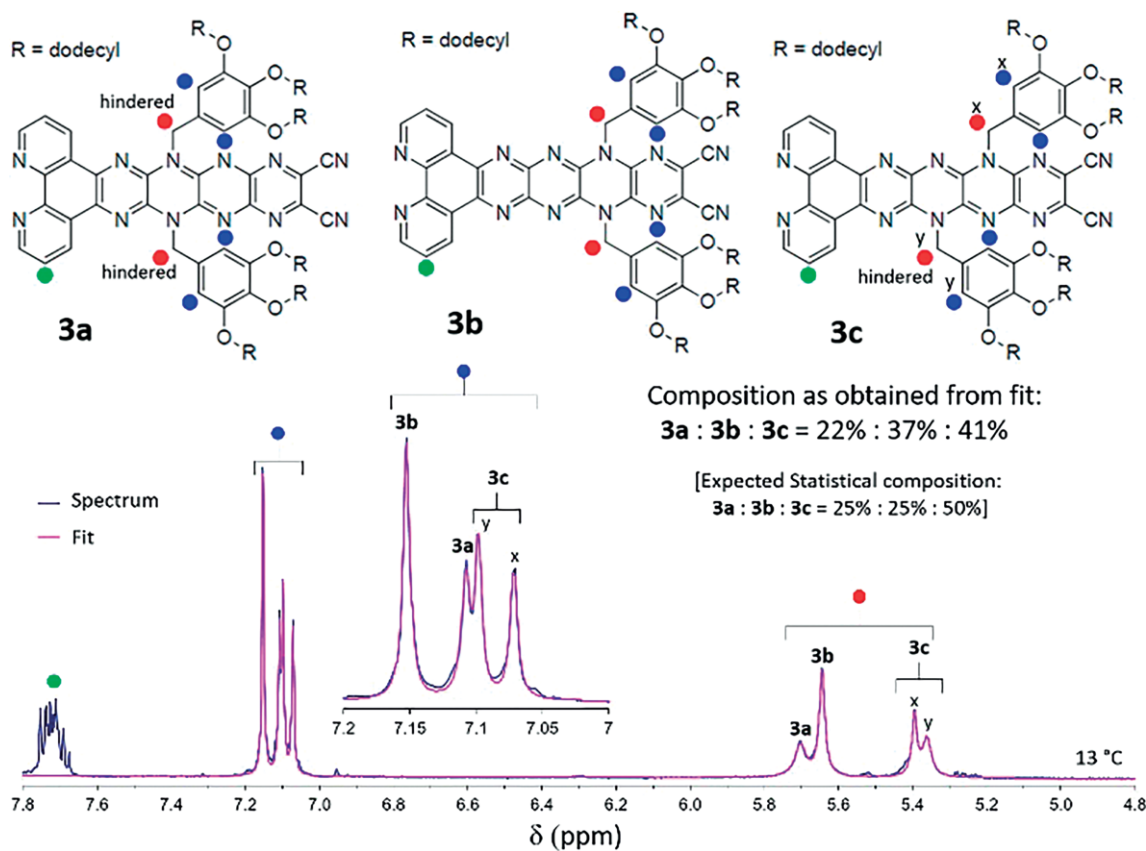


Figure 2. Analysis of the isomer mixture of compound **3** based on ¹H NMR spectroscopy. The fitted spectroscopic data is shown in magenta and is based on the structures **3a–c** at top. Other isomer structures may be present in small quantities but were neglected for this analysis. Peaks in the chemical shift ranges 7.2–7.0 and 5.8–5.3 ppm are due to the N-substituted *ortho* protons and benzylic protons, respectively. Expected percentage statistical composition is **3a:3b:3c = 25 %:25 %:50 %**. R = *n*-C₁₂H₂₅.

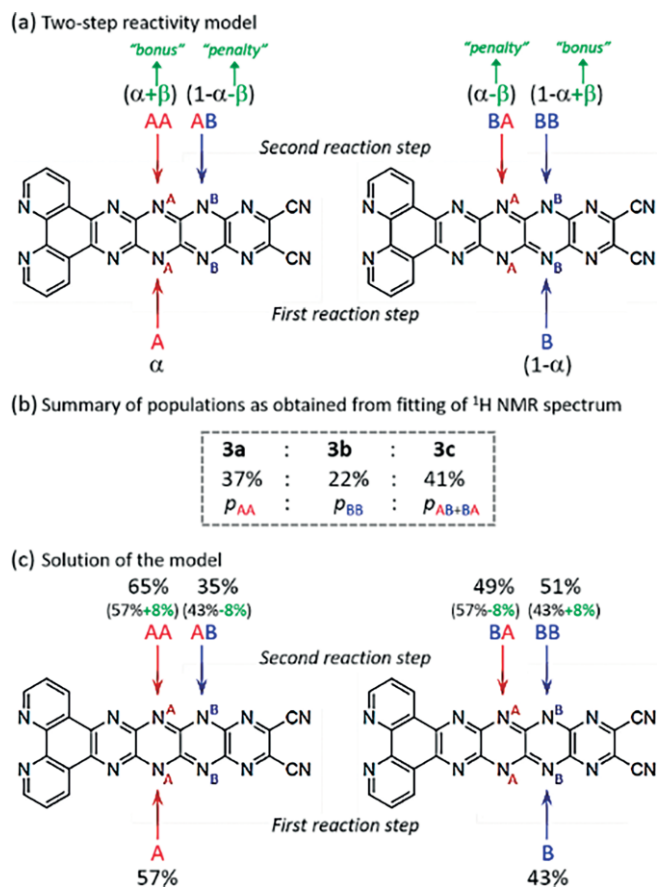


Figure 3. Reactivity towards N-alkylation of the pyrazine rings A (red) and B (blue) in octaazapentacene derivatives. (a) Effect of first N-alkylation step (at "A" or "B") on reactivity for the second step ("AA", "AB", "BA" and "BB"). (b) Populations of isomers based on the fitting of NMR spectrum shown in Figure 2. (c) Solution of the model shown in (a) where percentages given are the yields of the reactions steps based on the final isomer composition.

to probability "bonus" and "penalty" at the second step due to reaction at the same pyrazine ring or the neighboring ring, respectively. The populations can be expressed as:

$$p_{AA} = \alpha(\alpha + \beta) \quad (1a)$$

$$p_{BB} = (1 - \alpha)(1 - \alpha + \beta) \quad (1b)$$

$$p_{AB+BA} = \alpha(1 - \alpha - \beta) + (1 - \alpha)(\alpha - \beta) \quad (1c)$$

Combination of Equation (1a) and Equation (1b) yields cubic equation for α and an expression for β .

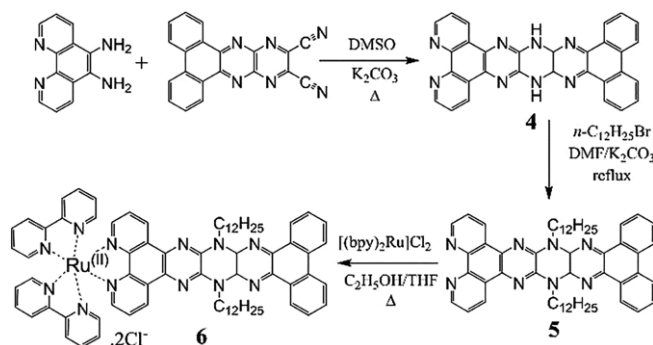
$$2\alpha^3 - 3\alpha^2 + p_{AB+BA}\alpha + p_{AA} = 0 \quad (2a)$$

$$\beta = \frac{p_{AA}}{\alpha} - \alpha \quad (2b)$$

Numerical solution of Equation (2a) with subsequent substitution to Equation (2b) gives $\alpha = 0.57$ and $\beta = 0.08$. This analysis indicates that nitrogens closer to the phenanthroline group are more reactive (57%), which is consistent with the preference of the dihydropyrazine group to be at this position.^[16] Also, values

of β indicate that the second step of reaction is slightly (8%) favoured at the already N-alkylated dihydropyrazine group (see Figure 3c).

Although our attempts to obtain pure examples of N-alkylated **2** have been so far unsuccessful, there remained the question of whether the properties of appropriate pyrazinacene-appended transition metal complexes could be of interest. Therefore, we designed and synthesized compound **4** (Scheme 2), which possesses a phenanthroline unit conjugated with a fluorubine core; a pyrazinacene unit that is known to form only centrally N-alkylated isomers since N-alkylation of terminal pyrazines is negligible in pyrazinacenes. The alkylated compound **5** was treated with *cis*-bis(2,2'-bipyridine)dichlororuthenium(II) complex under literature conditions^[28] yielding **6** containing a classical bipyridine-ruthenium(II) complex. Similar complexes have been intensively studied for DNA intercalation^[22,29] and it is known that replacing fused benzo groups with fused pyrazino units can have a significant effect on the properties of the resulting complexes.^[30]



Scheme 2. Synthesis of compound **4**, **5**, and **6**. The product **4** of the condensation between 1,10-phenanthroline-5,6-diamine and the dinitrile was used as isolated without further purification.

Compound **6** is an orange amorphous powder soluble in common solvents despite the presence of the tetrabenzo-fluorubine core whose large π -electron surface might induce aggregation. Its electronic spectrum (Figure 4a) contains bands assignable to the bpy ligands (300 nm) as well as to the acene unit with a four band structure with λ_{max} at 472 and 503 nm. An assignment of these transitions with regard to ligand-centred, MLCT or a combination of these will be reported in future for these compounds and related derivatives. It is weakly fluorescent with a broad band at 600 nm. An excitation spectrum recorded by holding the emission monochromator at 531 nm and scanning the excitation monochromator revealed peaks at 460 and 492 nm, that largely resembled the spectrum of **6** (see Figure S1). The fluorescence lifetime of **6** in Ar-purged DCB, evaluated using time correlated single photon counting (TCSPC) and excited at 529 nm by nanoLED sources, was found to be 2.11 ns. Upon purging with oxygen, a decrease in lifetime to 1.98 ns was observed (see Figure S2). Compound **6** undergoes two one-electron reversible oxidations at 1.15, 1.51 and three one-electron reversible reductions at -1.10, -1.36 and -1.75 V vs. Ag/AgCl in *o*-dichlorobenzene containing 0.1 M (TBA)ClO₄ [see Figure 4b] some of them involving the pyrazinacene unit.^[16] The measured electrochemical HOMO-LUMO

gap was found to be 2.25 eV, close to that of Ru(bpy)₃ complexes in literature.^[31] The use of acetonitrile as solvent for electrochemical measurements lead to irreversibility of the processes and surface adsorption.

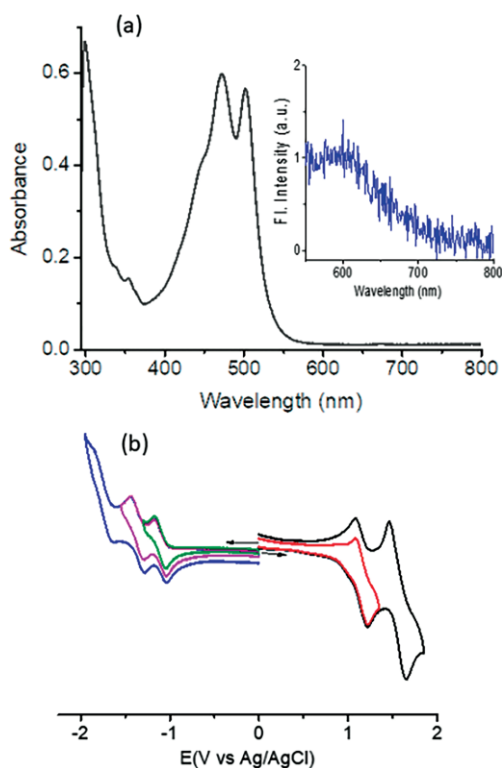


Figure 4. (a) Electronic absorption spectrum of **6** in *o*-dichlorobenzene (figure inset shows the emission spectrum, $\lambda_{\text{ex}} = 503$ nm). (b) Cyclic voltammograms of **6** in dichlorobenzene containing 0.1 M tetrabutylammonium perchlorate.

6 was incorporated into a dye-sensitized cell and the relevant measured data is shown in Figure 5.^[32] The compound was adsorbed on TiO₂ in a typical DSSC configuration with I⁻/I₃⁻ as the mediator. It should be mentioned here that addition of a slurry of TiO₂ into the solution of **6** lead to significant fluorescence quenching, suggesting occurrence of electron injection from excited **6** into the TiO₂ conduction band. The absence of any anchoring groups in **6** leads to its weaker adsorption onto TiO₂, and resulted in a modest overall DSSC performance.^[33] It is possible in this case that the dye is chemisorbed at the TiO₂ surface with the pyrazinacene group of **6** facilitating such an adsorption process. This point will be elaborated on in future work where the role of the pyrazinacene in adsorption will be investigated by introduction of other reactive groups such as carboxyl at different points on the structure. As shown in Figure 5a, average performance metrics of two cells were as follows: open circuit potential = 0.42 V, short circuit current = 0.58 mA/cm², fill factor = 0.45 and $\eta = 0.11$ %. Despite these relatively modest performance metrics, excellent reproducibility of voltage and current switching indicate that **6** is a robust DSSC sensitizer. Figure 5b shows the calculated structures of the highest occupied molecular orbital (HOMO) and lowest unoccupied molecular orbital (LUMO) for compound **6**. These reveal that the HOMO is accommodated largely on the pyrazinacene portion of the molecule while the LUMO lies on the

Ru(bpy)₂ moiety, suggesting their ability to promote directional electron transfer in DSSCs by means of push-pull effect.^[34]

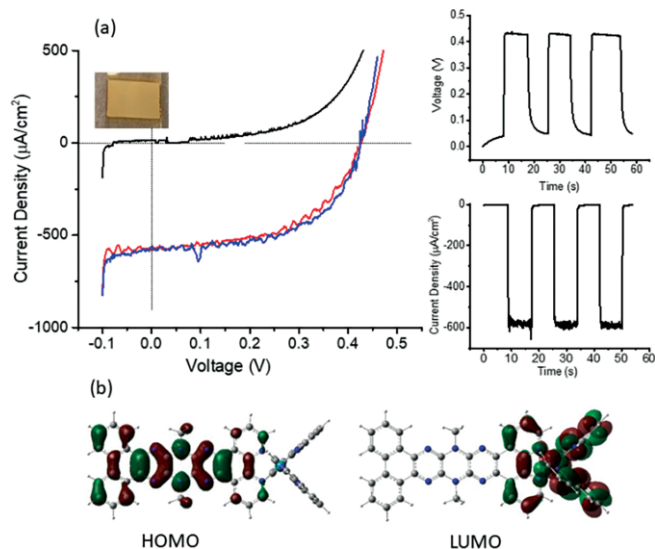


Figure 5. (a) Current density vs. voltage (J - V) curves of DSSC constructed from **6**. Voltage and current switching plots are shown in the right hand panels. (b) Structures of the HOMO and LUMO for **6**.^[35]

The photochemical properties of **6** might be improved by a variety of means that have already been addressed by other workers.^[36–38] In particular, the addition of extended aromatic ligands has been extensively studied for the corresponding Ru^{II} complexes. Those works have given insight into the structure parameters that might affect the materials' performances of the compounds,^[39–41] and the compounds themselves remain highly relevant.^[42,43] Beyond the already well-studied π -extended phenanthroline ligands,^[44–47] the introduction of the pyrazinacene-type ligands to these dyes present some prospects for developing a series of highly fluorescent compounds whose substituents can be easily modified either at (bpy)₂Ru^{II} moiety (as has already been done) or at the pyrazinacene (here a fluorubine) moiety where lateral substitution at nitrogen atoms could be advantageous for tuning the interaction of the complexes with TiO₂. The variation of the N-substituents could also be instrumental in reducing detrimental aggregative processes. NMR spectroscopy of **6** at different concentrations suggests that it tends to aggregate through (probably π - π stacking) interactions at the pyrazinacene unit as indicated by the upfield shift of NMR resonances of protons at those locations (see Figure S21) at higher concentrations. These and other aspects of derivatives of **6** ought to add a valuable extension to what is known about the already reported compounds.

Conclusions

In summary, we report the one-pot and stepwise syntheses of unusual unsymmetrical pyrazinacene derivatives. These novel chromophore compounds that may be adapted to include a transition metal chelating group (as in **2** and **5**) are significant from the point-of-view of their highly N-substituted flat acene-like cores, which suggest their investigation for the relevant ap-

lications including in molecular electronics and dye sensitization. Tautomerization in these systems containing four or more fused pyrazine rings introduces new aspects to the characterization of the N-alkylated compounds but also gives access to conjugation pathways and therefore optical properties not otherwise available by N-alkylative fixing of the isomer form.

Although initial studies of their use in photovoltaic applications reveal that the current compounds are not competitive with the state-of-the-art Grätzel-type dyes (most likely as a result of poor adsorption stemming from the absence of anchoring groups such as carboxyl groups), we believe that the simple synthesis of these derivatives and their structures will allow the exploitation of this new class of compounds despite the intractability of these initially reported materials. We are currently studying the potential benefits of the dihydrooctaazatetracene core based on its adaptable molecular recognition properties, which are available because of potential protic tautomeric processes revealed by the N-alkylation properties of the pyrazinacene congener reported here. Further, the introduction of anchoring groups on the bpy entities for better dye uptake and performance of DSSCs using the present push-pull type Ru dye is currently underway, as is the synthesis of other derivatives based on transformation of the nitrile groups in **2** and **3**-type compounds.

Experimental Section

General: Reagents and solvents were purchased from TCI Chemicals, Aldrich Chemical Co., Wako Chemical Co. or Nacalai Tesque Chemical Co. All reagents were used as received. Preparative thin layer chromatography (PTLC) was performed using Analtech UNIPATE™ PTLC silica plates (20 × 20 cm, 1500 microns, cat. no. Z513040). Gel permeation chromatography separations were performed using Bio-Beads™ S-X1 (tetrahydrofuran as eluent). Stabilizer-free tetrahydrofuran was used for Soxhlet extraction and chromatographic separations. Electronic absorption spectra were obtained using a Shimadzu UV-3600 UV/Vis/NIR spectrophotometer. Fluorescence spectra were similarly obtained using a JASCO FP-6500 spectrofluorometer. ¹H and ¹³C nuclear magnetic resonance (NMR) spectra were recorded using a JEOL AL300BX NMR spectrometer operating at 300 MHz for ¹H and 75 MHz for ¹³C. Infrared absorption spectra were obtained using a Thermo-Nicolet Nexus 670 FT-IR spectrometer from samples prepared as KBr pellets or by ATR using a Specac MKII Golden Gate Single Reflection ATR System with diamond crystal, (angle of incidence 45°) for neat solid samples. LDI-TOF-MS and MALDI-TOF-MS spectra were measured using a Shimadzu-Kratos Axima CR+ spectrometer. High resolution MALDI-TOF mass spectra were measured using an LTQ Orbitrap XL system using 2,5-dihydroxybenzoic acid as matrix. ESI-HR-MS spectra were measured using a Thermo Scientific Exactive Plus Orbitrap Mass Spectrometer. 1,10-Phenanthroline-5,6-dione,^[48] 1,10-phenanthroline-5,6-diamine^[49] and dibenzo[*f,h*]pyrazino[2,3-*b*]quinoxaline-11,12-dicarbonitrile^[50] were prepared according to the literature procedures.

Scanning Tunneling Microscopy: 5,12-Dihydro-2,3-diphenyl-1,4,6,7,10,11,12-octaazatetraacene-8,9-dicarbonitrile^[16] was dried in vacuo before use in STM experiments. Atomically clean single crystals of Cu(111) used as substrates were prepared by Ar⁺ sputtering and annealing (700 K) cycles. Sub-monolayer coverage of the substrate was obtained by sublimation for 10 min at 320 °C from a

Knudsen cell to the metal substrate over an intervening distance of 30 cm in ultra-high vacuum (1 × 10⁻⁸ Pa), followed by characterization using STM at room temperature.

6,13-Dihydrodibenzo[*a,c*]-5,6,7,8,11,12,13,14-octaazapentacene-9,10-dicarbonitrile (1): Phenanthrene-9,10-dione (1.5 g, 7.2 × 10⁻³ mol), 5,6-diamino-2,3-dicyanopyrazine (2.7 g, 1.69 × 10⁻² mol, 2.3 equiv.) and sodium carbonate (2.31 g, 3 equiv. based on dione) placed in a 100 mL round-bottomed flask and dimethylsulfoxide (50 mL) was poured in. The resulting mixture was stirred at 140 °C for 24 h then cooled. The reaction mixture was poured into a mixture of acetic acid (150 mL) in methanol (700 mL) and the resulting precipitate was filtered. The crude material was triturated with tetrahydrofuran (50 mL) and the mixture was filtered. The filtrand was subjected to column chromatography on neutral alumina eluting first with neat tetrahydrofuran (to remove unreacted phenanthrene-9,10-dione) then with THF/5 % methanol/0.2 % acetic acid. The product elutes as a purple band exiting the column as a bright orange solution, which gives a brick red solid when evaporated. This method allowed isolation of ≈ 180 mg of product with the remaining crude product as a dark red powder. ¹H NMR (300 MHz, CF₃COOD): 8.18 (dd, ³J = 7.8, ³J = 7.2 Hz, 2 H), 8.32 (dd, ³J = 7.8, ³J = 7.2 Hz, 2 H), 9.03 (d, ³J = 7.8 Hz, 2 H), 9.34 (d, ³J = 7.8 Hz, 2 H) ppm. FTIR (KBr pellet): $\tilde{\nu}$ = 3217.2 [m, br., NH (str.)]; 3130.9 [w, C–H (str.)]; 2236.7 [m, C≡N (str.)]; 1605.8 (w), 1581.7 (m), 1574.9 (m), 1555.1 (w) [C=C (str.), C=N (str.)]; 1516.7 (m); 1492.3 (w); 1476.3 [s, NH (def.)]; 1464.9 (w); 1456.8 (w); 1430.8 (s), 1401.6 (s) [C–H (def.)]; 1365.0 (m); 1323.3 (m); 1278.5 (m); 1222.7 [s, C–N (str.)]; 1168.8 (w); 1132.6 (w); 1116.2 (m); 1086.1 (w); 1043.1 (m); 959.4 (w); 858.9 (w); 848.2 (w) cm⁻¹. MALDI-TOF-MS (dithranol; negative ion mode): calcd. for C₂₄H₇N₁₀ *m/z* = 435.09, found 435.31 [(M – H)⁻]; M is in situ oxidized acene.

6,13-Dihydrodipyrido[3,2-*a*:2',3'-*c*]-5,6,7,8,11,12,13,14-octaazapentacene-9,10-dicarbonitrile (2): A 100 mL pear-shaped flask was loaded with a magnetic stirrer bar, phenanthroline-5,6-dione (1.00 g, 4.76 mmol, 1.00 equiv.), 5,6-diamino-2,3-dicyanopyrazine (2.00 g, 12.5 mmol, 2.63 equiv.), anhydrous sodium carbonate (1.00 g, 9.43 mmol, 1.98 equiv.), and dimethyl sulfoxide (50 mL). The flask was then equipped with a condenser and it was heated in an oil bath at 140 °C for 16 h. The reaction mixture was poured into a mixture of acetic acid (150 mL) in methanol (700 mL) and the resulting precipitate was filtered. The solid was washed with THF three times (total volume 150 mL to remove any excess 5,6-diamino-2,3-dicyanopyrazine) and while still wet was transferred into a 500 mL round-bottom flask containing acetic acid (300 mL) and THF (50 mL). Resulting suspension in acetic acid was refluxed for 1 h. The suspension was subsequently filtered through a Büchner funnel while still hot and the solid obtained was washed several times with THF. The product was finally dried under vacuum (50 °C) to yield the compound in the form of a black solid with a green metallic luster (1.03 g, 2.06 mmol, 43 %). The purity of this crude product was ≈ 90 % according to NMR analyses. However, the compound could be further purified by performing Soxhlet extraction using tetrahydrofuran/acetic acid (2 % v/v) and samples of the latter were used for analyses. The reaction can also be performed using a lower quantity of sodium carbonate at the cost of a somewhat lower yield. However, using more than 2 equiv. of base promotes formation of an unidentified inseparable by-product. ¹H NMR (300 MHz, [D₆]DMSO + few drops CF₃COOD): δ = 8.87 (dd, ³J = 8.1 Hz, ³J = 4.8 Hz, 2 H), 9.86 (d, ³J = 4.5 Hz, 2 H), 10.05 (d, ³J = 8.1 Hz, 2 H) ppm. ¹³C NMR (75 MHz, [D₆]DMSO + few drops CF₃COOD): δ = 114.20, 126.63, 127.04, 127.75, 135.24, 137.11, 138.64, 143.53, 145.84, 148.09, 149.14 ppm. FTIR (KBr pellet): $\tilde{\nu}$ = 3300–3000 [w, br., NH (str.)]; 2920.5, 2851.5 [w, C–H (str.) from trace acetic acid]; 2229.3

[m, C=N (str.); 1604.4 [m, C=C (str.); 1571.3 [m, C=N (str.); 1541.9 (w); 1513.9 (m); 1468.4 (m); 1378.9 (s); 1321.4 (w); 1255.6 (m), 1228.4 (m) [C-N (str.); 1177.6 (w); 1124.3 (w); 1083.3 (w); 1035.9 (w); 971.3 (w); 854.8 (w); 819.2 (w) cm⁻¹. MALDI-TOF-HR-MS (DHB): calcd. for C₂₂H₉N₁₂ m/z = 441.1073, found 441.1070 [(M + H)⁺].

6(7), 13(14)-Bis[3,4,5-tris(*n*-dodecyloxy)benzyl]-dipyrido[3,2-*a*:2',3'-*c*]-5,6,7,8,11,12,13, 14-octaazapentacene-9,10-dicarbonitrile (3): The crude product from the synthesis of **2** (100 mg) was suspended in DMF (10 mL) and 3,4,5-tris(dodecyloxy)benzyl chloride (400 mg, 2.5 equiv.) and potassium carbonate (100 mg) were added. The resulting mixture was heated at 120 °C overnight. The reaction mixture was cooled to room temperature then poured into water (50 mL) followed by partitioning with dichloromethane (50 mL). The organic fraction was collected dried with anhydrous sodium sulfate and the solvents removed under reduced pressure yielding a dark green solid, which was then applied to a column of Biobeads SX-1 prepared in tetrahydrofuran. Elution with tetrahydrofuran yielded two fractions. The high molecular weight fraction was collected and analyzed revealing a mixture of doubly-*N*-substituted isomers (see main manuscript). A minor low molecular weight fraction assigned as the mono-[3,4,5-tris(dodecyloxy)benzyl]-*N*-substituted compound was discarded. Yield of **3**: 230 mg (59 %). Isomers of the doubly-*N*-substituted compound could not be separated despite attempts using column chromatography and preparative thin layer chromatography. ¹H NMR (300 MHz, [D₂]THF): δ = 0.78 (m, 18 H, terminal-CH₃), 1.17 [m, 108 H, -(CH₂)₉-], 1.33 [m, 12 H, -(CH₂)₂-], 1.54 [m, 12 H, -(CH₂)₂-], 3.73 (m, 8 H, 3,5-OCH₂), 3.88 (m, 4 H, 4-OCH₂), 5.25–5.75 (4 singl., 4 H, benzylic CH₂), 7.05–7.2 (4 singl., 4 H, benzyl *ortho*-H), 7.65–7.76 (m, 2 H, phenanthroline *meta*-H), 9.05–9.15 (m, 2 H, phenanthroline *ortho*-H), 9.25–9.45 (m, 2 H, phenanthroline *para*-H) ppm. FTIR (KBr pellet): ν̄ = 2923.3, 2853.2 [s, C-H (str.); 1590.6 [m, C=C (str.); 1541.3, 1518.2, 1497.8 [s, C=C (str.), C=N (str.); 1459.1 [s, C-H (def.); 1430.9 [s, C-H (def.); 1399.1 [w); 1377.1 [s, C-H (def.); 1331.3 (m); 1280–1220 [s, C-N (str.); 1173.4 (w); 1114.2 [s, C-O (str.)] cm⁻¹. MALDI-TOF-HR-MS (DHB): calcd. for C₁₀₈H₁₆₅N₁₂O₆ m/z = 1726.298, found 1726.297 [(M + H)⁺].

6,13-Dihydrodipyrido[3,2-*a*:2',3'-*c*]dibenzo[*l,n*]-5,6,7,12,13,14-hexa-azapentacene (4): Dibenzo[*f,h*]pyrazino[2,3-*b*]quinoxaline-11,12-dicarbonitrile (200 mg, 6 × 10⁻⁴ mol) and 1,10-phenanthroline-5,6-diamine (140 mg, 6.7 × 10⁻⁴ mol) were dissolved in dimethylsulfoxide (10 mL) then potassium carbonate (170 mg, 2 equiv.) was added. The resulting mixture was heated at 110 °C overnight under a dry nitrogen atmosphere. The resulting light orange solid was filtered and washed with methanol. This material was used in the next step without further purification. Yield (crude): 245 mg (84 %). This compound was too insoluble for NMR analysis. MALDI-TOF-MS (DHB): calcd. for C₃₀H₁₄N₈ m/z = 486.1341, found 486.1592; [(M - 2H)⁺]: (due to in situ dehydrogenation).

6,13-Bis(*n*-dodecyl)-dipyrido[3,2-*a*:2',3'-*c*]dibenzo[*l,n*]-5,6,7,12,13, 14-hexaazapentacene (5): Compound **4** (100 mg, 1.21 × 10⁻⁴ mol) and potassium carbonate (50 mg, 3 equiv.) were suspended in *N,N*-dimethylformamide (10 mL) and *n*-1-dodecyl bromide (100 mg) was added. The resulting mixture was heated at reflux overnight under a dry nitrogen atmosphere. The reaction mixture was then cooled and the orange precipitate filtered then washed with methanol followed by drying in air at the pump. Yield: (95 %). ¹H NMR (300 MHz, CDCl₃): δ = 0.86 (t, ³J = 7.2, Hz, 6 H, CH₃) 1.16–1.4 [m, 36 H, (CH₂)_n], 1.48 (m, 4 H, -*N*-CH₂CH₂CH₂-), 1.84 (p, 4 H, -*N*-CH₂CH₂-), 4.26 (t, *J* = 7.4 Hz, 4 H, -*N*-CH₂-), 7.33 (m, 2 H), 7.50 (m, 2 H), 7.60 (dd, *J* = 8.1, 4.3 Hz, 2 H), 8.08 (d, ³J = 8.4 Hz, 2 H), 8.69 (d, ³J = 8.1 Hz, 2 H), 8.77 (dd, ³J = 8.2, ⁴J = 1.1 Hz, 2 H), 9.14

(dd, ³J = 4.2, ⁴J = 1.7 Hz, 2 H), ppm. ¹³C NMR (75 MHz, CDCl₃): δ = 14.11, 22.69, 25.83, 27.36, 29.80–29.20, 31.96, 41.11, 122.45, 123.09, 123.92, 126.50, 127.07, 129.22, 129.87, 131.66, 132.19, 133.44, 140.75, 141.75, 145.94, 150.09 ppm. FTIR (KBr pellet): ν̄ = 3063.5, 3036.3, 3014.7 [w, aromatic C-H (str.); 2955.4, 2920.2, 2851.3 [s, aliphatic C-H (str.); 1601.6, 1588.7, 1579.7, 1565.2 [all w, C=C (str.), C=N (str.); 1514.4 [m, C=N (str.); 1488–1420 [s, C-H (def.); 1404.9 (w); 1389.0 (w); 1372.6 [s, C-H (def.); 1285.6, 1277.2 [s, C-N (str.); 1222.7 [s, C-N (str.); 1173.2 (w); 11538.7 (w); 1153.5 (w); 1125.4 (w), 1084.9 (w); 1045.1 (w); 1039.6 (w); 1027.3 (w); 996.3 (w); 976.0 (w); 944.0 (w); 926.6 (w); 902.2 (w); 893.5 (w); 821.6 (w); 809.7 (w) cm⁻¹. MALDI-TOFHR-MS (DHB): calcd. for C₅₄H₆₅N₈ m/z = 824.525, found 824.540; [(M + H)⁺].

Bis(2,2'-bipyridine)[6,13-bis(*n*-dodecyl)-dipyrido(3,2-*a*:2',3'-*c*)dibenzo[*l,n*]-5,6,7,12,13,14-hexaazapentacene]ruthenium(II) Chloride (6): Compound **5** (70 mg, 8.5 × 10⁻⁵ mol) was dissolved in tetrahydrofuran (10 mL) and added dropwise to a solution of dichlorobis(2,2'-bipyridine)ruthenium(II) in ethanol (10 mL) and the mixture heated at reflux with stirring overnight under a nitrogen atmosphere. The reaction mixture was then cooled. Solvents were removed under reduced pressure and the resulting solid dissolved in the minimum of tetrahydrofuran, applied to a column of Biobeads SX-1 prepared using THF, followed by elution with THF. The dark orange band eluting first was collected and the solvents removed under reduced pressure. The resulting solid was suspended in a small quantity of methanol and filtered yielding **6** as a bright orange powder. Yield: 80 mg (71 %). ¹H NMR (300 MHz, [D₆]DMSO): δ = 0.78 (t, ³J = 7.2, Hz, 6 H), 1.3–1.1 (m, 28 H), 1.46 (m, 4 H), 1.55 (m, 4 H), 1.85 (m, 4 H), 4.30 (br. t, 4 H), 7.30 (t, ³J = 6.9 Hz, 2 H), 7.46 (t, ³J = 6.3 Hz, 2 H), 7.65–7.50 (m, 4 H), 7.79 (d, ³J = 5.3 Hz, 2 H), 7.90 (m, 4 H), 8.10 (d, ³J = 4.2 Hz, 2 H), 8.21–8.15 (m, 4 H), 8.25 (t, ³J = 7.9 Hz, 2 H), 8.77 (d, ³J = 8.3 Hz, 2 H), 8.84 (d, ³J = 8.1 Hz, 2 H), 8.91 (t, ³J = 8.7 Hz, 4 H) ppm. ¹³C NMR (75 MHz, [D₆]DMSO): δ = 13.59, 21.74, 24.82, 26.25, 28.35, 28.51, 28.70, 28.75, 30.97, 122.39, 123.19, 124.37, 124.43, 126.32, 127.04, 127.51, 127.68, 127.78, 128.22, 129.09, 131.43, 131.53, 132.64, 137.78, 137.86, 139.33, 140.71, 142.69, 146.04, 151.28, 151.36, 156.56, 156.71 ppm. FTIR (KBr pellet): ν̄ = 3127.2, 3068.6, 3025.2 [all w, aromatic C-H (str.); 2922.8, 2851.9 [s, alkyl C-H (str.)] 1971.4 (m), 1627.7, 1603.4, 1588.4, 1576.0 [all w, C=C (str.), C=N (str.); 1517.7 (m); 1482.0 [s, C-H (def.); 1464.9 (w); 1452.7 [s, C-H (def.); 1409.7 (w); 1372.7 [s, C-H (def.); 1345.1 (w); 1326.9 (w); 1286.1 [m, C-N (str.); 1223.8 [m, C-N (str.); 1157.9 (w); 1125.7 (w); 1090.4 (w); 1069.2 (w); 1045.4 (w); 1025.7 (w); 957.9 (w); 906.8 (w); 813.5 (w) cm⁻¹. ESI-HR-MS: calcd. for C₇₄H₈₀N₁₂Ru m/z = 619.2836, found 619.2828 [(M - 2(Cl)⁻)²⁺].

Acknowledgments

This work was financially supported by the National Science Foundation (Grant No. 1401188 to F. D.). The study was partially supported by the Grant Agency of Charles University (project GA UK, No. 718214), JSPS KAKENHI Grant No. JP15K13684 (Linear acene proton conductors for molecular electronics), JSPS KAKENHI Grant No. JP16H06518 (Coordination asymmetry), and CREST JST, Japan (Grant No. JPMJCR1665). This work was also partly supported by World Premier International Research Center Initiative (WPI Initiative), MEXT, Japan.

Keywords: Heteroacene · Pyrazinacene · Tautomerization · Phenanthroline · Dye-sensitized solar cells

- [1] U. H. F. Bunz, *Acc. Chem. Res.* **2015**, *48*, 1676–1686.
- [2] U. H. F. Bunz, J. U. Engelhart, *Chem. Eur. J.* **2016**, *22*, 4680–4689.
- [3] G. J. Richards, J. P. Hill, T. Mori, K. Ariga, *Org. Biomol. Chem.* **2011**, *9*, 5005–5017.
- [4] A. H. Endres, M. Schaffroth, F. Paulus, H. Reiss, H. Wadepohl, F. Rominger, R. Kraemer, U. H. F. Bunz, *J. Am. Chem. Soc.* **2016**, *138*, 1792–1795.
- [5] P.-Y. Gu, Z. Wang, G. Liu, H. Yao, Z. Wang, Y. Li, J. Zhu, S. Li, Q. Zhang, *Chem. Mater.* **2017**, *29*, 4172–4175.
- [6] L. V. Brownell, K. Jang, K. A. Robins, I. C. Tran, C. Heske, D.-C. Lee, *Phys. Chem. Chem. Phys.* **2013**, *15*, 5967–5974.
- [7] D. M. Gampe, S. Schramm, S. Ziemann, M. Westerhausen, H. Görls, P. Naumov, R. Beckert, *J. Org. Chem.* **2017**, *82*, 6153–6162.
- [8] D. Cortizo-Lacalle, C. Gozalvez, M. Olano, X. Sun, M. Melle-Franco, L. E. Hueso, A. Mateo-Alonso, *Org. Lett.* **2015**, *17*, 5902–5905.
- [9] Z. He, R. Mao, D. Liu, Q. Miao, *Org. Lett.* **2012**, *14*, 4190–4193.
- [10] Q. Tang, D. Zhang, S. Wang, N. Ke, J. Xu, J. C. Yu, Q. Miao, *Chem. Mater.* **2009**, *21*, 1400–1405.
- [11] J. Xiao, H. M. Duong, Y. Liu, W. Shi, L. Ji, G. Li, S. Li, X.-W. Liu, J. Ma, F. Wudl, Q. Zhang, *Angew. Chem. Int. Ed.* **2012**, *51*, 6094–6098; *Angew. Chem.* **2012**, *124*, 6198.
- [12] D. M. Gampe, M. Kaufmann, J. Dörthe, T. Sachse, M. Presselt, R. Beckert, H. Görls, *Chem. Eur. J.* **2015**, *21*, 7571–7581.
- [13] J. E. Anthony, *Chem. Rev.* **2006**, *106*, 5028–5048.
- [14] M. Bendikov, F. Wudl, D. F. Perepichka, *Chem. Rev.* **2004**, *104*, 4891–4945.
- [15] Z. Sun, Z. Zeng, J. Wu, *Acc. Chem. Res.* **2014**, *47*, 2582–2591.
- [16] G. J. Richards, J. P. Hill, N. K. Subbaiyan, F. D'Souza, M. R. J. Elsegood, S. J. Teat, T. Mori, K. Ariga, *J. Org. Chem.* **2009**, *74*, 8914–8923.
- [17] F. Stöckner, R. Beckert, D. Gleich, E. Birckner, W. Günther, H. Görls, G. Vaughan, *Eur. J. Org. Chem.* **2007**, *2007*, 1237–1243.
- [18] B. D. Lindner, J. U. Engelhart, O. Tverskoy, A. L. Appleton, F. Rominger, A. Peters, H.-J. Himmel, U. H. F. Bunz, *Angew. Chem. Int. Ed.* **2011**, *50*, 8588–8591; *Angew. Chem.* **2011**, *123*, 8747.
- [19] R. Scipioni, M. Boero, G. J. Richards, J. P. Hill, T. Ohno, T. Mori, K. Ariga, *J. Chem. Theory Comput.* **2010**, *6*, 517–525.
- [20] R. Scipioni, J. P. Hill, G. J. Richards, M. Boero, T. Mori, K. Ariga, T. Ohno, *Phys. Chem. Chem. Phys.* **2011**, *13*, 2145–2150.
- [21] J. Fleischhauer, S. Zahn, R. Beckert, U.-W. Grummt, E. Birckner, H. Görls, *Chem. Eur. J.* **2012**, *18*, 4549–4557.
- [22] H.-K. Liu, P. J. Sadler, *Acc. Chem. Res.* **2011**, *44*, 349–359.
- [23] Y. Zhang, M. Schulz, M. Waechtler, M. Karnahl, B. Dietzek, *Coord. Chem. Rev.* **2018**, *356*, 127–146.
- [24] G. J. Richards, J. P. Hill, K. Okamoto, A. Shundo, M. Akada, M. R. J. Elsegood, T. Mori, K. Ariga, *Langmuir* **2009**, *25*, 8408–8413.
- [25] G. J. Richards, J. P. Hill, J. Labuta, Y. Wakayama, M. Akada, K. Ariga, *Phys. Chem. Chem. Phys.* **2011**, *13*, 4868–4876.
- [26] G. J. Richards, S. Ishihara, J. Labuta, D. Miklik, T. Mori, S. Yamada, K. Ariga, J. P. Hill, *J. Mater. Chem. C* **2016**, *4*, 11514–11523.
- [27] J. Bolger, A. Gourdon, E. Ishow, J.-P. Launay, *Inorg. Chem.* **1996**, *35*, 2937–2944.
- [28] Y. Liu, R. Hammit, D. A. Lutterman, L. E. Joyce, R. P. Thummel, C. Turro, *Inorg. Chem.* **2009**, *48*, 375–385.
- [29] L. Troian-Gautier, C. Moucheron, *Molecules* **2014**, *19*, 5028–5087.
- [30] Y. Sun, S. N. Collins, L. E. Joyce, C. Turro, *Inorg. Chem.* **2010**, *49*, 4257–4262.
- [31] A. Juris, B. Balzani, F. Barigelletti, S. Campagna, P. Belser, A. V. Zelewsky, *Coord. Chem. Rev.* **1988**, *84*, 85–277.
- [32] For experimental procedure and instrumentation, please see S. Yellappa, W. A. Webre, H. B. Gobeze, A. Middleton, C. B. KC, F. D'Souza, *ChemPlus-Chem* **2017**, *82*, 896–903.
- [33] M. Bräutigam, J. Kubel, M. Schulz, J. G. Vos, B. Dietzek, *Phys. Chem. Chem. Phys.* **2015**, *17*, 7823–7830.
- [34] Y. Hu, S. Yellappa, M. B. Thomas, R. G. W. Jinadasa, A. Matus, M. Shulman, F. D'Souza, H. Wang, *Chem. Asian J.* **2017**, *12*, 2749–2762.
- [35] M. J. Frisch, G. W. Trucks, H. B. Schlegel, G. E. Scuseria, M. A. Robb, J. R. Cheeseman, G. Scalmani, V. Barone, B. Mennucci, G. A. Petersson, H. Nakatsuji, M. Caricato, X. Li, H. P. Hratchian, A. F. Izmaylov, J. Bloino, G. Zheng, J. L. Sonnenberg, M. Hada, M. Ehara, K. Toyota, R. Fukuda, J. Hasegawa, M. Ishida, T. Nakajima, Y. Honda, O. Kitao, H. Nakai, T. Vreven, J. A. Montgomery Jr., J. E. Peralta, F. Ogliaro, M. Bearpark, J. J. Heyd, E. Brothers, K. N. Kudin, V. N. Staroverov, R. Kobayashi, J. Normand, K. Raghavachari, A. Rendell, J. C. Burant, S. S. Iyengar, J. Tomasi, M. Cossi, N. Rega, J. M. Millam, M. Klene, J. E. Knox, J. B. Cross, V. Bakken, C. Adamo, J. Jaramillo, R. Gomperts, R. E. Stratmann, O. Yazyev, A. J. Austin, R. Cammi, C. Pomelli, J. W. Ochterski, R. L. Martin, K. Morokuma, V. G. Zakrzewski, G. A. Voth, P. Salvador, J. J. Dannenberg, S. Dapprich, A. D. Daniels, Ö. Farkas, J. B. Foresman, J. V. Ortiz, J. Cioslowski, D. J. Fox, T. Keith, M. A. Al-Laham, C. Y. Peng, A. Nanayakkara, C. Gonzalez, M. Challacombe, P. M. W. Gill, B. G. Johnson, W. Chen, M. W. Wong, J. L. Andres, M. Head-Gordon, E. S. Replogle, J. A. Pople, *Gaussian 09*, Rev. B.01, Gaussian Inc., Pittsburgh PA, **2009**.
- [36] L. Spiccia, G. B. Deacon, C. M. Kepert, *Coord. Chem. Rev.* **2004**, *248*, 1329–1341.
- [37] A. Stumper, T. D. Pilz, M. Schaub, H. Görls, D. Sorsche, K. Peuntiger, D. Guldi, S. Rau, *Eur. J. Inorg. Chem.* **2017**, *2017*, 3799–3810.
- [38] J. M. Aslan, D. J. Boston, F. M. MacDonnell, *Chem. Eur. J.* **2015**, *21*, 17314–17323.
- [39] D. Sorsche, M. Schaub, F. W. Heinemann, J. Habermehl, S. Kuhri, D. Guldi, J. Guthmuller, S. Rau, *Dalton Trans.* **2016**, *45*, 12846–12853.
- [40] M. B. Majewski, N. R. de Tacconi, F. M. MacDonnell, M. O. Wolf, *Chem. Eur. J.* **2013**, *19*, 8331–8341.
- [41] J. Schindler, Y. Zhang, P. Traber, J.-F. Lefebvre, S. Kupfer, M. Demeunynck, S. Graefe, M. Kerlidou-Chavarot, B. Dietzek, *J. Phys. Chem. C* **2018**, *122*, 83–95.
- [42] B. Pashaei, H. Shahroosvand, M. Graetzel, M. K. Nazeeruddin, *Chem. Rev.* **2016**, *116*, 9485–9564.
- [43] B. Happ, A. Winter, M. D. Hager, U. S. Schubert, *Chem. Soc. Rev.* **2012**, *41*, 2222–2255.
- [44] S. Tschierlei, B. Dietzek, M. Karnahl, S. Rau, F. M. MacDonnell, M. Schmitt, J. Popp, *J. Raman Spectrosc.* **2008**, *39*, 557–559.
- [45] C. Chiorboli, M. A. J. Rogers, F. Scandola, *J. Am. Chem. Soc.* **2003**, *125*, 483–491.
- [46] C. Kuhnt, M. Karnahl, S. Rau, M. Schmitt, B. Dietzek, J. Popp, *Chem. Phys. Lett.* **2011**, *516*, 45–50.
- [47] S. Singh, N. R. de Tacconi, N. R. G. Diaz, R. O. Lezna, J. Munoz-Zuniga, K. Abayan, F. M. MacDonnell, *Inorg. Chem.* **2011**, *50*, 9318–9328.
- [48] W. Paw, R. Eisenberg, *Inorg. Chem.* **1997**, *36*, 2287–2293.
- [49] S. Bodige, F. M. MacDonnell, *Tetrahedron Lett.* **1997**, *38*, 8159–8160.
- [50] J. Nishida Naraso, S. Murai, E. Fujiwara, H. Tada, M. Tomura, Y. Yamashita, *Org. Lett.* **2004**, *6*, 2007–2010.

Received: March 1, 2018

Eur. J. Inorg. Chem. ISSN 1099–0682

<https://doi.org/10.1002/ejic.201800283>

SUPPORTING INFORMATION

Title: Phenanthroline-Fused Pyrazinacenes: One-Pot Synthesis, Tautomerization and a Ru^{II}(2,2'-bpy)₂ Derivative

Author(s): Pavel Švec, Whitney A. Webre, Gary J. Richards,* Jan Labuta, Yutaka Wakayama, David Miklík, Paul A. Karr, Toshiyuki Mori, Katsuhiko Ariga, Francis D'Souza,* and Jonathan P. Hill*

Contents

1) Excitation spectrum and fluorescence lifetime data	S3
2) 6,13-Dihydrodibenzo[a,c]-5,6,7,8,11,12,13,14-octaazapentacene-9,10-dicarbonitrile (1)	
¹ H NMR spectrum (Region of aromatic resonances).....	S4
MALDI-TOF-MS	S5
3) 6,13-Dihydrodipyrido[3,2-a:2',3'-c]-5,6,7,8,11,12,13,14-octaazapentacene-9,10-dicarbonitrile (2)	
¹ H NMR spectrum	S6
¹³ C NMR spectrum	S7
HR-MS (MALDI-TOF)	S8
4) 6(7),13(14)-Bis[3,4,5-tris(<i>n</i> -dodecyloxy)benzyl]-dipyrido[3,2-a:2',3'-c]-5,6,7,8,11,12,13,14-octaazapentacene-9,10-dicarbonitrile (3)	
¹ H NMR spectrum	S9
HR-MS (MALDI-TOF)	S10
5) 6,13-Dihydrodipyrido[3,2-a:2',3'-c]-dibenzo[l,n]-5,6,7,12,13,14-hexaazapentacene, (4)	
HR-MS (MALDI-TOF)	S11
6) 6,13-Bis(<i>n</i> -dodecyl)-dipyrido[3,2-a:2',3'-c]-dibenzo[l,m]-5,6,7,8,11,12,13,14-octaazapentacene (5)	
¹ H NMR spectrum	S12
¹³ C NMR spectrum	S13
HR-MS (MALDI-TOF)	S14
7) Bis(2,2'-bipyridine)(6,13-bis(<i>n</i> -dodecyl)-dipyrido[3,2-a:2',3'-c]-dibenzo[l,n]-5,6,7,12,13,14-hexaazapentacene)ruthenium(II) chloride (6)	
¹ H NMR spectrum	S15
¹ H- ¹ H COSY spectrum	S16,S17
¹³ C NMR spectrum	S18,S19
HR-MS (ESI-Orbitrap)	S20
8) ¹ H NMR spectra of 6 at different concentrations in acetonitrile- <i>d</i> ₃	S21

1) Excitation spectrum and fluorescence lifetime data

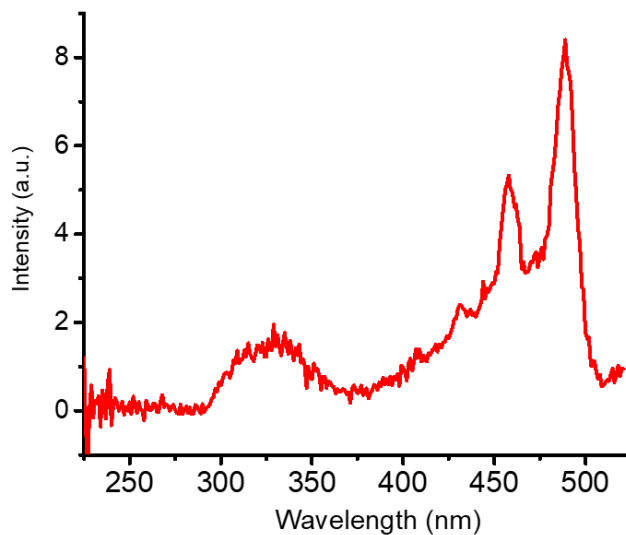


Figure S1. Excitation spectrum of **6** recorded by holding the emission monochromator at 531 nm and scanning the excitation monochromator. The spectrum resembles the electronic absorption spectrum of **6**.

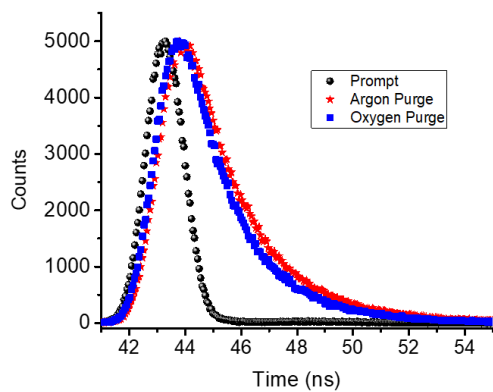


Figure S2. Time correlated single photon counting (TCSPC) after excitation at 529 nm using a nanoLED source used to evaluate the fluorescence lifetime of **6**.

2) 6,13-Dihydrodibenzo[a,c]-5,6,7,8,11,12,13,14-octaazapentacene-9,10-dicarbonitrile (**1**)

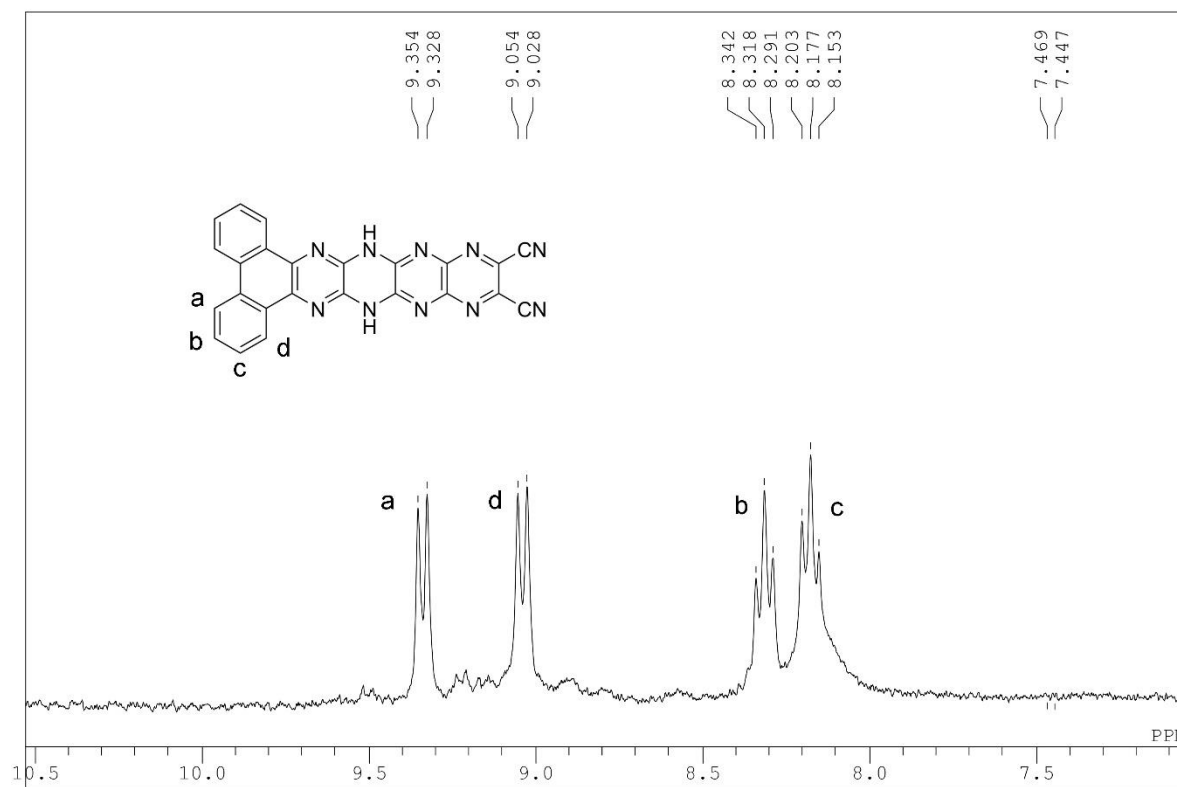


Figure S3. ¹H NMR spectrum of **1** in trifluoroacetic acid-*d*.

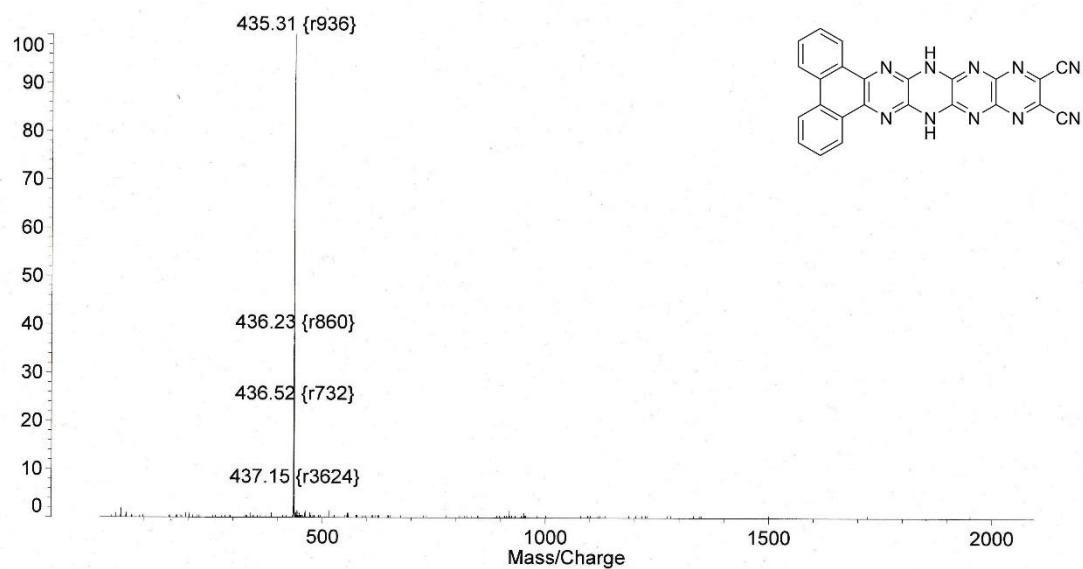


Figure S4. MALDI-TOF-MS of **1** with dithranol as matrix. Molecular ion is due to dehydrogenated product, dibenzo[a,c]-5,6,7,8,11,12,13,14-octaazapentacene-9,10-dicarbonitrile.

3) 6,13-Dihydrodipyrido[3,2-a:2',3'-c]-5,6,7,8,11,12,13,14-octaazapentacene-9,10-dicarbonitrile (**2**)

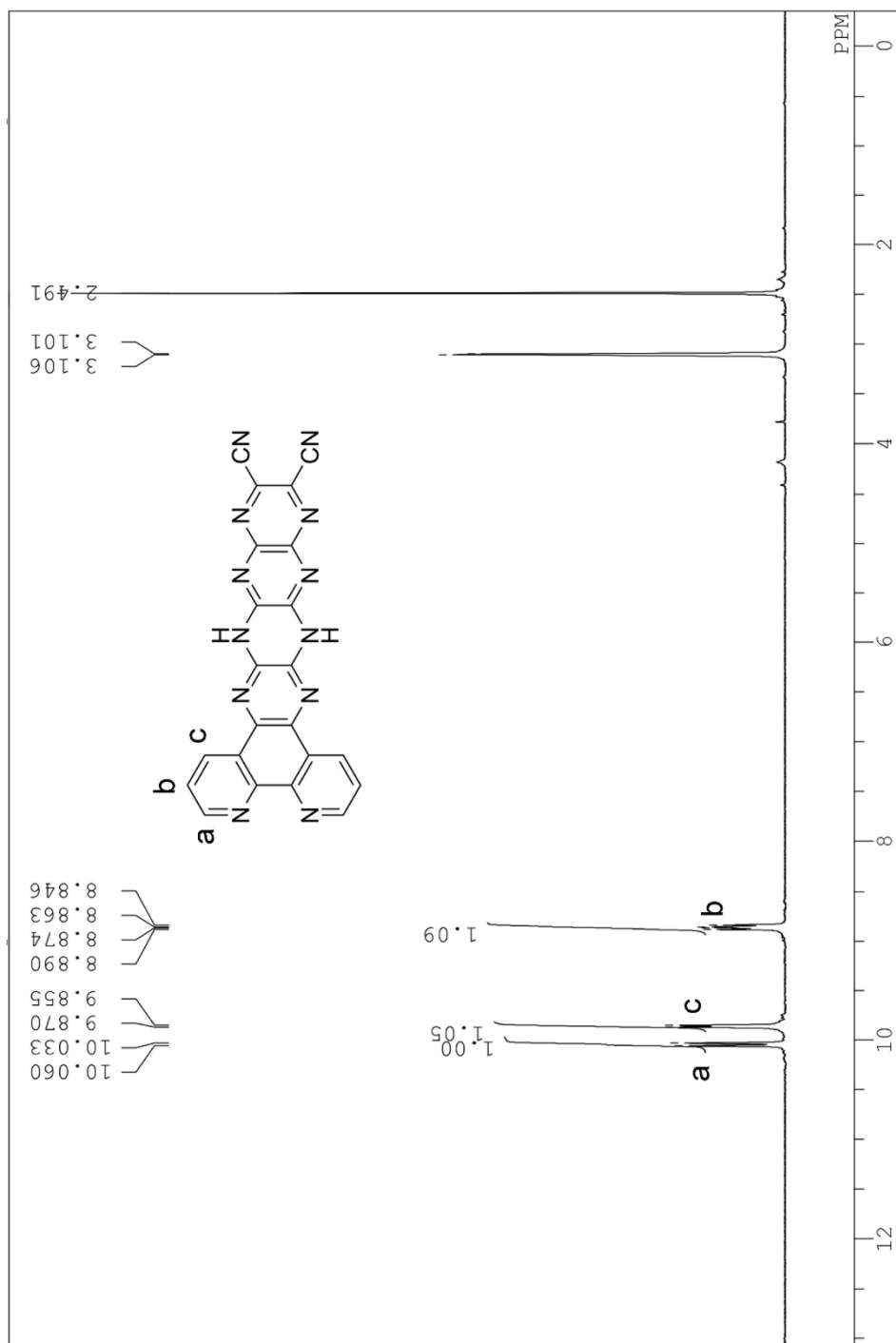


Figure S5. ¹H NMR spectrum of **2** in DMSO-d₆/trifluoroacetic acid-d₄.

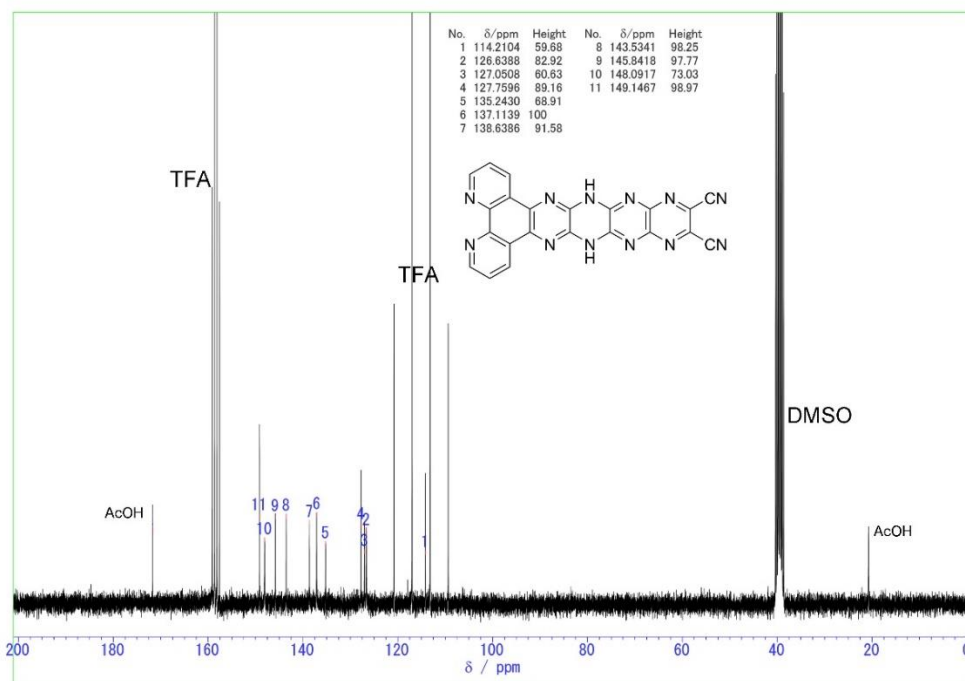


Figure S6. ^{13}C NMR spectrum of **2**. Samples of **2** isolated by Soxhlet extraction routinely contained small quantities of acetic acid.

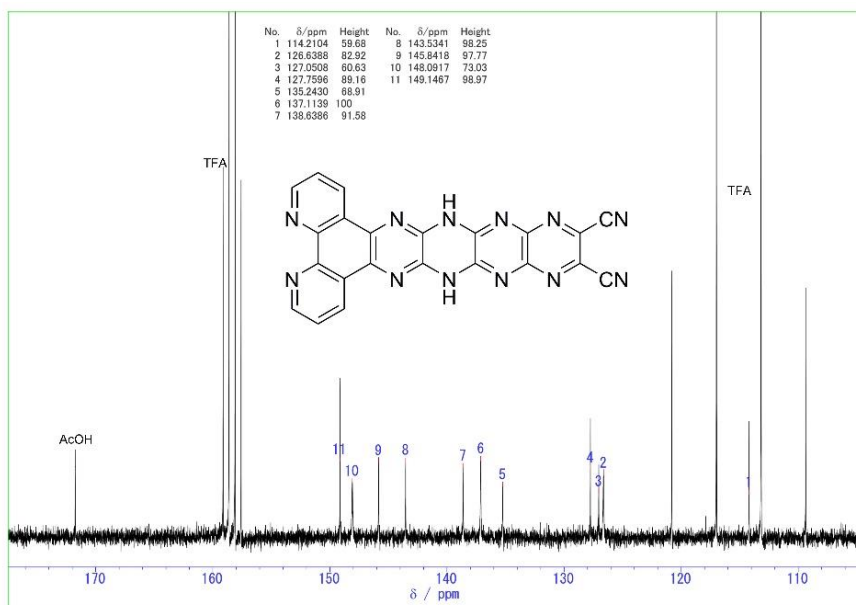


Figure S7. Expansion of ^{13}C NMR spectrum of **2**.

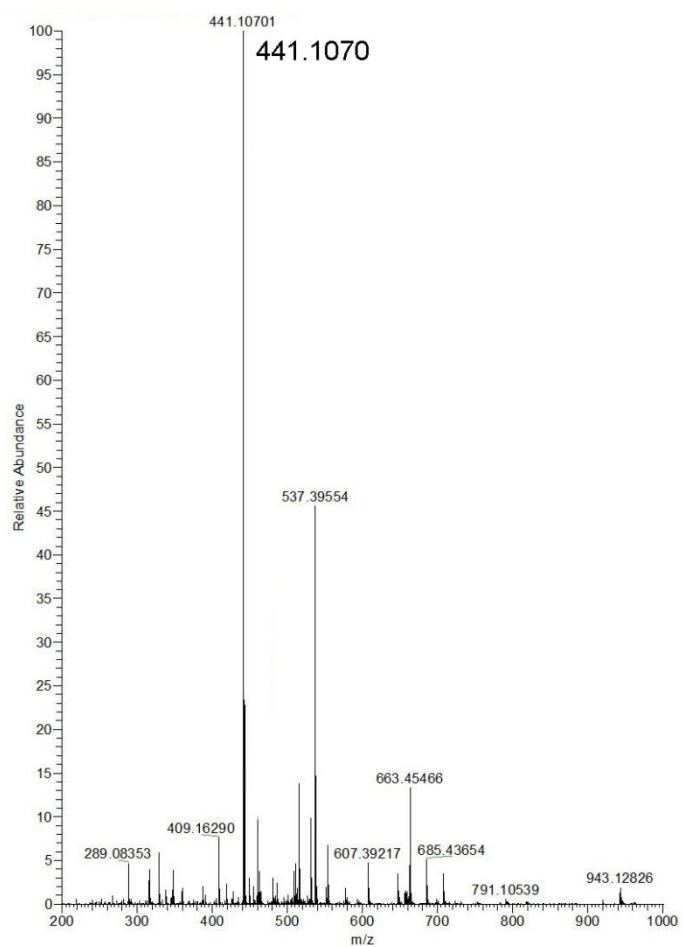


Figure S8. HR-MS (MALDI-TOF) for compound **2**.

4) 6(7),13(14)-Bis[3,4,5-tris(n-dodecyloxy)benzyl]-dipyrido[3,2-a:2',3'-c]-5,6,7,8,11,12,13, 14-octazaapentacene-9,10-dicarbonitrile (**3**)

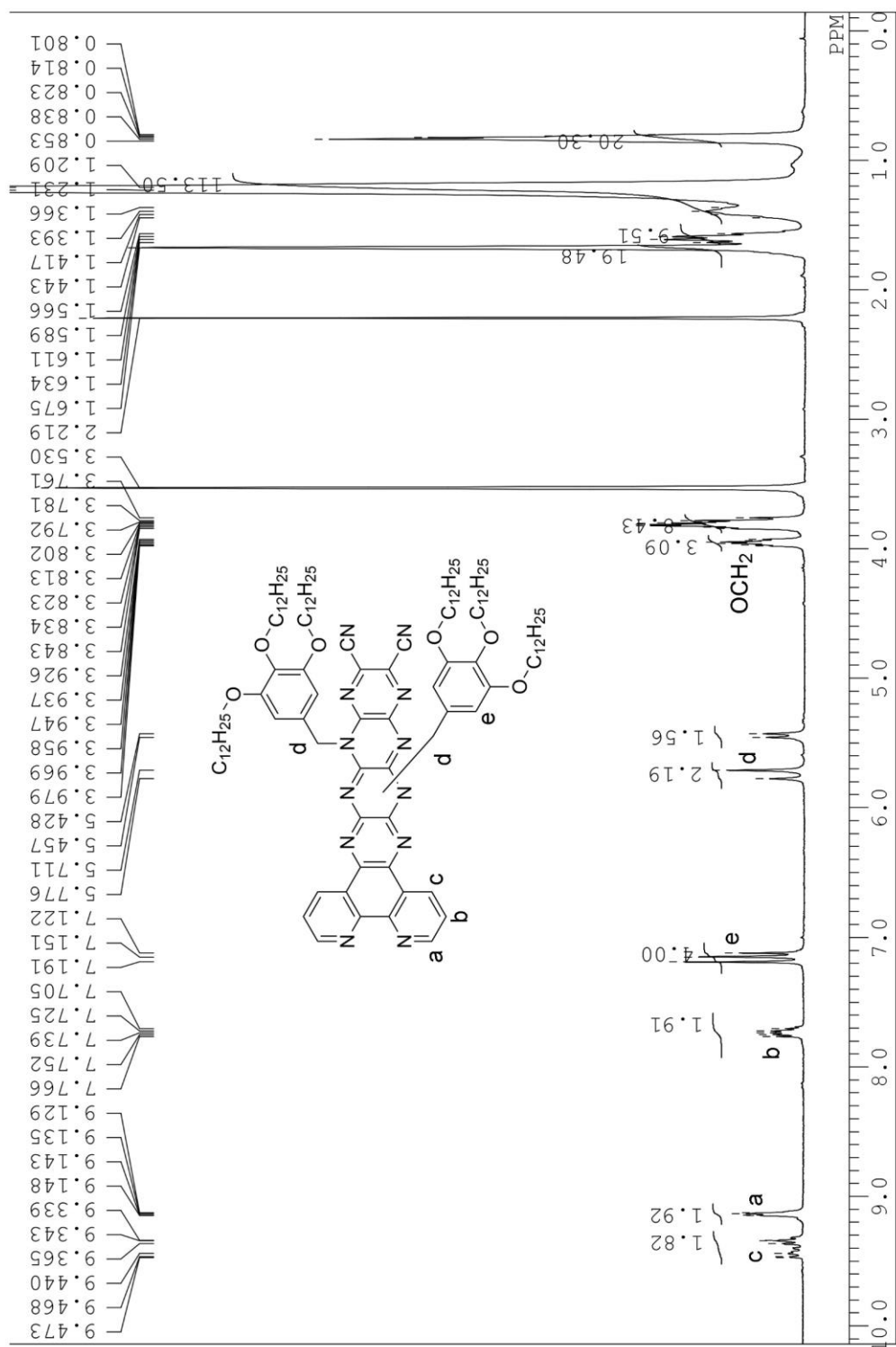


Figure S9. ¹H NMR spectrum of **3**(a-c) in tetrahydrofuran-*d*₈.

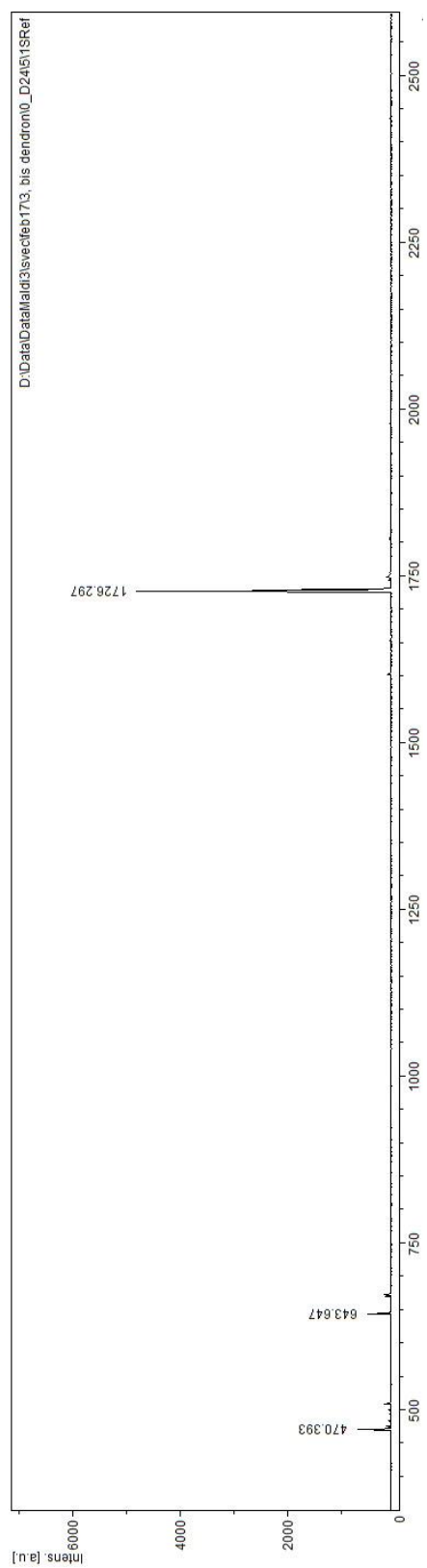


Figure S10. High resolution mass spectrum of **3(a-c)**.

5) 6,13-Dihydrodipyrido[3,2-a:2',3'-c]-dibenzo[*l,n*]-5,6,7,12,13,14-hexaazapentacene (**4**)

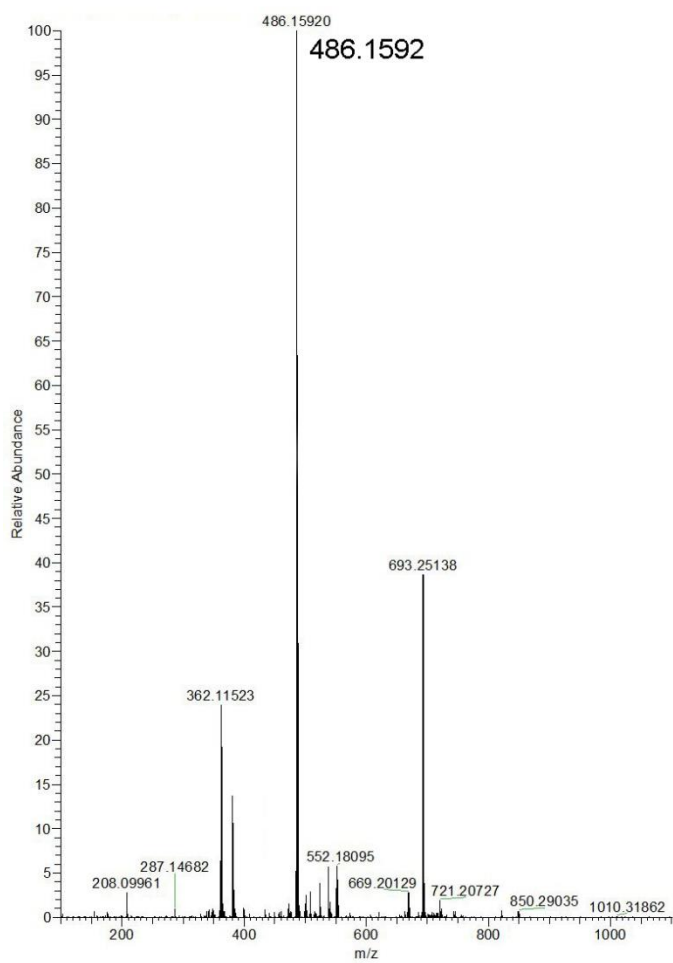


Figure S11. HR-MS (MALDI-TOF) for compound **4**.

6) 6,13-Bis(*n*-dodecyl)-dipyrido[3,2-*a*:2',3'-*c*]-dibenzo[*l,n*]-5,6,7,12,13,14-hexaazapentacene (**5**)

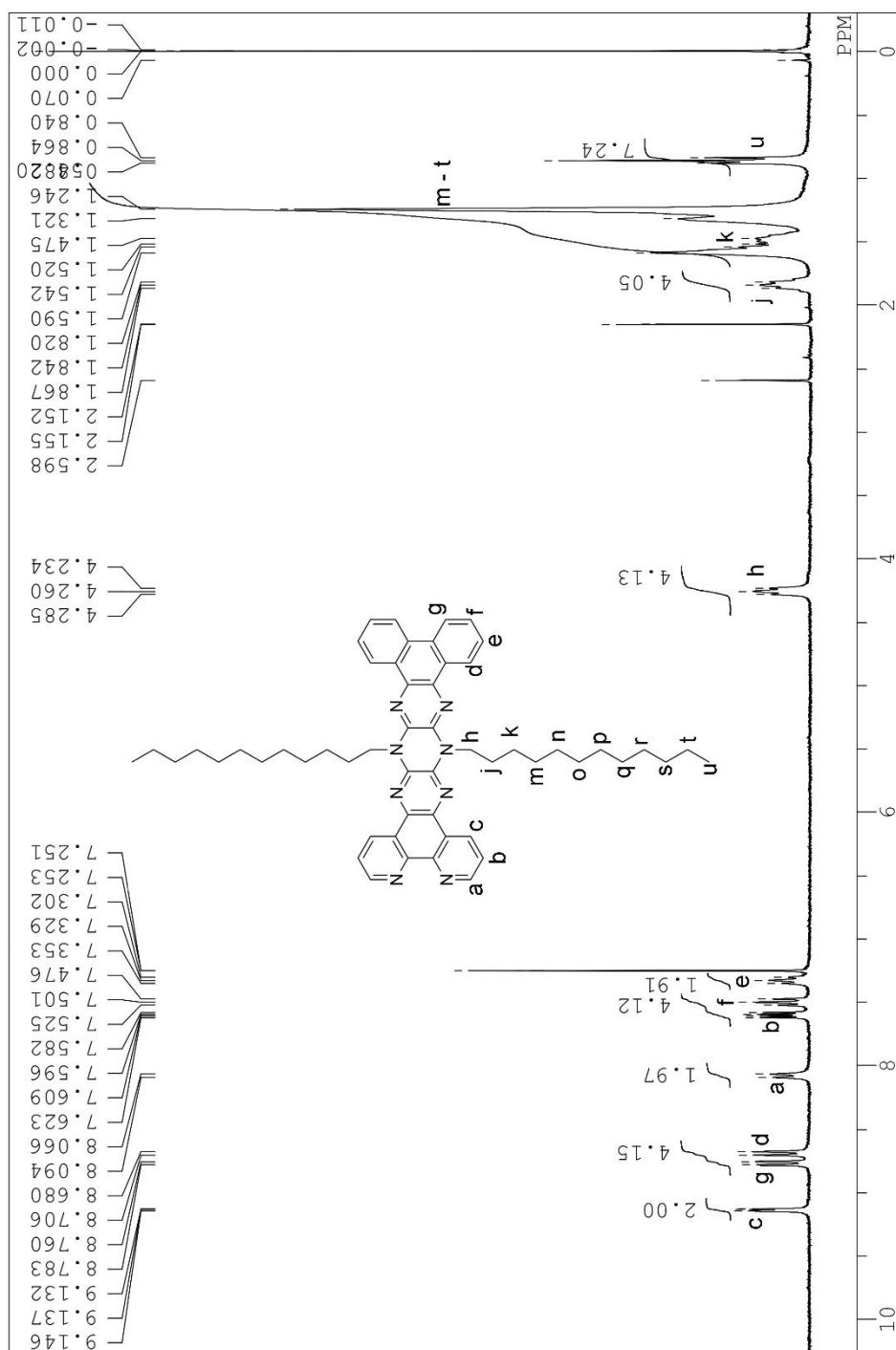


Figure S12. ¹H NMR spectrum of 6,13-Bis(*n*-dodecyl)-dipyrido[3,2-*a*:2',3'-*c*]-dibenzo[*l,n*]-5,6,7,12,13,14-hexaazapentacene (**5**) in CDCl₃.

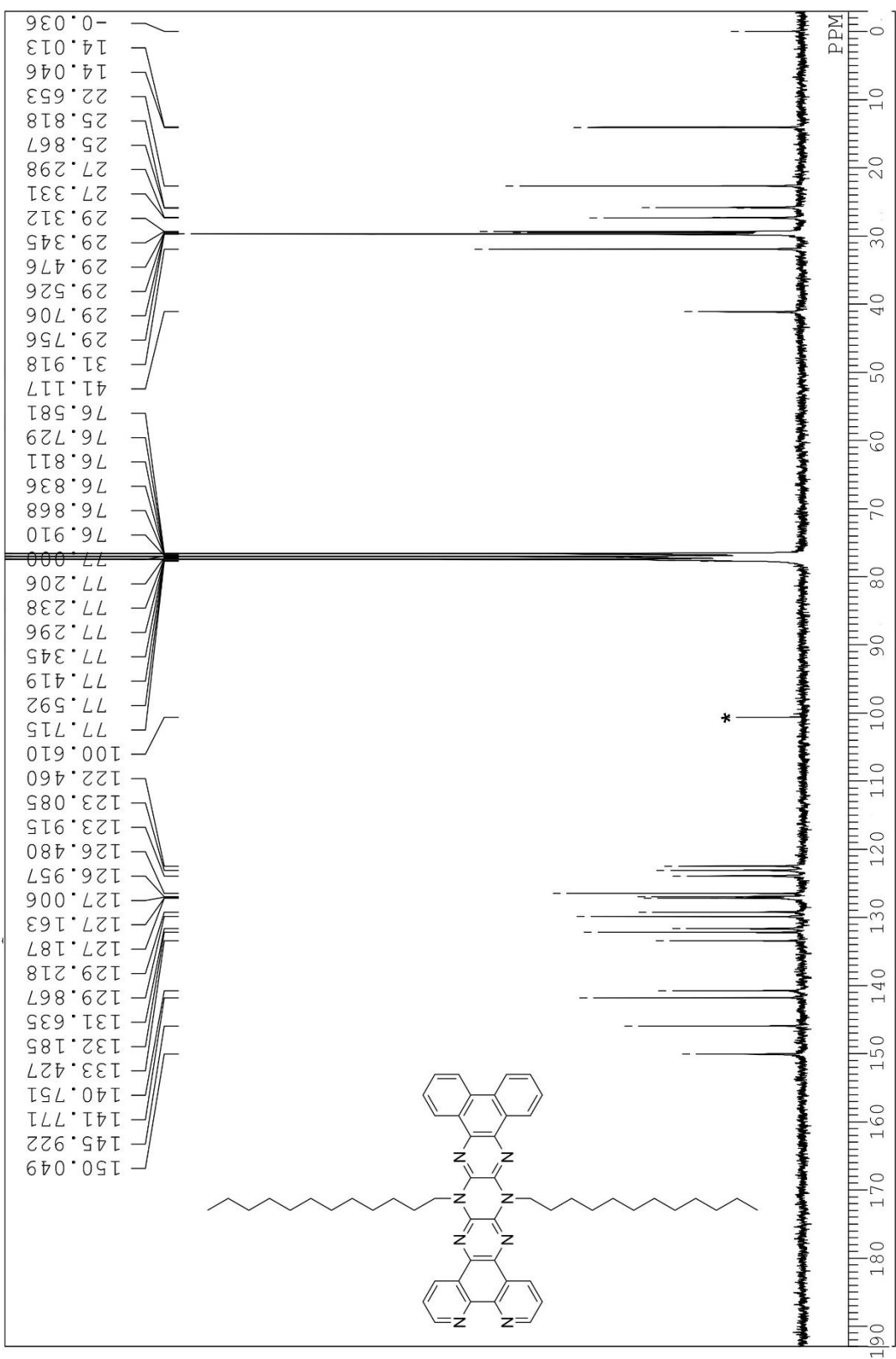


Figure S13. ¹³C NMR spectrum of 6,13-Bis(*n*-dodecyl)-dipyrido[3,2-*a*:2',3'-*c*]-dibenzo[1,1'-*n*]-5,6,7,12,13,14-hexaazapentacene (**5**) in CDCl₃. Asterisk denotes trace solvent impurity.

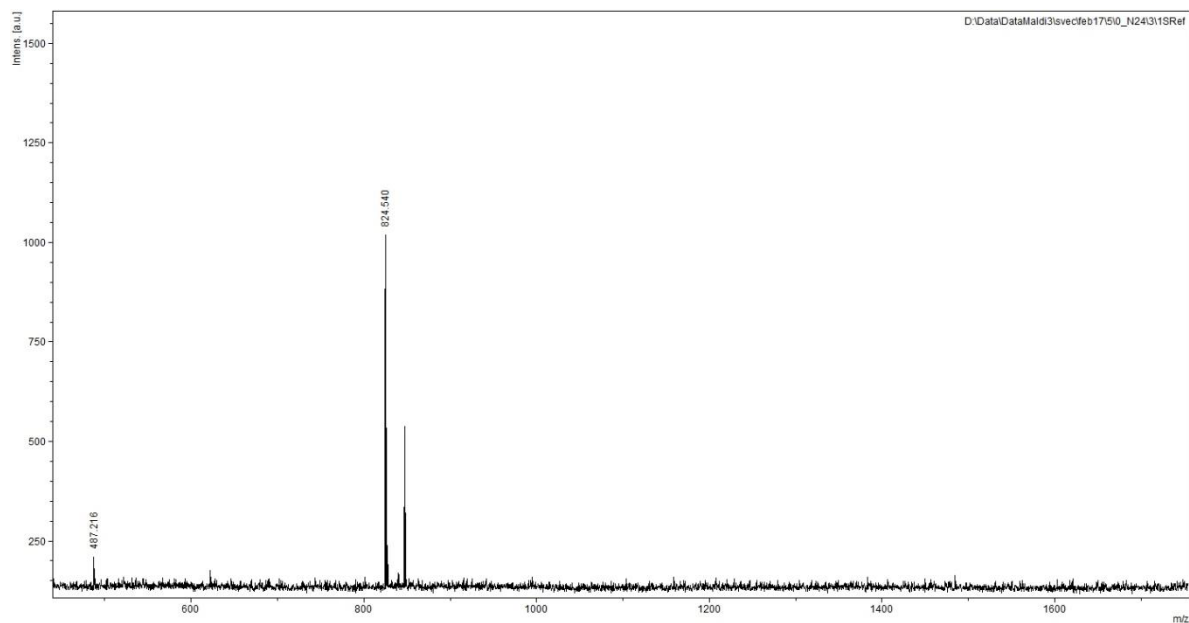


Figure S14. MALDI-TOF-HR-MS for compound 6,13-Bis(*n*-dodecyl)-dipyrido[3,2-*a*:2',3'-*c*]-dibenzo[*l*,*n*]-5,6,7,12,13,14-hexaazapentacene (**5**).

7) Bis(2,2'-bipyridine)(6,13-bis(*n*-dodecyl)-dipyrido[3,2-*a*:2',3'-*c*]-dibenzo[*l*,*n*]-5,6,7,12,13,14-hexaazapentacene)ruthenium(II) chloride (**6**)

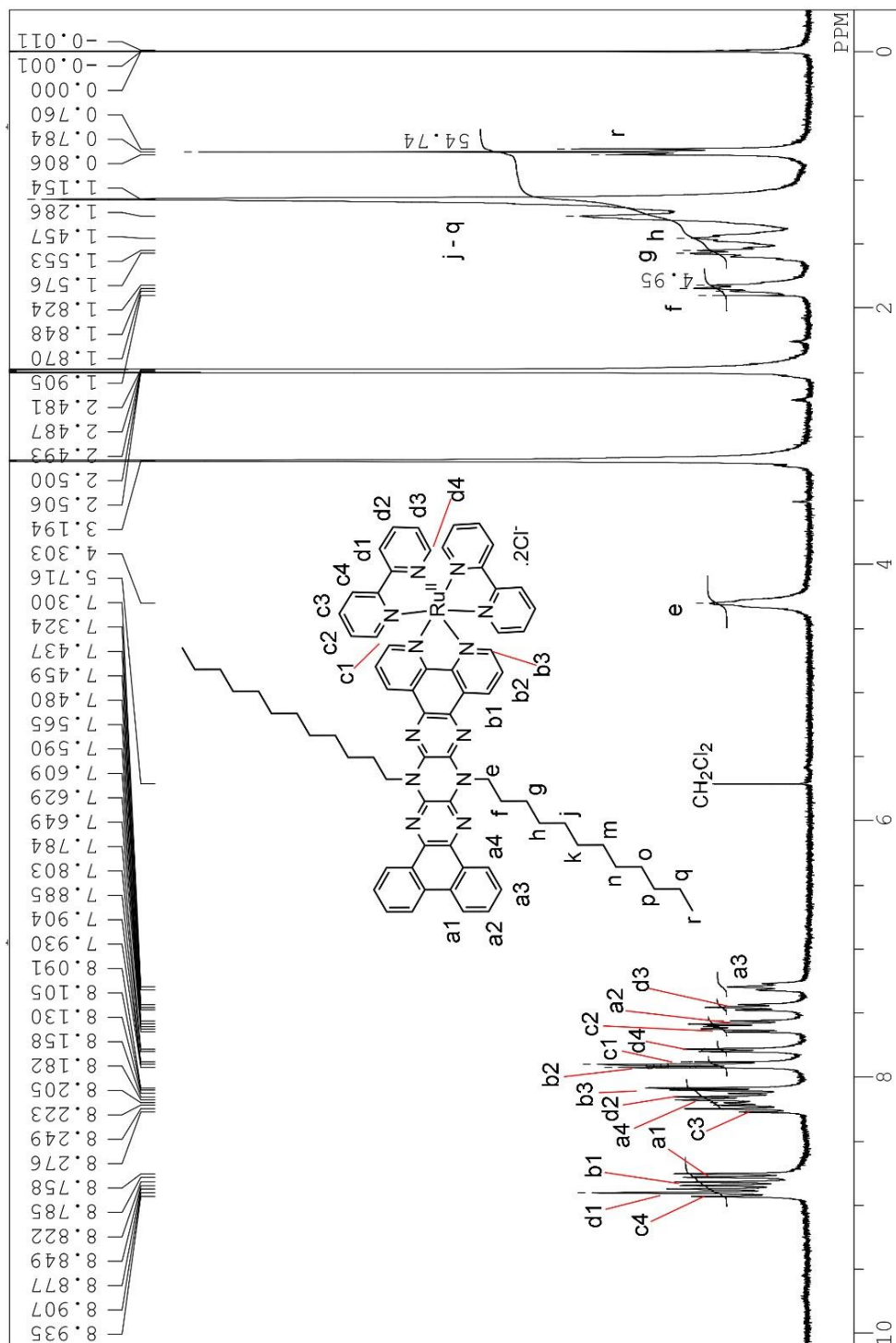


Figure S15. ¹H NMR spectrum of **6** in CDCl₃. Assignments based on ¹H-¹H COSY NMR spectrum and chemical shifts.

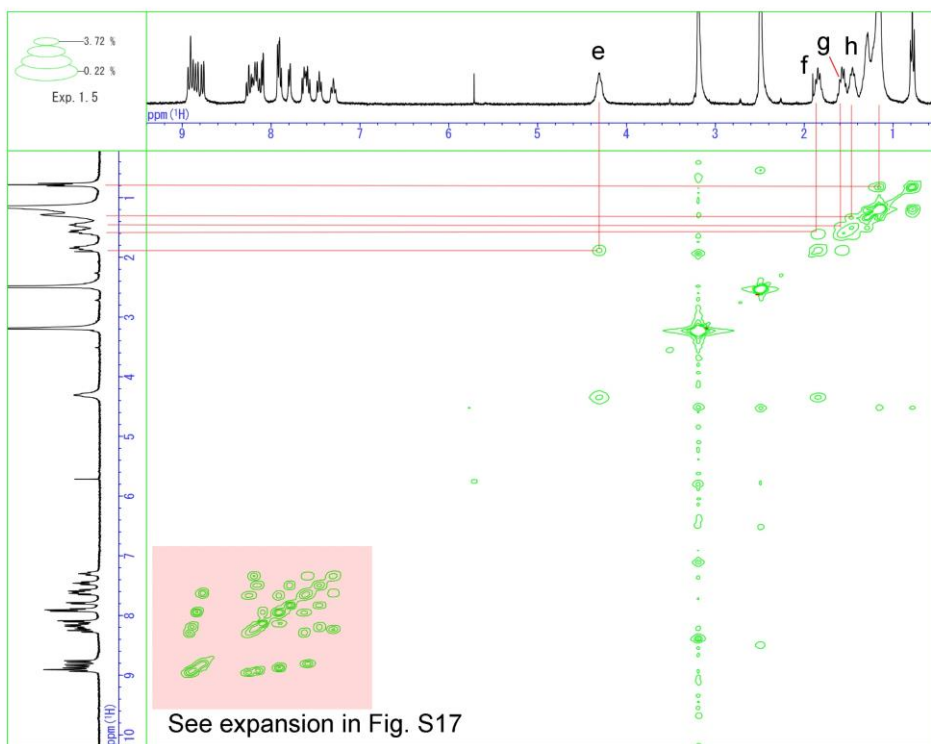


Figure S16. ^1H - ^1H COSY NMR Spectrum of compound **6** with partial assignment of alkyl chain resonances. For low field region see Fig. S17.

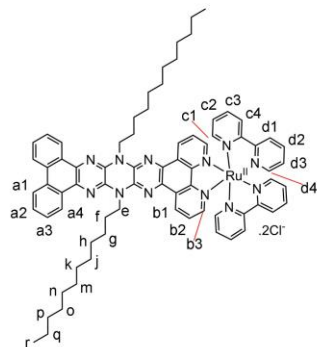
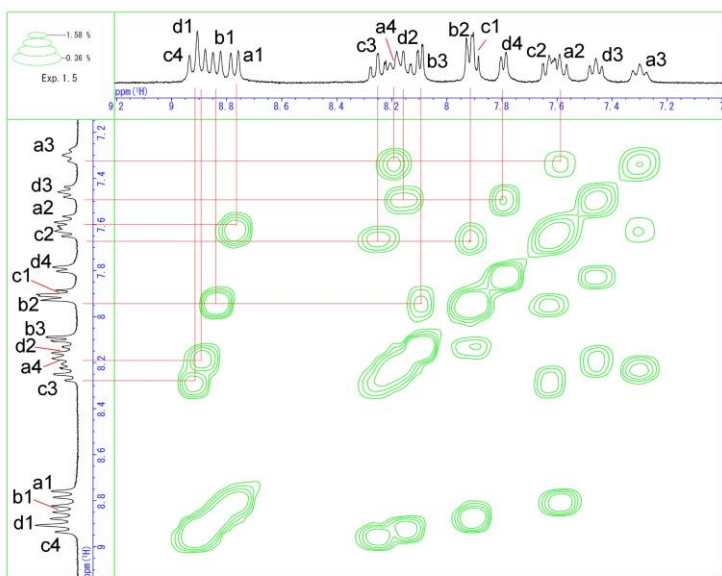


Figure S17. ^1H - ^1H COSY NMR Spectrum of compound **6** with assignments.

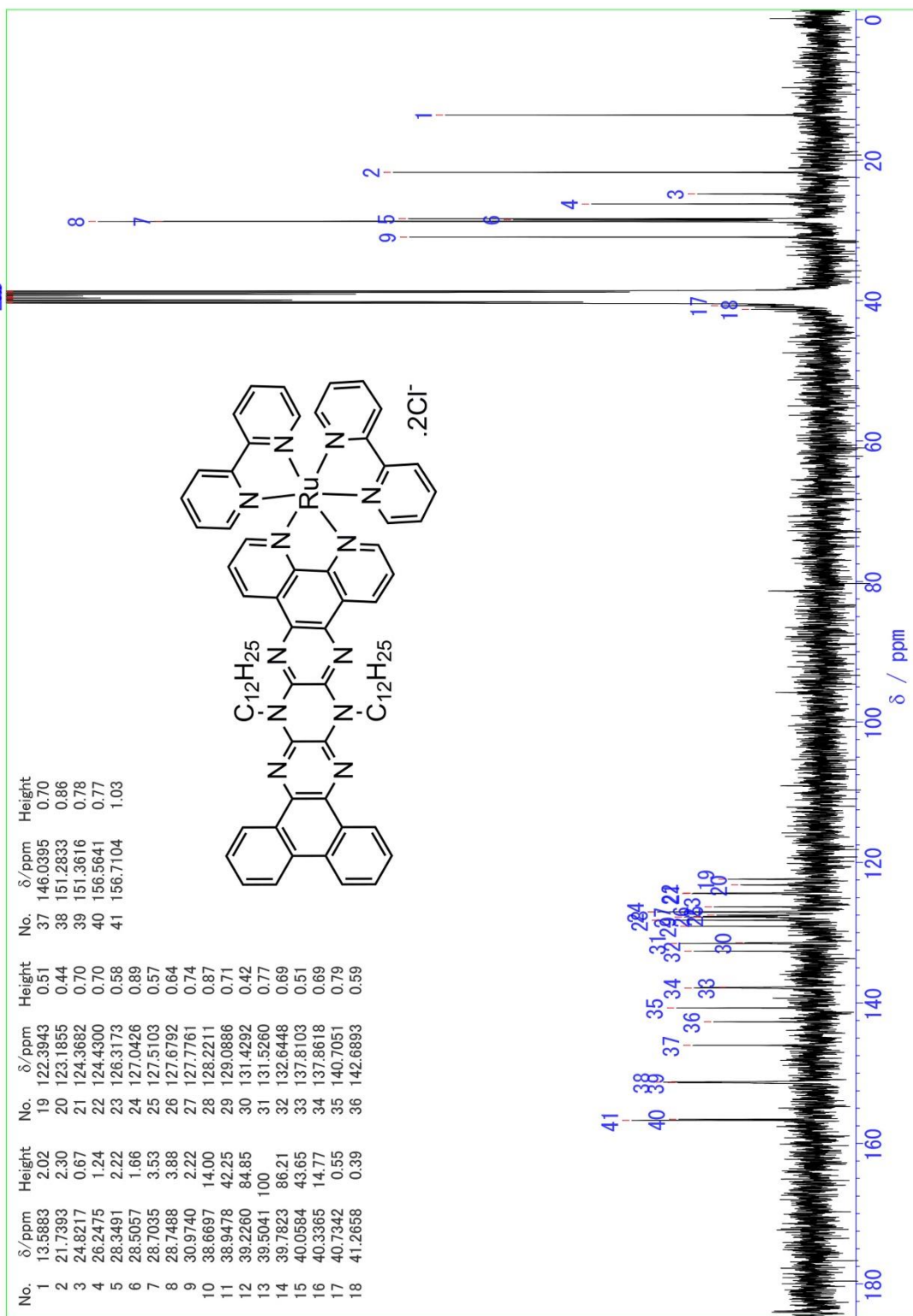


Figure S18. ^{13}C NMR spectrum of **6** in $DMSO-d_6$.

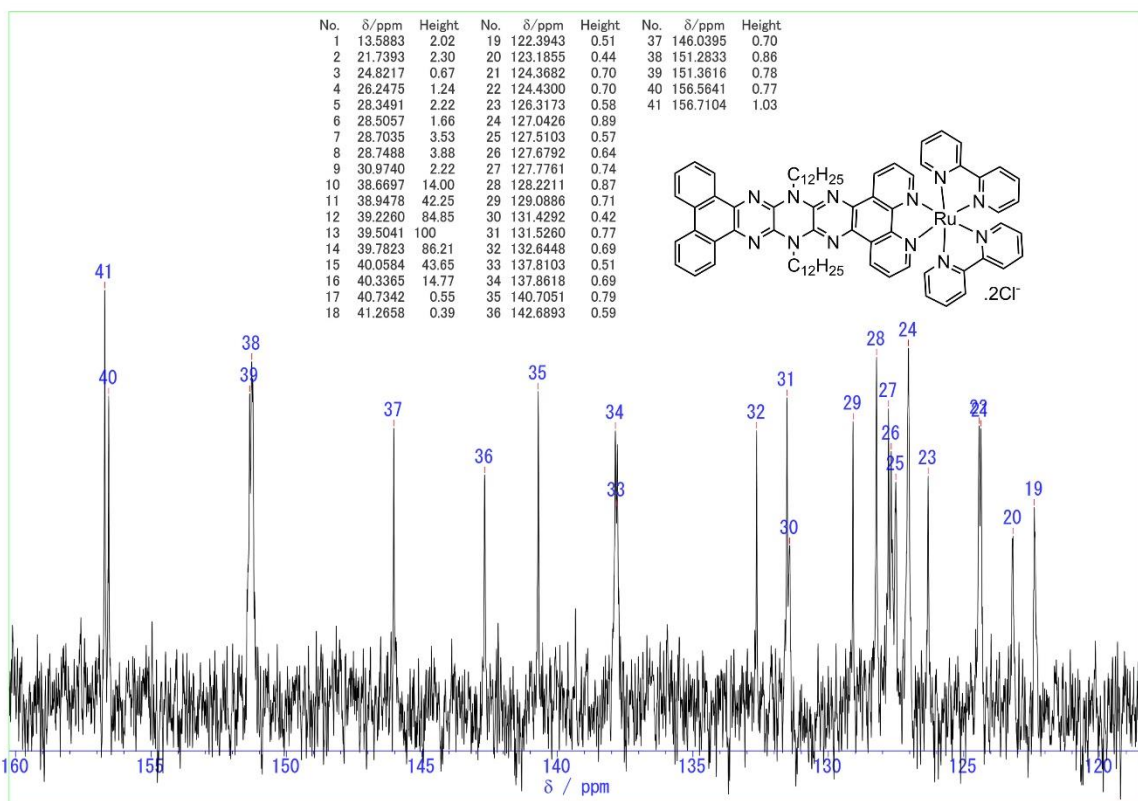


Figure S19. Detail of ^{13}C NMR spectrum of **6** in $\text{DMSO-}d_6$.

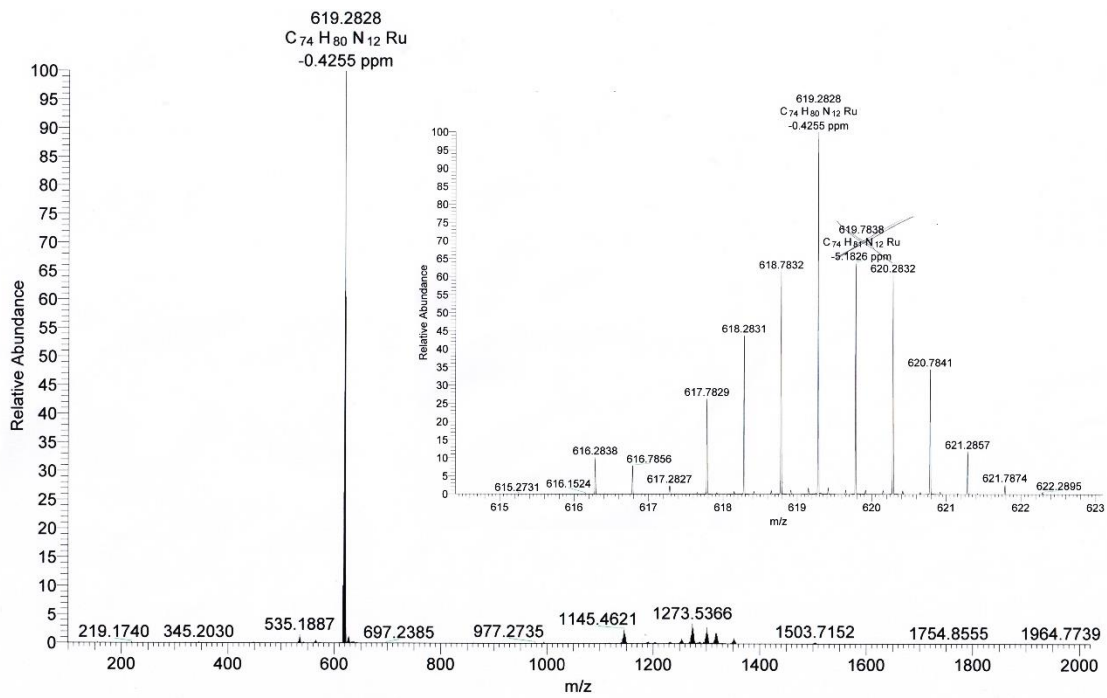


Figure S20. ESI-HR-MS for compound 6.

8) ^1H NMR spectra of **6** at different concentrations in acetonitrile- d_3 .

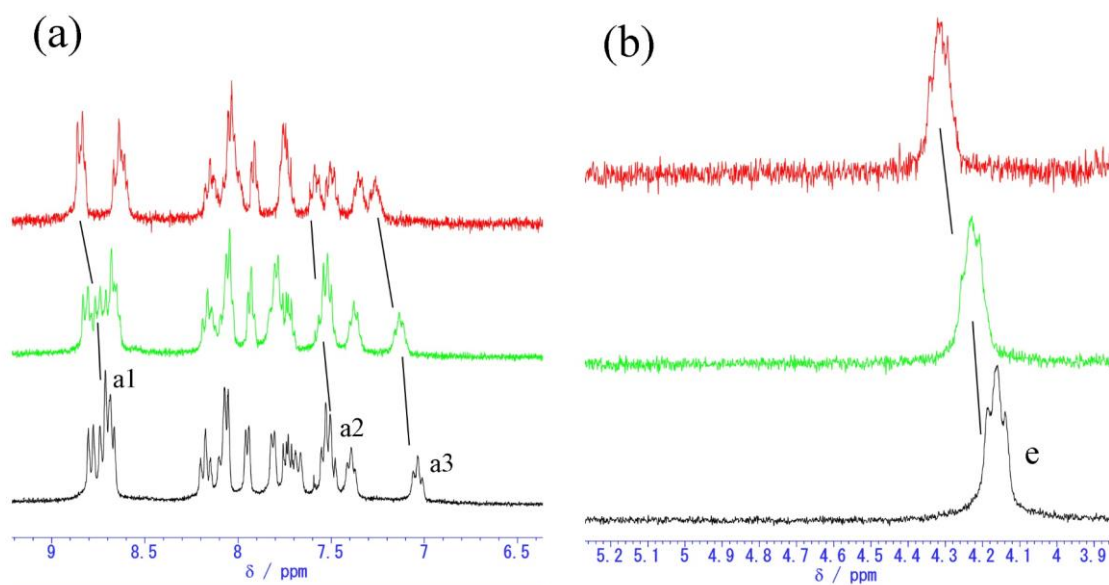


Figure S21. ^1H -NMR spectra of **6** in acetonitrile- d_3 at different concentrations (Black: $\sim 1 \times 10^{-2}$ M; green: $\sim 5 \times 10^{-3}$ M; red: $\sim 1 \times 10^{-3}$ M). (a) Low field region. (b) N- CH_2 group adjacent to the pyrazinacene unit. Black lines denote the downfield shift at increasing dilution of peaks due to the phenanthrenyl unit of the pyrazinacene ligand (protons a1, a2, a3 according to the assignment given in Figs. S15,S17) and the methylene unit attached at the fluorubine nitrogen atoms (assigned as e in Figs. S15,S17). Other peaks are less affected by change in concentration.

Appendix 2

Sedláček, O.; Filippov, S. K.; Švec, P.; Hrubý, M., SET-LRP Synthesis of Well-Defined Light-Responsible Block Copolymer Micelles. *Macromol. Chem. Phys.* **2019**, 220 (19), 1900238.

Times Cited: 10; IF = 2.34.

P. Švec performed the pilot NBA polymerization experiments, assisted with optimizing the polymerization conditions, collected polymer/nanoparticle characterization data (UV, DLS, and NMR - except the DOSY spectra), and performed the UV-induced micelle disassembly experiments.



SET-LRP Synthesis of Well-Defined Light-Responsive Block Copolymer Micelles

Ondrej Sedlacek,* Sergey K. Filippov, Pavel Svec, and Martin Hruby

Herein, the synthesis of well-defined light-sensitive amphiphilic diblock copolymers consisting of UV-responsive poly(2-nitrobenzyl acrylate) (PNBA) and hydrophilic poly(ethylene oxide) (PEO) blocks is reported. This is achieved by a single electron transfer living radical polymerization (SET-LRP) of 2-nitrobenzyl acrylate monomer initiated by PEO-containing macroinitiator. Despite several reports on PEO-*b*-PNBA copolymers, this is the first time the PNBA block is synthesized by a controlled radical polymerization leading to the copolymers with low dispersity ($\bar{D} = 1.10$). In water, the copolymers self-assemble into well-defined micelles with a hydrodynamic diameter of 25 nm. Upon irradiation with UV-light, the PNBA units degrade to hydrophilic poly(acrylate) resulting in disassembly of the micelles. Considering the robustness of the reported synthetic protocol, the prepared polymers represent an interesting platform for the construction of new stimuli-responsive drug delivery systems.

and hydrophilic blocks. After the administration of the drug-loaded micellar delivery system, its concentration in the body gradually decreases, resulting finally in disassembly of the micelles and release of the hydrophobic cargo.^[2] However, the release rate for systems with non-covalently bound drugs is much less controllable than in the case of systems with covalently bound drug via a degradable linker. Premature non-covalently bound drug release from the micelles could be prevented by the stabilization of the core using either increasing the content of a hydrophobic part or by its crosslinking preferably with a biodegradable linker. Also, the drug can be released based on the external stimuli^[3] such as change of pH,^[4–6] temperature,^[7–10] presence of light,^[11] or the redox stimuli,^[12] which is currently the preferred

1. Introduction

Polymeric micelles have recently gained substantial attention as effective nanocarriers for specific organ delivery of hydrophobic drugs.^[1] In most cases, they are assemblies of amphiphilic block or graft copolymers with hydrophilic shell and a hydrophobic core. The core can encapsulate hydrophobic drugs such as paclitaxel using non-covalent hydrophobic interactions, while the hydrophobic shell is responsive for the micelle water solubility and biocompatibility. Kinetic and thermodynamic stability of these micelles is controlled by the length and nature of the hydrophobic block as well as a weight ratio of hydrophobic

way providing extra control over drug release.

To achieve decomposition of micelles by light, the hydrophobic polymer block should hydrophilize upon irradiation^[11] to enable light-triggered disassembly. As an example, hydrophilic poly(meth)acrylate block can be retrieved upon UV-light irradiation when the side chains are esterified with photodegradable hydrophobic alcohols.^[13] Most of these systems are composed of poly(ethylene oxide) (PEO) hydrophilic block with the varying structure of a photodegradable block. This can be, for example, poly(1-pyrenemethyl methacrylate),^[14] poly([7-(diethylamino)coumarin-4-yl]methyl methacrylate),^[15] or poly(2-nitrobenzyl acrylate) (PNBA).^[16]

Ultraviolet light is extensively used in a biomedical application for sterilization. However, the dose delivered should be carefully monitored especially for colored samples with significant UV absorption where deeper layers may not receive dose sufficient for sterilization. The commonly used UV-source, the mercury lamp, has spectrum especially in the shorter wavelengths below 315 nm (i.e., the UV B and UV C region) crucial for sterilization perfectly matching the absorption of 2-nitrobenzyl ester, a photocleavable group.

Despite the extensive use of *o*-nitrobenzyl-based photodegradable polymers, the synthesis of 2-nitrobenzyl acrylate (NBA) polymers with narrow dispersity was challenging for a long time.^[17] Therefore, the already reported PEO-*b*-PNBA amphiphilic copolymers suffered either from rather high dispersities^[18,19] or the NBA was copolymerized with other monomers in rather low partial content (<12 mol%).^[16,20] The possibilities of controlled polymerization of *o*-nitrobenzyl (meth)acrylates were evaluated by Gohy and coworkers.^[21] As a result,

Dr. O. Sedlacek, Dr. S. K. Filippov, P. Svec, Dr. M. Hruby
 Institute of Macromolecular Chemistry
 Academy of Sciences of the Czech Republic
 Heyrovsky Sq. 2, 162 06 Prague 6, Czech Republic
 E-mail: sedlacek@imc.cas.cz

Dr. O. Sedlacek
 Department of Organic and Macromolecular Chemistry
 Ghent University
 Krijgslaan 281 S4, B-9000 Ghent, Belgium

Dr. S. K. Filippov
 School of Engineering and Applied Science
 Harvard University
 9 Oxford Street, Cambridge, MA 02138, USA

The ORCID identification number(s) for the author(s) of this article can be found under <https://doi.org/10.1002/macp.201900238>.

DOI: 10.1002/macp.201900238

the polymerization of NBA using atom transfer radical polymerization (ATRP), reversible addition-fragmentation chain transfer polymerization (RAFT), and nitroxide-mediated polymerization (NMP) proceed very slowly and in an uncontrolled way. The polymerization of 2-nitrobenzyl methacrylate (NBMA) by ATRP proved to be the method of choice, but the control over the molar mass and the dispersity was retained only at monomer conversions up to 30%. Only recently, Six and coworkers succeeded in controlled polymerization of NBA using single electron transfer living radical polymerization (SET-LRP), where the Cu(I) species are formed in situ by synproportionation of Cu(II) and Cu(0).^[13] Then, the formed Cu(I) disproportionates to yield highly reactive nascent Cu(0) (and Cu(II)), which activates the alkyl halide for the polymerization.

Herein, we report for the first time the protocol for the rapid synthesis of light-sensitive PEO-*b*-PNBA amphiphilic diblock copolymers having narrow molar mass distribution ($\mathcal{D} = 1.10$) necessary to obtain tailorable, well-defined, and reproducible micellar, and uniform biological behavior. This was achieved by SET-LRP of NBA monomer initiated by PEO-containing macroinitiator. Despite several reports on PEO-*b*-PNBA copolymers,^[18,19] this is the first time the PNBA block was synthesized by a controlled radical polymerization leading to the copolymers with low dispersity. The micellization of such copolymer was studied by dynamic light scattering, while the light responsivity of the system was demonstrated by successful degradation of formed micelles in aqueous solution upon UV irradiation. The system described herein may not only serve as a model biologically excretable micellar delivery system but also as an in situ dosimeter for monitoring UV dose received within, for example, sterilization. The output may be monitored/read by both UV-spectrophotometry (the photodegradation product *o*-nitrosobenzaldehyde has a different spectrum than 2-nitrobenzyl ester) and dynamic or static light scattering. The above-mentioned scattering methods have an advantage in colored samples with significant UV-absorption, because while 2-nitrospecies absorb in UV and short wavelength visible region, light scattering monitoring of micelles-to-unimer disassembly may be done with any wavelength including long wavelengths, where absorption may be low.

2. Experimental Section

2.1. Materials

All chemicals, including poly(ethylene oxide) monomethyl ether ($M_w = 5000$ Da), α -bromoisobutyryl bromide, triethylamine, 2-nitrobenzyl alcohol, acryloyl chloride, dimethyl sulfoxide (DMSO), hydrazine monohydrate, copper(II) chloride, tris[2-(dimethylamino)ethyl]amine (Me_6TREN) were purchased from Sigma-Aldrich Ltd. (Prague, Czech Republic) and were used without further purification. PEO-based macroinitiator PEO-Br ($M_{n(\text{SEC})} = 5100$ Da, $\mathcal{D} = 1.09$) was prepared by esterification of poly(ethylene oxide) monomethyl ether with α -bromoisobutyryl bromide according to ref. [16]. Cu(0) wire (20 gauge) was wrapped around a teflon-coated magnetic stir bar and activated for 30 min in hydrazine/DMSO solution (10 mM, 5 mL) followed by copious washing with ethanol and drying according to

the reference.^[22] Water was deionized with a Millipore Milli-Q (Merck) water purification system.

2.2. General Methods

The molar masses (M_w —mass-averaged molar mass, M_n —number-averaged molar mass) and dispersity ($\mathcal{D} = M_w/M_n$) of the polymers were determined by size exclusion chromatography (SEC) using a Viscotek GPC-Max VE 2001 equipment fitted with a 2×30 cm $5 \mu\text{m}$ mixed-C PLgel columns and coupled with a VE 3580 RI detector, VE 3210 UV/vis detector, and multiangle light scattering (MALS) DAWN EOS (Wyatt Technology Co., USA); with tetrahydrofuran (THF, flow rate of 1 mL min^{-1}) as mobile phase. The refractive index increment of the diblock polymer was calculated as a weighted average of refractive indexes of PEO ($dn/dc = 0.078 \text{ mL g}^{-1}$)^[23] and PNBA ($dn/dc = 0.137 \text{ mL g}^{-1}$)^[13] in THF based on the monomeric unit composition. UV/vis spectra were measured by Evolution 220 Spectrometer (Thermo Scientific, USA). Nuclear magnetic resonance (NMR) spectra were measured with a Bruker Advance MSL 400 MHz NMR spectrometer. All chemical shifts are given in ppm.

2.3. Synthesis of 2-Nitrobenzyl Acrylate

The 2-nitrobenzyl acrylate (NBA) monomer was synthesized analogously to the previously described procedure.^[16] Briefly, a solution of acryloyl chloride (7 g, 78 mmol) in dichloromethane (10 mL) was added dropwise to the ice-cooled mixture of *o*-nitrobenzyl alcohol (10 g, 65 mmol) and triethylamine (10.9 mL, 78 mmol) in dichloromethane (200 mL). Then, the reaction mixture was allowed to warm to the room temperature and stirred overnight (16 h). After quenching with saturated aqueous NaHCO_3 solution (200 mL), the organic phase was separated, washed with water (200 mL), dried with anhydrous magnesium sulfate, evaporated in vacuo, dissolved in ethyl acetate, filtered, and evaporated again. The crude product was separated by column chromatography on silica (hexane-ethyl acetate 5:1) to afford the title compound (10.1 g, 75%) as a colorless oil, which was stored at 4°C in the dark. ESI-MS: 230.1 ($M + \text{Na}^+$). ^1H NMR ($\text{DMSO}-d_6$): 8.09 (d, 1H), 7.61–7.73 (m, 3H), 6.37 (d, 1H), 6.23 (dd, 1H), 6.0 (d, 1H), 5.49 (s, 2H).

2.4. SET-LRP Synthesis of PEO-*b*-PNBA Copolymers

SET-LRP synthesis of PEO-*b*-PNBA copolymers was carried out by modifying the procedure described by Soliman and coworkers.^[13] Typically, NBA (4.14 g, 20 mmol), PEO-Br (2 g, 0.4 mmol), Me_6TREN (107 μL , 0.4 mmol), and CuBr_2 (8.9 mg, 40 μmol) were dissolved in DMSO (8.18 mL) in a Schlenk tube under argon atmosphere. After degassing the mixture by seven consecutive freeze–pump–thaw cycles, the magnetic stir bar with wrapped Cu(0) wire (diameter 0.8 mm) was added to initiate the reaction. The reaction mixture was protected from light by aluminum foil and stirred at room temperature (25°C). For kinetic analysis, small aliquots (100 μL) were taken in predetermined

Table 1. Characteristics of PEO-*b*-PNBA copolymers.

Entry ^{a)}	Cu(0) wire length [cm]	Time [min]	Conversion ^{b)} [%]	DP _(NBA) ^{b)}	M _{n(theo)} ^{c)} [Da]	M _{n(SEC)} [Da] ^{d)}	Đ _(SEC) ^{d)}
1	5	60	81	40	13 500	26 600	1.57
2	3	60	75	37	12 900	20 900	1.35
3	1.5	60	52	26	10 500	12 300	1.10
4	1.5	120	83	43	13 700	19 100	1.26

^{a)}Initial monomer feed ratio [NBA]₀:[PEO-Br]₀:[Me₆TREN]₀:[CuBr₂]₀ = 50:1:1:0.1 in DMSO [NBA]₀ = 1.61 M; ^{b)}Determined by ¹H NMR spectroscopy; ^{c)}Calculated by formula M_{n(theo)} = [(NBA)₀/([PEO-Br]₀ × conversion × M_{NBA}) + M_{PEO-Br}]; ^{d)}Determined by size-exclusion chromatography (SEC).

time points, purged with compressed air to quench the growing radicals and analyzed. The conversions were calculated from the ¹H NMR signal ratio of the peaks corresponding to the ethylenic proton of the monomer ($\delta = 6.0$ ppm) and the sum of the aromatic protons ($\delta = 7.29$ to 8.15 ppm). The polymer was separated by gel filtration on an LH-20 column using methanol as an eluent. Polymer-containing fractions were collected, evaporated under reduced pressure, and stored in the dark. The ratio of PEO and PNBA blocks was calculated from the ¹H NMR integral intensities of the peaks corresponding to the PNBA aliphatic protons (O-CH₂-, $\delta = 5.4$ ppm) and the PEG methylene protons (O-CH₂-, $\delta = 3.7$ ppm).

2.5. Preparation of Micelles

Block copolymer nanoparticles were obtained by so-called nanoprecipitation. Typically, 60 mg of the polymer was dissolved in acetone (20 mL). This solution was quickly added via syringe to 40 mL of rapidly stirred water or phosphate-buffered saline (PBS, pH = 7.4; 0.150 M). After stirring at room temperature for 30 min, the volume of the mixture was reduced to ≈ 20 mL by rotary evaporation. Then, distilled water was added to the acetone-free solution to adjust its total volume to 30 mL ($c_{\text{pol}} = 2$ mg mL⁻¹).

2.6. Determination of Critical Micelle Concentration

Micellar solution was prepared by the abovementioned nanoprecipitation in PBS (150 mM, pH 7.4) at a concentration of 1 mg mL⁻¹ and was successively diluted to a concentration of 10⁻⁵ mg mL⁻¹. Pyrene stock solution (1.2 × 10⁻⁴ mol L⁻¹ in methanol) was added to each polymer sample, so the final concentration of pyrene in PBS was 6 × 10⁻⁷ mol L⁻¹. Fluorescence spectra of the samples were recorded with Jasco spectrofluorometer using excitation at 333 nm. The ratio of the fluorescence emission intensities at 372 nm (*I*₁) and 383 nm (*I*₃) was plotted against the polymer concentration. The critical micelle concentration (cmc) was determined as the intersection between the plateau at $d(I_1/I_3)/dc \approx 0$ and the tangent of the curve where the *I*₁/*I*₃ ratio decreased with an increasing copolymer concentration.

2.7. Dynamic Light Scattering Measurements

The UV-light responsive degradation has been monitored by dynamic light scattering (DLS) method. Experimental

DLS setup was based on a homemade goniometer combined with ALV-7000 correlator (ALV-GmbH, Germany), Ar laser (Coherent) tuned to 514 nm wavelength, and two avalanche photodiodes. Cross-correlation setup with fiber optics was used to accumulate intensity autocorrelation function. Experiments were conducted at the scattering angle 90° at finite concentration 0.5 mg mL⁻¹ for different degradation times at room temperature. The obtained correlation functions were analyzed at each angle using the requirements engineering process for embedded systems (REPEs) algorithm. All solutions were filtered with 0.22 μm polyvinylidene fluoride (PVDF) filter into a dust-free cell before DLS experiments.

2.8. UV-Irradiation Induced Disassembly of the Prepared Micelles

The micellar solution ($c_{\text{pol}} = 0.5$ mg mL⁻¹, 4 mL) was transferred to a quartz cuvette and was irradiated using mercury vapor lamp Noblelight HPK125W (Heraeus, Hanau, Germany) while cooling in an ice-water bath, always a pair of cuvettes (one with PBS solution and one with aqueous solution) was irradiated at the same time. The distance between the irradiated sample and the lamp was 5 cm. In predetermined time points, the samples were measured by UV-vis and DLS. The degradation kinetics was performed in duplicates and the results were analyzed by one-way ANOVA.

3. Results and Discussion

To explore the feasibility of SET-LRP polymerization for the synthesis of PEO-*b*-PNBA copolymers, a series of test polymerizations was performed (Table 1, Figures 1 and 2). Polymerizations were carried out in DMSO at 25 °C with Me₆TREN as a ligand.^[13] PEO-Br was used as macroinitiator and the initial weight/volume ratio of NBA/DMSO was held at 1:2 ([NBA]₀ = 1.61 M) to ensure full solubility of PEO-Br. CuBr₂

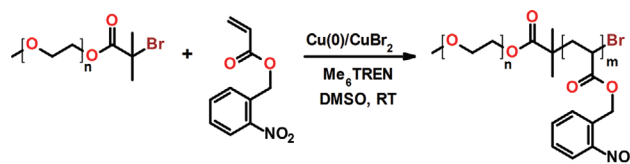


Figure 1. SET-LRP synthesis of PEO-*b*-PNBA copolymers.

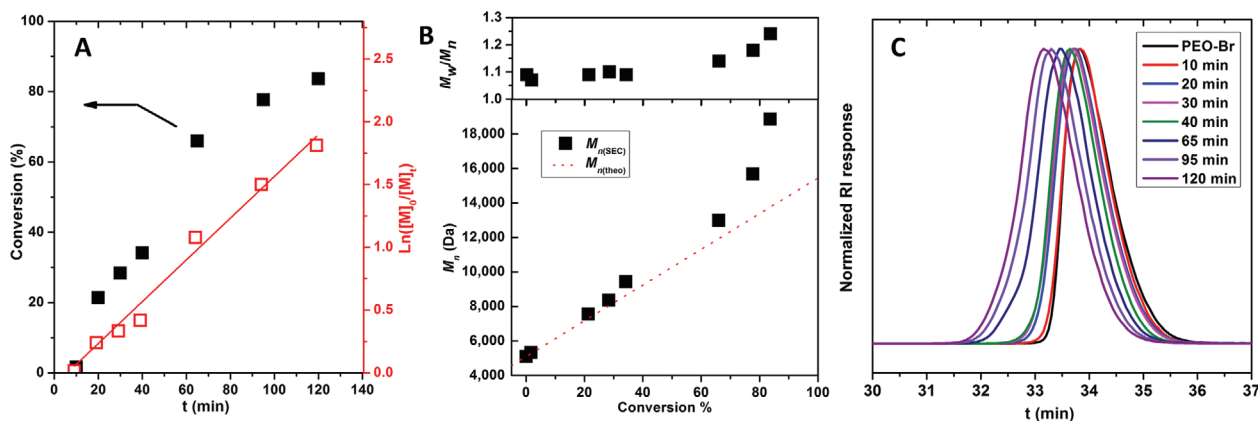


Figure 2. SET-LRP of NBA using $[\text{NBA}]_0:[\text{PEO-Br}]_0:[\text{Me}_6\text{TREN}]_0:[\text{CuBr}_2]_0 = 50:1:1:0.1$ in DMSO at 25 °C, initiated with 1.5 cm 20-gauge copper wire, using 3 g of NBA. A) Conversion plot of NBA monomer. B) Plot of molar masses and dispersities. C) SEC chromatograms of PEO-*b*-PNBA copolymers.

was added to prevent the formation of high molar mass by-products. The polymerization rate highly depends on the length of the copper(0) wire catalyst. The polymerization initiated with 5 cm wire (diameter = 0.8 mm) led to high conversions in the short reaction time (81% in 60 min), the dispersity of the final polymer was relatively high ($\mathcal{D} = 1.57$). On the other hand, excellent control over the polymerization was achieved using shorter copper wire (1.5 cm) (Table 1).

Furthermore, the polymerization kinetics was followed by ^1H NMR and SEC. After an induction period, the polymerization proceeds via pseudo-first-order kinetics with respect to the monomer (Figure 2A), with apparent propagation rate constant achieved from the linear fit of the kinetic plot being $k_p = 8.6 \pm 0.4 \times 10^{-3} \text{ L mol}^{-1} \text{ s}^{-1}$. Compared with the results obtained by Six and coworkers who polymerized NBA from ethyl 2-bromoisobutyrate initiator, the herein reported polymerization rate constant is approximately one order of magnitude higher, which can be explained by more effective activation of the copper wire surface using hydrazine solution.^[13,22] The increase in the copper surface reactivity can also explain the shorter induction period ($t_{\text{ind}} = 7 \text{ min}$) described in this work. The polymerization follows the first order kinetic for monomer conversions up to $\approx 65\%$. Then, the bimolecular chain coupling leads to deviation of the molar mass to the higher values as well as to the increase in polymer dispersity (Figure 2B). The final polymer, PEO₁₁₄-*b*-PNBA₂₆, was further characterized by diffusion-ordered NMR spectroscopy (DOSY, Figure 3), which revealed the same diffusion coefficient for each polymer peak, confirming the block-character for the synthesized copolymer.

For further irradiation studies, we used a diblock polymer of composition PEO₁₁₄-*b*-PNBA₂₆, that is, the polymer with the weight ratio of hydrophilic and hydrophobic blocks approximately 1:1. In water or PBS (pH = 7.4), this copolymer self-assembles by nanoprecipitation into the micelles with an average hydrodynamic diameter of 25 nm. Although we do not have direct proof of the micellar structure of nanoparticles, we will use henceforth the term “micelles” for the nanoparticles formed by the nanoprecipitation procedure. The formation of micelles for PEG-based block copolymers is widely reported in the literature, and therefore, our assumption is very realistic. The cmc of the block copolymer was measured

in PBS by fluorescence spectroscopy in the presence of pyrene (Figure S1, Supporting Information) and the obtained value ($\text{cmc} = 8.1 \text{ mg L}^{-1}$) was similar to the values previously reported for other block copolymers.^[24]

Irradiation of micellar solution with the mercury lamp led to the photo-triggered cleavage of the hydrophobic *o*-nitrobenzyl groups and hydrophilization of the whole polymer system. The *o*-nitrobenzyl ester decomposition can be followed by UV-vis spectroscopy, as its intensive absorption at 275 nm gradually drops upon irradiation, whereas the band at 326 nm appears, corresponding to the formed *o*-nitrosobenzaldehyde (Figure 4A).^[13] Therefore, absorption at 326 nm was used to compare the extent of UV-light triggered PNBA block degradation in water and PBS (Figure 4B), suggesting slightly faster degradation of micelles irradiated in pure water; however, this difference was not statistically significant ($p > 0.1$). Moreover, the reaction mixtures irradiated for 10 min were freeze-dried and analyzed by ^1H NMR

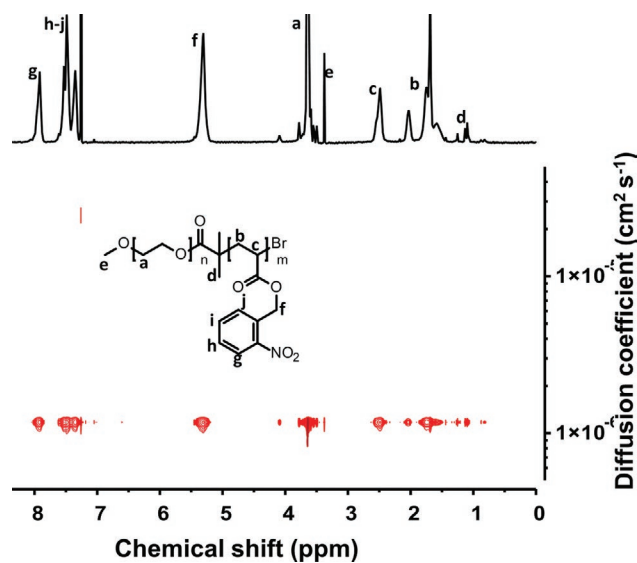


Figure 3. ^1H NMR (top) and DOSY (bottom) spectra of PEO₁₁₄-*b*-PNBA₂₆ in CDCl₃.

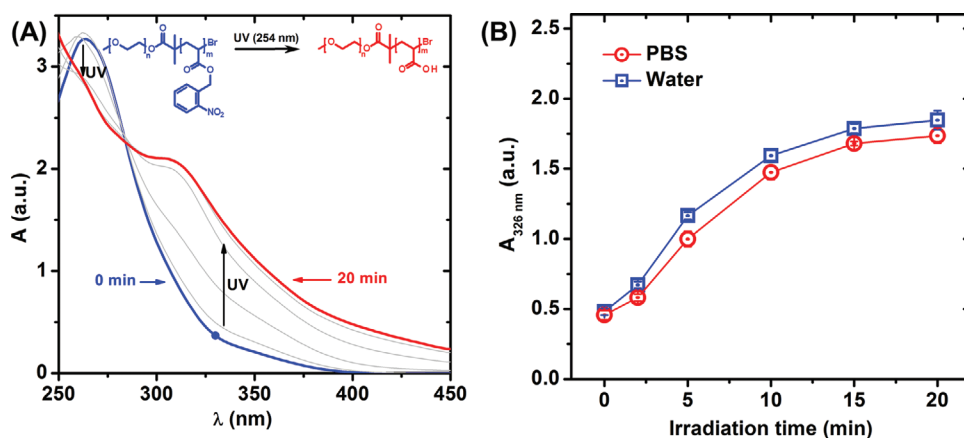


Figure 4. Absorption spectra measured following irradiation of PEO₁₁₄-*b*-PNBA₂₆ micelles in PBS ($c = 0.5 \text{ mg mL}^{-1}$) (A). The initial (blue line) and final (red line) spectra are highlighted. Dependence of polymer absorption at 326 nm on irradiation time (B).

spectroscopy (Figure 5). The spectrum of aromatic degradation products is relatively complex; however, the aldehyde signal at $\delta = 10.4 \text{ ppm}$ confirms the formation of *o*-nitrosobenzaldehyde. Furthermore, the degree of degradation was calculated from the decrease of the relative intensity of the aliphatic PNBA signals ($-\text{O}-\text{CH}_2-$, $\delta = 5.4 \text{ ppm}$) to the PEO signal at $\delta = 3.6 \text{ ppm}$ as 46.1% (micelles in PBS), respectively, 48.0% (micelles in pure water). It can be therefore concluded, that buffering the micelle solution does not have a significant effect on the rate of the *o*-nitrobenzyl group photocleavage.

The decomposition of the amphiphilic polymer micelles was studied by DLS, as well (Figures 6 and 7). The intensity of scattered light is the first intuitive parameter that someone should check if decomposition is expected due to the power law dependence of the scattered intensity of the size of a scattering object. Indeed, Figure 6A gives solid proof of the decomposition process that happens due to UV-light irradiation. With this finding in mind, we have inspected the distribution functions of hydrodynamic diameter at different irradiation times. At short irradiation times, the distribution function of PEO₁₁₄-*b*-PNBA₂₆ copolymer in water shows a monomodal peak with D_h around

25 nm (Figure 6B,C). This peak was attributed to micelles. With longer irradiation times, this peak is shifting to lower D_h , due to the micelle hydrophilization and disassembly. In the buffered solution, the D_h value dropped rapidly to $\approx 9 \text{ nm}$ and remained constant upon further irradiation. As the pH of the buffered solution after irradiation remained unchanged, the acrylic acid units were present in their anionic form, which leads to their hydrophilization and micelle disassembly.

On the other hand, micelles irradiated in pure water dissociate more gradually, leading to larger objects with D_h around 17 nm. This can be explained by the drop of the pH in the irradiated solutions to the values below the $\text{p}K_a$ of the acrylic acid units. This was experimentally confirmed by measurement of pH after 10 min (pH = 4.26), respectively 20 min (pH = 4.01) of irradiation. Low pH suppresses the dissociation of the poly(acrylic acid) block, which can form a polyplex with PEO blocks via hydrogen bonding. Similar behavior was observed in the mixtures of PEO and poly(acrylic acid) homopolymers.^[25] To prove this hypothesis, the pH of the micelle solution irradiated in pure water for 10 min, was adjusted to 7.4 by the addition of solid PBS. This resulted in the nanoparticle disassembly as observed by

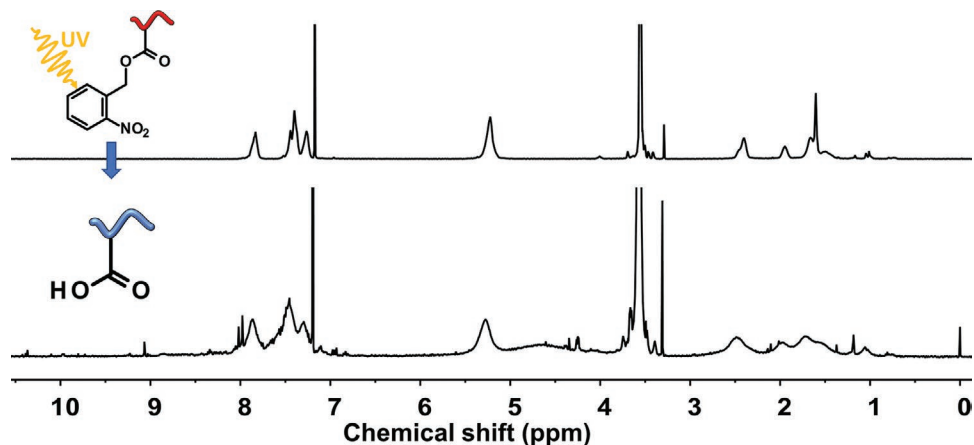


Figure 5. ¹H NMR spectra of PEO₁₁₄-*b*-PNBA₂₆ micelles before (top) and after (bottom) UV-irradiation in water for 10 min. Spectra measured in CDCl₃.

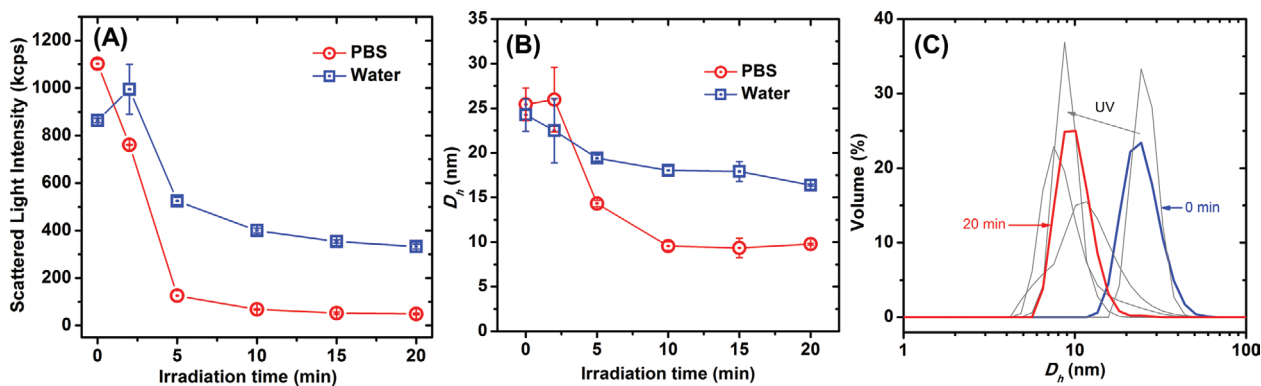


Figure 6. UV-light responsive degradation of the PEO₁₁₄-*b*-PNBA₂₆ micelles in water in PBS buffer. Dependence of the scattered light intensity (A) and hydrodynamic diameter (B) on the irradiation time. Hydrodynamic diameter distribution functions at different irradiation times in PBS (C).

DLS (a drop of D_h value from 18 to 8 nm, Figure 7). Surprisingly, the adjustment of pH to 7.4 in the sample irradiated for longer time (20 min) did not lead to the micelle disassembly, but to the larger objects with average D_h of 36 nm (Figure S3, Supporting Information). This can be explained by the UV-mediated crosslinking of the micelles irradiated in the assembled state for a longer time. Similar crosslinking of the nitrobenzyl groups was reported in the literature.^[26] Upon the pH adjustment, the repulsion of the charged acrylic acid units results in the nanoparticle swelling and size increase. To conclude, irradiation of PEO-*b*-PNBA micelles in pure water represents a complex system. It should be noted, however, that for the intended applications (stimuli-responsive drug delivery systems) micellar properties in buffered media (PBS) are relevant.

4. Conclusions

In summary, we report for the first time the synthesis of low-dispersity ($D = 1.10$) light-sensitive PEO-*b*-PNBA amphiphilic diblock copolymers by SET-LRP of NBA monomer initiated by PEO-containing macroinitiator. The screening of polym-

erization kinetics revealed a high propagation rate and short induction period even at room temperature. The prepared amphiphilic copolymer self-assembles in the aqueous conditions into the micelles with a hydrodynamic diameter of 25 nm. Upon irradiation with UV-light, these micelles gradually disassemble as the PNBA decomposes into the hydrophilic poly(acrylate) units. These properties, together with the robustness of the reported synthetic protocol, demonstrate the potential of these polymers for the construction of light-responsive drug delivery systems and UV-dosimeters with bimodal UV-absorption and light scattering output.

Supporting Information

Supporting Information is available from the Wiley Online Library or from the author.

Acknowledgements

This work was financially supported by the Ministry of Education, Youth and Sports of the Czech Republic (grant no. LM2015064 ERIC) and the Czech Grant Foundation (M.H., grant no. 18-07983S). O.S. and M.H. acknowledge the funding from the FWO (grant no. FWO-19-03) and European Union's Horizon 2020 research and innovation program under the Marie Skłodowska-Curie grant agreement no. 665501. S.K.F. acknowledges the financial support of the U.S.–Czech Republic Fulbright Commission.

Conflict of Interest

The authors declare no conflict of interest.

Keywords

amphiphilic block copolymers, nitrobenzyl acrylate, self-assembly, UV-responsive polymers

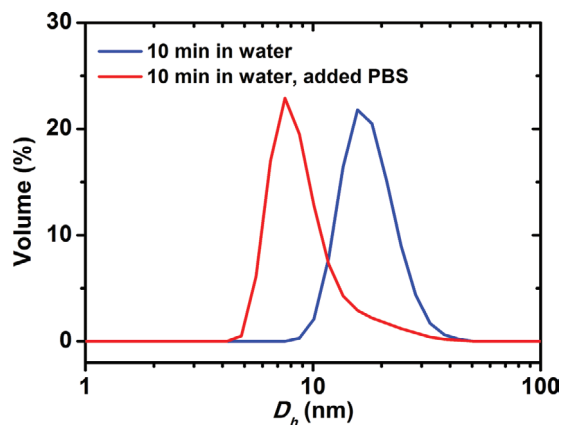


Figure 7. Hydrodynamic diameter distribution functions PEO₁₁₄-*b*-PNBA₂₆ micelles irradiated 10 min in water before (blue) and after (red) consequential addition of PBS.



- [1] G. S. Kwon, T. Okano, *Adv. Drug Delivery Rev.* **1996**, *21*, 107.
- [2] N. Rapoport, *Prog. Polym. Sci.* **2007**, *32*, 962.
- [3] M. Hrubý, S. K. Filippov, P. Štěpánek, *Eur. Polym. J.* **2015**, *65*, 82.
- [4] S. Filippov, M. Hrubý, C. E. R. Koňák, H. Macková, M. Špírková, P. Štěpánek, *Langmuir* **2008**, *24*, 9295.
- [5] A. Riabtseva, L. I. Kaberov, J. Kučka, A. Bogomolova, P. Stepanek, S. K. Filippov, M. Hruby, *Langmuir* **2017**, *33*, 764.
- [6] A. Bogomolova, L. Kaberov, O. Sedlacek, S. Filippov, P. Stepanek, V. Král, X. Wang, S. Liu, X. Ye, M. Hruby, *Eur. Polym. J.* **2016**, *84*, 54.
- [7] M. Hruby, S. K. Filippov, J. Panek, M. Novakova, H. Mackova, J. Kucka, D. Vetvicka, K. Ulbrich, *Macromol. Biosci.* **2010**, *10*, 916.
- [8] R. Laga, O. Janoušková, K. Ulbrich, R. Pola, J. Blažková, S. K. Filippov, T. S. Etrych, M. Pechar, *Biomacromolecules* **2015**, *16*, 2493.
- [9] S. K. Filippov, A. Bogomolova, L. Kaberov, N. Velychkivska, L. Starovoytova, Z. Cernochova, S. E. Rogers, W. M. Lau, V. V. Khutoryanskiy, M. T. Cook, *Langmuir* **2016**, *32*, 5314.
- [10] O. Sedlacek, K. Lava, B. Verbraeken, S. Kasmi, B. G. De Geest, R. Hoogenboom, *J. Am. Chem. Soc.* **2019**, *141*, 9617.
- [11] Y. Zhao, *Macromolecules* **2012**, *45*, 3647.
- [12] M. Huo, J. Yuan, L. Tao, Y. Wei, *Polym. Chem.* **2014**, *5*, 1519.
- [13] S. M. A. Soliman, C. Nouvel, J. Babin, J.-L. Six, *J. Polym. Sci., Part A: Polym. Chem.* **2014**, *52*, 2192.
- [14] J. Jiang, X. Tong, Y. Zhao, *J. Am. Chem. Soc.* **2005**, *127*, 8290.
- [15] J. Babin, M. Pelletier, M. Lepage, J.-F. Allard, D. Morris, Y. Zhao, *Angew. Chem., Int. Ed.* **2009**, *48*, 3329.
- [16] X. Jiang, C. A. Lavender, J. W. Woodcock, B. Zhao, *Macromolecules* **2008**, *41*, 2632.
- [17] H. Zhao, E. S. Sterner, E. B. Coughlin, P. Theato, *Macromolecules* **2012**, *45*, 1723.
- [18] J. Jiang, X. Tong, D. Morris, Y. Zhao, *Macromolecules* **2006**, *39*, 4633.
- [19] H. Huo, X. Ma, Y. Dong, F. Qu, *Eur. Polym. J.* **2017**, *87*, 331.
- [20] X. Jiang, S. Jin, Q. Zhong, M. D. Dadmun, B. Zhao, *Macromolecules* **2009**, *42*, 8468.
- [21] J.-M. Schumers, C.-A. Fustin, A. Can, R. Hoogenboom, U. S. Schubert, J.-F. Gohy, *J. Polym. Sci., Part A: Polym. Chem.* **2009**, *47*, 6504.
- [22] N. H. Nguyen, V. Percec, *J. Polym. Sci., Part A: Polym. Chem.* **2010**, *48*, 5109.
- [23] H. Gao, K. Matyjaszewski, *J. Am. Chem. Soc.* **2007**, *129*, 11828.
- [24] K. Kolouchova, O. Sedlacek, D. Jirak, D. Babuka, J. Blahut, J. Kotek, M. Vit, J. Trousil, R. Konefał, O. Janouskova, B. Podhorska, M. Slouf, M. Hruby, *Biomacromolecules* **2018**, *19*, 3515.
- [25] X. Yu, A. Tanaka, K. Tanaka, T. Tanaka, *J. Chem. Phys.* **1992**, *97*, 7805.
- [26] F. Guillier, D. Orain, M. Bradley, *Chem. Rev.* **2000**, *100*, 2091.



Supporting Information

for *Macromol. Chem. Phys.*, DOI: 10.1002/macp.201900238

SET-LRP Synthesis of Well-Defined Light-Responsible Block Copolymer Micelles

Ondrej Sedlacek,* Sergey K. Filippov, Pavel Svec, and Martin Hruby

Supplementary Information

SET-LRP synthesis of well-defined light-responsive block copolymer micelles

Ondrej Sedlacek,^{a,b*} Sergey K. Filippov,^{a,c} Pavel Svec^a and Martin Hruby^a

^aInstitute of Macromolecular Chemistry, v.v.i., Academy of Sciences of the Czech Republic, Heyrovsky Sq. 2, 162 06 Prague 6, Czech Republic

^bDepartment of Organic and Macromolecular Chemistry, Ghent University, Krijgslaan 281 S4, B-9000 Ghent, Belgium

^cSchool of Engineering and Applied Science, Harvard University, 9 Oxford St, Cambridge, MA 02138, USA

E-mail: sedlacek@imc.cas.cz

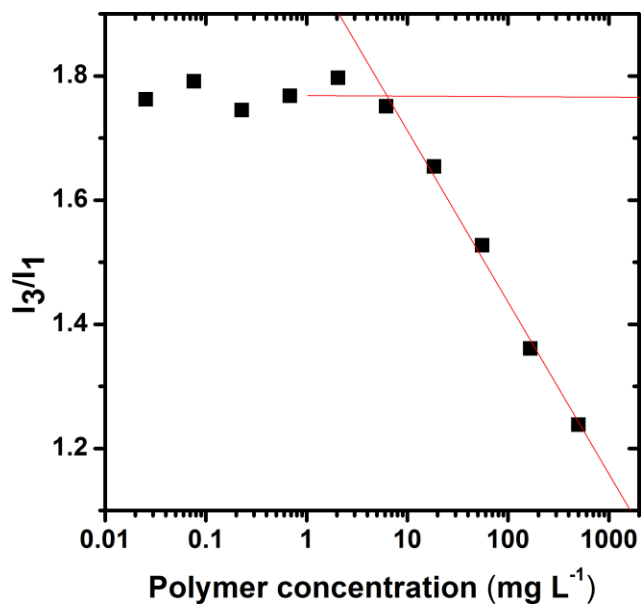


Figure S1. Dependence of the I_3/I_1 pyrene fluorescence ratio on the $\text{PEO}_{114}\text{-b-PNBA}_{26}$ copolymer concentration in PBS, used for the determination of critical micelle concentrations (cmc).

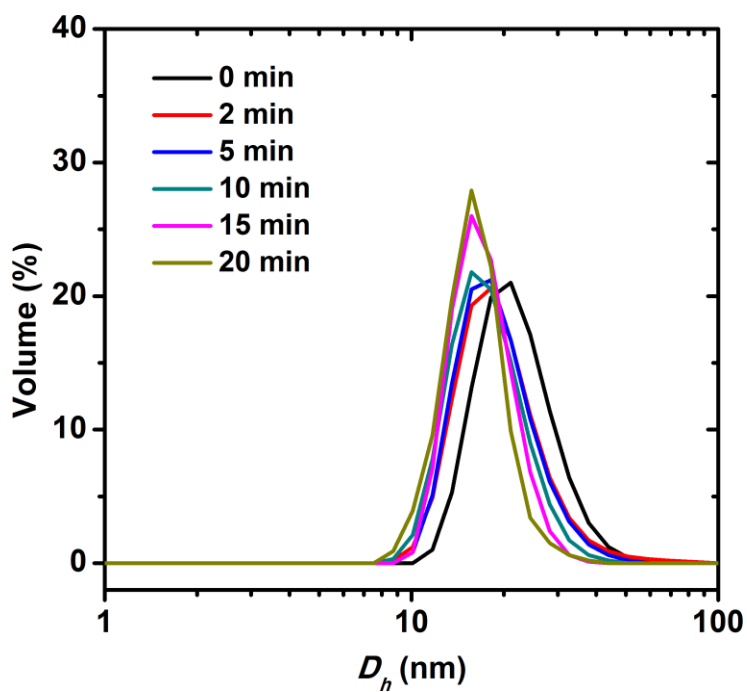


Figure S2. UV-light responsive degradation of the $\text{PEO}_{114}\text{-b-PNBA}_{26}$ micelles in water: Hydrodynamic diameter distribution functions at different irradiation times.

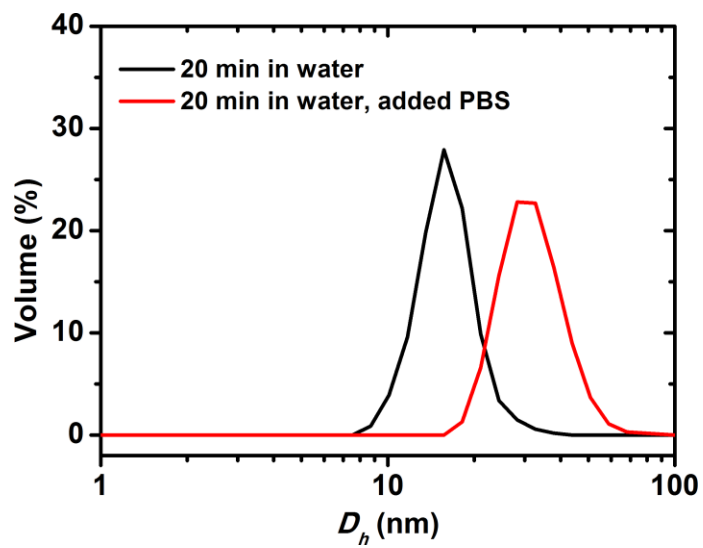


Figure S3. Hydrodynamic diameter distribution functions PEO₁₁₄-b-PNBA₂₆ micelles irradiated 20 min in water before (black) and after (red) consequential addition of PBS.

Appendix 3

Kolouchová, K.; Jiráček, D.; Groborz, O.; Sedláček, O.; Ziolkowska, N.; Vít, M.; Šticová, E.; Gálisová, A.; Švec, P.; Trousil, J.; Hájek, M.; Hrubý, M., Implant-forming polymeric ¹⁹F MRI-tracer with tunable dissolution. *J. Control. Release* **2020**, *327*, 50-60. **Times Cited: 21; IF = 9.78.**

P. Švec designed and performed the drug release experiments and assisted with writing the manuscript.



Implant-forming polymeric ^{19}F MRI-tracer with tunable dissolution

Kristyna Kolouchova^{a,b,1}, Daniel Jirak^{c,i,1,*}, Ondrej Groborz^{a,e,f,g}, Ondrej Sedlacek^h,
Natalia Ziolkowska^{c,f}, Martin Vit^{c,d}, Eva Sticova^c, Andrea Galisova^c, Pavel Svec^{a,b}, Jiri Trousil^a,
Milan Hajek^c, Martin Hruby^{a,*}

^a Institute of Macromolecular Chemistry CAS, Heyrovsky Square 2, 162 06 Prague 6, Czech Republic

^b Department of Physical and Macromolecular Chemistry, Faculty of Science, Charles University, Hlavova 8, Prague 2 128 00, Czech Republic

^c Department of Diagnostic and Interventional Radiology, Institute for Clinical and Experimental Medicine, Videnska 1958/9, 140 21 Prague 4, Czech Republic

^d Technical University of Liberec, Faculty of Mechatronics Informatics and Interdisciplinary Studies, Studentska 1402/2, 461 17 Liberec, Czech Republic

^e Department of Organic Chemistry, Charles University, Faculty of Science, Hlavova 8, 128 43 Prague 2, Czech Republic

^f Institute of Biophysics and Informatics, Charles University, First Faculty of Medicine, Salmovská 1, 120 00 Prague 2, Czech Republic

^g Institute of Organic Chemistry and Biochemistry, Czech Academy of Sciences, Flemingovo square 542/2, 162 06 Prague 6, Czech Republic

^h Department of Organic and Macromolecular Chemistry, Ghent University, Krijgslaan 281-S4, 9000 Ghent, Belgium

ⁱ Department of Science and Research, Faculty of Health Studies, Technical University of Liberec, Studentska 1402/2, 461 17 Liberec, Czech Republic



ARTICLE INFO

Keywords:

Polymer implant

^{19}F magnetic resonance imaging

Double-stimuli responsiveness

Tunable dissolution

ABSTRACT

Magnetic resonance imaging (MRI) using ^{19}F -based tracers has emerged as a promising multi-purpose noninvasive diagnostic tool and its application requires the use of various ^{19}F -based tracers for the intended diagnostic purpose. In this study, we report a series of double-stimuli-responsive polymers for use as injectable implants, which were designed to form implants under physiological conditions, and to subsequently dissolve with different dissolution rates ($t_{1/2}$ ranges from 30 to more than 250 days). Our polymers contain a high concentration of fluorine atoms, providing remarkable signal detectability, and both a hydrophilic monomer and a pH-responsive monomer that alter the biodistribution properties of the implant. The implant location and dissolution were observed using ^{19}F MRI, which allows the anatomic extent of the implant to be monitored. The dissolution kinetics and biocompatibility of these materials were thoroughly analyzed. No sign of toxicity *in vitro* or *in vivo* or pathology *in vivo* was observed, even in chronic administration. The clinical applicability of our polymers was further confirmed *via* imaging of a rat model by employing an instrument currently used in human medicine.

1. Introduction

Magnetic resonance imaging (MRI) is a commonly used noninvasive diagnostic tool in medicine and research. The vast majority of clinically used MRI scanners are ^1H MRI enabling the detection of the omnipresent water signal, thereby providing detailed anatomical and spatial information. ^{19}F MRI is a highly promising multi-purpose tool in the diagnostic field, because common MRI devices can be adjusted for the detection of ^{19}F nuclide by hardware modifications (as ^{19}F and ^1H have similar gyromagnetic ratios). A major benefit of ^{19}F MRI is, that there is only a negligible ^{19}F fluorine background in terms of ^{19}F MRI, which can be used to monitor the presence of a given tracer. The development of ^{19}F MRI and its availability has created a great demand for ^{19}F -based tracers. Many tracers have been developed and tested, yet most small-

molecule-based tracers frequently suffer from poor or very poor bio-distribution due to their hydrophobicity and lipophobicity [1]. Over the last few decades, ^{19}F MRI has become an important tool in many medical applications: [2] it can be used for cellular tracking [3–8], tumor diagnosis [9–12], metabolic studies [13], partial oxygen pressure determination [14,15], inflammation monitoring [16–18], and intra- / extracellular pH measurement [19].

In this study, we investigate stimuli-responsive polymers with a lower critical solution temperature (LCST) [20,21]. This means that below the a so-called cloud point temperature (T_{CP}), such polymers dissolve, e.g., in water, but above this temperature, they aggregate, forming rather lipophilic implants. Stimuli-responsive polymers were suggested to be used as drug-delivery systems for the controlled release of hydrophobic pharmaceuticals entrapped in the so called polymeric

* Corresponding author.

E-mail addresses: daji@ikem.cz (D. Jirak), mhruby@centrum.cz, hruby@imc.cas.cz (M. Hruby).

¹ Both authors equally contributed.

depots by noncovalent interactions [22,23] as well as for polymer-supported internal radiotherapy (brachytherapy), [24] immunoradiotherapy [25], injectable thermogelling tissue engineering scaffolds [26], or for cell cultivation purposes [27], due to the tendency to adhere to cells and the extracellular matrix [28,29]. If such an implant is based on a fluorinated material, ^{19}F MRI can be effectively used to detect and monitor its location and size, as has been reported in previous studies [22,23,25,30–43]. Such systems usually contain low concentration of fluorine and are designed for specific applications. Recently, an injectable fluorinated thermo- and pH-responsive polymer with high concentration of fluorine for use as a universal tracer for ^{19}F MRI was introduced in a communication study [44,45]. However, the *in vivo* dissolution of the reported polymer implant [44] under physiological conditions ranged from slow to virtually nonexistent, which compromises its possible biomedical applications.

In this paper, we describe a series of polymers, based on previously published tracers, for injectable implants with different dissolution rates under physiological conditions (with a biological half-life ranging from approximately 30 to more than 250 days in rats), overcoming the slow elimination of the previously described polymers. We have shown that different dissolution rates can be tailored by altering the polymer compositions to meet the demands of various applications. The mechanism of polymers' intended administration is illustrated in Fig. 1. At lower pH values of ≈ 5.0 (non-physiological, but biologically well tolerated) [46], these polymers dissolve readily in water; hence, their aqueous solution can be injected into the body. After the administration, the solution is exposed to the interstitial fluid within the tissue, which has a high buffer capacity [47,48]. Therefore, the pH rises very quickly to the physiological pH ≈ 7.4 , they form an implant due to aggregation, which can physically entrap (or dissolve in this separated phase) the co-administered drugs [31,49], forming the polymeric depot. The surrounding cells are exposed to the higher pH for only a short period of time. This is a major difference from previous studies, since they mostly used DMSO solutions of the polymer, which stays in the tissue for longer period of time and is then responsible for several side effects. Due to the chemical nature of our polymers (in aggregated form they are lipophilic and positively charged) they can be expected to accumulate lipophilic and/or negatively charged molecules rather well and release them slowly as we demonstrated with the *in vitro* drug release study. Moreover, it has been shown in similar pH responsive materials that if the pH in the certain tissue is lowered (e.g. tumor tissues tend to have pH ≈ 6 due to the Warburg effect [50] or in inflammations [51]), the solidified polymeric implant would dissolve and release the co-administered compound quickly (under the acidic conditions, their LCST is higher), while non-pathological tissues would be exposed to much lower concentrations of the drug (for a longer period of time) [21,31,52,53]. This property could potentially provide a

locally accelerated controlled release in acidic conditions in more specific applications.

The biocompatibility of the described polymers was studied *in vitro* and by *in vivo* chronic administrations, and their clinical applicability was further confirmed by ^{19}F and ^1H MR imaging in a rat model by employing a clinically used MR scanner. Finally, evaluation of the kinetic data revealed a relationship between physico-chemical properties, polymer composition, and *in vivo* biological half-life of the polymer. These data can be used to tailor properties of the polymer to meet the clinical demand.

Our newly reported polymeric system can, therefore, serve as an injectable implant with adjustable dissolution rates for variable applications. Dissolution of the polymer depot can be quantitatively monitored with ^{19}F MRI.

2. Materials and methods

2.1. Materials

2,2-Difluoroethylamine (97%) was purchased from FluorChem (Germany). Amphotericin B ($250\ \mu\text{g}\cdot\text{mL}^{-1}$), Dulbecco's modified Eagle's medium (DMEM, high glucose, GlutaMAX™), fetal bovine serum (FBS, heat-inactivated), penicillin-streptomycin-neomycin antibiotic mixture, Roswell Park Memorial Institute (RPMI) 1640 (ATCC modification), and TrypLE™ express enzyme were purchased from Life Technologies, Ltd. (Czech Republic). Isoflurane for anesthesia of the experimental animals was purchased (Baxter, Deerfield, United States). The Lewis rats (attested by Envigo+, Huntingdon, United Kingdom) were provided by AnLab s.r.o. (Czech Republic), and their feed (1324 mod. Velaz IRR - maintenance diet) was obtained from Velaz, Ltd. (Czech Republic). Normal human fibroblasts from stomach/intestine Hs 738.St/Int and normal human epithelial cells from lungs BEAS-2B were purchased from American Type Culture Collection (USA). The murine monocyte-macrophage cell line J774A.1 and all the remaining chemicals were purchased from Sigma-Aldrich (Czech Republic).

2.2. Methods

2.2.1. Synthesis of monomers

N-(2,2-Difluoroethyl)acrylamide (DFEAM) was synthesized as previously described by the reaction of acryloyl chloride with 2,2-difluoroethylamine in the presence of triethylamine (TEA) [54]. *N*-[3-(1*H*-imidazol-1-yl)propyl]acrylamide (ImpPAM) was synthesized by the reaction of acryloyl chloride with 3-(1*H*-imidazol-1-yl)propan-1-amine as previously described [44].

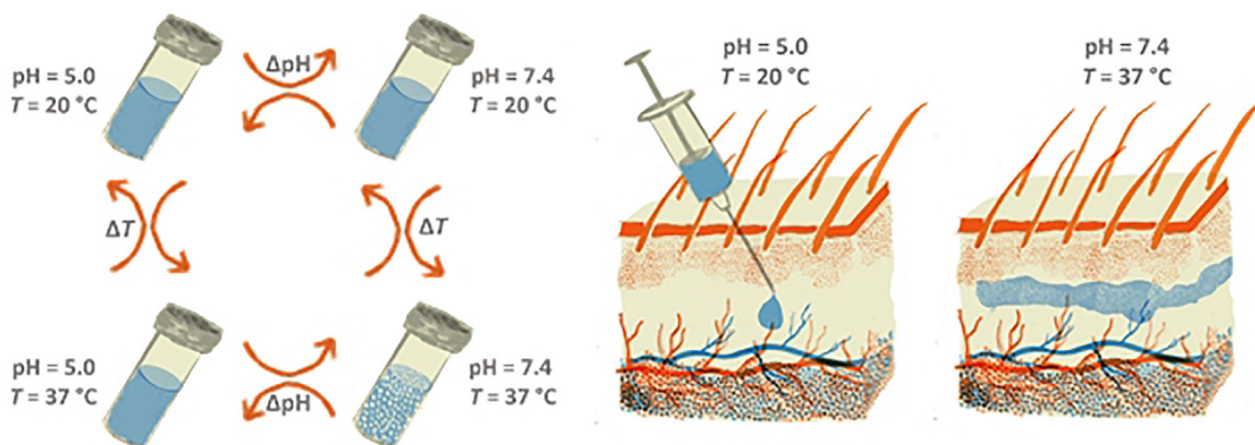
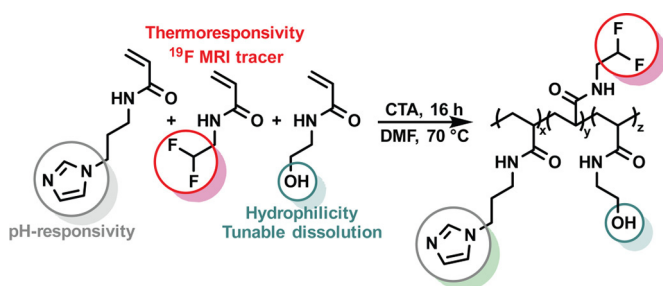


Fig. 1. (Left) Illustration of the pH-dependent LCST behavior of the proposed polymers (Right) Schematic illustration of ^{19}F MRI contrast implant formation.



Scheme 1. Structure and synthesis of multiresponsive fluorinated P(DFEAM-ImPAM-HEAM) copolymers F1-F5. Polymer chain-end groups were omitted for clarity.

2.2.2. Synthesis of polymers

Copolymers poly{*N*-(2,2-difluoroethyl)acrylamide-co-*N*-[3-(1*H*-imidazol-1-yl)propyl]acrylamide-co-*N*-(2-hydroxyethyl)acrylamide} (P(DFEAM-ImPAM-HEAM)) F1-F5 were prepared by reversible addition-fragmentation chain transfer (RAFT) copolymerization with 4-cyano-4-(dodecylsulfanylthiocarbonyl)sulfanyl]pentanoic acid as the chain transfer agent (CTA) (Scheme 1). The polymerization mixture consisting of the monomers *N*-(2-hydroxypropyl)methacrylamide, *N*-[3-(1*H*-imidazol-1-yl)propyl]acrylamide and *N*-(2-hydroxyethyl)acrylamide (initial monomer ratios and amounts are shown in Table S1), the CTA (8.5 mg, 23.4 μmol) and AIBN (1.0 mg, 6.2 μmol) in DMF (4 mL) was purged with argon in a dried Schlenk flask and polymerized overnight in an oil bath heated to 70 °C. Afterward, the resulting copolymers were precipitated into diethyl ether and purified by gel filtration using a Sephadex LH-20 column with methanol as eluent. The solvent was removed under reduced pressure, and the polymers (F1-F5) were isolated by freeze-drying (yields 65–74%, Table S1) as off-white powders.

2.2.3. Size exclusion chromatography (SEC)

The number-average molecular weight (M_n), weight-average molecular weight (M_w) and polymer dispersity ($\bar{D} = M_w/M_n$) were analyzed by SEC using an HPLC Ultimate 3000 system (Dionex, Sunnyvale, USA) equipped with an SEC column (TSKgel SuperAW3000 150 \times 6 mm, 4 μm). Three detectors, UV/VIS, refractive index (RI) Optilab®-rEX and multiangle light scattering (MALS) DAWN EOS (Wyatt Technology Co., USA), were employed with a methanol and sodium acetate buffer (0.3 M, pH 6.5) mixture (80:20 v/v, flow rate of 0.6 mL·min⁻¹) as the mobile phase (Fig. S1).

2.2.4. NMR spectroscopy

Each polymer (10 mg) was dissolved in DMSO-*d*₆ (550 μL). ¹H NMR spectra ($D_1 = 30.00$ s, $NS = 32$, Fig. S2 and S3) and HSQC-edited spectra ($D_1 = 1.5$ s, $NS = 2$, $TD = 2048$ for H and 256 for C, Fig. S4). Each polymer (15.0 mg) was dissolved in fetal bovine serum (150 μL), ECM gel (150 μL), phosphate-buffered saline solution (40 mM, 150 μL , pH = 7.4) and phosphate-buffered saline solution (40 mM) with its pH adjusted to 5.0 by the addition of hydrochloric acid. The solution was placed inside a coaxial NMR tube insert (3.00 mm outer diameter, 1.84 mm inner diameter), and the insert was placed inside a standard 5.00 mm NMR tube filled with D₂O (200 μL), potassium carbonate (6.3 mg, 46 μmol) and trifluoroacetic acid (6.0 μL , 8.9 mg, 78 μmol). Then, ¹⁹F NMR ($D_1 = 8.00$ s, $NS = 64$) spectra of each sample were measured at both 20.0 °C and 37.0 °C. The integral ratio of the polymer peak and trifluoroacetate peak, as well as the height of the polymer peak at both temperatures, was evaluated. All spectra were acquired with a Bruker Advance III 400 MHz (Bruker, Rheinstetten, Germany) equipped with a broad-band probe.

2.2.5. Turbidity measurements

The cloud point temperature (T_{CP}) was indicated by a decrease in sample transmittance below 90 % (Fig. S7). The polymer was dissolved

in 150 mM phosphate buffer or 150 mM sodium acetate buffer at a polymer concentration of 5.0 mg·mL⁻¹. The transmittance was measured at $\lambda = 600$ nm with a Thermo Scientific Evolution 220 UV/VIS spectrophotometer equipped with a Thermo Scientific single cell Peltier element (Thermo-Fisher, Waltham, USA). The temperature increments were 0.1 °C, and the samples were stirred at 700 rpm.

2.2.6. Cytotoxicity assay

J774A.1 and Hs 738. St/Int cells were grown in full DMEM containing 10% FBS, 50 $\mu\text{g/mL}$ penicillin, 50 $\mu\text{g/mL}$ streptomycin, 100 $\mu\text{g/mL}$ neomycin, and 2.5 $\mu\text{g/mL}$ amphotericin B in a humidified atmosphere containing 5% CO₂ at 37 °C. BEAS-2B cells were grown in full RPMI containing 10% FBS, 50 $\mu\text{g/mL}$ penicillin, 50 $\mu\text{g/mL}$ streptomycin, 100 $\mu\text{g/mL}$ neomycin, and 2.5 $\mu\text{g/mL}$ amphotericin B in a humidified atmosphere containing 5% CO₂ at 37 °C. For subculturing, J774A.1 cells were detached using a cell scraper; Hs 738.St/Int and BEAS-2B cells were detached using TrypLE™ express enzyme. The cytotoxicities of the copolymers were assessed via an MTT assay using J774A.1, Hs 738.St/Int, and BEAS-2B cells. The cells were seeded in 96-well plates at a concentration of 1·10⁴ cells/well and left to incubate overnight. For the assays, the F1-F5 copolymers were directly dissolved in the culture medium (DMEM or RPMI). The cell culture medium was replaced with 100 μL of fresh culture medium (DMEM or RPMI) containing the formulations to be tested. After 24 h of incubation, the medium was aspirated, and the cells were incubated with complete culture medium containing MTT reagent (0.5 mg·mL⁻¹) for 3–4 h. The MTT solution was subsequently aspirated before adding 100 μL of DMSO. A Sunrise microplate reader (Tecan Group Ltd., Switzerland) was used to assess cell viability via spectrophotometry at 570 nm. The results of the MTT assay are expressed as the percentage of the control value (obtained from cells in the control medium). A reduction in cell viability by more than 30% is considered a cytotoxic effect, according to ISO 10993-5. The testing consisted of at least three experiments. The results are shown in Fig. S8.

2.2.7. MRS and MRI phantom measurement (in vitro)

All *in vitro* MRS and MRI experiments were performed using a custom-made dual ¹H/¹⁹F surface single-loop circular radiofrequency (RF) coil with a diameter of 4 cm optimized for rat experiments on a 4.7 T scanner (Bruker BioSpec, Ettlingen, Germany). The coil was designed to allow an on-machine tuning and matching at the ¹H and ¹⁹F Larmor frequencies.

Phantoms (0.5 mL Eppendorf tubes with aqueous solution of F3 polymer, polymer concentration $c_{\text{pol}} = 100, 50, 25, 12.5, 6.25, 3.13, 1.56$ and 0.00 mg·mL⁻¹) in 40 mM phosphate-buffered saline (pH = 7.4) at 37 °C were used for setting the ¹H Larmor frequency of water and ¹⁹F frequency of the polymer (200,486 \pm 1 kHz and 188,620 \pm 1 kHz, respectively). The phantom was subsequently used for optimization of the excitation block-pulse width. Afterwards, a MRS single-pulse sequence was used to measure the MRS spectrum (repetition time $TR = 1000$ ms; number of averaging $NA = 64$; total scanning time $TA = 1$ min 8 s). The dependency of acquired signal as a function of concentration can be seen in Figs. 3 and S13. After the spectroscopy experiments, Rapid Acquisition with Relaxation Enhancement (RARE) [55] sequence was employed to acquire ¹H and ¹⁹F MR images. The images were processed with ParaVision 4 (Bruker, Billerica, USA) and fused in ImageJ 1.48 (National Institutes of Health, Bethesda, USA) and are presented in Fig. 3.

¹H MRI: $TR = 3000$ ms; echo time $TE = 36$ ms; turbo factor $TF = 8$; $NA = 2$; spatial resolution 0.25 \times 0.25 \times 1.5 mm; field of view 65 \times 65 mm, digital matrix 256 \times 256, number of slices 15 (longitudinal axis), $TA = 2$ min 24 s.

¹⁹F MRI: $TR = 500$ ms; $TE = 43.5$ ms; $TF = 4$; $NA = 512$; spatial resolution 0.94 \times 0.94 \times 5.0 mm; field of view 60 \times 60 mm; digital matrix 64 \times 64, number of slices 3 (longitudinal axis); $TA = 17$ min 4 s.

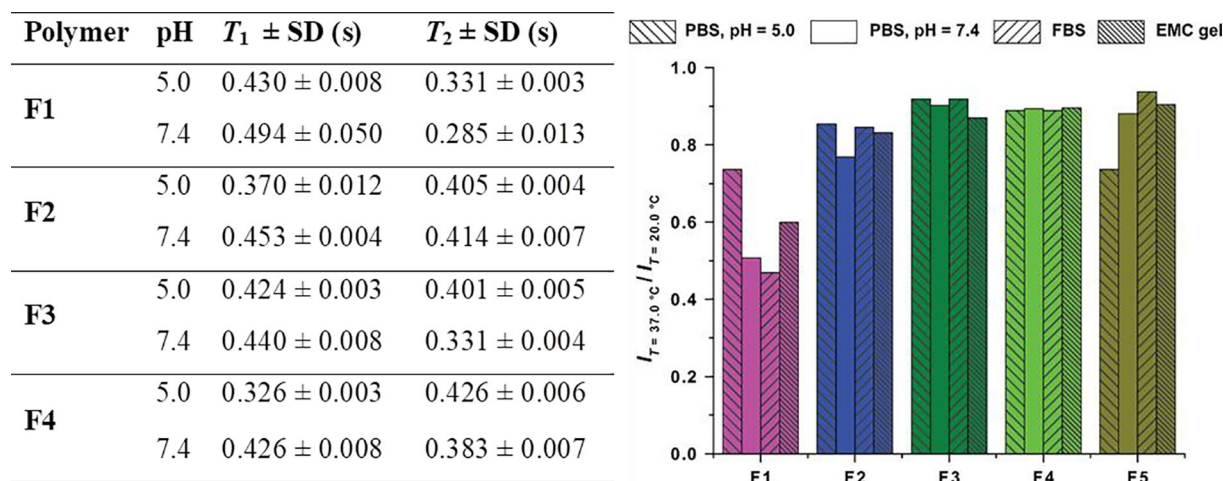


Fig. 2. Left: Summary of the relaxation times for F1-F4 under a 4.7 T field at 37.0 °C (mean value \pm SD based on the fitting residue). Right: Relative ^{19}F signal amplitude in buffer with pH 5.0 or 7.4 or in FBS or EMC gel after a change in temperature from 20.0 °C to 37.0 °C.

2.2.8. ^{19}F MR relaxations (in vitro study)

Relaxation times for *in vivo* experiments were assessed using the ^{19}F MRS performed at 4.7 T MRI scanner. The T_1 and T_2 relaxation times were assessed for polymers F1, F2, F3, and F4 using a non-localized saturation recovery [56] and Carr-Purcell-Meiboom-Gill (CPMG) [57] sequences, respectively. The polymer sample solution ($c_{\text{pol}} = 100 \text{ mg}\cdot\text{mL}^{-1}$ in 40 mM phosphate-buffered saline solution, the pH was adjusted to 5.0 or 7.4 with an addition of concentrated hydrochloric acid) was placed inside a 0.5 mL Eppendorf tube and measured at 25.0 or 37.0 °C.

Saturation recovery (for T_1): single square pulse; flip angle 90°; bandwidth: 25 kHz; $TR = 64, 96, 128, 184, 256, 384, 512, 740, 1024, 2048, \text{ and } 4096 \text{ ms}$.

CPMG sequence (for T_2): TE ranged from 7.2 ms to 1440 ms, increment 7.2 ms (200 echoes in total). Only data from $TE = 7.2$ to 720 were used to calculate the T_2 . The data was fitted with corresponding functions using Origin 8.0 (OriginLab, Northampton, USA). The T_1 and T_2 relaxation times are shown in Fig. 2.

2.2.9. In vivo experiments

All animal experiments described in this manuscript were performed in accordance with the Protection of Animals Against Cruelty Act (No. 359/2012) of the Czech Republic, which fully corresponds with European Union directives, and were approved by IKEM's ethics committee as stipulated in the legislation above. All animals were kept in a conventional breeding facility under a 12/12 h light cycle regimen with free access to water and pelleted food.

Healthy male Lewis rats (5 months old, $n = 15$, AnLab, Czech Republic) were divided into 4 groups based on the administration of different copolymers (control group: $n = 4$, F1: $n = 3$, F2: $n = 4$, F3: $n = 4$, F4: $n = 4$). Polymer implants were injected into the muscle of the left hind leg and the subcutaneous area of the right hind leg (in MRI perspective) ($200 \mu\text{L}$, $c_{\text{pol}} = 100 \text{ mg}\cdot\text{mL}^{-1}$ in 40 mM phosphate-buffered saline, the pH was adjusted to 5.0 by the addition of concentrated hydrochloric acid) under anesthesia using isoflurane (3% for induction, 0.8–1.5% for maintenance). The respiratory function during anesthesia was monitored with a trigger unit (Rapid Biomedical, Berlin, Germany). Animals weight was monitored, and blood samples were collected from two rats from each group using a catheter administered into the tail vein. The blood samples were left to clot at room temperature for 20 min and then centrifuged (6000 rpm, 10 min); the resulting serum was then removed. Before examination, using a DRI-CHEM 500 (Fujifilm, Tokyo, Japan) with original testing slides, serum was stored at -20°C . The activities of alanine aminotransferase (ALT) and aspartate aminotransferase (AST) and the concentrations of bilirubin,

creatinine and albumin in this serum were assessed. The results are shown in Fig. S9.

2.2.10. MRI and MRS experiments (in vivo)

Long-term *in vivo* MRI experiments were performed with the same 4.7 T scanner and RF coil as was used in the phantom study. Animals were scanned over the course of 9 months with the following procedure.

Firstly, the tested animal was placed into the MR scanner. A phantom containing an aqueous solution of the same polymer as the one implanted into the animal's leg was placed between its hind legs ($c_{\text{pol}} = 100 \text{ mg}\cdot\text{mL}^{-1}$, $200 \mu\text{L}$, pH = 5.0). A single-pulse MRS experiment with the same parameters as the ones used the *in vitro* was conducted. The phantom was used to set the ^1H and ^{19}F frequencies at the given local field and to determine the 90° and 180° pulse width. Next the phantom was removed without moving the animal and the same MRS sequence was repeated to quantify the signal of the polymer within the implant formed in the body.

If a ^{19}F signal was detected within the animal implant during the MRS experiment, a MRI experiment was conducted to provide anatomical details of the implant location, to visualize the implant size, volume and its signal. The visualization encompassed acquisitions of both ^1H MRI in 3 anatomical axes and ^{19}F MRI in transversal axis using a RARE sequence (with the same parameters as used for *in vitro* experiments). The results of both MRS and MRI data were used for quantification of the implant dissolution by means of signal decrease and volume decrease (for details see the chapter 2.2.12. *Pharmacokinetics*, Fig. 3, Table S2, S3, S4, S5 and S6).

One rat was scanned with a 3 T Tim Trio clinical scanner (Siemens Medical Solutions, Erlangen, Germany) intended for use in human medicine (Fig. 6). The ^1H and ^{19}F frequencies were set using aqueous solution of polymer F3 (123,258 and 115,963 kHz, respectively). The phantom and rat were scanned 24 h after the administration of the F3 polymer ($200 \mu\text{L}$, $c_{\text{pol}} = 100 \text{ mg}\cdot\text{mL}^{-1}$) into the muscle of the right hind leg in a whole-body clinical system with a dedicated ^{19}F transmit/receive birdcage coil for rodents (MRI. TOOLS GmbH, Berlin, Germany).

For precise localization, T_2 -weighted proton ^1H MR images were acquired (turbo spin-echo sequence, animal imaging: $TR = 3000 \text{ ms}$, $TE = 34 \text{ ms}$, $TF = 16$, $NA = 4$; $TA = 2 \text{ min } 33 \text{ s}$, field of view $63.75 \times 80 \text{ mm}$; digital matrix 204×256 ; number of slices 7; spatial resolution: $0.32 \times 0.32 \times 3.0 \text{ mm}$).

^{19}F MR spectroscopy was performed in 3 T scanner using a single block pulse sequence ($TR = 1500 \text{ ms}$), and imaging was performed using a fast low-angle shot (FLASH) [58] gradient sequence

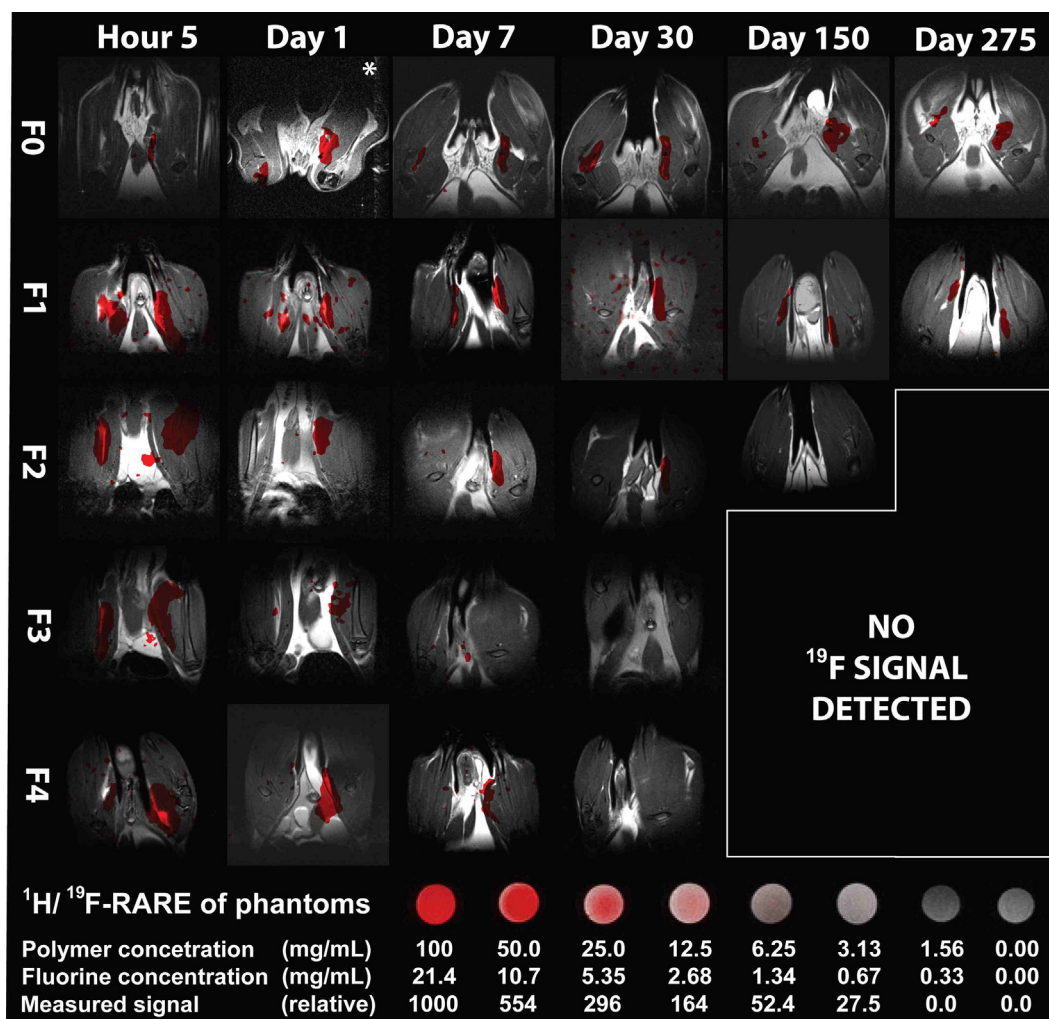


Fig. 3. Top: Merged ^1H and ^{19}F MR images of rats injected with fluorinated polymers. Images were acquired at (from left) 5 h, 1 day, 7 days, 1 month and 9 months after administration. Images of F0 were from a previous study [44] and were acquired with the same procedure. Image (*) from day 1 was not available, and an image from day 4 was used instead. Because of the lack of a detectable ^{19}F signal, *in vivo* experiments for F3 and F4 were discontinued after 1 month, and those for F2 were discontinued after 5 months. Bottom: Phantoms with a decreasing concentration of F3 polymer in 40 mM PBS (pH 7.4), merged $^1\text{H}/^{19}\text{F}$ -RARE images (17 min acquisition) subjected to the same processing procedure as those from the *in vivo* experiments, and relative measured signals used as a reference.

($TR = 500$ ms, $TE = 3.8$ ms, $NA = 64$; number of slices 3; digital matrix 30×32 ; field of view 75×80 mm; spatial resolution $2.5 \times 2.5 \times 8$ mm, flip angle 30° , $TA = 17$ min 4 s).

All MR images used for quantification were post-processed using a sine-squared filter implemented in ParaVision 4 (Bruker, Billerica, USA) on a 4.7 T scanner console with the same weight. The volume and mean intensity of the implant were assessed from the ^{19}F MR images using ImageJ 1.48 (National Institutes of Health, Bethesda, USA).

2.2.11. Histological examination

At the end of the imaging experiments, animals were sacrificed; the sites of injection for rat in the F1 and F2 groups (those injected with polymer F1 and F2, respectively) were visually inspected for any pathology, and their liver, spleen, kidneys, injected muscle, and contralateral muscle were excised for histological examination. Tissues were fixed in 10% buffered formaldehyde for 2 days and then embedded in paraffin, after which 5-mm thick sections were stained according to standard hematoxylin & eosin and Verhoeff-van Gieson staining procedures. The results are shown in Fig. S10.

2.2.12. Pharmacokinetics

Using ^{19}F MRI, the signal integral of the polymer and the volume of the implant formed in muscle and subcutaneously were measured as a

function of time.

$$I_{\text{SNR}} = 0.655 \cdot \frac{S}{\sigma_S} \quad (1)$$

I_{SNR} is the signal integral of the ^{19}F signal with the normalized noise level, S is the mean signal integral in the region of interest, σ_S is the standard deviation of the background noise, and the constant 0.655 reflects the Rician distribution of background noise in a magnitude MR image [59].

The observed implant-dissolution kinetics were characterized by parameter A , which is a ratio of the signal integral (or implant volume) observed immediately after the administration and the signal intensity (or implant volume) after period t_1 (from when the dissolution follows the 1st order kinetics). Lastly, the signal integral (or implant volume) were fitted with Formulas 2 and 3 (SD-weighted fit; outlier values were excluded) using Origin 8.0 (OriginLab, Northampton, USA).

$$I_{\text{SNR},t} = F_I \cdot e^{-k_{e,I} \cdot t} \quad (2)$$

$$V_t = F_V \cdot e^{-k_{e,V} \cdot t} \quad (3)$$

where I_t and V_t are the signal integral and implant volume, respectively, as a function of time, F_I and F_V are the corresponding normalization factors, $k_{e,I}$ and $k_{e,V}$ are the elimination constants for signal intensity

and implant volume, respectively, and t is the time after administration. The results are shown in Tables 2 and 3.

The biological half-lives were calculated with Formula 4.

$$t_{1/2} = \frac{\ln(2)}{k_e} \quad (4)$$

where k_e represents any elimination constant. Finally, the parameter A was calculated based on signal integral (A_{MRS} or A_{MRI}) and volume (A_V) based on MRS or MRI data.

$$A_{\text{MRS}} = \frac{F_I}{I_0} \quad (5)$$

$$A_V = \frac{F_V}{V_0} \quad (6)$$

where I_0 and V_0 are signal integral and implant volume detected after the administration, respectively.

2.2.13. Drug release (DR)

The stock solution of dexamethasone was prepared by sonicating dexamethasone (10 mg) in PBS (25 mL) at 40 °C for 30 min. After that, the resulting suspension was centrifuged to remove the undissolved dexamethasone (solubility approx. 80 mg·L⁻¹) and the supernatant (1.000 mL) was transferred to an Eppendorf tube containing polymer F1 or F4 (50 mg, experiments run in duplicates). The polymer was subsequently dissolved by sonication in an ice/water bath and subsequent vortexing. The cooled polymer solution containing dexamethasone was quickly transferred into a minidialysis kit (Float-A-lyzer G2–1 mL, 300 kDa) and the minidialysis kit was immersed into a 50 mL centrifugation tube containing pre-heated PBS (25 mL, 37 °C) and a magnetic stir bar. The solution (150 µL) at the outer side of the dialysis membrane was taken by a pipette at specific time-points for determination of the released amount of dexamethasone by UV HPLC. HPLC Gradient: Phase A: 95% water, 5% ACN, 0.1% TFA, Phase B: 5% water, 95% ACN, 0.1% TFA, $t = 0$ min – 20% B, 0.5 mL·min⁻¹; $t = 0.1$ min – 20% B, 3.5 mL·min⁻¹; $t = 2.25$ min – 60% B, 3.5 mL·min⁻¹ (linear gradient); $t = 2.5$ min – 90% B, 3.5 mL·min⁻¹ (linear gradient); $t = 3.0$ min – 90% B, 3.5 mL·min⁻¹; $t = 3.3$ min – 20% B, 3.5 mL·min⁻¹ (linear gradient); $t = 4.0$ min – 20% B, 3.5 mL·min⁻¹.

The data was subsequently fitted with the Formula (7).

$$x_{\text{dex},t} = \frac{Ae^{-k_A \cdot t} + Be^{-k_B \cdot t}}{c_{\text{dex,max}}} \cdot 100\% \quad (7)$$

Where $x_{\text{dex},t}$ is the fraction of the released drug (described in %), $c_{\text{dex,max}}$ is the maximal concentration of the dexamethasone in the control experiment; A and B are coefficients that describe the drug binding, and k_A and k_B are kinetics constant of non-bound drug release (k_A) and polymer-bound drug release (k_B).

3. Result and discussion

3.1. Synthesis of polymers and characterization

P(DFEAM-ImPAM-HEAM) multiresponsive fluorinated copolymers were prepared by the reversible addition and fragmentation transfer (RAFT) statistical copolymerizations of the corresponding monomers with 4-cyano-4-[(dodecylsulfanylthiocarbonyl)sulfanyl]pentanoic acid as the chain transfer agent (CTA) (Scheme 1). While the *N*-(2,2-difluoroethyl)acrylamide units endowed the copolymers with ¹⁹F MRI contrast and LCST properties, the pendant imidazole moieties ensured their pH-responsive character. Finally, the *N*-(2-hydroxyethyl)acrylamide units were used to modulate the polymer hydrophilicity. The copolymers were prepared in five different monomer unit ratios (Table 1) to develop tracers with variable *in vivo* dissolution rates. All copolymers had a narrow molecular mass distribution (dispersity $D \leq 1.20$), and their molar mass was approximately 40 kDa, which is

below the renal filtration threshold [60]. This property, together with the positive charge of the polymer, allows the renal elimination of the polymer from the body after implant dissolution [60]. Polymers with LCST properties have often been shown to be eliminated by kidneys and bile even if the LCST of the given polymer was well below body temperature due to equilibration between the phase-separated and dissolved phase [61].

¹H NMR spectroscopy was used for composition determination (Fig. S2 and S3). The monomeric composition was calculated from the integrals of the corresponding signals in the ¹H NMR spectrum of each monomer: PDFEA (CHF₂ moiety, $\delta = 5.9$), imidazole-containing monomer (aromatic CH moiety, $\delta = 6.9$), and HEAM (OH moiety, $\delta = 4.6$) (Table 1). HSQC-edited spectra were used for signal assignment (Fig. S4); ¹⁹F NMR spectra were used for purity confirmation (Fig. S5 and S6).

The pH- and thermoresponsive behavior of the polymers was analyzed by turbidimetry (Fig. S7) based on a temperature-dependent change in the sample transmittance in PBS buffer (pH = 7.4) and acetate buffer (pH = 5.0). The polymers were optimized to exhibit the maximum difference in T_{CP} (Table 1) under physiological versus acidic conditions, which is beneficial for the intended application. The polymers were designed to dissolve at pH 5.0, at which the T_{CP} value of the copolymer needs to be well above body temperature to prevent obstruction of the needle by polymer aggregates during administration into the body. [62] On the other hand, the T_{CP} needs to be below the body temperature at pH 7.4 to enable the rapid formation of the implant. The polymers that exhibit T_{CP} values within the required range are copolymers F1, F2, and F3. Even though F3 precipitates at ≈ 37 °C at pH 7.4, this temperature is too close to body temperature (36.5 °C in rats [63]) to guarantee the formation of a sufficiently stable implant. As the content of the hydrophilic *N*-(2-hydroxyethyl) acrylamide monomeric unit increased, T_{CP} was observed to increase, in accordance with the general trend observed for LCST copolymers [52,64], due to the pronounced hydration of the polymeric chains. The most hydrophilic copolymers (F4, F5) exhibited LCST behavior within a temperature range far above the body temperature and were therefore not suitable as injectable implants. For the biological evaluation, we therefore focused mostly on polymers F1, F2, F3, and F4. Polymer F4 is used as a reference material expected to have the fastest dissolution rate.

3.2. *In vitro* ¹⁹F NMR spectroscopy and relaxation properties

These tracers have relatively unique chemical shift (–124 ppm), which allows a parallel use of ‘traditional’ perfluorocarbon tracers if needed (they usually have shifts from –80 ppm to –70 ppm). Their T_1 and T_2 relaxation times were measured with a 4.7 T MRI scanner at 37.0 °C and pH 5.0 and 7.4, respectively, because these parameters are essential for the choice of the MRI sequence (Fig. 2). Both T_1 and T_2 for the given magnetic field (4.7 T) were approximately in range 380 ± 50 ms (they were equal within the margin of the experimental error) for all polymers in both the non-aggregated (pH = 5.0) and aggregated forms (pH = 7.4), which enables the use of the most common MRI sequences [30]. In spite of the fact that T_2 cannot be longer than T_1 , the resulting relaxations in the case of copolymer F2 and pH 5.0, where $T_2 > T_1$ corresponds to the experimental error. Interestingly, there was a relatively minor difference between the relaxation times with the change of the pH, indicating that the aggregation has only a minor effect on the observable relaxation times of our polymers.

The effect of polymer aggregation on its signal was investigated further with 400 MHz NMR (9.4 T). The ¹⁹F NMR signal was measured in PBS (pH 5.0 and 7.4), FBS or EMC gel at 20.0 °C and 37.0 °C. Trifluoroacetate solution inside a coaxial insert was used as a reference in each measurement. The integrals and amplitudes of the polymer signals at different conditions were compared. The temperature increase to body temperature had a negligible effect on the overall measured signal integral (Fig. 2). However, the increased temperature

Table 1
The composition and physicochemical properties of the prepared polymers.

Polymer	Polymer composition ^a (mol. %)			Fluorine content (wt%)	M_w (kDa) ^b	(M_w/M_n)	T_{CP} (°C) ^c	
	DFEAM	ImPAM	HEAM				pH 7.4	pH 5.0
F0 [44]	92	8	0	25.8	41.9	1.10	22	43
F1	88	7	5	24.8	37.8	1.12	27	60
F2	84	8	8	23.6	37.9	1.09	31	71
F3	76	9	15	21.4	32.8	1.19	37	> 85 ^d
F4	70	9	21	20.2	43.7	1.05	54	(85) ^d
F5	58	9	33	16.3	47.4	1.09	(67) ^d	(85) ^d

Determined by ¹H NMR spectroscopy^a, SEC^b or turbidimetry^c. Inaccurate data^d.

caused a signal broadening and amplitude decrease (most pronounced in F1 and F2; Fig. 2, Fig. S5 and S6). As our polymers have a high T_{CP} under acidic pH, the signal broadening was also significantly smaller. Lastly, the presence of naturally occurring proteins in biological media (FBS and EMC gel) did not cause additional signal broadening above T_{CP} and the broadening was similar to buffer solutions. The general ¹⁹F NMR behavior of this system is similar to a system we have described before [65].

3.3. *In vitro* cytotoxicity assay

Before conducting the *in vivo* experiments, we analyzed the cytotoxicity of the studied copolymers in several relevant cell lines. None of the F1-F5 copolymers were found to decrease cell viabilities below 70% (Fig. S8); the non-cytotoxicity of the polymers to all the tested cell lines within the concentration range used (8–1000 $\mu\text{g}\cdot\text{mL}^{-1}$) was confirmed.

3.4. *In vivo* ¹⁹F MR imaging and implant dissolution

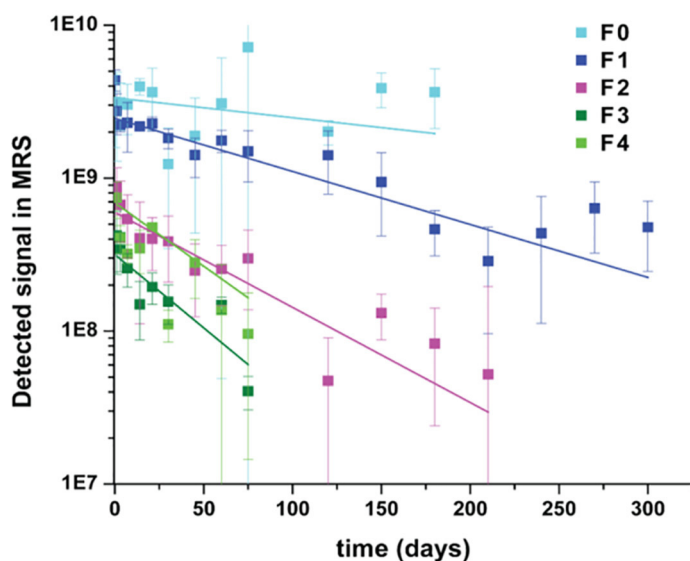
Although many theoretical and experimental studies have been conducted on the prospective usage of LCST polymers for implant drug formulations and the controlled release of *co*-administered drugs, very little work involving the pharmacokinetics and dissolution rates of the polymer implant has been previously conducted. The polymers were injected subcutaneously and intramuscularly into healthy rats.

We collected data from MR spectroscopy (Table S2) and MRI signal intensity (signal-to-noise ratio, Table S4 and S6) and MRI-assessed implant volume (Fig. 3, Tables S3 and S5), and converted these data

into specific pharmacokinetic data (Fig. 4, Table S7 and Fig. S12). As the MR spectroscopy measurement evaluates the absolute integral of the ¹⁹F signal of the measured implant, these kinetic data are the most accurate. The MRI signal and MRI-assessed implant volume are more prone to be influenced by geometry of the implant and other factors. Therefore, the exact description of the kinetics in rats is less accurate, but the data seem to comply with MRS-based descriptions. The ¹⁹F MR signal of isoflurane (a fluorinated inhalation anesthetic) did not interfere with the signal acquired from the fluorinated polymer implants, because its signals are well beyond the measured region of the MRI (Fig. S11) [66,67].

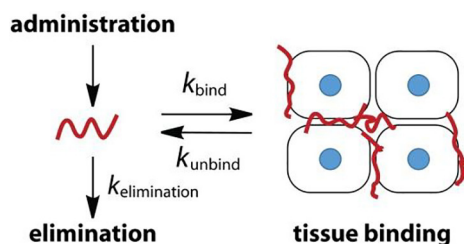
After administration (simultaneous intramuscular and subcutaneous), a ¹⁹F MR spectroscopy signal was detected. Similar to our previous study with *N*-isopropylacrylamide [68], the administration was followed by a fast decrease in signal intensity over a short period of 2 to 3 days. The initial decrease in the signal (characterized by the parameter A_{MRS}) was more significant for the more hydrophilic polymers, probably due to their faster dissolution into the blood and subsequent elimination during the first phase. After this initial period, the decrease in the signal closely followed pseudo-1st order kinetics (Fig. 4). The kinetics during this phase can be described with a mono-exponential function (Formulas 2, 4 and 5), and the results can be seen in Fig. 4.

The kinetic study reveals a possible mechanism of the thermo-responsive polymeric implant dissolution (Scheme 2), although this mechanism needs to be investigated in more detail. In previous studies, it has been reported that as the aggregated polymers lose hydration (especially above their LCST), they tend to adhere to the cell membrane



Polymer	A_{MRS}	$t_{1/2} \pm \text{SD}$ (days)	R^2
F0	1.0	> 200	-
F1	0.6	86 ± 18	0.92
F2	0.2	48 ± 8	0.75
F3	0.1	36 ± 31	0.14
F4	0.2	31 ± 8	0.62

Fig. 4. The non-localized ¹⁹F MR spectroscopy from thigh part of rat body performed with 4 cm circular ¹H/¹⁹F RF surface coil dissolution kinetics of polymers F0-F4 as a function of time. Parameters A_{MRS} and $t_{1/2}$ of the polymers, the fitting-based SD, the fitting R^2 .



Scheme 2. Scheme of polymer forms, interactions with tissues and their kinetics.

and become bound to tissue [28,29]. It has also been shown that thermoresponsive polymers may be retained in organisms for a rather long time, e.g., poly(*N*-isopropylacrylamide with $M_w = 28$ kDa, $T_{LCST} = 32$ °C is after IM administration retained with half-life of $t_{1/2} \geq 50$ days [68,69], which is in agreement with our findings. The binding and renal excretion of the polymer are parallel processes (Scheme 2); therefore, during the period a fast decrease in the signal was observed. This fast decrease is followed by a short and steady excretion of the tissue-bound polymer, which can be described with 1st order kinetics.

In summary, the properties of synthesized polymers, changed by altering the composition, are compared in Fig. 5. The T_{CP} of the polymer at the given pH grows linearly with the addition of the hydrophilic monomer, in agreement with previous studies [64]. The dissolution constant k_e increases (in other words $t_{1/2}$ decreases) with the amount of hydrophilic monomer, which fulfills the primary intentions of this study - to obtain polymers with various biological dissolution rates. The parameter A_{MRS} decreases with the amount of hydrophilic monomer, possibly due to faster elimination of the polymer before its tissue binding.

Implant dissolution times can be also summarized by the biological half-life of dissolution (ranging from approximately 30 days to more than 250 days). In comparison, the polymer F0 dissolution rate from a previous study [44] ranged very slow to almost negligible (the signal from ^{19}F MR images was detectable during the entire experiment, $t_{1/2} \gg 200$ d). Despite F3 having a T_{CP} close to body temperature and F4 even having a T_{CP} far higher than body temperature, the dissolution rates of the polymers were still significantly slower than they would be in the case of mere diffusion-driven dissolution, proving that the polymer binds to tissues upon the administration.

As has been discussed before, such polymer could find numerous

applications in the medical field. These polymers could be used as tracers for tracing cells and tissues (e.g. for purposes of transplantations) because of their long, but tunable retention within tissues. They can be further used for injectable-depot formulations, which could serve for slow and controlled release of pharmaceutically active substances. Due to the chemical nature of our polymers (in aggregated form they are lipophilic and positively charged) can be expected to accumulate lipophilic and/or negatively charged co-administered drugs rather well and release them slowly into the surrounding tissues.

3.5. *In vivo* compatibility

Throughout the duration of the above mentioned *in vivo* ^{19}F MR imaging experiments in rats, blood samples were taken and evaluated once a week for the first month and then once a month until the end of the experiment. A standard blood test was performed for the assessment of aspartate aminotransferase (AST, EC 2.6.1.1) and alanine aminotransferase (ALT, EC 2.6.1.2) activities and bilirubin, creatinine, and albumin concentrations since their altered blood levels could indicate pathology or organ toxicity. Rat weights were monitored because weight gain retardation or even a decrease in weight could indicate pathology, pain or discomfort to the animal. The results are shown in Fig. S9. The biomarker values were consistent throughout the entire duration of the experiment, despite the steady decrease in the polymer concentration, indicating that the polymers had a minor to negligible influence on the biomarker values. Only at a few time points did the values deviate with statistical importance, but no general trend or long-term deviation between the test groups was observed. All biomarker values were within the ranges measured in the control group (Fig. S9). The biomarker values in all animals were consistent with those found in the literature [70].

Anatomical ^1H MRI revealed no foreign-body responses to the administered polymer. Similar polymer implants have been shown to secondarily accumulate in the liver, kidneys, and spleen [61,68]; therefore, at the end of the experiment, the rats were sacrificed, the sites of injections were inspected for any pathology, and a histological examination was performed. No pathology was found, and the histology is shown in Fig. S10. In summary, the results of *in vitro* and *in vivo* testing indicated the biological tolerance of the polymers.

3.6. $^{19}\text{F}/^1\text{H}$ MR imaging of polymer implant F3 with a clinically used instrument

To demonstrate the potential use of our polymers in clinical

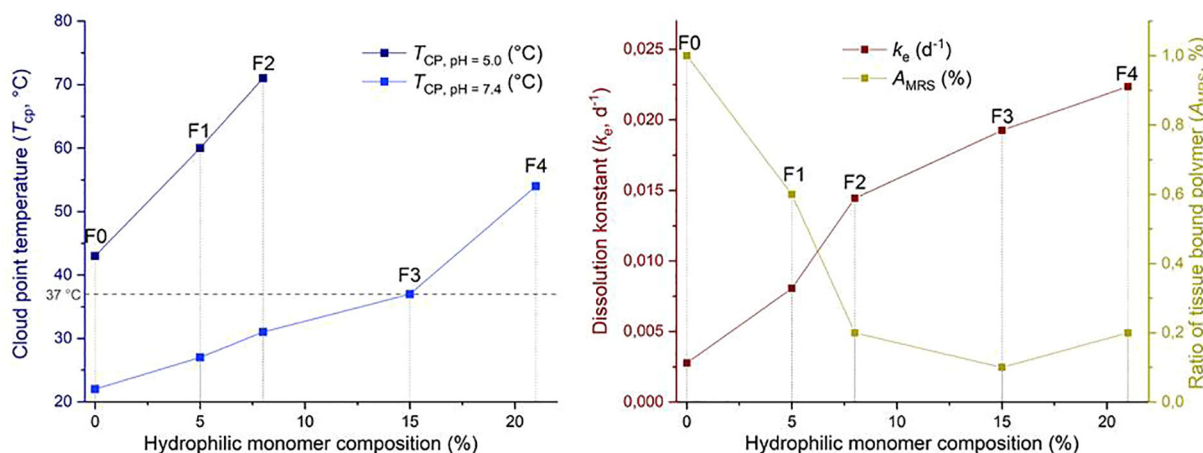


Fig. 5. Correlation among composition, physicochemical properties and biological behavior of the polymers. The compared parameters are based on MRS-assessed implant volumes after subcutaneous administration. Blue: Cloud point temperatures of each polymer at pH 5.0 and 7.4; red: dissolution constant of each polymer; yellow: fraction of tissue-bound polymer. All parameters are plotted as a function of the polymer (F0-F5) composition (% of hydrophilic monomer). (For interpretation of the references to colour in this figure legend, the reader is referred to the web version of this article.)

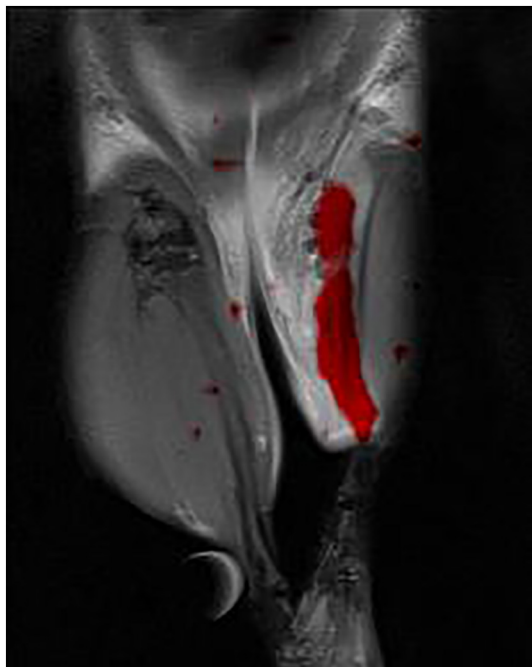


Fig. 6. *In vivo* experiment with the clinically used 3 T MRI showing a merged ^{19}F MRI (red) and ^1H MRI (grayscale). (For interpretation of the references to colour in this figure legend, the reader is referred to the web version of this article.)

practice, a rat was measured on a clinically used 3 T MRI scanner equipped with rat $^1\text{H}/^{19}\text{F}$ volume coil, capable of measuring both ^1H MRI and ^{19}F MRI. The merged images can be seen in Fig. 6. This image shows a high potential of this tracer for clinical use.

3.7. Drug release study

To demonstrate the effect of polymer and their aggregation on the drug release, an *in vitro* experiment was performed with dexamethasone as a chosen drug for this study. Dexamethasone was used due to its biological activity in minute biologically efficient concentrations. It is relatively lipophilic ($\log P = 1.8$) [71], but soluble enough to perform this study, *i.e.*, its aqueous concentration during the measurements was high enough to be determined by HPLC.

In this experiment, the polymer (F1 or F4) was dissolved in a saturated solution of dexamethasone. This solution was transferred into a mini-dialysis kit and placed into a pre-heated ($37\text{ }^\circ\text{C}$) PBS solution. Upon heating, the polymer F1 solidified and formed a depot; in contrast, polymer F4 did not, as its T_{CP} is higher than $37\text{ }^\circ\text{C}$, and therefore it was used as a reference. Samples ($20\text{ }\mu\text{L}$) of the outer solution were taken and analyzed using HPLC equipped with a UV–vis detector to quantify the dexamethasone concentration.

In both cases (for both polymers), a rather fast release was observed during the first 10 h, which corresponds to the release of non-polymer bound drug. After this initial burst release, a significantly slower release was observed in F1. For this polymer, the release was sustained and accounted for less than 10% of the contained drug per day (the $t_{1/2}$ of the release was 2.2 days). The release may depend on the lipophilicity of the drug, as reported in similar systems [72–75], and may be even slower *in vivo*, given that the *in vivo* release of the polymer has been shown to be considerably slower than *in vitro* [76,77]. The obtained results indicate that the polymeric depot can incorporate a portion of the drug (in function of the $\log P$ of the drug) and sustain the release over time (see Fig. 7). The collected data also evidences the inability of the control polymer F4 to sustain the drug release. Given the *in vitro* results, we can assume that our system can be used for a controlled

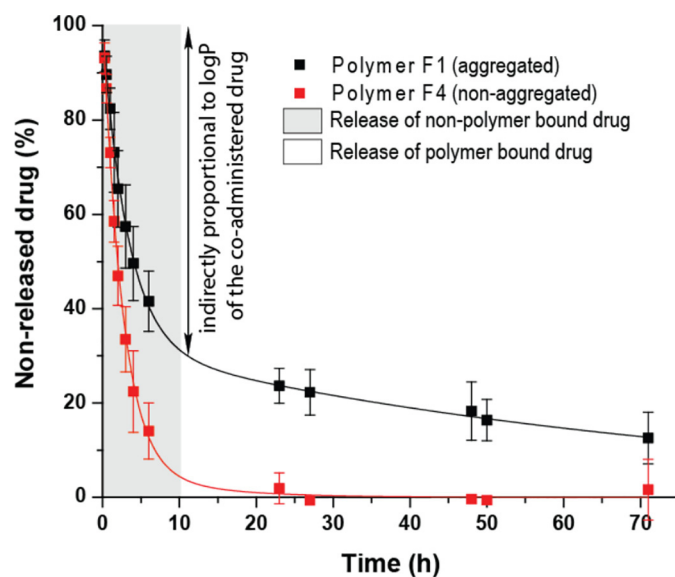


Fig. 7. Drug release from 50 mg depot *in vitro*; the graph shows the concentration of dexamethasone released from the depot F1 and the control F4 as a function of time. The data were fitted with the Formula (7).

release of hydrophobic drugs.

4. Conclusion

This study demonstrates that the presented fluorinated polymers can be used for cells/tissue tracing or as injectable implants that can be easily visualized via ^{19}F MRI with equipment that is used in clinical practice. These tracers have relatively unique chemical shift (-124 ppm), which allows a simultaneous use of the ‘traditional’ perfluorocarbon tracers if needed (they usually have shifts from -80 ppm to -70 ppm). We showed that the addition of pH-responsive and hydrophilic monomers in various ratios can be used to tailor the polymer properties to meet the demands of the desired application. The polymers described herein have excellent imaging properties such as a high fluorine concentration, high atomic mobility even in the aggregated state and almost ideal relaxation times. Our *in vivo* experiments confirmed that the addition of a hydrophilic monomer to the polymer results in these multiresponsive polymers having a tunable dissolution rate. The formed implants demonstrated the potential of these systems in both experimental and clinical medicine. Finally, we used the data to propose the mechanism of aggregated implant dissolution in a biological system.

Acknowledgements

Financial support from MH CZ-DRO (Institute for Clinical and Experimental Medicine - IKEM, IN00023001) is acknowledged. M.H. and K.K. acknowledge financial support from the Ministry of Education, Youth and Sports of the Czech Republic (grant # LTC19032), National Programme for Sustainability NPU I, grant # POLYMAT LO 1507 and from the Czech Grant Foundation (grant # 18-07983S). K.K. and P.S. acknowledge financial support from the Grant Agency of Charles University (Project No. 602119 and No. 766119).

The authors would like to acknowledge the help of Kateřina Kolouchová with the graphical artwork and help of Dr. Zdeněk Tošner with MR-related data interpretation.

MV thanks SGS-TUL for funding. J.T. thanks Dr. Olga Šebestová-Janoušková (Institute of Macromolecular Chemistry CAS) for allowing us to work on cell culture experiments in her lab and Dr. Oto Pavliš (Center of Biological Defense, Military Health Institute, Těchonín, Czech Republic) for lending the Sunrise microplate reader.

Appendix A. Supplementary data

Supplementary data to this article can be found online at <https://doi.org/10.1016/j.jconrel.2020.07.026>.

References

- [1] J.W. Bulte, Hot spot MRI emerges from the background, *Nat. Biotechnol.* 23 (2005) 945.
- [2] J.C. Knight, P.G. Edwards, S.J. Paisley, Fluorinated contrast agents for magnetic resonance imaging; a review of recent developments, *RSC Adv.* 1 (2011) 1415–1425.
- [3] E.T. Ahrens, R. Flores, H. Xu, P.A. Morel, In vivo imaging platform for tracking immunotherapeutic cells, *Nat. Biotechnol.* 23 (2005) 983.
- [4] C. Fink, J.M. Gaudet, M.S. Fox, S. Bhatt, S. Viswanathan, M. Smith, J. Chin, P.J. Foster, G.A. Dekaban, 19 F-perfluorocarbon-labeled human peripheral blood mononuclear cells can be detected in vivo using clinical MRI parameters in a therapeutic cell setting, *Sci. Rep.* 8 (2018) 590.
- [5] M. Srinivas, P.A. Morel, L.A. Ernst, D.H. Laidlaw, E.T. Ahrens, Fluorine-19 MRI for visualization and quantification of cell migration in a diabetes model, *Magn. Reson. Med.* 58 (2007) 725–734.
- [6] P. Boehm-Sturm, M. Aswendt, A. Minassian, S. Michalk, L. Mengler, J. Adamczak, L. Mezzanotte, C. Löwik, M. Hoehn, A multi-modality platform to image stem cell graft survival in the naïve and stroke-damaged mouse brain, *Biomaterials* 35 (2014) 2218–2226.
- [7] A. Tennstaedt, A. Mastropietro, M. Nelles, A. Beyrau, M. Hoehn, In vivo fate imaging of intracerebral stem cell grafts in mouse brain, *PLoS One* 10 (2015) e0144262.
- [8] B.P. Barnett, J. Ruiz-Cabello, P. Hota, R. Ouwerkerk, M.J. Shablott, C. Lauzon, P. Walczak, W.D. Gilson, V.P. Chacko, D.L. Kraitchman, Use of perfluorocarbon nanoparticles for non-invasive multimodal cell tracking of human pancreatic islets, *Contrast Media Mol. Imaging* 6 (2011) 251–259.
- [9] B.E. Rolfe, I. Blakey, O. Squires, H. Peng, N.R. Boase, C. Alexander, P.G. Parsons, G.M. Boyle, A.K. Whittaker, K.J. Thurecht, Multimodal polymer nanoparticles with combined 19F magnetic resonance and optical detection for tunable, targeted, multimodal imaging in vivo, *J. Am. Chem. Soc.* 136 (2014) 2413–2419.
- [10] M. Oishi, S. Sumitani, Y. Nagasaki, On – off regulation of 19F magnetic resonance signals based on pH-sensitive PEGylated Nanogels for potential tumor-specific smart 19F MRI probes, *Bioconj. Chem.* 18 (2007) 1379–1382.
- [11] S. Young, D. Enzmann, D. Long, H. Muller, Perfluorocarbon contrast enhancement of malignant neoplasms: preliminary observations, *Am. J. Roentgenol.* 137 (1981) 141–146.
- [12] C. Zhang, S.S. Moonshi, H.T. Ta, Y. Han, F.Y. Han, H. Peng, P. Král, B.E. Rolfe, A.K. Whittaker, High F-Content Perfluoropolyether-Based Polymers for Targeted Detection of Breast Cancer by 19F Magnetic Resonance and Optical Imaging, (2018).
- [13] A. Stevens, P. Morris, R. Iles, P. Sheldon, J. Griffiths, 5-fluorouracil metabolism monitored in vivo by 19F NMR, *Br. J. Cancer* 50 (1984) 113.
- [14] S.R. Thomas, R.G. Pratt, R.W. Millard, R.C. Samarantunga, Y. Shiferaw, A.J. McGoron, K.K. Tan, In vivo PO₂ imaging in the porcine model with perfluorocarbon F-19 NMR at low field, *Magn. Reson. Imaging* 14 (1996) 103–114.
- [15] P.M. Winter, A.M. Morawski, S.D. Caruthers, R.W. Fuhrhop, H. Zhang, T.A. Williams, J.S. Allen, E.K. Lacy, J.D. Robertson, G.M. Lanza, Molecular imaging of angiogenesis in early-stage atherosclerosis with $\alpha\beta 3$ -integrin-targeted nanoparticles, *Circulation* 108 (2003) 2270–2274.
- [16] U. Flögel, Z. Ding, H. Hardung, S. Jander, G. Reichmann, C. Jacoby, R. Schubert, J. Schrader, In vivo monitoring of inflammation after cardiac and cerebral ischemia by 19F magnetic resonance imaging, *Circulation* 118 (2008) 140.
- [17] E.T. Ahrens, W.-B. Young, H. Xu, L.K. Pusateri, Rapid quantification of inflammation in tissue samples using perfluorocarbon emulsion and fluorine-19 nuclear magnetic resonance, *Biotechniques* 50 (2011) 229–234.
- [18] H. Waiczies, S. Lepore, S. Drechsler, F. Qadri, B. Purfürst, K. Sydow, M. Dathe, A. Kühne, T. Lindel, W. Hoffmann, Visualizing brain inflammation with a shingled-leg radio-frequency head probe for 19 F/1 H MRI, *Sci. Rep.* 3 (2013) 1280.
- [19] C.J. Deutsch, J. Taylor, New class of 19F pH indicators: fluoroanilines, *Biophys. J.* 55 (1989) 799–804.
- [20] M. Hruby, J. Kucka, H. Mackova, O. Lebeda, K. Ulbrich, Thermoresponsive polymers. From laboratory curiosity to advanced materials for medicinal applications, *Chem. List.* 102 (2008) 21–27.
- [21] M.A. Ward, T. Georgiou, Thermoresponsive polymers for biomedical applications, *Polymers* 3 (2011).
- [22] Y.Y. Lang, S.M. Li, W.S. Pan, L.Y. Zheng, Thermo- and pH-sensitive drug delivery from hydrogels constructed using block copolymers of poly(N-isopropylacrylamide) and guar gum, *J. Drug Deliv. Sci. Technol.* 16 (2006) 65–69.
- [23] Y. Tang, M. Oak, R. Mandke, B. Layek, G. Sharma, J. Singh, Thermosensitive Polymers for Controlled Delivery of Hormones, in, (2011).
- [24] M. Hruby, P. Pouckova, M. Zadinova, J. Kucka, O. Lebeda, Thermoresponsive polymeric radionuclide delivery system—an injectable brachytherapy, *Eur. J. Pharm. Sci.* 42 (2011) 484–488.
- [25] L. Loukotová, J. Kučka, M. Rabyk, A. Höcherl, K. Venclíková, O. Janoušková, P. Páral, V. Kolářová, T. Heizer, L. Šefc, P. Štěpánek, M. Hruby, Thermoresponsive β -glucan-based polymers for bimodal immunoradiotherapy – are they able to promote the immune system? *J. Control. Release* 268 (2017) 78–91.
- [26] M. Liu, X. Zeng, C. Ma, H. Yi, Z. Ali, X. Mou, S. Li, Y. Deng, N. He, Injectable hydrogels for cartilage and bone tissue engineering, *Bone Res* 5 (2017) 17014.
- [27] M.A. Cooperstein, P.A.H. Nguyen, H.E. Canavan, Poly(N-isopropyl acrylamide)-coated surfaces: Investigation of the mechanism of cell detachment, *Biointerphases* 12 (2017) 02C401.
- [28] J. Wang, E. Ayano, Y. Maitani, H. Kanazawa, Tunable surface properties of temperature-responsive polymer-modified liposomes induce faster cellular uptake, *ACS Omega* 2 (2017) 316–325.
- [29] T. Takezawa, Y. Mori, K. Yoshizato, Cell culture on a thermo-responsive polymer surface, *Bio/Technology* 8 (1990) 854–856.
- [30] D. Jirak, A. Galisova, K. Kolouchova, D. Babuka, M. Hruby, Fluorine polymer probes for magnetic resonance imaging: quo vadis? *MAGMA* 32 (2019) 173–185.
- [31] H. Priya James, R. John, A. Alex, K.R. Anoop, Smart polymers for the controlled delivery of drugs – a concise overview, *Acta Pharm. Sin. B* 4 (2014) 120–127.
- [32] C. Fu, J. Tang, A. Pye, T. Liu, C. Zhang, X. Tan, F. Han, H. Peng, A.K. Whittaker, Fluorinated glycopolymers as reduction-responsive 19F MRI agents for targeted imaging of cancer, *Biomacromolecules* 20 (2019) 2043–2050.
- [33] C. Zhang, R.J.P. Sanchez, C. Fu, R. Clayden-Zabik, H. Peng, K. Kempe, A.K. Whittaker, Importance of thermally induced aggregation on 19F magnetic resonance imaging of Perfluoropolyether-based comb-shaped poly(2-oxazolines), *Biomacromolecules* 20 (2019) 365–374.
- [34] C. Zhang, S.S. Moonshi, Y. Han, S. Puttick, H. Peng, B.J.A. Magoling, J.C. Reid, S. Bernardi, D.J. Searles, P. Král, A.K. Whittaker, PFPE-based polymeric 19F MRI agents: a new class of contrast agents with outstanding sensitivity, *Macromolecules* 50 (2017) 5953–5963.
- [35] C. Fu, A. Bongers, K. Wang, B. Yang, Y. Zhao, H. Wu, Y. Wei, H.T.T. Duong, Z. Wang, L. Tao, Facile synthesis of a multifunctional copolymer via a concurrent RAFT-enzymatic system for theranostic applications, *Polym. Chem.* 7 (2016) 546–552.
- [36] K. Wang, H. Peng, K.J. Thurecht, S. Puttick, A.K. Whittaker, Multifunctional hyperbranched polymers for CT/19F MRI bimodal molecular imaging, *Polym. Chem.* 7 (2016) 1059–1069.
- [37] K. Wang, H. Peng, K.J. Thurecht, A.K. Whittaker, Fluorinated POSS-star polymers for 19F MRI, *Macromol. Chem. Phys.* 217 (2016) 2262–2274.
- [38] A.V. Fuchs, A.P. Bapat, G.J. Cowin, K.J. Thurecht, Switchable 19F MRI polymer theranostics: towards in situ quantifiable drug release, *Polym. Chem.* 8 (2017) 5157–5166.
- [39] T. Lammers, M.E. Mertens, P. Schuster, K. Rahimi, Y. Shi, V. Schulz, A.J.C. Kuehne, S. Jockenhoevel, F. Kiessling, Fluorinated polyurethane scaffolds for 19F magnetic resonance imaging, *Chem. Mater.* 29 (2017) 2669–2671.
- [40] Z.-X. Jiang, X. Liu, E.-K. Jeong, Y.B. Yu, Symmetry-guided design and Fluorous synthesis of a stable and rapidly excreted imaging tracer for 19F MRI, *Angew. Chem. Int. Ed.* 48 (2009) 4755–4758.
- [41] X. Yang, Y. Sun, S. Kootala, J. Hilborn, A. Heerschap, D. Ossipov, Injectable hyaluronic acid hydrogel for 19F magnetic resonance imaging, *Carbohydr. Polym.* 110 (2014) 95–99.
- [42] G. Brix, A. Schlicker, W. Mier, P. Peschke, M.E. Bellemann, Biodistribution and pharmacokinetics of the 19F-labeled radiosensitizer 3-aminobenzamide: assessment by 19F MR imaging, *Magn. Reson. Imaging* 23 (2005) 967–976.
- [43] D.R. Arifin, M. Kulkarni, D. Kadayakkara, J.W.M. Bulte, Fluorocapsules allow in vivo monitoring of the mechanical stability of encapsulated islet cell transplants, *Biomaterials* 221 (2019) 119410.
- [44] O. Sedlacek, D. Jirak, A. Galisova, E. Jager, J.E. Laaser, T.P. Lodge, P. Stepanek, M. Hruby, 19F magnetic resonance imaging of injectable polymeric implants with multiresponsive behavior, *Chem. Mater.* 30 (2018) 4892–4896.
- [45] K. Kolouchova, O. Sedlacek, D. Jirak, D. Babuka, J. Blahut, J. Kotek, M. Vit, J. Trousil, R. Konefał, O. Janouškova, Self-assembled Thermoresponsive polymeric Nanogels for 19F MR imaging, *Biomacromolecules* 19 (2018) 3515–3524.
- [46] Y.-C. Lee, P.D. Zocharski, B. Samas, An intravenous formulation decision tree for discovery compound formulation development, *Int. J. Pharm.* 253 (2003) 111–119.
- [47] R.L. Clancy, E.B. Brown, In vivo CO-2 buffer curves of skeletal and cardiac muscle, *Am. J. Physiol. Legacy Content* 211 (1966) 1309–1312.
- [48] D. Böning, C. Klarholz, B. Himmelsbach, M. Hütler, N. Maassen, Extracellular bicarbonate and non-bicarbonate buffering against lactic acid during and after exercise, *Eur. J. Appl. Physiol.* 100 (2007) 457–467.
- [49] N. Kamaly, B. Yameen, J. Wu, O.C. Farokhzad, Degradable controlled-release polymers and polymeric nanoparticles: mechanisms of controlling drug release, *Chem. Rev.* 116 (2016) 2602–2663.
- [50] O.A. Khalid, T.S.A.L.S. Claudiu, The Warburg effect and the hallmarks of cancer, *Anti-Cancer Agents Med. Chem.* 17 (2017) 164–170.
- [51] A. Punnia-Moorthy, Evaluation of pH changes in inflammation of the subcutaneous air pouch lining in the rat, induced by carrageenan, dextran and staphylococcus aureus, *J. Oral Pathol. Med.* 16 (1987) 36–44.
- [52] M. Hruby, J. Kucka, H. Mackova, C. Konak, M. Vetric, J. Kozempel, O. Lebeda, New binary thermoresponsive polymeric system for local chemoradiotherapy, *J. Appl. Polym. Sci.* 111 (2009) 2220–2228.
- [53] L. Zhao, L. Zhu, F. Liu, C. Liu, D. Shan, Q. Wang, C. Zhang, J. Li, J. Liu, X. Qu, Z. Yang, pH triggered injectable amphiphilic hydrogel containing doxorubicin and paclitaxel, *Int. J. Pharm.* 410 (2011) 83–91.
- [54] J.M. Bak, K.-B. Kim, J.-E. Lee, Y. Park, S.S. Yoon, H.M. Jeong, H.-I. Lee, Thermoresponsive fluorinated polyacrylamides with low cytotoxicity, *Polym. Chem.* 4 (2013) 2219–2223.
- [55] J. Hennig, H. Friedburg, Clinical applications and methodological developments of the RARE technique, *Magn. Reson. Imaging* 6 (1988) 391–395.
- [56] C. Karunakaran, R. Rajkumar, M. Balamurugan, Chapter one - principles of nuclear magnetic resonance and pulsed nuclear magnetic resonance, in: C. Karunakaran (Ed.), *Spin Resonance Spectroscopy*, Elsevier, 2018, pp. 1–47.
- [57] H.Y. Carr, E.M. Purcell, Effects of diffusion on free precession in nuclear magnetic

- resonance experiments, *Phys. Rev.* 94 (1954) 630–638.
- [58] J. Frahm, A. Haase, D. Matthaei, Rapid NMR imaging of dynamic processes using the FLASII technique, *Magn. Reson. Med.* 3 (1986) 321–327.
- [59] M. Vít, M. Burian, A. Gálišová, D. Jiráček, Construction of a Wide tuneable Volume Coil for Small-Animal MR Imaging, 8 (2019), pp. 8–17.
- [60] A.C. Guyton, J.E. Hall, *Textbook of Medical Physiology*, Elsevier Saunders, Philadelphia, 2006, pp. 316–317.
- [61] N. Bertrand, J.G. Fleischer, K.M. Wasan, J.-C. Leroux, Pharmacokinetics and bio-distribution of N-isopropylacrylamide copolymers for the design of pH-sensitive liposomes, *Biomaterials* 30 (2009) 2598–2605.
- [62] A. Bogomolova, L. Kaberov, O. Sedlacek, S. Filippov, P. Stepanek, V. Král, X. Wang, S. Liu, X. Ye, M. Hruby, Double stimuli-responsive polymer systems: how to use crosstalk between pH-and thermosensitivity for drug depots, *Eur. Polym. J.* 84 (2016) 54–64.
- [63] B.J. Myles, L.A. Jarrett, S.L. Broom, H.A. Speaker, K.E. Sabol, The effects of methamphetamine on core body temperature in the rat—PART 1: chronic treatment and ambient temperature, *Psychopharmacology* 198 (2008) 301.
- [64] E.S. Gil, S. Hudson, Stimuli-Responsive polymers and their bioconjugates, *Prog. Polym. Sci.* 29 (2004) 1173–1222.
- [65] D. Babuka, K. Kolouchova, M. Hruby, O. Groborz, Z. Tosner, A. Zhigunov, P. Stepanek, Investigation of the internal structure of thermoresponsive diblock poly(2-methyl-2-oxazoline)-b-poly[N-(2,2-difluoroethyl)acrylamide] copolymer nanoparticles, *Eur. Polym. J.* 121 (2019) 109306.
- [66] R.K. Harris, E.D. Becker, S.M. Cabral de Menezes, R. Goodfellow, P. Granger, NMR nomenclature: nuclear spin properties and conventions for chemical shifts: IUPAC recommendations 2001, *Solid State Nucl. Magn. Reson.* 22 (2002) 458–483.
- [67] M.N. Kinde, V. Bondarenko, D. Granata, W. Bu, K.C. Grasty, P.J. Loll, V. Carnevale, M.L. Klein, R.G. Eckenhoff, P. Tang, Y. Xu, Fluorine-19 NMR and computational quantification of isoflurane binding to the voltage-gated sodium channel NaChBac, *Proc. Natl. Acad. Sci.* 113 (2016) 13762.
- [68] J. Kucka, M. Hruby, O. Lebeda, Biodistribution of a radiolabelled thermoresponsive polymer in mice, *Appl. Radiat. Isot.* 68 (2010) 1073–1078.
- [69] M. Hrubý, V. Šubr, J. Kučka, J. Kozempel, O. Lebeda, A. Sikora, Thermoresponsive polymers as promising new materials for local radiotherapy, *Appl. Radiat. Isot.* 63 (2005) 423–431.
- [70] T. Küme, B. Sağlam, C. Ergon, A.R. Sisman, Evaluation and comparison of Abbott Jaffe and enzymatic creatinine methods: could the old method meet the new requirements? *J. Clin. Lab. Anal.* 32 (2018) e22168.
- [71] G. Jóhannesson, E. Stefánsson, T. Loftsson, Microspheres and nanotechnology for drug delivery, *Dev. Ophthalmol.* 55 (2015) 93–103.
- [72] H.R. Kranzler, D.R. Wesson, L. Billot, G. DrugAbuse Sciences Naltrexone Depot Study, Naltrexone depot for treatment of alcohol dependence: a multicenter, randomized, placebo-controlled clinical trial, *Alcohol. Clin. Exp. Res.* 28 (2004) 1051–1059.
- [73] E.J. Park, S. Amatya, M.S. Kim, J.H. Park, E. Seol, H. Lee, Y.-H. Shin, D.H. Na, Long-acting injectable formulations of antipsychotic drugs for the treatment of schizophrenia, *Arch. Pharm. Res.* 36 (2013) 651–659.
- [74] J.M. Davis, L. Metalon, M.D. Watanabe, L. Blake, Depot antipsychotic drugs, *Drugs* 47 (1994) 741–773.
- [75] E. Roese, H. Bunjes, Drug release studies from lipid nanoparticles in physiological media by a new DSC method, *J. Control. Release* 256 (2017) 92–100.
- [76] M.M. Nounou, L.K. El-Khordagui, N.A. Khalafallah, S.A. Khalil, In vitro release of hydrophilic and hydrophobic drugs from liposomal dispersions and gels, *Acta Pharma.* 56 (2006) 311–324.
- [77] C. Washington, Drug release from microdisperse systems: a critical review, *Int. J. Pharm.* 58 (1990) 1–12.

Supporting information for the article

Implant-forming polymeric ¹⁹F MRI-tracer with tunable dissolution

Kristyna Kolouchova^{#1,2}, Daniel Jirak^{#3,4}, Ondrej Groborz^{1,5,6,7}, Ondrej Sedlacek⁸, Natalia Ziolkowska^{3,6}, Martin Vit^{3,4}, Eva Sticova³, Andrea Galisova³, Pavel Svec^{1,2}, Jiri Trousil¹, Milan Hajek³, Martin Hruby^{*1}*

¹Institute of Macromolecular Chemistry CAS v.v.i., Heyrovsky square 2, 162 06 Prague 6, Czech Republic

²Department of Physical and Macromolecular Chemistry, Faculty of Science, Charles University, Hlavova 8, Prague 2, 128 00, Czech Republic

³Department of Diagnostic and Interventional Radiology, Institute for Clinical and Experimental Medicine, Videnska 1958/9, 140 21 Prague 4, Czech Republic

⁴Technical University of Liberec, Faculty of Mechatronics Informatics and Interdisciplinary Studies, Studentska 1402/2, 461 17 Liberec, Czech Republic

⁵Department of Medicinal Chemistry, Charles University, Faculty of Science, Hlavova 8, 128 43 Prague 2, Czech Republic

⁶Institute of Biophysics and Informatics, Charles University, First Faculty of Medicine, Salmovská 1, 120 00 Prague 2, Czech Republic

⁷Institute of Organic Chemistry and Biochemistry, Czech Academy of Sciences, Flemingovo square 542/2, 162 06 Prague 6, Czech Republic

⁸Department of Organic and Macromolecular Chemistry, Ghent University, Krijgslaan 281-S4, 9000 Ghent, Belgium

#-both authors (K. Kolouchova, D. Jirak) contributed equally to the manuscript. * mhruby@centrum.cz,

* daji@ikem.cz

Keywords: polymer implant, ¹⁹F magnetic resonance imaging, double-stimuli responsivity, tunable dissolution

Table S1. Initial monomer ratios, amounts and resulting yields of polymers F1-F5, prepared by the RAFT copolymerization of DFEA, ImPAM and HEAM in dry DMF at 70 °C.

Polymer	Initial monomer ratios (mol. %)			Monomer amounts (mg)			Yields (%)
	DFEAM	ImPAM	HEAM	DFEAM	ImPAM	HEAM	
F1	85	10	5	720	280	30	69
F2	80	10	10	680	280	80	71
F3	75	10	15	640	280	100	74
F4	70	10	20	600	280	200	65
F5	60	10	30	500	280	300	71

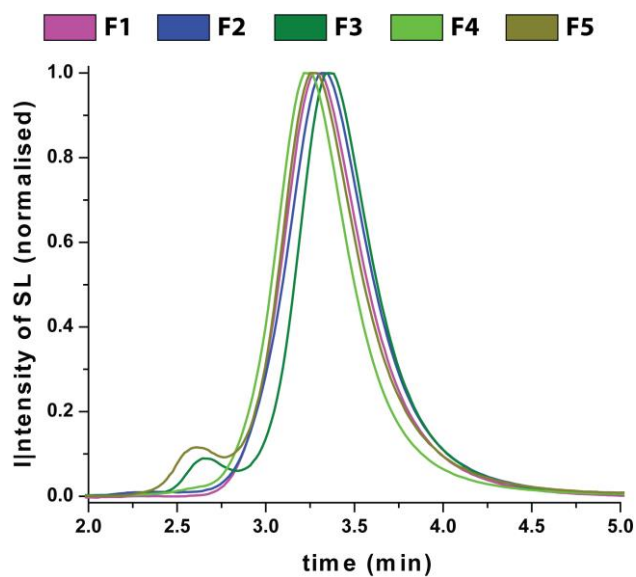


Figure S1. Size exclusion chromatography (SEC) traces for prepared polymers F1-F5 using an HPLC Ultimate 3000 system (Dionex, Sunnyvale, USA) equipped with a SEC column (TSKgel SuperAW3000 150 × 6 mm, 4 μm) and employed with a methanol and sodium acetate buffer (0.3 M, pH 6.5) mixture (80:20 v/v, flow rate of 0.6 mL min⁻¹) as the mobile phase.

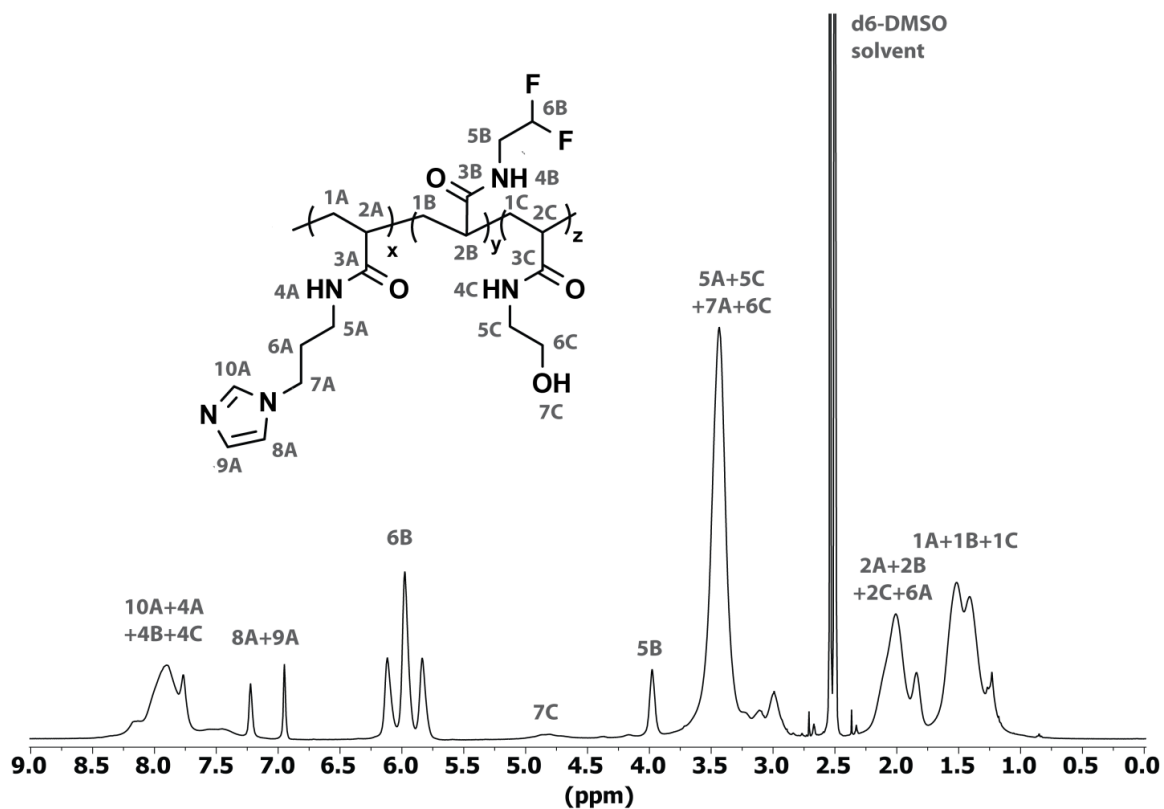


Figure S2. ^1H NMR spectrum acquired on Bruker 300MHz of polymer F2, measured in $\text{DMSO-}d_6$ ($c_{\text{pol}} = 0.5 \text{ mg}\cdot\text{mL}^{-1}$), $NS = 32$, $DI = 30.00 \text{ s}$.

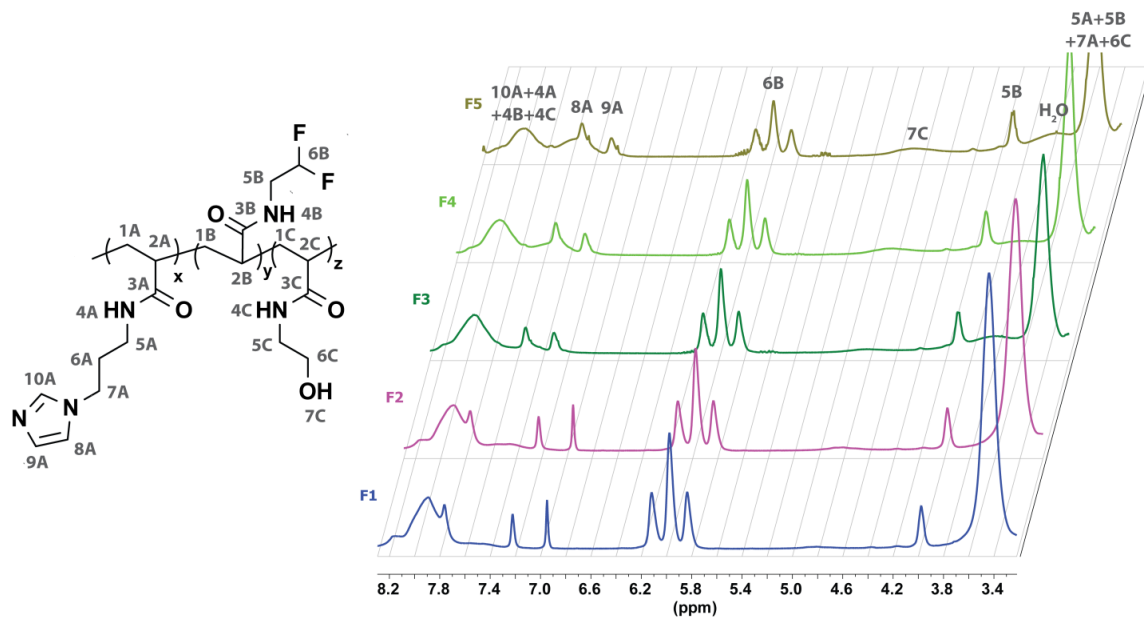


Figure S3. ^1H NMR spectrum acquired on Bruker 300MHz of polymers F1-F5 measured in $\text{DMSO-}d_6$ ($c_{\text{pol}} = 0.5 \text{ mg}\cdot\text{mL}^{-1}$), $NS = 32$, $DI = 30.00 \text{ s}$.

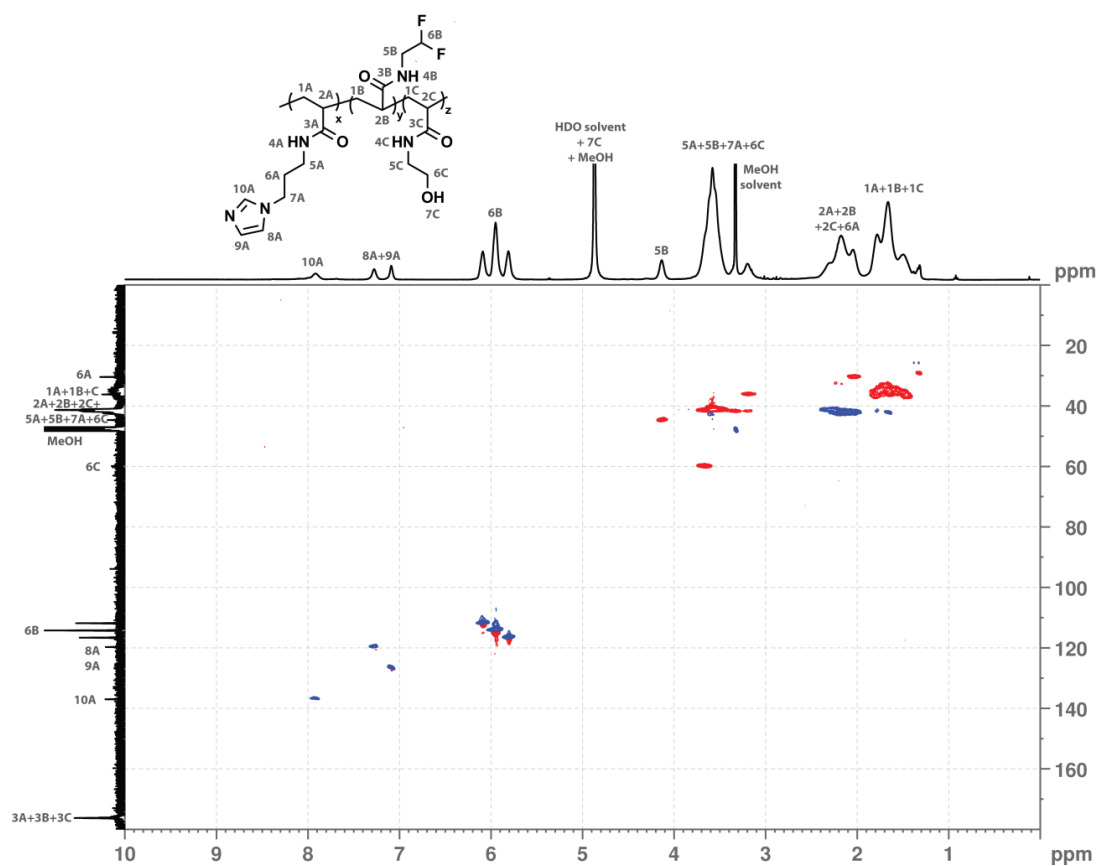


Figure S4. HSQC-edit F1 (25 mg in DMSO- d_6 , 550 μ L), $NS = 2$, $DI = 1.50$ s, 2048 to 512 points in spectrum, external projection was used.

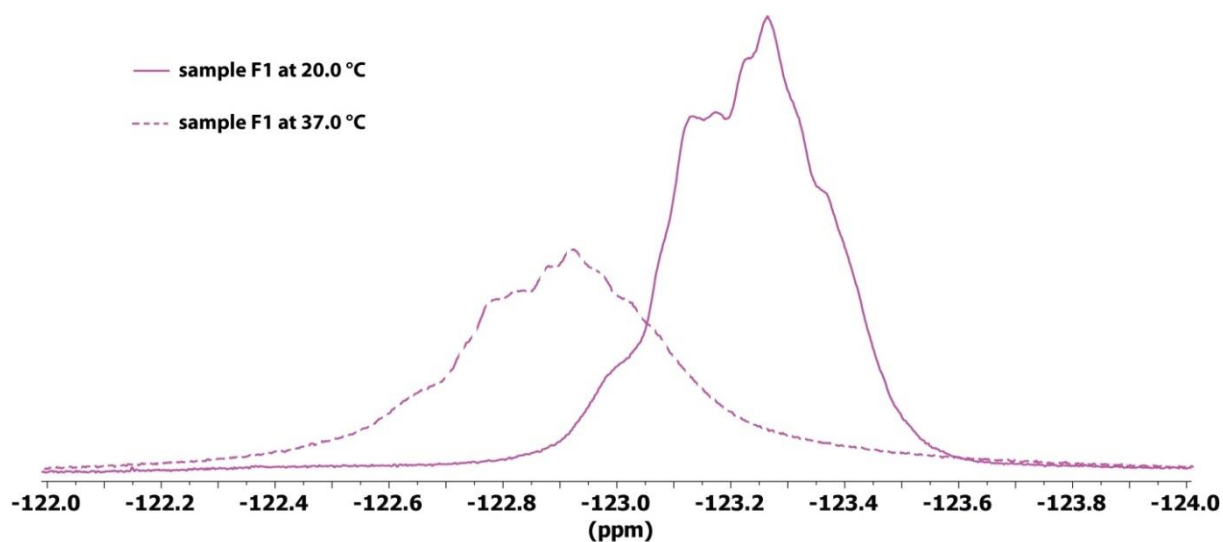


Figure S5. ^{19}F NMR scan, F1 ($c_{\text{pol}} = 15.0$ mg·mL $^{-1}$ in 40 mM phosphate buffered saline with pH adjusted by addition of hydrochloric acid to 5.0), $DI = 8.00$ s, $NS = 64$, measured at 20.0 °C and 37.0 °C with Bruker Avance III 400 MHz (Bruker, Billerica, USA). A slight change in chemical shifts at different temperatures is due to the solvent (D_2O) locking.

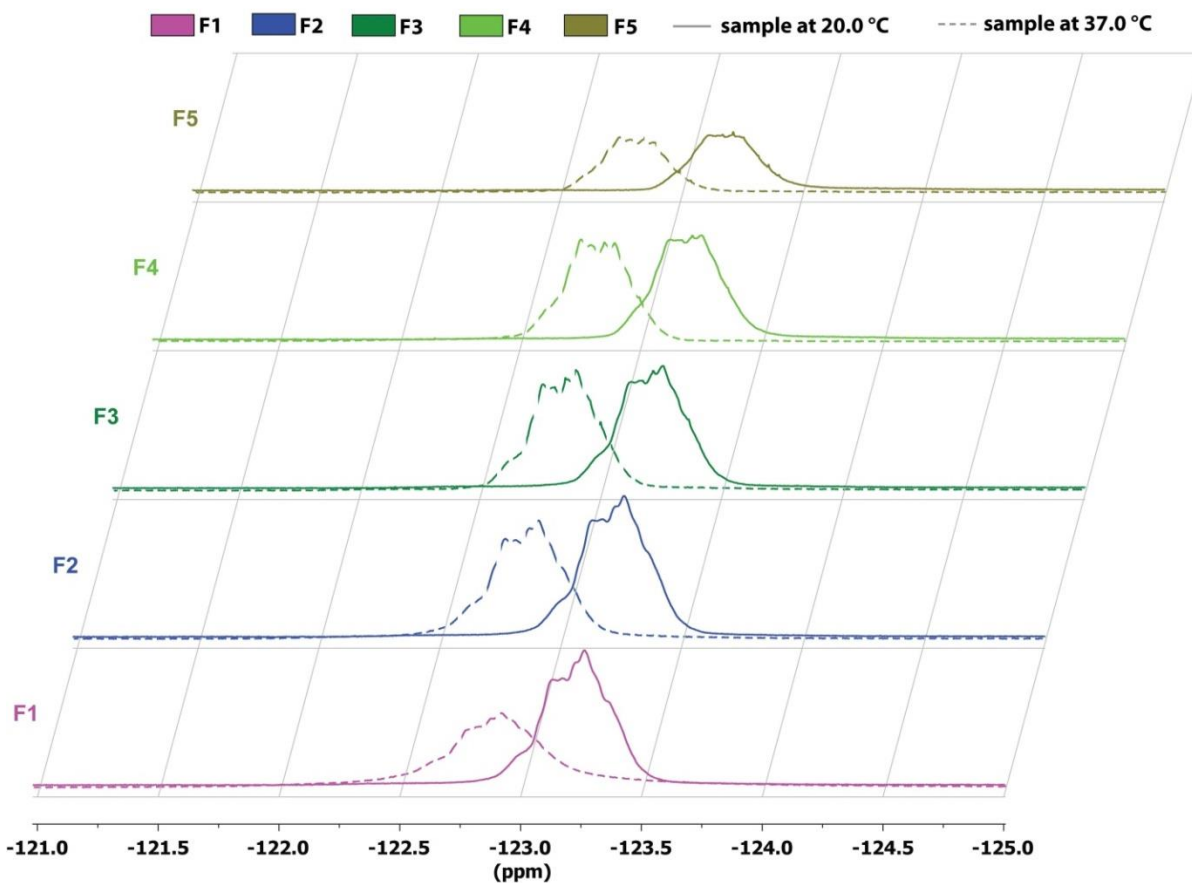


Figure S6. ^{19}F NMR scan, F1-F5 ($c_{\text{pol}} = 15.0 \text{ mg}\cdot\text{mL}^{-1}$ in 40 mM phosphate buffered saline, pH = 7.4), $DI = 8.00 \text{ s}$, $NS = 64$, measured at 20.0 °C and 37.0 °C with Bruker Avance III 400 MHz (Bruker, Billerica, USA). A slight change in chemical shifts at different temperatures is due to the solvent (D_2O) locking.

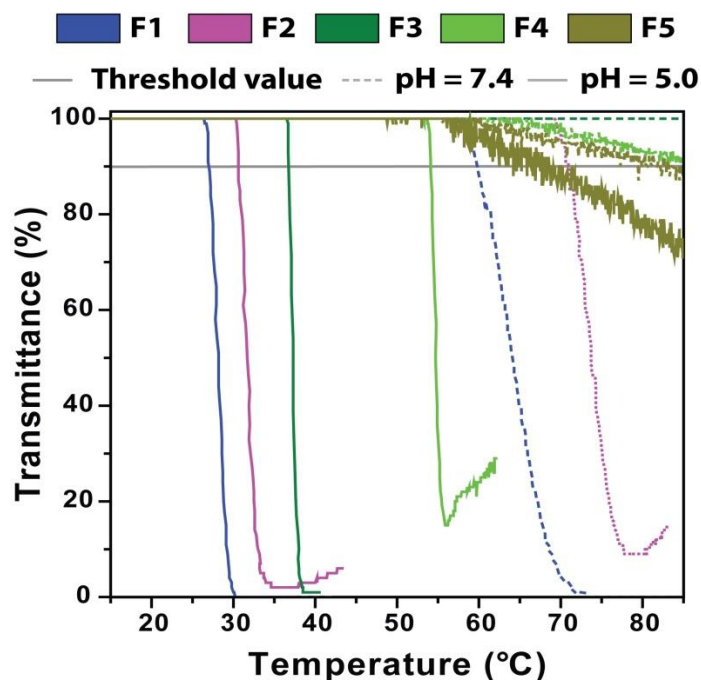


Figure S7. Transmittance ($\lambda = 600 \text{ m}$) of the polymer solutions F0-F5 ($c_{\text{pol}} = 5.0 \text{ mg}\cdot\text{mL}^{-1}$) as a function of temperature at pH 5.0 or 7.4, respectively. Gray horizontal lines are transmittance levels 30% and 70%, omitted for clarity.

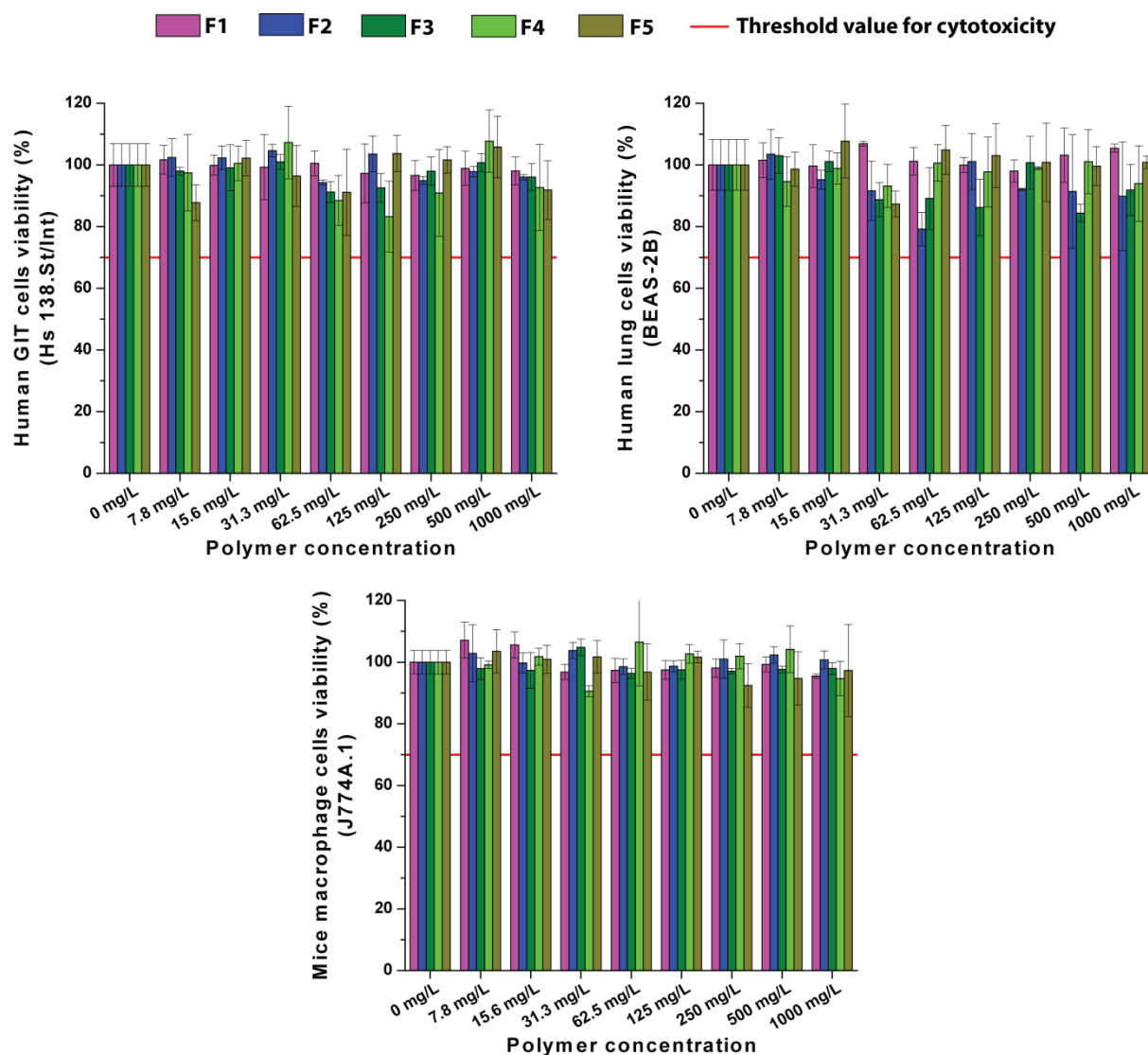


Figure S8. Viability of different cells (J774A.1, Hs 738.St/Int and BEAS-2B) with an increasing concentration (0-1000 mg·L⁻¹) of polymer F1-F5.

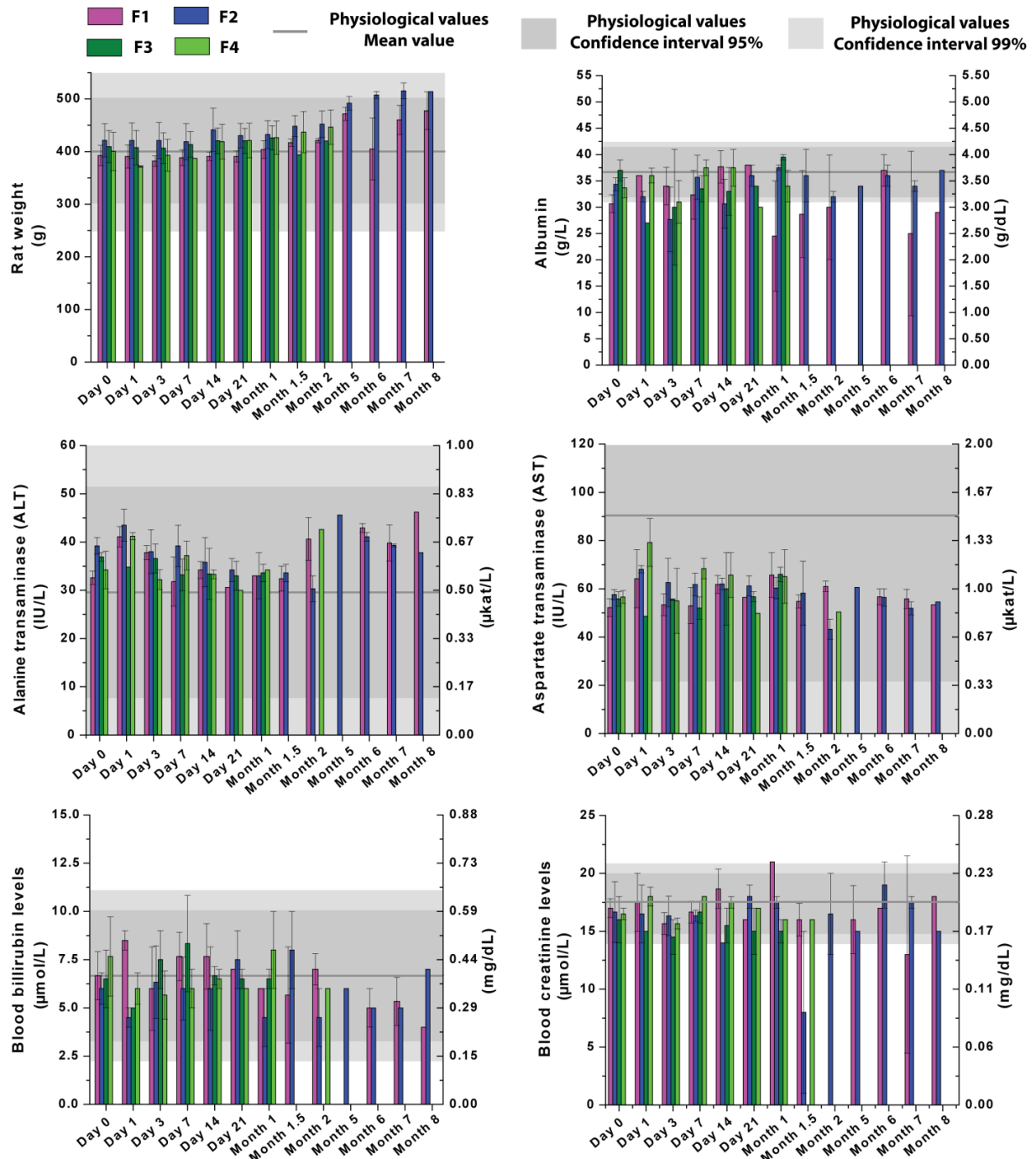


Figure S9. Tested biomarkers of systemic toxicity: body weight, albumin, ALT, AST, blood bilirubin and creatinine.

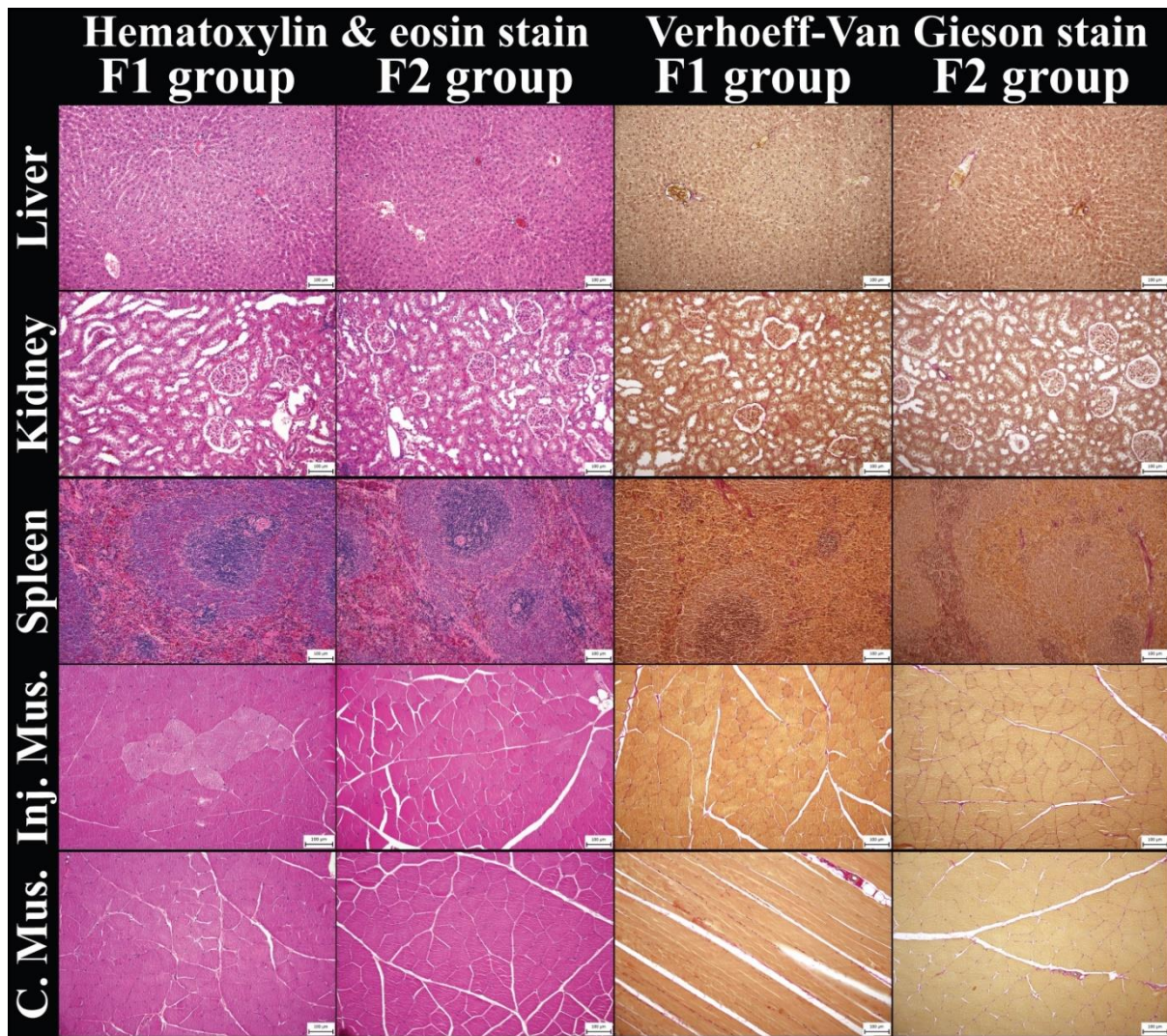


Figure S10. Histological examination of test animals: liver, kidney, spleen, muscle after administration and contralateral muscle, respectively, of groups F1 and F2 1 year after administration. Stained with haematoxylin&eosin and Verhoeff-Van Gieson stain, respectively, all magnified 200 times.

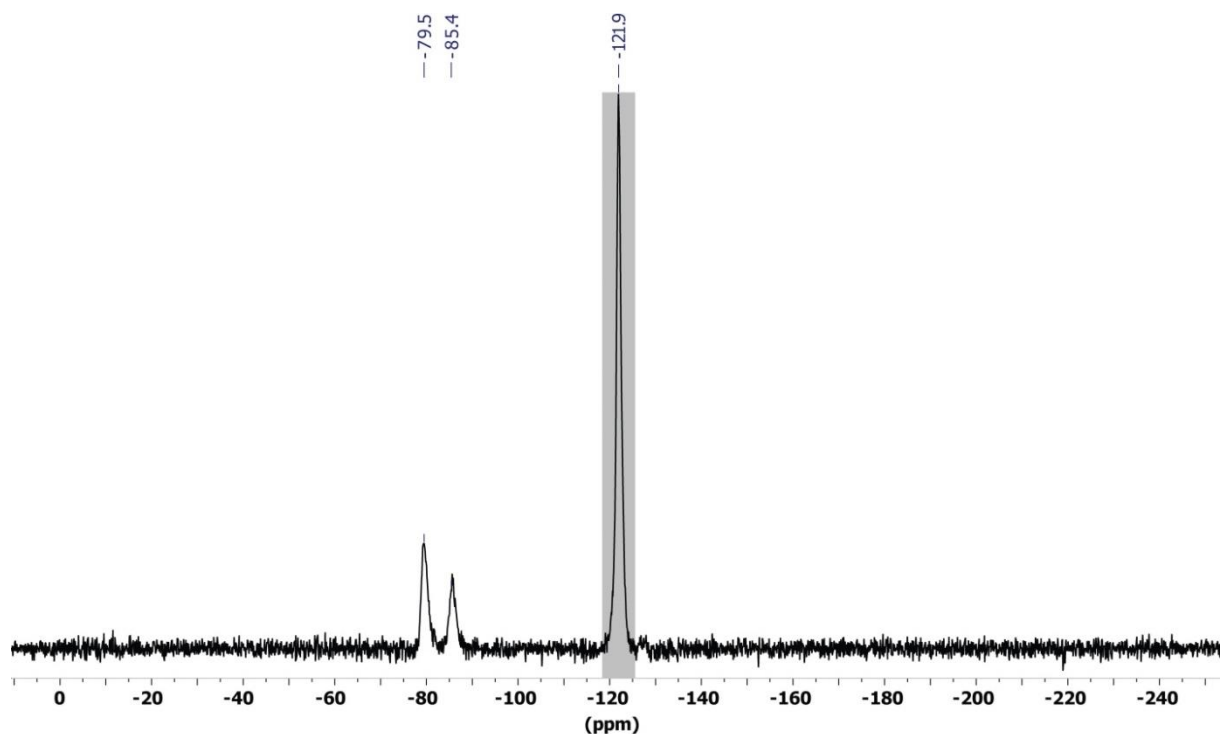


Figure S11. An in vivo ^{19}F spectrum at 4.7 T; polymer signal and isoflurane signals can be seen. The gray rectangle shows the measured area during the MRI experiments (-125.4 to -118.4 ppm). No apodization was involved.

Table S2. Whole body MR spectroscopy and calculated standard deviation. Data for F0 polymer were used from a previous study [S1].

Polymer Day	F0		F1		F2		F3		F4	
	MRS	SD	MRS	SD	MRS	SD	MRS	SD	MRS	SD
0	$3.2 \cdot 10^9$	$1.6 \cdot 10^9$	$4.4 \cdot 10^9$	$6.9 \cdot 10^8$	$3.9 \cdot 10^9$	$9.1 \cdot 10^8$	$3.8 \cdot 10^9$	$7.4 \cdot 10^8$	$3.6 \cdot 10^9$	$5.6 \cdot 10^7$
1	$3.1 \cdot 10^9$	$1.8 \cdot 10^9$	$2.7 \cdot 10^9$	$8.1 \cdot 10^8$	$8.7 \cdot 10^8$	$3.0 \cdot 10^8$	$4.2 \cdot 10^8$	$1.9 \cdot 10^8$	$7.5 \cdot 10^8$	$2.0 \cdot 10^8$
3	$3.1 \cdot 10^9$	$1.1 \cdot 10^9$	$2.2 \cdot 10^9$	$2.0 \cdot 10^8$	$6.7 \cdot 10^8$	$2.9 \cdot 10^8$	$3.4 \cdot 10^8$	$9.9 \cdot 10^7$	$4.1 \cdot 10^8$	$8.4 \cdot 10^7$
7	$3.0 \cdot 10^9$	$1.1 \cdot 10^9$	$2.3 \cdot 10^9$	$8.2 \cdot 10^8$	$5.4 \cdot 10^8$	$2.4 \cdot 10^8$	$2.6 \cdot 10^8$	$6.4 \cdot 10^7$	$3.2 \cdot 10^8$	$4.6 \cdot 10^7$
14	$4.0 \cdot 10^9$	$4.9 \cdot 10^8$	$2.2 \cdot 10^9$		$4.0 \cdot 10^8$	$2.9 \cdot 10^8$	$1.5 \cdot 10^8$	$6.2 \cdot 10^7$	$3.5 \cdot 10^8$	$1.1 \cdot 10^8$
21	$3.6 \cdot 10^9$	$1.6 \cdot 10^9$	$2.3 \cdot 10^9$	$2.4 \cdot 10^8$	$4.0 \cdot 10^8$	$1.5 \cdot 10^8$	$1.9 \cdot 10^8$	$4.5 \cdot 10^7$	$4.8 \cdot 10^8$	$5.0 \cdot 10^6$
30	$1.2 \cdot 10^9$	$8.9 \cdot 10^8$	$1.8 \cdot 10^9$	$2.7 \cdot 10^8$	$3.9 \cdot 10^8$	$1.8 \cdot 10^8$	$1.6 \cdot 10^8$	$4.5 \cdot 10^7$	$1.1 \cdot 10^8$	$2.6 \cdot 10^7$
45	$1.9 \cdot 10^9$	$1.5 \cdot 10^9$	$1.4 \cdot 10^9$	$4.1 \cdot 10^8$	$2.5 \cdot 10^8$	$1.2 \cdot 10^8$	$6.5 \cdot 10^6$	$3.9 \cdot 10^6$	$2.8 \cdot 10^8$	$1.2 \cdot 10^8$
60	$3.1 \cdot 10^9$	$3.0 \cdot 10^9$	$1.8 \cdot 10^9$	$2.9 \cdot 10^8$	$2.5 \cdot 10^8$	$1.1 \cdot 10^8$	$1.5 \cdot 10^8$	$1.8 \cdot 10^7$	$1.4 \cdot 10^8$	$1.4 \cdot 10^8$
75	$7.2 \cdot 10^9$	$7.4 \cdot 10^9$	$1.5 \cdot 10^9$	$5.5 \cdot 10^8$	$3.0 \cdot 10^8$	$1.6 \cdot 10^8$	$4.0 \cdot 10^7$		$9.6 \cdot 10^7$	$8.1 \cdot 10^7$
120	$2.0 \cdot 10^9$	$3.6 \cdot 10^8$	$1.4 \cdot 10^9$	$6.2 \cdot 10^8$	$4.7 \cdot 10^7$	$4.3 \cdot 10^7$				
150	$3.9 \cdot 10^9$		$9.4 \cdot 10^8$	$5.2 \cdot 10^8$	$1.3 \cdot 10^8$	$4.3 \cdot 10^7$				
180	$3.6 \cdot 10^9$	$1.5 \cdot 10^9$	$4.6 \cdot 10^8$	$1.5 \cdot 10^8$	$8.3 \cdot 10^7$	$5.9 \cdot 10^7$				
210			$2.9 \cdot 10^8$	$1.9 \cdot 10^8$	$5.2 \cdot 10^7$	$1.4 \cdot 10^8$				
240			$4.4 \cdot 10^8$	$3.2 \cdot 10^8$						
270			$6.4 \cdot 10^8$	$3.1 \cdot 10^8$						
300			$4.8 \cdot 10^8$	$2.3 \cdot 10^8$						

Table S3. Average volume of intramuscular implant and calculated standard deviation. Data for F0 polymer were used from a previous study [S1].

Polymer Day	F0		F1		F2		F3		F4	
	V	SD V	V	SD V	V	SD V	V	SD V	V	SD V
0	0.39	0.45	0.77	0.73	1.82	1.84	1.54	1.28	1.04	0.67
1	0.38	0.09	0.27	0.15	0.30	0.54	0.08	0.11	0.43	0.46
2					0.12	0.00			0.00	0.00
3			0.33	0.34	0.40	0.37	0.04	0.06	0.06	0.11
4	0.62	0.31								
7	0.54	0.32	0.90	0.28	0.30	0.24			0.13	0.19
14			1.07	0.31	0.11	0.16	0.06	0.09		
21	0.92	0.35	0.86	0.14	0.03	0.06				
30	0.64	0.19	0.77	0.75	0.15	0.30				
45			0.33	0.28	0.07	0.12				
60	0.54	0.76	0.44	0.21	0.05	0.07				
75			0.40	0.19	0.07	0.12				
90	0.03	0.05								
120	0.46	0.65	0.26	0.45	0.29	0.12				
150	0.34	0.13	0.28	0.27	0.00	0.00				
180	0.71	1.01	0.40	0.13	0.00	0.00				
210			0.11	0.15	0.00	0.00				
240			0.24	0.00						
270	0.46	0.26	0.11	0.19						
300			0.16	0.27						
330										
360			0.13	0.19						

Table S4. Average volume of subcutaneous implant and calculated standard deviation. Data for F0 polymer were used from a previous study [S1].

Polymer Day	F0		F1		F2		F3		F4	
	V	SD V	V	SD V	V	SD V	V	SD V	V	SD V
0	1.36	0.34	2.61	0.61	2.96	1.88	2.95	1.59	2.84	0.95
1	0.56	0.24	0.67	0.21	1.37	0.27	1.17	0.20	1.62	1.25
2					0.38				0.21	
3			0.84	0.29	1.07	0.37	0.50	0.02	0.52	0.29
4	0.80	0.84								
7	0.88	0.45	1.21	0.30	1.01	0.12			0.92	0.01
14			1.16	0.61	0.55	0.19	0.33	0.07	1.11	
21	1.31	0.43	0.81	0.77	0.63	0.28	0.27		0.23	
30	1.67	0.29	0.93	0.22	0.97	0.38				
45			0.87	0.08	0.32	0.17				
60	0.40	0.57	0.73	0.11	0.51	0.06				
75			0.70	0.21	0.46	0.13				
90	0.69	0.57								
120	1.08	0.55	0.60	0.21	0.08	0.13				
150	1.41	0.03	0.34	0.32						
180	0.58	0.38	0.11	0.19						
210	1.61		0.27	0.17						
240			0.44							
270	1.66	1.25	0.40	0.17						
300			0.33	0.12						
330			0.49	0.18						
360			0.50	0.14						

Table S5. Signal to noise ratio of intramuscular implant and calculated standard deviation. Data for F0 polymer were used from a previous study [S1].

Polymer Day	F0		F1		F2		F3		F4	
	SNR	SD	SNR	SD	SNR	SD	SNR	SD	SNR	SD
0	2.92	1.95	6.54	8.16	17.94	15.38	10.61	1.37	11.43	4.57
1	5.24	1.96	3.65	0.94	1.94	2.24	1.59	2.25	7.40	9.69
2					3.17	0.00				
3			3.45	3.44	3.25	2.32	1.58	2.24	0.91	1.57
4	6.35	2.95								
7	6.02	1.75	4.06	1.26	2.51	1.90			1.42	2.01
14			4.42	0.46	2.21	2.84	1.53	2.17	0.00	0.00
21	4.07	3.19	4.98	0.99	0.79	1.59	0.00	0.00	0.00	0.00
30	7.09	3.36	3.36	2.91	0.73	1.46	0.00	0.00	0.00	0.00
45			3.03	3.03	1.81	3.13	0.00	0.00	0.00	0.00
60	4.04	5.72	6.14	4.01	1.60	2.27	0.00	0.00	0.00	0.00
75			5.93	3.78	1.26	2.18	0.00	0.00	0.00	0.00
90	1.36	1.92								
120	2.48	3.50	2.46	4.26	3.29	0.63				
150	3.36	0.15	3.12	2.96	0.00	0.00				
180	4.06	5.75	4.18	1.21	0.00	0.00				
210			2.33	3.29	0.00	0.00				
240			5.02	0.00						
270	4.68	1.30	1.91	3.30						
300			1.05	1.82						
330			0.00	0.00						
360			2.12	2.99						

Table S6. Signal to noise ratio of subcutaneous implant and calculated standard deviation. Data for F0 polymer were used from a previous study [S1].

Polymer Day	F0		F1		F2		F3		F4	
	SNR	SD	SNR	SD	SNR	SD	SNR	SD	SNR	SD
0	3.29	2.48	8.78	3.71	25.06	19.05	65.88	68.58	57.06	34.35
1	4.67	4.95	5.10	1.58	8.31	4.90	4.22	1.01	9.85	11.67
2					3.26				2.55	
3			7.32	2.15	9.81	4.75	3.86	0.06	3.37	0.92
4	5.50	3.23								
7	7.80	4.28	6.27	3.13	6.49	2.40			3.10	0.33
14			8.74	1.92	9.26	5.24	3.21	0.45	2.60	
21	5.75	1.97	8.63	7.49	5.08	2.29	2.73		3.37	
30	7.32	1.43	12.89	4.63	5.60	1.72				
45			7.73	5.41	4.94	1.68				
60	5.58	7.89	14.58	5.98	4.50	1.70				
75			11.53	3.53	3.79	0.96				
90	4.50	0.42								
120	6.11	1.28	12.03	4.19	1.79	2.53				
150	5.21	0.91	8.19	7.71						
180	4.97	1.40	1.63	2.81						
210	8.38		3.93	1.31						
240			5.87							
270	6.76	1.24	4.71	0.68						
300			4.48	1.21						
330			6.62	2.89						
360			4.69	1.87						

Table S7. Parameters A_{MRI} , t_{peak} , $t_{1/2}$ and the fitting-based SD, and the fitting R^2 as they were calculated based on MRI data. Data for F0 polymer were used from a previous study [S1].

Polymer		A_{MRI}	$t_{1/2} \pm \text{SD}$ (days)	R^2	A_{MRI}	$t_{1/2} \pm \text{SD}$ (days)	R^2
Administ.		SC administration			IM administration		
F0	Signal intensity noise	1.0	$\gg 350$	-	1.0	$\gg 250$	-
F1		1.0	168 ± 35	0.55	1.0	319 ± 119	0.54
F2		0.3	72 ± 12	0.81	0.2	56 ± 10	0.89
F3		0.2	40 ± 5	0.97	0.1	$< 40^*$	-
F4		0.2	30 ± 3	0.98	0.1	$< 40^*$	-
F0	Implant volume	1.0	$\gg 350$	-	1.0	169 ± 73	0.48
F1		1.0	242 ± 39	0.82	0.9	103 ± 20	0.76
F2		0.3	48 ± 6	0.91	0.2	20 ± 2	0.91
F3		0.2	$< 30^*$	-	< 0.1	$< 30^*$	-
F4		0.1	$< 30^*$	-	0.1	$< 30^*$	-

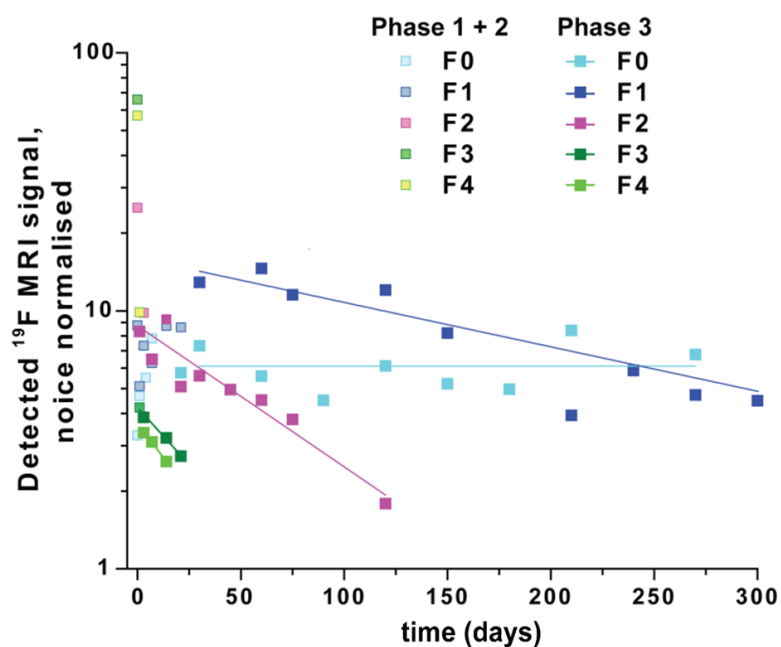


Figure S12. ^{19}F MRI intensity dissolution kinetics of polymers F0-F4 after subcutaneous injection as a function of time. Demonstration of 1st order kinetics of Phase 3 including data of more complex behavior in Phases 1 and 2. Standard deviations are not shown for clarity.

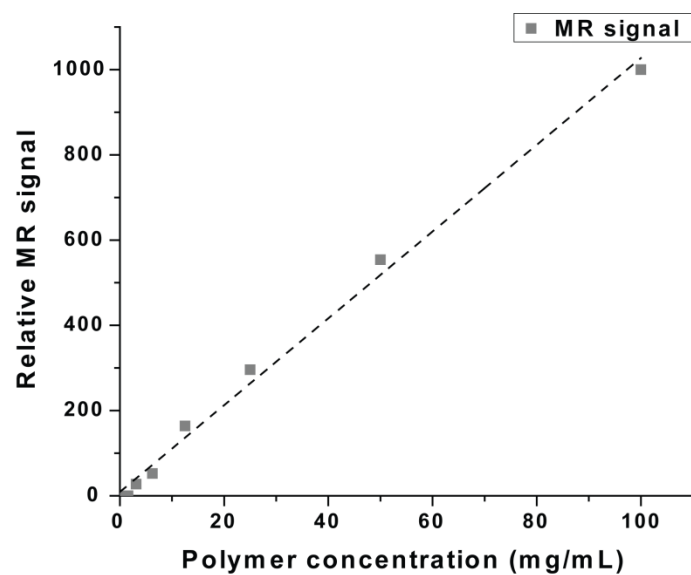


Figure S13. The dependency of MRI signal intensity as a function of concentration, polymer F3 in 40 mM phosphate-buffered saline, pH = 7.4 at 37 °C.

Reference

[S1] O. Sedlacek, D. Jirak, A. Galisova, E. Jager, J.E. Laaser, T.P. Lodge, P. Stepanek, M. Hruby, ^{19}F Magnetic Resonance Imaging of Injectable Polymeric Implants with Multiresponsive Behavior, *Chemistry of Materials*, 30 (2018) 4892-4896.

Appendix 4

Kolouchová, K.; Groborz, O.; Černochohá, Z.; Škárková, A.; Brábek, J.; Rosel, D.; Švec, P.; Starčuk, Z.; Šlouf, M.; Hrubý, M., Thermo- and ROS-Responsive Self-Assembled Polymer Nanoparticle Tracers for ^{19}F MRI Theranostics. *Biomacromolecules* **2021**, 22 (6), 2325-2337.

Times Cited: 26; IF = 6.98.

P. Švec assisted with the synthesis of ferrocenecarboxylic acid, with designing and performing the oxidative disassembly experiments, and writing the manuscript.

Thermo- and ROS-Responsive Self-Assembled Polymer Nanoparticle Tracers for ^{19}F MRI Theranostics

Kristyna Kolouchova, Ondrej Groborz, Zulfiya Cernochova, Aneta Skarkova, Jan Brabek, Daniel Rosel, Pavel Svec, Zenon Starcuk, Miroslav Slouf, and Martin Hruby*

Cite This: *Biomacromolecules* 2021, 22, 2325–2337

Read Online

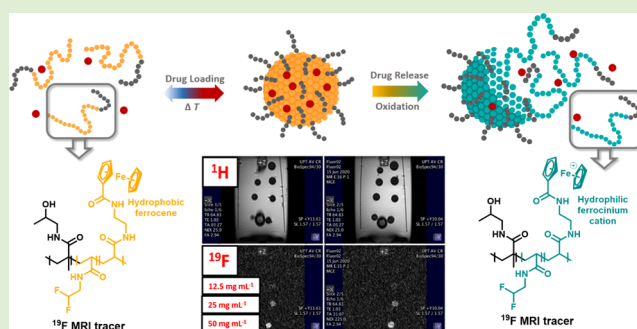
ACCESS |

Metrics & More

Article Recommendations

Supporting Information

ABSTRACT: Fluorine-19 magnetic resonance imaging (^{19}F MRI) enables detailed *in vivo* tracking of fluorine-containing tracers and is therefore becoming a particularly useful tool in noninvasive medical imaging. In previous studies, we introduced biocompatible polymers based on the hydrophilic monomer *N*-(2-hydroxypropyl)methacrylamide (HPMA) and the thermoresponsive monomer *N*-(2,2-difluoroethyl)acrylamide (DFEA). These polymers have abundant magnetically equivalent fluorine atoms and advantageous properties as ^{19}F MRI tracers. Furthermore, in this pilot study, we modified these polymers by introducing a redox-responsive monomer. As a result, our polymers changed their physicochemical properties once exposed to an oxidative environment. Reactive oxygen species (ROS)-responsive polymers were prepared by incorporating small amounts (0.9–4.5 mol %) of the *N*-[2-(ferrocenylcarboxamido)ethyl]acrylamide (FcCEA) monomer, which is hydrophobic and diamagnetic in the reduced electronneutral (Fe(II), ferrocene) state but hydrophilic and paramagnetic in the oxidized (Fe(III), ferrocenium cation) state. This property can be useful for theranostic purposes (therapy and diagnostic purposes), especially, in terms of ROS-responsive drug-delivery systems. In the reduced state, these nanoparticles remain self-assembled with the encapsulated drug but release the drug upon oxidation in ROS-rich tumors or inflamed tissues.



INTRODUCTION

Drug-delivery systems (DDSs) may improve the pharmacodynamics and pharmacokinetics of drugs. Modern medicine depends heavily on pharmaceuticals, which may nevertheless cause side effects in patients and have unfavorable chemical and physicochemical properties or biodistribution. DDSs can solve many of these problems, especially those with improved bioavailability, biodistribution, and pharmacokinetics.¹ Tissue-specific DDSs use one or several specific properties of the target tissue that, ideally, cannot be found anywhere else in the body.^{2–4} Arguably, the most studied drug-delivery principle is the enhanced permeability and retention (EPR) effect.^{5,6} Most solid tumors passively accumulate more nanoparticles (approximately 200 nm and smaller) than healthy tissues. Furthermore, most solid tumors lack lymphatic drainage systems; thus, these nanoparticles remain trapped in the tumor, and drug-loaded nanoparticles may accumulate in solid tumors more selectively than the corresponding free drug.

An ideal DDS does not release its drug content reaching the target tissue (once exposed to target-specific conditions). This targeted delivery can be achieved by designing drug-delivery systems responsive to specific stimuli under external conditions that trigger the release of the drug.⁷ For these purposes, stimulus-responsive systems exploiting pH responsiveness^{8–15}

(tumors are usually more acidic than the surrounding tissues due to the Warburg effect,¹⁶ $\text{pH} \approx 6$), thermoresponsiveness^{17–20} (increased temperature in tumor tissue), light responsiveness^{21–24} (release of the drug after irradiation), and enzyme responsiveness,^{25–28} as well as redox-responsive systems,^{22–24,29–34} have been extensively researched. However, some of these properties are nonspecific: several tissues in the body have low pH values (e.g., stomach³⁵ and the female reproductive system³⁶) or temperatures higher than the rest of the body,³⁷ which can interfere with drug delivery (by triggering premature drug release). Light irradiation depends on external sources of radiation, which can be very advantageous for topical applications but have only limited use in internal applications because radiation does not extensively penetrate tissues. Nevertheless, inflammation and tumors are associated with a significant increase in the concentration of reactive oxygen species (ROS), which is quite unique among

Received: September 9, 2020

Revised: April 6, 2021

Published: April 21, 2021



healthy tissues.^{38–40} These ROS (such as ClO^- , H_2O_2 , and O_2^-) are commonly formed by the both immune system and cancer cells.^{38,40–42} Therefore, redox responsiveness can be used for the selective disassembly of DDSs.

DDSs can also be attached to a tracer moiety to track the fate of DDSs and to diagnose diseases. These systems combine therapeutic and diagnostic modalities, often called theranostics.^{43,44} Traditionally, radioisotope tracers have been used for single-photon emission computed tomography (SPECT) and positron emission tomography (PET), but radioisotopes have several drawbacks (mostly related to administration, cost, and safety). However, ^{19}F magnetic resonance imaging (^{19}F MRI) has emerged as a highly promising noninvasive imaging method without radioisotopes.^{45–50} To date, most MRI systems used in clinical practice detect the proton signal (^1H MRI) of omnipresent water; therefore, xenobiotic tracers are not required. Nevertheless, the gyromagnetic ratios of ^{19}F and ^1H are very similar; therefore, ^1H MRI scanners can be modified into ^{19}F MRI scanners with only minor hardware adjustments (or both ^1H and ^{19}F MRI scanners can be used with advanced hardware).⁵¹ Because the concentration of fluorine in the body is negligible, the use of ^{19}F MRI requires a xenobiotic tracer.⁵² However, this also means that ^{19}F MRI can be used to monitor the distribution of administered fluorine-containing molecules highly selectively and with a very low background, thereby increasing its diagnostic value. Thus, the fate of the fluorinated DDS may be monitored by ^{19}F MRI.

Thermoresponsive copolymers can form nanoparticles with noncovalently bound drugs and thus be used for drug delivery. The amphiphilic copolymers containing hydrophilic blocks and thermoresponsive blocks (e.g., poly[*N*-(2,2'-difluoroethyl)acrylamide], PDFEA) exhibit a lower critical solution temperature (LCST). Consequently, they can be injected into the body at room temperature in aqueous solution; upon heating to body temperature, the PDFEA block rapidly loses its hydration layer, forming defined nanogel particles. In our previous studies, we explained that these thermoresponsive fluorinated diblock copolymers^{53–57} can self-assemble into nanoparticles of ideal sizes upon heating past their cloud point temperature (T_{CP}). We previously described the numerous benefits of using PDFEA polymers for MRI tracers:^{53–57} PDFEA is noncytotoxic and contains a high content of chemically equivalent fluorine atoms that provide a sharp signal in ^{19}F MRI. Moreover, even after aggregation, the ^{19}F signal exhibits only minor signal broadening and a small change in relaxation parameters.^{53–57} Considering all of these properties, PDFEA copolymers are ideal not only for ^{19}F MRI but also for DDSs.

In this study, we investigate a PDFEA-based dual thermo- and ROS-responsive diblock copolymeric DDS that can be monitored via ^{19}F MRI for theranostics. The thermoresponsiveness of these PDFEA-based copolymers enables the convenient formation of nanoparticles in their aqueous solution upon heating, thus encapsulating the drugs. Furthermore, our polymeric nanoparticles contain various amounts (0.9–4.5 mol %) of ferrocene derivatives, endowing the polymers with ROS-responsive behavior. This covalently bound hydrophobic ferrocene (Fc) can be oxidized to a hydrophilic ferrocenium cation (Fc^+),⁵⁸ thereby changing the phase transition temperature and triggering the disassembly of the nanoparticles. Therefore, our polymers are quickly oxidized in an ROS-rich environment (typical for inflammation and tumor tissues),⁵⁹ dissolving and noncovalently releasing their

cargo.^{60,61} Because these polymers in the form of PDFEA contain abundant fluorine (16.5–18.0 wt %), they can be visualized using ^{19}F MRI. As described in the literature, the combination of the MRI contrast agent or tracer with the redox-switch modality enables MRI signal regulation with oxidation.^{62,63} Nevertheless, in our case, the concentration of ferrocene is too low to enable us to detect changes in signal intensity upon oxidation, that is, to track the signal in the oxidized state as well. We used dynamic light scattering (DLS) to study the ability of polymers to self-assemble into particles with increasing temperature and their disassembly upon oxidation. Our approach yielded more advanced polymeric systems, which form nanoparticles when heated to physiological temperature and disassemble under oxidative stress, as confirmed by DR *in vitro* measurements and in spheroidal cancer cell clusters (spheroids) mimicking *in vivo* microtumors.^{64,65}

EXPERIMENTAL SECTION

Materials. 2,2-Difluoroethylamine (97%) was purchased from Fluorochem (Chempur Feinchemikalien GmbH, Germany). Dimethyl sulfoxide- d_6 (99.80% D, water content $\leq 0.02\%$) and methanol- d_4 (99.80% D, water content $\leq 0.03\%$) were purchased from Eurisotop (Saint-Aubin, France). All solvents and magnesium sulfate were purchased from Lach-Ner (Neratovice, Czech Republic). Collagen solution from rat tails was purchased from Millipore (Burlington, MA). The remaining chemicals and cell cultures were purchased from Sigma-Aldrich s.r.o. (Prague, Czech Republic). All chemicals and solvents were of analytical grade. Solvents and liquid chemicals were dried and purified by conventional procedures or distilled before use.

Synthesis of Monomers. *N*-(2-Hydroxypropyl)methacrylamide (HPMA) was synthesized by the reaction of methacryloyl chloride, 1-amino-propan-2-ol, and sodium carbonate in dry dichloromethane (DCM) according to ref 66.

N-(2,2-Difluoroethyl)acrylamide (DFEA) was prepared by the reaction of acryloyl chloride, 2,2-difluoroethylamine, and triethylamine (TEA) in tetrahydrofuran (THF), according to ref 67.

N-(2*N'*-Boc-aminoethyl)acrylamide was prepared by the reaction of acryloyl chloride with *N*-Boc-ethylenediamine in the presence of triethylamine. *N*-Boc-ethylenediamine (2.00 mL, 12.5 mmol) was dissolved in dry THF (20 mL) and cooled in an ice bath. TEA (1.50 mL, 6.85 mmol, 1.20 equiv) was added, followed by the dropwise addition of acryloyl chloride (1.20 mL, 15.0 mmol, 1.20 equiv) in dry THF (1.20 mL). The reaction mixture was stirred overnight at room temperature. Then, the reaction mixture was washed with water and dried with anhydrous magnesium sulfate, and the product was purified by column chromatography on silica (mobile phase, 1:4 v/v hexane/ethylacetate). ^1H NMR (400 MHz, DMSO) δ 8.10 (t, $J = 5.0$ Hz, 1H), 6.82 (t, $J = 5.6$ Hz, 1H), 6.18 (dd, $J = 17.1, 10.0$ Hz, 1H), 6.06 (dd, $J = 17.1, 2.3$ Hz, 1H), 5.57 (dd, $J = 10.0, 2.4$ Hz, 1H), 3.15 (q, $J = 6.3$ Hz, 2H), 3.00 (q, $J = 6.3$ Hz, 2H), and 1.37 (s, 9H). ^{13}C NMR (101 MHz, DMSO) δ 165.19, 156.08, 132.26, 125.44, 78.12, 40.13, 39.18, and 28.68.

Ferrocene carboxylic acid was prepared by ferrocene lithiation with Schlosser's base according to ref 68.

Synthesis of PHPMA. Poly[*N*-(2-hydroxypropyl)methacrylamide] (PHPMA) was prepared by RAFT polymerization. The polymerization mixture consisting of *N*-(2-hydroxypropyl)methacrylamide (3.00 g, 21.0 mmol), 4-cyano-4-[(dodecylsulfanylthiocarbonyl)sulfanyl]pentanoic acid (CTA, 105 mg, 0.260 mmol), and AIBN (31.5 mg, 0.192 mmol) in *tert*-butanol (24 mL) was flushed with argon in a dried Schlenk flask and heated in an oil bath to 70 °C for 7 h. Then, the resulting polymer was precipitated in diethyl ether and purified by gel chromatography using a Sephadex LH-20 column with methanol as the eluent. The polymer-containing fractions were evaporated under reduced pressure, and the polymer was isolated by freeze-drying, yielding 2.1 g (70%) of macro-CTA. The concentration of CTA in macro-CTA was determined by

UV-vis spectrometry to be $21.5 \text{ mmol}\cdot\text{g}^{-1}$ at $\lambda = 308 \text{ nm}$ in methanol ($\epsilon = 4.91 \times 10^3 \text{ cm}^{-1}\cdot\text{M}^{-1}$).

Synthesis of Diblock Copolymers. We prepared three diblock copolymers with different *N*-(2*N'*-Boc-aminoethyl)acrylamide contents with both types of hydrophilic blocks. First, three reaction mixtures containing macro-CTA (PHPMA-CTA, 0.5 g), AIBN (5 mg, 0.03 mmol), *N*-(2,2-difluoroethyl)acrylamide (1.20 g, 8.89 mmol), and three different amounts of *N*-(2*N'*-Boc-aminoethyl)acrylamide (11.0, 22.0, or 44.0 mg; corresponding to 0.05, 0.09, and 0.18 mmol, respectively) were dissolved in dry DMF (4.50 mL), flushed with argon, and polymerized overnight in an oil bath heated to 70 °C. After polymerization, the resulting three polymers were precipitated in diethyl ether and purified by gel chromatography using Sephadex LH-20 in methanol. Methanol was evaporated under reduced pressure, and the polymers were isolated by freeze-drying. The yield was from 133 to 180 mg (from 26 to 36% of the theoretical yield) of PHPMA-*block*-P(DFEA-*stat*-BocAEA), polymers HF1 to HF3.

Modification of the Polymers. The polymers (100 mg) were dissolved in a 10% aqueous solution of trifluoroacetic acid (TFA, 5.00 mL) and stirred for 1 h at room temperature to remove the Boc-protecting groups. Then, we partially evaporated TFA under reduced pressure, and the remaining solution was neutralized with a saturated solution of aqueous sodium bicarbonate to obtain a neutral pH. The polymers were purified using gel chromatography on Sephadex LH-20 with methanol as the eluent. The solvent was evaporated using a rotatory evaporator, and the product was redissolved in water and isolated by freeze-drying, yielding approximately 80 mg of product. The content of the amine moieties in the polymers was determined by labeling the polymers with 2,4,6-trinitrobenzene-1-sulfonic acid (TNBSA) according to the literature.⁶⁹ The content of the TNBS amides was measured at 415 nm ($\epsilon = 1.12 \times 10^4 \text{ cm}^{-1}\cdot\text{M}^{-1}$) and was determined to be 0.0054, 0.0113, and 0.0315 mmol per 70 mg of the HF1-NH₂, HF2-NH₂, and HF3-NH₂ polymers, respectively.

Subsequently, ferrocenecarboxylic acid (FcCOOH, 23.5 mg, 0.102 mmol), *N,N'*-dicyclohexylcarbodiimide (DCC, 25.3 mg, 0.123 mmol), and a catalytic amount ($\approx 0.1 \text{ mg}$) of 4-dimethylaminopyridine (DMAP) were dissolved in cool, dry DMF (1.0 mL), and the mixture was stirred for 30 min at 0 °C. Then, *N*-hydroxysuccinimide (NHS, 17.0 mg, 0.148 mmol) was added to the reaction mixture; the mixture was stirred for 2 h at room temperature to form reactive ferrocenecarboxy-*N*-hydroxysuccinimide ester (FcCOO-NHS). This humidity-sensitive NHS ester was not isolated, and its solution was used without modification for further transformations of the polymer.

The HF1-NH₂, HF2-NH₂, and HF3-NH₂ polymers (70 mg each) were dissolved in dry DMF (1.0 mL). Then, we added 100, 220, and 630 μL of the freshly prepared FcCOO-NHS solution in DMF to the polymer solutions, and the reaction mixture was stirred overnight. After the reaction, the polymers were purified by gel chromatography using Sephadex LH-20 in methanol. The solvent was evaporated under reduced pressure, and the polymers were isolated by freeze-drying, yielding from 55 to 60 mg (70–86%) of the final poly[*N*-(2-hydroxypropyl)methacrylamide]-*block*-poly[*N*-(2,2-difluoroethyl)acrylamide-*stat*-*N*-[2-(ferrocenylcarboxamido)ethyl]acrylamide] (PHPMA-*block*-P(DFEA-*stat*-FcCEA)) HF1, HF2, and HF3 copolymers.

ICP-MS-MS (Determination of the Fe Content). Each polymer (from 1 to 4 mg) was dissolved in nitric acid (v/v 65%, 900 μL) and hydrogen peroxide (v/v 30%, 100 μL). This mixture was heated to 130 °C in capped vials in a single-mode Biotage Initiator Sixty microwave (IR temperature sensor, Biotage, Uppsala, Sweden). Then, the solution was diluted in deionized water to a final volume of 15.0 mL. Subsequently, this solution (1.00 mL) was mixed with nitric acid (5.00 mL, v/v 2%), and the concentration of iron was determined using ICP-MS-MS (Agilent 8900, Agilent, Santa Clara, CA) in O₂ mode. External calibration was performed.

NMR. All NMR spectra were acquired with a Bruker Avance III 400 MHz system (Bruker, Billerica, MA) operating at 400.13 MHz and equipped with a broad-band probe. The ¹H, ¹³C{¹H}, ¹H–¹H correlation spectroscopy (COSY), ¹H–¹³C heteronuclear multiple bond correlation (HMBC), and multiplicity-edited ¹H–¹³C hetero-

nuclear single quantum coherence spectroscopy (HSQC) spectra of the monomer *N*-(2*N'*-Boc-aminoethyl)acrylamide were recorded in dimethyl sulfoxide-*d*₆.

Each polymer (10.0 mg) was dissolved in methanol-*d*₄ (600 μL). We used their ¹H NMR (NS = 32, *D*₁ = 30.0 s) spectra to determine the polymer purity. Furthermore, we assessed the ratio of the proton signals in the –CHF₂ moiety of PDFEA ($\delta = 5.9 \text{ ppm}$) and the CHOH moiety of PHPMA ($\delta = 3.9 \text{ ppm}$) to determine the ratios of the incorporated monomers.

We recorded the ¹⁹F NMR spectra of aqueous HF1, HF2, and HF3 polymers (0.6 mg·mL⁻¹, 64 scans, *D*₁ = 1.00 s) in their reduced and oxidized forms.

¹⁹F Relaxation. We determined the relaxation properties (*T*₁ and *T*₂) of ¹⁹F atoms with a Varian Inova 400 MHz spectrometer equipped with an ID-PFG (pulsed field gradient) probe. Both parameters were measured for each sample (*c*_{pol} = 15 mg·mL⁻¹) at 37.0 °C in their reduced form. The samples were incubated for at least 15 min at the given temperature before assessment. The *T*₁ parameter was measured with an inversion recovery sequence (*D*₂ = 0.2, 0.4, 0.8, 1.6, 3.2, 6.4, 12.8, 25.6, 51.2, 102.4, 204.8, 409.6, 819.2, 1638.4, and 3276.8 ms; the 180° pulse width was optimized to $\approx 180^\circ$; and the 90° pulse was derived from the 180° pulse width). The *T*₂ parameter was measured with the CPMG sequence⁷⁰ (*D*₂ = 0.05 ms; *n* = 4, 8, 16, 32, 64, 128, 256, 512, 1024, 2048, 4096, 8192, 16384, 32768, and 65536; the 180° pulse width was optimized to $\approx 180^\circ$; the 90° pulse was derived from the 180° pulse width).

Size Exclusion Chromatography (SEC). The number-average molecular weight (*M*_n), weight-average molecular weight (*M*_w), and dispersity ($\mathcal{D} = M_w/M_n$) of the polymers were assessed using an HPLC Ultimate 3000 system (Dionex, Sunnyvale, CA) equipped with an SEC column (TSKgel SuperAW3000 150 × 6 mm², 4 μm) and three different types of detectors, a UV-vis detector, an Optilab-REX refractive index (RI) detector, and a DAWN EOS multiangle light scattering (MALS) detector (Wyatt Technology Corporation, Santa Barbara, CA). For the analysis, a methanol and sodium acetate buffer (0.3 M, pH 6.5) mixture was used as the mobile phase (80:20 v/v%, a flow rate of 0.5 mL·min⁻¹).

Dynamic Light Scattering (DLS). We measured the intensity-weighted hydrodynamic diameter (*R*_H) and the scattering intensity of the polymeric assemblies as a function of polymer temperature using a Zetasizer NanoZS instrument, model ZEN3600 (Malvern Instruments, Malvern, U.K.). *R*_H was measured at a scattering angle of $\theta = 173^\circ$, and the data were processed with the Repes algorithm.⁷¹ All solutions were filtered before measurement using a 0.22 μm PVDF syringe filter. The measurement step was 0.5 °C. The set points of the temperature values were kept within an accuracy level of ± 0.2 °C, and the samples were incubated at the given temperature for 5 min before taking measurements. The stability of the polymeric particles over time was measured using the same procedure as that followed in the assessment of the variation of temperature as a function of the particle size. Samples HF1, HF2, and HF3 (polymer concentration 1.0 mg·mL⁻¹ in 140 mM PBS) were incubated at 37 °C for 72 h, and the DLS of each sample was measured at specific time points.

We measured the size distribution of the polymeric assemblies in the polymer solutions (1.0 mg·mL⁻¹, PBS, 140 mM, pH 7.4) as a function of temperature (15.0–48.0 °C). Then, we measured the size distribution of the polymeric assemblies in the polymer solutions in acetate buffer (40 mM, pH 5.0) containing a catalytic amount of CuCl₂·2H₂O ($\approx 0.1 \text{ mg}$) and from 0.003 to 0.01 v/v % hydrogen peroxide as a function of temperature.

Finally, we measured the size distribution of the polymeric assemblies in the HF1 solution (8.00 mL, 1.0 mg·mL⁻¹) in PBS (140 mM, pH 7.4) at constant temperature (37.0 °C) with increasing concentrations of hydrogen peroxide; at each step, we added 30 μL of 30% (v/v) hydrogen peroxide.

Static Light Scattering (SLS). *M*_w and radii of gyration (*R*_g) at 37 °C were determined by SLS using an ALV-6000 equipment (ALV-GmbH, Langen (Hesse), Germany). The *z*-average radii of gyration of particles, $\langle R_g \rangle_z$, and their *M*_w were derived from a wide range of scattering angles (60–146°, increment 2°) and polymer concen-

trations (0.25, 0.35, 0.5, 0.75, and 1.0 mg·mL⁻¹ in 140 mM PBS). All solutions were filtered using a 0.22 μm PVDF syringe filter. The SLS was measured three times, and the SLS acquisition time was 40 s. Subsequently, we constructed Zimm plots from the data and analyzed them by ALV/static and Dynamic FIT and PLOT 4.31 10/01 software (Langen/Hessen, Germany).

Furthermore, we measured the differential refractive index (dn/dc) using a differential refractometer (Brookhaven Instruments, Holtsville, NY) and analyzed by Brookhaven Refractometer Software Ver. 5.32 at different polymer concentrations (0.25, 0.35, 0.5, 0.75, and 1.0 mg·mL⁻¹ in 140 mM PBS) and temperature 37 °C.

Critical Association Concentration (CAC). We assessed the CAC via fluorescence spectrometry using Nile red (NR) in two independent experiments. We prepared a series of HF1 solutions in PBS: a twofold dilution series starting from a concentration of 1.0 mg·mL⁻¹ and decreased to 3.8×10^{-6} mg·mL⁻¹ was prepared (19 samples, each 100 μL), and we added a stock solution of NR (5 μL, 2.0×10^{-5} mol·L⁻¹ in ethanol) to each of the samples, which were incubated for 10 min at 37 °C. Then, we recorded the fluorescence spectra of all samples using black Nunc cell culture microplates (Nalge Nunc International, Rochester, NY) and a Synergy H1 hybrid reader (BioTek, Winooski, VT) at 37 °C and excitation/emission wavelengths of 485/636 nm. The intensities of the fluorescence were plotted as a function of polymer concentration, and the CAC was determined as the intersection between two fit linear functions, one decreasing with decrease in polymer concentration and the other remaining constant regardless of the polymer concentration.

Transmission Electron Microscopy (TEM). The morphology of the nanoparticles was visualized under a transmission electron microscope (Tecnai G2 Spirit Twin 12; FEI Company, Brno, Czech Republic) equipped with a Cryo-holder (Gatan, CA). The polymer solution (polymer concentrations 1.0 and 10 mg·mL⁻¹ in 140 mM PBS, pH 7.4) and tools for sample preparation (tweezers, microscopic grids, etc.) were incubated in an electric oven at 50 °C for at least 30 min. Then, 2.0 μL of the heated solution was deposited on a carbon-coated copper TEM grid and left to evaporate for 1 min (still in the oven at $T = 50$ °C). Subsequently, the grid was removed from the oven and then the excess solvent on the grid was removed by touching the bottom of the grid with a small piece of filter paper. This fast removal of the solution is a key step of the fast-drying method, which minimizes drying artifacts, as shown in our previous studies.^{72–74} The dried samples were equilibrated for at least 1 h in air and were then observed under TEM at room temperature using bright field imaging at 120 kV.

MRS and MRI Phantom Measurements. Both MRS and MRI were performed on a Bruker BioSpec 94/30 Advanced III 9.4 T MRI system (Bruker BioSpin MRI GmbH, Ettlingen, Germany) equipped with a ¹H/¹⁹F dual probe (RF RES ¹H/¹⁹F 075/040 LIN/LIN, outer diameter of 75 mm, and inner diameter of 40 mm). We prepared small Eppendorf vial phantoms containing PBS solutions (200 μL) of H1 polymer (50.0, 25.0, or 12.5 mg·mL⁻¹) with trace amounts of trifluoroacetic acid as a chemical shift reference. Then, the phantoms were sealed and placed into a large plastic vial connected to a thermostat (the heat transfer fluid was an aqueous solution of manganese(II) chloride), which enabled us to carefully control the sample temperature during the measurements. With this setup, MRS was performed at 24 and 37 °C (Figure 3), and MRS was used for excitation pulse length optimization.

¹⁹F MRS (376.7 MHz): single-pulse sequence; repetition time TR = 1000 ms; number of averages NA = 128; total scanning time TA = 2 min 8 s.

Subsequently, ¹H MRI and ¹⁹F MRI were performed at 37 °C, and their data were combined.

¹H MRI (400.3 MHz): MGE gradient sequence; flip angle = 2.94°; repetition time TR = 64.8 ms; echo time TE = 1.03/2.93/4.83/6.73/8.63/10.5 ms; TF = 1; slice thickness = 1.57 mm; sw = 100 kHz; number of averages NA = 25; number of slices, 5; digital matrix, 64 × 128; field of view, 40 × 40 mm²; spatial resolution, 0.313 × 0.313 mm²; TA = 3 m 27 s.

¹⁹F MRI (376.4 MHz): MGE gradient sequence; flip angle = 2.94°; repetition time TR = 64.8 ms; echo time TE = 1.03/2.93/4.83/6.73/8.63/10.5 ms; TF = 1; slice thickness = 1.57 mm; sw = 100 kHz; number of averages NA = 225; number of slices, 5; digital matrix, 64 × 128; field of view, 40 × 40 mm²; spatial resolution, 0.313 × 0.313 mm²; TA = 31 m 7 s.

Drug Loading (DL). The drug-loading factor f_{DL} (sometimes referred to as DL) and the entrapment efficiency factor f_{EE} (sometimes referred to as EE) were calculated using eqs 1 and 2.

$$f_{DL} = \frac{m_{drug,II}}{m_{polymer} + m_{drug,II}} \times 100\% \quad (1)$$

$$f_{EE} = \frac{m_{drug,II}}{m_{drug,I}} \times 100\% \quad (2)$$

where $m_{polymer}$ is the mass of the polymer, $m_{drug,I}$ is the mass of the drug added to the system (cumulative mass of the drug within both the aqueous and polymer phases), $m_{drug,II}$ is the mass of the drug found in the formulation, and m_{aq} is the mass in the aqueous phase.

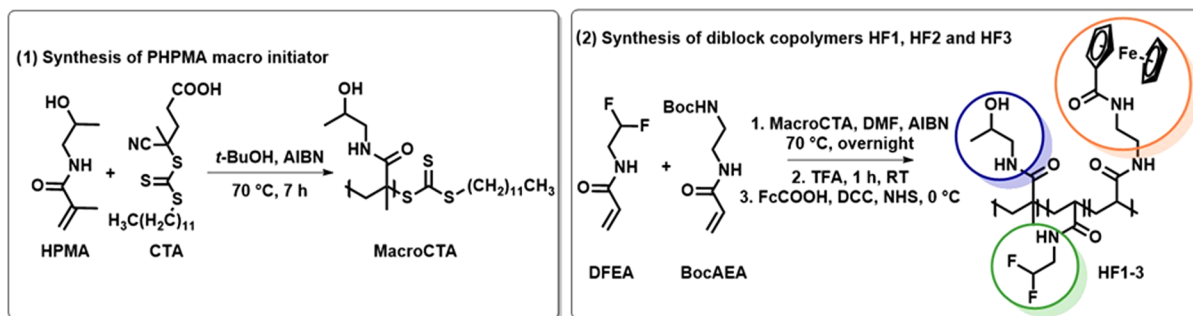
The mass of the non-encapsulated drug was determined by UV-vis spectroscopy after ultrafiltration (Amicon Ultra-15 centrifugal filter unit with an Ultracel 30 kDa membrane, Millipore, Burlington, MA). Particle solutions at 0.1 mg·mL⁻¹ in PBS buffer, pH 7.4, with varying concentrations of the drug doxorubicin (DOX) or the inhibitor (GSK 429286) (drug concentration range: from 0.025 to 0.100 mg·mL⁻¹) were tested at 37 °C in two independent experiments. For the determination of the non-encapsulated drug, an aliquot (45 μL) of each filtrate was diluted with methanol (55 μL), and the absorbance was compared to the absorbance of the particle solution (45 μL) also diluted with methanol (55 μL) to dilute the particles and avoid measurement errors. The concentration of DOX ($m_{drug,II}$) was determined by UV-vis spectroscopy (measured at 480 nm) with a Synergy H1 hybrid reader (BioTek, Winooski, VT) and black Nunc cell culture microplates (Thermo Scientific, Nalge Nunc International, Rochester). The concentration of the inhibitor (GSK 429286) was determined by UV HPLC.

The HPLC gradient was as follows: phase A: 95% water, 5% ACN, and 0.1% TFA; phase B: 5% water, 95% ACN, 0.1% and TFA; $t = 0$ min for 20% B, 0.5 mL·min⁻¹; $t = 0.1$ min for 20% B, 3.5 mL·min⁻¹; $t = 2.25$ min for 60% B; 3.5 mL·min⁻¹ (linear gradient); $t = 2.5$ min for 90% B; 3.5 mL·min⁻¹ (linear gradient); $t = 3.0$ min for 90% B; 3.5 mL·min⁻¹; $t = 3.3$ min for 20% B; 3.5 mL·min⁻¹ (linear gradient); and $t = 4.0$ min for 20% B, 3.5 mL·min⁻¹.

Drug Release (DR). The doxorubicin stock solution (10 μL) in DMSO (10 mg·mL⁻¹) was transferred to an Eppendorf tube containing 1.00 mL of polymer HF1 solutions (1.0 mg in 140 mM PBS, pH 7.4, or 40 mM acetate buffer, pH 5.0, containing a catalytic amount of (≈0.1 mg) CuCl₂·2H₂O and 0.003 vol % hydrogen peroxide), and the final concentration of DOX is 0.1 mg·mL⁻¹. A measure of 0.1 mg of doxorubicin was dissolved in 1.00 mL of 140 mM PBS buffer and used as a control measurement. The preheated polymer solution containing DOX and free DOX solution was quickly transferred into a minidialysis kit (Spectra-Por Float-A-Lyzer G2 black, 1 mL, MWCO 3.5–5 kDa, Sigma-Aldrich, Prague, Czech Republic), and the minidialysis kit was immersed into a 150 mL beaker containing preheated PBS (125 mL, 37 °C) and a magnetic stir bar. The solution (5 μL) at the inner side of the dialysis membrane was taken using a pipette at specific time points to determine the amount of released doxorubicin by fluorescence ($\lambda_{ex}/\lambda_{em} = 480/590$).

Cell Culture. Human embryonic lung fibroblasts (IMR90) and human fibrosarcoma (HT1080) cell lines were routinely cultivated in DMEM supplemented with 10% FBS and 10 μg·μL⁻¹ gentamicin in a humidified atmosphere with 5% CO₂ at 37 °C.

In Vitro Cytotoxicity. *In vitro* cytotoxicity was assessed by an Alamar Blue assay (Invitrogen, Grand Island, NY). Briefly, HT1080 and IMR90 cells were seeded in 96-well plates (1 × 10⁴ cells per well, Figure S13). The next day, polymer solutions in complete medium (DMEM supplemented with 10% FBS and antibiotics) were prepared

Scheme 1. Synthesis of Multiresponsive Fluorinated PHPMA-*block*-P(DFEA-*stat*-FcCEA) Copolymers HF1, HF2, and HF3^a

^aThe polymer chain end moieties were omitted for clarity.

Table 1. Composition and Physicochemical Properties of Polymers

polymer	block ratio ^a	M_w^b (kDa)	M_n^b (kDa)	\mathcal{D}^b (M_w/M_n)	wt % of fluorine ^{a,d}	wt % of ferrocene ^{c,d}
PHPMA	— ^d	8.68	8.02	1.09	—	—
HF1	1:1.8	32.3	26.3	1.22	16.7	0.49 ± 0.12
HF2	1:1.9	29.1	26.0	1.12	18.0	0.80 ± 0.12
HF3	1:1.8	34.0	27.9	1.22	16.6	2.63 ± 0.66

^aDetermined by ¹H NMR spectroscopy. ^bDetermined by SEC. ^cDetermined by ICP-MS-MS. ^dNot applicable (—).

from a stock solution (10 mg·mL⁻¹ in PBS) by serial dilution and added to cells (100 μL per well). A complete medium without polymer solutions was used as a positive control, and wells containing only medium were used as blanks. After 24 h, the medium was aspirated, and the cells were incubated with 50 μL of Alamar Blue solution per well (10% Alamar Blue reagent in phenol-red free DMEM) for 3 h. Subsequently, 40 μL of the Alamar Blue solution was transferred to a new 96-well plate, and fluorescence ($\lambda_{\text{ex}} = 560$ nm; $\lambda_{\text{em}} = 590$ nm) was determined using an Infinite M200 PRO fluorescent plate reader (Tecan Life Sciences, San Jose, CA). Two independent experiments were performed, and the average results of the treated cells were plotted relative to the positive control. Statistical significance was assessed by a two-way ANOVA with Sidak multiple comparison tests.

3D Spheroid Assay. HT1080 cells were grown to create multicellular spheroids using agarose micromolds (MicroTissues 3D Petri Dish micromold spheroids) according to the manufacturer's instructions. After 48 h, the spheroids were rinsed in medium and embedded in a collagen matrix prepared by mixing a buffer solution with rat tail collagen (4 mg·mL⁻¹) on ice. The resulting composition of the collagen matrix was 1.0 mg·mL⁻¹ rat tail collagen, 1× RPMI medium, 15 mM HEPES, 1% fetal bovine serum, and 50 μg·mL⁻¹ gentamicin (Sigma Aldrich, St. Louis, MO). After 30 min, the spheroids were overlaid with the medium without polymer or the medium with 0.2 mg·mL⁻¹ polymer; for both conditions, DMSO or an inhibitor of invasion (1.0 and 10 μM GSK 429286) was used as a control. Images of the spheroids were taken using a Nikon-Eclipse TE2000-S microscope immediately after embedding and after 24 h. The area of the spheroids at 0 and 24 h was assessed using Fiji software. The "relative invasion index" was calculated as the ratio of the spheroid area at 24/0 h. The presented data show the results of two independent experiments and 6–8 spheroids per condition. Statistical significance was assessed by a two-way ANOVA with Sidak multiple comparison tests. To determine the DOX distribution in 3D spheroids, doxorubicin (10 μM) was added to the overlaid control medium or the medium with 0.2 mg·mL⁻¹ polymer directly after cells were embedded in 3D collagen. After 24 h, doxorubicin fluorescence in the spheroids was imaged by a 10× objective lens using the Thunder Imager configuration of a Leica DMI8 microscope (excitation wavelength of 470 nm). For each spheroid, the representative image is a maximum projection of 100 stacked images. Doxorubicin fluorescence was quantified with ImageJ software based

on three independent experiments, and significance was assessed using the Student's *t* test.

RESULTS AND DISCUSSION

The PHPMA-*block*-P(DFEA-*stat*-FcCEA) (HF1, HF2, and HF3) amphiphilic diblock copolymers at a 1:2 ratio and with varying ferrocene content (from 0.5 to 3.0 wt %) were prepared by two subsequent RAFT polymerizations of the corresponding monomers using the chain transfer agent (CTA) and AIBN, as the initiator (Scheme 1), followed by postpolymerization modifications. First, we polymerized the hydrophilic HPMA monomer, purified, and determined the concentration of CTA using UV–vis spectroscopy. Then, the second polymerization of the DFEA monomer was performed with small amounts (from 0.9 to 4.5 mol %) of the *N*-(2'-Boc-aminoethyl)acrylamide monomer (determined by NMR, Figures S1–S5) for statistical copolymerization. After polymerization, the Boc-protecting groups were removed under acidic conditions, neutralized, and purified. The concentration of amine moieties was determined by the reaction with TNBSA and measured by UV–vis spectroscopy according to the literature.⁶⁹ Then, the amine moieties were coupled with *in situ*-generated ferrocenecarboxy-*N*-hydroxysuccinimide ester to form the resulting HF1, HF2, and HF3 polymers. The structure and purity of all copolymers and the relative content of the comonomers were determined by ¹H NMR (Figure S6). Then, the narrow molecular weight distribution (dispersity $\mathcal{D} \leq 1.22$) and molar mass of approximately 30 kDa (Table 1) of all copolymers was determined by size exclusion chromatography (Figure S7).

Thus, the polymer consists of three different components (Scheme 1). First, PDFEA with a high concentration of fluorine is suitable for ¹⁹F MRI and ensures the LCST properties of the polymer, thus enabling particle self-assembly with the increase in temperature. Second, the *N*-[2-(ferrocenylcarboxamido)ethyl]acrylamide monomer (FcCEA) incorporated in the PDFEA block provides the redox-responsive character of the polymers and possible controlled drug release properties. Last, the nanoparticle that colloiddally

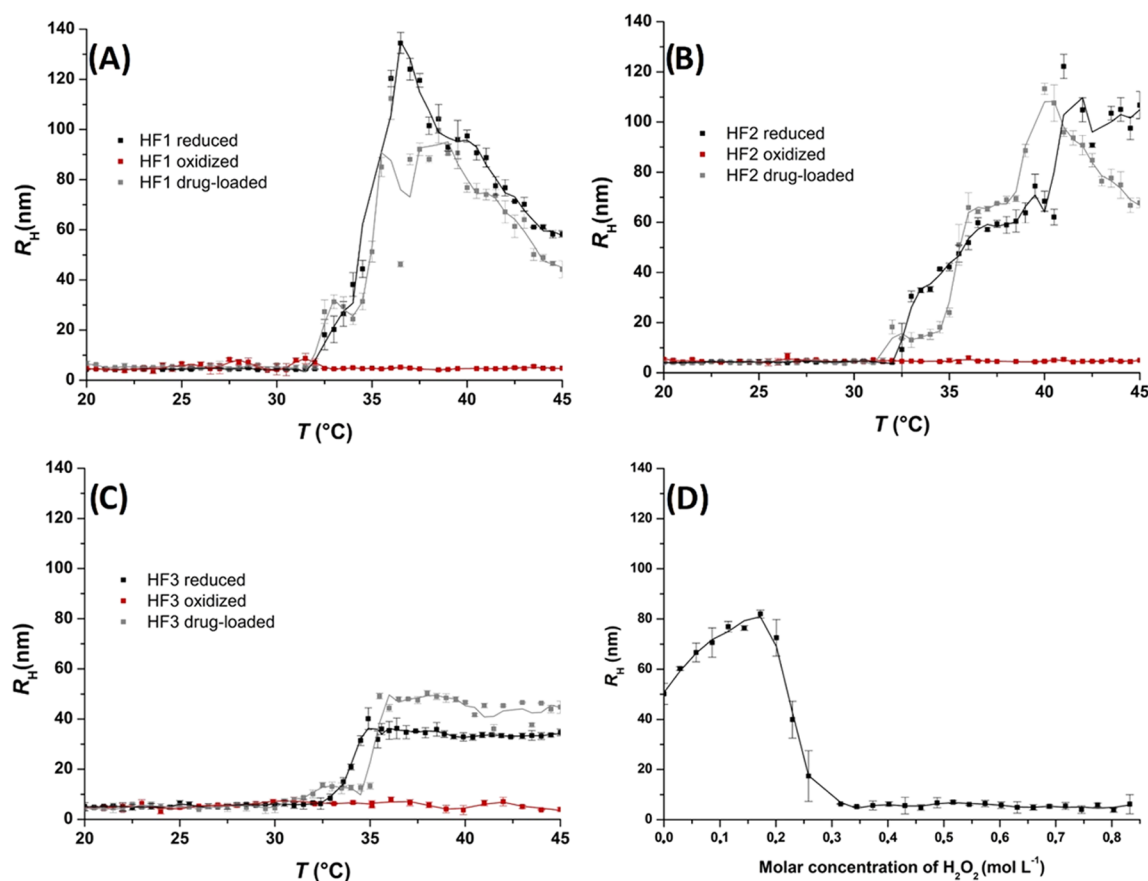


Figure 1. Graphs (A–C) show the particle size (determined by DLS) as a function of temperature for HF1, HF2, and HF3 in their reduced forms in PBS (black trends), in their oxidized forms in acetate buffer (red trends), and in their reduced drug-loaded form in PBS (GSK 429286, 0.1 mg·mL⁻¹, gray trends). Graph (D) shows the HF1 particle size (by DLS) as a function of the H₂O₂ concentration used for titration. The trendlines, smoothed using a Savitzky–Golay filter, serve as guides to the eye.

stabilizes the hydrophilic block consists of a single monomer, HPMA. The copolymers were prepared with three different ferrocene contents (approximately 0.5, 1.0, and 3.0 wt %, Table 1) to assess the concentration effect of the redox-responsive monomer on the general physicochemical properties of the polymer.

The temperature change-induced self-assembly of the copolymers in the aqueous PBS solution was measured by DLS as a function of temperature (Figure 1, black trends) and as a drug formulation with hydrophobic drugs (GSK 429286, 0.1 mg·mL⁻¹, Figure 1, gray trends). A phosphate-buffered saline (PBS) solution (pH 7.4) was chosen as a simple biologically relevant model (pH, ion concentration). Particle hydrodynamic radii (R_H) and T_{CP} are outlined in Table 2. The morphology of the particles based on the reduced form of HF1 was visualized by transmission electron microscopy (TEM) (Figure 2) to further corroborate and confirm DLS results. The particle size of the sample HF1 measured by TEM above

Table 2. DLS and SLS Data of HF1, HF2, and HF3 Polymers (1.0 mg·mL⁻¹ in 140 mM PBS, 37 °C)

polymer	$R_H \pm SD$ (nm)	$R_g \pm SD$ (nm)	M_m of particle (kg·mol ⁻¹)	ρ (g·cm ⁻³)	T_{CP} (°C)
HF1	124 ± 4	133 ± 27	175 ± 35	0.03	32.5
HF2	57 ± 1	75 ± 14	63 ± 7	0.06	33.0
HF3	35 ± 3	36 ± 3	24 ± 1	0.02	33.6

LCST (Figure 2; diameter approximately 100 nm) was in fair agreement with the DLS results (Figure 1; diameters approximately 120 nm). The difference between the two methods is given by different sample preparations: In TEM, we used the fast-drying method in which the sample was heated up to 50 °C (to ensure that the temperature remained above the LCST throughout the sample preparation), and the solvent was quickly removed before the particles collapse, albeit without completely avoiding particle shrinking (due to solution removal). In DLS, we measured swollen particles directly in the solution and with the precise temperature gradient. Therefore, DLS is a more precise method for determining the particle size of our system as it measures particles in their natural state in the solution. Eventually, the architecture was described in more detail with SLS. Thus, the DLS and SLS results together with TEM images provide a comprehensive insight into the structure of each copolymer and suggest that the internal structure of these polymers resembles a nanogel, which we have described previously.^{53,55,57} These nanogels have a low density and relatively large sizes and particle weights. With the increase in the content of ferrocene, the particles became more compact, most likely due to the hydrophobicity of ferrocene. In the polymer HF1, we observed an equilibrium between small particles and larger nanogels (Figure S9) as described in a previous study.⁵⁵

The R_H of the particles ranges from approximately 34.8 to 124 nm, and the T_{CP} is 33.0 ± 0.6 °C for all three polymers. The initial increased R_H value corresponds to a cluster of

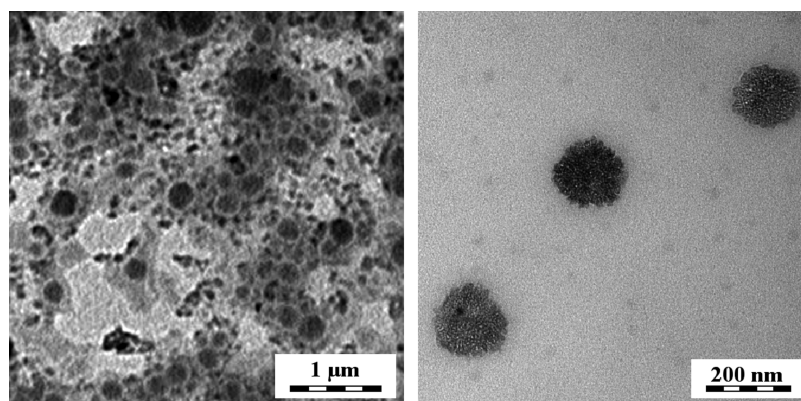


Figure 2. TEM micrograph of polymeric HF1 particles. Left: polymer concentration of 10 mg·mL⁻¹, right: polymer concentration of 1.0 mg·mL⁻¹.

particles moving together, which is a well-known behavior of particles with hydrophobic coronas.⁷⁵ Particles were stable over 3 days at 37 °C in 140 mM PBS. Particles (or their clusters, Figure S8) are stable over time, and no disassembly or oxidation occurs. Additional depictions of the intensity-based size distributions of particles, which provide a comparative picture of size distributions from Figure 1 below and above the T_{CP} , are presented in Figures S9–S11.

To determine the ROS-responsive behavior, we oxidized ferrocene in the polymer and measured the size distributions as a function of temperature using the same DLS setup (Figure 1). Numerous ferrocene oxidation methods have been reported, e.g., with hydrogen peroxide in the presence of enzymes and metal ions and acids.^{76–79} The oxidation of ferrocene can be observed by the color change from yellow-orange ferrocene (Fc^0) to greenish and dark blue ferrocenium (Fc^+). For our intended application, as DDSs for cancer treatment, we decided to simulate the conditions for *in vitro* measurements in acidic environments containing hydroxyl radicals (pH 5.0, corresponding to acidic environments in tumor endosomes).⁸⁰ Therefore, for our measurement, we used Fenton oxidation conditions in the 40 mM acetate buffer (pH 5.0).⁸¹ The results revealed that oxidation prevents all three polymers from forming particles within the measured temperature range (Figure 1, red trends), which indicates that oxidation shifts to the temperatures outside the physiological range, thus triggering particle disassembly. Furthermore, we also titrated the polymer solution using a hydrogen peroxide solution under neutral conditions to determine the concentration of H_2O_2 , into which the particles decompose. The 0.2 mol % concentration of H_2O_2 (corresponding to approximately 11 μ L of H_2O_2 to 0.02 mg of ferrocene) was sufficient to oxidize/disassemble the polymer with the lowest concentration of ferrocene, showing the great sensitivity of the system to even a slightly oxidative environment. In conclusion, the ferrocene moiety acts as a ROS-responsive switch between self- and disassembled states at physiological temperatures.

The suitability of using the tracers for routine ^{19}F MRI techniques is highly dependent on several key parameters. First, it is beneficial if the ^{19}F atoms are chemically and magnetically equivalent (this ensures a very intense and narrow peak of the ^{19}F signal), and the content of the ^{19}F atom needs to be as high as possible. Second, the choice of applicable ^{19}F MRI scanning techniques and, therefore, the quality of the image strongly depend on the T_2 and T_2^* relaxation properties of fluorine atoms. For the purposes of routinely used MRI scanning techniques (e.g., RARE and FLASH),⁸² T_2 should be

longer than 10 ms.⁵⁴ Short T_2 relaxation requires using particular sequences, such as ultrashort echo time (UTE)⁸³ or zero echo time (ZTE)⁸³ sequences, which, in turn, require a high hardware capacity.

Usually, polymer aggregation significantly decreases the ^{19}F signal (partly due to the significantly faster T_2 relaxation of the aggregates, ultimately lowering the intensity of the tracer signal).⁵⁵ Although the PDFEA copolymers generally do not undergo changes in their MR properties upon aggregation, the MR properties may be influenced by the surrounding conditions.^{56,57} Therefore, we measured the T_1 and T_2 relaxation times at 37 °C in 140 mM PBS buffer (pH 7.4) to simulate physiologically relevant conditions.⁵⁶ The results show a decrease in both relaxation times with the increase in ferrocene content (Table 3). T_2 is above the threshold value for the ^{19}F MRI sequences of polymers HF1 and HF2 ($T_2 \approx 17$ ms), making them suitable for currently used ^{19}F MRI scanners.

Table 3. T_1 and T_2 Relaxation Times for ^{19}F in a 9.4 T Field of All Three Polymer Solutions at 37 °C in PBS-D₂O Buffer (140 mM, pH 7.4)^a

polymer	T_1 (ms)	T_2 (ms)
HF1	460 ± 4	16.9 ± 0.6
HF2	458 ± 6	11.0 ± 0.4
HF3	395 ± 10	7.0 ± 0.6

^aAll data were fitted with $R^2 \geq 0.998$.

Moreover, the oxidation of the diamagnetic ferrocene to paramagnetic Fc^+ may affect the ^{19}F signal. Hence, we recorded the NMR spectrum of the polymers before and after oxidation, and we did not observe any change in chemical shift (both forms had a chemical shift of ≈ -123 ppm) or any significant signal broadening (indicating no observable change in T_2^*) (Figure S14). Furthermore, the similarity of spectra, regardless of the oxidation state, was confirmed in MRS experiments (Figure 5). No changes were observed in the NMR spectra most likely because the polymer contains a relatively minor amount of Fc and its oxidation affects only the surrounding DFEA monomers. Most moieties remain unaffected, and thus the ^{19}F NMR signal remains unchanged.

Based on our results, we decided to use the polymer HF1 for further measurements owing to its well-defined self-assembling properties, thoroughly studied in previous research,⁵³ and its suitable T_1 and T_2 relaxation times for ^{19}F MRI purposes.

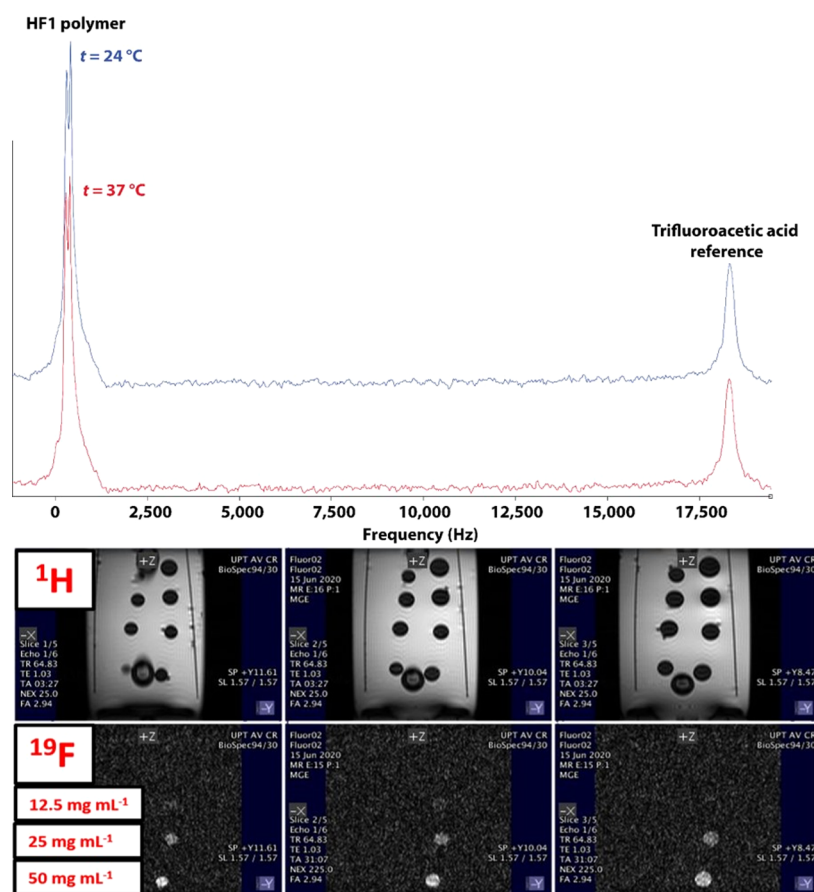


Figure 3. Top: ¹⁹F MRS spectra of the HF1 polymer with trifluoroacetic acid as a chemical shift reference at 24 °C (blue curve) and 37 °C (red curve). Bottom: *In vitro* phantom ¹H MRI and ¹⁹F MRI images with decreasing polymer concentrations. Signal-to-noise ratio (SNR) = 6.9.

However, our results indicated that the ferrocene content might differ considerably without severely changing the T_{CP} or MR properties (only particle size changes).

Subsequently, we performed ¹H/¹⁹F MRS and MRI: the polymer HF1 with the best MR relaxation properties was dissolved in a 140 mM PBS solution to achieve various polymer concentrations (Figure 3). The phantoms were placed inside a container connected to a thermostat to closely control the temperature of the samples during the measurement. We used water as a heat transfer medium, but we added manganese(II) chloride to decrease the relaxation times of the medium and thus shortened the ¹H MRI acquisition time. First, we measured ¹⁹F MRS at 24 °C (Figure 3, blue curve) and 37 °C (body temperature, Figure 3, red curve). No significant signal decrease was observed upon heating (and particle formation), which is ideal for ¹⁹F MRI purposes. Subsequently, we performed ¹H and ¹⁹F MRI for the entire setup (Figure 3); this method enables the study of phantoms with polymer concentrations as low as 12.5 mg·mL⁻¹.

The HF1 polymer, selected for further testing, was subjected to a drug-loading (DL) study. We determined the drug-loading factor f_{DL} and the entrapment efficiency factor f_{EE} , which were calculated with eqs 1 and 2. The DL was measured for three different concentrations of doxorubicin (DOX) and the inhibitor (GSK 429286) in the presence of the polymer (1.0 mg·mL⁻¹ in 140 mM PBS buffer, pH 7.4) at 37 °C by ultracentrifugation (Table 4). The lowest concentration of the drug (0.025 mg of the drug to 1.0 mg of polymer) has an $f_{EE} \approx 92.1 \pm 2.4\%$ for DOX and an $f_{EE} \approx 74.5 \pm 2.7\%$ for GSK

Table 4. Data from the DL Study for the HF1 Polymer in PBS Buffer, pH 7.4, Loaded with the DOX/GSK 429286 Drug at Concentrations of 0.10, 0.05, and 0.025 mg·mL⁻¹^a

	doxorubicin		
$m_{drug,I}$ (μ g)	100	50.0	25.0
$m_{drug,II}$ (μ g)	35.2 \pm 1.6	27.8 \pm 1.7	22.8 \pm 0.3
f_{EE} (%)	34.1 \pm 3.2	58.0 \pm 6.7	92.1 \pm 2.4
f_{DL} (%)	3.2 \pm 0.2	2.7 \pm 0.2	2.23 \pm 0.03
	GSK 429286		
$m_{drug,I}$ (μ g)	100	50.0	25.0
$m_{drug,II}$ (μ g)	30.2 \pm 2.5	17.8 \pm 1.7	18.6 \pm 0.8
f_{EE} (%)	30.5 \pm 2.9	35.3 \pm 3.1	74.5 \pm 2.7
f_{DL} (%)	2.9 \pm 0.3	1.8 \pm 0.2	1.8 \pm 0.1

^aThe mean and SD were calculated from two independent experiments.

429286, which corresponds to the approximate concentration in the following *in vitro* measurements, showing efficient drug encapsulation.

To determine the biocompatibility of the polymer HF1, we measured the cytotoxicity on two relevant cell lines, human embryonic lung fibroblasts and human fibrosarcoma (IMR90 and HT1080). The polymer HF1 did not significantly affect cell viability, with no decreases below 70% (Figure S13) within the tested concentration range (0.125–2.00 mg·mL⁻¹). Furthermore, we measured the critical association concentration (CAC) to determine the biocompatibility and stability of the polymer particles.⁶⁴ Serial dilution was used to measure

the critical association concentration of the polymer solution in phosphate-buffered saline (140 mM, pH 7.4) containing the same concentration of Nile red (NR) used as the fluorescent probe with a low fluorescence signal in aqueous solution and a high fluorescence signal in micelles. The fluorescence of the samples was recorded ($\lambda_{\text{ex}}/\lambda_{\text{em}} = 485/636$) and plotted as a function of polymer concentration. The CAC of the polymer HF1 was $14.1 \pm 1.9 \text{ mg}\cdot\text{L}^{-1}$, as determined by intersecting both fitted linear functions (Figure S12). The standard deviation was evaluated from two independent experiments.

To demonstrate the effect of the oxidative state of the polymers on drug release, we performed *in vitro* drug-release experiments with the hydrophobic drug doxorubicin. In this experiment, both doxorubicin and HF1 polymer were dissolved in either PBS (140 mM, pH 7.4, as a model of reduced state) or acetate buffer (40 mM, pH 5.0, and oxidized via Fenton oxidation). We used doxorubicin solution in PBS as a drug release control (no added polymer). DR was performed using a dialysis method. The DR was determined by the fluorescence ($\lambda_{\text{ex}}/\lambda_{\text{em}} = 480/590$).

In both cases (reduced and oxidized states), the DOX concentration increased rather quickly during the first 5 h, which corresponds to the release of the nonpolymer-bound drug. Upon this quick initial release, a significantly slower release is observed in the HF1-reduced polymer formulation (Figure 4). In contrast, in the oxidized state of HF1, DOX

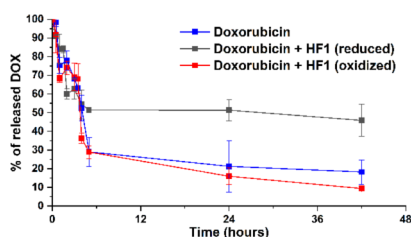


Figure 4. DOX DR from the HF1 polymer formulation *in vitro*. The graph shows the concentration of DOX released from the drug formulation of polymer HF1 in the oxidized and reduced states and the corresponding control (free DOX) as a function of time. The drug release was measured in two independent experiments.

release follows the kinetics of the free DOX. The final release of DOX from the HF1 (reduced form) formulation was very slow ($\approx 45\%$ of the remaining encapsulated drug after 42 h).

This shows that the polymeric formulation can incorporate hydrophobic drugs and that DR can be effectively accelerated by polymer oxidation.

To demonstrate the ability of the formulations to entrap and subsequently release drugs under conditions naturally mediated by standard cancer cells, we chose two *in vitro* experiments with spheroidal cancer cell clusters known as “spheroids”. In this study, we monitored spheroid proliferation in the presence of polymer particles loaded with cytostatic drugs (doxorubicin, DOX) or with an inhibitor of proliferation (GSK 429286).

First, we determined the *in vitro* distribution of cytostatic DOX in 3D spheroids, which provides important information about the availability of the drug encapsulated in the polymeric particle (Figure 5). Although low-molecular-weight drugs can easily penetrate cell clusters crossing into the core of spheroids, the presence of nanoscale particles can limit their penetration and, therefore, the effect of cytostatic drugs. However, our results suggest that the penetration of the polymer formulation and of the free DOX are similar to that of the control, showing effective tissue penetration and DR of the encapsulated drug, even inside the core of the spheroids, mediated by the oxidative environment of cancer cells. The experiment with the DOX distribution was performed by adding doxorubicin (to a final $10 \mu\text{M}$ DOX solution, corresponding to $f_{\text{EE}} > 90\%$) to the cells incubated with control medium or the medium with $0.2 \text{ mg}\cdot\text{mL}^{-1}$ polymer (more than 10-fold higher than the CAC of polymer HF1) directly after embedding in 3D collagen, acquiring images after 3 h of incubation.

We performed a second experiment with a selective Rock (Rho-kinase) inhibitor (GSK 429286), that is, a cell invasion inhibitor, to describe the efficiency of the DR of the encapsulated drug by comparing the activities of the free inhibitor and inhibitor–polymer formulation (Figure 6). The experiment was performed at two different inhibitor concentrations (1 and $10 \mu\text{M}$ inhibitor solution), and data were collected in duplicates to assess their statistical distribution (Figure S15). Images of the spheroids were taken immediately after they were embedded into the medium and 24 h later. Four different culture media were prepared. First, a control medium containing $1.0 \mu\text{L}\cdot\text{mL}^{-1}$ DMSO was used to rule out any DMSO effect on cell proliferation (this DMSO content is labeled as DMSO hereafter), whereas the hydrophobic inhibitor must be applied in a DMSO solution. The first

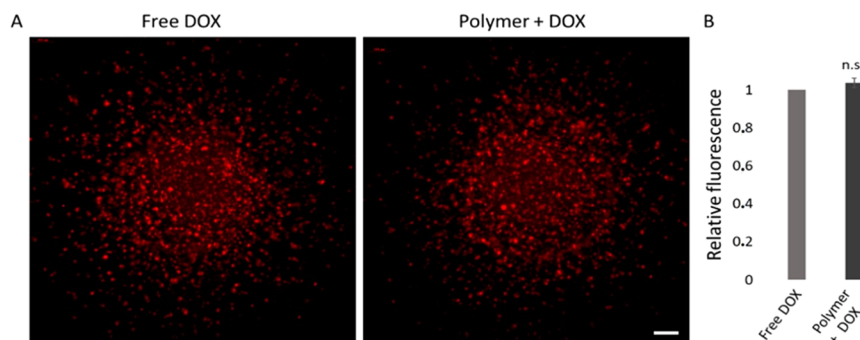


Figure 5. Distribution of free DOX and the DOX–polymer formulation in 3D spheroidal clusters of HT1080 cancer cells. Left: representative maximum projection images of spheroids treated with free DOX and the DOX–polymer formulation imaged with a $10\times$ objective lens using Thunder Imager configuration of a Leica DMi8 microscope (excitation 470 nm). Scale bar $100 \mu\text{m}$. Right: quantification of doxorubicin fluorescence in HT1080 spheroids treated with free DOX and DOX–polymer formulation. Doxorubicin fluorescence was quantified in ImageJ based on three independent experiments, and significance was assessed using the Student’s *t* test.

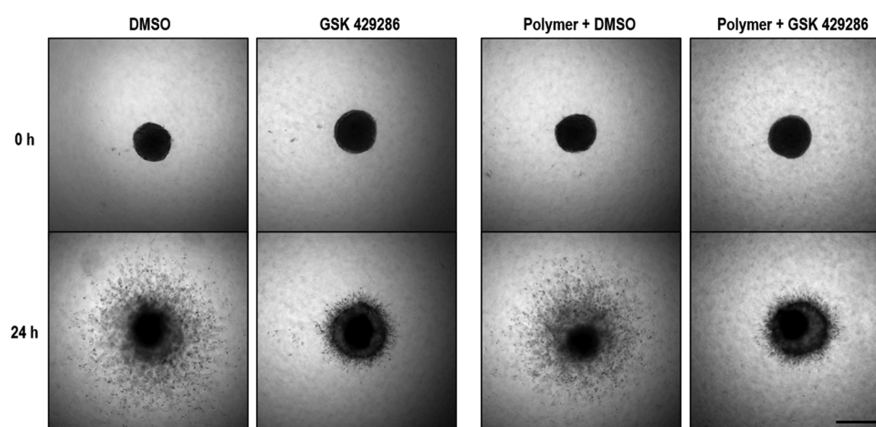


Figure 6. *In vitro* HT1080 spheroid proliferation study. Left: control medium with DMSO and control medium containing the free inhibitor GSK 429286 (10 μ M). Right: the polymer solution (0.2 mg·mL⁻¹ with DMSO) and the medium with the inhibitor–polymer formulation (polymer concentration 0.2 mg·mL⁻¹ with 10 μ M inhibitor). Images were taken using the microscope immediately after incubation with the medium and then after 24 h. Representative images are shown with a scale bar (500 μ m).

control medium was used to observe, quantify, and compare the invasion of cancer cells by spheroids. The second culture medium was a control medium containing free inhibitor (applied in a DMSO solution to a final 10 μ M concentration of inhibitor) to observe and quantify the relative inhibition of proliferation after exposure to the free inhibitor. The third culture medium was a control medium with polymer (0.2 mg·mL⁻¹ polymer in DMSO) to eliminate the possible impact of the polymer on the experiment. The last culture medium contained the inhibitor–polymer formulation (0.2 mg·mL⁻¹ polymer with 10 μ M inhibitor), and the relative inhibition of proliferation was quantified and compared to that of the control media. After 24 h, the control groups without the inhibitor proliferated naturally; neither the free polymer nor DMSO affected the invasion of cancer cells. The comparison of the results between the experimental and control groups showed a similar spheroid growth inhibition in the free inhibitor and inhibitor–polymer formulation groups at both inhibitor concentrations (Figures 6 and S10). These results again indicate that the polymer effectively releases the inhibitor under such conditions, which are naturally mediated by standard cancer cells, and that the drug encapsulated in the polymeric particle reached its target.

CONCLUSIONS

In this study, we developed a promising polymeric ¹⁹F MRI theranostic tracer that forms particles when heated above 33 °C but disassembles when exposed to oxidative conditions. By combining self-assembly and disassembly with ¹⁹F magnetic resonance imaging, we introduce a novel theranostic system for drug delivery in cancer tissues with simultaneous functional detection. Even our polymer with the lowest concentration of redox-responsive ferrocene (HF1, 0.5 wt % of ferrocene) loads hydrophobic drugs (doxorubicin and GSK-429286) in reduced state and releases them in oxidized state while maintaining suitable imaging properties, such as a high fluorine concentration and relaxation times in both states. This ability to monitor the location and amount of drug release in cell cultures highlights the potential to quantitatively analyze the therapeutic effects in target tissues of cancer patients using this approach. As such, our findings contribute to advancing theranostics by providing a more sophisticated system for such purposes toward improving the efficacy of clinical treatments.

Further research may show the applicability of this system to other classes of drugs and other oxidative-stress-related diseases, thereby maximizing the value of this theranostic system.

ASSOCIATED CONTENT

Supporting Information

The Supporting Information is available free of charge at <https://pubs.acs.org/doi/10.1021/acs.biomac.0c01316>.

Figures with ¹H NMR, ¹³C{¹H} NMR, ¹H–¹H COSY, ¹H–¹³C HMBIC and multiplicity-edited ¹H–¹³C HSQC spectra of monomer *N*-(2*N'*-Boc-aminoethyl)-acrylamide; ¹H NMR spectra of diblock copolymer; summary from SEC; DLS measurement of particle stability over time; chart showing the CAC of copolymer HF1; summary of the cytotoxicity assay, ¹⁹F NMR spectra of HF1, HF2 and HF3 in D₂O before and after oxidation; and relative invasion index evaluated for the spheroids in different media with the polymer HF1 (PDF)

AUTHOR INFORMATION

Corresponding Author

Martin Hruby – Institute of Macromolecular Chemistry, Czech Academy of Sciences, 16206 Prague 6, Czech Republic; orcid.org/0000-0002-5075-261X; Email: mhruby@centrum.cz

Authors

Kristyna Kolouchova – Institute of Macromolecular Chemistry, Czech Academy of Sciences, 16206 Prague 6, Czech Republic; Department of Physical and Macromolecular Chemistry, Faculty of Science, Charles University, 12800 Prague 2, Czech Republic

Ondrej Groborz – Institute of Macromolecular Chemistry, Czech Academy of Sciences, 16206 Prague 6, Czech Republic; Department of Organic Chemistry, Faculty of Science, Charles University, 12800 Prague 2, Czech Republic; Institute of Biophysics and Informatics, Charles University, First Faculty of Medicine, 12000 Prague 2, Czech Republic

Zulfiya Cernochova – Institute of Macromolecular Chemistry, Czech Academy of Sciences, 16206 Prague 6, Czech Republic

Aneta Skarkova – Department of Cell Biology, Charles University, 12843 Prague, Czech Republic; Biotechnology and Biomedicine Centre of the Academy of Sciences and Charles University (BIOCEV), 25242 Vestec u Prahy, Czech Republic

Jan Brabek – Department of Cell Biology, Charles University, 12843 Prague, Czech Republic; Biotechnology and Biomedicine Centre of the Academy of Sciences and Charles University (BIOCEV), 25242 Vestec u Prahy, Czech Republic

Daniel Rosel – Department of Cell Biology, Charles University, 12843 Prague, Czech Republic; Biotechnology and Biomedicine Centre of the Academy of Sciences and Charles University (BIOCEV), 25242 Vestec u Prahy, Czech Republic

Pavel Svec – Institute of Macromolecular Chemistry, Czech Academy of Sciences, 16206 Prague 6, Czech Republic; Department of Physical and Macromolecular Chemistry, Faculty of Science, Charles University, 12800 Prague 2, Czech Republic; orcid.org/0000-0002-6604-2815

Zenon Starcuk – Institute of Scientific Instruments, Czech Academy of Sciences, 61264 Brno, Czech Republic

Miroslav Slouf – Institute of Macromolecular Chemistry, Czech Academy of Sciences, 16206 Prague 6, Czech Republic; orcid.org/0000-0003-1528-802X

Complete contact information is available at:

<https://pubs.acs.org/10.1021/acs.biomac.0c01316>

Notes

The authors declare no competing financial interest.

ACKNOWLEDGMENTS

Financial support from the Ministry of Education, Youth and Sports of the Czech Republic (grant # LTC19032 and # LM2018133), the Academy of Sciences of the Czech Republic [grant Strategy AV21 # VP06 (Diagnostic Methods and Techniques; K.K., O.G., Z.C.) and # RP10 (Molecules and Materials for Life; M.H.)], and the Czech Science Foundation (grant # 19-01438S) is gratefully acknowledged. K.K., P.S., and O.G. acknowledge financial support from the Grant Agency of Charles University (Project No. 602119 and No. 766119). Z.S. acknowledges financial support from the Ministry of Education, Youth and Sports of the Czech Republic (grant # LM2018129). The authors would like to acknowledge the help of Kateřina Kolouchová and Kristina Bártová with the graphical artwork.

REFERENCES

- (1) Wagner, V.; Dullaart, A.; Bock, A.-K.; Zweck, A. The Emerging Nanomedicine Landscape. *Nat. Biotechnol.* **2006**, *24*, 1211–1217.
- (2) Pridgen, E. M.; Langer, R.; Farokhzad, O. C. Biodegradable, Polymeric Nanoparticle Delivery Systems for Cancer Therapy. *Nanomedicine* **2007**, *2*, 669–680.
- (3) Bamrungsap, S.; Zhao, Z.; Chen, T.; Wang, L.; Li, C.; Fu, T.; Tan, W. Nanotechnology in Therapeutics: A Focus on Nanoparticles as a Drug Delivery System. *Nanomedicine* **2012**, *7*, 1253–1271.
- (4) Zhang, G.; Zeng, X.; Li, P. Nanomaterials in Cancer-Therapy Drug Delivery System. *J. Biomed. Nanotechnol.* **2013**, *9*, 741–750.
- (5) Maeda, H.; Bharate, G. Y.; Daruwalla, J. Polymeric Drugs for Efficient Tumor-Targeted Drug Delivery Based on EPR-Effect. *Eur. J. Pharm. Biopharm.* **2009**, *71*, 409–419.
- (6) Maeda, H.; Wu, J.; Sawa, T.; Matsumura, Y.; Hori, K. Tumor Vascular Permeability and the EPR Effect in Macromolecular Therapeutics: A Review. *J. Controlled Release* **2000**, *65*, 271–284.

- (7) Iyer, A. K.; Khaled, G.; Fang, J.; Maeda, H. Exploiting the Enhanced Permeability and Retention Effect for Tumor Targeting. *Drug Discovery Today* **2006**, *11*, 812–818.

- (8) Gupta, P.; Vermani, K.; Garg, S. Hydrogels: From Controlled Release to PH-Responsive Drug Delivery. *Drug Discovery Today* **2002**, *7*, 569–579.

- (9) Pang, X.; Jiang, Y.; Xiao, Q.; Leung, A. W.; Hua, H.; Xu, C. PH-Responsive Polymer–Drug Conjugates: Design and Progress. *J. Controlled Release* **2016**, *222*, 116–129.

- (10) Schmaljohann, D. Thermo- and PH-Responsive Polymers in Drug Delivery. *Adv. Drug Delivery Rev.* **2006**, *58*, 1655–1670.

- (11) Popat, A.; Liu, J.; Lu, G. Q. M.; Qiao, S. Z. A PH-Responsive Drug Delivery System Based on Chitosan Coated Mesoporous Silica Nanoparticles. *J. Mater. Chem.* **2012**, *22*, 11173–11178.

- (12) Xing, L.; Zheng, H.; Cao, Y.; Che, S. Coordination Polymer Coated Mesoporous Silica Nanoparticles for PH-Responsive Drug Release. *Adv. Mater.* **2012**, *24*, 6433–6437.

- (13) Gao, Q.; Xu, Y.; Wu, D.; Sun, Y.; Li, X. PH-Responsive Drug Release from Polymer-Coated Mesoporous Silica Spheres. *J. Phys. Chem. C* **2009**, *113*, 12753–12758.

- (14) Li, M.; Song, W.; Tang, Z.; Lv, S.; Lin, L.; Sun, H.; Li, Q.; Yang, Y.; Hong, H.; Chen, X. Nanoscaled Poly(l-Glutamic Acid)/Doxorubicin-Amphiphile Complex as PH-Responsive Drug Delivery System for Effective Treatment of Nonsmall Cell Lung Cancer. *ACS Appl. Mater. Interfaces* **2013**, *5*, 1781–1792.

- (15) Yang, X.; Grailer, J. J.; Rowland, I. J.; Javadi, A.; Hurley, S. A.; Matson, V. Z.; Steeber, D. A.; Gong, S. Multifunctional Stable and PH-Responsive Polymer Vesicles Formed by Heterofunctional Triblock Copolymer for Targeted Anticancer Drug Delivery and Ultrasensitive MR Imaging. *ACS Nano* **2010**, *4*, 6805–6817.

- (16) Alfarouk, K. O.; Schwartz, C. T. S.; L. The Warburg Effect and the Hallmarks of Cancer. *Anticancer Agents Med. Chem.* **2017**, *17*, 164–170.

- (17) Gandhi, A.; Paul, A.; Sen, S. O.; Sen, K. K. Studies on Thermoresponsive Polymers: Phase Behaviour, Drug Delivery and Biomedical Applications. *Asian J. Pharm. Sci.* **2015**, *10*, 99–107.

- (18) Sanoj Rejinold, N.; Muthunarayanan, M.; Divyarani, V. V.; Sreerakha, P. R.; Chennazhi, K. P.; Nair, S. V.; Tamura, H.; Jayakumar, R. Curcumin-Loaded Biocompatible Thermoresponsive Polymeric Nanoparticles for Cancer Drug Delivery. *J. Colloid Interface Sci.* **2011**, *360*, 39–51.

- (19) Chung, J. E.; Yokoyama, M.; Yamato, M.; Aoyagi, T.; Sakurai, Y.; Okano, T. Thermo-Responsive Drug Delivery from Polymeric Micelles Constructed Using Block Copolymers of Poly(N-Isopropylacrylamide) and Poly(Butylmethacrylate). *J. Controlled Release* **1999**, *62*, 115–127.

- (20) Zhang, X.-Z.; Zhuo, R.-X.; Cui, J.-Z.; Zhang, J.-T. A Novel Thermo-Responsive Drug Delivery System with Positive Controlled Release. *Int. J. Pharm.* **2002**, *235*, 43–50.

- (21) Linsley, C. S.; Wu, B. M. Recent Advances in Light-Responsive on-Demand Drug-Delivery Systems. *Ther. Delivery* **2017**, *8*, 89–107.

- (22) Luo, Z.; Cai, K.; Hu, Y.; Li, J.; Ding, X.; Zhang, B.; Xu, D.; Yang, W.; Liu, P. Redox-Responsive Molecular Nanoreservoirs for Controlled Intracellular Anticancer Drug Delivery Based on Magnetic Nanoparticles. *Adv. Mater.* **2012**, *24*, 431–435.

- (23) Vogt, A. P.; Sumerlin, B. S. Temperature and Redox Responsive Hydrogels from ABA Triblock Copolymers Prepared by RAFT Polymerization. *Soft Matter* **2009**, *5*, 2347–2351.

- (24) Wen, H.; Dong, C.; Dong, H.; Shen, A.; Xia, W.; Cai, X.; Song, Y.; Li, X.; Li, Y.; Shi, D. Engineered Redox-Responsive PEG Detachment Mechanism in PEGylated Nano-Graphene Oxide for Intracellular Drug Delivery. *Small* **2012**, *8*, 760–769.

- (25) de la Rica, R.; Aili, D.; Stevens, M. M. Enzyme-Responsive Nanoparticles for Drug Release and Diagnostics. *Adv. Drug Delivery Rev.* **2012**, *64*, 967–978.

- (26) Hu, Q.; Katti, P. S.; Gu, Z. Enzyme-Responsive Nanomaterials for Controlled Drug Delivery. *Nanoscale* **2014**, *6*, 12273–12286.

- (27) Liu, Y.; Ding, X.; Li, J.; Luo, Z.; Hu, Y.; Liu, J.; Dai, L.; Zhou, J.; Hou, C.; Cai, K. Enzyme Responsive Drug Delivery System Based on

Mesoporous Silica Nanoparticles for Tumor Therapy *in Vivo*. *Nanotechnology* **2015**, *26*, No. 145102.

(28) Zhang, C.; Pan, D.; Luo, K.; She, W.; Guo, C.; Yang, Y.; Gu, Z. Peptide Dendrimer–Doxorubicin Conjugate-Based Nanoparticles as an Enzyme-Responsive Drug Delivery System for Cancer Therapy. *Adv. Healthcare Mater.* **2014**, *3*, 1299–1308.

(29) Huo, M.; Yuan, J.; Tao, L.; Wei, Y. Redox-Responsive Polymers for Drug Delivery: From Molecular Design to Applications. *Polym. Chem.* **2014**, *5*, 1519–1528.

(30) Sun, J.-T.; Piao, J.-G.; Wang, L.-H.; Javed, M.; Hong, C.-Y.; Pan, C.-Y. One-Pot Synthesis of Redox-Responsive Polymers-Coated Mesoporous Silica Nanoparticles and Their Controlled Drug Release. *Macromol. Rapid Commun.* **2013**, *34*, 1387–1394.

(31) Zhang, X.; Han, L.; Liu, M.; Wang, K.; Tao, L.; Wan, Q.; Wei, Y. Recent Progress and Advances in Redox-Responsive Polymers as Controlled Delivery Nanoplatfoms. *Mater. Chem. Front.* **2017**, *1*, 807–822.

(32) Yang, Q.; Tan, L.; He, C.; Liu, B.; Xu, Y.; Zhu, Z.; Shao, Z.; Gong, B.; Shen, Y.-M. Redox-Responsive Micelles Self-Assembled from Dynamic Covalent Block Copolymers for Intracellular Drug Delivery. *Acta Biomater.* **2015**, *17*, 193–200.

(33) Zhuang, Y.; Deng, H.; Su, Y.; He, L.; Wang, R.; Tong, G.; He, D.; Zhu, X. Aptamer-Functionalized and Backbone Redox-Responsive Hyperbranched Polymer for Targeted Drug Delivery in Cancer Therapy. *Biomacromolecules* **2016**, *17*, 2050–2062.

(34) Shi, C.; Guo, X.; Qu, Q.; Tang, Z.; Wang, Y.; Zhou, S. Actively Targeted Delivery of Anticancer Drug to Tumor Cells by Redox-Responsive Star-Shaped Micelles. *Biomaterials* **2014**, *35*, 8711–8722.

(35) Fiddian-Green, R. G.; Baker, S. Predictive Value of the Stomach Wall PH for Complications after Cardiac Operations: Comparison with Other Monitoring. *Crit. Care Med.* **1987**, *15*, 153–156.

(36) Caillouette, J. C.; Sharp, C. F.; Zimmerman, G. J.; Roy, S. Vaginal PH as a Marker for Bacterial Pathogens and Menopausal Status. *Am. J. Obstet. Gynecol.* **1997**, *176*, 1270–1277.

(37) Stefanadis, C.; Chrysohoou, C.; Panagiotakos, D. B.; Passalidou, E.; Katsi, V.; Polychronopoulos, V.; Toutouzas, P. K. Temperature Differences Are Associated with Malignancy on Lung Lesions: A Clinical Study. *BMC Cancer* **2003**, *3*, 1.

(38) Irani, K.; Xia, Y.; Zweier, J. L.; Sollott, S. J.; Der, C. J.; Fearon, E. R.; Sundaresan, M.; Finkel, T.; Goldschmidt-Clermont, P. J. Mitogenic Signaling Mediated by Oxidants in Ras-Transformed Fibroblasts. *Science* **1997**, *275*, 1649–1652.

(39) Gorrini, C.; Harris, I. S.; Mak, T. W. Modulation of Oxidative Stress as an Anticancer Strategy. *Nat. Rev. Drug Discovery* **2013**, *12*, 931–947.

(40) Sztatrowski, T. P.; Nathan, C. F. Production of Large Amounts of Hydrogen Peroxide by Human Tumor Cells. *Cancer Res.* **1991**, *51*, 794–798.

(41) Akong-Moore, K.; Chow, O. A.; von Köckritz-Blickwede, M.; Nizet, V. Influences of Chloride and Hypochlorite on Neutrophil Extracellular Trap Formation. *PLoS One* **2012**, *7*, No. e42984.

(42) Leto, T. L.; Geiszt, M. Role of Nox Family NADPH Oxidases in Host Defense. *Antioxid. Redox Signaling* **2006**, *8*, 1549–1561.

(43) Alexis, F.; Anker, J. N. Theranostic Nanotechnologies: Moving beyond Imaging Drug Localization? *Ther. Delivery* **2014**, *5*, 97–100.

(44) Sumer, B.; Gao, J. Theranostic Nanomedicine for Cancer. *Nanomedicine* **2008**, *3*, 137–140.

(45) Fuchs, A. V.; Bapat, A. P.; Cowin, G. J.; Thurecht, K. J. Switchable ¹⁹F MRI Polymer Theranostics: Towards in Situ Quantifiable Drug Release. *Polym. Chem.* **2017**, *8*, 5157–5166.

(46) Shin, S. H.; Park, E.-J.; Min, C.; Choi, S.; Il, Jeon, S.; Kim, Y.-H.; Kim, D. Tracking Perfluorocarbon Nanoemulsion Delivery by ¹⁹F MRI for Precise High Intensity Focused Ultrasound Tumor Ablation. *Theranostics* **2017**, *7*, 562–572.

(47) Vu-Quang, H.; Vinding, M. S.; Nielsen, T.; Ullisch, M. G.; Nielsen, N. C.; Kjems, J. Theranostic Tumor Targeted Nanoparticles Combining Drug Delivery with Dual near Infrared and ¹⁹F Magnetic Resonance Imaging Modalities. *Nanomedicine* **2016**, *12*, 1873–1884.

(48) Dewitte, H.; Geers, B.; Liang, S.; Himmelreich, U.; Demeester, J.; De Smedt, S. C.; Lentacker, I. Design and Evaluation of Theranostic Perfluorocarbon Particles for Simultaneous Antigen-Loading and ¹⁹F-MRI Tracking of Dendritic Cells. *J. Controlled Release* **2013**, *169*, 141–149.

(49) Porsch, C.; Zhang, Y.; Östlund, Å.; Damberg, P.; Ducani, C.; Malmström, E.; Nyström, A. M. In Vitro Evaluation of Non-Protein Adsorbing Breast Cancer Theranostics Based on ¹⁹F-Polymer Containing Nanoparticles. *Part. Part. Syst. Charact.* **2013**, *30*, 381–390.

(50) Higashino, T.; Nakatsuji, H.; Fukuda, R.; Okamoto, H.; Imai, H.; Matsuda, T.; Tochio, H.; Shirakawa, M.; Tkachenko, N. V.; Hashida, M.; Murakami, T.; Imahori, H. Hexaphyrin as a Potential Theranostic Dye for Photothermal Therapy and ¹⁹F Magnetic Resonance Imaging. *ChemBioChem* **2017**, *18*, 951–959.

(51) Kovacs, H.; Kupčič, Ě. Simultaneous Dual-Nuclei Imaging for Motion Corrected Detection and Quantification of ¹⁹F Imaging Agents. *Magn. Reson. Chem.* **2016**, *66* (4), 1116–1122.

(52) Bennett, K. M.; Jo, J.; Cabral, H.; Bakalova, R.; Aoki, I. MR Imaging Techniques for Nano-Pathophysiology and Theranostics. *Adv. Drug Delivery Rev.* **2014**, *74*, 75–94.

(53) Kolouchova, K.; Sedlacek, O.; Jirak, D.; Babuka, D.; Blahut, J.; Kotek, J.; Vit, M.; Trousil, J.; Konefal, R.; Janouskova, O.; Podhorska, B.; Slouf, M.; Hruby, M. Self-Assembled Thermoresponsive Polymeric Nanogels for ¹⁹F MR Imaging. *Biomacromolecules* **2018**, *19*, 3515–3524.

(54) Jirak, D.; Galisova, A.; Kolouchova, K.; Babuka, D.; Hruby, M. Fluorine Polymer Probes for Magnetic Resonance Imaging: Quo Vadis? *Magn. Reson. Mater. Phys., Biol. Med.* **2019**, *32*, 173–185.

(55) Babuka, D.; Kolouchova, K.; Hruby, M.; Groborz, O.; Tosner, Z.; Zhigunov, A.; Stepanek, P. Investigation of the Internal Structure of Thermoresponsive Diblock Poly(2-Methyl-2-Oxazoline)-*b*-Poly[N-(2,2-Difluoroethyl)Acrylamide] Copolymer Nanoparticles. *Eur. Polym. J.* **2019**, *121*, No. 109306.

(56) Kolouchova, K.; Jirak, D.; Groborz, O.; Sedlacek, O.; Ziolkowska, N.; Vit, M.; Sticova, E.; Galisova, A.; Svec, P.; Trousil, J.; Hajek, M.; Hruby, M. Implant-Forming Polymeric ¹⁹F MRI-Tracer with Tunable Dissolution. *J. Controlled Release* **2020**, *327*, 50–60.

(57) Babuka, D.; Kolouchova, K.; Groborz, O.; Tosner, Z.; Zhigunov, A.; Stepanek, P.; Hruby, M. Internal Structure of Thermoresponsive Physically Crosslinked Nanogel of Poly[N-(2-Hydroxypropyl) Methacrylamide]-Block-Poly[N-(2,2-Difluoroethyl) Acrylamide], Prominent ¹⁹F MRI Tracer. *Nanomaterials* **2020**, *10*, 2231.

(58) Liu, L.; Rui, L.; Gao, Y.; Zhang, W. Self-Assembly and Disassembly of a Redox-Responsive Ferrocene-Containing Amphiphilic Block Copolymer for Controlled Release. *Polym. Chem.* **2015**, *6*, 1817–1829.

(59) Pavlides, S.; Tsigros, A.; Migneco, G.; Whitaker-Menezes, D.; Chiavarina, B.; Flomenberg, N.; Frank, P. G.; Casimiro, M. C.; Wang, C.; Pestell, R. G.; Martinez-Outschoorn, U. E.; Howell, A.; Sotgia, F.; Lisanti, M. P. The Autophagic Tumor Stroma Model of Cancer. *Cell Cycle* **2010**, *9*, 3485–3505.

(60) Jäger, E.; Höcherl, A.; Janoušková, O.; Jäger, A.; Hrubý, M.; Konefal, R.; Netopilik, M.; Pánek, J.; Šlouf, M.; Ulbrich, K.; Štěpánek, P. Fluorescent Boronate-Based Polymer Nanoparticles with Reactive Oxygen Species (ROS)-Triggered Cargo Release for Drug-Delivery Applications. *Nanoscale* **2016**, *8*, 6958–6963.

(61) Jäger, E.; Sincari, V.; Albuquerque, L. J. C.; Jäger, A.; Humajova, J.; Kucka, J.; Pankrac, J.; Paral, P.; Heizer, T.; Janouskova, O.; Konefal, R.; Pavlova, E.; Sedlacek, O.; Giacomelli, F. C.; Pouckova, P.; Sefc, L.; Stepanek, P.; Hruby, M. Reactive Oxygen Species (ROS)-Responsive Polymersomes with Site-Specific Chemotherapeutic Delivery into Tumors via Spacer Design Chemistry. *Biomacromolecules* **2020**, *21*, 1437–1449.

(62) Tanaka, K.; Kitamura, N.; Takahashi, Y.; Chujo, Y. Reversible Signal Regulation System of ¹⁹F NMR by Redox Reactions Using a Metal Complex as a Switching Module. *Bioorg. Med. Chem.* **2009**, *17*, 3818–3823.

- (63) Wang, H.; Jordan, V. C.; Ramsay, I. A.; Sojoodi, M.; Fuchs, B. C.; Tanabe, K. K.; Caravan, P.; Gale, E. M. Molecular Magnetic Resonance Imaging Using a Redox-Active Iron Complex. *J. Am. Chem. Soc.* **2019**, *141*, 5916–5925.
- (64) Wang, X.; Zhen, X.; Wang, J.; Zhang, J.; Wu, W.; Jiang, X. Doxorubicin Delivery to 3D Multicellular Spheroids and Tumors Based on Boronic Acid-Rich Chitosan Nanoparticles. *Biomaterials* **2013**, *34*, 4667–4679.
- (65) Gandaloyičová, A.; Rosel, D.; Fernandes, M.; Veselý, P.; Heneberg, P.; Čermák, V.; Petruželka, L.; Kumar, S.; Sanz-Moreno, V.; Brábek, J. Migrastatics—Anti-Metastatic and Anti-Invasion Drugs: Promises and Challenges. *Trends Cancer* **2017**, *3*, 391–406.
- (66) Tucker, B. S.; Stewart, J. D.; Aguirre, J. I.; Holliday, L. S.; Figg, C. A.; Messer, J. G.; Sumerlin, B. S. Role of Polymer Architecture on the Activity of Polymer–Protein Conjugates for the Treatment of Accelerated Bone Loss Disorders. *Biomacromolecules* **2015**, *16*, 2374–2381.
- (67) Bak, J. M.; Kim, K.-B.; Lee, J.-E.; Park, Y.; Yoon, S. S.; Jeong, H. M.; Lee, H. Thermoresponsive Fluorinated Polyacrylamides with Low Cytotoxicity. *Polym. Chem.* **2013**, *4*, 2219–2223.
- (68) Roemer, M.; Wild, D. A.; Sobolev, A. N.; Skelton, B. W.; Nealon, G. L.; Piggott, M. J.; Koutsantonis, G. A. Carbon-Rich Trinuclear Octamethylferrocenophanes. *Inorg. Chem.* **2019**, *58*, 3789–3799.
- (69) Snyder, S. L.; Sobocinski, P. Z. An Improved 2,4,6-Trinitrobenzenesulfonic Acid Method for the Determination of Amines. *Anal. Biochem.* **1975**, *64*, 284–288.
- (70) Pell, G. S.; Briellmann, R. S.; Waites, A. B.; Abbott, D. F.; Lewis, D. P.; Jackson, G. D. Optimized Clinical T2 Relaxometry with a Standard CPMG Sequence. *J. Magn. Reson. Imaging* **2006**, *23*, 248–252.
- (71) Jakeš, J. Regularized Positive Exponential Sum (REPES) Program - A Way of Inverting Laplace Transform Data Obtained by Dynamic Light Scattering. *Collect. Czech. Chem. Commun.* **1995**, *60*, 1781–1797.
- (72) Bildziukevich, U.; Kaletová, E.; Šaman, D.; Sievänen, E.; Kolehmainen, E. T.; Slouf, M.; Wimmer, Z. Spectral and Microscopic Study of Self-Assembly of Novel Cationic Spermine Amides of Betulinic Acid. *Steroids* **2017**, *117*, 90–96.
- (73) Paiuk, O.; Mitina, N.; Slouf, M.; Pavlova, E.; Finiuk, N.; Kinash, N.; Karkhut, A.; Manko, N.; Gromovoy, T.; Hevus, O.; Shermolovich, Y.; Stoika, R.; Zaichenko, A. Fluorine-Containing Block/Branched Polyamphiphiles Forming Bioinspired Complexes with Biopolymers. *Colloids Surf., B* **2019**, *174*, 393–400.
- (74) Štěpánek, M.; Hajduová, J.; Procházka, K.; Šlouf, M.; Nebesářová, J.; Mountrichas, G.; Mantzaridis, C.; Pispas, S. Association of Poly(4-Hydroxystyrene)-Block-Poly(Ethylene Oxide) in Aqueous Solutions: Block Copolymer Nanoparticles with Intermixed Blocks. *Langmuir* **2012**, *28*, 307–313.
- (75) Bianchi, A.; Mauri, M.; Bonetti, S.; Koynov, K.; Kappl, M.; Lieberwirth, I.; Butt, H.-J.; Simonutti, R. Hierarchical Self-Assembly of PDMA-b-PS Chains into Granular Nanoparticles: Genesis and Fate. *Macromol. Rapid Commun.* **2014**, *35*, 1994–1999.
- (76) Lubach, J.; Drenth, W. Enolization and Oxidation: II. Oxidation of Ferrocene by Molecular Oxygen and Hydrogen Peroxide in Acidic Media. *Recl. Trav. Chim. Pays-Bas* **1973**, *92*, 586–592.
- (77) Epton, R.; Hobson, M. E.; Marr, G. Oxidation of Ferrocene and Some Substituted Ferrocenes in the Presence of Horseradish Peroxidase. *J. Organomet. Chem.* **1978**, *149*, 231–244.
- (78) Traverso, O.; Scandola, F. Photooxidation of Ferrocene in Halocarbon Solvents. *Inorg. Chim. Acta* **1970**, *4*, 493–498.
- (79) Bao, D.; Millare, B.; Xia, W.; Steyer, B. G.; Gerasimenko, A. A.; Ferreira, A.; Contreras, A.; Vullev, V. I. Electrochemical Oxidation of Ferrocene: A Strong Dependence on the Concentration of the Supporting Electrolyte for Nonpolar Solvents. *J. Phys. Chem. A* **2009**, *113*, 1259–1267.
- (80) Ganta, S.; Devalapally, H.; Shahiwal, A.; Amiji, M. A Review of Stimuli-Responsive Nanocarriers for Drug and Gene Delivery. *J. Controlled Release* **2008**, *126*, 187–204.
- (81) Chatterjee, S. Oxidative Stress, Inflammation, and Disease. In *Oxidative Stress and Biomaterials*; Dziubla, T.; Butterfield, D. A., Eds.; Elsevier, 2016; p 404.
- (82) Gufler, H.; Laubenberger, J.; DeGregorio, G.; Dohnicht, S.; Langer, M. Pelvic Floor Descent: Dynamic MR Imaging Using a Half-Fourier RARE Sequence. *J. Magn. Reson. Imaging* **1999**, *9*, 378–383.
- (83) Larson, P. E. Z.; Han, M.; Krug, R.; Jakary, A.; Nelson, S. J.; Vigneron, D. B.; Henry, R. G.; McKinnon, G.; Kelley, D. A. C. Ultrashort Echo Time and Zero Echo Time MRI at 7T. *Magn. Reson. Mater. Phys., Biol. Med.* **2016**, *29*, 359–370.

Supporting information for the article

Thermo- and ROS-Responsive Self-Assembled Polymer Nanoparticle Tracers for ^{19}F MRI Theranostics

Kristyna Kolouchova,^{1,2} Ondrej Groborz,^{1,3,4} Zulfiya Cernochova,¹ Aneta Skarkova,^{5,6} Jan Brabek,^{5,6} Daniel Rosel,^{5,6} Pavel Svec,^{1,2} Zenon Starcuk,⁷ Miroslav Slouf[†] and Martin Hruby^{1}*

¹Institute of Macromolecular Chemistry, Czech Academy of Sciences, Heyrovského sq. 2,
Prague 6, 16206, Czech Republic

²Department of Physical and Macromolecular Chemistry, Faculty of Science, Charles
University, Hlavova 8, Prague 2, 128 00, Czech Republic

³Department of Organic Chemistry, Faculty of Science, Charles University, Hlavova 8,
Prague 2, 128 00, Czech Republic

⁴Institute of Biophysics and Informatics, Charles University, First Faculty of Medicine,
Salmovská 1, 12000 Prague 2, Czech Republic

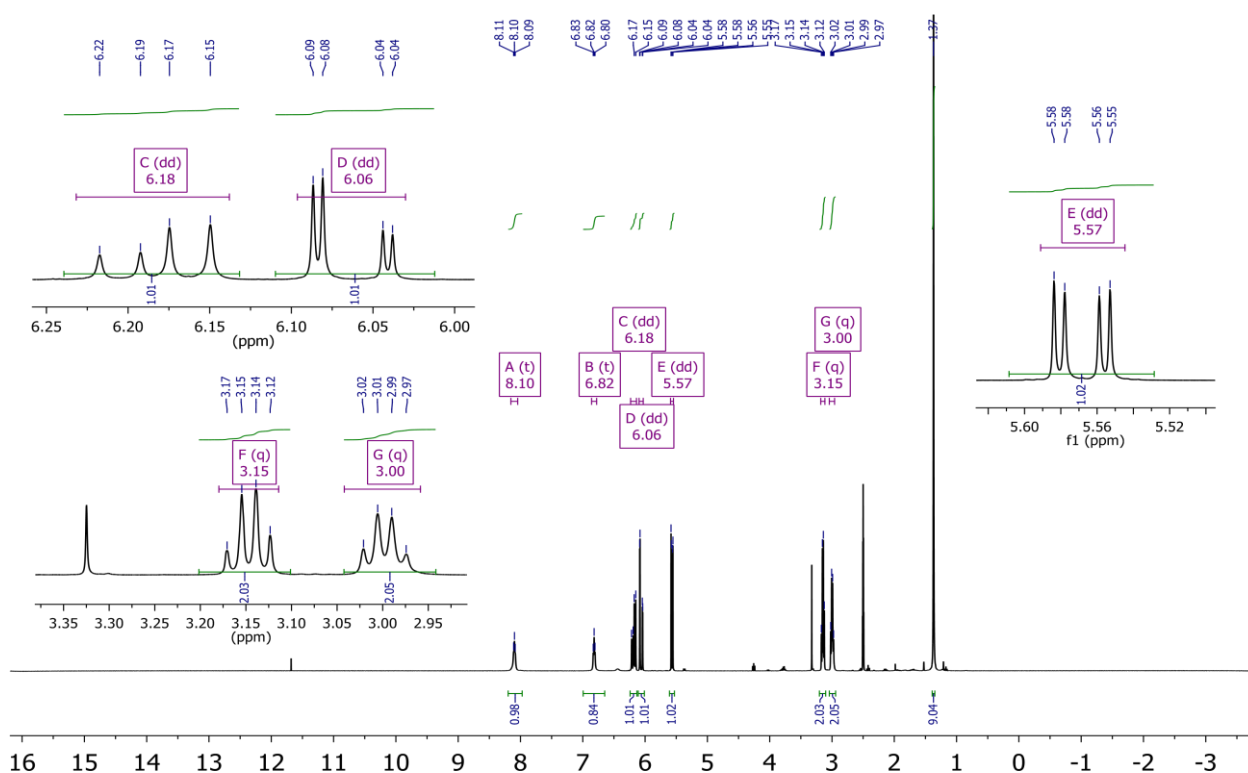
⁵Department of Cell Biology, Charles University, Viničná 7, 12843 Prague, Czech Republic

⁶Biotechnology and Biomedicine Centre of the Academy of Sciences and Charles University
(BIOCEV), Průmyslová 595, 25242 Vestec u Prahy, Czech Republic

⁷ Institute of Scientific Instruments, Czech Academy of Sciences, Královopolská 147, Brno, 612 64, Czech Republic

*corresponding author, e-mail: mhruby@centrum.cz

Keywords: thermoresponsiveness, redox responsive, reactive oxygen species, fluorine-19, magnetic resonance imaging, drug delivery system, nanotracer



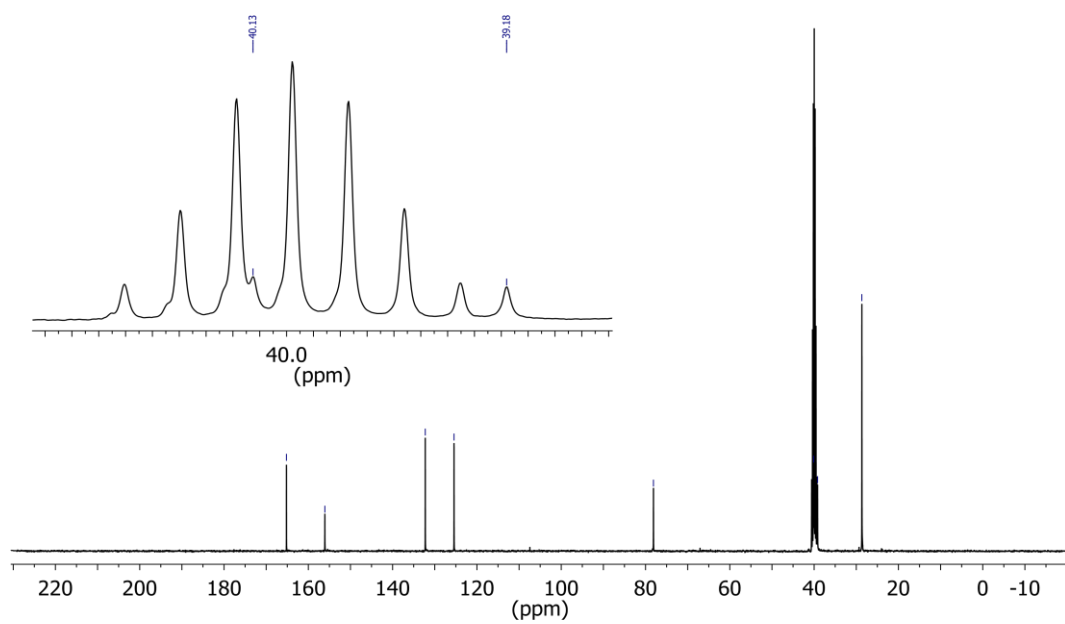


Figure S2. $^{13}\text{C}\{^1\text{H}\}$ NMR spectrum of monomer *N*-(2*N'*-Boc-aminoethyl)acrylamide in dimethyl sulfoxide- D_6 ; $NS = 1024$; $D_1 = 2.00$ s; recorded with a Bruker 400 MHz instrument.

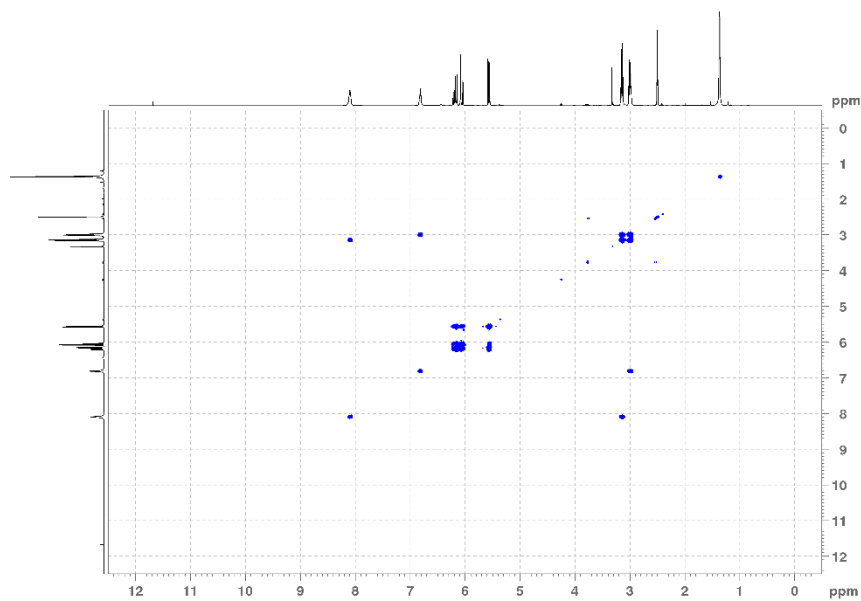


Figure S3. ^1H - ^1H COSY spectrum of monomer *N*-(2*N'*-Boc-aminoethyl)acrylamide in dimethyl sulfoxide- D_6 ; $NS = 4$; $D_1 = 1.50$ s; recorded with a Bruker 400 MHz. instrument

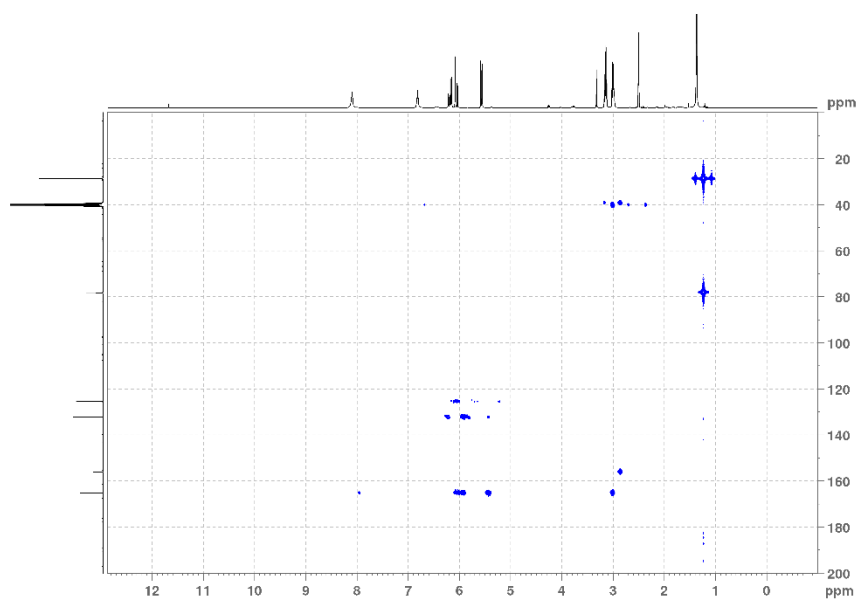


Figure S4. ^1H - ^{13}C HMBC spectrum of monomer *N*-(2*N'*-Boc-aminoethyl)acrylamide in dimethyl sulfoxide- D_6 ; $NS = 4$; $D_1 = 1.50$ s; recorded with a Bruker 400 MHz instrument.

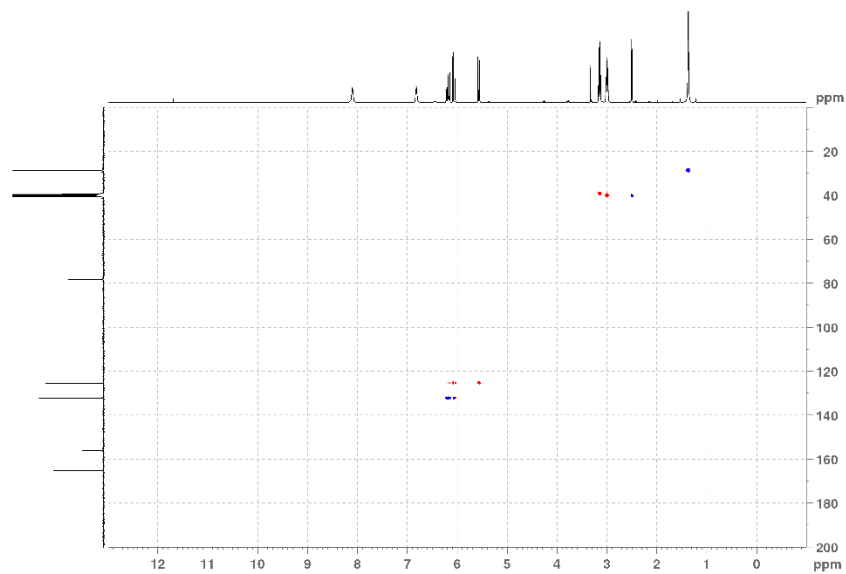


Figure S5. Multiplicity-edited ^1H - ^{13}C HSQC spectrum of *N*-(2*N'*-Boc-aminoethyl)acrylamide measured in dimethyl sulfoxide- D_6 ; $NS = 4$; $D_1 = 2.00$ s; recorded with a Bruker 400 MHz instrument.

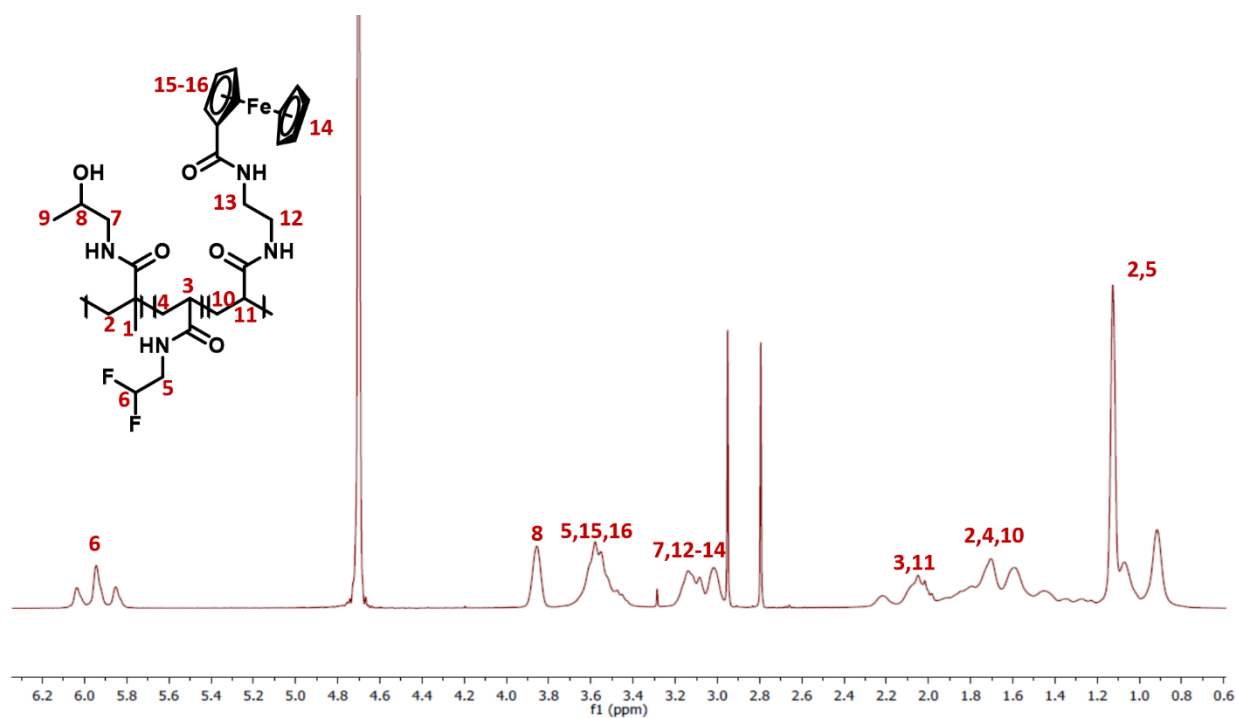


Figure S6. ^1H NMR spectrum of polymer HF2 in MeOH-D_4 ($c_{\text{pol}} = 16.7 \text{ mg}\cdot\text{mL}^{-1}$); $NS = 32$; $D_1 = 30.00$ s; recorded with a Bruker 400 MHz instrument.

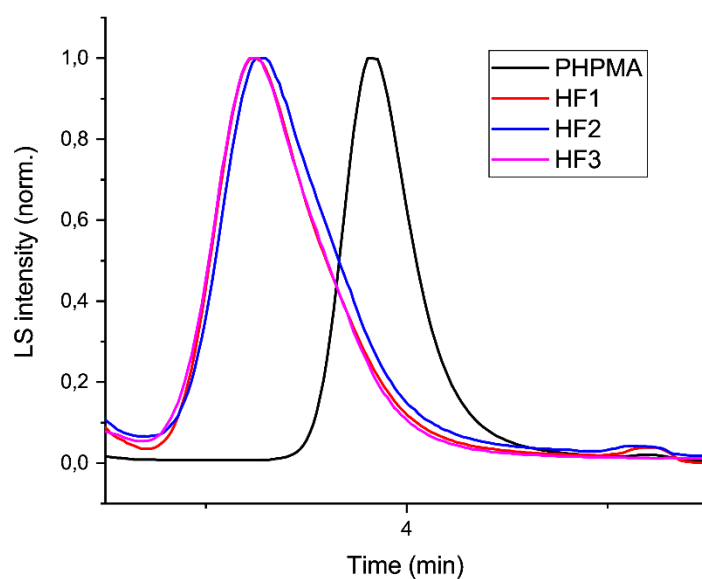


Figure S7. Size exclusion chromatography (SEC) traces for polymers PHPMA-*b*-P(DFEA-co-BocAEA) 1-3 prepared using a methanol and sodium acetate buffer (0.3 M, pH 6.5) mixture (80:20 v/v; flow rate of $0.6 \text{ mL} \cdot \text{min}^{-1}$) as the mobile phase.

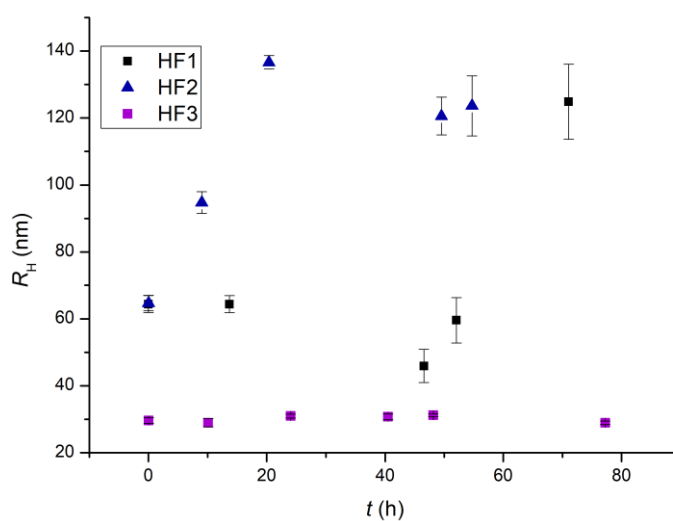


Figure S8. DLS determination of particle stability as a function of time. Samples were incubated at $37 \text{ }^\circ\text{C}$ (polymer concentration of $1 \text{ mg} \cdot \text{mL}^{-1}$ in 140 PBS buffer).

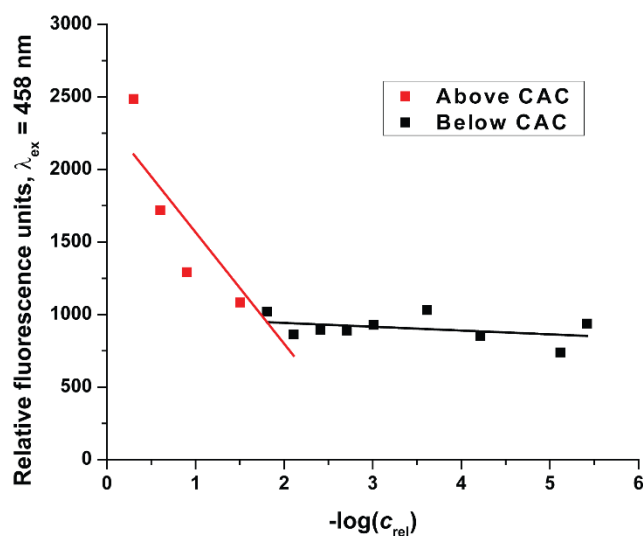


Figure S9. The intensity of the fluorescence emission ($\lambda = 636 \text{ nm}$) of Nile red as a function of decreasing polymer concentration. The critical association concentration is evaluated as the intersection between the enhanced Nile red emission spectrum by the concentration of polymers and the concentration of polymer where the Nile red fluorescence emission is static.

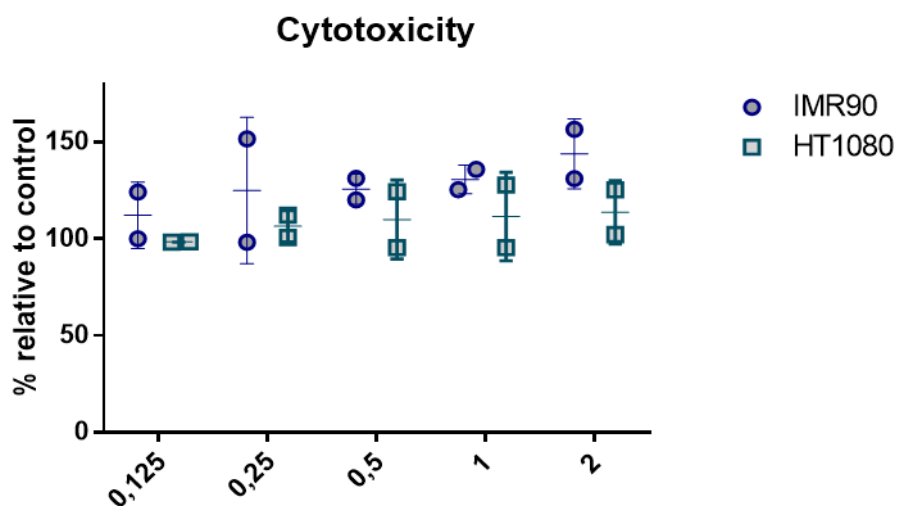


Figure S10. Viability of different cells (IMS90 and HT1080) with increasing concentrations (0.125 to $2 \text{ mg}\cdot\text{mL}^{-1}$) of polymer HF1.

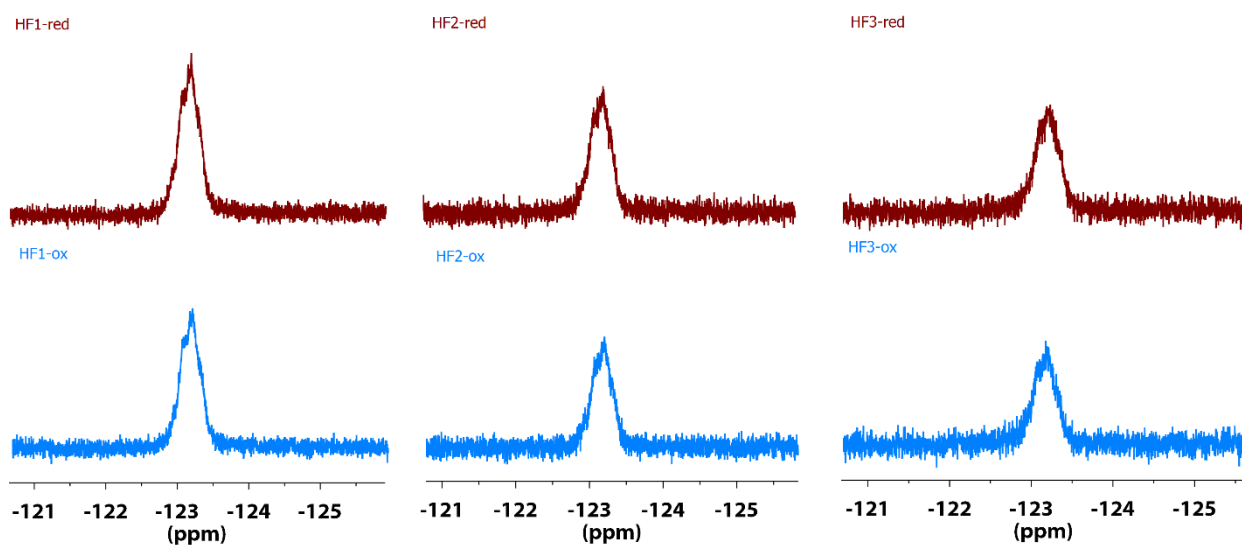


Figure S11. Comparison of the ^{19}F NMR spectra (64 scans, $D_1 = 1.00$ s) of HF1, HF2 and HF3 in D_2O before (**red**) and after oxidation (**ox**) with ammonium persulfate. Recorded with a Bruker 400 MHz instrument.

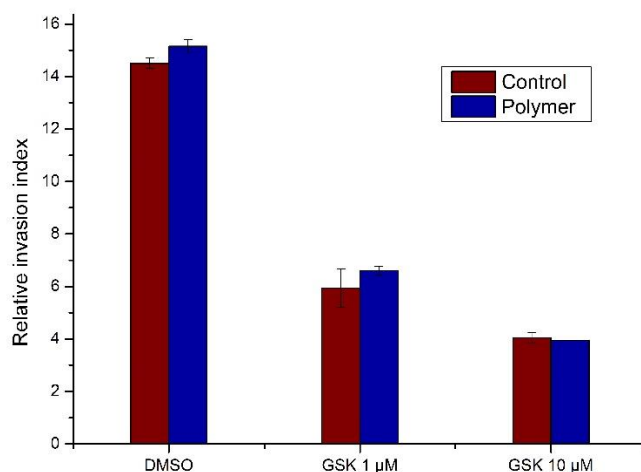


Figure S12. Relative invasion index evaluated for the spheroids in different media. The gray trend line corresponds to the control media (medium containing DMSO and medium containing the free inhibitor GSK 429286 at a 1 or 10 μM concentration), which is compared to the blue trend line corresponding to the polymer solutions (medium with the free polymer and DMSO; medium containing the polymer with the encapsulated inhibitor GSK 429286 at a 1 or 10 μM concentration).

Appendix 5

Švec, P.; Petrov, O. V.; Lang, J.; Štěpnička, P.; Groborz, O.; Dunlop, D.; Blahut, J.; Kolouchová, K.; Loukotová, L.; Sedláček, O.; Heizer, T.; Tošner, Z.; Šlouf, M.; Beneš, H.; Hoogenboom, R.; Hrubý, M., Fluorinated Ferrocene Moieties as a Platform for Redox-Responsive Polymer ¹⁹F MRI Theranostics. *Macromolecules* **2022**, *55* (2), 658-671.

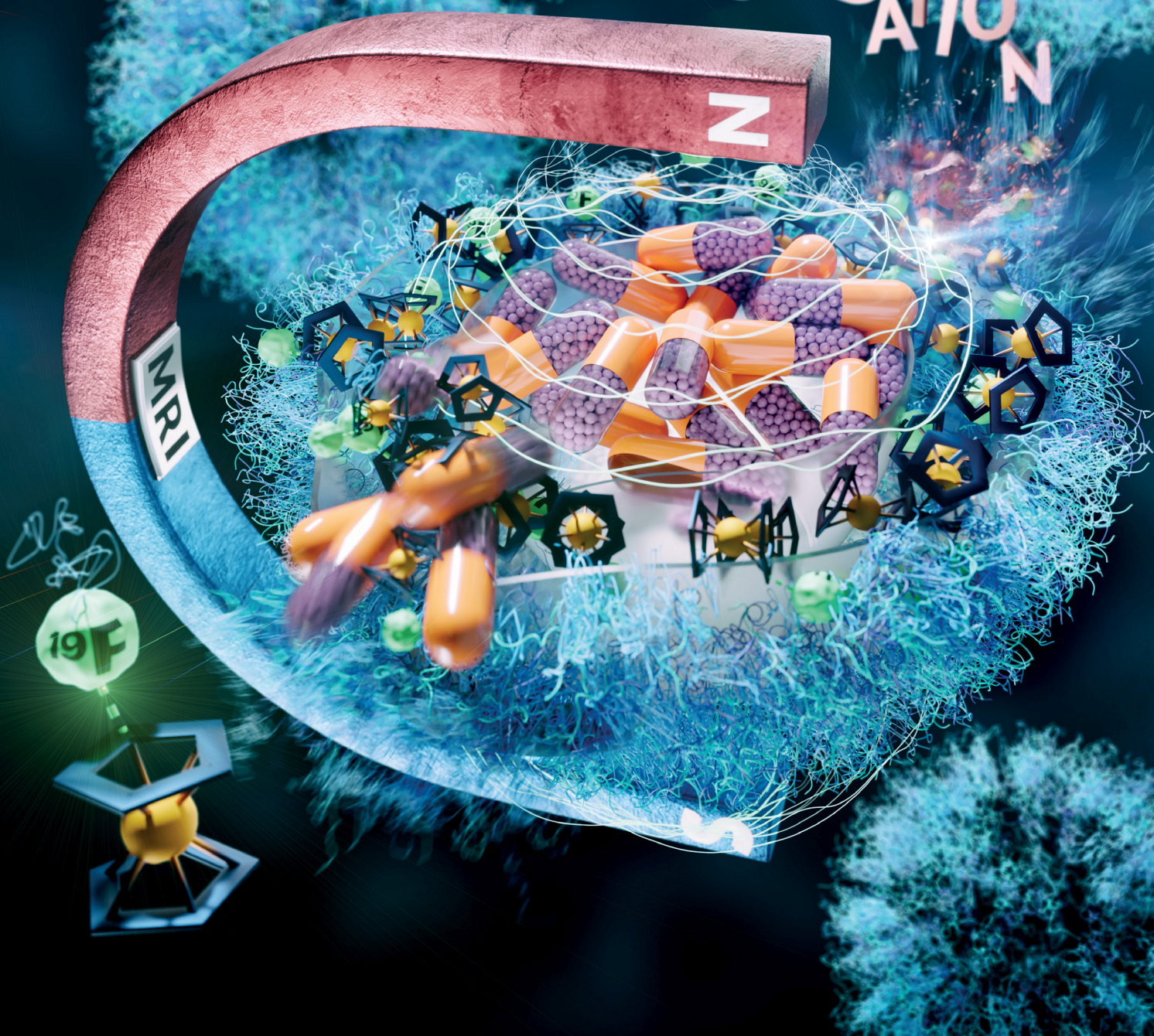
Times Cited: 9; IF = 5.46.

P. Švec and K.K. conceived this research study; P. Švec designed and performed the synthesis of fluorinated ferrocene derivatives, prepared the final polyoxazolines modified with fluorinated ferrocene moieties, collected the DLS data, and wrote the manuscript (except the NMR/MRI section).

January 25, 2022
Volume 55
Number 2

Macromolecules

OXIDATION



ACS Publications
Most Trusted. Most Cited. Most Read.

www.acs.org

Fluorinated Ferrocene Moieties as a Platform for Redox-Responsive Polymer ^{19}F MRI Theranostics

Pavel Švec,* Oleg V. Petrov, Jan Lang, Petr Štěpnička, Ondřej Groborz, David Dunlop, Jan Blahut, Kristýna Kolouchová, Lenka Loukotová, Ondřej Sedláček, Tomáš Heizer, Zdeněk Tošner, Miroslav Šlouf, Hynek Beneš, Richard Hoogenboom, and Martin Hrubý*



Cite This: *Macromolecules* 2022, 55, 658–671



Read Online

ACCESS |



Metrics & More

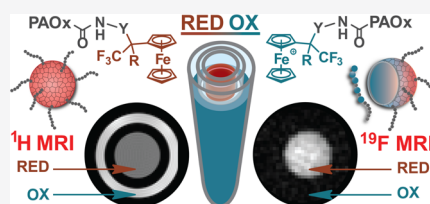


Article Recommendations



Supporting Information

ABSTRACT: Fluorine-19 magnetic resonance imaging (^{19}F MRI) stands out as a powerful tool for noninvasive diagnostics. In particular, polymer-based ^{19}F MRI tracers offer tunable physicochemical properties, including solubility and thermoresponsiveness, and enhanced ^{19}F MRI performance. However, these tracers do not detectably respond to redox changes or do so in only one redox state, thereby preventing potential applications to reactive oxygen species (ROS) bioimaging. Herein, we report the first amphiphilic redox-responsive, poly(2-oxazoline)-based polymers bearing fluorinated ferrocene moieties. Their hydrophobicity and redox responsiveness were tailored by changing the monomer ratio and substitution pattern of the fluorinated ferrocene units. Converting the diamagnetic fluorinated ferrocene moieties into paramagnetic ferrocenium markedly changed the chemical shift and relaxation times of the ^{19}F nuclei distinguishable by ^{19}F MRI. In turn, the statistical–diblock copolymers formed nanoparticles that disassemble upon oxidation, with no toxicity to cultured cells. Therefore, these polymers may be used to release lipophilic drugs in ROS-rich malignancies.



INTRODUCTION

Magnetic resonance imaging (MRI) is currently one of the most important anatomical imaging tools for medical purposes. Using appropriate tracers, MRI even enables us to visualize specific molecular targets, including metabolites.¹ Standard MRI techniques visualize ^1H in water as the most sensitive and abundant nuclei in many tissues of living organisms, but ^{19}F MRI is currently emerging as a highly promising supplementary method because the ^{19}F nucleus sensitivity and the resonance frequency/gyromagnetic ratio are almost identical to those of ^1H . This similarity enables us to acquire ^{19}F MRI images on standard ^1H MRI machines with only minor adjustments of the radiofrequency hardware for dual-mode $^{19}\text{F}/^1\text{H}$ MRI patient imaging² and even for simultaneous acquisition.³ Thanks to the monoisotopic composition of natural fluorine and to its negligible content in the body, fluorinated tracers provide high contrast with almost no background.⁴ Unsurprisingly, numerous ^{19}F MRI tracers have already been described for various applications, such as cell tracking,^{5–10} amyloid plaque detection,^{11–13} pO_2 determination,^{14–16} and polymers with glutathione¹⁷ or drug-release switchable ^{19}F MRI signal.¹⁸

Some of these systems have a high fluorine content but lack fluorine mobility and consequently display strong F–F dipolar interactions,^{19,20} resulting in unfavorable relaxation times. In addition, magnetically inequivalent fluorine atoms also contribute to a lower ^{19}F MRI signal-to-noise ratio due to peak broadening or multiple peaks, thus accounting for poor tracer performance despite the high fluorine content. Previous

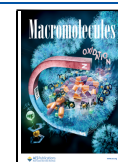
studies have demonstrated that ^{19}F MRI tracers based on fluorinated polymers display unique tunable physicochemical and ^{19}F MRI properties.²¹ For instance, we recently introduced thermoresponsive copolymers based on poly[*N*-(2,2-difluoroethyl)acrylamide]²² that combine an exceptionally high fluorine content (up to 28 wt % for the homopolymer) with excellent relaxation properties, even in the collapsed state above the lower critical solution temperature (LCST) of these tracers.^{23–27} As even more versatile platforms, poly(2-alkyl-2-oxazoline)s (PAOx) stand out for their biocompatibility and tunable properties and for the possibility to synthesize well-defined PAOx polymers with narrow dispersity by controlled cationic ring-opening polymerization (CROP).^{28–34} For example, we have recently developed a promising ^{19}F MRI tracer with a high fluorine content based on PAOx, poly[(2-methyl-2-oxazoline)-*stat*-(2-difluoromethyl-2-oxazoline)].³⁵ Overall, considerable efforts have been made to tap into the potential of these tracers for applications in both basic and applied research, including biomedical sciences.

Both physiological (immune response, cell signaling, and aging) and pathological (cancer) processes are associated with reactive oxygen species (ROS), namely, hydroxyl radicals

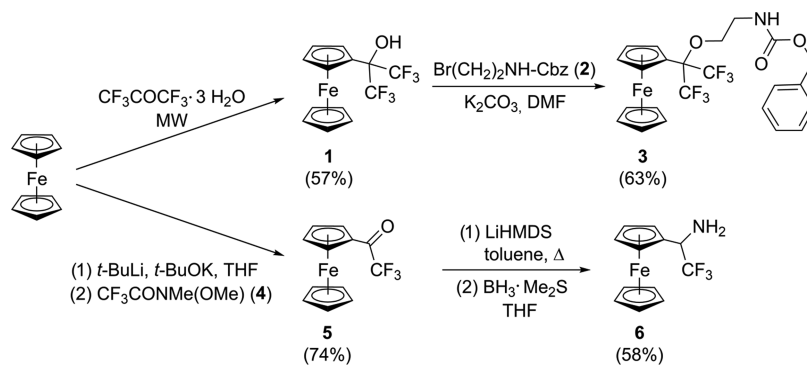
Received: August 15, 2021

Revised: December 10, 2021

Published: December 29, 2021



Scheme 1. Synthesis of Fluorinated Ferrocenes with a Pendant Amino Group (MW, Microwave-Assisted)



($\bullet\text{OH}$), superoxide radicals ($\bullet\text{O}_2^-$), alkyl peroxy radicals ($\text{ROO}\bullet$), hydrogen peroxide (H_2O_2), hypochlorous acid (HClO), and peroxyxynitrite (ONOO^-).^{36–38} Cancer cells, in particular, may exhibit increased levels of ROS. On the one hand, these increased levels of ROS stabilize hypoxia-inducible factor 1- α (HIF-1 α),^{39–41} which is required for cell survival under the hypoxic conditions of solid tumor microenvironments and for rapid tumor neovascularization.⁴² On the other hand, human neutrophils selectively generate HClO and ONOO^- during oxidative burst and netosis^{43,44} (production of neutrophil extracellular traps), which are vital defense mechanisms against pathogens. Therefore, ROS-responsive drug delivery systems (DDSs) and tracers for noninvasive visualization of processes involving increased concentrations of reactive oxygen species may be used as powerful research and diagnostic tools.

Many redox-responsive fluorinated metal-complex ^{19}F MRI tracers,^{45,46} fluorinated polymers showing changes in T_2 upon oxidation,^{47–49} and ferrocene-based redox-responsive materials^{50–52} and DDSs⁵³ have been described previously. Furthermore, 2-[2-(ferrocenyl)ethyl]-2-oxazoline has been reported as a CROP-polymerizable building block for redox-responsive polyoxazolines.⁵⁴ More recently, we have also described ^{19}F MRI tracers/DDSs based on poly[*N*-(2,2-difluoroethyl)acrylamide] modified with ferrocene groups for ROS-induced nanoparticle disassembly and drug release.⁵⁵ However, the ^{19}F MRI signal of this polymer does not change upon oxidation due to its low ferrocene content.

In this study, we present, for the first time, fluorinated ferrocenes as a platform for polymeric redox-responsive ^{19}F MRI tracers/DDSs. Our noncytotoxic, water-soluble amphiphilic polymers form redox-responsive nanoparticles and change their relaxation times and ^{19}F chemical shifts upon oxidation of the ferrocene moieties. These characteristics differentiate them from other ^{19}F MRI polymer tracers because both reduced and oxidized forms can be visualized selectively. Furthermore, the fluorinated ferrocene-based polymers do not employ potentially immunogenic and/or toxic metals such as nickel or cobalt. The nanoparticles of some of our polymers disassemble in an aqueous environment through the action of ROS and may be thus used to deliver lipophilic drugs. The polymers contain 4–11 wt % fluorine, and their localization and oxidation state can be monitored by ^{19}F MRI thanks to the trifluoromethyl groups attached only one atom away from the ferrocene moiety. We also synthesized fluorinated ferrocene amino derivatives suitable for conjugation with polymers using common peptide chemistry, available on a multigram scale from relatively inexpensive common reagents. In addition, we

characterized the morphology, redox properties, and MRI performance of our systems by dynamic light scattering (DLS) and cryogenic transmission electron microscopy (cryo-TEM), by cyclic voltammetry (CV), and by ^{19}F NMR/MRI, respectively.

RESULTS AND DISCUSSION

Synthesis of Fluorinated Ferrocene Derivatives with a Pendant Amino Group. Strong ^{19}F MRI signals require materials with mobile magnetically equivalent fluorine atoms and a high fluorine content.^{19,20} For this reason, we designed polymers containing trifluoromethylated ferrocenes as the sensing units that were anticipated to change their ^{19}F nuclear magnetic resonance signal in response to ROS species while simultaneously triggering nanoparticle disassembly and potential drug release. ^{19}F nuclei will experience the strongest changes in relaxation times and chemical shift when they are close to the ferrocene moiety that is being oxidized. However, introducing strong electron-withdrawing groups, such as the trifluoromethyl group, to the ferrocene moiety can significantly increase its redox potential. The resulting redox potential of the polymer-bound ferrocene derivative could thus impact the ease and rate of oxidation/disassembly of nanoparticles formed from these amphiphilic polymers. Furthermore, fluorinated groups tend to increase material lipophilicity markedly, and highly fluorinated materials may even exhibit both hydro- and lipophobicity (i.e., fluorophilic behavior).⁵⁶ Therefore, we prepared polymers based on two different fluorinated ferrocene chemotypes in this study (Scheme 1).

Compound 1 was prepared using a previously reported microwave-assisted Friedel–Crafts-like reaction.⁵⁷ After optimizing the reaction conditions, we easily synthesized the fluorinated precursor on a multigram scale. To introduce the amine group, necessary for amide coupling with the polymer, we used the Williamson ether synthesis with (benzyloxy)-carbonyl-protected amine 2 (Cbz) as the alkylating agent. The hydroxyl group in compound 1 is expected to be strongly acidic given the presence of two electron-withdrawing $-\text{CF}_3$ groups (the $\text{p}K_a$ of hexafluoroisopropanol is 9.3⁵⁸ and the phenyl analog of 1 has a $\text{p}K_a$ value of 8.8^{59,60}), which accounts for the relatively high yield of the $\text{S}_{\text{N}}2$ reaction that leads to the desired product 3 (63%). Considering the above, we selected the Cbz group in compound 3 as the most suitable amine-protecting group for its clean and fast cleavage by H_2/Pd and straightforward free amine isolation.

The synthesis of the second fluorinated ferrocene derivative with a pendant amino group starts with 2,2,2-trifluoroacetylferrocene (5). In turn, 5 can be synthesized by Friedel–Crafts

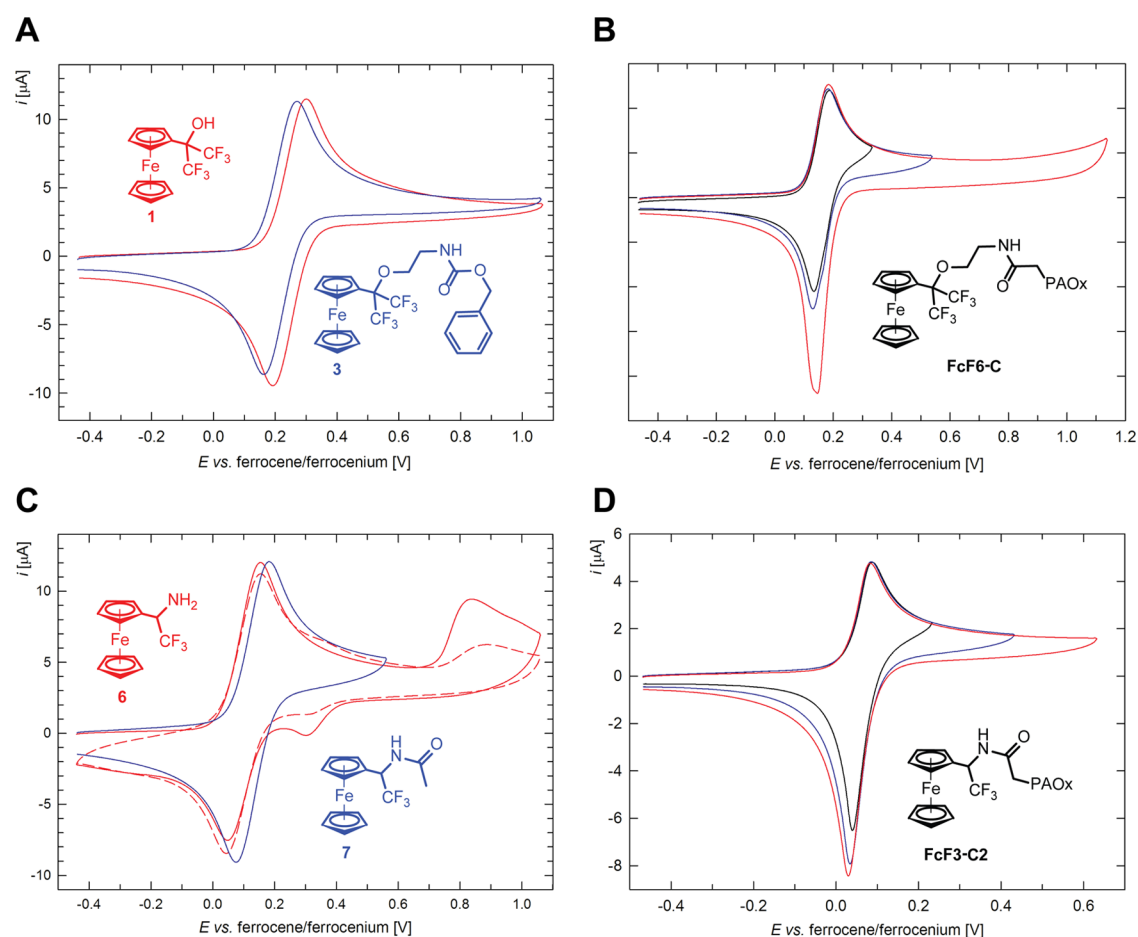
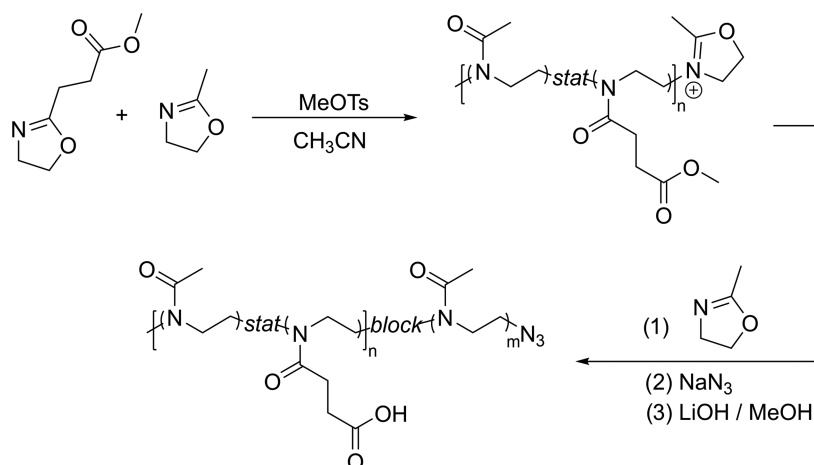


Figure 1. (A, C) Cyclic voltammograms of **1** and **3** (A) and **6** and **7** (C) as recorded in dichloromethane (0.1 M Bu₄N[PF₆]) on a glassy carbon disk electrode at 0.1 V·s⁻¹ scan rate showing the first scans; the reversible nature of the redox transitions is maintained over the following scans except for **6**, for which the second scan is also shown by a dashed line. (B, D) Representative cyclic voltammograms recorded over different potential ranges for **FcF6-C** (B) and **FcF3-C2** (D) in dichloromethane under the same conditions.

Scheme 2. Synthesis of Starting Polyoxazolines with a Pendant Carboxyl Group



acylation of ferrocene with trifluoroacetic anhydride in the presence of AlCl₃ as the catalyst.⁶¹ Unfortunately, this approach resulted in very low yields (≈15%) with a rather demanding purification of the product on a larger scale. For this reason, we prepared 2,2,2-trifluoroacetylferrocene (**5**) on a larger scale by selective monolithiation of ferrocene⁶² followed by a reaction of the *in situ*-formed lithioferrocene with Weinreb

amide of trifluoroacetic acid (**4**). This reaction is straightforward, yielding the product on a multigram scale and allowing further upscaling.

The next step toward the desired amine **6** was reductive amination of the ketone moiety, which is usually performed through *in situ* imine formation and reduction with, e.g., sodium cyanoborohydride. However, under these conditions,

we were able to isolate only the product of ketone reduction [(2,2,2-trifluoro-1-hydroxyethyl)ferrocene; perfluoromethylated ketones generally perform poorly in reductive amination⁶³ with NaBH₃CN]. By following a previously reported protocol for 1-aryl-2,2,2-trifluoroethylamine synthesis from the corresponding ketones,⁶³ we were able to prepare more than 1 g of pure compound **6** in a single run. Compound **6** was easily isolated by chromatography on silica without adding any base into the mobile phase, indicating the low basicity of its amino group, *vide infra*. The amine **6** was converted into the corresponding acetamide **7** (Figure 1C) to study its electrochemical behavior as a low-molecular-weight counterpart of polymers prepared by coupling with compound **6**.

Polymer Synthesis and Modification with Fluorinated Ferrocene Derivatives. A series of three methyl ester-containing diblock copoly(2-oxazoline)s (A_{Me_e}, B_{Me_e}, and C_{Me_e}; Scheme 2) were targeted to have a first block consisting of a statistical copolymer of 2-methyl-2-oxazoline (MeOx) and 2-(3-methoxy-3-oxopropyl)-2-oxazoline (MestOx),⁶⁴ which will serve for coupling with the fluorinated ferrocene moieties leading to a hydrophobic block and a second hydrophilic PMeOx block.

The block copolymers were synthesized by microwave-assisted cationic ring-opening polymerization (CROP) of the respective 2-oxazoline monomers in acetonitrile at 140 °C initiated by methyl 4-methylbenzenesulfonate (MeOTs). To avoid preparing an excessively hydrophobic ferrocene-containing block, statistical copolymerization of MestOx with hydrophilic MeOx was used to synthesize the first block. Hydrophobic statistical copolymers may also offer some advantages over classical block copolymers, such as higher hydration of the core and increased mobility, which leads to longer T₂⁶⁵ and higher drug loading capacity.⁶⁶

After both monomers were completely consumed, the second portion of MeOx was added, and the polymerization was continued to yield the second block of fully hydrophilic MeOx homopolymer to ensure water solubility. The polymerization was terminated with sodium azide to introduce a chain-end azide moiety for functionalization, which was not further employed in this work. The three copolymers differed in the content of MestOx repeating units, whereas the target total theoretical degree of polymerization (DP = 100) and target block molar ratio remained the same in all polymers ([MeOx-MestOx]/[MeOx] = 40:60). For subsequent conjugation, the methyl ester side chains were converted into carboxylic acids by alkaline saponification (for molecular weights and dispersities, see Table 1).

The polymers with free carboxyl groups were subsequently conjugated with the fluorinated ferrocenes by amide coupling using (benzotriazol-1-yloxy)tripyrrolidinophosphonium hexafluorophosphate (PyBOP). The hexafluorinated amine **8** (Scheme 3) was prepared by deprotection of **3** by hydrogen in MeOH with a Pd/C catalyst immediately prior to coupling with polymers A–C. Amide coupling with compound **8** and PyBOP proceeded smoothly and with virtually full conversion of the carboxyl groups, yielding polymers FcF6-A, FcF6-B, and FcF6-C with 5, 10, and 15 mol % fluorinated ferrocene moiety content, respectively, according to NMR analysis. These values correspond to 5–11 wt % fluorine content (Table 1). Polymers FcF6-A and FcF6-B were soluble/dispersible in water at room temperature, and the polymer FcF6-C dissolved/dispersed in water after briefly heating to approximately 50 °C without any

Table 1. Molecular Weight and Dispersity as Determined by Multiangle Light Scattering Coupled with Size-Exclusion Chromatography (SEC-MALS), Proportion of Ferrocene-Containing Repeating Units (Fc % ru) as Determined by NMR in DMSO-*d*₆, and the Corresponding Calculated Weight Content of Fluorine in the Polymers

polymer	M _w ^a [kDa]	D _M ^a	Fc % ru ^b	F [wt %]
A	11.0	1.03		
B	9.66	1.03		
C	8.52	1.03		
FcF6-A	12.8	1.03	5	5.3
FcF6-B	14.2	1.04	10	8.9
FcF6-C	16.8	1.01	15	11
FcF3-C1	14.9	1.02	6.8	3.4
FcF3-C2	25.8	1.14	13	5.8

^aDetermined by SEC; the dn/dc in a mixture (80:20 vol %) of MeOH and aqueous AcONa buffer (0.3 M, pH = 6.5) at 620 nm and 29 °C: dn/dc (FcF6-C) = 0.183 ± 0.005 mL·g⁻¹; dn/dc (FcF3-C1) = 0.187 ± 0.005 mL·g⁻¹; dn/dc (FcF3-C2) = 0.182 ± 0.009 mL·g⁻¹.

^bDetermined by ¹H NMR in DMSO-*d*₆.

apparent precipitation when cooling to room temperature (*c* = 20–30 mg·mL⁻¹).

Because the fluorine content was lower in compound **6**, only polymer C, which had the highest amount of free carboxyl groups, was chosen for modification with this fluorinated ferrocene moiety. Using the same reaction conditions as those applied to **8**, the conversion of the carboxyl groups of C in the reaction with **6** was always incomplete, with a relatively high amount of HOCH₂CH₂NH-moieties (coupling reactions were quenched with 2-hydroxyethylamine). Polymer FcF3-C1 (Table 1) contains 6.8 mol % of ferrocene moieties and 5.8 mol % of *N*-(2-hydroxyethyl)amide moieties. This phenomenon is most likely caused by low nucleophilicity (and basicity, as mentioned above) of the amino group geminal to the trifluoromethyl group in compound **6**. For this reason, we decided to employ a more reactive coupling reagent (7-azabenzotriazol-1-yloxy)tripyrrolidinophosphonium hexafluorophosphate (PyAOP) added in two portions. This procedure yielded polymer FcF3-C2 with a high functionalization degree (13 mol %), but the high functionalization was unfortunately accompanied by higher polymer dispersity than in FcF6-A-C and FcF3-C1 (Table 1). As with the FcF6 polymers, the most hydrophilic polymer of the FcF3 chemotype (FcF3-C1) was soluble/dispersible at room temperature, whereas the polymer with the highest ferrocene content (FcF3-C2) required heating to 60 °C for dissolution/dispersion, with no apparent precipitation after cooling to room temperature. Although FcF3-C2 should be less hydrophobic than its FcF6-C counterpart (1 vs 2 CF₃ groups on the ferrocene moiety), the former is surprisingly almost insoluble in water without heating the sample. This kinetically impeded solubility may be explained by a higher rigidity of the ferrocene-containing repeating units in FcF3-C2 (*T*_g = 98 °C for FcF3-C2 vs 80 °C for FcF6-C; see Table S5 and Figure S37, SI).

Cyclic Voltammetry. The redox properties of the amphiphilic polymers and low-molecular-weight fluorinated ferrocene precursors were studied by cyclic voltammetry in dichloromethane containing Bu₄N[PF₆] as the supporting electrolyte. Our results showed that alcohol **1** and ether **3** undergo simple redox transitions attributable to reversible oxidation of the ferrocene unit at 0.25 and 0.22 V vs ferrocene/

Scheme 3. Synthesis of the Final Polymers: Amide Coupling with 8 (R = $-\text{CF}_3$, Y = $-\text{CH}_2\text{CH}_2\text{O}-$) or 6 (R = $-\text{H}$, Y = Void; Racemate)

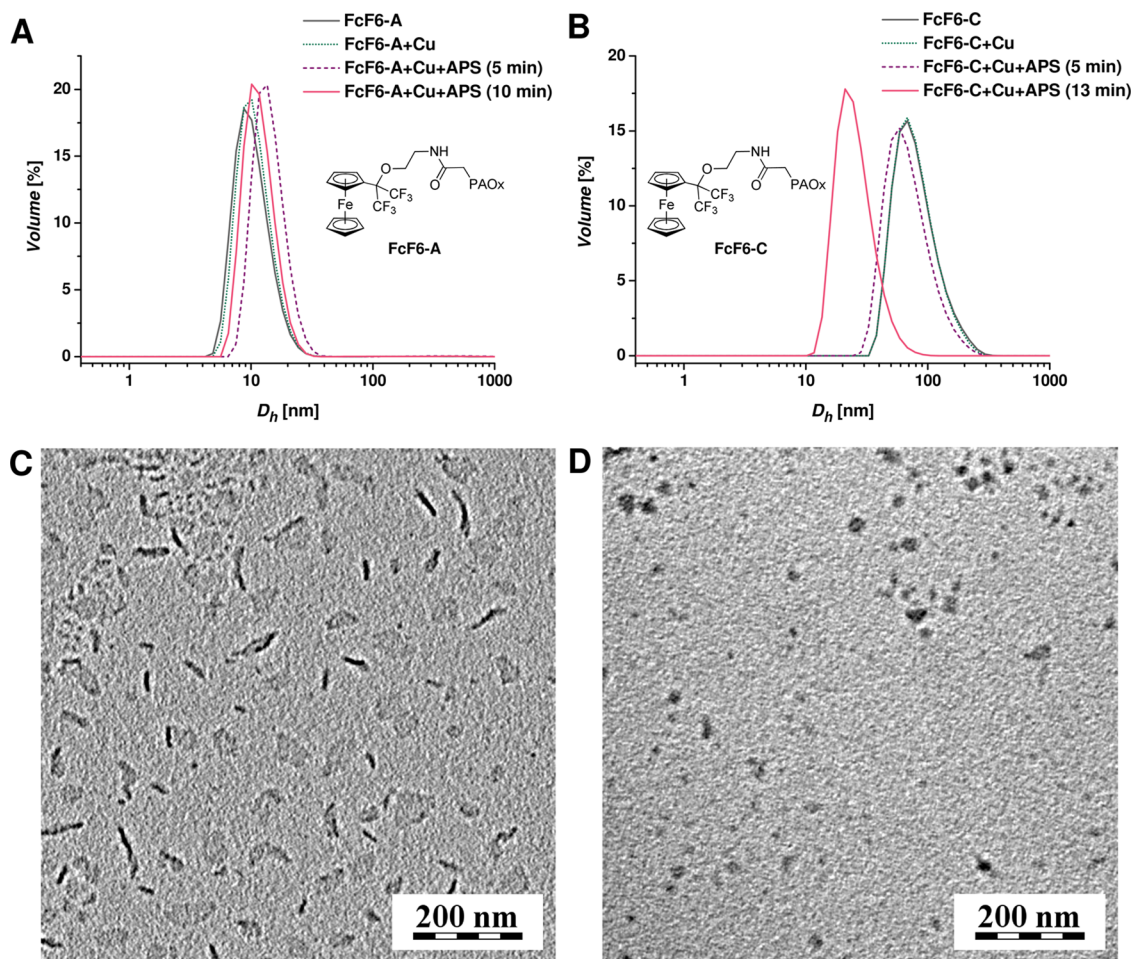
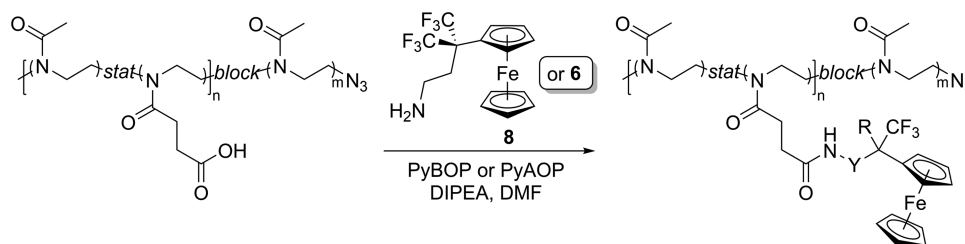


Figure 2. (A, B) Hydrodynamic diameter of FcF6-A and FcF6-C polymer samples ($2 \text{ mg}\cdot\text{mL}^{-1}$) dissolved in citrate buffer (0.08 M , $\text{pH} = 6.2$) before oxidation, after Cu^{2+} (catalytic amount) addition, and after APS addition at different timepoints. (C) Cryo-TEM image of FcF6-C dissolved in citrate buffer (0.08 M , $\text{pH} = 6.2$). (D) Cryo-TEM image of FcF6-C dissolved in citrate buffer (0.08 M , $\text{pH} = 6.2$) after oxidation with APS.

ferrocenium (Figure 1A). Both oxidations occur at more positive potentials than the oxidation of ferrocene itself due to the electron-withdrawing character of the substituents at the ferrocene unit, which hinders oxidation. Thus, our findings corroborate previous data on compound 1.⁵⁷ In contrast, we observed that ether 3 derived from compound 1 is more easily oxidized than its parent alcohol, unlike the methyl ether derivative 3-(1,1,1,3,3,3-hexafluoro-2-methoxypropan-2-yl)-ferrocene, whose oxidation potential is higher than that of compound 1.⁵⁷ Nevertheless, this discrepancy may be merely caused by different experimental conditions (MeCN vs CH_2Cl_2), as found when comparing FcCH_2OH with FcCH_2OMe .^{67,68} Moreover, the difference in oxidation potentials between 1 and 3 is small.

The oxidation of compound 6, which bears a single $-\text{CF}_3$ group, was also reversible ($E^{\circ'}$ 0.10 V) but followed by an irreversible redox transition at more positive potentials (Figure 1C). The second wave, presumably due to irreversible oxidation of the amine moiety,⁶⁹ was associated with a weak reduction counter wave and changed its position and intensity upon repeated scanning. Conversely, the oxidation of amide 7 was electrochemically reversible and, due to the presence of an electron-withdrawing substituent at the nitrogen atom, occurred at a more positive potential ($E^{\circ'}$ 0.13 V) than for the parent amine.

The $\text{Fc}(\text{CF}_3)_2\text{OCH}_2\text{CH}_2\text{NHC}(\text{O})$ moieties in the FcF6-C polymer were oxidized independently during a single redox event at potentials similar to that of compound 3 (an anodic

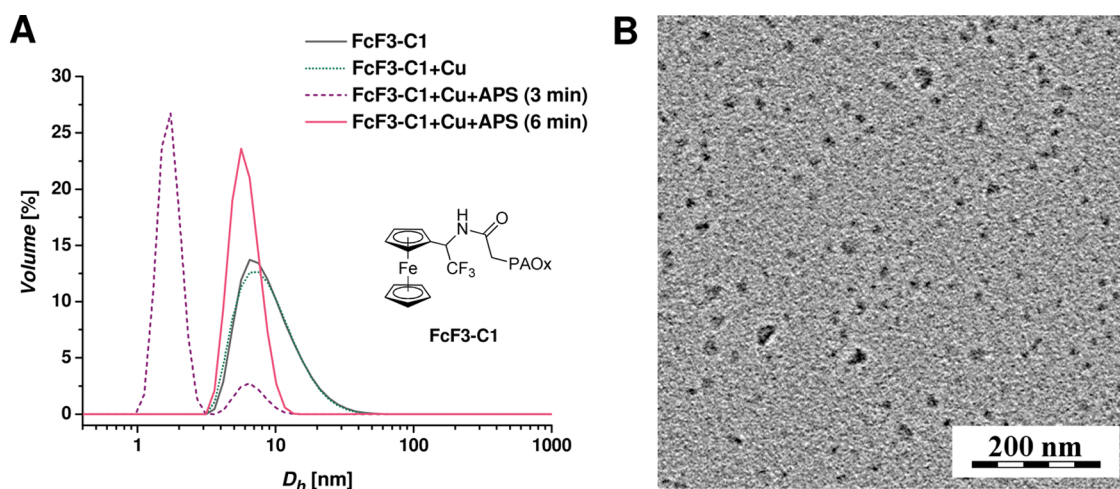


Figure 3. (A) Hydrodynamic diameter of FcF3-C1 polymer samples ($2 \text{ mg}\cdot\text{mL}^{-1}$) dissolved in citrate buffer (0.08 M, pH = 6.2) before oxidation, after Cu^{2+} (catalytic amount) addition, and after APS addition at different timepoints. (B) Cryo-TEM image of FcF3-C1 dissolved in citrate buffer (0.08 M, pH = 6.2).

peak potential of 0.19 V, see Figure 1B). However, the associated reduction was strongly affected by adsorption of the oxidized polymer on the electrode surface. For instance, changing the scan direction immediately after the oxidative wave resulted in a convolution of the reduction counter wave with a stripping peak during back scanning. Upon increasing the switching potential, the stripping peak became the dominant feature of the reverse scan. The redox behavior of polymers FcF6-C and FcF6-B was virtually identical. Similarly, the redox responses of the polymers FcF3-C2 and FcF3-C1 did not differ from each other and were comparable to those of FcF6-C and FcF6-B, except for the lower oxidation potential of the amido-ferrocene pendants in FcF3-C2 (Figure 1D) and FcF3-C1. This shift to lower potential stems from the presence of only one $-\text{CF}_3$ group and a less electronegative nitrogen atom at the pivotal carbon atom (anodic peak potentials: 0.08 V).

To further support the results of CV, we also investigated the redox potentials of fluorinated ferrocene derivatives 1, 3, 6, and 7 computationally using a combined (U-)DFT/(U-)DLPNO-CCSD(T) approach, (for details, see the SI, Quantum Chemical Study).^{70–73} The calculated redox potentials were in good agreement⁷⁴ with the experimental data.

Dynamic Light Scattering and Cryogenic Transmission Electron Microscopy. Polymer responsivity to oxidation in an aqueous environment was assessed by dynamic light scattering (DLS) and cryogenic transmission electron microscopy (cryo-TEM). Polymers with fluorinated ferrocene moieties can be oxidized using hydrogen peroxide, but similarly to the oxidation of ferrocene with H_2O_2 , this reaction is autocatalytic, with relatively slow kinetics.⁷⁵ Furthermore, the ferrocenium species can be decomposed by oxygen or some nucleophiles on a longer time scale.^{76–80} To perform the oxidation as fast as possible and in a controlled manner, we used ammonium peroxydisulfate (APS), together with a CuCl_2 catalyst as the oxidant. Under these Fenton-like conditions, the polymers of the FcF3 chemotype were fully oxidized almost instantaneously, whereas polymers of the FcF6 chemotype with two CF_3 groups on the ferrocene moiety became gradually oxidized with an induction period of approximately 1 min. Isotonic citrate buffer was selected as the aqueous

medium for its ability to strongly complex Fe^{III} that was slowly released upon ferrocenium decomposition. Citrate chelates Fe^{III} and prevents the formation of larger Fe^{III} hydroxide aggregates that interfere with DLS measurements.

The polymers FcF6-A and FcF6-B formed micelles with a hydrodynamic diameter (D_h) from 10 to 20 nm, whose size did not change significantly upon oxidation (possible slight swelling observed during FcF6-A oxidation, Figure 2A). In contrast, the D_h of FcF6-C polymer particles was close to 100 nm (Figure 2B). This value cannot correspond to the size of a “classical micelle” because the maximum theoretical diameter of a classical micelle is limited by the fully stretched polymer chain contour length (L), and, therefore, cannot exceed $2L$ (for MeOx DP = 100 approx. 70 nm).⁸¹ Upon oxidation, the hydrodynamic diameter of the FcF6-C nanoparticles changes to approximately 20 nm, which is similar to that of unoxidized FcF6-A and FcF6-B (Figure S2) nanoparticles.

To better understand these unexpected DLS results, we examined the morphology of these nanoparticles by cryo-TEM. Cryo-TEM images of unoxidized FcF6-C revealed approximately 100 nm long, thin “rod-like” particles resembling rod-/worm-like micelles⁶⁶ and flake objects of a similar size (Figure 2C). The flake objects could be either different nanoparticles of FcF6-C or an artifact resulting from the cryogenic sample preparation process (such as the occasionally occurring “leopard skin” artifact of unclear origin).^{82,83} In contrast, the oxidized polymer FcF6-C resembled classical micelles, as shown by the isometric objects, approximately 20 nm in size, observed in the cryo-TEM images (Figure 2D) and in line with our DLS results.

The D_h of the nanoparticles formed from FcF3-C1 and FcF3-C2 (close to 10 nm) was lower than that of FcF6 samples. Unlike the nanoparticles derived from FcF6 polymers, those formed from FcF3-C1 and FcF3-C2 at least partly disintegrated to unimers upon oxidation (Figures 3A and S8). After 6 min, the D_h returned to slightly higher values indicating a gradual reassociation process. The cryo-TEM images of the aqueous FcF3-C1 sample (Figure 3B) revealed micelle-like particles, which disappeared after oxidation (image not shown).

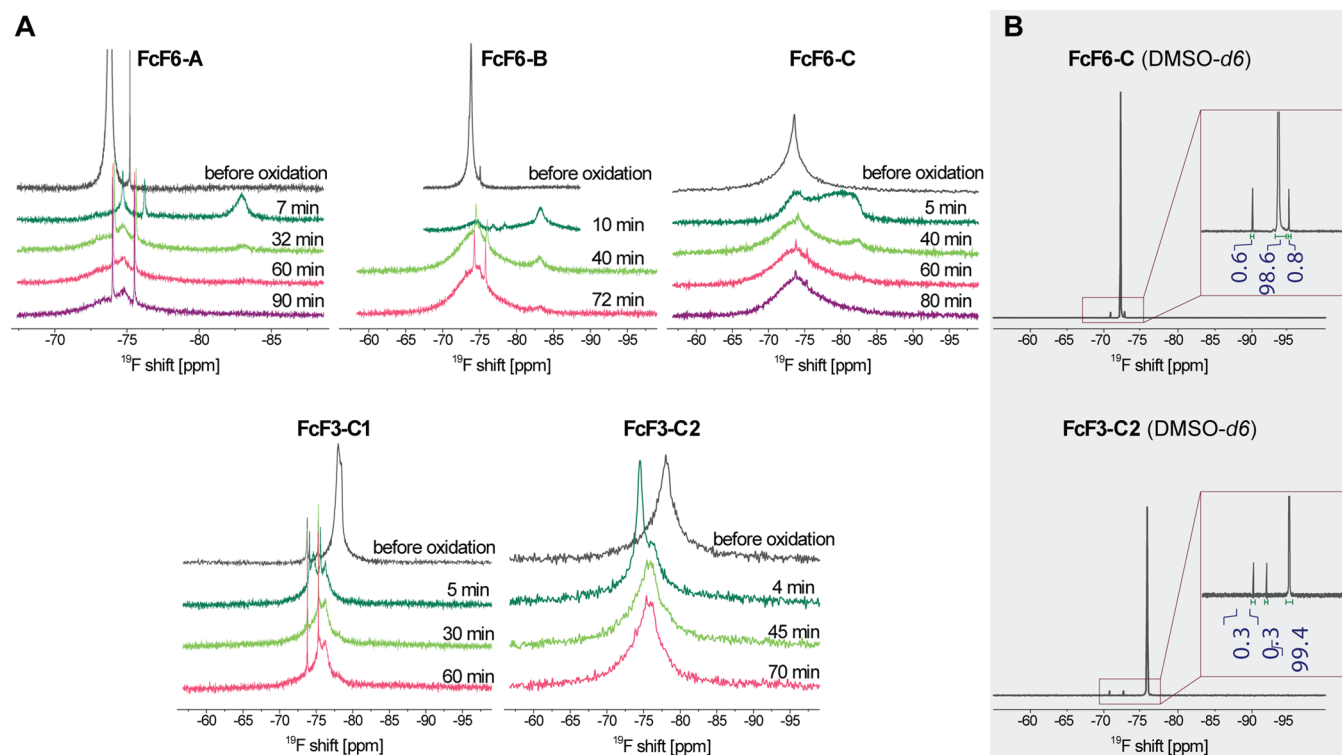


Figure 4. (A) ^{19}F NMR spectra of FcF6-A, -B, -C, FcF3-C1, and FcF3-C2 in citrate buffer (0.08 M, pH = 6.2) at $B_0 = 11.75$ T. The timepoints indicate the time elapsed after adding APS to the sample. The ^{19}F chemical shifts are referenced to external CFCl_3 . (B) ^{19}F NMR spectra of FcF6-C and FcF3-C2 in $\text{DMSO-}d_6$.

These substantial differences between FcF6 and FcF3 polymer chemotypes during oxidation suggest that the (hexafluoroisopropyl)ferrocenyl moiety remains hydrophobic after oxidation to its cationic ferrocenium counterpart and/or that the oxidation of the ferrocene moieties in FcF6 polymers is incomplete even when using a powerful oxidizing agent such as peroxydisulfate. These two possible mechanisms would act in cooperation because the redox potential of ferrocene significantly increases in a nonpolar environment.⁸⁴ Furthermore, excessive hydrophobicity decreases the amount of APS and reactive oxidative species available in the micelle core. During the oxidation, the aqueous polymer samples change from orange-brown (ferrocene) to blue (ferrocenium); more specifically, the FcF3 samples turn deep blue almost immediately after adding APS, whereas FcF6 samples reach only a faint blue-green hue even when using a high excess of APS (the incomplete oxidation is also supported by the results of the NMR/MRI experiments, *vide infra*).

Cytotoxicity. Polymer cytotoxicity was assessed using the standard 3-(4,5-dimethylthiazol-2-yl)-2,5-diphenyltetrazolium bromide (MTT) assay. For this purpose, we selected a human prostate cancer PC3 cell line for its considerably high ROS levels⁸⁵ and normal human dermal fibroblast (NHDF) line as a “ROS-negative” control. The cells were cultivated with the polymers at four different concentrations of up to $1 \text{ mg}\cdot\text{mL}^{-1}$. The polymers had no detrimental effect on the cell viability of the NHDF line, but at the two highest concentrations (1.0 and $0.75 \text{ mg}\cdot\text{mL}^{-1}$), they had a minor, albeit significant, negative impact on the viability of PC3 cells after 24 h of incubation (Figures S30 and S31, SI). This result indicates that both FcF3 and FcF6 polymers are oxidized and slightly cytotoxic to cancer cells that produce high amounts of ROS. Both the oxidation of the ferrocene moieties to

ferrocenium and the subsequent, gradual release of Fe(II) by hydrolysis cause cytotoxicity by generating further ROS species through Fenton-type pathways.^{86–88}

NMR and MRI Properties. Fluorinated ferrocenes **8** and **6** are diamagnetic before their oxidation to the corresponding paramagnetic ferrocenium ions. Similarly to isopropylferrocene and (*tert*-butyl)ferrocene, the CF_3 groups in **8** and **6** should have low rotational barriers, thus allowing high group mobility at room temperature.⁸⁹ Accordingly, the $\text{DMSO-}d_6$ solutions of FcF6 and FcF3 polymers exhibited sharp signals in ^{19}F NMR (FWHM = 0.02 kHz) at -72.3 and -75.8 ppm, respectively (Figure 4B). The ^{19}F NMR peak of the polymer was always accompanied by two ^{19}F NMR signals with low integral intensities but distinctively sharp peaks. These minor signals likely derive from slow oxidation and decomposition of the ferrocene units by oxygen and are therefore unavoidable impurities; a higher impurity signal was observed in the more hydrophilic polymers (Figure 4A).

When dissolved in water, FcF6 and FcF3 polymers formed nanoparticles. With a few exceptions,^{25,26} polymer aggregation significantly decreases T_2 (and/or T_2^*) and increases T_1 due to the lower mobility of the polymers. This is generally an undesirable effect for MRI imaging because the decrease in the T_2 -to- T_1 ratio lowers the signal-to-noise ratio and leads to longer acquisition times. As expected, the decrease in T_2 due to FcF6 and FcF3 polymer aggregation strengthened with the increase in polymer hydrophobicity. Consequently, FcF6-C and FcF3-C2 exhibited shorter spin–spin relaxation times (T_2 0.4 and 1.6 ms, respectively) than their more hydrophilic counterparts FcF6-A and FcF3-C1 (T_2 8.2 and 6.9 ms, respectively; for complete data, see Table 2 and Figures S20–S24, SI).

Table 2. Full Width at Half-Maximum (FWHM) and Mean T_1 and T_2 Relaxation Times of Polymer Samples in Citrate Buffer (0.08 M, pH = 6.2) at $B_0 = 11.75$ T

polymer	reduced			oxidized (>60 min)		
	FWHM [kHz]	T_1 [ms]	T_2 [ms]	FWHM [kHz]	T_1 [ms]	T_2 [ms]
FcF6-A	0.07	620	8.2	1.1	280	20
FcF6-B	0.17	670	1.6	2.1	810	2.1
FcF6-C	0.86	740	0.4	3.2	280	1.3
FcF3-C1	0.45	560	6.9	1.1	290	n/a
FcF3-C2	1.60	690	1.6	2.0	280	3.0

The polymer oxidation effect on ^{19}F NMR parameters differed between FcF3 and FcF6 chemotypes. However, these chemotypes follow a similar reaction pathway via a short-living (≈ 10 min) intermediate stage with the sharpest changes in NMR lineshape and T_1 relaxation. For the FcF6 chemotype, this stage of oxidation manifests as broadening and shifting of the ^{19}F peak around -73 ppm to a lower frequency (upfield) and as a second peak that emerges around -82 ppm (Figure 4A). For the FcF3 chemotype, the peak at -77 ppm shifts to a higher frequency (downfield), and the second peak emerges at -73 ppm (Figure 4A). These changes are accompanied by a decrease of more than one order of magnitude in the T_1 relaxation time (Figures S20–S24, SI).

The second ^{19}F peak emerging during oxidation is attributed to the newly formed paramagnetic ferrocenium. Paramagnetic metal centers are known to shift the NMR frequency of the nucleus, and the value and sign of this shift are determined by the electron spin–nuclear spin coupling.^{90,91} The second ^{19}F peak appeared at opposite sides to the original peaks in FcF6 versus FcF3 polymers (upfield vs downfield, respectively). At the early stage of oxidation (Figure 4A), these two ^{19}F signals may be interpreted as a transient coexistence of both ferrocenium and ferrocene moieties. The concomitant faster T_1 relaxation of the ^{19}F signal is attributed to the paramagnetic relaxation enhancement (PRE) caused by Fe^{III} of ferrocenium (Fe^{II} in ferrocene is diamagnetic). The moieties with unoxidized ferrocene also exhibited enhanced ^{19}F T_1 relaxation resulting from the surrounding paramagnetic species and higher mobility due to polymer hydrophilization/nanoparticle disassembly, which caused the T_1 distribution to spread to 100 ms and lower values. In contrast, the T_2 relaxation did not exhibit dramatic changes at this early stage of oxidation (see Figures S20–S24). This observation could be explained by two opposing oxidation effects on T_2 —PRE of the ferrocenium moieties (lowering T_2) and by polymer hydrophilization/nanoparticle disassembly (increasing T_2 and/or T_2^*). Considering the high T_1/T_2 ratio and the micelle size, unlike in smaller dendrimer systems,⁴⁹ in our FcF3 and FcF6 systems, the ^{19}F relaxation conditions approach the solid-state limit, where T_1 and T_2 have an opposite dependence on the molecular mobility. In other words, polymer nanoparticle disintegration and the concomitant increase in molecular mobility would lead to longer T_2 and shorter T_1 values. The formation of paramagnetic ferrocenium upon oxidation further shortens the T_1 values while counteracting the increase in T_2 .

As the reaction proceeded, the newly formed peak gradually disappeared in both FcF3 and FcF6, whereas the parent peak was shifted and broadened compared to the reduced polymer (except for the initially broad spectrum of FcF3-C2, where the oxidation effect on the FWHM may be disregarded because

the peak is already broad) (Figure 4A). Two different phenomena may explain the displacement of this peak from the original ^{19}F chemical shift. On the one hand, both polymer micelles and “free” unimers are present but a fast chemical exchange now gives rise to an average signal. This explanation is also supported by DLS measurements, especially for FcF3 polymers. In FcF3-C1 and FcF3-C2, after their initial “oxidative” disintegration, the nanoparticles gradually reassociate, albeit considerably less so than in the starting polymers. On the other hand, ferrocenium compounds gradually decompose similarly to ferrocene. Ferrocenium reacts with common nucleophiles (e.g., water and chloride ions) and oxygen. These reactions partly regenerate ferrocene and form Fe^{II} and Fe^{III} ions together with other byproducts such as cyclopentadiene, cyclopenta-2,4-dien-1-one, and cyclopent-4-ene-1,3-dione, which can further react through Diels–Alder reactions, leading to complex mixtures of products.^{76,77,80} A small amount of regenerated ferrocene units on the polymer chain inevitably leads to fast ferrocenium–ferrocene electron self-exchange, as shown by NMR line broadening.^{75,76} The ^{19}F NMR signals did not change any further 60 min after oxidation and the blue color caused by ferrocenium had disappeared completely. To compare the relaxation times of the reduced and oxidized samples at the late stage of the reaction (>60 min), see Table 2.

T_1 relaxation times increased at the late stage of the reaction toward the initial values but exhibited a wider distribution (Figures S20–S24). In contrast to T_1 , the mean T_2 relaxation times were slightly higher at the late stage of oxidation than before oxidation (see Table 2). In some samples of oxidized polymers, T_1 determination was negatively affected by minor impurities, which, however, displayed long T_1 and very sharp peaks compared to the significantly broadened signal of the redox tracers.

The contrast in MR images is most often achieved by spatial variation of nuclear spin relaxation properties. In general, 3 quantities can be used: T_1 (spin-lattice relaxation time), T_2 (spin-echo decay time), and T_2^* (free induction decay time, FID, $T_2^* \leq T_2$). The short ^{19}F T_2 relaxation times of the FcF3/FcF6 polymers in aqueous medium render the most commonly used echo-based MRI pulse sequences impractical and require FID-based techniques (free induction decay). Hence, we employed the ultrashort echo time (UTE) MRI sequence in FID mode (see the SI, Section 5.3).^{92,93} The difference in chemical shift of the reduced and oxidized state is an excellent tool for probing the redox state of our tracers by ^{19}F magnetic resonance spectroscopy (MRS) and ^{19}F MRI. Yet, this property also presents a challenge because the chemical shift is used to encode spatial information in MRI. The first approach to resolve this issue was late-stage imaging of the oxidized sample because only a single ^{19}F NMR peak was present 60 min after sample oxidation. The second approach included selective excitation to exclusively visualize ^{19}F signal of the ferrocenium species.

MRI contrast between late-stage oxidized and reduced FcF3/FcF6 polymers within UTE can be achieved in at least two ways. One approach is to exploit the longer T_1 relaxation of the ^{19}F signal in the reduced sample to saturate this signal more than that of the oxidized sample. This technique was implemented by setting a short repetition time in conjunction with a 90° flip angle (henceforth referred to as “positive” contrast in the following text). The other approach is to use the difference in linewidth (FWHM = $1/\pi T_2^*$) and to

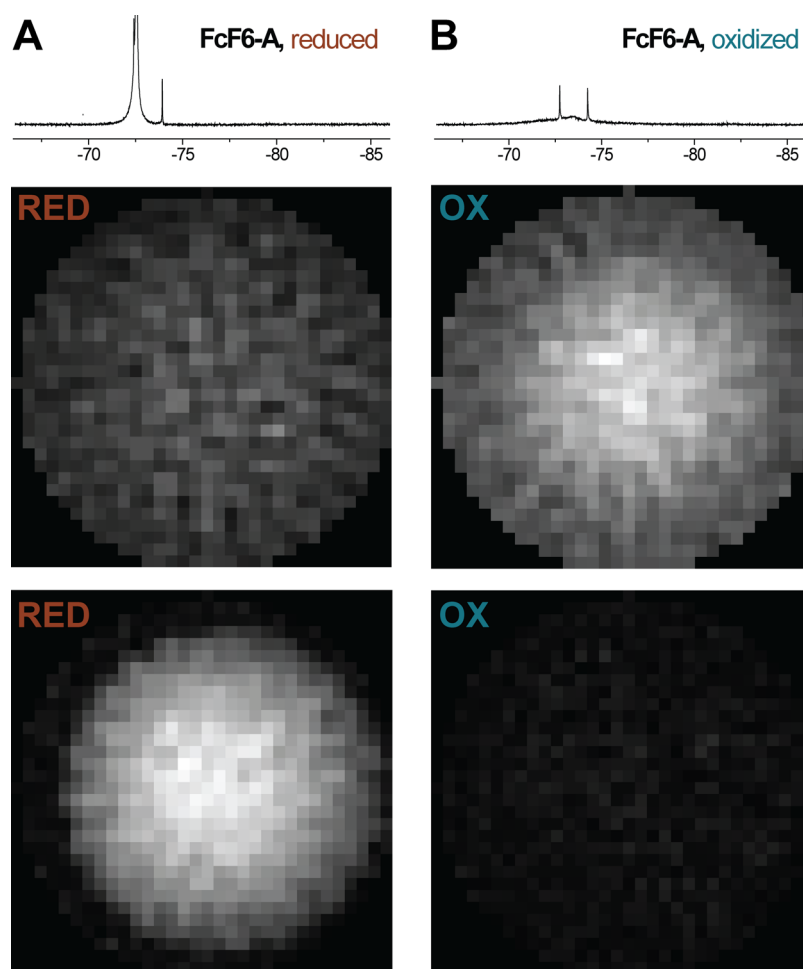


Figure 5. FcF6-A: ^{19}F NMR spectra and ^{19}F UTE images of a polymer sample ($18\text{ mg}\cdot\text{mL}^{-1}$) in citrate buffer (0.08 M , $\text{pH} = 6.2$) before (A) and after oxidation (B) with APS ($>60\text{ min}$). The UTE provides a circular field of view ($d = 5\text{ mm}$, the inscribed circles in the square images), and the tube position is slightly shifted with respect to the center (tube inner diameter $d = 4.2\text{ mm}$). A blurring of sample edges in panel (B) is due to the greater FWHM of the ^{19}F NMR signal. Top: UTE parameters set in favor of the oxidized sample with a shorter T_1 : $22\ \mu\text{s}$ acquisition delay; 10.5 ms repetition time; 90° flip angle. The brighter image is displayed in the full range of a 16-bit grayscale, whereas the darker image is rescaled according to its true intensity ratio. Bottom: UTE parameters set in favor of the reduced sample with a slower ^{19}F FID (a narrower spectral peak): $680\ \mu\text{s}$ acquisition delay; 11.2 ms repetition time; 12° flip angle.

attenuate the signal from the oxidized sample by setting a sufficient delay between the excitation pulse and acquisition while applying a small flip angle (henceforth referred to as “negative” contrast).

Figure 5 shows axial views of a 5 mm NMR tube filled with FcF6-A in aqueous medium before and after oxidation (late stage, $>60\text{ min}$). The top two images were acquired with the UTE parameters for positive MRI contrast based on T_1 relaxation enhancement upon oxidation. The bottom images show MR images of the same sample, albeit with negative MRI contrast, exploiting the difference in signal FWHM (note the respective ^{19}F NMR spectra shown above the images). In FcF6 polymers, the ^{19}F line broadening resulting from oxidation yielded a significantly better contrast than the T_1 relaxation enhancement ($6:1$ vs $1:2$). The UTE images of FcF6-B had similar contrasts (Figure S25, SI). FcF6-C (Figure S26, SI) exhibited a positive contrast albeit much weaker than the negative contrast of FcF6-A and FcF6-B.

FcF3-C1 and FcF3-C2 polymers (Figures S27 and S28, SI) offered good contrast when exploiting the T_1 relaxation enhancement ($>4:1$), but unlike FcF6-A and FcF6-B, showed no negative contrast related to differences in FWHM because

the ^{19}F signal of FcF3 polymers was already broad in the reduced state. The short T_2 relaxation of the diamagnetic reduced polymers results from the low mobility of the nanoparticle core and may be improved by altering the polymer composition or changing the structure of the fluorinated ferrocene moieties. For example, switching the trifluoromethyl substituents for difluoromethyl groups may significantly reduce the hydrophobicity^{94,95} and, therefore, increase mobility and make the tracers suitable for echo-based MRI pulse sequences when using a T_2 contrast scheme.

Of all our polymers, FcF6-A gave the highest contrast ^{19}F images. Figure 6A illustrates the negative contrast of this polymer within a single-image axial view of coaxial NMR tubes (the inner tube is filled with the reduced polymer and the outer tube with the oxidized polymer). Figure 6B shows ^1H MRI contrast caused by paramagnetic relaxation enhancement of ^1H water signal in a common gradient-echo experiment.

Furthermore, selective excitation may enable us to selectively detect ferrocenium species in FcF6-A or FcF6-B formed at an early stage of the oxidation process by exploiting the large ($\approx 10\text{ ppm}$) difference in ^{19}F chemical shift between ferrocene and ferrocenium. In fact, we briefly tested this option

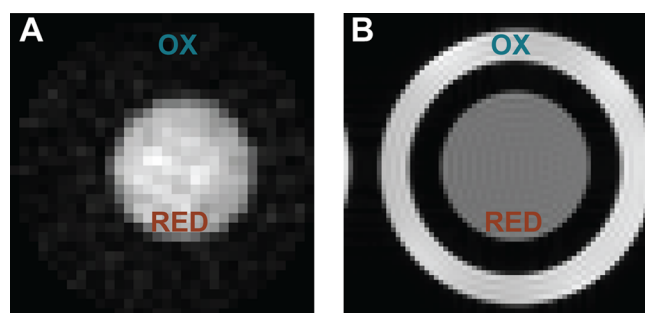


Figure 6. (A) ^{19}F UTE image of a composite sample of FcF6-A ($30\text{ mg}\cdot\text{mL}^{-1}$) in citrate buffer (0.08 M , $\text{pH} = 6.2$) comprising two coaxial NMR tubes; the inner tube is filled with the reduced polymer and the outer with the oxidized polymer. The UTE parameters are identical to those shown in Figure 5 favoring the reduced sample. (B) ^1H 64×64 FLASH image of the same sample, demonstrating paramagnetic relaxation enhancement of the ^1H water signal in the oxidized sample and outlining the geometry of the setup.

in two-dimensional (2D) UTE without performing any slice selection (Figure 7). When using selective excitation, the ^{19}F MRI signal derives solely from the “paramagnetic” ferrocenium species at -82 ppm . These selective pulses can be applied without any resolution restriction in the three-dimensional (3D) UTE pulse sequence as long as the whole imaging experiment can be performed within the lifetime of the paramagnetic molecular tracer.

The initial *in vitro* UTE experiments establish the link between MRI and redox-triggered FcF3/FcF6 changes necessary for their potential biomedical applications as hybrid drug-delivery/tracer materials. Based on these findings, suitable MRI methods may be thus further developed to fully exploit the properties of these new redox-responsive tracers. For example, the intermediate paramagnetic state with a significantly shorter T_1 may create a positive contrast by adding an

inversion recovery filter at the beginning of the UTE pulse sequence.

CONCLUSIONS

In summary, in this study, we describe the first synthesis of amphiphilic poly(2-oxazoline)s with fluorinated ferrocene moieties. We also report the straightforward and scalable synthesis of trifluoromethylated and bis(trifluoromethylated) ferrocenes with a pendant amino group to introduce these moieties into polymers through common peptide chemistry. The poly(2-oxazoline)s bearing fluorinated ferrocene moieties are amphiphilic and form nanoparticles with a hydrophobic core in an aqueous environment. Their ferrocene moieties are susceptible to oxidation by ROS, resulting in a partial or full hydrophilization of the hydrophobic block through the formation of charged ferrocenium cations. The redox properties of differently substituted low-molecular fluorinated ferrocenes are closely correlated with those of the corresponding polymers, as shown by cyclic voltammetry. Upon oxidation, the polymer nanoparticles disassemble and/or the morphology changes, as confirmed by DLS and cryo-TEM. In principle, this redox responsiveness may be employed for selective drug delivery and release into ROS-rich loci *in vivo* because our polymers were noncytotoxic *in vitro* for healthy cells and mildly cytotoxic only in PC3 cancer cells, indicating preferential polymer oxidation in ROS-rich cells. Based on our pilot ^{19}F MRI study with these materials and appropriate sequences, the described polymers *in vitro* can be selectively visualized in their reduced and oxidized states. In conclusion, our results lay the foundation for the development of ^{19}F MRI theranostic materials toward selectively imaging ROS-related processes and drug delivery *in vivo*.

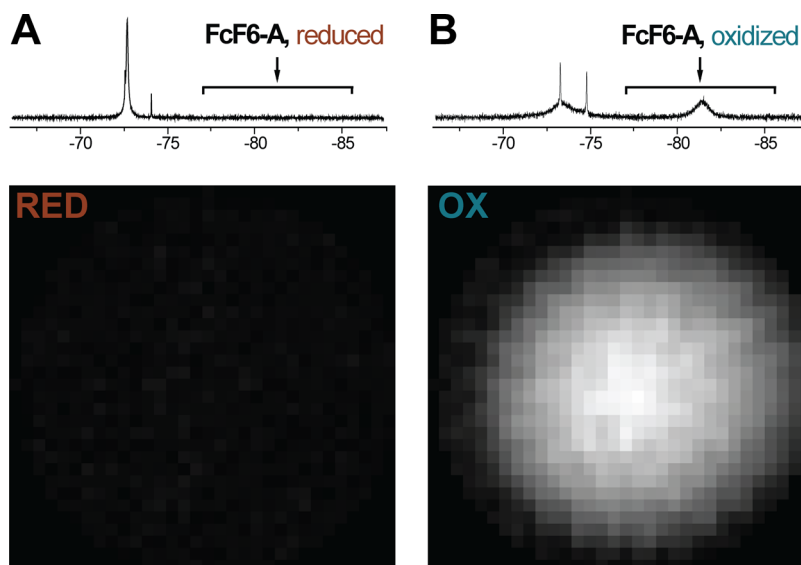


Figure 7. (A) ^{19}F UTE images of FcF6-A ($16\text{ mg}\cdot\text{mL}^{-1}$) in citrate buffer (0.08 M , $\text{pH} = 6.2$) before oxidation recorded with a frequency-selective pulse of a Gaussian shape. The carrier frequency of the pulse is indicated by the arrow and the excitation bandwidth by the brace in the spectra above the image. (B) ^{19}F UTE image of the sample shortly after oxidation with APS ($\approx 10\text{ min}$), recorded with the same pulse sequence parameters as in panel (A). The MRI signal derives solely from the paramagnetic ^{19}F signal at -82 ppm , which enables us to detect the onset of FcF6-A oxidation directly from the emergence of the new peak.

■ ASSOCIATED CONTENT

SI Supporting Information

The Supporting Information is available free of charge at <https://pubs.acs.org/doi/10.1021/acs.macromol.1c01723>.

Experimental procedures; copies of ^1H , ^{13}C , and ^{19}F NMR spectra; SEC traces; DLS data; cryo-TEM images; cytotoxicity results; DSC data; *in silico* results; and additional ^{19}F NMR/MRI data (PDF)

■ AUTHOR INFORMATION

Corresponding Authors

Pavel Švec – Institute of Macromolecular Chemistry, CAS, Prague 6 162 06, Czech Republic; Department of Physical and Macromolecular Chemistry, Faculty of Science, Charles University, Prague 2 128 43, Czech Republic; orcid.org/0000-0002-6604-2815; Email: prion2@seznam.cz

Martin Hrubý – Institute of Macromolecular Chemistry, CAS, Prague 6 162 06, Czech Republic; orcid.org/0000-0002-5075-261X; Email: mhruby@centrum.cz

Authors

Oleg V. Petrov – Department of Low Temperature Physics, Faculty of Mathematics and Physics, Charles University, Prague 8 180 00, Czech Republic; orcid.org/0000-0003-1728-6896

Jan Lang – Department of Low Temperature Physics, Faculty of Mathematics and Physics, Charles University, Prague 8 180 00, Czech Republic

Petr Štěpnička – Department of Inorganic Chemistry, Faculty of Science, Charles University, Prague 2 128 43, Czech Republic; orcid.org/0000-0002-5966-0578

Ondřej Groborz – Institute of Macromolecular Chemistry, CAS, Prague 6 162 06, Czech Republic; Institute of Organic Chemistry and Biochemistry, CAS, Prague 6 160 00, Czech Republic; Institute of Biophysics and Informatics, Charles University, Prague 2 120 00, Czech Republic; orcid.org/0000-0002-3164-6168

David Dunlop – Department of Inorganic Chemistry, Faculty of Science, Charles University, Prague 2 128 43, Czech Republic; Institute of Organic Chemistry and Biochemistry, CAS, Prague 6 160 00, Czech Republic; J. Heyrovský Institute of Physical Chemistry, CAS, Prague 8 182 23, Czech Republic

Jan Blahut – Department of NMR Spectroscopy, Faculty of Science, Charles University, Prague 2 128 43, Czech Republic

Kristýna Kolouchová – Institute of Macromolecular Chemistry, CAS, Prague 6 162 06, Czech Republic; orcid.org/0000-0002-8874-8632

Lenka Loukotová – Institute of Macromolecular Chemistry, CAS, Prague 6 162 06, Czech Republic; Institute of Organic Chemistry and Biochemistry, CAS, Prague 6 160 00, Czech Republic; orcid.org/0000-0002-8087-1425

Ondřej Sedláček – Department of Physical and Macromolecular Chemistry, Faculty of Science, Charles University, Prague 2 128 43, Czech Republic; Supramolecular Chemistry Group, Centre of Macromolecular Chemistry (CMaC), Department of Organic and Macromolecular Chemistry, Ghent University, Ghent B-9000, Belgium; orcid.org/0000-0001-5731-2687

Tomáš Heizer – Center for Advanced Preclinical Imaging, First Faculty of Medicine, Charles University, Prague 2 120 00, Czech Republic

Zdeněk Tošner – Department of NMR Spectroscopy, Faculty of Science, Charles University, Prague 2 128 43, Czech Republic

Miroslav Slouf – Institute of Macromolecular Chemistry, CAS, Prague 6 162 06, Czech Republic; orcid.org/0000-0003-1528-802X

Hynek Beneš – Institute of Macromolecular Chemistry, CAS, Prague 6 162 06, Czech Republic; orcid.org/0000-0002-6861-1997

Richard Hoogenboom – Supramolecular Chemistry Group, Centre of Macromolecular Chemistry (CMaC), Department of Organic and Macromolecular Chemistry, Ghent University, Ghent B-9000, Belgium; orcid.org/0000-0001-7398-2058

Complete contact information is available at:

<https://pubs.acs.org/doi/10.1021/acs.macromol.1c01723>

Author Contributions

P. Švec and K.K. conceived this research study; P. Švec designed and performed the synthesis of fluorinated ferrocene derivatives, prepared the final polymers, collected the DLS data, and wrote the manuscript; J.L. and O.V.P. designed and performed the NMR/MRI analysis of polymers and wrote the manuscript; P. Štěpnička measured and evaluated the CV; O.G. and L.L. measured NMR spectra, SEC-MALS, and helped with the synthesis; O.G. and D.D. performed the quantum chemical study; J.B. and Z.T. performed the initial evaluation of the ^{19}F NMR relaxation times; R.H. and O.S. proposed the starting poly(2-oxazoline)s; O.S. synthesized the starting poly(2-oxazoline)s; T.H. measured and evaluated the cytotoxicity; M.Š. acquired, measured, and evaluated cryo-TEM images; H.B. measured and evaluated the DSC; and M.H. proposed the introduction of ferrocene into fluorinated polymer tracers and supervised the project.

Notes

The authors declare the following competing financial interest(s): P. Švec is a former scientist in Avroxa BV, R.H. is one of the founders of Avroxa BV. Avroxa BV commercializes poly(2-oxazoline)s as Ultroxa. The other authors have no conflicts of interest to declare.

■ ACKNOWLEDGMENTS

This work was supported by the Charles University Grant Agency (Project Nos. 766119 and 379321), the Ministry of Education, Youth, and Sports of the Czech Republic (grant #LTC19032 and #LM2018133), the Czech Academy of Sciences [grant Strategy AV21 #VP06 (Diagnostic Methods and Techniques) and #RP10 (Molecules and Materials for Life)], Charles University (project UNCE/SCI/014), and the Czech Science Foundation (grant #19-01438S). The authors thank Dr. Carlos V. Melo for editing the manuscript.

■ ABBREVIATIONS

APS, ammonium persulfate; $\text{Bu}_4\text{N}[\text{PF}_6]$, tetrabutylammonium hexafluorophosphate; CBz, (benzyloxy)carbonyl; CROP, cationic ring-opening polymerization; cryo-TEM, cryogenic transmission electron microscopy; CV, cyclic voltammetry; D_{M} , dispersity (M_w/M_n); DCM, dichloromethane; DDS, drug delivery system; D_h , hydrodynamic diameter; DIPEA, *N,N*-diisopropylethylamine; DLS, dynamic light scattering; DMF, *N,N*-dimethylformamide; $\text{DMSO-}d_6$, deuterated dimethylsulfoxide; DP, degree of polymerization; Et_3N , triethylamine; Fc,

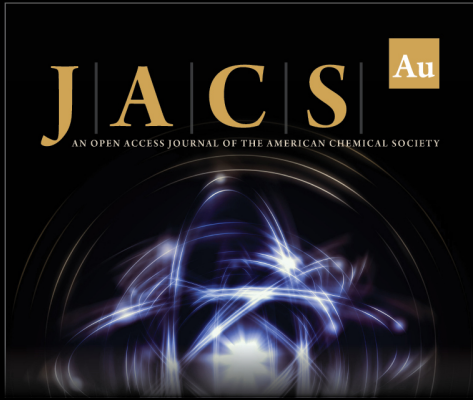
ferrocene; FLASH, fast low-angle shot; FID, free induction decay; DSC, differential scanning calorimetry; FWHM, full width at half-maximum; HIF-1 α , hypoxia-inducible factor 1- α ; *L*, chain contour length; LiHDMS, lithium bis(trimethylsilyl)-amide; MALS, multiangle light scattering; MeCN, acetonitrile; MeOH, methanol; MeOTs, methyl 4-methylbenzenesulfonate; MeOx, 2-methyl-2-oxazoline; MestOx, 2-(3-methoxy-3-oxopropyl)-2-oxazoline; MRI, magnetic resonance imaging; MRS, magnetic resonance spectroscopy; MTT, 3-(4,5-dimethylthiazol-2-yl)-2,5-diphenyltetrazolium bromide; MW, microwave assisted; M_n , number average molecular weight; M_w , weight average molecular weight; NHDF, normal human dermal fibroblast; PAOx, poly(2-alkyl-2-oxazoline); PC3, human prostate cancer; ppm, parts per million; PRE, paramagnetic relaxation enhancement; PyAOP, (7-azabenzotriazol-1-yloxy)-tripyrrolidinophosphonium hexafluorophosphate; PyBOP, (benzotriazol-1-yloxy)tripyrrolidinophosphonium hexafluorophosphate; ROS, reactive oxygen species; ru, repeating units; SEC, size-exclusion chromatography; *t*-BuLi, *tert*-butyllithium; *t*-BuOK, potassium *tert*-butoxide; THF, tetrahydrofuran; UTE, ultrashort echo time

REFERENCES

- (1) Wahsner, J.; Gale, E. M.; Rodríguez-Rodríguez, A.; Caravan, P. Chemistry of MRI Contrast Agents: Current Challenges and New Frontiers. *Chem. Rev.* **2019**, *119*, 957–1057.
- (2) Tirotta, I.; Dichiarante, V.; Pigliacelli, C.; Cavallo, G.; Terraneo, G.; Bombelli, F. B.; Metrangolo, P.; Resnati, G. ^{19}F Magnetic Resonance Imaging (MRI): From Design of Materials to Clinical Applications. *Chem. Rev.* **2015**, *115*, 1106–1129.
- (3) Keupp, J.; Rahmer, J.; Grässlin, I.; Mazurkewitz, P. C.; Schaeffter, T.; Lanza, G. M.; Wickline, S. A.; Caruthers, S. D. Simultaneous Dual-Nuclei Imaging for Motion Corrected Detection and Quantification of ^{19}F Imaging Agents. *Magn. Reson. Med.* **2011**, *66*, 1116–1122.
- (4) Ruiz-Cabello, J.; Barnett, B. P.; Bottomley, P. A.; Bulte, J. W. M. Fluorine (^{19}F) MRS and MRI in biomedicine. *NMR Biomed.* **2011**, *24*, 114–129.
- (5) Ahrens, E. T.; Bulte, J. W. M. Tracking Immune Cells In Vivo Using Magnetic Resonance Imaging. *Nat. Rev. Immunol.* **2013**, *13*, 755–763.
- (6) Blahut, J.; Bernásek, K.; Gáliková, A.; Herynek, V.; Císářová, I.; Kotek, J.; Lang, J.; Matějková, S.; Hermann, P. Paramagnetic ^{19}F Relaxation Enhancement in Nickel(II) Complexes of *N*-Trifluoroethyl Cyclam Derivatives and Cell Labeling for ^{19}F MRI. *Inorg. Chem.* **2017**, *56*, 13337–13348.
- (7) Srinivas, M.; Boehm-Sturm, P.; Figdor, C. G.; de Vries, I. J.; Hoehn, M. Labeling Cells for In Vivo Tracking Using ^{19}F MRI. *Biomaterials* **2012**, *33*, 8830–8840.
- (8) Ahrens, E. T.; Helfer, B. M.; O'Hanlon, C. F.; Schirda, C. Clinical Cell Therapy Imaging Using a Perfluorocarbon Tracer and Fluorine-19 MRI. *Magn. Reson. Med.* **2014**, *72*, 1696–1701.
- (9) Jacoby, C.; Temme, S.; Mayenfels, F.; Benoit, N.; Krafft, M. P.; Schubert, R.; Schrader, J.; Flögel, U. Probing different perfluorocarbons for in vivo inflammation imaging by ^{19}F MRI: image reconstruction, biological half-lives and sensitivity. *NMR Biomed.* **2014**, *27*, 261–271.
- (10) Ahrens, E. T.; Zhong, J. In Vivo MRI Cell Tracking Using Perfluorocarbon Probes and Fluorine-19 Detection. *NMR Biomed.* **2013**, *26*, 860–871.
- (11) Higuchi, M.; Iwata, N.; Matsuba, Y.; Sato, K.; Sasamoto, K.; Saido, T. C. ^{19}F and ^1H MRI Detection of Amyloid β Plaques In Vivo. *Nat. Neurosci.* **2005**, *8*, 527–533.
- (12) Amatsubo, T.; Morikawa, S.; Inubushi, T.; Urushitani, M.; Taguchi, H.; Shirai, N.; Hirao, K.; Kato, M.; Morino, K.; Kimura, H.; Nakano, I.; Yoshida, C.; Okada, T.; Sano, M.; Tooyama, I. Trifluoromethoxy-Benzylated Ligands Improve Amyloid Detection in the Brain Using ^{19}F Magnetic Resonance Imaging. *Neurosci. Res.* **2009**, *63*, 76–81.
- (13) Yanagisawa, D.; Amatsubo, T.; Morikawa, S.; Taguchi, H.; Urushitani, M.; Shirai, N.; Hirao, K.; Shiino, A.; Inubushi, T.; Tooyama, I. In Vivo Detection of Amyloid β Deposition Using ^{19}F Magnetic Resonance Imaging With a ^{19}F -Containing Curcumin Derivative in a Mouse Model of Alzheimer's Disease. *Neuroscience* **2011**, *184*, 120–127.
- (14) Taylor, N. G.; Chung, S. H.; Kwansa, A. L.; Johnson, R. R., III; Teator, A. J.; Milliken, N. J. B.; Koshlap, K. M.; Yingling, Y. G.; Lee, Y. Z.; Leibfarth, F. A. Partially Fluorinated Copolymers as Oxygen Sensitive ^{19}F MRI Agents. *Chem. - Eur. J.* **2020**, *26*, 9982–9990.
- (15) Diepart, C.; Magat, J.; Jordan, B. F.; Gallez, B. In Vivo Mapping of Tumor Oxygen Consumption Using ^{19}F MRI Relaxometry. *NMR Biomed.* **2011**, *24*, 458–463.
- (16) Zhao, D.; Jiang, L.; Hahn, E. W.; Mason, R. P. Comparison of ^1H Blood Oxygen Level-Dependent (BOLD) and ^{19}F MRI to Investigate Tumor Oxygenation. *Magn. Reson. Med.* **2009**, *62*, 357–364.
- (17) Fu, C.; Tang, J.; Pye, A.; Liu, T.; Zhang, C.; Tan, X.; Han, F.; Peng, H.; Whittaker, A. K. Fluorinated Glycopolymers as Reduction-Responsive ^{19}F MRI Agents for Targeted Imaging of Cancer. *Biomacromolecules* **2019**, *20*, 2043–2050.
- (18) Fuchs, A. V.; Bapat, A. P.; Cowin, G. J.; Thurecht, K. J. Switchable ^{19}F MRI Polymer Theranostics: Towards In Situ Quantifiable Drug Release. *Polym. Chem.* **2017**, *8*, 5157–5166.
- (19) Jiráček, D.; Gáliková, A.; Kolouchová, K.; Babuka, D.; Hrubý, M. Fluorine Polymer Probes for Magnetic Resonance Imaging: Quo Vadis? *Magn. Reson. Mater. Phys., Biol. Med.* **2019**, *32*, 173–185.
- (20) Fu, C.; Zhang, C.; Peng, H.; Han, F.; Baker, C.; Wu, Y.; Ta, H.; Whittaker, A. K. Enhanced Performance of Polymeric ^{19}F MRI Contrast Agents Through Incorporation of Highly Water-Soluble Monomer MSEA. *Macromolecules* **2018**, *51*, 5875–5882.
- (21) Fu, C.; Yu, Y.; Xu, X.; Wang, Q.; Chang, Y.; Zhang, C.; Zhao, J.; Peng, H.; Whittaker, A. K. Functional Polymers As Metal-Free Magnetic Resonance Imaging Contrast Agents. *Prog. Polym. Sci.* **2020**, *108*, No. 101286.
- (22) Bak, J. M.; Kim, K.-B.; Lee, J.-E.; Park, Y.; Yoon, S. S.; Jeong, H. M.; Lee, H.-i. Thermoresponsive Fluorinated Polyacrylamides with Low Cytotoxicity. *Polym. Chem.* **2013**, *4*, 2219–2223.
- (23) Sedláček, O.; Jiráček, D.; Gáliková, A.; Jäger, E.; Laaser, J. E.; Lodge, T. P.; Štěpánek, P.; Hrubý, M. ^{19}F Magnetic Resonance Imaging of Injectable Polymeric Implants with Multiresponsive Behavior. *Chem. Mater.* **2018**, *30*, 4892–4896.
- (24) Kolouchová, K.; Sedláček, O.; Jiráček, D.; Babuka, D.; Blahut, J.; Kotek, J.; Vít, M.; Trousil, J.; Konefal, R.; Janoušková, O.; Podhorská, B.; Šlouf, M.; Hrubý, M. Self-Assembled Thermoresponsive Polymeric Nanogels for ^{19}F MR Imaging. *Biomacromolecules* **2018**, *19*, 3515–3524.
- (25) Kolouchová, K.; Jiráček, D.; Groborz, O.; Sedláček, O.; Ziolkowska, N.; Vít, M.; Šticová, E.; Gáliková, A.; Svec, P.; Trousil, J.; Hájek, M.; Hrubý, M. Implant-Forming Polymeric ^{19}F MRI-Tracer with Tunable Dissolution. *J. Controlled Release* **2020**, *327*, 50–60.
- (26) Babuka, D.; Kolouchová, K.; Groborz, O.; Tošner, Z.; Zhigunov, A.; Štěpánek, P.; Hrubý, M. Internal Structure of Thermoresponsive Physically Crosslinked Nanogel of Poly[N-(2-hydroxypropyl)methacrylamide]-Block-Poly[N-(2,2-difluoroethyl)acrylamide], Prominent ^{19}F MRI Tracer. *Nanomaterials* **2020**, *10*, No. 2231.
- (27) Babuka, D.; Kolouchová, K.; Hrubý, M.; Groborz, O.; Tošner, Z.; Zhigunov, A.; Štěpánek, P. Investigation of the Internal Structure of Thermoresponsive Diblock Poly(2-methyl-2-oxazoline)-b-poly[N-(2,2-difluoroethyl)acrylamide] Copolymer Nanoparticles. *Eur. Polym. J.* **2019**, *121*, No. 109306.
- (28) Verbraeken, B.; Monnery, B. D.; Lava, K.; Hoogenboom, R. The Chemistry of Poly(2-oxazoline)s. In *Encyclopedia of Polymer Science and Technology*; John Wiley & Sons, Inc., 2002; pp 1–59.

- (29) Zahoranová, A.; Luxenhofer, R. Poly(2-oxazoline)- and Poly(2-oxazine)-Based Self-Assemblies, Polyplexes, and Drug Nanoformulations—An Update. *Adv. Healthcare Mat.* **2021**, *10*, No. 2001382.
- (30) Sedláček, O.; Hoogenboom, R. Drug Delivery Systems Based on Poly(2-Oxazoline)s and Poly(2-Oxazine)s. *Adv. Ther.* **2020**, *3*, No. 1900168.
- (31) de la Rosa, V. R. Poly(2-oxazoline)s As Materials for Biomedical Applications. *J. Mater. Sci. Mater. Med.* **2014**, *25*, 1211–1225.
- (32) Lorson, T.; Lübtow, M. M.; Wegener, E.; Haider, M. S.; Borova, S.; Nahm, D.; Jordan, R.; Sokolski-Papkov, M.; Kabanov, A. V.; Luxenhofer, R. Poly(2-oxazoline)s Based Biomaterials: A Comprehensive and Critical Update. *Biomaterials* **2018**, *178*, 204–280.
- (33) Sedláček, O.; Monnery, B. D.; Filippov, S. K.; Hoogenboom, R.; Hrubý, M. Poly(2-Oxazoline)s—Are They More Advantageous for Biomedical Applications Than Other Polymers? *Macromol. Rapid Commun.* **2012**, *33*, 1648–1662.
- (34) Luxenhofer, R.; Han, Y.; Schulz, A.; Tong, J.; He, Z.; Kabanov, A. V.; Jordan, R. Poly(2-oxazoline)s as Polymer Therapeutics. *Macromol. Rapid Commun.* **2012**, *33*, 1613–1631.
- (35) Sedláček, O.; Jiráček, D.; Vít, M.; Ziolkowska, N.; Janoušková, O.; Hoogenboom, R. Fluorinated Water-Soluble Poly(2-oxazoline)s as Highly Sensitive ¹⁹F MRI Contrast Agents. *Macromolecules* **2020**, *53*, 6387–6395.
- (36) Winterbourn, C. C. Reconciling the Chemistry and Biology of Reactive Oxygen Species. *Nat. Chem. Biol.* **2008**, *4*, 278–286.
- (37) Chio, I. I. C.; Tuveson, D. A. ROS in Cancer: The Burning Question. *Trends Mol. Med.* **2017**, *23*, 411–429.
- (38) Radi, R. Oxygen Radicals, Nitric Oxide, and Peroxynitrite: Redox Pathways in Molecular Medicine. *Proc. Natl. Acad. Sci. U.S.A.* **2018**, *115*, 5839–5848.
- (39) Brunelle, J. K.; Bell, E. L.; Quesada, N. M.; Vercauteren, K.; Tiranti, V.; Zeviani, M.; Scarpulla, R. C.; Chandel, N. S. Oxygen Sensing Requires Mitochondrial ROS But Not Oxidative Phosphorylation. *Cell Metab.* **2005**, *1*, 409–414.
- (40) Guzy, R. D.; Hoyos, B.; Robin, E.; Chen, H.; Liu, L.; Mansfield, K. D.; Simon, M. C.; Hammerling, U.; Schumacker, P. T. Mitochondrial Complex III is Required for Hypoxia-Induced ROS Production and Cellular Oxygen Sensing. *Cell Metab.* **2005**, *1*, 401–408.
- (41) Mansfield, K. D.; Guzy, R. D.; Pan, Y.; Young, R. M.; Cash, T. P.; Schumacker, P. T.; Simon, M. C. Mitochondrial Dysfunction Resulting from Loss of Cytochrome C Impairs Cellular Oxygen Sensing and Hypoxic HIF- α Activation. *Cell Metab.* **2005**, *1*, 393–399.
- (42) Ryan, H. E.; Lo, J.; Johnson, R. S. HIF-1 α is Required for Solid Tumor Formation and Embryonic Vascularization. *EMBO J.* **1998**, *17*, 3005–3015.
- (43) Akong-Moore, K.; Chow, O. A.; von Köckritz-Blickwede, M.; Nizet, V. Influences of Chloride and Hypochlorite on Neutrophil Extracellular Trap Formation. *PLoS One* **2012**, *7*, No. e42984.
- (44) Manda-Handzlik, A.; Bystrzycka, W.; Cieloch, A.; Glodkowska-Mrowka, E.; Jankowska-Steifer, E.; Heropolitanska-Pliszka, E.; Skrobot, A.; Muchowicz, A.; Ciepiela, O.; Wachowska, M.; Demkow, U. Nitric Oxide and Peroxynitrite Trigger and Enhance Release of Neutrophil Extracellular Traps. *Cell. Mol. Life Sci.* **2020**, *77*, 3059–3075.
- (45) Pinto, S. M.; Tomé, V.; Calvete, M. J. F.; Castro, M. M. C. A.; Tóth, É.; Geraldes, C. F. G. C. Metal-Based Redox-Responsive MRI Contrast Agents. *Coord. Chem. Rev.* **2019**, *390*, 1–31.
- (46) Li, A.; Tang, X.; Gong, X.; Chen, H.; Lin, H.; Gao, J. A Fluorinated bihydrazide Conjugate for Activatable Sensing and Imaging of Hypochlorous Acid by ¹⁹F NMR/MRI. *Chem. Commun.* **2019**, *55*, 12455–12458.
- (47) Yu, M.; Xie, D.; Phan, K. P.; Enriquez, J. S.; Luci, J. J.; Que, E. L. A CoII Complex for ¹⁹F MRI-Based Detection of Reactive Oxygen Species. *Chem. Commun.* **2016**, *52*, 13885–13888.
- (48) Fu, C.; Herbst, S.; Zhang, C.; Whittaker, A. K. Polymeric ¹⁹F MRI Agents Responsive to Reactive Oxygen Species. *Polym. Chem.* **2017**, *8*, 4585–4595.
- (49) Tanaka, K.; Kitamura, N.; Takahashi, Y.; Chujo, Y. Reversible signal regulation system of ¹⁹F NMR by redox reactions using a metal complex as a switching module. *Biorg. Med. Chem.* **2009**, *17*, 3818–3823.
- (50) Abbott, N. L.; Whitesides, G. M. Potential-Dependent Wetting of Aqueous Solutions on Self-Assembled Monolayers Formed from 15-(Ferrocenylcarbonyl)pentadecanethiol on Gold. *Langmuir* **1994**, *10*, 1493–1497.
- (51) Elbert, J.; Gallei, M.; Rüttiger, C.; Brunsen, A.; Didzoleit, H.; Stühn, B.; Rehahn, M. Ferrocene Polymers for Switchable Surface Wettability. *Organometallics* **2013**, *32*, 5873–5878.
- (52) Rüttiger, C.; Mehlhase, S.; Vowinkel, S.; Cherkashin, G.; Liu, N.; Dietz, C.; Stark, R. W.; Biesalski, M.; Gallei, M. Redox-mediated flux control in functional paper. *Polymer* **2016**, *98*, 429–436.
- (53) Gu, H.; Mu, S.; Qiu, G.; Liu, X.; Zhang, L.; Yuan, Y.; Astruc, D. Redox-Stimuli-Responsive Drug Delivery Systems with Supramolecular Ferrocenyl-Containing Polymers for Controlled Release. *Coord. Chem. Rev.* **2018**, *364*, 51–85.
- (54) Borchers, P. S.; Dirauf, M.; Strumpf, M.; Görls, H.; Weber, C.; Hager, M. D.; Schubert, U. S. Ferrocene Containing Redox-Responsive Poly(2-oxazoline)s. *Chem. Commun.* **2021**, *57*, 1308–1311.
- (55) Kolouchová, K.; Groborz, O.; Černochová, Z.; Škárková, A.; Brábek, J.; Rösel, D.; Švec, P.; Starčuk, Z.; Šlouf, M.; Hrubý, M. Thermo- and ROS-Responsive Self-Assembled Polymer Nanoparticle Tracers for ¹⁹F MRI Theranostics. *Biomacromolecules* **2021**, *22*, 2325–2337.
- (56) Huque, F. T. T.; Jones, K.; Saunders, R. A.; Platts, J. A. Statistical and Theoretical Studies of Fluorophilicity. *J. Fluorine Chem.* **2002**, *115*, 119–128.
- (57) Maschke, M.; Alborzina, H.; Lieb, M.; Wöfl, S.; Metzler-Nolte, N. Structure–Activity Relationship of Trifluoromethyl-Containing Metallocenes: Electrochemistry, Lipophilicity, Cytotoxicity, and ROS Production. *ChemMedChem* **2014**, *9*, 1188–1194.
- (58) Filler, R.; Schure, R. M. Highly Acidic Perhalogenated Alcohols. A New Synthesis of Perfluoro-tert-butyl Alcohol. *J. Org. Chem.* **1967**, *32*, 1217–1219.
- (59) Chang, I. S.; Price, J. T.; Tomlinson, A. J.; Willis, C. J. Studies on Fluorinated Vinylic and Aromatic Alcohols and Esters. *Can. J. Chem.* **1972**, *50*, 512–520.
- (60) Vuluga, D.; Legros, J.; Crousse, B.; Slawin, A. M. Z.; Laurence, C.; Nicolet, P.; Bonnet-Delpon, D. Influence of the Structure of Polyfluorinated Alcohols on Bronsted Acidity/Hydrogen-Bond Donor Ability and Consequences on the Promoter Effect. *J. Org. Chem.* **2011**, *76*, 1126–1133.
- (61) Sobociková, M.; Štěpnička, P.; Ramella, D.; Kotora, M. Synthesis of 1-Alkanoyl-1'-(trifluoroacetyl)ferrocenes. *Collect. Czech. Chem. Commun.* **2006**, *71*, 190–196.
- (62) Sanders, R.; Mueller-Westerhoff, U. T. The Lithiation of Ferrocene and Ruthenocene: a Retraction and an Improvement. *J. Organomet. Chem.* **1996**, *512*, 219–224.
- (63) Gosselin, F.; O'Shea, P. D.; Roy, S.; Reamer, R. A.; Chen, C.-y.; Volante, R. P. Unprecedented Catalytic Asymmetric Reduction of N–H Imines. *Org. Lett.* **2005**, *7*, 355–358.
- (64) Bouten, P. J. M.; Hertsen, D.; Vergaalen, M.; Monnery, B. D.; Boerman, M. A.; Goossens, H.; Catak, S.; van Hest, J. C. M.; Van Speybroeck, V.; Hoogenboom, R. Accelerated Living Cationic Ring-Opening Polymerization of a Methyl Ester Functionalized 2-Oxazoline Monomer. *Polym. Chem.* **2015**, *6*, 514–518.
- (65) Filippov, S. K.; Verbraeken, B.; Konarev, P. V.; Svergun, D. I.; Angelov, B.; Vishnevetskaya, N. S.; Papadakis, C. M.; Rogers, S.; Radulescu, A.; Courtin, T.; Martins, J. C.; Starovoytova, L.; Hrubý, M.; Štěpánek, P.; Kravchenko, V. S.; Potemkin, I. I.; Hoogenboom, R. Block and Gradient Copoly(2-oxazoline) Micelles: Strikingly Different on the Inside. *J. Phys. Chem. Lett.* **2017**, *8*, 3800–3804.

- (66) Loukotová, L.; Švec, P.; Groborz, O.; Heizer, T.; Beněš, H.; Raabová, H.; Bělinová, T.; Herynek, V.; Hrubý, M. Direct Comparison of Analogous Amphiphilic Gradient and Block Polyoxazolines. *Macromolecules* **2021**, *54*, 8182–8194.
- (67) Golovin, M. N.; Wilkinson, D. P.; Dudley, J. T.; Holonko, D.; Woo, S. Applications of Metallocenes in Rechargeable Lithium Batteries for Overcharge Protection. *J. Electrochem. Soc.* **1992**, *139*, 5–10.
- (68) Gubin, S. P.; Pendin, A. A.; Balusov, V. A.; Solomatina, V. T. Constancy of the Redox Potential of a Ferrocene-Ferricenium System in Mixed Solvents. *Dokl. Akad. Nauk SSSR* **1979**, *248*, 385–388.
- (69) Steckhan, E. *Organic Electrochemistry*, 4th ed.; Lund, H.; Hammerich, O.; Speiser, B., Eds.; Dekker: New York, 2001; pp 545–588.
- (70) Neese, F. The ORCA Program System. *Wiley Interdiscip. Rev.: Comput. Mol. Sci.* **2012**, *2*, 73–78.
- (71) Neese, F. Software Update: the ORCA Program System, version 4.0. *Wiley Interdiscip. Rev.: Comput. Mol. Sci.* **2018**, *8*, No. e1327.
- (72) Riplinger, C.; Neese, F. An Efficient and Near Linear Scaling Pair Natural Orbital Based Local Coupled Cluster Method. *J. Chem. Phys.* **2013**, *138*, No. 034106.
- (73) Riplinger, C.; Sandhoefer, B.; Hansen, A.; Neese, F. Natural Triple Excitations in Local Coupled Cluster Calculations with Pair Natural Orbitals. *J. Chem. Phys.* **2013**, *139*, No. 134101.
- (74) Isegawa, M.; Neese, F.; Pantazis, D. A. Ionization Energies and Aqueous Redox Potentials of Organic Molecules: Comparison of DFT, Correlated Ab Initio Theory and Pair Natural Orbital Approaches. *J. Chem. Theory Comput.* **2016**, *12*, 2272–2284.
- (75) Lubach, J.; Drenth, W. Enolization and Oxidation: II. Oxidation of Ferrocene by Molecular Oxygen and Hydrogen Peroxide in Acidic Media. *Recl. Trav. Chim. Pays-Bas* **1973**, *92*, 586–592.
- (76) Zotti, G.; Schiavon, G.; Zecchin, S.; Favretto, D. Dioxygen-Decomposition of Ferrocenium Molecules in Acetonitrile: The Nature of the Electrode-Fouling Films During Ferrocene Electrochemistry. *J. Electroanal. Chem.* **1998**, *456*, 217–221.
- (77) Tabbi, G.; Cassino, C.; Cavigliolo, G.; Colangelo, D.; Ghiglia, A.; Viano, I.; Osella, D. Water Stability and Cytotoxic Activity Relationship of a Series of Ferrocenium Derivatives. ESR Insights on the Radical Production during the Degradation Process. *J. Med. Chem.* **2002**, *45*, 5786–5796.
- (78) Zhang, J.; Ren, L.; Hardy, C. G.; Tang, C. Cobaltocenium-Containing Methacrylate Homopolymers, Block Copolymers, and Heterobimetallic Polymers via RAFT Polymerization. *Macromolecules* **2012**, *45*, 6857–6863.
- (79) Hurvois, J. P.; Moinet, C. Reactivity of Ferrocenium Cations with Molecular Oxygen in Polar Organic Solvents: Decomposition, Redox Reactions and Stabilization. *J. Organomet. Chem.* **2005**, *690*, 1829–1839.
- (80) Prins, R.; Korswagen, A. R.; Kortbeek, A. G. T. G. Decomposition of the Ferricenium Cation by Nucleophilic Reagents. *J. Organomet. Chem.* **1972**, *39*, 335–344.
- (81) Chen, W.-Y.; Alexandridis, P.; Su, C.-K.; Patrickios, C. S.; Hertler, W. R.; Hatton, T. A. Effect of Block Size and Sequence on the Micellization of ABC Triblock Methacrylic Polyampholytes. *Macromolecules* **1995**, *28*, 8604–8611.
- (82) Cheng, Y.; Grigorieff, N.; Penczek, P. A.; Walz, T. A Primer to Single-Particle Cryo-Electron Microscopy. *Cell* **2015**, *161*, 438–449.
- (83) Franken, L. E.; Boekema, E. J.; Stuart, M. C. A. Transmission Electron Microscopy as a Tool for the Characterization of Soft Materials: Application and Interpretation. *Adv. Sci.* **2017**, *4*, No. 1600476.
- (84) Bao, D.; Millare, B.; Xia, W.; Steyer, B. G.; Gerasimenko, A. A.; Ferreira, A.; Contreras, A.; Vullev, V. I. Electrochemical Oxidation of Ferrocene: A Strong Dependence on the Concentration of the Supporting Electrolyte for Nonpolar Solvents. *J. Phys. Chem. A* **2009**, *113*, 1259–1267.
- (85) Kumar, B.; Koul, S.; Khandrika, L.; Meacham, R. B.; Koul, H. K. Oxidative Stress Is Inherent in Prostate Cancer Cells and Is Required for Aggressive Phenotype. *Cancer Res.* **2008**, *68*, 1777–1785.
- (86) Gasser, G.; Ott, I.; Metzler-Nolte, N. Organometallic Anticancer Compounds. *J. Med. Chem.* **2011**, *54*, 3–25.
- (87) Neuse, E. W. Macromolecular Ferrocene Compounds as Cancer Drug Models. *J. Inorg. Organomet. Polym. Mater.* **2005**, *15*, 3–31.
- (88) Salmain, M.; Metzler-Nolte, N. Bioorganometallic Chemistry of Ferrocene. In *Ferrocenes*; Štěpnička, P., Ed.; John Wiley & Sons: Chichester, U.K., 2008; pp 499–639.
- (89) Morrison, C. A.; Bone, S. F.; Rankin, D. W. H.; Robertson, H. E.; Parsons, S.; Coxall, R. A.; Fraser, S.; Howell, J. A. S.; Yates, P. C.; Fey, N. Conformational Properties of Substituted Ferrocenes: Experimental and Theoretical Studies of the Molecular Structures of 1,1'-Di-tert-butylferrocene and Isopropylferrocene. *Organometallics* **2001**, *20*, 2309–2320.
- (90) Pell, A. J.; Pintacuda, G.; Grey, C. P. Paramagnetic NMR in Solution and the Solid State. *Prog. Nucl. Magn. Reson. Spectrosc.* **2019**, *111*, 1–271.
- (91) Blahut, J.; Benda, L.; Kotek, J.; Pintacuda, G.; Hermann, P. Paramagnetic Cobalt(II) Complexes with Cyclam Derivatives: Toward ¹⁹F MRI Contrast Agents. *Inorg. Chem.* **2020**, *59*, 10071–10082.
- (92) Bergin, C. J.; Pauly, J. M.; Macovski, A. Lung Parenchyma: Projection Reconstruction MR Imaging. *Radiology* **1991**, *179*, 777–781.
- (93) Robson, M. D.; Gatehouse, P. D.; Bydder, M.; Bydder, G. M. Magnetic Resonance: An Introduction to Ultrashort TE (UTE) Imaging. *J. Comput. Assisted Tomogr.* **2003**, *27*, 825–846.
- (94) Xing, L.; Blakemore, D. C.; Narayanan, A.; Unwalla, R.; Lovering, F.; Denny, R. A.; Zhou, H.; Bunnage, M. E. Fluorine in Drug Design: A Case Study with Fluoroanisoles. *ChemMedChem* **2015**, *10*, 715–726.
- (95) Zafrani, Y.; Yeffet, D.; Sod-Moriah, G.; Berliner, A.; Amir, D.; Marciano, D.; Gershonov, E.; Saphier, S. Difluoromethyl Bioisostere: Examining the “Lipophilic Hydrogen Bond Donor” Concept. *J. Med. Chem.* **2017**, *60*, 797–804.



JACS Au
AN OPEN ACCESS JOURNAL OF THE AMERICAN CHEMICAL SOCIETY

Editor-in-Chief
Prof. Christopher W. Jones
Georgia Institute of Technology, USA

Open for Submissions

pubs.acs.org/jacsau ACS Publications
Most Trusted. Most Cited. Most Read.

Supporting Information for:

**Fluorinated Ferrocene Moieties as a Platform for Redox-Responsive
Polymer ¹⁹F MRI Theranostics**

Pavel Švec^{a,b,}, Oleg V. Petrov^e, Jan Lang^e, Petr Štěpnička^c, Ondřej Groborz^{a,f,g}, David Dunlop^{c,f,i}, Jan Blahut^d, Kristýna Kolouchová^a, Lenka Loukotová^{a,f}, Ondřej Sedláček^{b,j}, Tomáš Heizer^h, Zdeněk Tošner^d, Miroslav Šlouf^a, Hynek Beneš^a, Richard Hoogenboom^j, and Martin Hrubý^{a,*}*

^a Institute of Macromolecular Chemistry, CAS, Heyrovského nám. 2, Prague 6, 162 06, Czech Republic

^b Department of Physical and Macromolecular Chemistry; ^c Department of Inorganic Chemistry; ^d Department of NMR Spectroscopy;

Faculty of Science, Charles University, Hlavova 8, Prague 2, 128 43, Czech Republic

^e Department of Low Temperature Physics, Faculty of Mathematics and Physics, Charles University, V Holešovičkách 2, Prague 8, 180 00, Czech Republic

^f Institute of Organic Chemistry and Biochemistry, CAS, Flemingovo nám. 2, Prague 6, 160 00, Czech Republic

^g Institute of Biophysics and Informatics; ^h Center for Advanced Preclinical Imaging, First Faculty of Medicine, Charles University, Salmovská 3, Prague 2, 120 00, Czech Republic

ⁱ J. Heyrovský Institute of Physical Chemistry, CAS, Dolejškova 2155/3, 182 23 Prague 8, Czech Republic

^j Supramolecular Chemistry Group, Centre of Macromolecular Chemistry (CMaC), Department of Organic and Macromolecular Chemistry, Ghent University, Krijgslaan 281-S4, Ghent, B-9000, Belgium

*Corresponding authors, e-mail: prion2@seznam.cz, mhruby@centrum.cz

Table of contents

1	Materials and Methods	3
1.1	Materials	3
1.2	Methods	3
2	Synthesis	6
2.1	Synthesis of fluorinated ferrocene derivatives	6
2.2	Synthesis of polymers	10
3	Dynamic light scattering and cryoTEM	18
4	Size-exclusion chromatography	22
5	¹⁹ F relaxation times and MRI	29
5.1	¹⁹ F relaxation times	29
5.2	¹⁹ F UTE MRI images	32
5.3	UTE imaging technique	36
6	Cytotoxicity	37
7	Quantum chemical study	38
7.1	Method	38
7.2	Results: Electrochemical properties	39
7.3	Results: Optimized geometries in dichloromethane	40
8	Differential scanning calorimetry	50
9	¹ H, ¹³ C, and ¹⁹ F NMR spectra	52
10	References	69

1 Materials and Methods

1.1 Materials

All solvents were purchased from Lach-Ner s.r.o. (Neratovice, Czech Republic) and of analytical grade. Hexafluoroacetone trihydrate and trifluoroacetic anhydride were purchased from Fluorochem Ltd. (Hadfield, United Kingdom). Deuterated solvents were purchased from Eurisotop (Saint-Aubin, France). 2-Methyl-2-oxazoline (MeOx) was purchased from Acros Organics and distilled from barium oxide before use. Methyl *p*-toluenesulfonate (MeOTs) was purchased from Sigma-Aldrich and distilled from calcium hydride before use. Acetonitrile (Sigma-Aldrich) was purified over aluminum oxide using a solvent purification system from J.C. Meyer. Dry tetrahydrofuran and all other chemicals were purchased from Sigma-Aldrich (Prague, Czech Republic) and used as received. 2-(3-Methoxy-3-oxopropyl)-2-oxazoline (MestOx) was synthesized according to a previously reported procedure.¹ Water was deionized with a Millipore Milli-Q water purification system.

1.2 Methods

The reactions were monitored by thin-layer chromatography (TLC) unless stated otherwise. Flash chromatography was performed using Puriflash XS 420 (Interchim, France) system and spherical silica gel (40-75 μm). Polymers were purified by size exclusion chromatography using an F0080 column cartridge (Interchim, France) packed with Sephadex LH-20 (Cytiva Sweden AB, Uppsala, Sweden) and a flow rate 10 mL \cdot min⁻¹. TLC plates (silica gel 60 F254 or silica gel-RP18 60 F254) were visualized under UV and/or with KMnO₄/Na₂CO₃.

Polymer synthesis

All polymerization stock solutions were prepared in a VIGOR Sci-Lab SG 1200/750 glovebox system with a water concentration \leq 0.1 ppm. For the polymerizations, a Biotage Initiator EXP microwave system with Robot Sixty was used. CROP conversion was monitored by Gas chromatography (GC) on an Agilent 7890A system equipped with a VWR Carrier-160 hydrogen generator and an Agilent HP-5 column 30 m in length and 0.32 mm in diameter. A flame ionization detector (FID) was used, and the inlet was set to 240 °C, with a split injection ratio of 25:1. Hydrogen was used as carrier gas at a flow rate of 2 mL \cdot min⁻¹.

¹H, ¹³C NMR, and ¹⁹F NMR

NMR spectra were recorded at 298 K using Bruker Avance III 400 (¹H 400.13 MHz, ¹³C 100.62 MHz, ¹⁹F 376.46 MHz) spectrometer. The chemical shifts (δ /ppm) of the small-molecule compounds in ¹⁹F NMR are reported and referenced to an internal standard of 2,2,2-trifluoroethanol (1.0 μL TFE in 0.5 mL of the corresponding deuterated solvent; ¹⁹F NMR signal of TFE was set to -77.0 ppm).

Size-exclusion chromatography

The molecular weights of polymers were determined by size-exclusion chromatography (SEC) using an HPLC Ultimate 3000 system (Dionex, USA) equipped with a SEC column (TSKgel SuperAW3000 150 × 6 mm, 4 μm) coupled with a UV/VIS DAD, refractive index (RI) Optilab®-rEX and multi-angle light scattering (MALS) DAWN EOS (Wyatt Technology Co., USA). A mixture (80:20 vol.%) of methanol and sodium acetate buffer (0.3 M, pH = 6.5) was used as the mobile phase at a flow rate of 0.6 mL · min⁻¹.

Refractive index increment (dn/dc)

The refractive index increment was measured at four different concentrations (0.5, 1.0, 1.5, and 2.0 mg · mL⁻¹) in a mixture (80:20 vol.%) of methanol and aqueous sodium acetate buffer (0.3 M, pH = 6.5) using a PSS DnDc-2010/620 differential refractometer (Polymer Standard Service, Mainz, Germany) at 620 nm and 29 °C. The data were processed using Differential Refractometer Software (version 5.32, Brookhaven Instruments Corp., Holtsville, NY, USA). The refractometer was calibrated with a series of aqueous solutions of potassium chloride, according to the user manual.

Cyclic voltammetry

Cyclic voltammograms were recorded on a μAUTOLAB III instrument (EcoChemie, Netherlands) at room temperature using a glassy carbon disc working electrode (2 mm diameter), a platinum auxiliary electrode, and Ag/AgCl (KCl) reference electrode. The samples were dissolved in anhydrous dichloromethane containing 0.1 M Bu₄N[PF₆] (Fluka, purissimum for electrochemistry) as the supporting electrolyte to make approximately 1 mM solution of the low-molecular weight precursors and 1 mg · 1 mL solution of the polymers. The solutions were deaerated by argon bubbling prior to the measurement and then maintained under an argon atmosphere. Decamethylferrocene (Alfa-Aesar) was added as an internal standard during the final scans, and the redox potentials were converted into the ferrocene/ferrocenium scale by subtracting 0.548 V.² The formal redox potentials E° for reversible redox transitions were determined as an average of the anodic and cathodic peak potentials in the cyclic voltammograms recorded at 0.1 V s⁻¹ scan rate, $E^{\circ} = \frac{1}{2}(E_{pa} + E_{pc})$. Due to the higher resistance of the solutions, the separations of the counter-waves, $\Delta E_p = E_{pa} - E_{pc}$, exceeded the theoretical value (59 mV for a reversible one-electron transfer at 25°C); the typical value was near 100 mV.

Cryogenic transmission electron microscopy (cryoTEM)

TEM micrographs were acquired with a Tecain G2 Spirit Twin 12 microscope (FEI, Czech Republic) equipped with a cryo-attachment (Gatan, CA, USA). The sample solution (3 μL) was dropped to an electron microscopy grid covered with a holey carbon supporting film (Electron Microscopy Science), which was hydrophilized just before the experiment by glow discharge (Expanded Plasma Cleaner, Harrick Plasma, USA). The excess solution was removed by blotting (Whatman no. 1 filter paper) for 1 s, and the grid was plunged into liquid ethane held at -181 °C. The frozen sample was

immediately inserted in the cryo-holder, transferred into the TEM microscope, and observed by bright field imaging at -173 °C using an accelerating voltage of 120 kV.

Dynamic light scattering

The hydrodynamic diameter (D_h) of the polymer samples was measured in aqueous citrate buffer (0.08 M, pH = 6.2) on a Zetasizer Nano-ZS, Model ZEN3600 (Malvern Instruments, UK) at the scattering angle $\theta = 173^\circ$ (using the DTS software – version 6.20 for data evaluation) at 25 °C.

Differential scanning calorimetry

DSC measurements were performed on a Q2000 DSC calorimeter (TA Instruments, USA) calibrated for indium. The sample (2 mg) was placed in Tzero aluminum pan with a pinhole and measured in a nitrogen atmosphere (flow rate 50 ml · min⁻¹) at the temperature range of -80 – 200 °C. The sample was measured in a heating-cooling-heating cycle with a heating / cooling rate of 10 °C · min⁻¹. A 2-minute isotherm was inserted between the cycles. The glass transition temperature (T_g) was determined as the inflection point of the second heating curve.

***In vitro* cytotoxicity**

Normal Human Dermal Fibroblast (NHDF, Lonza) and PC3 (prostate adenocarcinoma, ATCC) cells were cultured in Dulbecco's Modified Eagle Medium (DMEM, SigmaAldrich) with the addition of 10% fetal bovine serum (SigmaAldrich) and 1% penicillin streptomycin (SigmaAldrich) at 37 °C in a humidified CO₂ incubator containing 5% CO₂. The NHDF and PC3 cells were pre-cultivated for 24 hours in 96-well plates (clear, flat bottom plate; density 10⁴ cells per cm²). The cells were incubated with an appropriate volume of polymer dissolved in phosphate buffered saline (PBS) to reach final concentrations 1.0 mg · mL⁻¹; 0.75 mg · mL⁻¹; 0.5 mg · mL⁻¹ and 0.25 mg · mL⁻¹ for 24 h. A solution of PBS without any polymer was used as a control. The cell viability was determined via a 3-(4,5-dimethylthiazol-2-yl)-2,5-diphenyltetrazolium bromide assay (MTT, Sigma-Aldrich). MTT is reduced to formazan in mitochondria of living cells, and thus the cell viability can be spectrophotometrically determined at 570 nm after cell lysis (sodium dodecyl sulphate lysis buffer). The MTT assay results were compared with the control samples (PBS without any polymer added), and cell viability in these control samples was set to 100 %. Data in graphs are shown as the mean of three independent experiments ± SEM.

¹⁹F MRI and determination of relaxation times

NMR/MRI experiments were performed on a Bruker Avance III HD spectrometer in a magnetic field of 11.75 T (¹⁹F Larmor frequency of 470.9 MHz). The spectra were referenced with respect to external CFC₃ since no internal standard was added. A Micro-5 microimaging probe head by Bruker with a 5-mm radio-frequency insert (tunable to ¹⁹F) was used in conjunction with the GREAT 60 gradient amplifier and x,y,z gradient coil (maximum gradient amplitude 300 G/cm). For ¹⁹F T_2 relaxometry, a Carr-Purcell-Meiboom-Gill spin-echo pulse sequence with an echo period of 0.4 to 0.8 ms was employed, while T_1 relaxation was measured with an inversion-recovery sequence with logarithmically spaced relaxation delays up to $\sim 5 \times T_1$. The recorded relaxation curves were submitted to

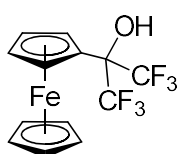
the inverse Laplace transformation³ to obtain T_1 , T_2 histograms (Fig. S20), from which the mean T_1 , T_2 values were finally computed to represent characteristic relaxation rates of the samples. MRI experiments were performed on a Bruker's ParaVision software platform (v6.0). The ultrashort echo time (UTE) pulse program from the Paravision library was used without any modification. The images of size of 32×32 pixels were acquired with an axial slice orientation, while the slice thickness parameter was set to maximum to excite the whole sample. The excitation pulse of a rectangular shape was applied; the pulse length was calibrated either for a 90° flip angle or for the Ernst angle (11-12°) depending on the required contrast. UTE parameters in favor of the oxidized sample: acquisition delay 22 μs; repetition time 10.5 ms; flip angle 90°. UTE parameters are set in favor of the reduced sample: acquisition delay 680 μs; repetition time 11.2 ms; flip angle 12°. The acquisition bandwidth (the FID sampling rate) was set to 10 kHz. The k-space trajectory measurement for the given bandwidth and image resolution was performed using a ¹H signal from the actual sample. One ¹⁹F UTE image was acquired in ca. 10 min. Lastly, the image data were finally exported from the ParaVision (Bruker) format into Matlab (The MathWorks Inc., Natick, Massachusetts) using the function read_2dseq.m⁴ and the image intensities were rescaled using the actual signal amplitude.

2 Synthesis

2.1 Synthesis of fluorinated ferrocene derivatives

Preparation of (1,1,1,3,3,3-hexafluoro-2-hydroxypropan-2-yl)ferrocene (1)

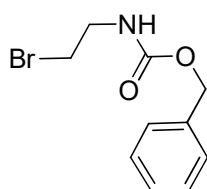
Compound **1** was synthesized as described in a previously reported procedure, albeit under modified conditions.⁵ A microwave pressure vial equipped with a magnetic stir bar was loaded with ferrocene (3.50 g, 18.8 mmol, 1 equiv.) and hexafluoroacetone trihydrate (15 mL, 108 mmol, 5.72 equiv.) and flushed with argon. The reaction was performed at 150 °C for 200 min in a Biotage Initiator+ microwave synthesizer (Biotage, Uppsala, Sweden). After cooling, the green residue in the reaction vial was dissolved in DCM (40 mL), and the resulting solution was poured into EtOAc (300 mL). The organic phase was subsequently washed with aqueous Na₂S₂O₃ (200 mL; reduction of the blue ferrocenium species) and two times with water (200 mL) in a separatory funnel, dried over anhydrous MgSO₄ and evaporated. The crude product was purified by flash chromatography (spherical silica, gradient 0-15% EtOAc in cyclohexane). Product **1** was obtained as an orange crystalline solid (3.79 g, 10.8 mmol, 57%).



¹H NMR (400 MHz, DMSO-*d*₆) δ 7.77 (s, 1H), 4.37 – 4.33 (m, 4H), 4.27 (s, 5H). ¹³C NMR (101 MHz, DMSO-*d*₆) δ 122.72 (q, $J = 289.1$ Hz), 80.35, 76.15 (septet, $J = 28.0$ Hz), 69.45, 68.50, 67.08. ¹⁹F NMR (376 MHz, DMSO-*d*₆) δ -76.08 (*d*, $J = 8.4$ Hz).

Preparation of *benzyl (2-bromoethyl)carbamate (2)*

A dry Schlenk flask equipped with a magnetic stir bar was loaded with 2-bromoethylamine hydrobromide (6.00 g, 29.3 mmol, 1.03 equiv.) and the 4-(dimethylamino)pyridine catalyst (70.0 mg, 0.573 mmol, 2 mol%). The flask was closed with a rubber septum, and the atmosphere was exchanged for argon using three cycles of vacuum-argon and cooled to 0 °C. Subsequently, DCM (100 mL, dried over 4 Å sieves) followed by benzyl chloroformate (4.04 mL, 4.83 g, 28.3 mmol, 1 equiv.) were added through the septum using a syringe and needle. Lastly, DIPEA (12.6 mL, 9.35 g, 72.3 mmol, 2.56 equiv.) was added dropwise through the septum. The reaction mixture was allowed to slowly warm to room temperature and stirred overnight. The reaction mixture was then diluted with DCM (250 mL) and extracted with water (200 mL), dilute aqueous HCl (2 × 200 mL) and brine/NaHCO₃ mixture (2 × 200 mL). The organic phase was dried over anhydrous MgSO₄, and all volatiles were then removed on a rotary evaporator. The crude product was purified by flash chromatography (spherical silica, gradient of EtOAc in cyclohexane 0-30%) yielding product **2** (6.30 g, 86%) as a colorless oil which crystallized upon cooling.

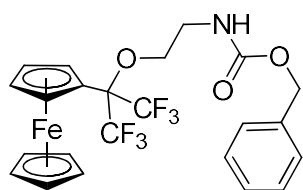


¹H NMR (400 MHz, DMSO-*d*₆) δ 7.57 (t, *J* = 5.2 Hz, 1H), 7.40 – 7.28 (m, 5H), 5.03 (s, 2H), 3.50 – 3.44 (m, 2H), 3.41 – 3.35 (m, 2H). ¹³C NMR (101 MHz, CDCl₃) δ 156.27, 136.37, 128.69, 128.37, 128.27, 67.12, 42.89, 32.58.

Preparation of *{2-[2-(benzyloxycarbonyl)aminoethoxy]-1,1,1,3,3,3-hexafluoropropan-2-yl}ferrocene (3)*

A flask equipped with a magnetic stir bar was loaded with NaH (60% dispersion in mineral oil, 203 mg, 8.46 mmol, 2.50 equiv.), closed with a rubber septum and flushed with argon. Dry Et₂O (2.0 mL, dried over 4 Å sieves) was added through the septum with a needle and syringe, and then a solution of compound **1** (1.100 g, 3.384 mmol, 1 equiv.) in dry Et₂O (6.0 mL) was added dropwise to the suspension of NaH. The mixture was stirred at rt for 15 min, and the solution was then aspirated into a syringe and filtered into a pear-shaped flask through a PTFE syringe filter to remove the solid NaH. Subsequently, the Et₂O was quickly evaporated on a rotary evaporator, the flask was immediately equipped with a magnetic stir bar, closed with a rubber septum, and put under argon (3 × vacuum-argon). Dry DMF (4 mL, dried over 4 Å sieves) was added into the flask with the solid residue using a needle and syringe, followed by a solution of compound **2** (961 mg, 3.722 mmol, 1.1 equiv.) and NaI (152 mg, 1.015 mmol, 0.3 equiv.) in dry DMF (6 mL). The reaction mixture was then heated to 40 °C for 30 h. The DMF was removed on a rotary evaporator, and the residue was dissolved in Et₂O (130 mL) and washed with water (3 × 100 mL) in a separatory funnel. The organic phase was dried over anhydrous MgSO₄ and evaporated *in vacuo*. The crude product was purified by flash chromatography using spherical silica as the stationary phase (ternary gradient 4% EtOAc / 96% cyclohexane / 0% DCM →

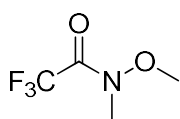
4% EtOAc / 46% cyclohexane / 50% DCM). The product **3** (1.136 g, 2.146 mmol, 63 %) was obtained as an orange oil, which crystallized upon cooling.



$^1\text{H NMR}$ (400 MHz, $\text{DMSO-}d_6$) δ 7.45 (t, $J = 5.8$ Hz, 1H), 7.40 – 7.28 (m, 5H), 5.05 (s, 2H), 4.47 – 4.45 (m, 2H), 4.31 – 4.21 (m, 7H), 3.87 (t, $J = 5.6$ Hz, 2H), 3.22 (td, $J = 5.8, 5.8$ Hz, 2H). $^{13}\text{C NMR}$ (101 MHz, $\text{DMSO-}d_6$) δ 156.23, 137.16, 128.31, 127.75, 127.64, 122.23 (q, $J = 290.6$ Hz), 80.71 (septet, $J = 28.0$ Hz), 75.35, 69.87, 69.15, 67.57, 65.25 (2C), 40.25. $^{19}\text{F NMR}$ (376 MHz, $\text{DMSO-}d_6$) δ -72.25 (s).

Preparation of 2,2,2-trifluoro-*N*-methoxy-*N*-methylacetamide (**4**)

A round-bottom flask equipped with a magnetic stir-bar was charged with *N,O*-dimethylhydroxylamine hydrochloride (12.0 g, 123 mmol, 1.00 equiv.), and the flask was closed with a rubber septum and flushed with argon via piercing the septum with a needle. Subsequently, dry DCM (250 mL, 4 Å sieves) was added using a syringe and a needle, and the flask was cooled to -20°C in an ice-salt bath. Trifluoroacetic anhydride (17.4 mL, 26.4 g, 126 mmol, 1.02 equiv.) was added, followed by a dropwise addition of dry pyridine (20.2 mL, 19.9 g, 251 mmol, 2.04 equiv.). The reaction mixture was then allowed to warm to rt and stirred for 1 h. The reaction mixture was diluted with DCM (300 mL) and extracted with water (60 mL), dilute aqueous HCl (100 mL), and finally with aqueous NaCl/NaHCO₃ (80 mL). The organic phase was dried over anhydrous MgSO₄ and evaporated *in vacuo*, yielding product **4** as a colorless viscous liquid (17.0 g, 108 mmol, 88%).

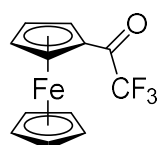


$^1\text{H NMR}$ (400 MHz, CDCl_3) δ 3.77 (s, 3H), 3.29 (s, 3H). $^{13}\text{C NMR}$ (101 MHz, Chloroform-*d*) δ 157.04 (q, $J = 38.3$ Hz), 116.25 (q, $J = 286.4$ Hz), 62.32, 33.00. $^{19}\text{F NMR}$ (376 MHz, CDCl_3) δ -71.78.

Preparation of 2,2,2-trifluoroacetylferrocene (**5**)

A flame-dried Schlenk flask equipped with a magnetic stir bar was loaded with ferrocene (3.163 g, 17.00 mmol, 1.0 equiv.) and *t*-BuOK (477 mg, 4.25 mmol, 0.125 equiv.) and closed with a rubber septum. The atmosphere in the flask was exchanged for argon with four cycles of vacuum-argon, and dry THF (160 mL) was added through the septum with a syringe and needle. The flask was cooled to -78°C and *t*-BuLi (1.7 M in pentane, 20 mL, 34.00 mmol; DANGER: extremely pyrophoric!) was slowly added dropwise via a needle and syringe over approx. 15 min (minimalization of local overheating resulting in ferrocene dilithiation⁶). The reaction mixture was stirred at -78°C for 1 h, and then 2,2,2-trifluoro-*N*-methoxy-*N*-methylacetamide (**4**) (4.16 mL, 5.341 g, 34.00 mmol, 2.0 equiv.), was added dropwise using a syringe and needle. The cooling bath was exchanged for acetonitrile-dry ice bath (-46°C), and the reaction mixture was stirred for another 1 h. Subsequently, the reaction mixture was left to warm slowly to rt and then hydrolyzed with water, diluted with DCM (250 mL) and extracted

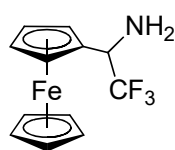
with dilute aqueous HCl (3×200 mL) followed by aqueous NaHCO₃ (200 mL). The organic phase was dried over anhydrous MgSO₄, and all volatiles were subsequently removed on a rotary evaporator. The crude product was purified from ferrocene and 1,1'-bis(2,2,2-trifluoroacetyl)ferrocene by flash chromatography (spherical silica, gradient of 0-15% EtOAc in cyclohexane). Dark red 2,2,2-trifluoroacetylferrocene (**5**) (3.561 g, 12.63 mmol, 74%) was isolated as a liquid, which formed large dark red crystals after cooling in the fridge. Even a freshly purified sample of compound **5** dissolved in DMSO-*d*₆ exhibited very broad peaks in ¹H NMR, possibly due to the fast formation of trace Fe³⁺ species.



¹H NMR (400 MHz, DMSO-*d*₆) δ 4.98 (br s, 4H), 4.35 (br s, 5H). ¹³C NMR (101 MHz, DMSO-*d*₆) δ 185.20 (q, $J = 33.8$ Hz), 116.39 (q, $J = 292.2$ Hz), 75.09, 70.50, 70.21, 69.97.

Preparation of (1-amino-2,2,2-trifluoroethyl)ferrocene (**6**)

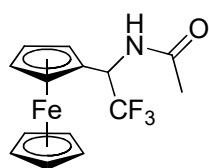
Compound **6** was prepared using a modified procedure reported for the synthesis of 1-aryl-2,2,2-trifluoroethylamines.⁷ A flame-dried Schlenk flask equipped with a magnetic stir bar was loaded with 2,2,2-trifluoroacetylferrocene (**5**) (2.00 g, 7.09 mmol, 1 equiv.) and closed with a rubber septum, and the atmosphere in the flask was exchanged for argon (4 vacuum-argon cycles). Subsequently, dry toluene (60 mL, dried over 4 Å sieves) was added through the septum using a syringe and needle, followed by a dropwise addition of LiHMDS solution in THF (1M, 13.5 mL, 13.5 mmol, 1.90 equiv.). The reaction mixture was stirred at room temperature for 20 min. Subsequently, the flask was immersed in an oil bath and heated to 80 °C for 30 min and then to 100 °C for another 45 min and finally 15 min at rt. At room temperature, a solution BH₃ · Me₂S in THF (1M, 25 mL, 25 mmol, 3.53 equiv.) was carefully added dropwise via a syringe and needle. The reaction was stirred at rt for 30 min and then heated to 55 °C for 45 min. After cooling down to rt, the reaction mixture was quenched by a dropwise addition of aqueous NaOH (2N, 20 mL) (exothermic reaction, hydrogen gas evolution!) and stirred overnight at rt. The crude product was extracted into Et₂O in a separatory funnel, and the organic phase was washed with aqueous Na₂CO₃. The organic phase was dried over anhydrous MgSO₄, and all volatiles were removed on a rotary evaporator. The crude product was purified by flash chromatography using spherical silica as the stationary phase (gradient EtOAc in cyclohexane 5-70%) yielding compound **6** (1.17 g, 4.14 mmol, 58%) as an orange solid.



¹H NMR (400 MHz, DMSO-*d*₆) δ 4.42 – 4.38 (m, 1H), 4.31 – 4.27 (m, 1H), 4.24 (s, 5H), 4.20 – 4.12 (m, 3H), 2.26 (s, 2H). ¹³C NMR (101 MHz, DMSO-*d*₆) δ 125.73 (q, $J = 282.4$ Hz), 84.54 (q, $J = 2.2$ Hz), 68.66, 68.46 (q, $J = 1.3$ Hz), 67.72, 67.58, 65.81, 52.58 (q, $J = 28.8$ Hz). ¹⁹F NMR (376 MHz, DMSO-*d*₆) δ -77.47 (d, $J = 8.0$ Hz).

Preparation of (1-acetamido-2,2,2-trifluoroethyl)ferrocene (7)

A dry pear-shaped flask was loaded with (1-amino-2,2,2-trifluoroethyl)ferrocene (6) (142 mg, 0.500 mmol, 1 equiv.), closed with a rubber septum and flushed with argon. Subsequently, dry DMF (1 mL, dried over 4 Å sieves) was added through the septum using a syringe and a needle, followed by DIPEA (192 μL, 142 mg, 1.10 mmol, 2.2 equiv.) and acetic acid (31 μL, 33 mg, 0.55 mmol, 1.10 equiv.). Finally, a solution of PyBOP (339 mg, 0.650 mmol, 1.30 equiv.) in DMF (1 mL) was added dropwise at rt, and the reaction mixture was stirred for 90 min. All volatiles from the reaction mixture were removed *in vacuo*, and the crude product was purified by flash chromatography using spherical silica as the stationary phase (gradient 15-35% EtOAc in cyclohexane) yielding product 7 (126 mg, 0.386 mmol, 77%) as an orange solid.



¹H NMR (400 MHz, DMSO-*d*₆) δ 8.80 (d, *J* = 9.9 Hz, 1H), 5.47 (dq, *J* = 9.9, 8.4 Hz, 1H), 4.53 – 4.51 (m, 1H), 4.46 – 4.41 (m, 1H), 4.24 – 4.19 (m, 2H), 4.14 (s, 5H), 2.06 (s, 3H). ¹³C NMR (101 MHz, DMSO-*d*₆) δ 169.27, 124.23 (q, *J* = 282.8 Hz), 81.04, 69.26, 68.64, 68.20, 68.03, 66.42, 49.22 (q, *J* = 30.6 Hz), 22.26. ¹⁹F NMR (376 MHz, DMSO-*d*₆) δ -75.84 (s).

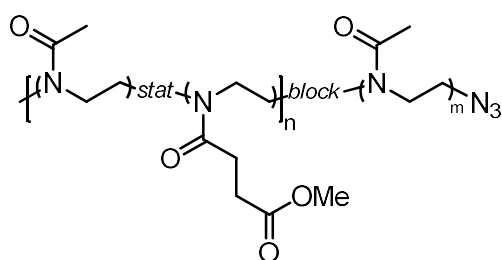
2.2 Synthesis of polymers

Synthesis of *P*(MeOx-*stat*-MestOx)₄₀-*block*-PMeOx₆₀-N₃ (A_{Me}-C_{Me}).

The corresponding amount of MeOx, MestOx (see Table S1) and MeOTs (108.8 μL, 0.72 mmol) were dissolved in acetonitrile (the total monomer concentration was 4 M, see Table S1) in 20 mL Biotage microwave vial. The vial was sealed and heated in a microwave reactor for 7 min at 140°C. After cooling to ambient temperature, the vial was transferred into the glovebox. A small aliquot (20 μL) was taken for the GC measurement to confirm the complete consumption of both monomers (conversion > 99%). The second portion of MeOx (3.67 g, 43.2 mmol) and acetonitrile (7.13 mL) was added, the vial was sealed, heated at 140 °C in a microwave reactor for 7 min and subsequently cooled to ambient temperature. After cooling the vial to ambient temperature, a small aliquot (20 μL) was taken under argon for GC measurement to confirm the complete consumption of MeOx (conversion > 99%), solid sodium azide (3 eq. of initial MeOTs amount) was added, and the mixture was stirred at ambient temperature overnight. The solution was evaporated under reduced pressure, dissolved in dichloromethane (DCM), filtered through a short pad of basic alumina, precipitated in diethyl ether, and dried under vacuum. The crude polymer was purified by dialysis (molecular weight cut-off 1 kDa) against distilled water, followed by freeze-drying.

Table S1. The amounts of monomers and solvent used for the synthesis of the first block of polymers **A_{Me}-C_{Me}**.

Polymer	MeOx	MestOx	Acetonitrile
A_{Me}	2.20 g, 25.9 mmol	452 mg, 2.88 mmol	4.54 mL
B_{Me}	1.96 g, 23.0 mmol	904 mg, 5.76 mmol	4.34 mL
C_{Me}	1.71 g, 20.2 mmol	1.71 g, 8.64 mmol	4.13 mL



Polymer A_{Me}

¹H NMR (400 MHz, CDCl₃) δ 3.66 – 3.58 (m, 16.5H, -OCH₃), 3.58 – 3.34 (m, 409H, -NCH₂CH₂-), 3.34 – 3.19 (m, 18.4H, -NCH₂CH₂-), 2.74 – 2.49 (m, 18.8H, -CO-CH₂CH₂-), 2.19 – 2.02 (m, 300H, -CO-CH₃). SEC-MALS: $M_n = 12.28$ kDa, $M_w = 12.89$ kDa, $D_M = 1.050$

Polymer B_{Me}

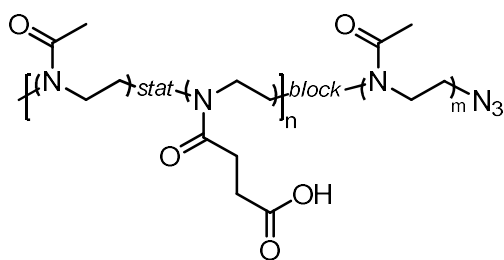
¹H NMR (400 MHz, CDCl₃) δ 3.66 – 3.58 (m, 35.5H, -OCH₃), 3.58 – 3.34 (m, 458H, -NCH₂CH₂-), 2.74 – 2.49 (m, 40.4H, -CO-CH₂CH₂-), 2.19 – 2.02 (m, 300H, -CO-CH₃). SEC-MALS: $M_n = 11.57$ kDa, $M_w = 12.07$ kDa, $D_M = 1.043$

Polymer C_{Me}

¹H NMR (400 MHz, CDCl₃) δ 3.66 – 3.58 (m, 52.5H, -OCH₃), 3.58 – 3.34 (m, 482H, -NCH₂CH₂-), 2.74 – 2.49 (m, 62.2H, -CO-CH₂CH₂-), 2.19 – 2.02 (m, 300H, -CO-CH₃). SEC-MALS: $M_n = 12.25$ kDa, $M_w = 12.58$ kDa, $D_M = 1.027$

Synthesis of P(MeOx-stat-(COOH)Ox)₄₀-block-PMeOx₆₀-N₃ (A-C).

A solution of LiOH (10 eq. relative to the methyl ester groups amount) in distilled water (20 mL) was added to a solution of methyl ester-containing polymer precursor A_{Me}-C_{Me} (5 g) in distilled water (40 mL), and the resulting mixture was stirred at room temperature for 4 h. Then, the mixture was acidified by concentrated hydrochloric acid to pH ~ 3, transferred to the dialysis tubing (molecular weight cut-off 1 kDa) and dialyzed against distilled water for two days, followed by polymer recovery by freeze-drying. The full ester conversion to carboxylic acid was confirmed by ¹H NMR (absence of the signal at 3.66 – 3.58 ppm corresponding to the methyl ester group).



Polymer A

SEC-MALS: $M_n = 10.67$ kDa, $M_w = 10.98$ kDa, $D_M = 1.029$

Polymer B

SEC-MALS: $M_n = 9.350$ kDa, $M_w = 9.662$ kDa, $D_M = 1.033$

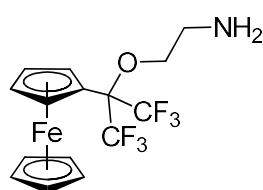
Polymer C

SEC-MALS: $M_n = 8.318$ kDa, $M_w = 8.522$ kDa, $D_M = 1.025$

Preparation of [2-(2-aminoethoxy)-1,1,1,3,3,3-hexafluoropropan-2-yl]ferrocene (8)

A Schlenk flask equipped with a magnetic stir bar was loaded with palladium on carbon (10% Pd, 110 mg, 0.103 mmol, 8.6 mol%) and compound **3** (468 mg, 0.885 mmol). The flask was closed with a rubber septum, and the atmosphere was exchanged for argon (3 cycles vacuum-argon). Subsequently, MeOH (6 mL) was added through the septum using a needle and syringe. The argon tubing connected to the sidearm of the Schlenk flask was carefully exchanged for hydrogen tubing to prevent the introduction of air. The flask was then connected to a gas bubbler via piercing the septum with a needle (the needle tip placed close to the liquid), and the flask was thoroughly flushed with hydrogen. After reducing the hydrogen flow, the flask was immersed in an oil bath and heated to 45 °C. A TLC analysis was run after 45 min, confirming a full conversion to the deprotected amine **8**. The hydrogen atmosphere was then exchanged for argon, and the suspension was filtered through a PTFE syringe filter to remove the Pd catalyst. All volatiles were thoroughly removed *in vacuo*, and the product **8** was dissolved in dry DMF (dried over 4 Å sieves) and used immediately for the synthesis of the ferrocene-modified polymers

(FcF6 polymers). The sample of compound **8** dissolved in DMSO-*d*₆ exhibited very broad peaks in ¹H NMR, possibly due to the fast formation of trace Fe³⁺ species by oxidation with atmospheric oxygen.

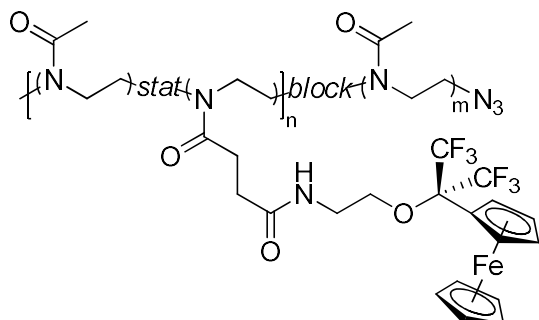


¹H NMR (400 MHz, DMSO-*d*₆) δ 4.50 (br s, 2H), 4.35 (br s, 2H), 4.28 (br s, 5H), 3.72 (br s, 2H), 2.77 (br s, 2H), 1.56 (br s, 2H). ¹³C NMR (101 MHz, DMSO-*d*₆) δ 122.40 (q, *J* = 290 Hz), 80.69 (septet, *J* = 27 Hz), 75.51, 69.85, 69.20, 69.03, 67.84, 41.34.

Preparation of polymer **FcF6-A**

A Schlenk flask equipped with a magnetic stir bar was loaded with polymer A (500 mg, 0.28 mmol COOH, 1 equiv.) and closed with a rubber septum, and the atmosphere in the flask was exchanged for argon (3 cycles argon-vacuum). Subsequently, dry DMF (6 mL, dried over 4 Å sieves) was added through the septum using a needle and syringe, followed by DIPEA (123 μL, 91 mg, 0.71 mmol, 2.5 equiv.), and the mixture was gently heated with a heat gun to fully dissolve the polymer. After cooling the flask to rt, the freshly prepared solution of [2-(2-aminoethoxy)-1,1,1,3,3,3-hexafluoropropan-2-yl]ferrocene (**8**) (0.294 mmol, 1.05 equiv.) in dry DMF (1.3 mL) was added through the septum using a syringe and needle, followed by a solution of PyBOP (153 mg, 0.294 mmol, 1.05 equiv.) in dry DMF (2 mL). The reaction mixture was stirred overnight at rt and subsequently quenched by adding 2-aminoethan-1-ol (100 μL, stirred 30 min). The volatiles from the reaction mixture were removed on a rotary evaporator, and the polymer was purified by size-exclusion chromatography in methanol using a flash chromatography system (LH-20 in F0080 column, 10 mL · min⁻¹), yielding polymer **FcF6-A** (579 mg) as an orange amorphous solid. The extent of polymer functionalization by the ferrocene moiety was approximately 5 mol% relative to all monomeric units (100%) according to the ¹H NMR analysis.

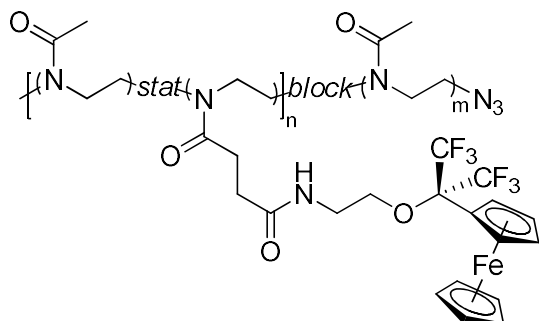
¹H NMR (400 MHz, DMSO-*d*₆) δ 8.11 – 7.96 (m, 5.0H, -NH-), 4.54 – 4.43 (m, 10.5H, Fc-H), 4.37 – 4.22 (m, 34.6H, Fc-H), 3.90 – 3.76 (m, 11.5H, -O-CH₂-), 3.60 – 3.21 (m, 468H), 2.40 – 2.29 (m, 10.8H), 2.09 – 1.87 (m, 300H, -CO-CH₃). SEC-MALS: *M*_n = 12.43 kDa, *M*_w = 12.75 kDa, *D*_M = 1.026



Preparation of polymer **FcF6-B**

A Schlenk flask equipped with a magnetic stir bar was loaded with the polymer **B** (500 mg, 0.55 mmol COOH, 1 equiv.) and closed with a rubber septum, and the atmosphere in the flask was exchanged for argon (3 cycles vacuum-argon). Subsequently, dry DMF (6 mL, dried over 4 Å sieves) was added through the septum using a needle and syringe, followed by DIPEA (246 μL, 182 mg, 1.41 mmol, 2.56 equiv.), and the mixture was gently heated with a heat gun to fully dissolve the polymer. After cooling the flask to rt, the freshly prepared solution of [2-(2-aminoethoxy)-1,1,1,3,3,3-hexafluoropropan-2-yl]ferrocene (**8**) (0.589 mmol, 1.07 equiv.) in dry DMF (2.6 mL) was added through the septum using a syringe and needle, followed by a solution of PyBOP (307 mg, 0.590 mmol, 1.07 equiv.) in dry DMF (2 mL). The reaction mixture was stirred overnight at rt and subsequently quenched by adding 2-aminoethan-1-ol (100 μL, stirred 30 min). The volatiles from the reaction mixture were removed on a rotary evaporator, and the polymer was purified by size-exclusion chromatography in methanol using a flash chromatography system (LH-20 in F0080 column, 10 mL · min⁻¹), yielding polymer **FcF6-B** (696 mg) as an orange amorphous solid. The extent of polymer functionalization by the ferrocene moiety was approximately 10 mol% relative to all monomeric units (100%) according to the ¹H NMR analysis.

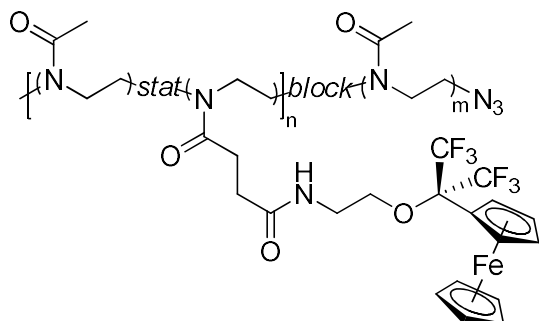
¹H NMR (400 MHz, DMSO-*d*₆) δ 8.11 – 7.96 (m, 10.1H, -NH-), 4.54 – 4.43 (m, 20.8H, Fc-H), 4.37 – 4.22 (m, 72.4H, Fc-H), 3.90 – 3.76 (m, 20.28H, -O-CH₂-), 3.60 – 3.21 (m, 495H), 2.40 – 2.29 (m, 21.8H), 2.09 – 1.87 (m, 300H, -CO-CH₃). SEC-MALS: $M_n = 13.66$ kDa, $M_w = 14.23$ kDa, $D_M = 1.042$



Preparation of polymer **FcF6-C**

A Schlenk flask equipped with a magnetic stir bar was loaded with the polymer **C** (250 mg, 0.400 mmol COOH, 1 equiv.) and closed with a rubber septum, and the atmosphere in the flask was exchanged for argon (3 cycles argon-vacuum). Subsequently, dry DMF (3 mL, dried over 4 Å sieves) was added through the septum using a needle and syringe, followed by DIPEA (183 μL, 134 mg, 1.04 mmol, 2.6 equiv.), and the mixture was gently heated with a heat gun to fully dissolve the polymer. After cooling the flask to rt, the freshly prepared solution of [2-(2-aminoethoxy)-1,1,1,3,3,3-hexafluoropropan-2-yl]ferrocene (**8**) (0.460 mmol, 1.15 equiv.) in dry DMF (2 mL) was added through the septum using a syringe and needle, followed by a solution of PyBOP (240 mg, 0.461 mmol, 1.15 equiv.) in dry DMF (2 mL). The reaction mixture was stirred overnight at rt and subsequently quenched by adding 2-aminoethan-1-ol (100 μL, stirred 30 min). The volatiles from the reaction mixture were removed on a rotary evaporator, and the polymer was purified by size-exclusion chromatography in methanol using a flash chromatography system (LH-20 in F0080 column, 10 mL · min⁻¹) yielding polymer **FcF6-C** (334 mg) as an orange amorphous solid. The extent of polymer functionalization by the ferrocene moiety was approximately 15 mol% relative all monomeric units (100%) according to the ¹H NMR analysis.

¹H NMR (400 MHz, DMSO-*d*₆) δ 8.11 – 7.96 (m, 15.9H, -NH-), 4.54 – 4.43 (m, 34.2H, Fc-H), 4.37 – 4.22 (m, 119.2H, Fc-H), 3.90 – 3.76 (m, 32.2H, -O-CH₂-), 3.60 – 3.21 (m, 508H), 2.40 – 2.29 (m, 31.8H), 2.09 – 1.87 (m, 300H, -CO-CH₃). SEC-MALS: *M*_n = 16.62 kDa, *M*_w = 16.82 kDa, *D*_M = 1.012

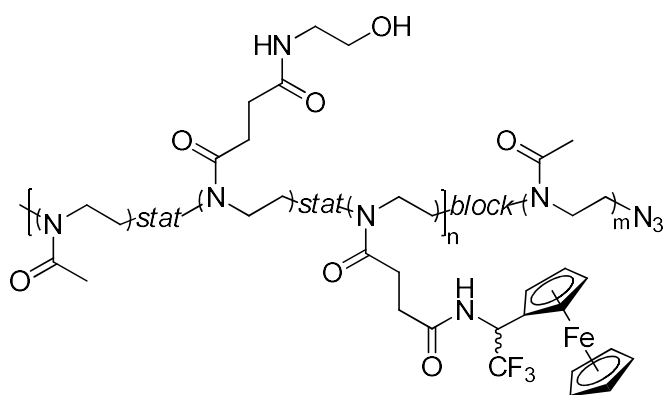


Preparation of polymer **FcF3-C1**

A Schlenk flask equipped with a magnetic stir bar was loaded with the polymer **C** (400 mg, 0.640 mmol COOH, 1 equiv.) and compound **6** (240 mg, 0.848 mmol, 1.33 equiv.) and closed with a rubber septum, and the atmosphere in the flask was exchanged for argon (3 cycles vacuum-argon). Subsequently, dry DMF (6 mL, dried over 4 Å sieves) was added through the septum using a needle and syringe, followed by DIPEA (365 μL, 271 mg, 2.10 mmol, 3.3 equiv.), and the mixture was gently heated with a heat gun to fully dissolve the polymer. After cooling the flask to rt, a solution of PyBOP (551 mg, 1.06 mmol, 1.65 equiv.) in dry DMF (3 mL) was added through the septum using a syringe and needle. The reaction mixture was stirred overnight at rt and subsequently quenched by adding

2-aminoethan-1-ol (100 μL , stirred 30 min). The volatiles from the reaction mixture were removed on a rotary evaporator, and the polymer was purified by size-exclusion chromatography in methanol using a flash chromatography system (LH-20 in F0080 column, 10 mL \cdot min $^{-1}$), yielding polymer **FcF3-C1** (500 mg) as an orange amorphous solid. The extent of polymer functionalization by the ferrocene moiety was 6.8 mol% and 5.8 mol% by 2-hydroxyethylamide moiety relative to all monomeric units (100%) according to the ^1H NMR analysis.

^1H NMR (400 MHz, DMSO- d_6) δ 8.90 – 8.67 (m, 7.8H, ((CF $_3$, Fc)CH)-NH-CO-), 7.87 – 7.61 (m, 6.6H, -CO-NH-CH $_2$ CH $_2$ -), 5.58 – 5.35 (m, 8.0H, ((CF $_3$, Fc)CH-), 4.65 – 4.57 (m, 7.0H), 4.56 – 4.49 (m, 7.7H, Fc-H), 4.45 – 4.36 (m, 8H, Fc-H), 4.23 – 4.17 (m, 17H, Fc-H), 4.15 – 4.11 (m, 41H, Fc-H), 3.62 – 3.22 (m, 455H), 3.13 – 3.04 (m, 15.2H), 2.10 – 1.82 (m, 300H, -CO-CH $_3$). SEC-MALS: M_n = 15.09 kDa, M_w = 15.44 kDa, D_M = 1.024

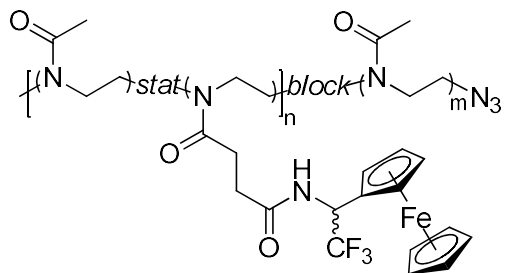


Preparation of polymer **FcF3-C2**

A Schlenk flask equipped with a magnetic stir bar was loaded with polymer **C** (200 mg, 0.320 mmol COOH, 1 equiv.) and closed with a rubber septum, and the atmosphere in the flask was exchanged for argon (3 cycles vacuum-argon). Subsequently, dry DMF (2.5 mL, dried over 4 Å sieves) was added through the septum using a needle and syringe, and the flask was heated to 70 °C. After the complete dissolution of the polymer, the flask was cooled to rt, and DIPEA (184 μL , 137 mg, 1.06 mmol, 3.3 equiv.) was added through the septum using a syringe and needle, followed by a solution of compound **6** (147 mg, 0.519 mmol, 1.62 equiv.) in dry DMF (1 mL). Subsequently, a solution of PyAOP (270 mg, 0.518 mmol, 1.62 equiv.) in dry DMF (1 mL) was added through the septum, and the reaction mixture was stirred at rt for 1 h. Finally, a second portion of PyAOP (120 mg, 0.230 mmol, 0.72 equiv.) in dry DMF (0.5 mL) was added, and the reaction mixture was stirred at rt for another 30 min. The reaction mixture was then quenched by adding 2-aminoethan-1-ol (150 μL , stirred 30 min), and the volatiles were removed on a rotary evaporator. The polymer was purified by size-exclusion chromatography in methanol using a flash chromatography system (LH-20 in F0080 column, 10 mL \cdot min $^{-1}$), yielding polymer **FcF3-C2** (265 mg) as an orange amorphous solid. The extent of

polymer functionalization by the ferrocene moiety was approximately 13% relative to all monomeric units (100%) according to the ^1H NMR analysis.

^1H NMR (400 MHz, $\text{DMSO-}d_6$) δ 8.89 – 8.66 (m, 13.8H, $-\text{NH}-$), 5.55 – 5.36 (m, 15.2H, $((\text{CF}_3, \text{Fc})\text{CH}-)$), 4.60 – 4.48 (m, 15.5H, Fc-H), 4.45 – 4.32 (m, 17.7H, Fc-H), 4.22 – 4.16 (m, 31H, Fc-H), 4.16 – 4.11 (m, 73H, Fc-H), 3.65 – 3.21 (m, 438H), 2.07 – 1.88 (m, 300H, $-\text{CO}-\text{CH}_3$). SEC-MALS: $M_n = 22.87$ kDa, $M_w = 26.03$ kDa, $D_M = 1.138$.



3 Dynamic light scattering and cryoTEM

The corresponding polymer was dissolved in isotonic citrate buffer (0.08 M, pH = 6.2) at a polymer concentration of $2 \text{ mg} \cdot \text{mL}^{-1}$ (more hydrophobic polymers **FcF6-C** and **FcF3-C2** had to be briefly heated to approx. 50-60 °C to obtain a clear solution). The samples were filtered through a $0.45 \mu\text{M}$ PVDF syringe filter into a cuvette (1 mL). After the first DLS measurement, a CuCl_2 solution in citrate buffer ($10 \mu\text{L}$, $10 \text{ mg} \cdot \text{mL}^{-1}$) was added, and another measurement was run. Finally, an aqueous solution of $(\text{NH}_4)_2\text{S}_2\text{O}_8$ ($20 \mu\text{L}$, $100 \text{ mg} \cdot \text{mL}^{-1}$) was added into the cuvette, and the change of polymer particle size was observed at different timepoints. The same polymer sample preparation was used in cryoTEM measurements (Fig. S4, S5 and S7).

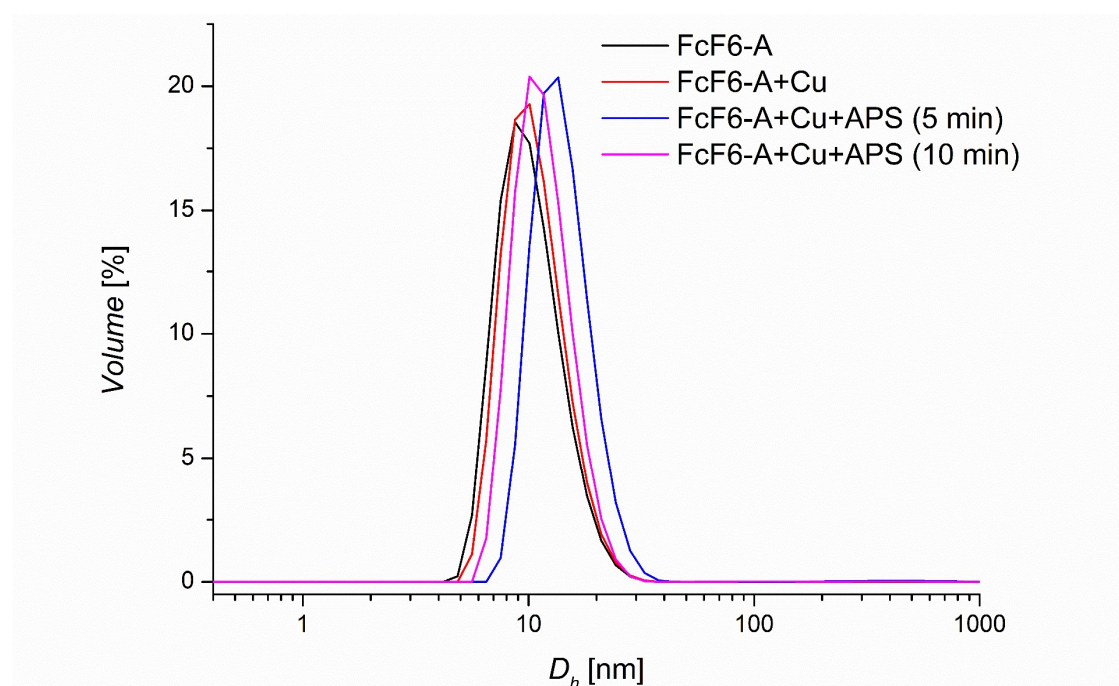


Figure S1. Hydrodynamic diameter of **FcF6-A** polymer sample ($2 \text{ mg} \cdot \text{mL}^{-1}$) dissolved in citrate buffer (0.08 M, pH = 6.2) before oxidation, after Cu^{2+} (catalytic amount) addition, and after addition of APS at different timepoints

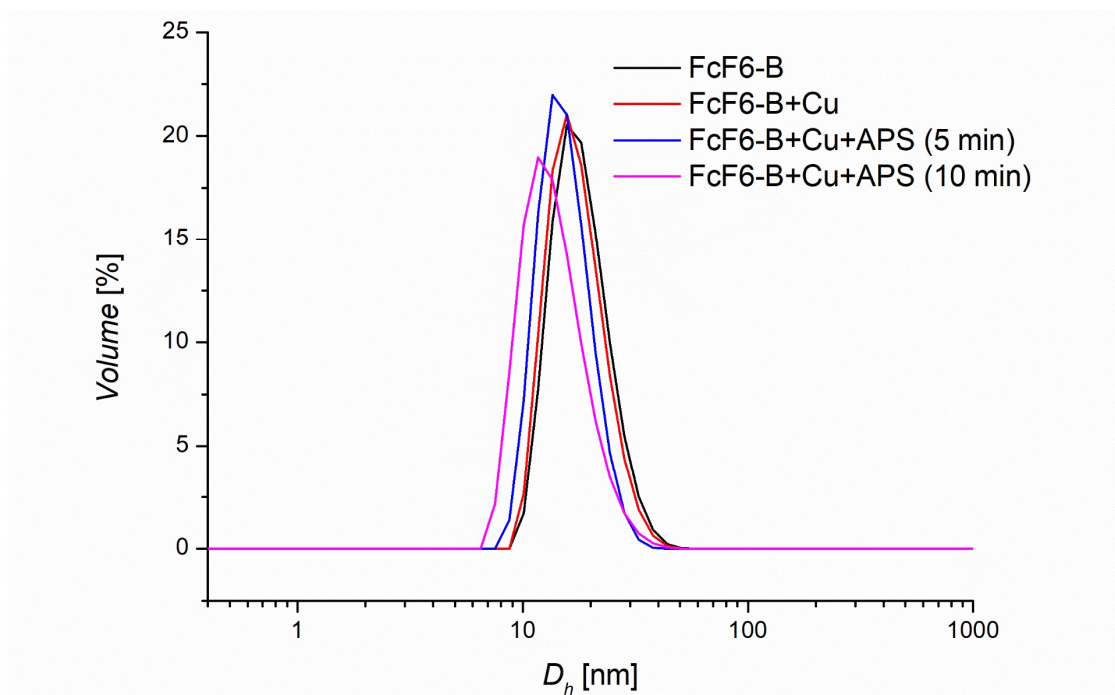


Figure S2. Hydrodynamic diameter of **FcF6-B** polymer sample ($2 \text{ mg} \cdot \text{mL}^{-1}$) dissolved in citrate buffer (0.08 M , $\text{pH} = 6.2$) before oxidation, after Cu^{2+} (catalytic amount) addition, and after addition of APS at different timepoints

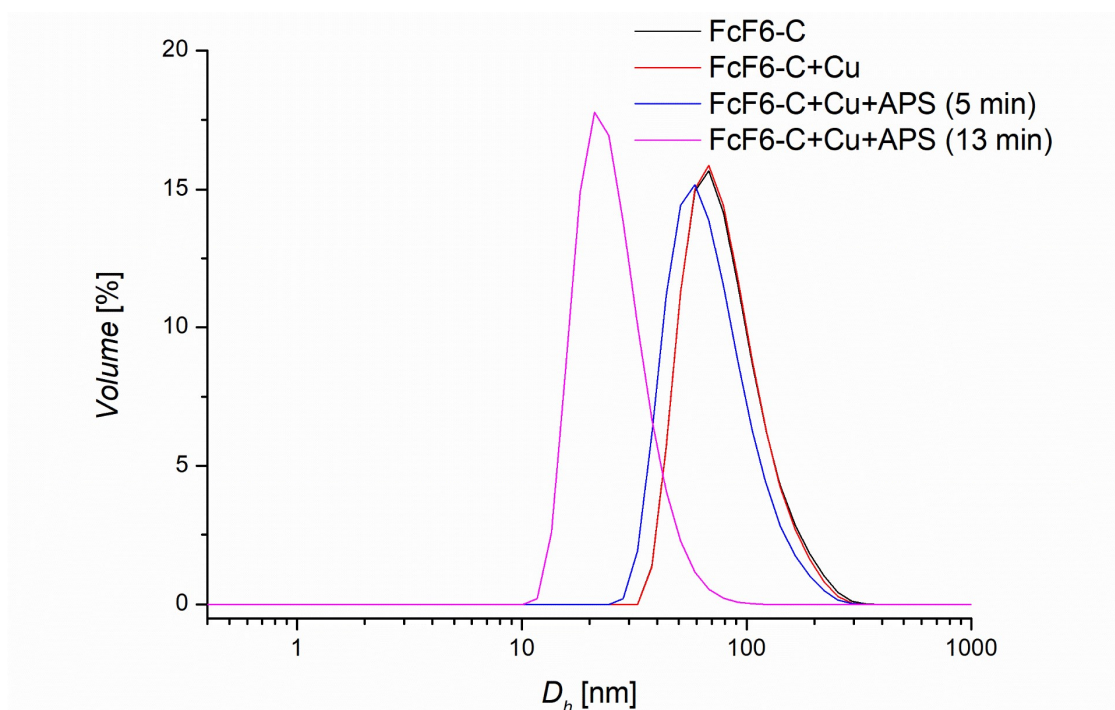


Figure S3. Hydrodynamic diameter of **FcF6-C** polymer sample ($2 \text{ mg} \cdot \text{mL}^{-1}$) dissolved in citrate buffer (0.08 M , $\text{pH} = 6.2$) before oxidation, after Cu^{2+} (catalytic amount) addition, and after addition of APS at different timepoints

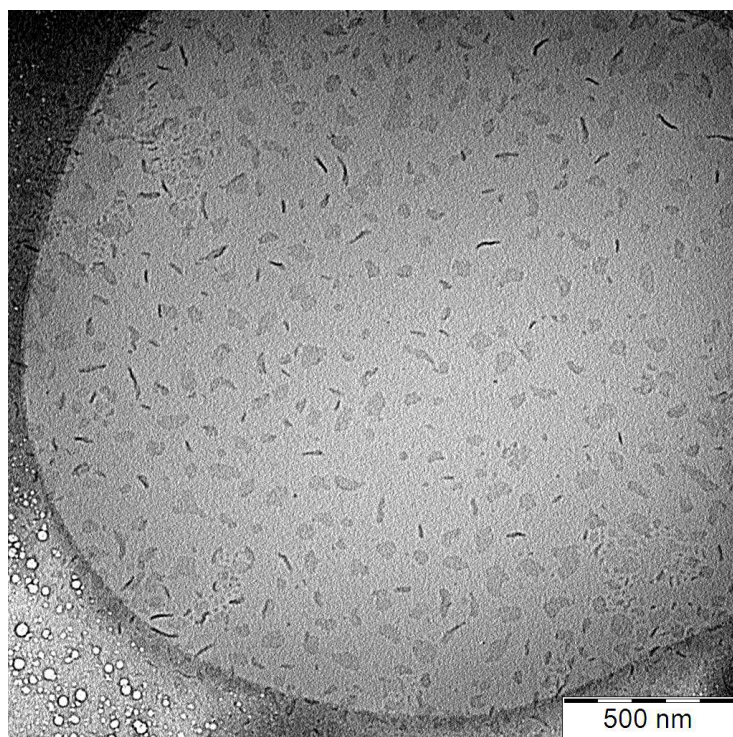


Figure S4. CryoTEM image of **FcF6-C** polymer sample ($2 \text{ mg} \cdot \text{mL}^{-1}$) dissolved in citrate buffer (0.08 M , $\text{pH} = 6.2$) before oxidation showing the 100-nm-long, “rod-like” micelles and flake structures

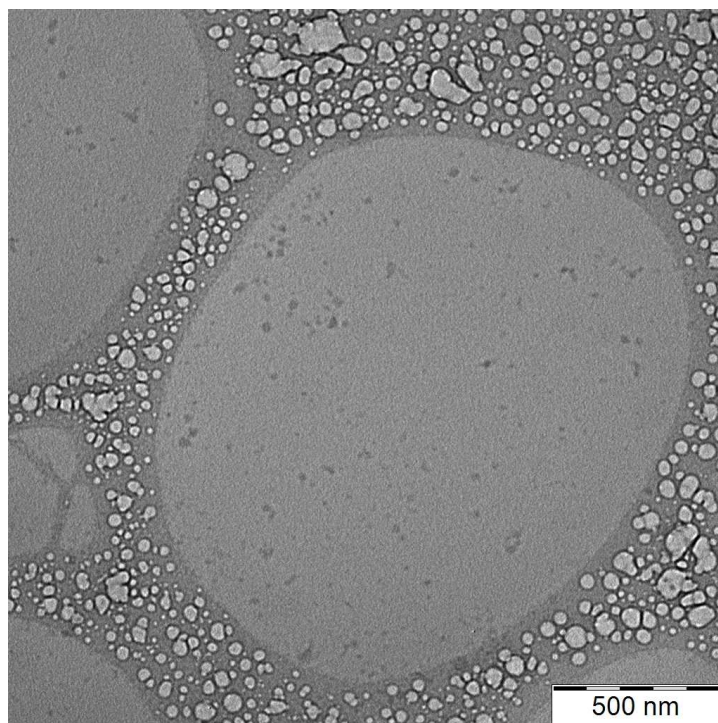


Figure S5. CryoTEM image of **FcF6-C** polymer sample ($2 \text{ mg} \cdot \text{mL}^{-1}$) dissolved in citrate buffer (0.08 M , $\text{pH} = 6.2$) after Cu^{2+} and APS addition (approx. 10 min) showing approximately 20 nm isometric objects resembling classical micelles after polymer oxidation (compare with Fig. S4)

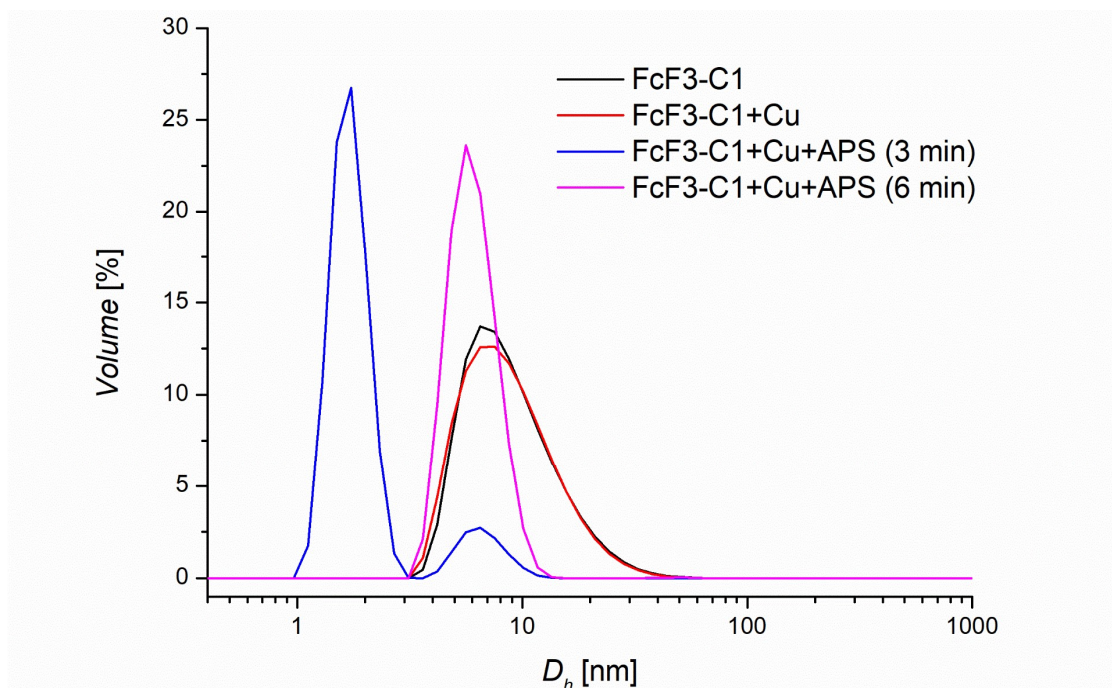


Figure S6. Hydrodynamic diameter of **FcF3-C1** polymer sample ($2 \text{ mg} \cdot \text{mL}^{-1}$) dissolved in citrate buffer (0.08 M , $\text{pH} = 6.2$) before oxidation, after Cu^{2+} (catalytic amount) addition, and after addition of APS at different timepoints

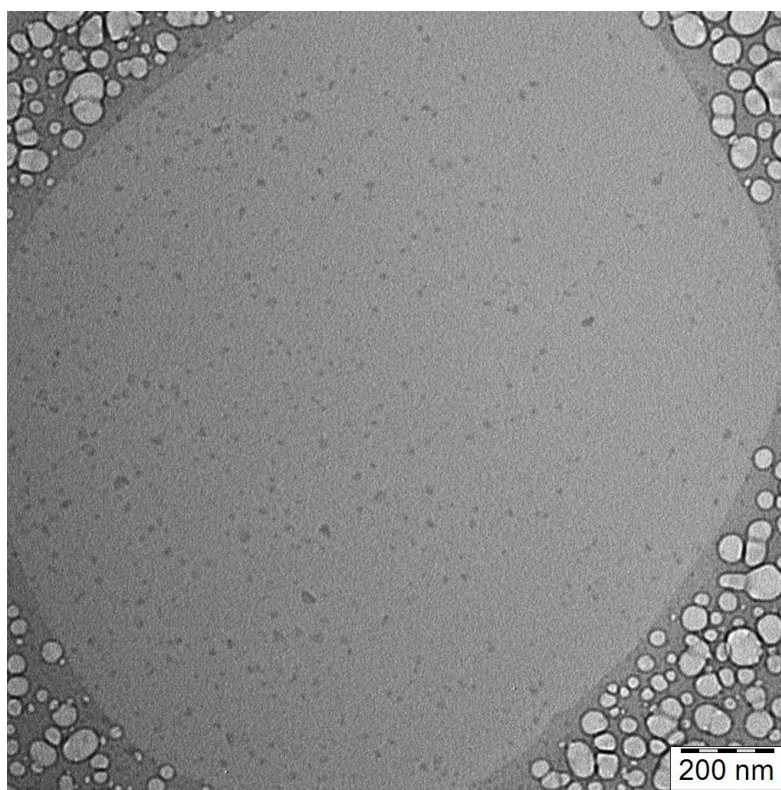


Figure S7. CryoTEM image of **FcF3-C1** polymer sample ($2 \text{ mg} \cdot \text{mL}^{-1}$) dissolved in citrate buffer (0.08 M , $\text{pH} = 6.2$) showing approximately 10-20 nm isometric objects resembling classical micelles

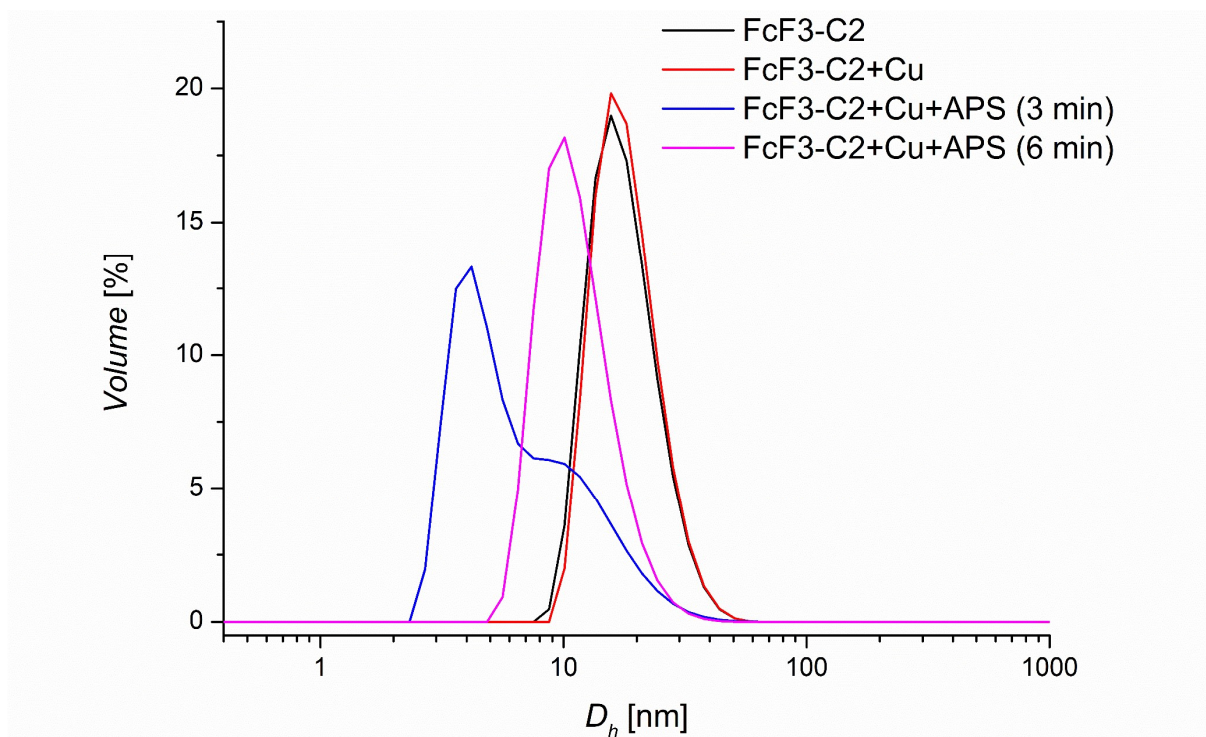


Figure S8. Hydrodynamic diameter of **FcF3-C2** polymer sample ($2 \text{ mg} \cdot \text{mL}^{-1}$) dissolved in citrate buffer (0.08 M , $\text{pH} = 6.2$) before oxidation, after Cu^{2+} (catalytic amount) addition, and after addition of APS at different timepoints

4 Size-exclusion chromatography

The peaks in SEC chromatograms (Fig. S9-S19) at 6 min correspond to system peaks, which are more prominent in polymers with free carboxyl groups (polymers **A**, **B**, **C** - Fig. S10, S12, S14). Their intensity also increases with the increasing content of free carboxyl groups. This relationship could be explained, for example, by the increase in the amount of water in polymer samples with the higher content of free carboxyl groups or by partial depletion of sodium ions in the mobile phase, bound by the polymer carboxylate groups, resulting in a greater change in the refractive index of the buffer in the system peak.

The apparent shoulders of the polymer peaks in SEC chromatograms of the free carboxyl group containing polymers **A**, **B**, **C** (Fig. S10, S12, S14) is a tailing arising from the polymer interaction with the column stationary phase. The tailing increased with the content of free carboxyl groups (especially **B**, **C**) but was not present in the corresponding parent polymers with methyl ester groups (**A_{Me}**, **B_{Me}**, **C_{Me}** - Fig. S9, S11, S13) or in the final polymers **FcF6-A**, **FcF6-B**, **FcF6-C** or **FcF3-C1**.

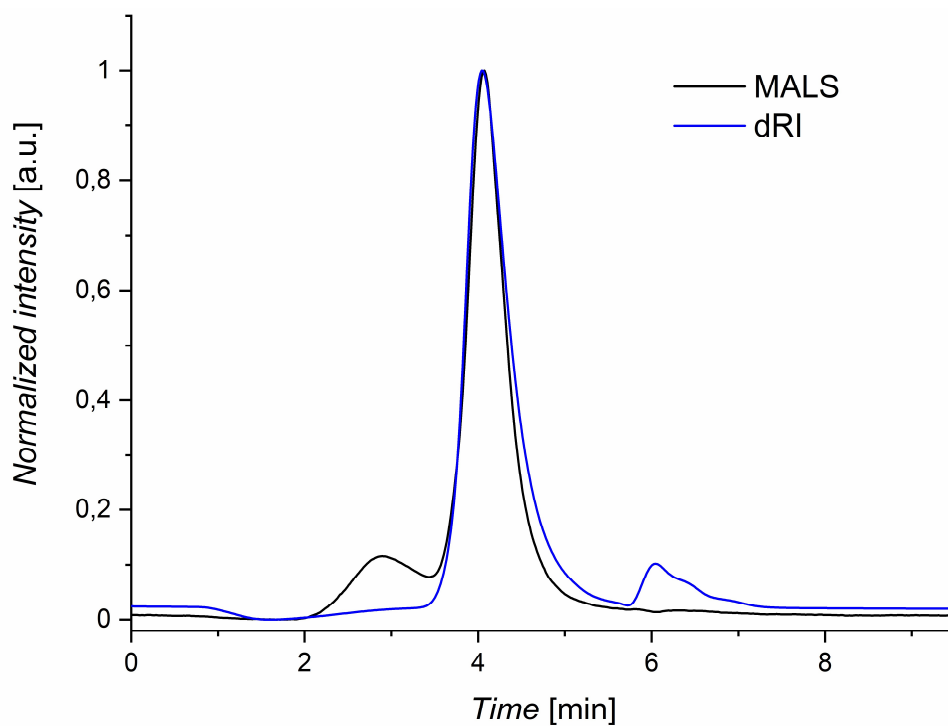


Figure S9. SEC chromatogram of polymer A_{Me}

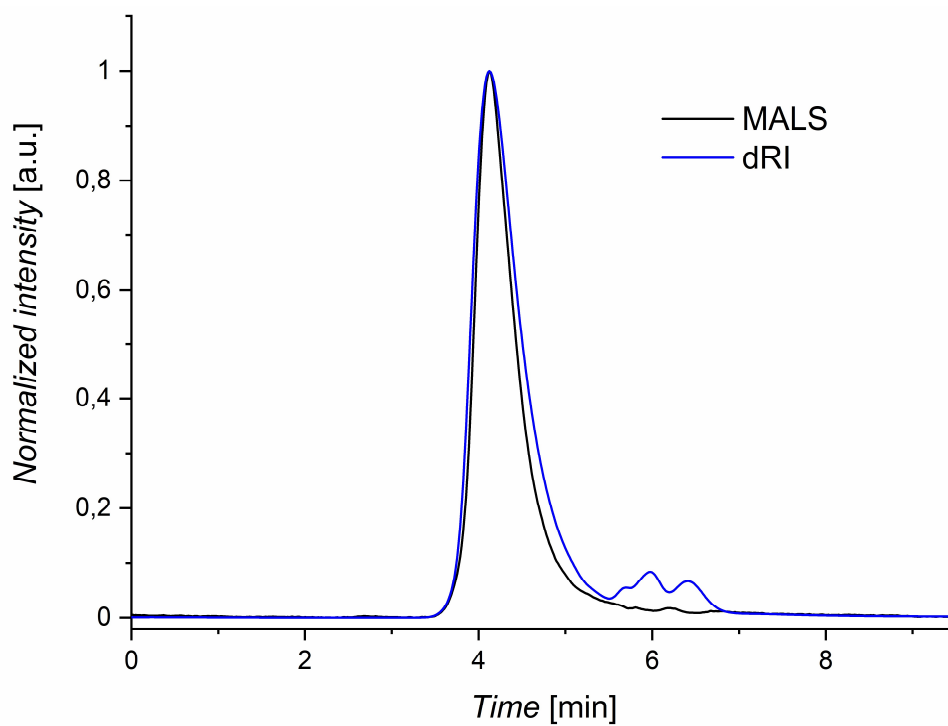


Figure S10. SEC chromatogram of polymer **A**, slight peak tailing due to free carboxyl groups

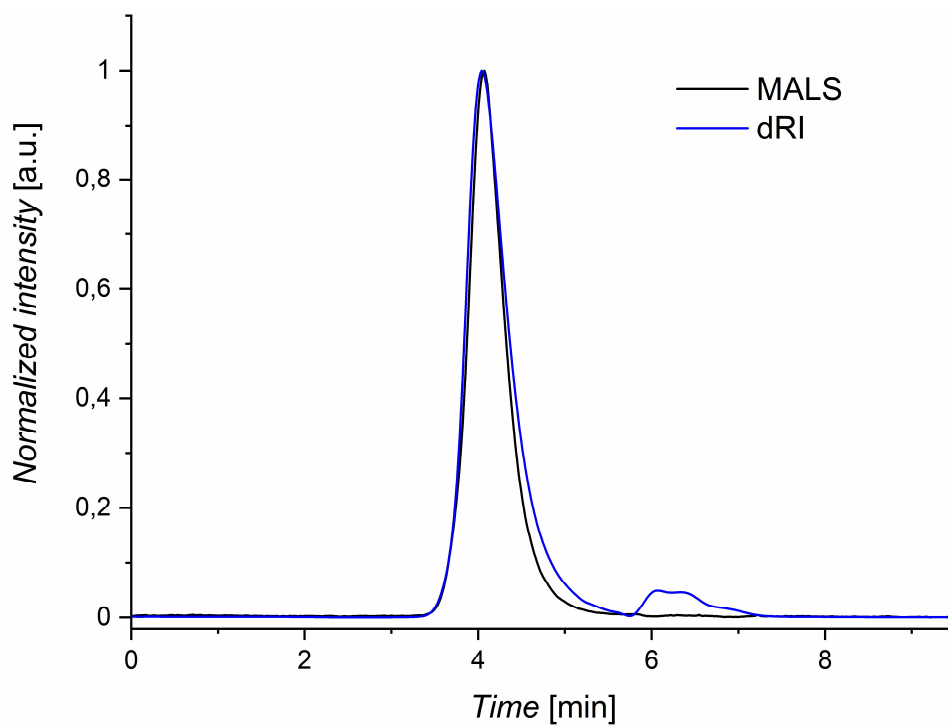


Figure S11. SEC chromatogram of polymer **B_{Me}**

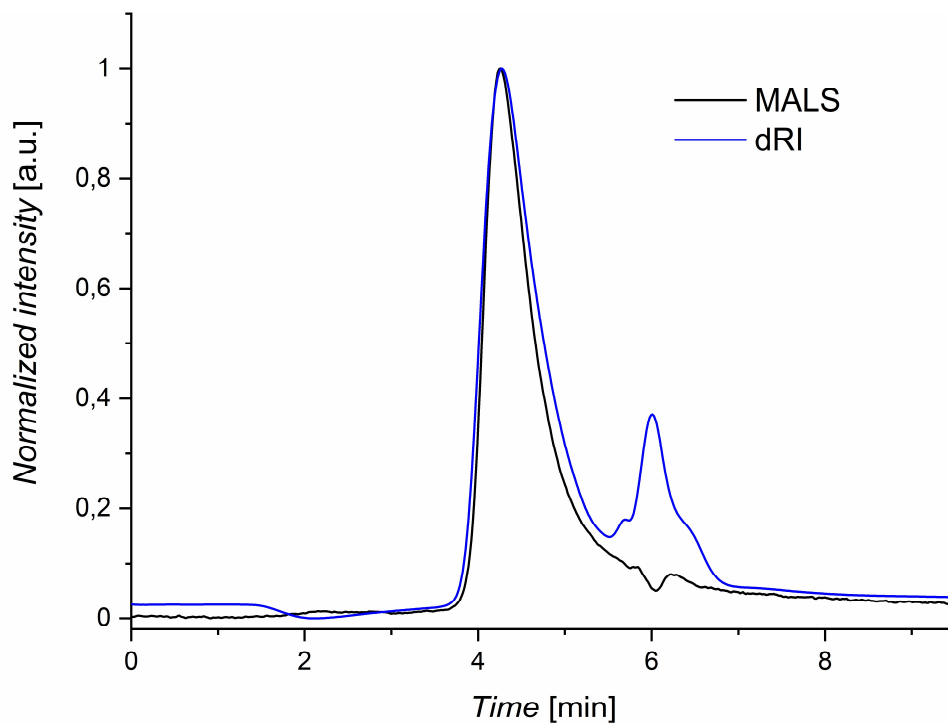


Figure S12. SEC chromatogram of polymer **B**, peak tailing due to free carboxyl groups

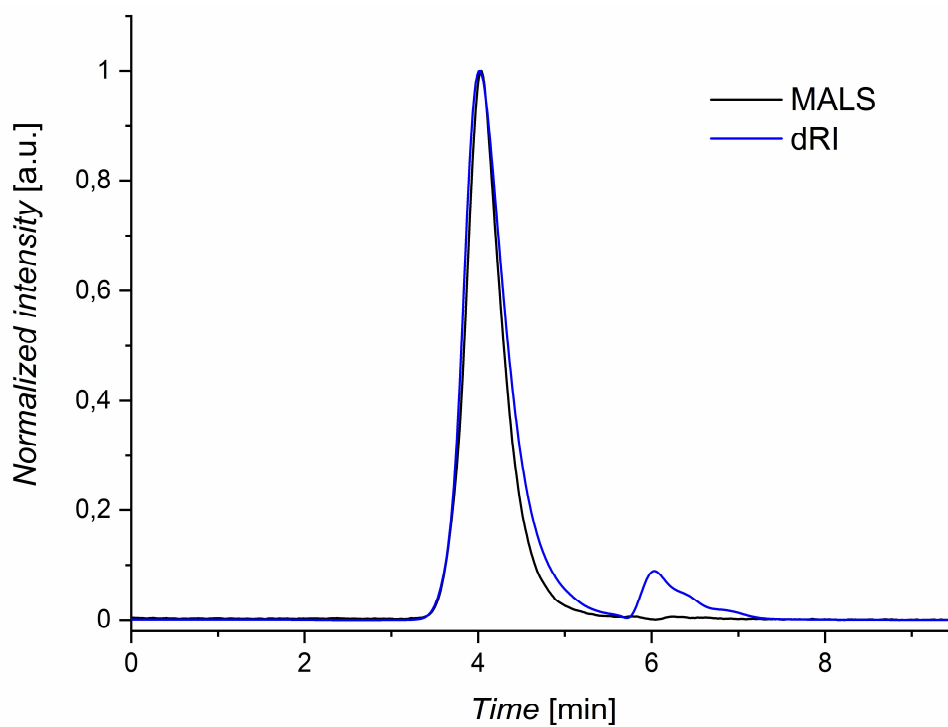


Figure S13. SEC chromatogram of polymer C_{Me}

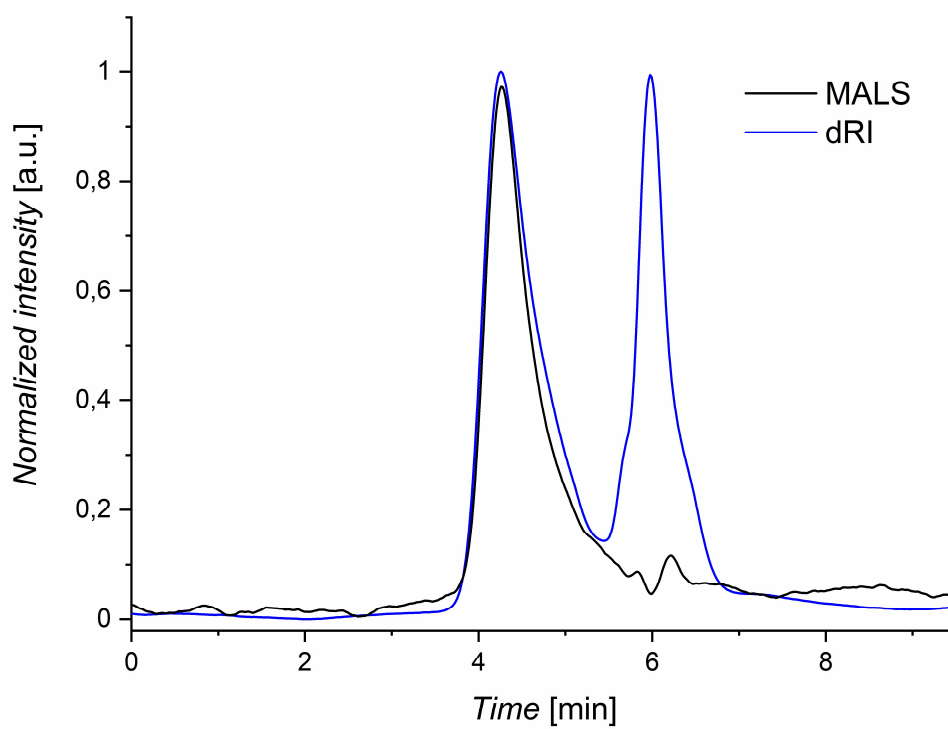


Figure S14. SEC chromatogram of polymer C, peak tailing due to free carboxyl groups

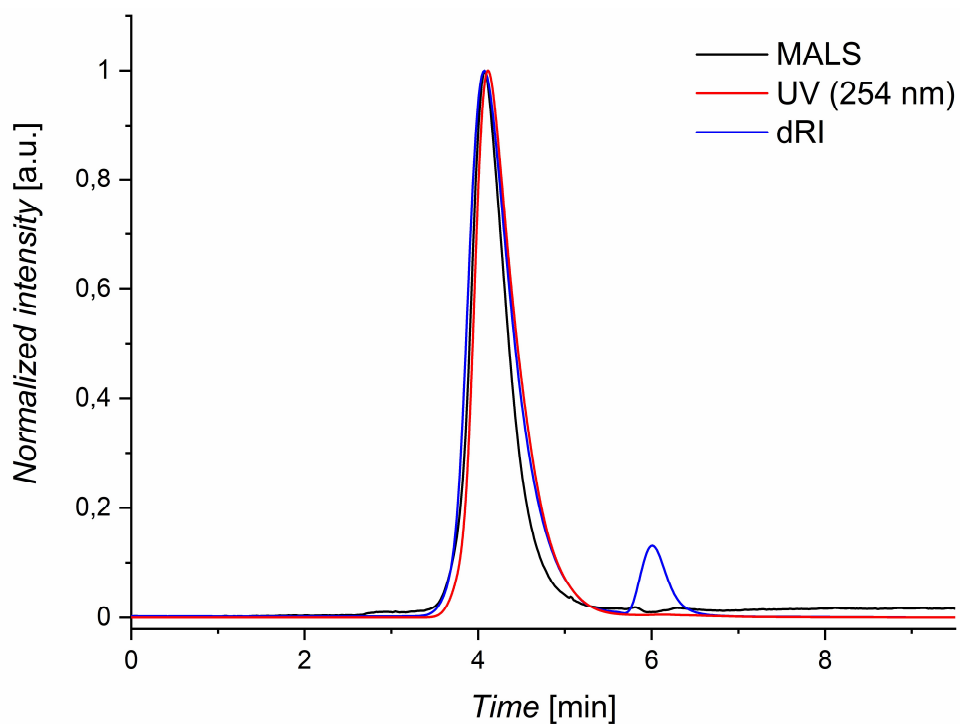


Figure S15. SEC chromatogram of polymer **FcF6-A** with a UV trace confirming that the polymer **FcF6-A** is free of the excess unbound ferrocene derivative **8** used for coupling

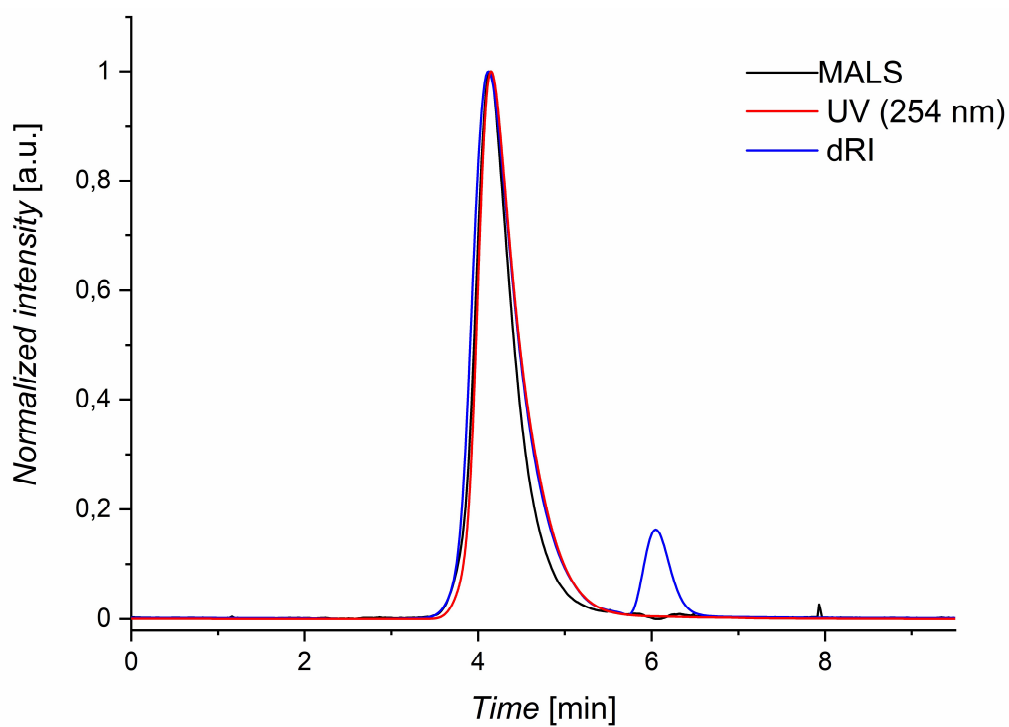


Figure S16. SEC chromatogram of polymer **FcF6-B** with a UV trace confirming that the polymer **FcF6-B** is free of the excess unbound ferrocene derivative **8** used for coupling

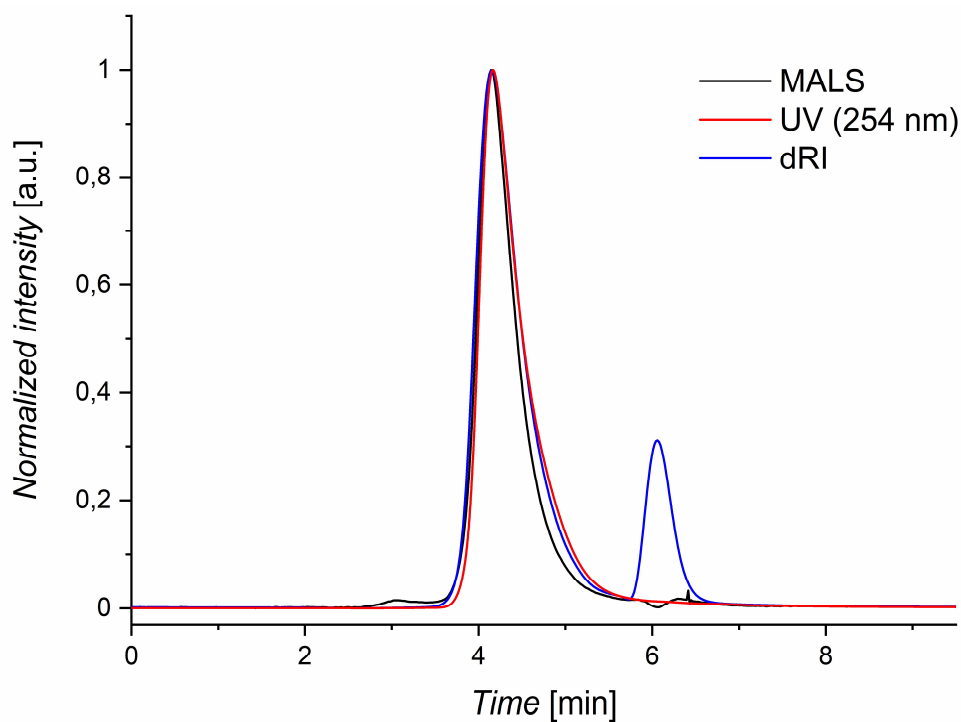


Figure S17. SEC chromatogram of polymer **FcF6-C** with a UV trace confirming that the polymer **FcF6-C** is free of the excess unbound ferrocene derivative **8** used for coupling

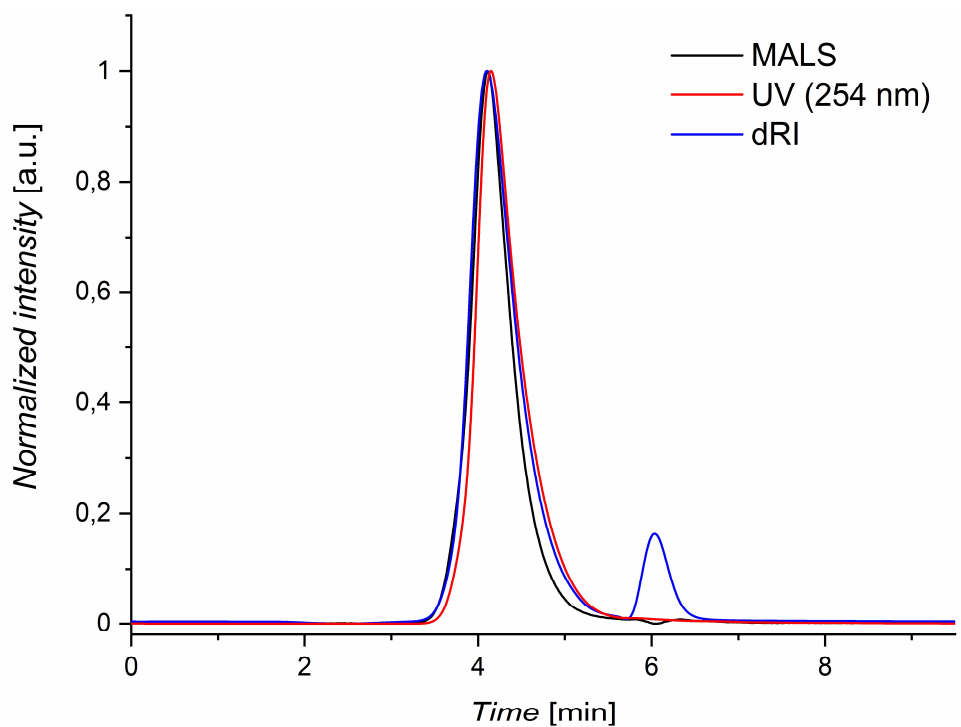


Figure S18. SEC chromatogram of polymer **FcF3-C1** with a UV trace confirming that the polymer **FcF3-C1** is free of the excess unbound ferrocene derivative **6** used for coupling

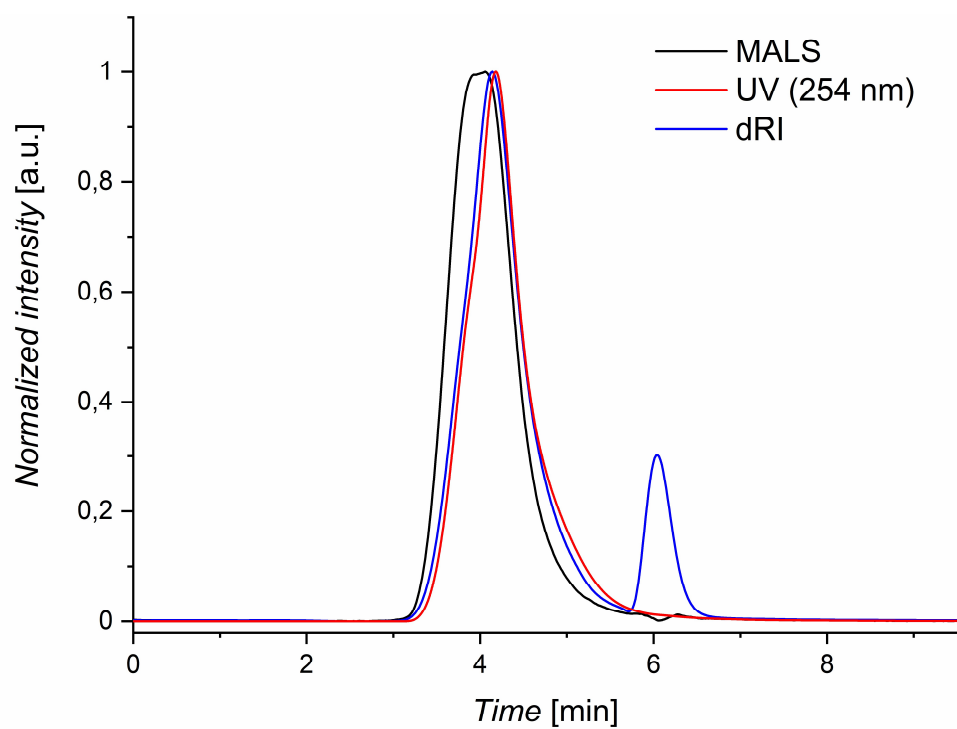


Figure S19. SEC chromatogram of polymer **FcF3-C2** with a UV trace confirming that the polymer **FcF3-C2** is free of the excess unbound ferrocene derivative **6** used for coupling

5 ^{19}F relaxation times and MRI

5.1 ^{19}F relaxation times

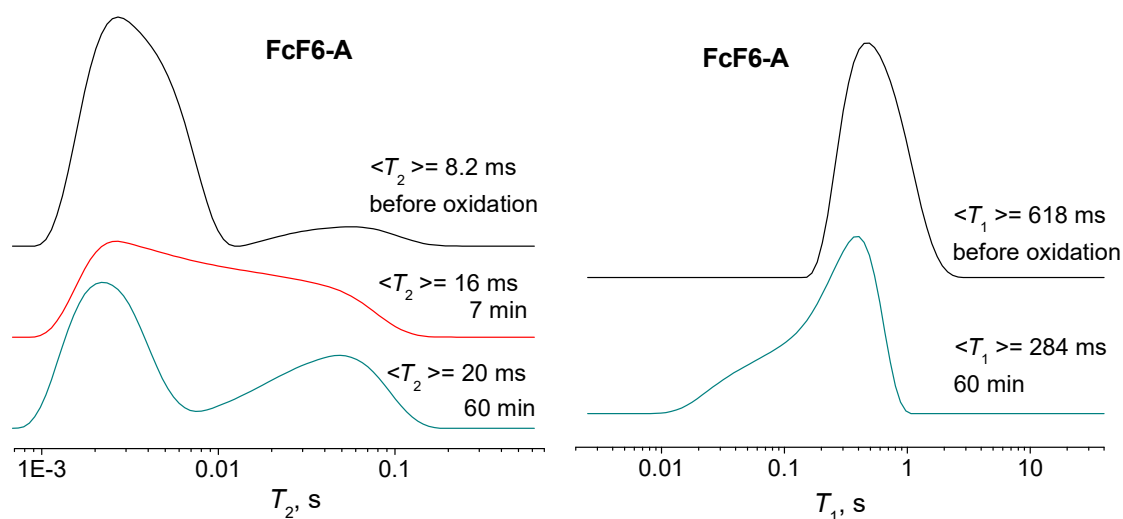


Figure S20. ^{19}F T_2 and T_1 relaxation time distributions in a FcF6-A polymer sample in citrate buffer (0.08 M, pH=6.2) before oxidation and at various stages of oxidation. The T_1/T_2 values in the brackets represent arithmetic-mean relaxation times of the respective distributions.

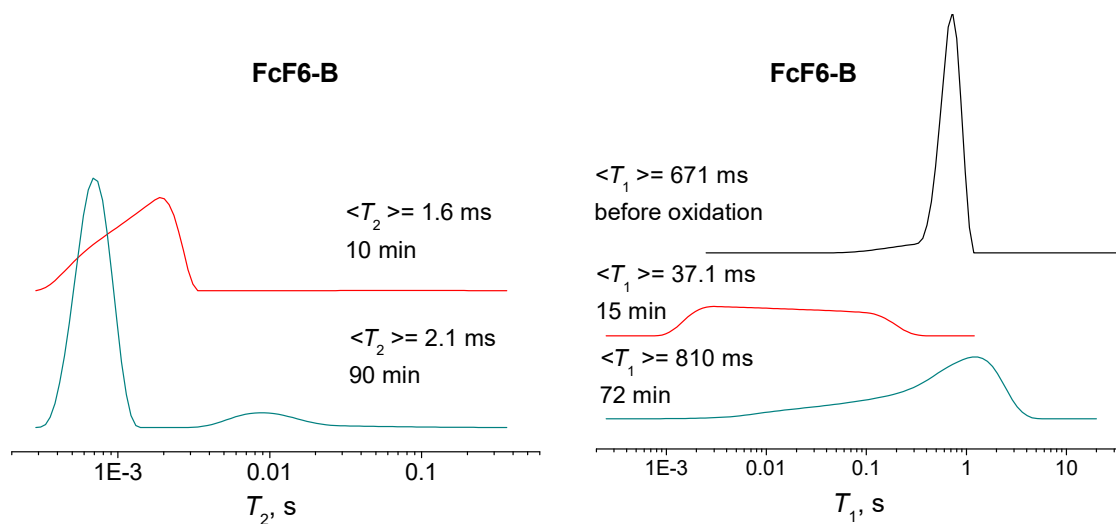


Figure S21. ^{19}F T_2 and T_1 relaxation time distributions in a FcF6-B

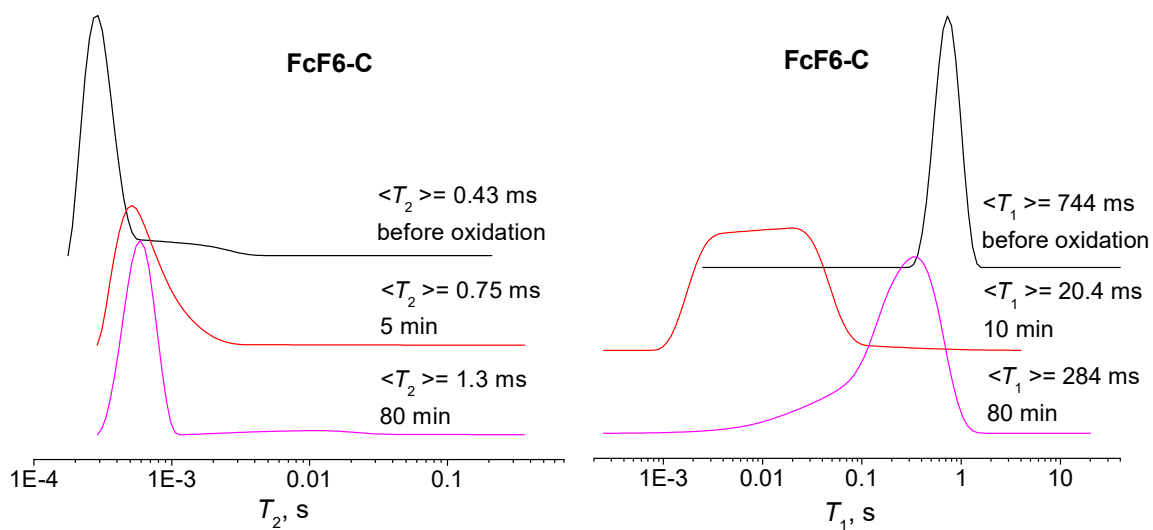


Figure S22. ^{19}F T_2 and T_1 relaxation time distributions in a **FcF6-C**

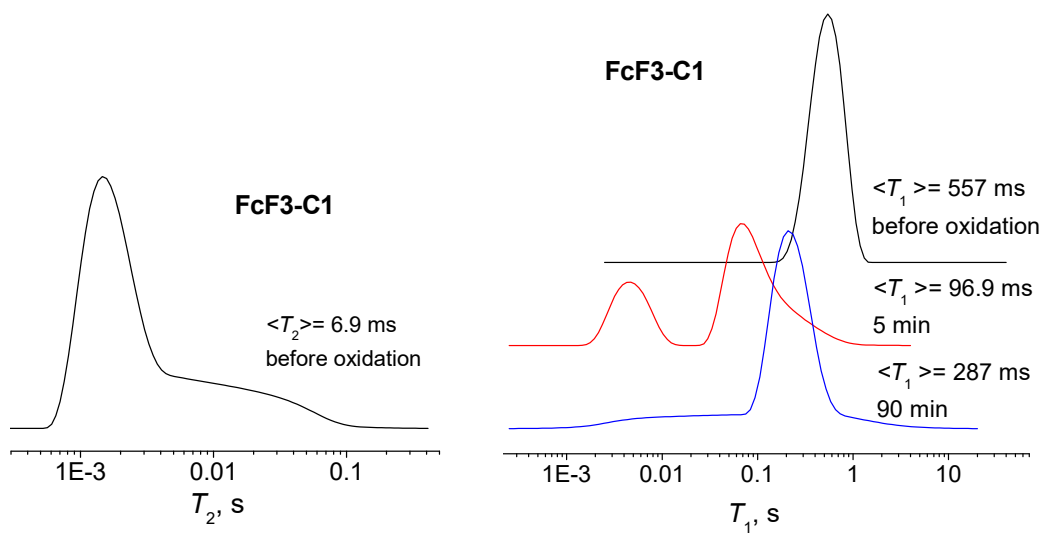


Figure S23. ^{19}F T_2 and T_1 relaxation time distributions in a **FcF3-C1**

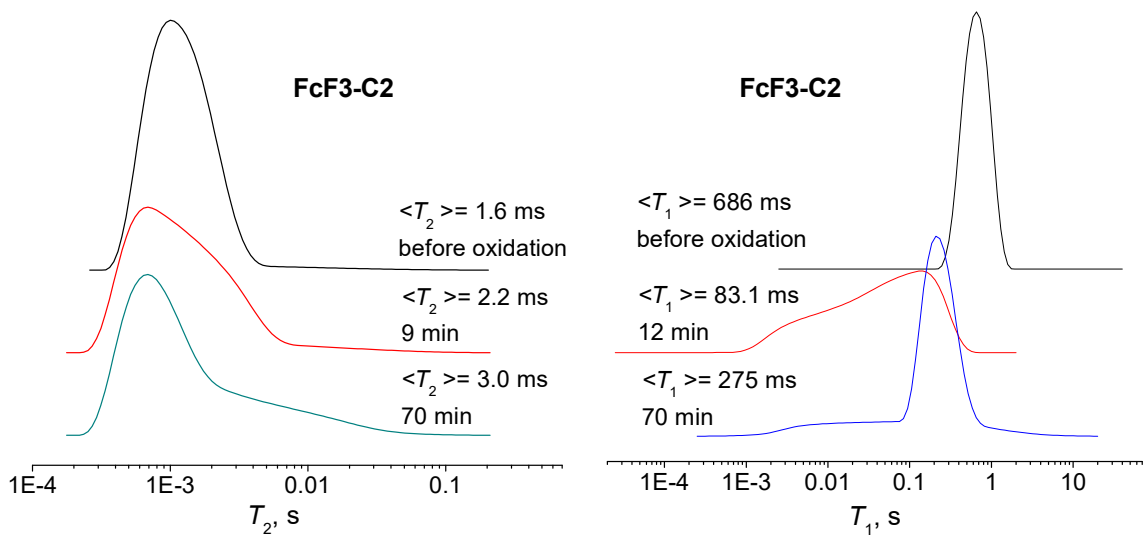


Figure S24. ^{19}F T_2 and T_1 relaxation time distributions in a **FcF3-C2**

5.2 ^{19}F UTE MRI images

The polymer concentration between $10\text{-}20\text{ mg} \cdot \text{mL}^{-1}$ was chosen for ^{19}F MRI experiments for lying within both the solubility limit of all polymers and a reasonable concentration window for potential bioapplications and drug delivery systems.

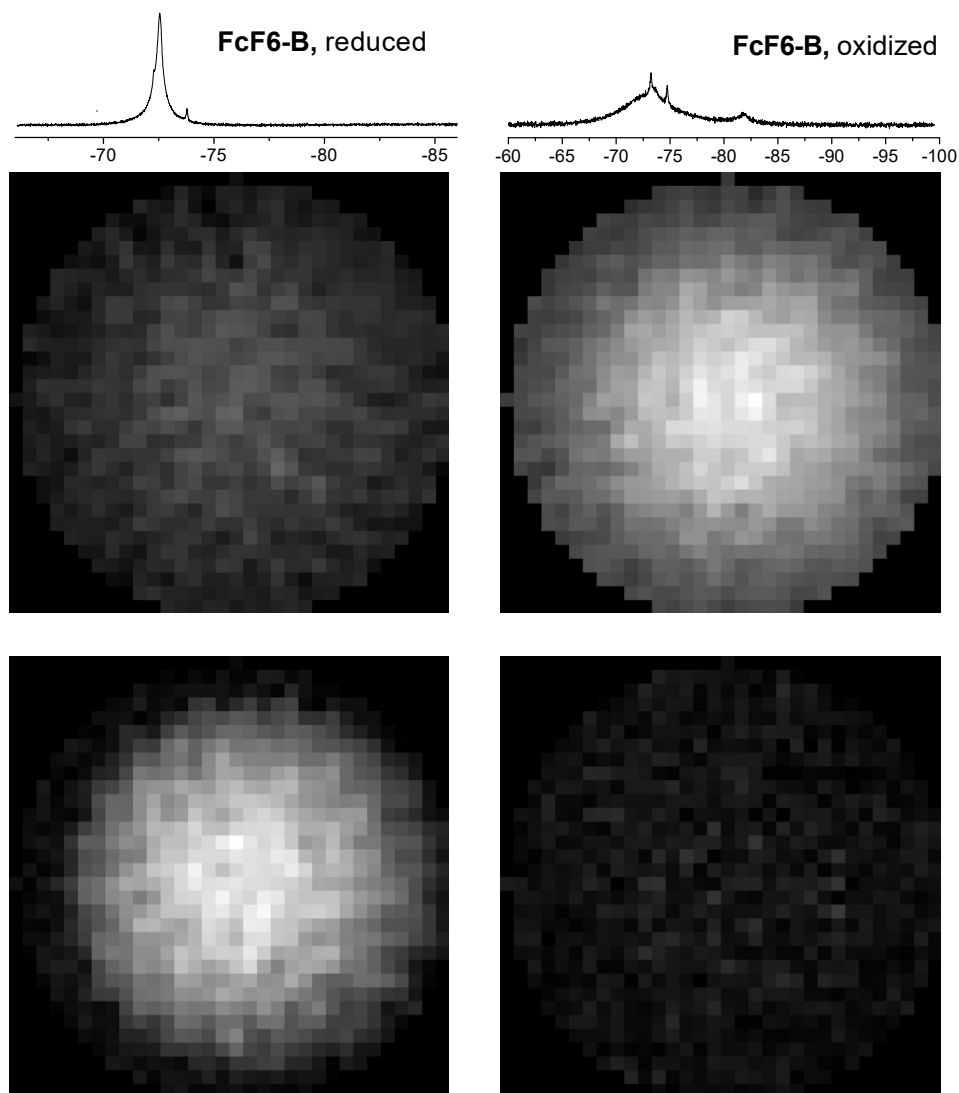


Figure S25. ^{19}F UTE images of a **FcF6-B** polymer sample ($19\text{ mg} \cdot \text{mL}^{-1}$) in citrate buffer (0.08 M , $\text{pH}=6.2$) before and after oxidation ($> 60\text{ min}$). *Top:* UTE parameters are set in favor of the oxidized sample with a shorter T_1 : acquisition delay $22\text{ }\mu\text{s}$; repetition time 10.5 ms ; flip angle 90° . The brighter image is displayed in the full range of a 16-bit gray scale, while the darker image is rescaled according to their true intensity ratio. *Bottom:* UTE parameters are set in favor of the reduced sample with a slower ^{19}F FID (a narrower spectral peak): acquisition delay $680\text{ }\mu\text{s}$; repetition time 11.2 ms ; flip angle 12° . The UTE provides a circular field of view (the inscribed circles in the square images), the tube position is slightly shifted with respect to the center.

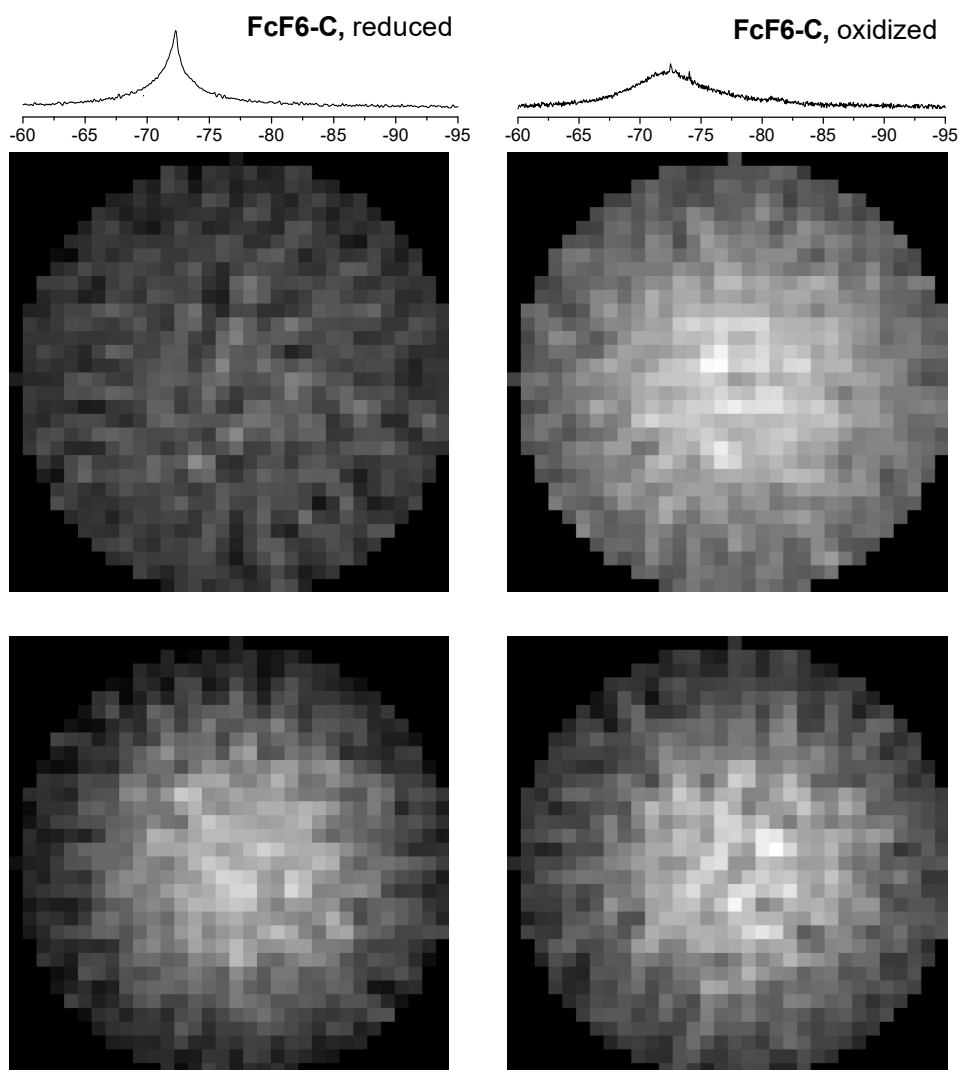


Figure S26. ^{19}F UTE images of a **FcF6-C** polymer sample ($10 \text{ mg} \cdot \text{mL}^{-1}$) in citrate buffer (0.08 M , $\text{pH}=6.2$) before and after oxidation ($> 60 \text{ min}$). *Top:* UTE parameters are set in favor of the oxidized sample with a shorter T_1 : acquisition delay $22 \mu\text{s}$; repetition time 10.5 ms ; flip angle 90° . The brighter image is displayed in the full range of a 16-bit gray scale, while the darker image is rescaled according to their true intensity ratio. *Bottom:* UTE parameters are set in favor of the reduced sample with a slower ^{19}F FID (a narrower spectral peak): acquisition delay $680 \mu\text{s}$; repetition time 11.2 ms ; flip angle 12° . The UTE provides a circular field of view (the inscribed circles in the square images), the tube position is slightly shifted with respect to the center.

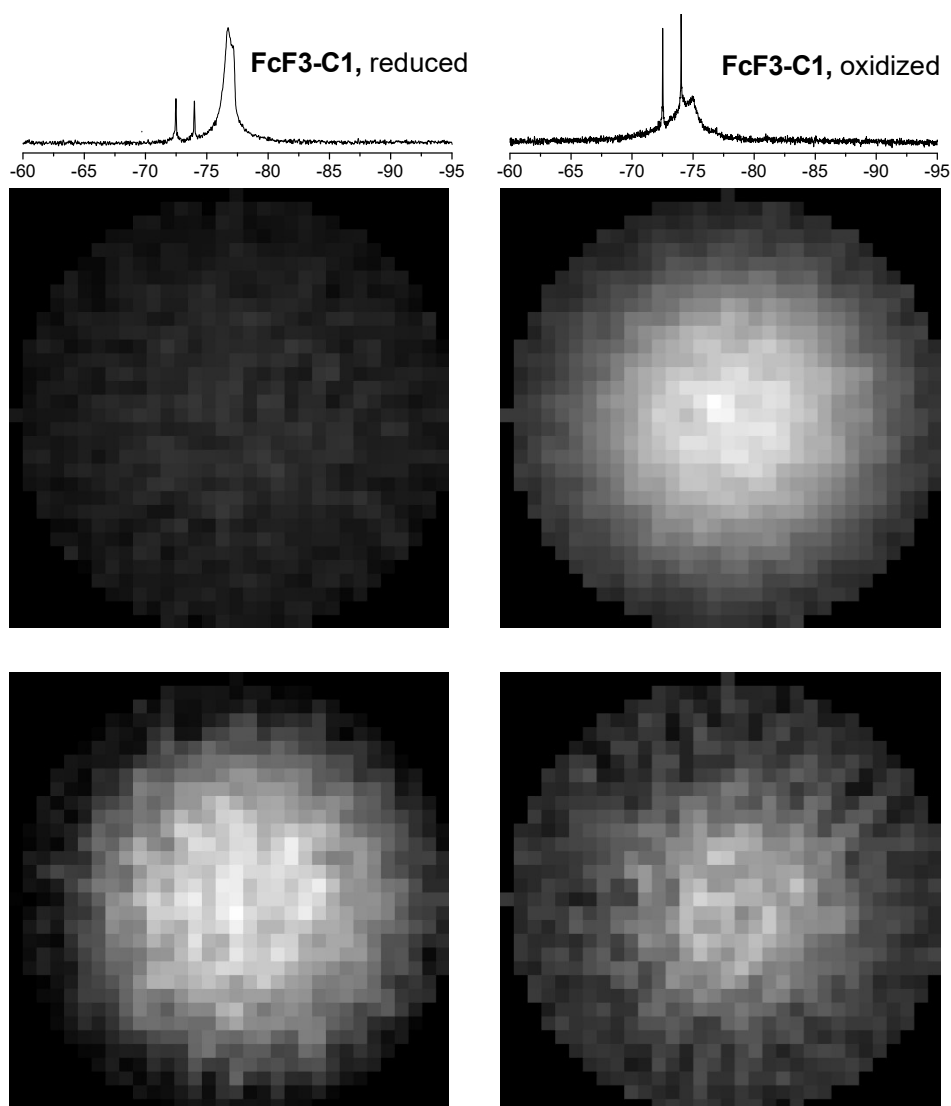


Figure S27. ^{19}F UTE images of a FcF3-C1 polymer sample ($18 \text{ mg} \cdot \text{mL}^{-1}$) in citrate buffer (0.08 M , $\text{pH}=6.2$) before and after oxidation ($> 60 \text{ min}$). *Top:* UTE parameters are set in favor of the oxidized sample with a shorter T_1 : acquisition delay $22 \mu\text{s}$; repetition time 10.5 ms ; flip angle 90° . The brighter image is displayed in the full range of a 16-bit gray scale, while the darker image is rescaled according to their true intensity ratio. *Bottom:* UTE parameters are set in favor of the reduced sample with a slower ^{19}F FID (a narrower spectral peak): acquisition delay $680 \mu\text{s}$; repetition time 11.2 ms ; flip angle 12° . The UTE provides a circular field of view (the inscribed circles in the square images), the tube position is slightly shifted with respect to the center.

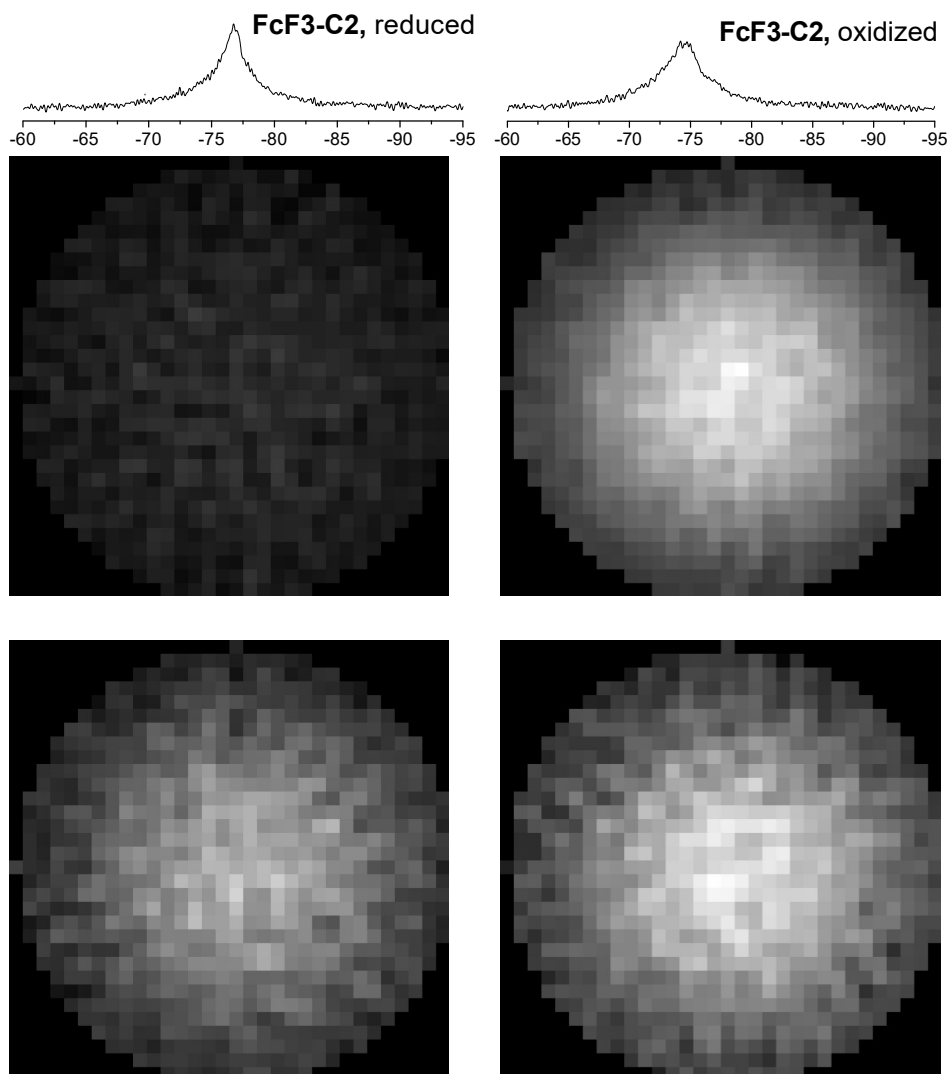


Figure S28. ^{19}F UTE images of a **FcF3-C2** polymer sample ($12 \text{ mg} \cdot \text{mL}^{-1}$) in citrate buffer (0.08 M , $\text{pH}=6.2$) before and after oxidation ($> 60 \text{ min}$). *Top:* UTE parameters are set in favor of the oxidized sample with a shorter T_1 : acquisition delay $22 \mu\text{s}$; repetition time 10.5 ms ; flip angle 90° . The brighter image is displayed in the full range of a 16-bit gray scale, while the darker image is rescaled according to their true intensity ratio. *Bottom:* UTE parameters are set in favor of the reduced sample with a slower ^{19}F FID (a narrower spectral peak): acquisition delay $680 \mu\text{s}$; repetition time 11.2 ms ; flip angle 12° . The UTE provides a circular field of view (the inscribed circles in the square images), the tube position is slightly shifted with respect to the center.

5.3 UTE imaging technique

UTE (ultrashort echo time) is a purely frequency-encoding MRI technique with radial k-space sampling trajectories (Fig. S29). In free induction decay (FID) acquisition mode, trajectories are taken starting from the center of the k-space, and their polar angle is incremented between 0 and 2π after each excitation α -pulse every TR (repetition time). To include the k-space center at each increment of the gradients, sampling begins already on the rising gradient ramps. The minimum acquisition delay (TE) is therefore limited by the duration of the RF pulse and of the refocusing gradient for slice selection and can be set as short as 0.1 ms or less. As a result, the UTE in FID mode becomes suitable for acquiring the k-space signal from samples with very fast T_2/T_2^* relaxation, for which echo-based sequences are not a viable option.

The radial sampling of the k-space requires a regridding procedure whereby acquired data are resampled on a uniform Cartesian grid prior to the Fourier transform. The regridding procedure relies on the actual k-space trajectories measured on a phantom with a long T_2 and high signal-to-noise ratio and with identical geometry.⁸ In particular, the k-space trajectory measurements are needed to account for transient currents during the rising gradient ramps at the beginning of the signal acquisition.

In the 3D UTE, the slice-selection gradient is replaced with the third read gradient. The k-space trajectories span a sphere with an even distribution of the “end points” with the density that is required by the field of view. The 3D UTE allows even shorter acquisition delays than the slice-selective 2D UTE because delay for a refocusing lobe of the slice selection gradient is avoided.

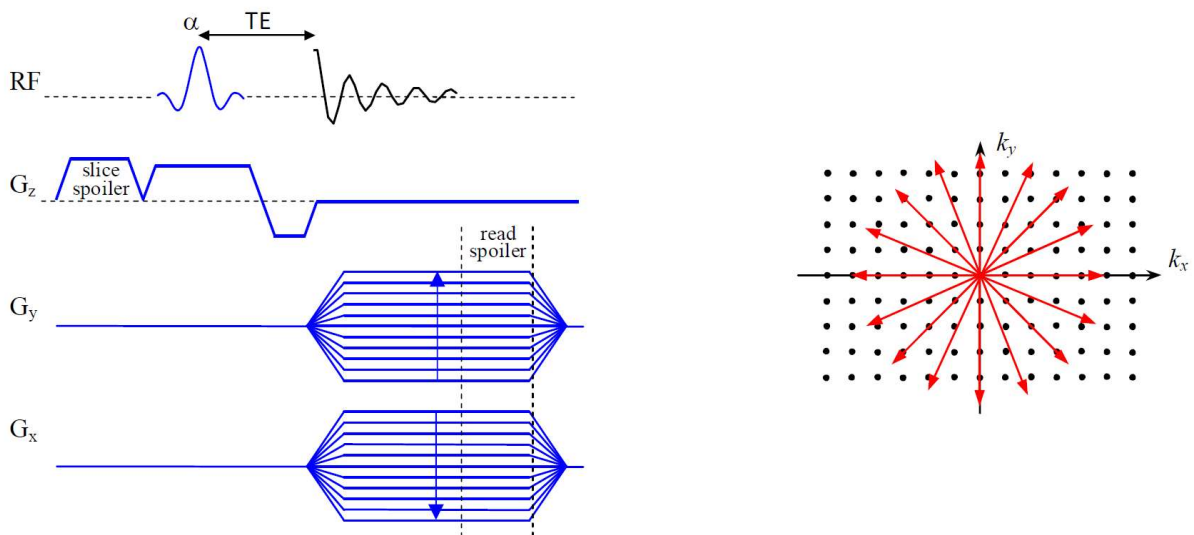


Figure S29. *Left:* Diagram of the 2D UTE pulse sequence in the FID acquisition mode (adapted from Bruker Paravision 6.0. Operating manual. Bruker BioSpin GmbH, 2014). *Right:* The radial k-space sampling employed for the 2D UTE – the ray direction is determined by the sum of two read gradients.

6 Cytotoxicity

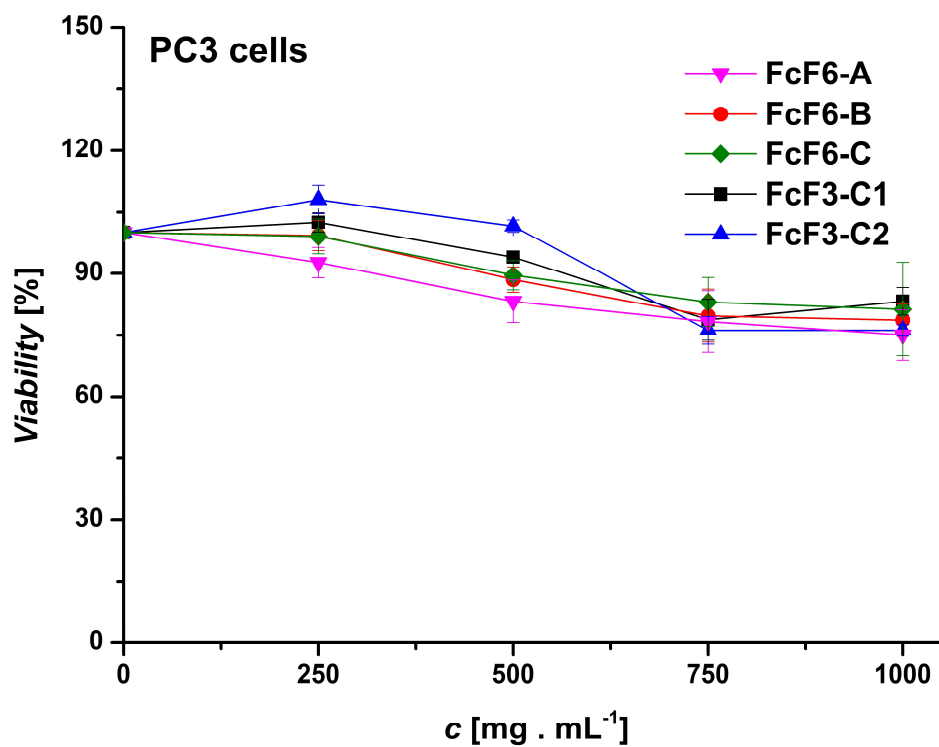


Figure S30. PC3 line viability (% of control) after incubating the cells with the polymers for 24 h

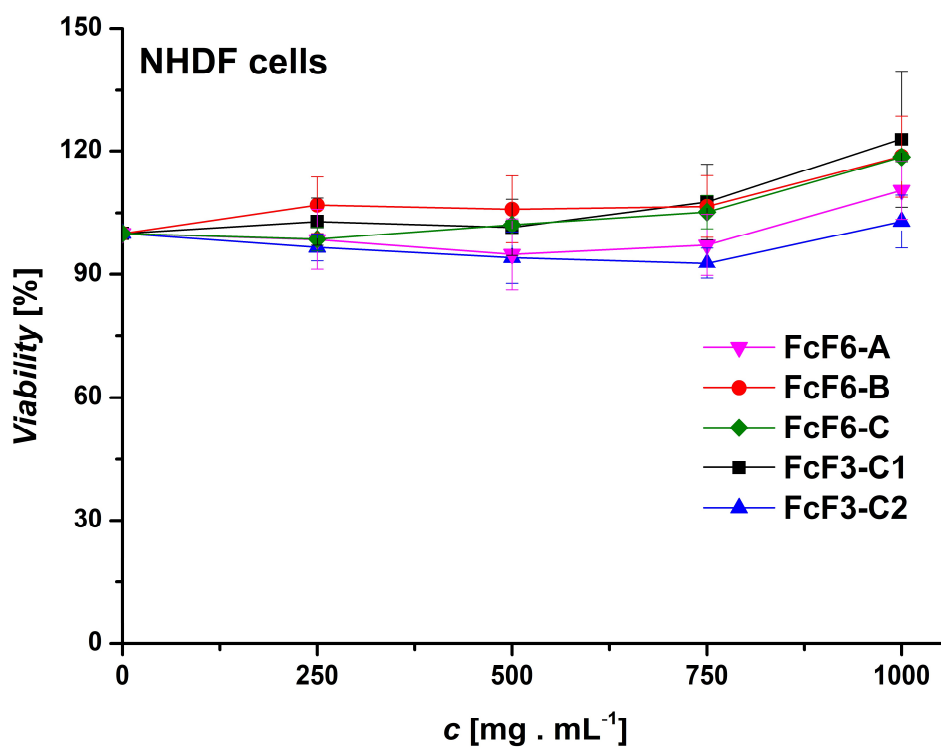


Figure S31. NHDF line viability (% of control) after incubating the cells with the polymers for 24 h

7 Quantum chemical study

We conducted a quantum chemical study to examine geometries of the complexes as well as the electronic structures of reduced (Fe(II)) and oxidized (Fe(III)) ferrocene derivatives to support the results of cyclic voltammetry measurements. The scope of the study is limited to compounds **1**, **3**, **5**, **6**, and **7** which are considered the redox-responsive moieties of the studied polymers. We selected Kohn-Sham DFT (at B3LYP/def2-TZVP level) as the most suitable method for obtaining molecular geometries. Then, we performed an additional DLPNO-CCSD(T) single point energy calculation to obtain improved electronic energies of the compounds, which were used to model redox behavior. Solvation was considered implicitly, using the SMD formalism.

7.1 Method

We performed the quantum chemical calculations using ORCA 4.2.1. software package.^{9, 10} Initial and final geometries and their properties were constructed and analyzed by Avogadro 1.2.0^{11, 12} and Chemcraft (version b595),¹³ respectively. Visualizations were rendered in VMD 1.9.3.¹⁴ All geometry optimizations were conducted at B3LYP/def2-TZVP level^{15, 16} with D3BJ dispersion correction^{17, 18}, and inclusion of SMD implicit solvent model of dichloromethane.¹⁹ RIJCOSX density fitting scheme was applied in all calculations,^{20, 21} with corresponding def2 auxiliary basis sets.²²⁻²⁴ All procedures were conducted under the “VERYTIGHT” criteria, as applied in ORCA 4.2.1 and integration grids were expanded to the “GRID6” and GRID6X” parameters. All geometries were verified by a subsequent calculation of their analytical Hessians.^{25, 26} Vibrational frequencies were obtained without any imaginary frequencies.

Compounds **1**, **3**, **5**, **6**, and **7** were pre-optimized (to their minimum energy geometries) in their neutral singlet and cation doublet multiplicities, in vacuum, and thereafter perturbed by implicit solvent model of dichloromethane. Subsequent optimizations used the optimized ground state singlet geometries as initial geometries.

Properties were collected from calculations perturbed by implicit solvent models, per experimental conditions. Redox properties, including calculations of single electron oxidation potentials were calculated using an additional single point DLPNO-CCSD(T)^{27 28} energy calculation for a more accurate treatment of the electronic energy, which was added to the DFT-calculated $\Delta G - E_{el}$ energy to give a more rigorous ΔG . Internally referenced isodesmic model, which was found suitable for metallocene-type compounds in previously published works,^{29 30} was applied to calculate oxidation potentials (**Table S4**), referenced to compound **1**.

7.2 Results: Electrochemical properties

Calculated single-electron oxidation of **1**, **3**, **5**, **6**, and **7** leads to the proposed metal centered oxidation of Fe(II) species to Fe(III) which is supported by Löwdin atomic charges and spin population of the optimized geometries (Tables S2 and S3). Calculated oxidation potentials in dichloromethane, based on an internally referenced isodesmic model are consistent with the experimentally determined oxidation potentials by cyclic voltammetry in the expected error margin³¹ (Table S4).

Table S2. Löwdin atomic charge analysis of **1**, **3**, **5**, **6**, **7** Fe(II)/Fe(III) redox pairs, listed for redox non-innocent atoms, in atomic units

Cmpnd.	Reduced compound – Fe(II)			Oxidized compound – Fe(III)		
	Fe	N	O	Fe	N	O
1	-0.16	-	0.08	0.09	-	0.08
3^a	-0.15	0.13	0.23 ^b	0.08	0.13	0.23 ^a
	-	-	0.22 ^c	-	-	0.23 ^b
	-	-	0.02 ^d	-	-	0.02 ^c
5	-0.15	-	0.12	0.10	-	0.12
6	-0.17	-0.13	-	0.16	-0.13	-
7	-0.17	0.17	0.03	0.05	0.17	0.04

^aCompound **3** contains more than three oxygen atoms; they are listed in 3 lines of the table and references with a/b/c; ^batom 32; ^catom 47; ^datom 48 (as listed in coordinates of the optimized compounds). Symbol “-” indicates that no such atom is present in the molecule.

Table S3: Löwdin spin population analysis of **1**, **3**, **5**, **6**, and **7** Fe(II)/Fe(III) redox pairs, listed for redox non-innocent atoms, in atomic units

Compound	Fe	N	O	Rest of the compound ^a
1	1.17	-	0.00	-0.17
3	1.18	0.00	0.00 ^b	-0.18
5	1.18	-	-0.01	-0.18
6	1.17	0.00	-	-0.17
7	1.18	0.00	0.00	-0.18

^aCalculated as (signed) sum over all atoms; Fe, N, O subtracted; ^bsum over all O atoms. Symbol “-” indicates that no such atom is present in the molecule.

Table S4. Calculated change of Gibbs free energy of Fe(II)/Fe(III) single oxygen oxidation ΔG , first oxidation potentials E_{ox} , orbital energies of HOMO ϵ_{HOMO} and SOMO ϵ_{SOMO} , of **1**, **3**, **5**, **6**, **7** Fe(II)/Fe(III) redox pairs in atomic units (au)

Compound	ΔG_{ox} [V]	E_{ox} [V]	ϵ_{HOMO}^a [au]	ϵ_{SOMO}^b [au]
1	5.03	0.25 ^c	-0.3443	-0.3518
3	4.95	0.17	-0.3395	-0.3519
6	4.90	0.12	-0.3413	-0.3436
7	4.95	0.17	-0.3442	-0.3510

^aParent Fe(II) species; ^boxidized Fe(III) species; ^cselected internal standard

7.3 Results: Optimized geometries in dichloromethane

Compound 1 - reduced form - Fe(II)

Fe	-0.05028766315935	-0.02789331648786	-0.02802425256427
C	0.10896415887957	-0.44583144344463	1.95719574023734
C	1.39544709895607	-0.20652722966764	1.37150519809557
C	1.58932318610113	-1.16745912077702	0.32415324931611
C	0.42764606898856	-1.98733616277794	0.26612877627689
C	-0.48336146886173	-1.54233302822558	1.26894636406072
H	-0.34444780310547	0.11222660883658	2.76058775064368
H	2.45497454029029	-1.23684856256233	-0.31448773170160
H	0.25158284811116	-2.77971392580924	-0.44497669415147
H	-1.46989882185449	-1.93887308271432	1.45315268341469
C	0.20647163182847	0.81226147497361	-1.86839391826927
C	-0.98078065936448	0.02009999803841	-1.83822245671380
C	-1.83538836606437	0.54493700541192	-0.82209558047982
C	-1.17537318764411	1.66019124893427	-0.22309092477551
C	0.08519781967128	1.82488968857221	-0.87192608598366
H	1.06063228954982	0.65140321092354	-2.50825216705242
H	-1.18159933744471	-0.84649596473147	-2.44961196268431
H	-2.79560657698083	0.14546927642343	-0.53296859635869
H	-1.55046540591690	2.25301856557339	0.59686110661525
H	0.83522355311674	2.55916644377722	-0.62542698427028
F	4.08831606205514	-1.00191610163422	1.93370401333022
F	2.90841072659316	-0.70979923114584	3.72718717712048
C	3.48666707884212	-0.07433409936021	2.69492446069962
F	4.46388438134355	0.71163439613755	3.19721446102274
H	3.88572953413853	1.81725344650892	1.03215590160587
C	2.46257401994827	0.74046699697260	1.83969259567046
O	3.14382246225044	1.27049998139549	0.72583171916965
C	1.90036817228510	1.92501634792027	2.67860206216094
F	1.43236954181106	1.54247876913524	3.88112504155814
F	2.86505584767470	2.84497827718816	2.89974810330966
F	0.90756126796124	2.55261553261548	2.03714895069708

Compound 1 - oxidized form - Fe(III)

Fe	-0.04933383989702	-0.03631444306547	-0.02830031081991
C	0.13954968867226	-0.54709876262911	2.02547754177001
C	1.40199612495591	-0.25330710714775	1.42755748446632
C	1.60199681669277	-1.18567972149890	0.35552462813589
C	0.46197344436918	-2.03701730398210	0.30417327734184
C	-0.43310398017197	-1.63890108783625	1.33154089291709
H	-0.31876222831736	-0.00895513991847	2.84048236695102
H	2.46835315262976	-1.22530691156295	-0.28465044619083
H	0.29424691304666	-2.82762906389554	-0.41131811697716
H	-1.40966409892100	-2.05881627857871	1.52112239185859
C	0.21409200788562	0.77869426275882	-1.89035399039537
C	-1.02727471330315	0.07127438293232	-1.85359523033925
C	-1.85425983364001	0.69115359953956	-0.87523879782968

C	-1.13452110895843	1.77210082642615	-0.30848331554060
C	0.14359848947737	1.82991301469651	-0.92742832587838
H	1.05700084883762	0.55532495688166	-2.52574525496606
H	-1.28868889650968	-0.78984582817662	-2.44953241505817
H	-2.84141009975697	0.36629749741361	-0.58200896162240
H	-1.47400369055951	2.40446607621909	0.49776450212119
H	0.93653736744892	2.51823077618075	-0.68274597916240
F	4.09245211041016	-0.97201497919137	1.90695656474459
F	2.99690905361108	-0.66415228960955	3.75276011229476
C	3.52610203728432	-0.04609428358896	2.69387779175019
F	4.49242741084432	0.78376488410416	3.11080155295228
H	3.81548708646845	1.80539169361247	0.97611648985304
C	2.44531023848743	0.73903335874907	1.87400360232260
O	3.04156045934583	1.27772704599778	0.72116645488985
C	1.84313548795815	1.90292953180956	2.71933145952218
F	1.37863776511047	1.49461045996772	3.90599194468901
F	2.75852216320509	2.85466818878312	2.92018120458115
F	0.81414682329376	2.46879664460937	2.05295788161855

Compound 3 - reduced form - Fe(II)

Fe	-3.12086992494919	-1.71368803824278	-0.09165070460353
C	-1.81990699352464	-0.98656147449244	1.33795950965031
C	-1.82179063420696	-0.13723984290567	0.18140161716552
C	-1.39530503966386	-0.93938881789715	-0.92973091107007
C	-1.14543781119337	-2.25126314267368	-0.45921873612957
C	-1.40837529388061	-2.28161402135584	0.93619716029724
H	-2.09874911513746	-0.70812299416046	2.33880018449487
H	-1.27663086162971	-0.60794578785241	-1.94533915235830
H	-0.84712556556674	-3.08866927952720	-1.06906384577970
H	-1.34920471951078	-3.14709479526665	1.57609972636432
C	-4.76385398574183	-1.42708357369211	-1.32093389678769
C	-4.34241504070604	-2.78496497509111	-1.37759280124000
C	-4.42272691512217	-3.32614615826945	-0.06374930338080
C	-4.89814496086309	-2.30339557467920	0.80482843244687
C	-5.10821999464852	-1.13120390370943	0.02916321257621
H	-4.78947676094279	-0.73752669786046	-2.14860397719488
H	-3.98665007882402	-3.30235238983067	-2.25434852835800
H	-4.13824057969533	-4.32441565393374	0.22815857618678
H	-5.03675480767677	-2.39105560972588	1.87051643730045
H	-5.43659904463235	-0.17746879215191	0.40528160591972
H	8.57531396919777	-2.24746729044781	2.22494199271523
H	10.39930669903180	-0.99150808712758	1.11491372198649
C	8.36499668387408	-1.64522795078230	1.34994685396503
C	9.39002887074202	-0.94000633417078	0.72593842994522
C	7.07059310704393	-1.58269146478936	0.84609191075067
H	6.27441124088292	-2.13672242968752	1.32941004030721
C	9.11574906228344	-0.17303824572996	-0.40241549422233
F	-1.63086714197649	1.69183507755347	2.51745572703031
H	9.91087082883444	0.37306899695668	-0.89456328012693
C	6.78653678029477	-0.81455512508864	-0.28311772596117
C	7.81999992847138	-0.11179827770279	-0.90282366324658
H	3.46473899364899	2.05460299188825	0.87968793736026
O	4.71356125507889	0.35499106892275	-0.13621129822897

F	-3.66956347187719	1.35441321443513	1.86083074016040
C	-2.50071269875699	1.91777044872848	1.51551207355141
H	0.60166305041146	0.38363352115063	0.05510234356944
H	0.58849594736526	1.43893725454006	1.48483758043292
N	2.95041127546720	1.69360995711609	0.09302111240495
C	5.38968410033069	-0.73271449241993	-0.81914379184643
C	0.52851147709528	1.41549063538715	0.39537951625717
F	-2.69727080277415	3.24546667743320	1.47279562797102
C	3.48747002269621	0.67463141570229	-0.61317610540369
H	7.60766541060640	0.48220302401668	-1.78394930478202
C	-1.93012131393467	1.36868073924253	0.16659013681340
H	4.83703303035359	-1.65480167030569	-0.63677338951169
C	1.64776133289682	2.24113291414593	-0.22252553139001
H	5.38808261241184	-0.53208252375321	-1.88936596520083
O	-0.69280047075318	2.01600999874831	-0.06084338754887
O	2.95562570160163	0.12057873755770	-1.55860018562989
H	1.52056875453209	2.26152778063355	-1.30488504201559
H	1.60885191735668	3.26505509215061	0.14726451090317
F	-4.11118773811612	1.64235506159815	-0.82889541614780
C	-2.80878396437210	1.91165718808829	-1.00649297896673
F	-2.69639504050560	3.24282750070278	-1.13946123626324
F	-2.43681928132747	1.38039211862524	-2.18104206513125

Compound 3 - oxidized form - Fe(III)

Fe	-2.64552872131286	-1.63808901004169	-0.21632699399730
C	-1.35102958580100	-0.92478688077557	1.21915833300470
C	-1.55260965351423	0.06254638762421	0.19228100618420
C	-1.07663117157870	-0.51001809936876	-1.03620583991107
C	-0.59299698745453	-1.80823982212525	-0.76461337670039
C	-0.76443255481001	-2.06925050168111	0.61680949786027
H	-1.60535723573426	-0.83488342170412	2.26251209278874
H	-1.09466169908683	-0.03991018545169	-2.00543930096055
H	-0.22664704132927	-2.50557034702273	-1.50194001863147
H	-0.54541726744002	-2.99867057090408	1.11968905110076
C	-4.52234056256696	-1.43378671049820	-1.18244131542235
C	-3.83955871925777	-2.60068679005183	-1.61871730485106
C	-3.60998906596740	-3.42751632654288	-0.47691408185858
C	-4.15225081189135	-2.75840457294728	0.66246392868412
C	-4.71415203836348	-1.52980321163404	0.22013498886162
H	-4.79576800772375	-0.59483425766260	-1.80329574530689
H	-3.51692866892595	-2.80543166136477	-2.62797026547925
H	-3.09106484932467	-4.37357473812344	-0.47200805813715
H	-4.11044114868553	-3.10417945295600	1.68379627575115
H	-5.15987369988282	-0.77756900181890	0.85195737960062
H	7.93227731136689	-1.54684184444655	2.86611967706367
H	9.85086811247744	-1.17904003007260	1.33843891067226
C	7.75977425285796	-1.35505215172521	1.81320931330580
C	8.83751247744662	-1.14891002430588	0.95467114790370
C	6.45981731127881	-1.31982644409645	1.31803834433360
H	5.62021340094488	-1.48398436855105	1.98548316728925
C	8.61106914245155	-0.91012518544029	-0.39899771893356
F	-1.09197736569901	1.63714388382488	2.61087216713783
H	9.44746504915663	-0.75476838759662	-1.07085677757398

C	6.22439624125809	-1.07842257998767	-0.03694421534094
C	7.30983990248444	-0.87545345697421	-0.89140828043168
H	3.43101601106774	2.50743101875858	-0.31419328816667
O	4.37192924617319	0.35870811572568	-0.45857356141424
F	-3.18594723927656	1.12402380784428	2.35972090139326
C	-2.18385486947825	1.87033048376212	1.85841594438752
H	0.61463286033911	0.97634630105232	0.54644672513369
H	0.82430128730142	2.64501914282178	1.12437602869142
N	2.75786474312848	1.87215805030693	-0.71568880344923
C	4.82242452221171	-1.02306594786283	-0.56274416265401
C	0.52933361081146	2.02835574800883	0.27391425111280
F	-2.51101336663999	3.15772607330861	2.02046191768786
C	3.08563710140110	0.56342710922423	-0.82291984271273
H	7.13354689405150	-0.69319393993991	-1.94639623866937
C	-1.87972575174402	1.53766482160305	0.36431290992482
H	4.14837667516510	-1.65023206341171	0.02137635755739
C	1.39723979664963	2.31389513513655	-0.94540599734933
H	4.77209563031743	-1.32370048448877	-1.61001501440448
O	-0.83267391669663	2.35660844925003	-0.08925010547807
O	2.32903825301968	-0.31592859897212	-1.20820965999014
H	0.99609091060626	1.78216060666184	-1.80866372817239
H	1.41148986167054	3.38052173264637	-1.16702932454022
F	-4.24706859050079	1.51680049567841	-0.08140523659311
C	-3.07408324963259	1.99972005482334	-0.52681375555703
F	-3.17536936690706	3.33164918797540	-0.56847346854711
F	-2.91192539841190	1.57257046450957	-1.79118983619666

Compound 5 - reduced form - Fe(II)

Fe	0.04303286843321	-0.00652165853149	0.04921546824370
C	-0.03203165384276	-0.09867878637329	2.07039990135512
C	1.33267224595823	-0.14549647004764	1.59371158520841
C	1.45596926728511	-1.29224924269111	0.72652933310240
C	0.19904709798105	-1.94690927071855	0.70155169740750
C	-0.71050745787430	-1.21778194993817	1.52560159626082
H	-0.46066076270615	0.64570980486659	2.72166728051459
H	2.34751318629602	-1.58091531268649	0.19341802806379
H	-0.04204165757139	-2.82459032397579	0.12223810276560
H	-1.75304966044386	-1.45163319283408	1.67560477910613
C	0.58799524892069	0.52002563755777	-1.84716848365848
C	-0.67462542297968	-0.14666732941246	-1.85033834367625
C	-1.57180059702363	0.60241870992370	-1.03121566034149
C	-0.86508294195004	1.73133458834368	-0.51872448759600
C	0.46686053309068	1.68018929896631	-1.02772226944849
H	1.48364497244453	0.18841310906177	-2.34930088752015
H	-0.90107364642899	-1.07466925748674	-2.35240497324756
H	-2.59375601278138	0.33871330831896	-0.80617406507302
H	-1.25809171319341	2.47390849763052	0.15810723674347
H	1.26045550639489	2.37511152316170	-0.79770673636464
O	3.48627759906279	0.79455152651737	1.26941065560029
F	0.93723068121673	2.77307813627825	2.15176037614825
C	2.35952803912427	0.85795780796967	1.74107990418242
C	2.01609868744530	2.10434754316361	2.60758909873916
F	3.03829450763960	2.96700392219844	2.63821915318124
F	1.75281108550251	1.73720638073746	3.88171671030318

Compound 5 - oxidized form - Fe(III)

Fe	0.01544305804483	-0.02208585745307	0.02377705087255
C	-0.01614921971686	-0.12937268021431	2.10637440407036
C	1.32377838051057	-0.10795211133535	1.58596355324158
C	1.48840954991303	-1.27565743267329	0.76411355678223
C	0.26979195898314	-1.99796285798753	0.79165348878444
C	-0.65039098632886	-1.29556385157555	1.61356316003104
H	-0.46453868916096	0.61506654430507	2.74566126867511
H	2.38914792731097	-1.53397104254306	0.22877086272583
H	0.06075029525435	-2.90616562697780	0.24609320992213
H	-1.67733957726131	-1.57714476036463	1.79423429107813
C	0.53840705098633	0.49675194671596	-1.90449395597260
C	-0.75768260446303	-0.09377251439030	-1.93931641551383
C	-1.62427004196532	0.69274953738926	-1.13648069848533
C	-0.87451191372350	1.76912228860698	-0.59453230419368
C	0.46710023390354	1.65516399998140	-1.06998159030684
H	1.41923482971927	0.12935774687601	-2.40852785485742
H	-1.02716060775207	-1.00374731581184	-2.45443856965780
H	-2.66152204691797	0.47616402125974	-0.92767356179570
H	-1.24391836755695	2.52313511896699	0.08384401230327
H	1.28325708261023	2.32116113098388	-0.83448745033506
O	3.47228296316953	0.80980248683888	1.25375357266483
F	1.00666778447279	2.79458602206590	2.12353470681812
C	2.39322162004681	0.90295865436120	1.77659292142902
C	2.04903627950432	2.11871144414634	2.67960382707893
F	3.07031411863257	2.94124606170096	2.80424759204468
F	1.65535092178454	1.70127504712814	3.89521492259599

Compound 6 - reduced form - Fe(II)

Fe	-0.01506385620100	-0.02298551273119	-0.00051229003919
C	0.16123162727252	-0.28510422611981	2.01219852182652
C	1.44932348317061	-0.14241417628041	1.40252563929633
C	1.58394289546674	-1.18961892782643	0.43275738762927
C	0.38947702960085	-1.96724862265983	0.44486055596439
C	-0.49105256454806	-1.40538580013564	1.41672944576959
H	-0.26217475078119	0.35968019692136	2.76633075607187
H	2.44066337548973	-1.34458878164631	-0.20629193844677
H	0.17432052626935	-2.80847485856059	-0.19637422901961
H	-1.49052679328522	-1.74550195140153	1.64161099959172
C	0.26908800520825	0.67486901593471	-1.89438554789774
C	-0.96419616006167	-0.03898833375452	-1.80401838916409
C	-1.77369142070190	0.60255580565349	-0.81820473444643
C	-1.03972188709099	1.71098117379436	-0.29754739466817
C	0.22253482971343	1.75548455066466	-0.96378898002764
H	1.10364967737574	0.42155136145863	-2.53045957267528
H	-1.22569414391485	-0.92687659411972	-2.35954072608945
H	-2.75496698861678	0.28548059470883	-0.49901938257068
H	-1.36746034203433	2.37720859328942	0.48558890868497
H	1.01539729409510	2.46257966831240	-0.77515194739286
H	4.11072021801354	-0.51637933977323	1.92800114274189

H	3.21652817859900	-0.39486779901496	3.27634175046615
N	3.64571814610696	0.15363946347464	2.53405140437522
C	2.57787098824388	0.79210579420892	1.74965596245344
H	3.02679574648633	1.17265104607578	0.83140100282098
F	1.71288882079755	1.72094842319678	3.77797598705821
C	2.13475045710398	2.02512504777855	2.52401837449160
F	3.14544812299876	2.91183126267516	2.66668134548574
F	1.12437448522364	2.69117392587644	1.92711694771002

Compound 6 - oxidized form - Fe(III)

Fe	-0.00399584429301	-0.00972359943693	-0.04653102683607
C	0.27336755598005	-0.37924917646096	2.00541193168974
C	1.56355216142739	-0.20279635228789	1.42687831496233
C	1.69327749692988	-1.16508259109297	0.38324655605143
C	0.51101795916131	-1.95860924360941	0.34126396167453
C	-0.37320488556757	-1.46685290795895	1.34842766227916
H	-0.15002680869951	0.22256345275338	2.79447296333375
H	2.54754959611121	-1.26783417467187	-0.27019053444892
H	0.31680529051452	-2.77423354530053	-0.33809746025482
H	-1.36080737026497	-1.84133740022293	1.57004619988231
C	0.04663917889661	0.72799130640084	-2.03918333936142
C	-1.14359423734805	-0.00836265757347	-1.78344382395118
C	-1.83554070084873	0.63510428530803	-0.71240050695164
C	-1.05919672465379	1.76402914931309	-0.30909613638357
C	0.09507880609260	1.81839956385018	-1.13688436446999
H	0.80266797348310	0.47493852176622	-2.76730370606620
H	-1.45817365448094	-0.90325837788085	-2.29831613208967
H	-2.77482972024443	0.32252933522217	-0.28289095008393
H	-1.29269633984521	2.44712789121479	0.49271228127631
H	0.89743907978011	2.53474973749978	-1.05164960837113
H	4.08940696252448	-0.65060160010870	2.50954419156031
H	2.97649917772505	-0.26204181568672	3.66951163714305
N	3.51468714695952	0.09310686632189	2.88646952891325
C	2.68136812468785	0.71465179224030	1.87390232986999
H	3.31238764357774	0.95767694932222	1.01666472498531
F	1.48529637652605	1.89662465199718	3.56301634693919
C	2.19212162660902	2.05794597462881	2.42304087745216
F	3.20341806109908	2.88159918342983	2.67151098859376
F	1.36966106816063	2.67037778102346	1.53241909266194

Compound 7 - reduced form - Fe(II)

Fe	-0.29004903030655	-0.02176608985851	-0.06435191009430
C	0.05773486332449	-0.21070299800391	1.93352880006718
C	1.28277770206175	-0.23402120998085	1.19169004778783
C	1.21544037378364	-1.33253439610079	0.27326969755035
C	-0.04223895319677	-1.97820029525333	0.44787270189782
C	-0.75824024509110	-1.28254291609956	1.46696350202758
H	-0.21884517806063	0.50670452739378	2.68975657792811
H	1.98368672383030	-1.60631156435891	-0.43399166883478
H	-0.40439732462830	-2.82108457982642	-0.12057714606716
H	-1.75812647576685	-1.50534986323635	1.80677314524196

C	-0.12422770148377	0.55792151023731	-2.01078055221659
C	-1.40645816166563	-0.02140647903972	-1.76825159828749
C	-2.05017332635252	0.74286649688558	-0.74843007804008
C	-1.16490921994685	1.79300634546835	-0.35894039252411
C	0.02462813937633	1.67849792525342	-1.14027029277852
H	0.61644504814959	0.19154712037574	-2.70523988274078
H	-1.80491656787647	-0.90291652020168	-2.24716033686338
H	-3.02120820495156	0.54102280721800	-0.32224396534727
H	-1.34825625858052	2.52365111362842	0.41370913902920
H	0.89725004070470	2.30872560142006	-1.06374105870159
F	1.27705378437007	2.67086708113937	1.61860546034890
F	1.94638706917084	1.67126029022412	3.42656264937401
C	2.26503615572907	1.91603315809067	2.13336159525792
F	3.37769645674880	2.68298558161645	2.15056042490426
C	2.50270531701637	0.63063798178693	1.34099073016475
H	2.87032218340064	0.94324904745078	0.36295651992802
H	3.37168535305218	-0.66367493944425	2.78361262876254
N	3.58852427895501	-0.10063744328271	1.97378293646504
C	4.84327511392921	-0.13408860688431	1.46680421838258
O	5.16151699251688	0.49687061912540	0.45102175855694
H	5.39116108204807	-1.45784847252585	3.09900749581232
C	5.82382554045490	-0.99604388624445	2.21184898012770
H	6.18255126474674	-1.77586448780665	1.53676513926910
H	6.67894916453787	-0.38272745916614	2.50149473361191

Compound 7 - oxidized form - Fe(III)

Fe	-0.24119430373086	0.01670790309728	-0.08698580892616
C	0.12594954424229	-0.23749882214815	1.97457642433992
C	1.37487361670341	-0.18142427013523	1.29652408416001
C	1.38953757962765	-1.22479931037472	0.32428743771438
C	0.15777032861053	-1.93461365169354	0.41145709413304
C	-0.62935403803278	-1.31704854368416	1.43214443910334
H	-0.20967926235398	0.44432430117233	2.74059078892874
H	2.20743715652881	-1.41068361517051	-0.35618121117353
H	-0.13169732986477	-2.78038945680742	-0.19296703638200
H	-1.62257026425056	-1.60784240261870	1.73811764508720
C	-0.09871239451024	0.71711321122480	-2.06651138171459
C	-1.30995448358258	-0.00358417962209	-1.84655234435523
C	-2.04482595402027	0.67882948375457	-0.82712044072906
C	-1.27886023592180	1.81241748531533	-0.42460297762713
C	-0.08677104846629	1.83413946550195	-1.19348686589726
H	0.68939298663390	0.44140691132380	-2.75093008953924
H	-1.61395695093508	-0.90453919215536	-2.35675800082946
H	-3.00481334277983	0.38710209053251	-0.42999199921257
H	-1.53899988087416	2.51421272619751	0.35304880858316
H	0.71814424782566	2.54541853350980	-1.08595746099851
F	1.16276371628620	2.66156129145528	1.70889149740413
F	1.84599637576577	1.73600980065951	3.55748968362613
C	2.20396304452666	2.01613130719613	2.28359562026846
F	3.23612794988727	2.85777048485713	2.32454316748178
C	2.54843739629247	0.74964397684566	1.50612881014665
H	2.92554499473255	1.05939783131653	0.52819330893457
H	3.67336069770165	-0.00302183479625	3.15810212131308

N	3.64476476021646	0.06259500950842	2.15145122489913
C	4.58630236108297	-0.57006479520003	1.37103318427102
O	4.47283423035148	-0.57604076148606	0.15458631570485
H	5.60352908417080	-1.21042712306351	3.18901227426631
C	5.72874592282695	-1.21749323598876	2.10597486308711
H	5.83642949229310	-2.24393824309270	1.75463943178115
H	6.64608800301657	-0.68325237543135	1.85061639215056

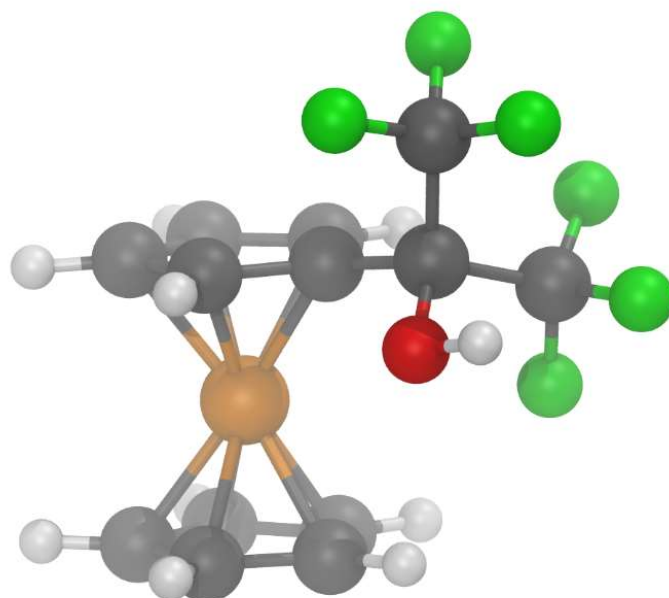


Figure S32. Optimized structure of compound **1** (reduced)

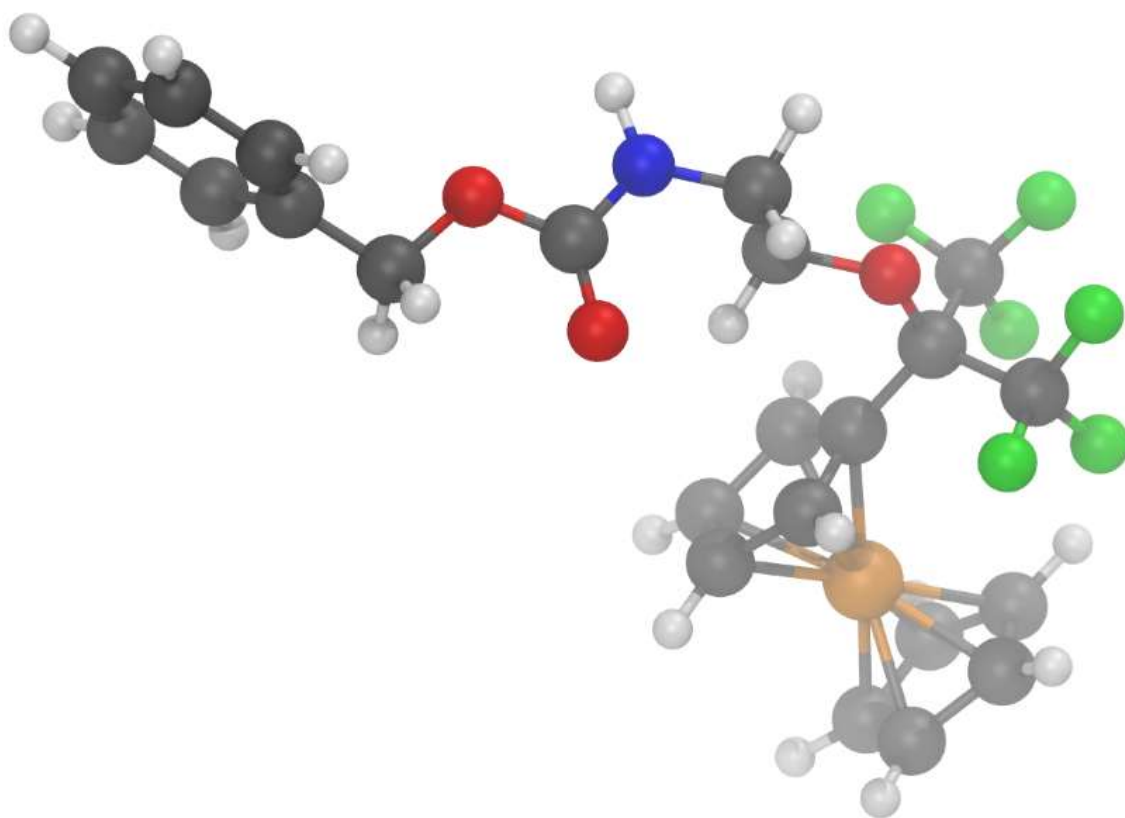


Figure S33. Optimized structure of compound **3** (reduced)

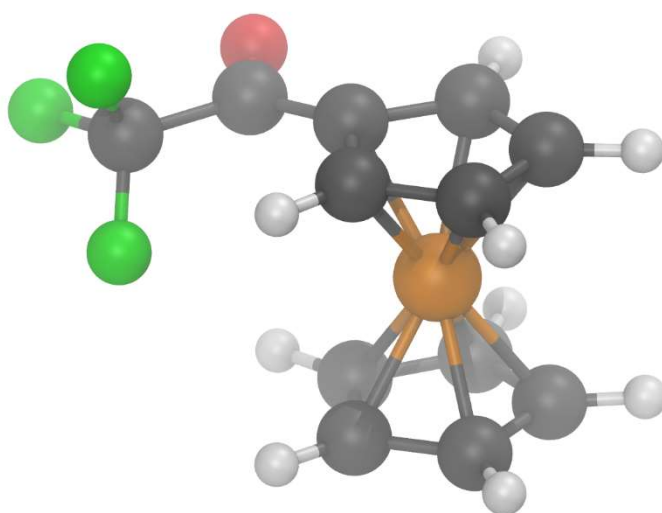


Figure S34. Optimized structure of compound **5** (reduced)

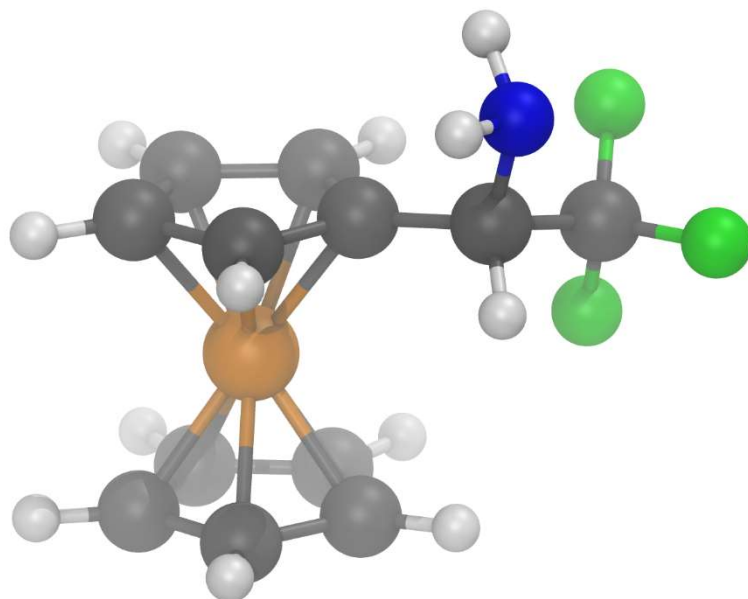


Figure S35. Optimized structure of compound **6** (reduced)

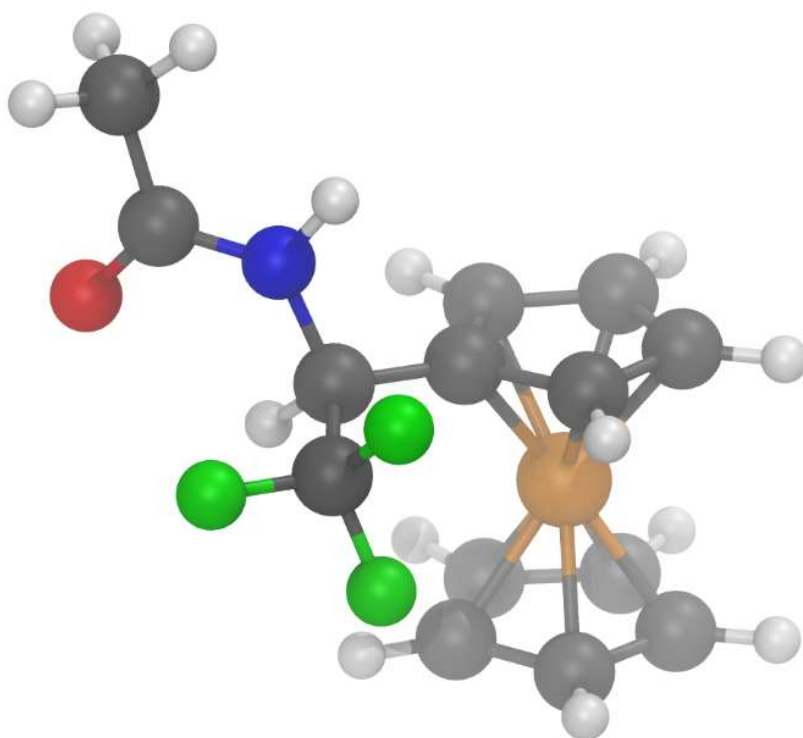


Figure S36. Optimized structure of compound **7** (reduced)

8 Differential scanning calorimetry

All samples were amorphous materials with similar behavior showing one T_g (see Table S5).

Table S5. Glass transition temperatures of the starting and ferrocene-modified polymers prepared in this study (standard deviation: ± 1 °C)

Sample	T_g [°C]
A	90
B	90
C	93
FcF6-A	79
FcF6-B	79
FcF6-C	80
FcF3-C1	91
FcF3-C2	98

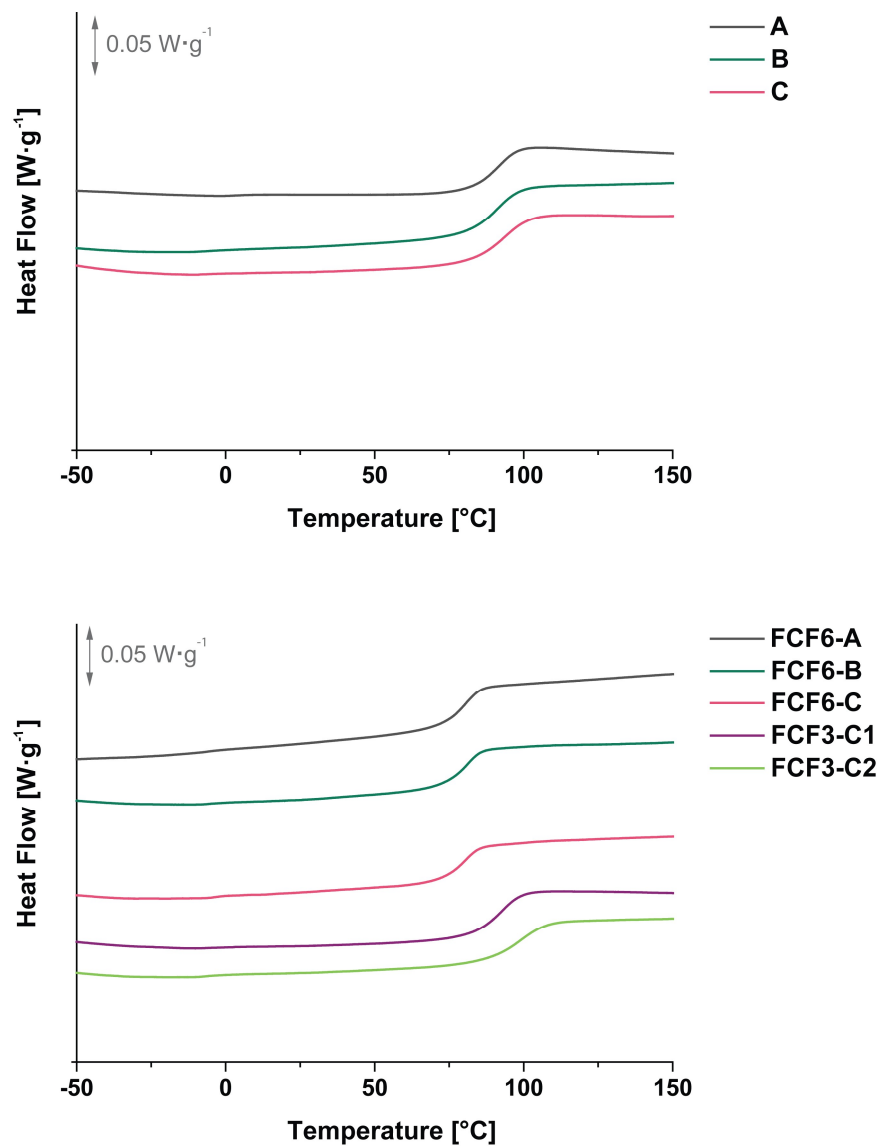
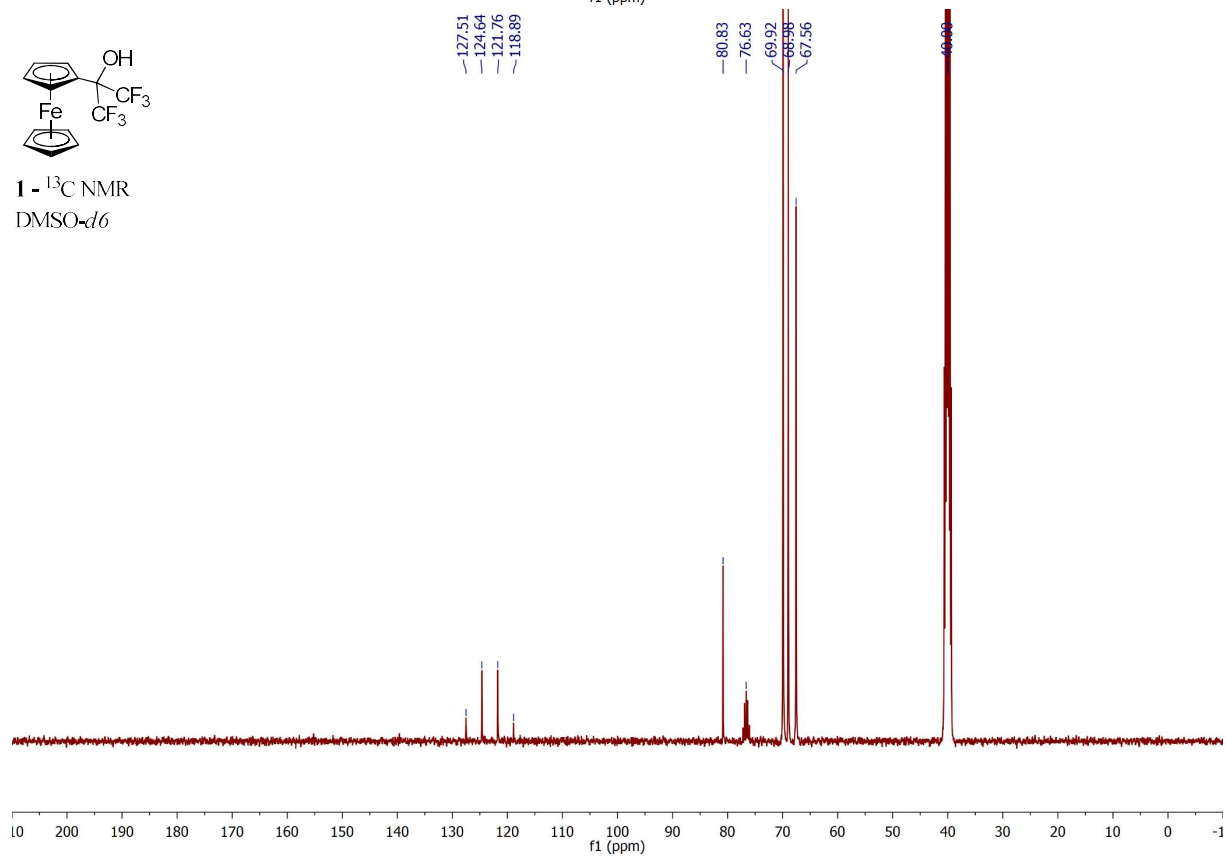
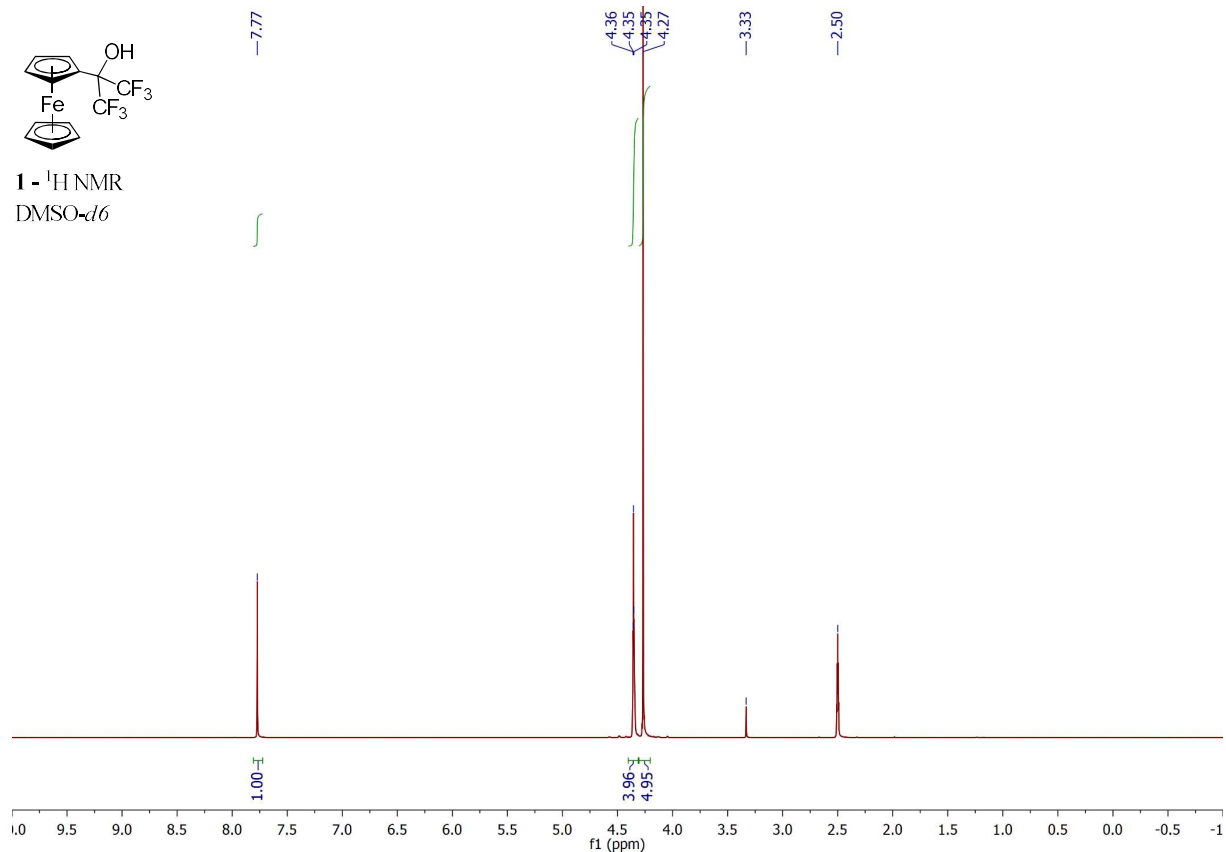
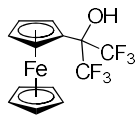


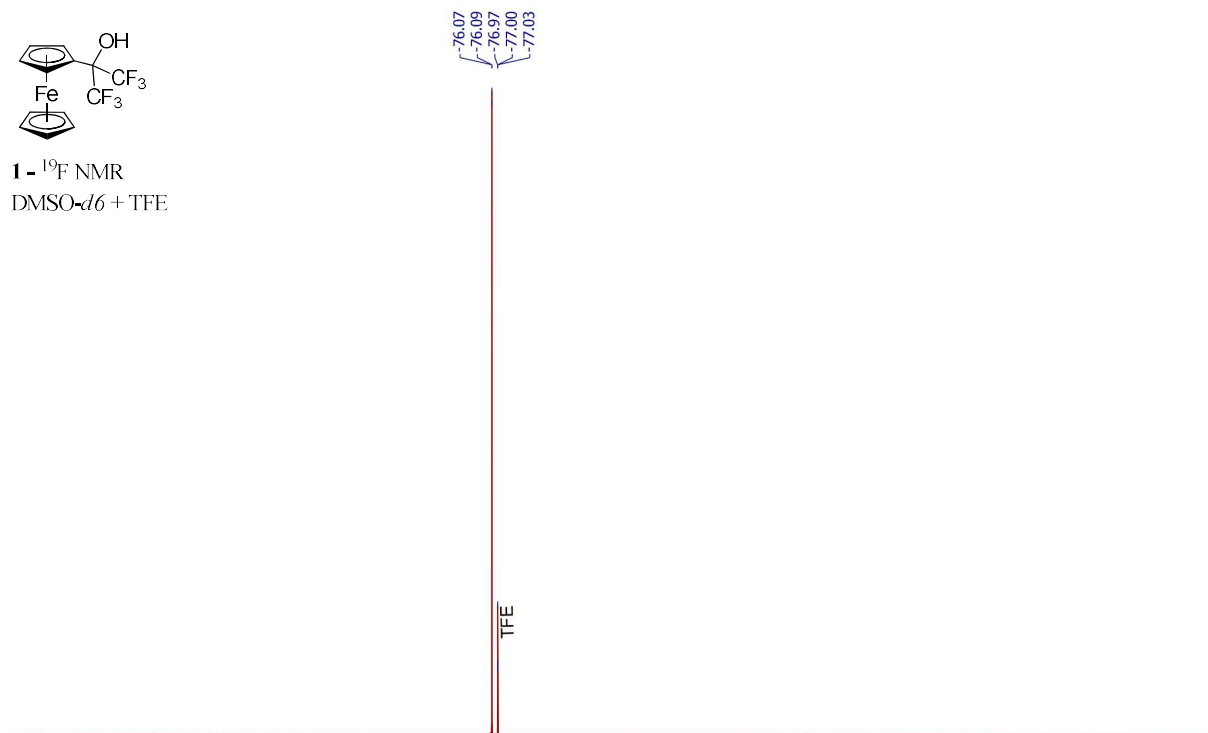
Figure S37. *Top:* DSC thermograms of polymers with free carboxyl groups A-C; *bottom:* DSC thermograms of polymers with fluorinated ferrocene moieties FcF6-A-C, FcF3-C1, and FcF3-C2.

9 ^1H , ^{13}C , and ^{19}F NMR spectra

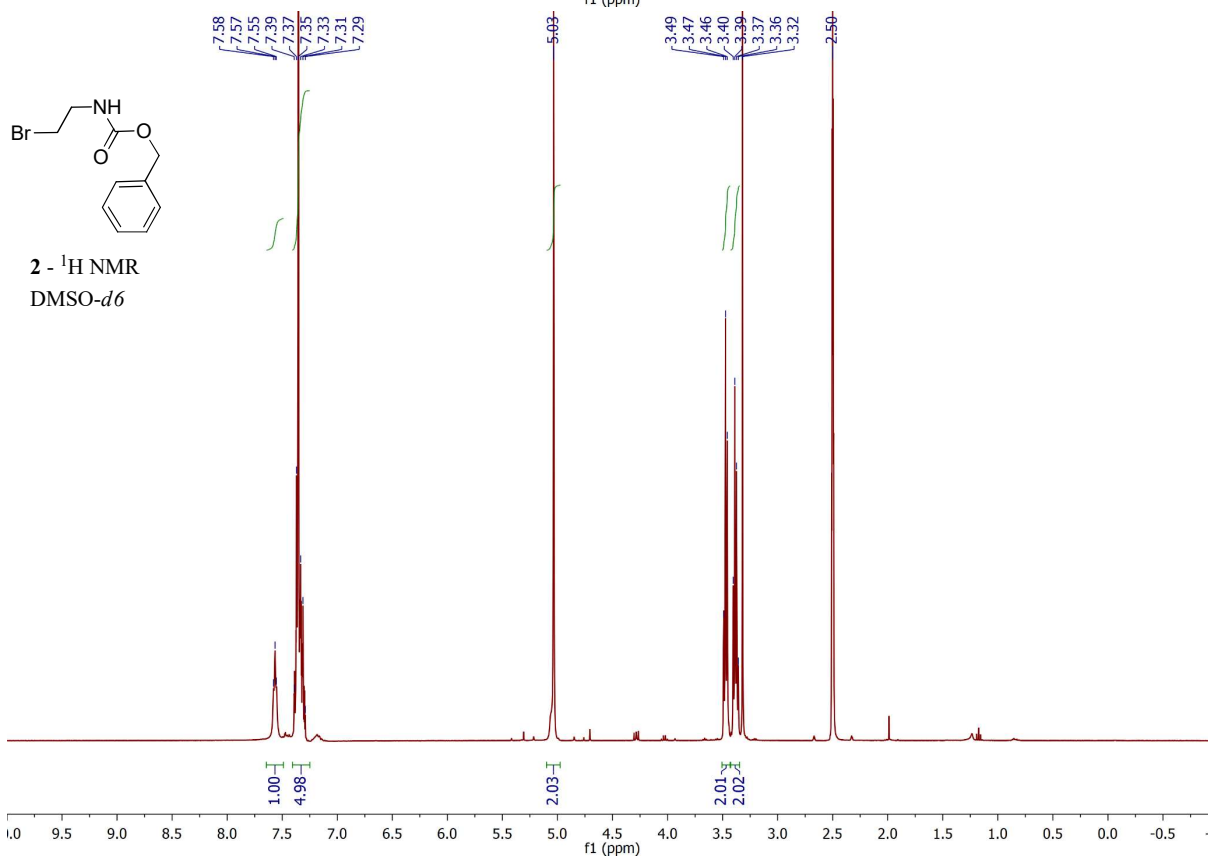




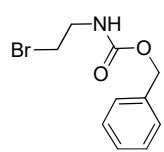
1 - ^{19}F NMR
DMSO- d_6 + TFE



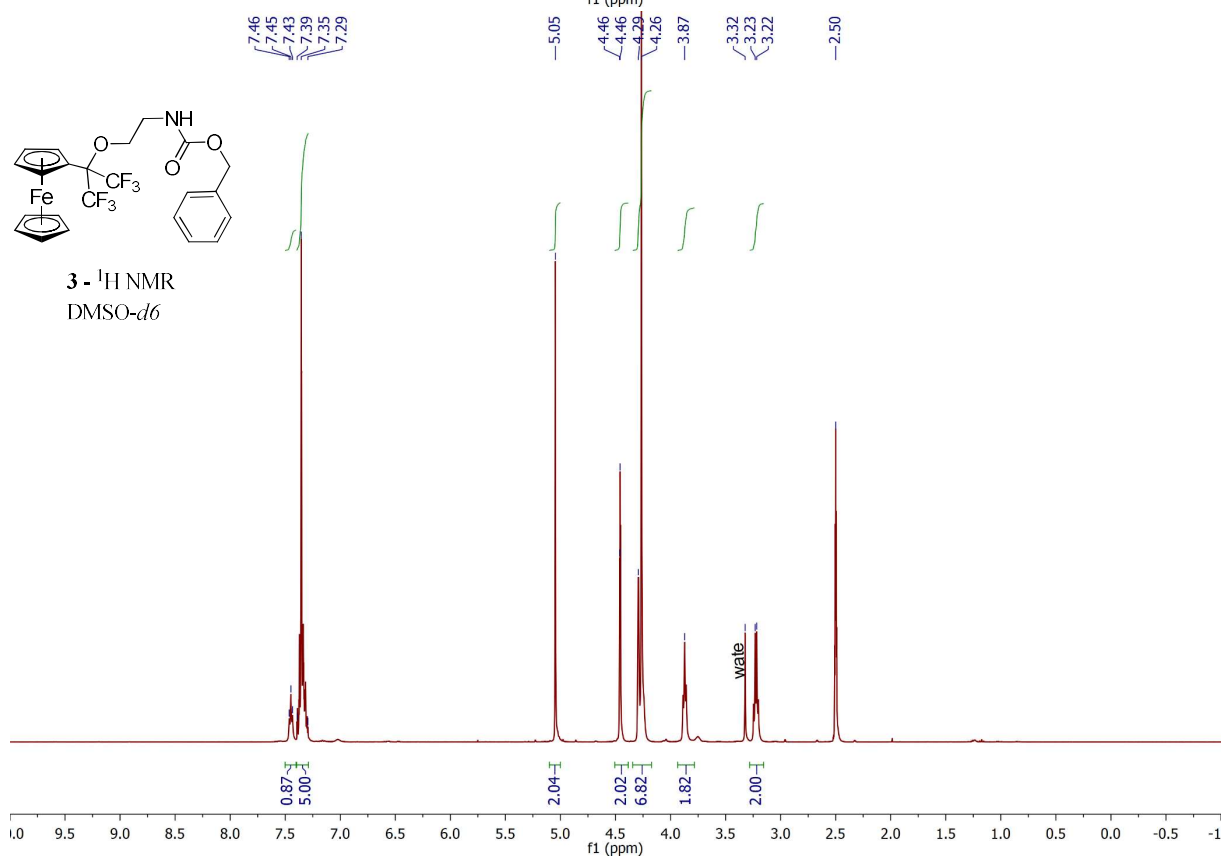
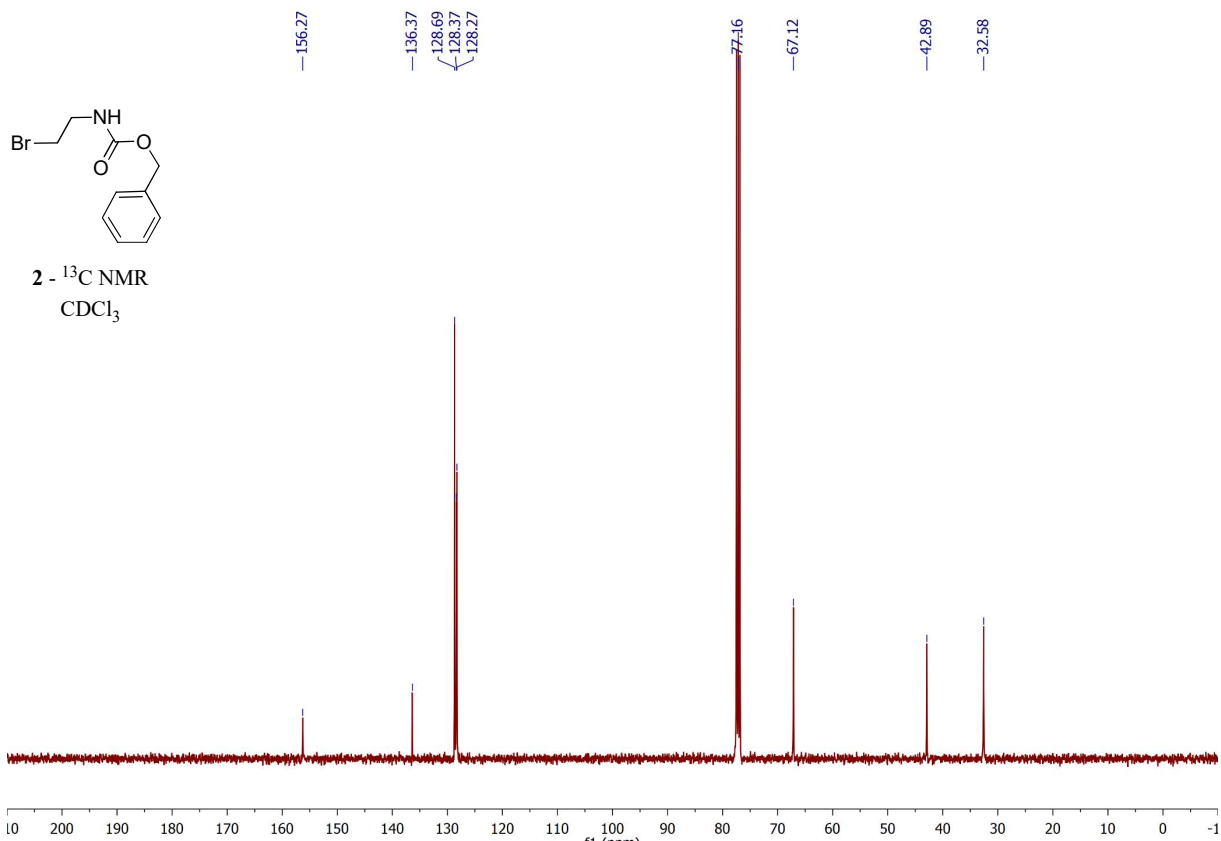
f1 (ppm)

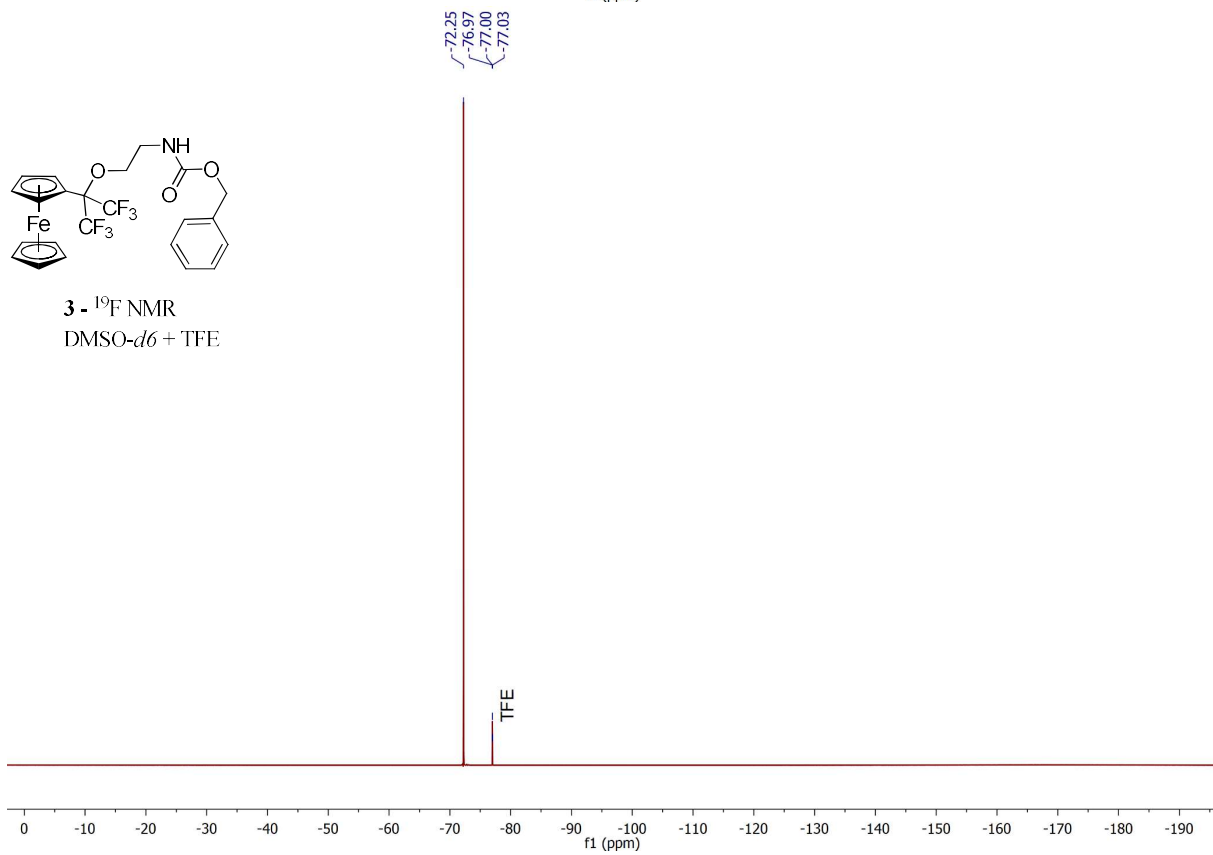
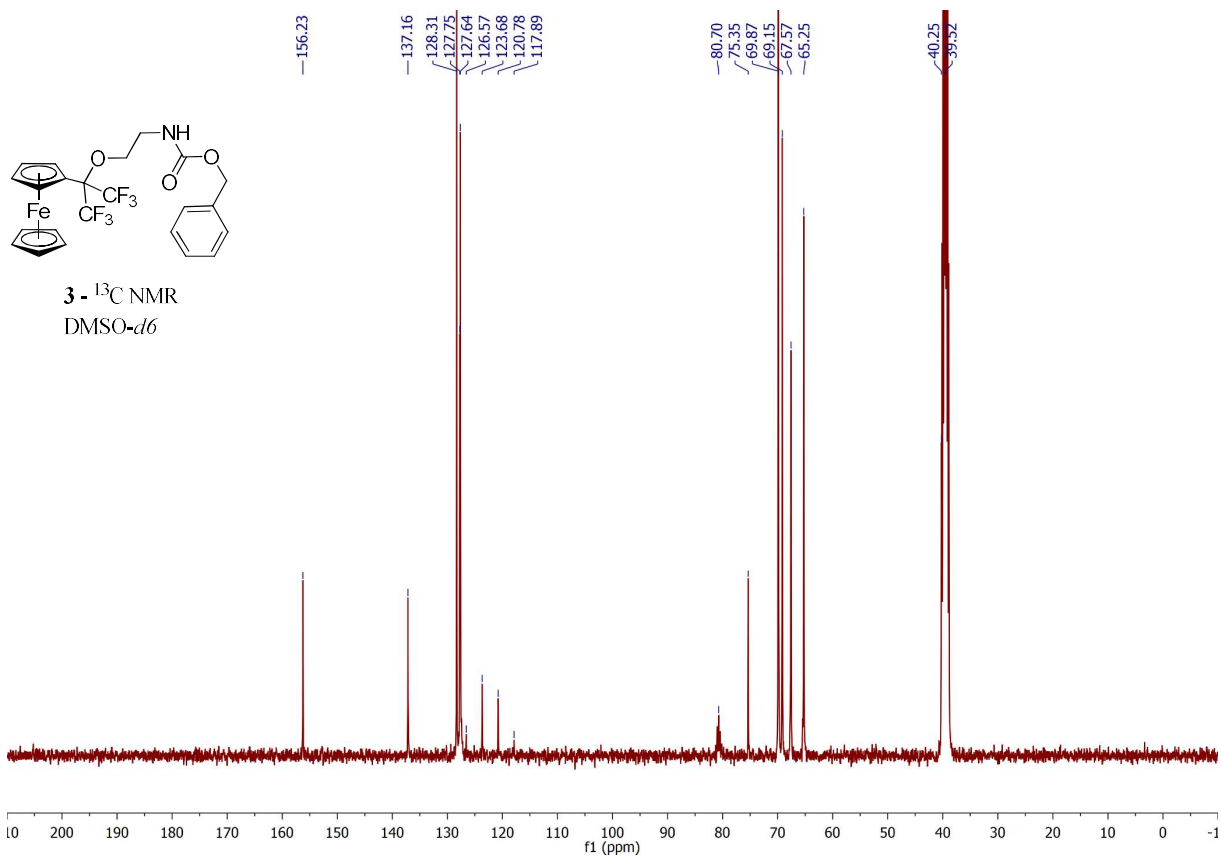


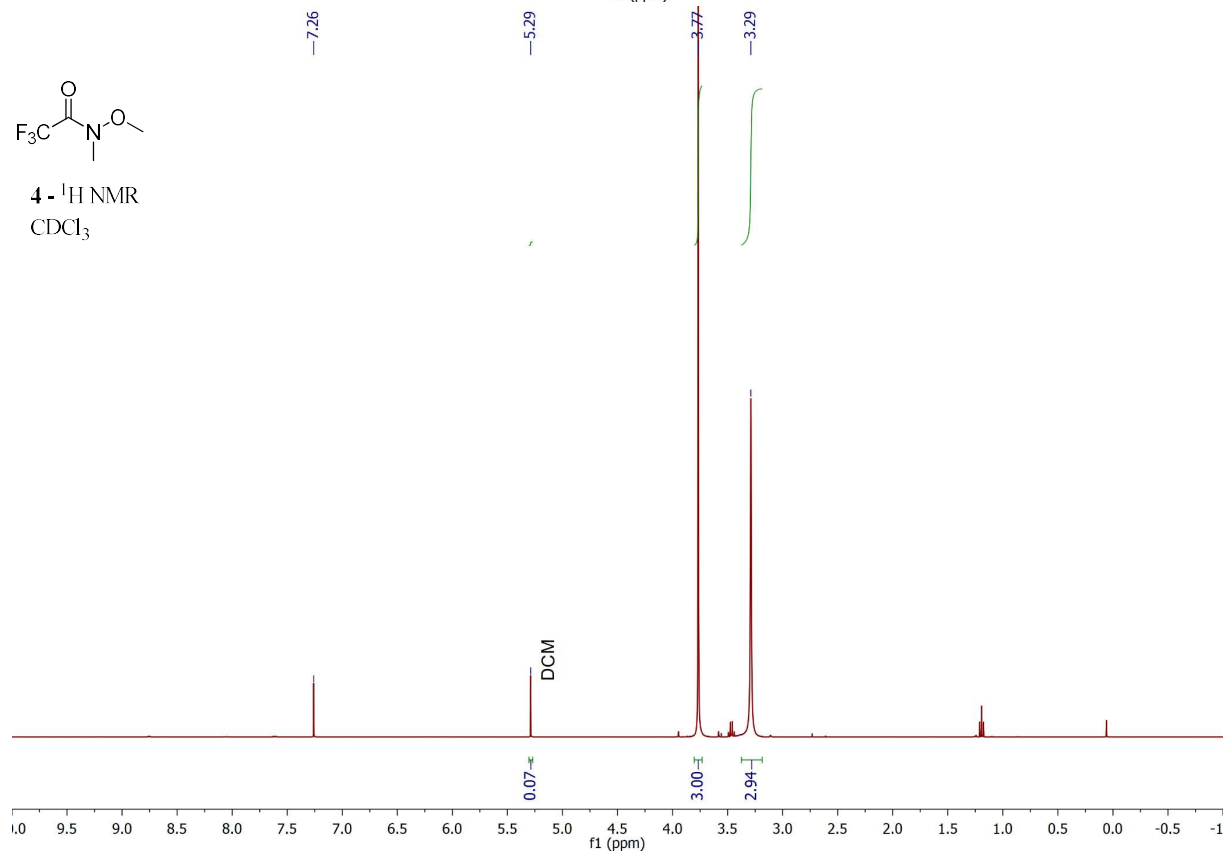
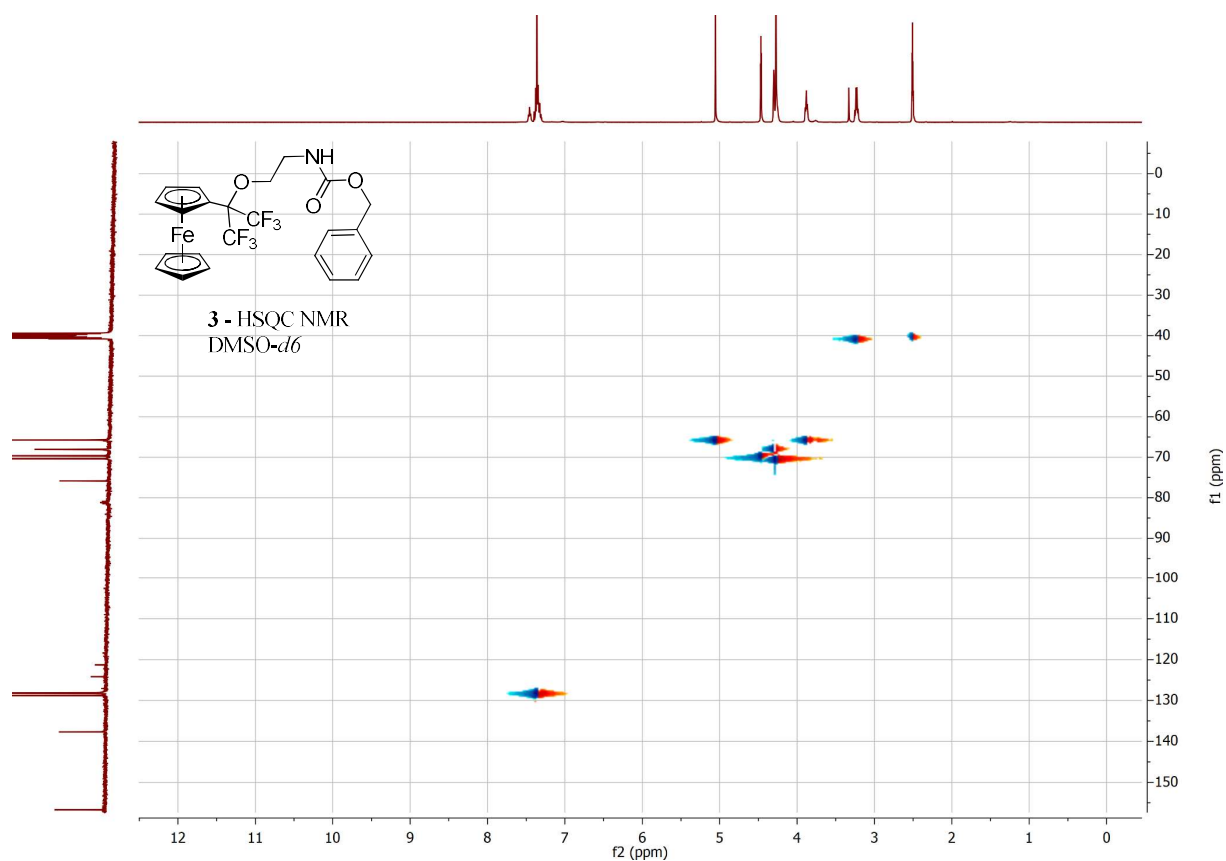
f1 (ppm)

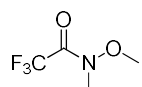


2 - ^1H NMR
DMSO- d_6

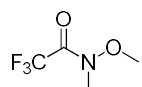
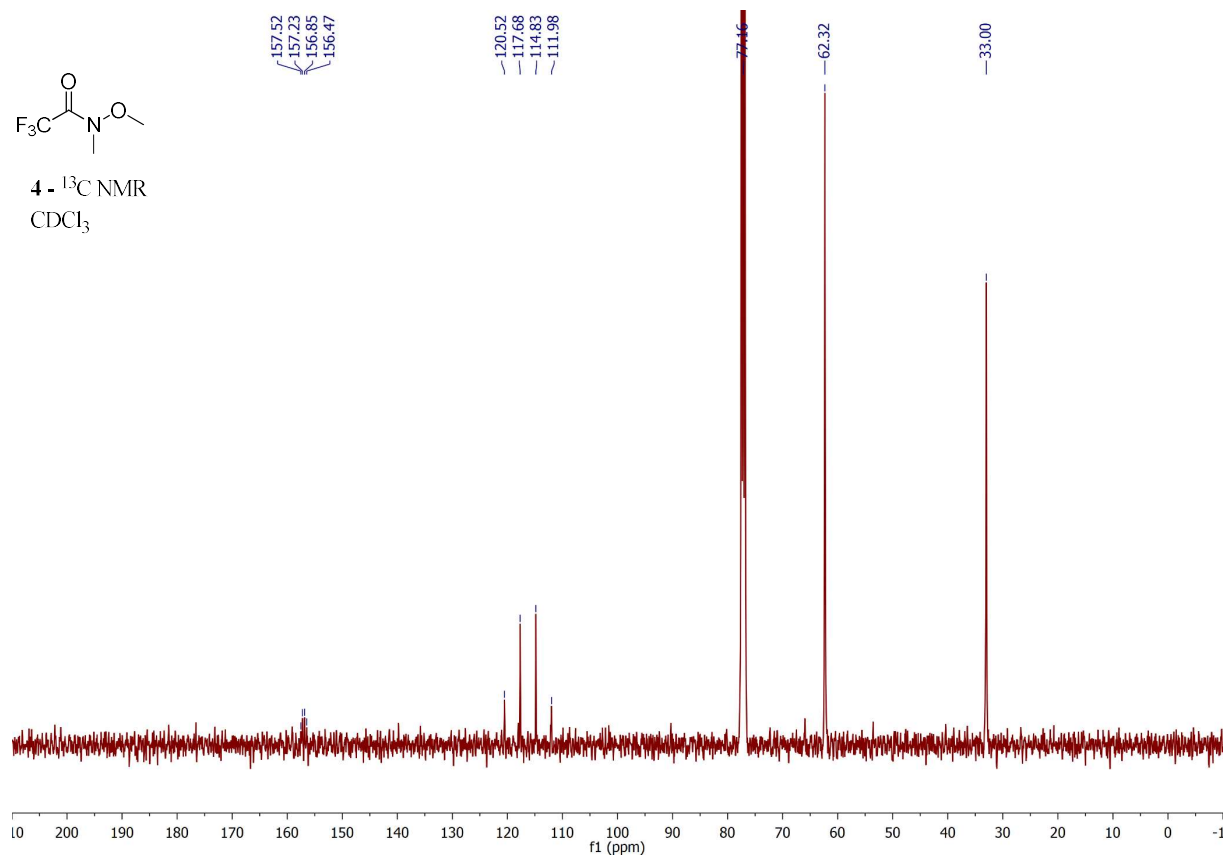




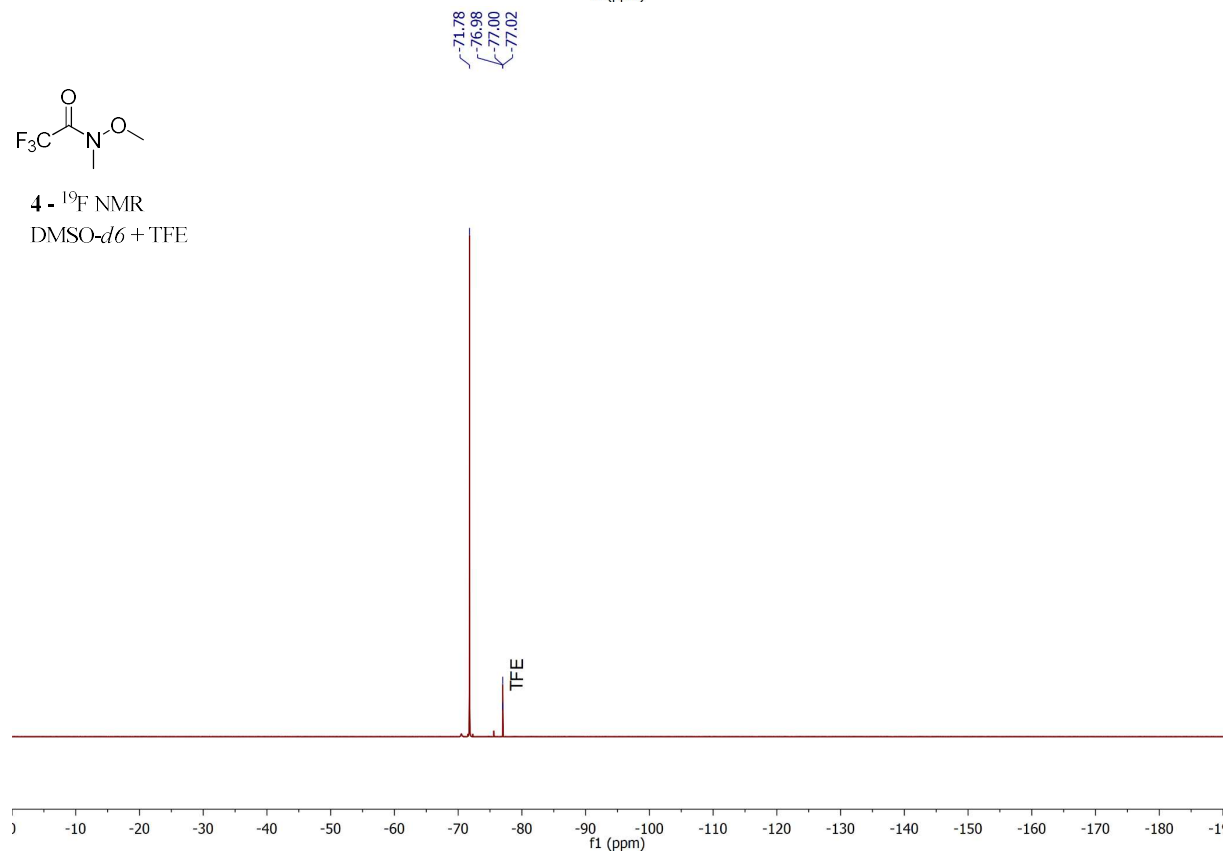


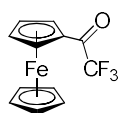


4 - ^{13}C NMR
 CDCl_3

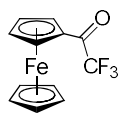
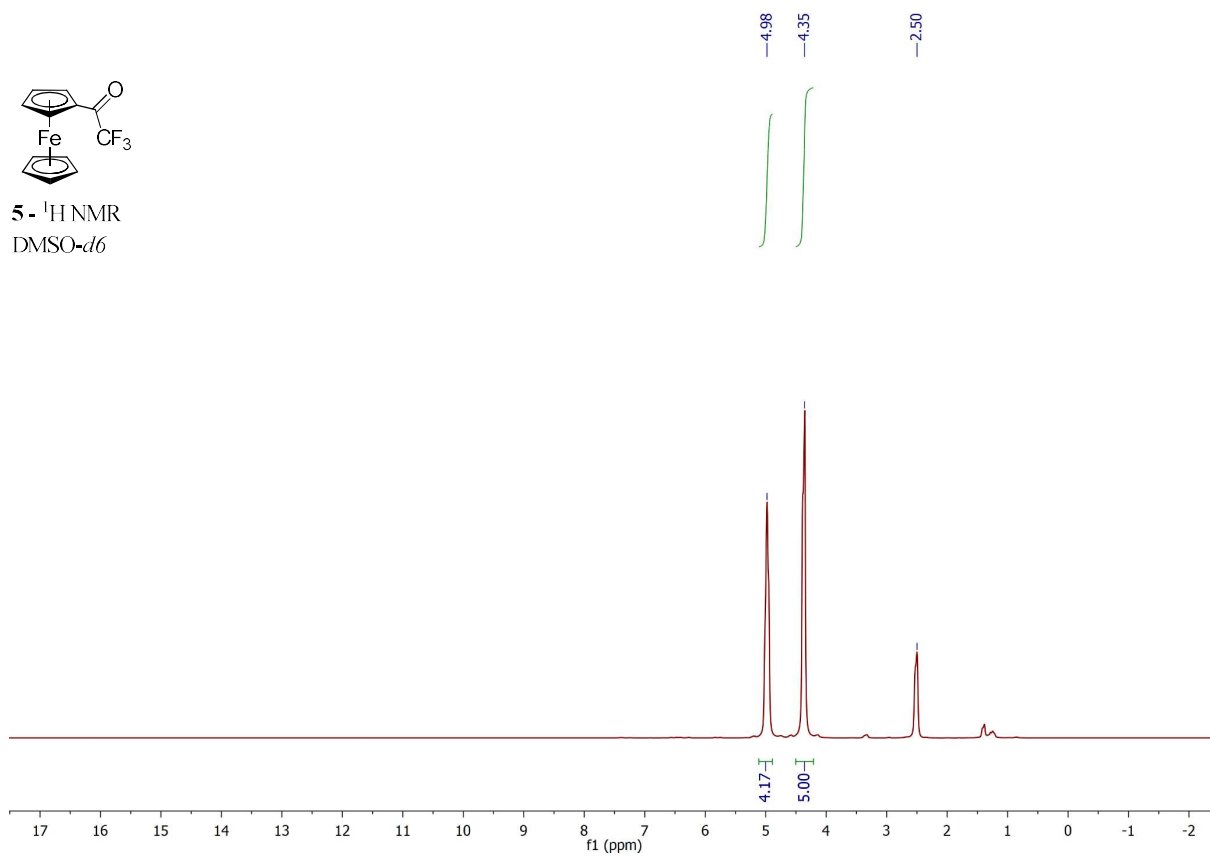


4 - ^{19}F NMR
 $\text{DMSO-}d_6 + \text{TFE}$

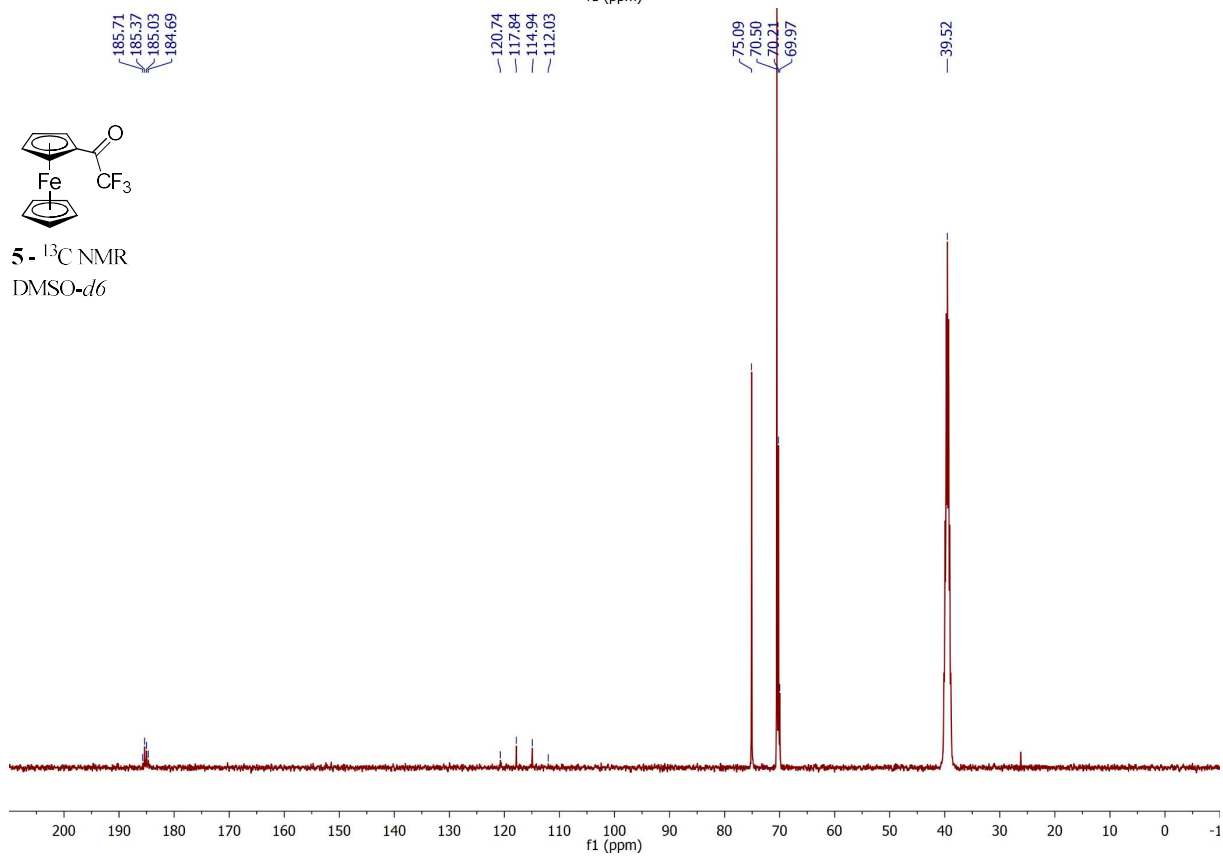


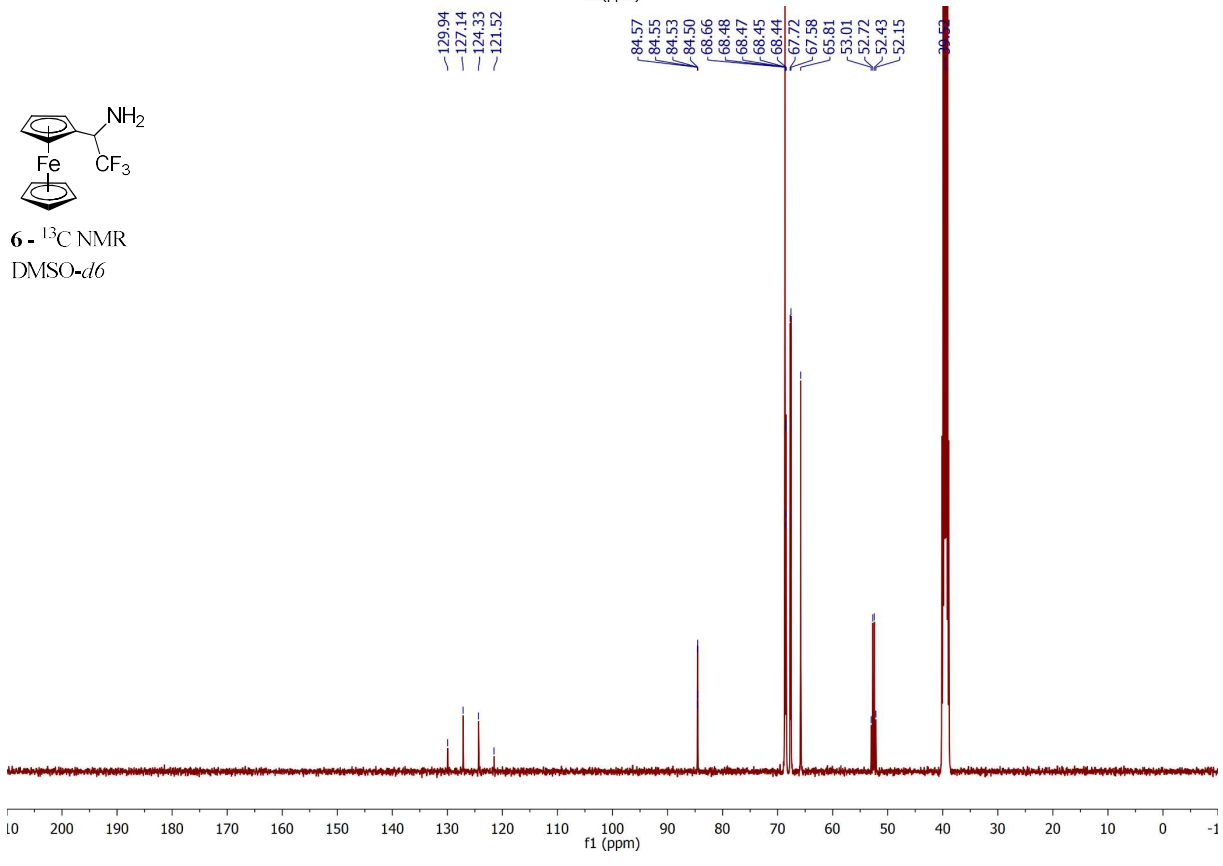
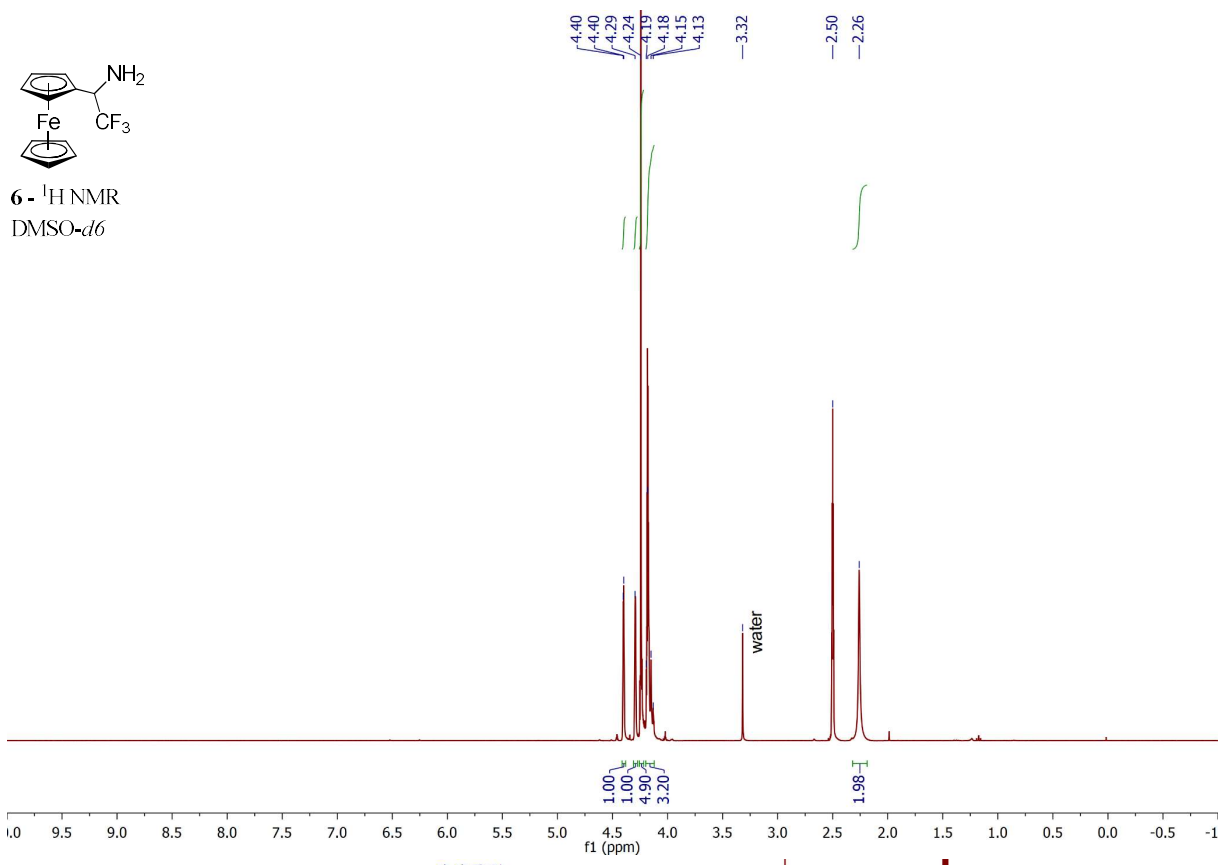


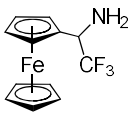
5. ^1H NMR
DMSO-*d*₆



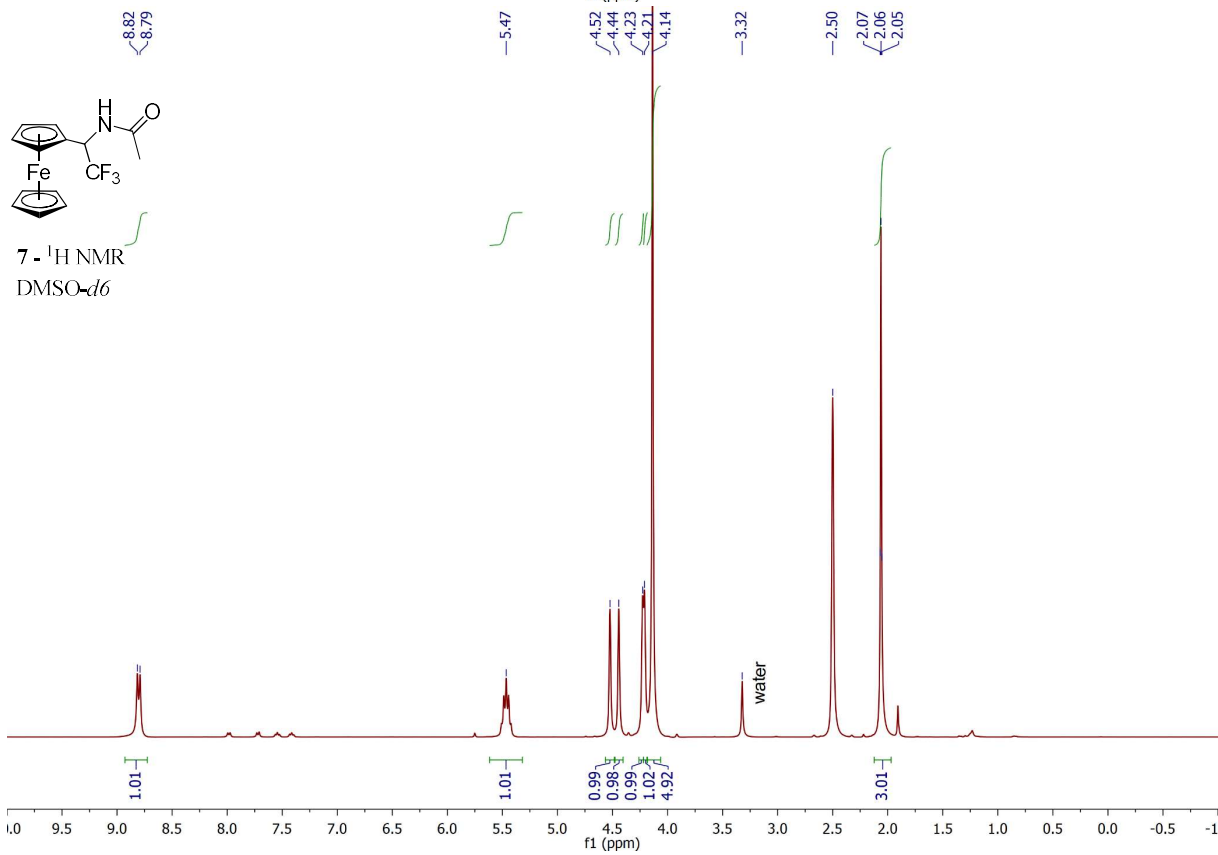
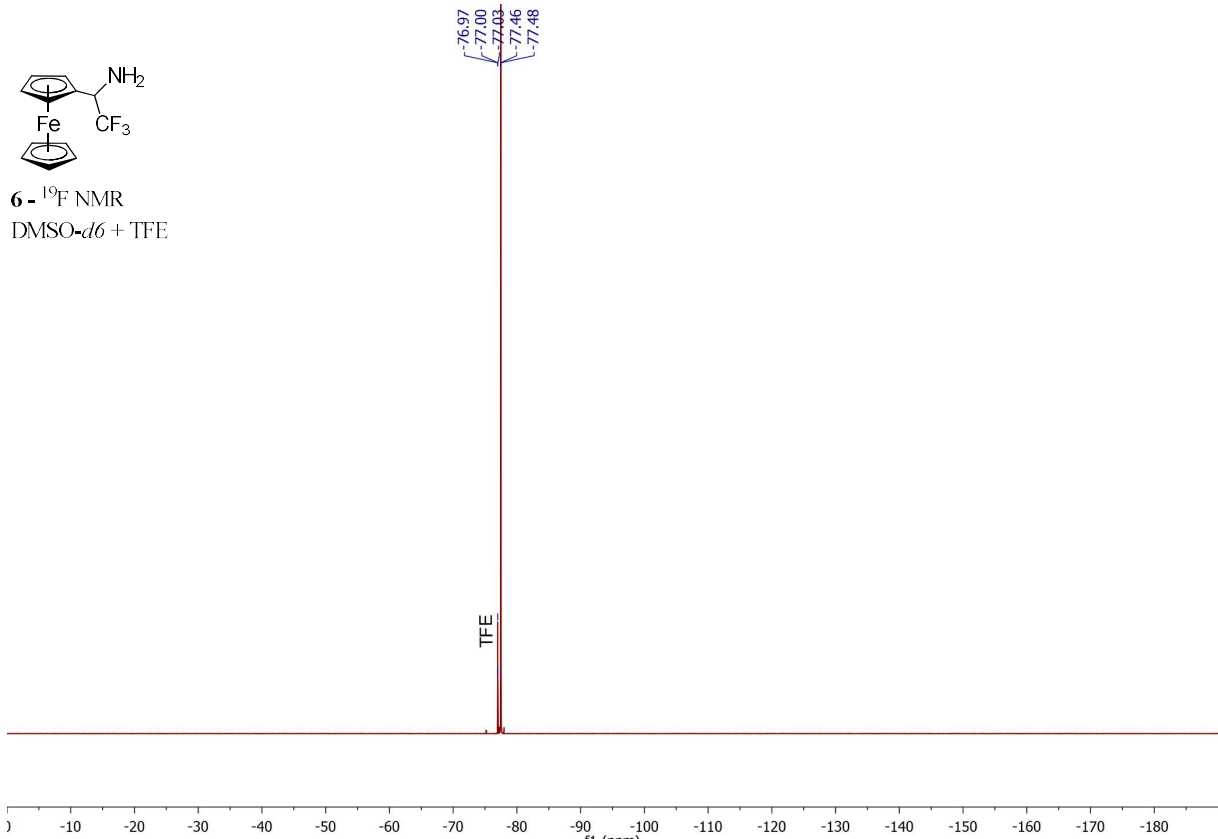
5. ^{13}C NMR
DMSO-*d*₆

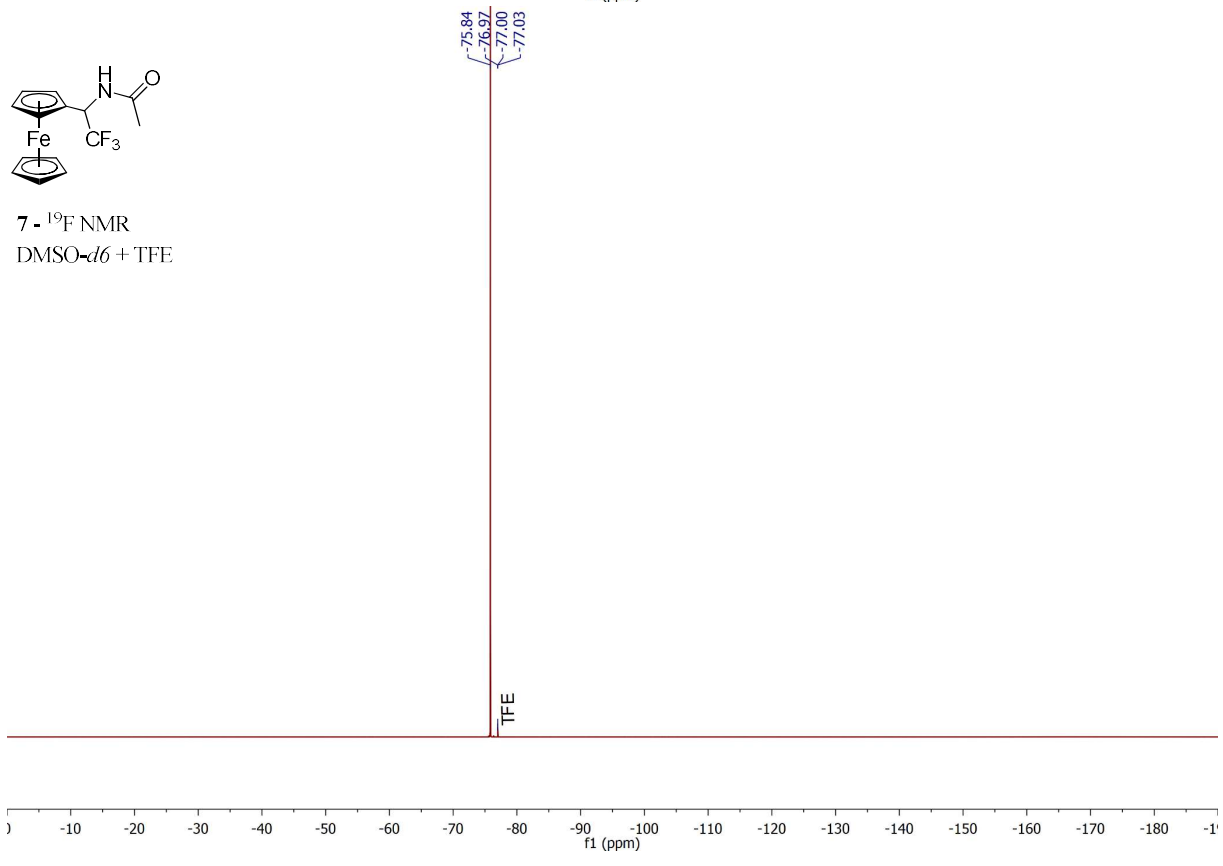
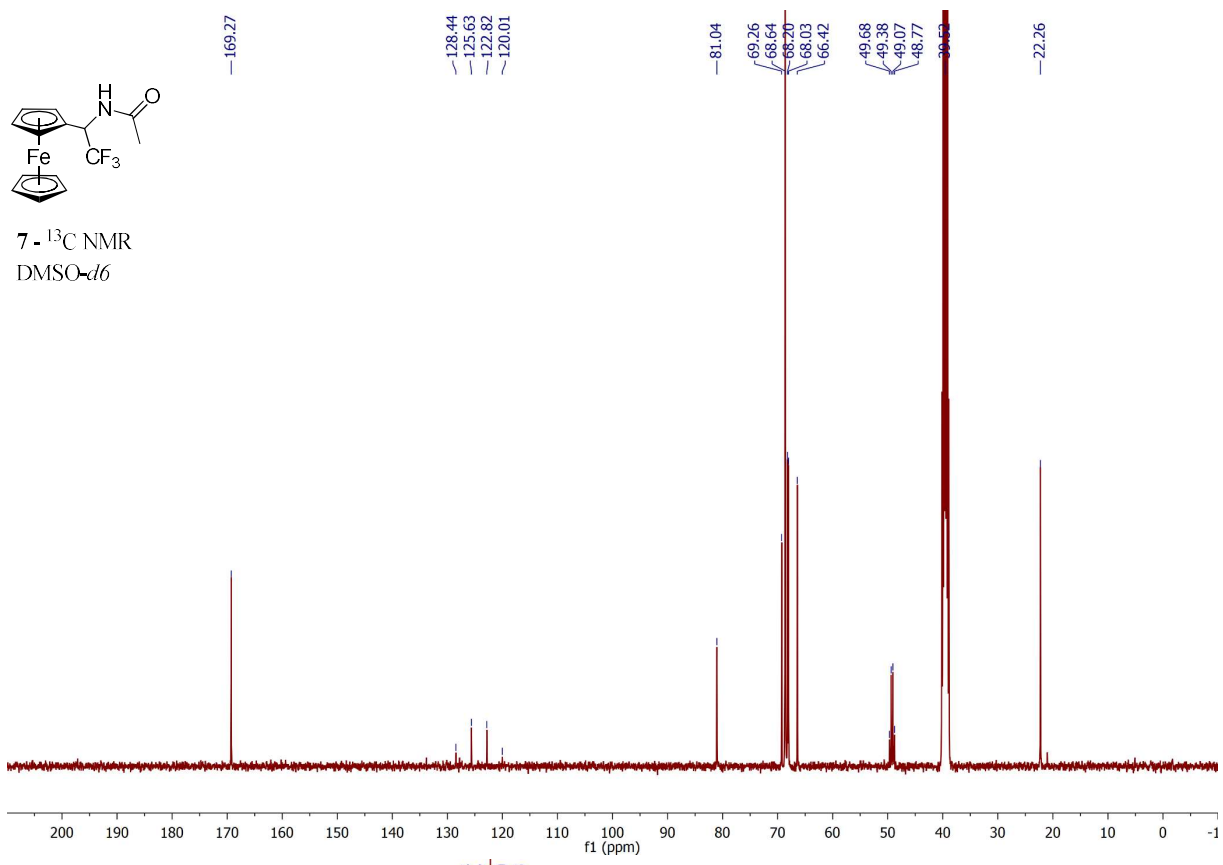


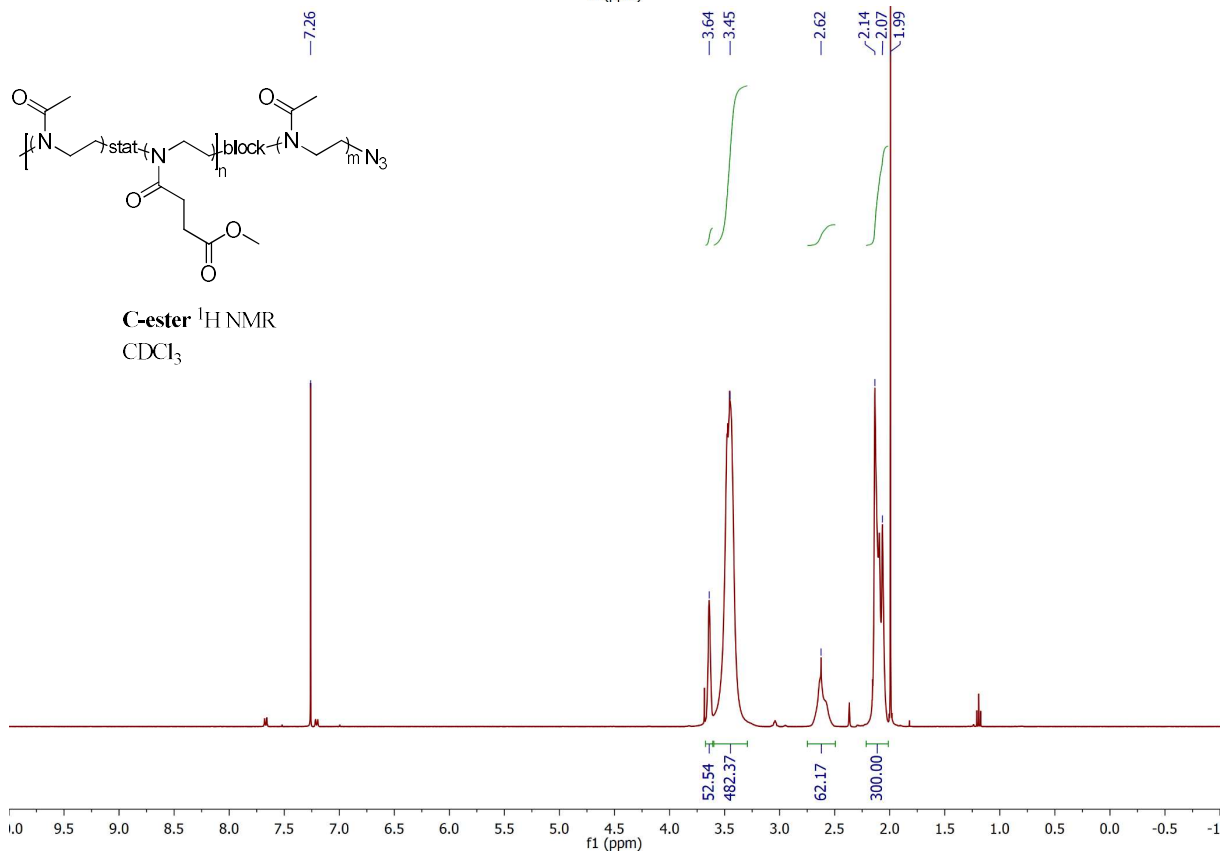
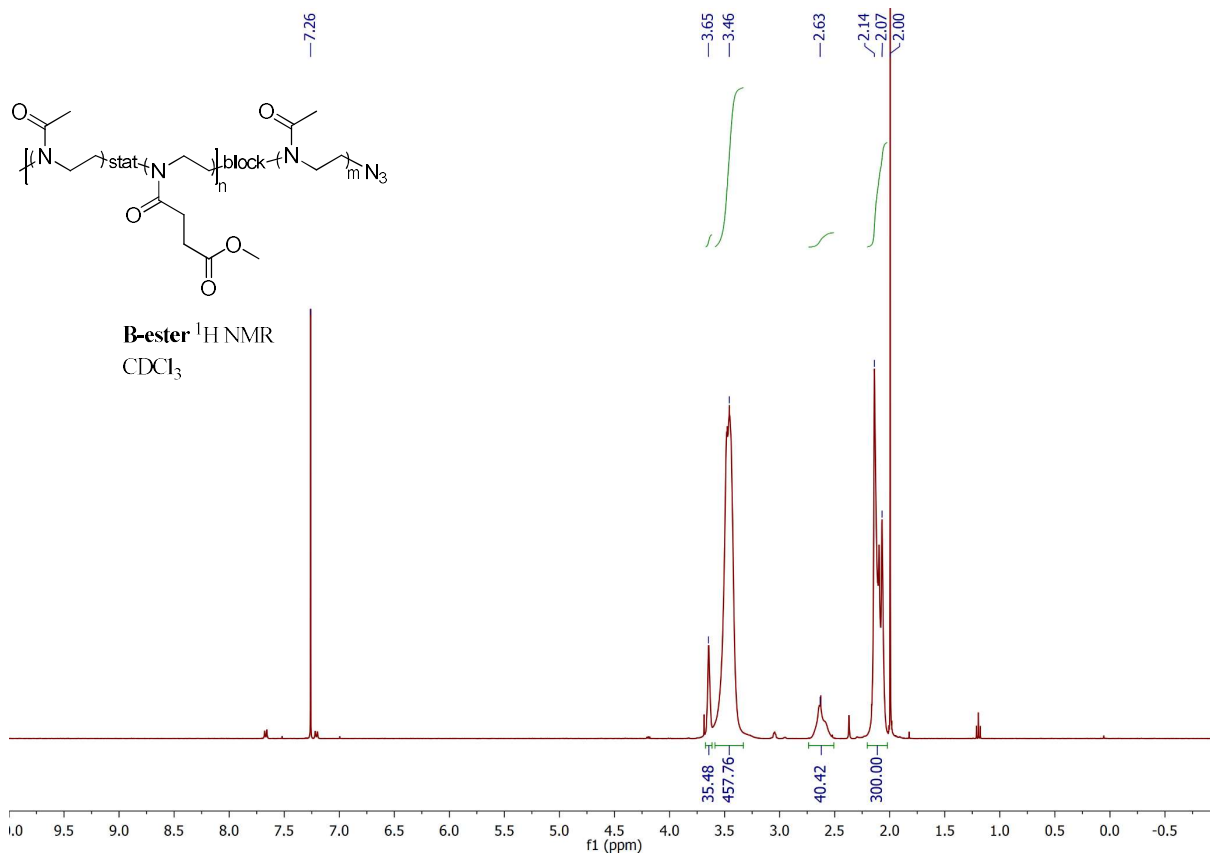


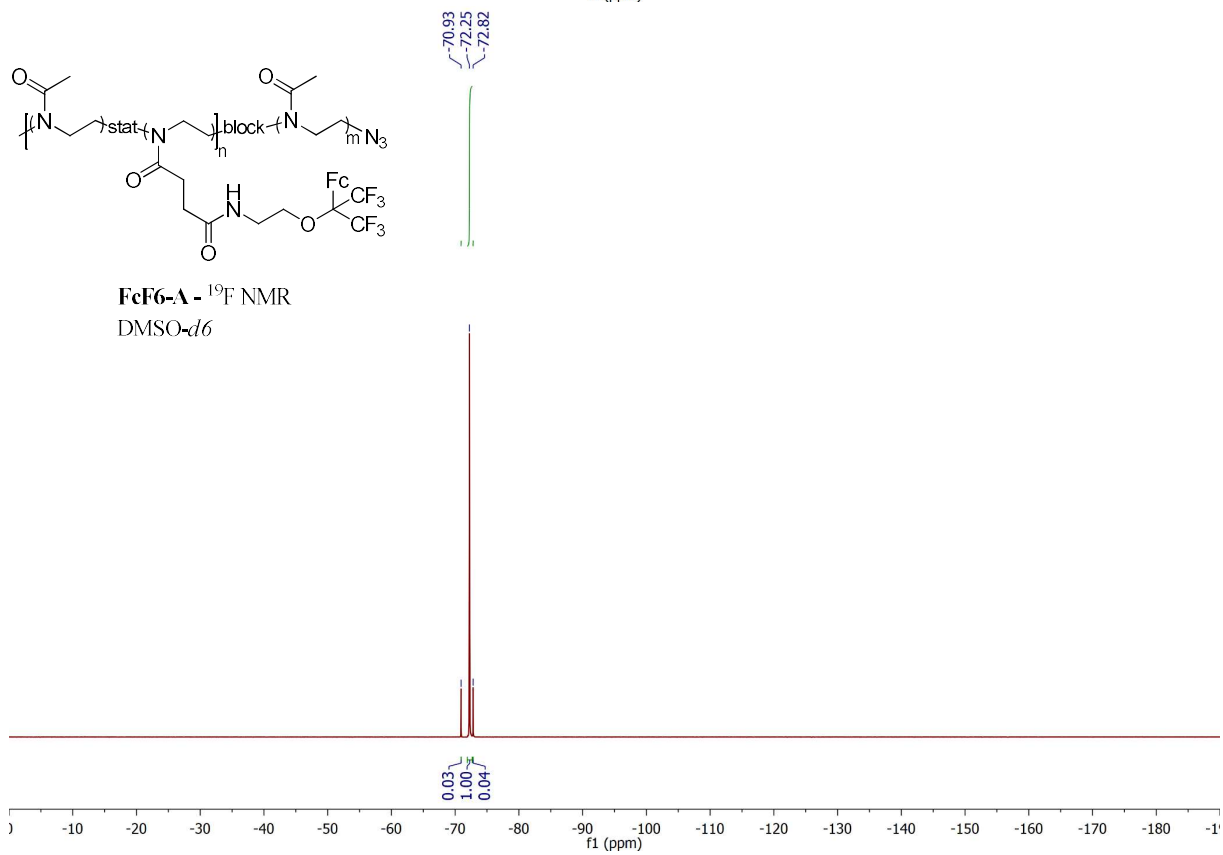
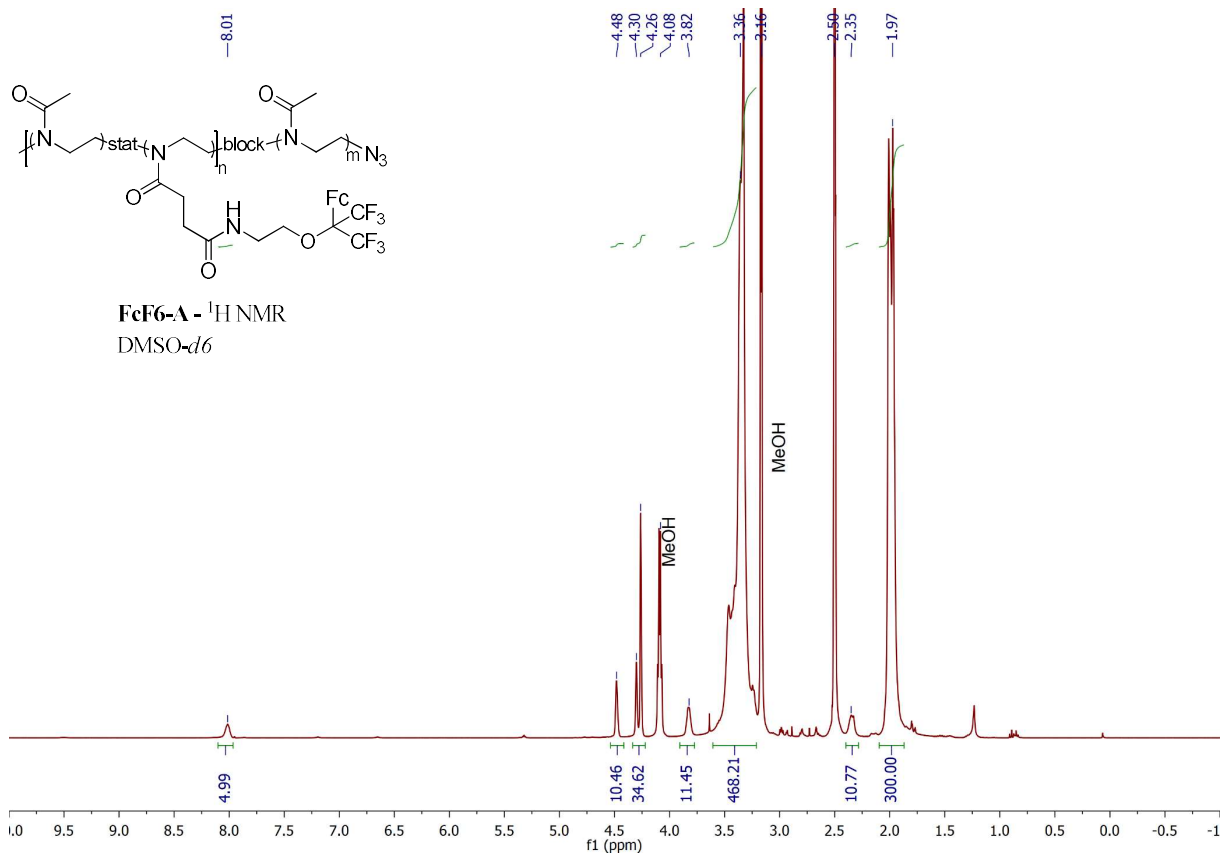


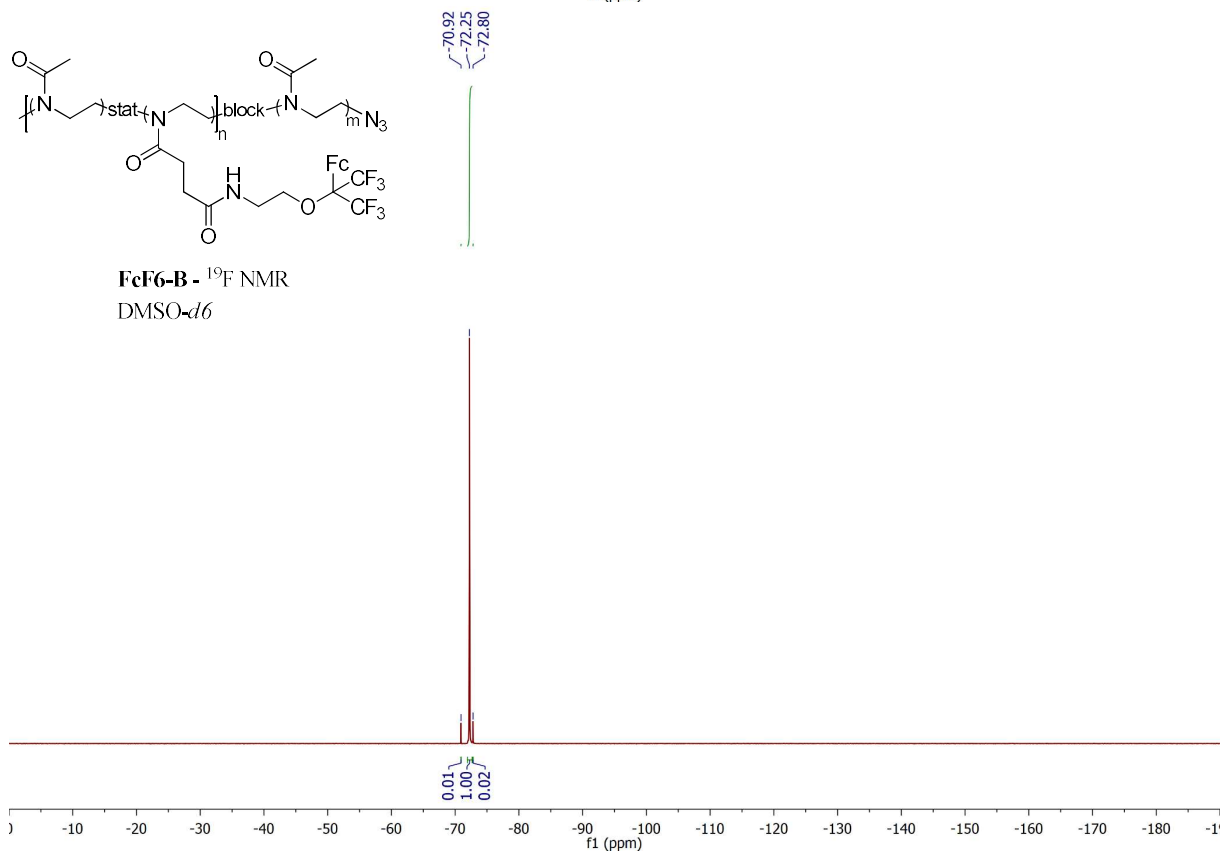
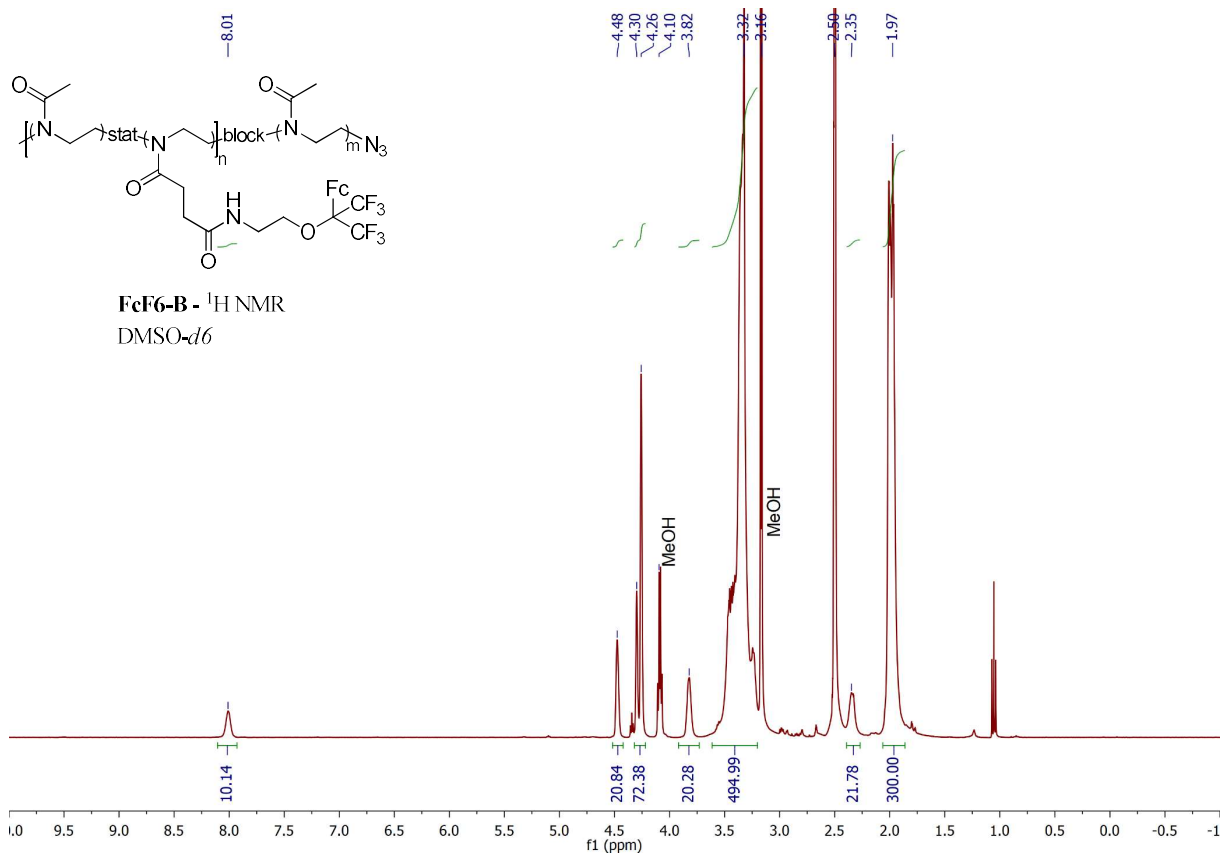
6 - ^{19}F NMR
DMSO- d_6 + TFE

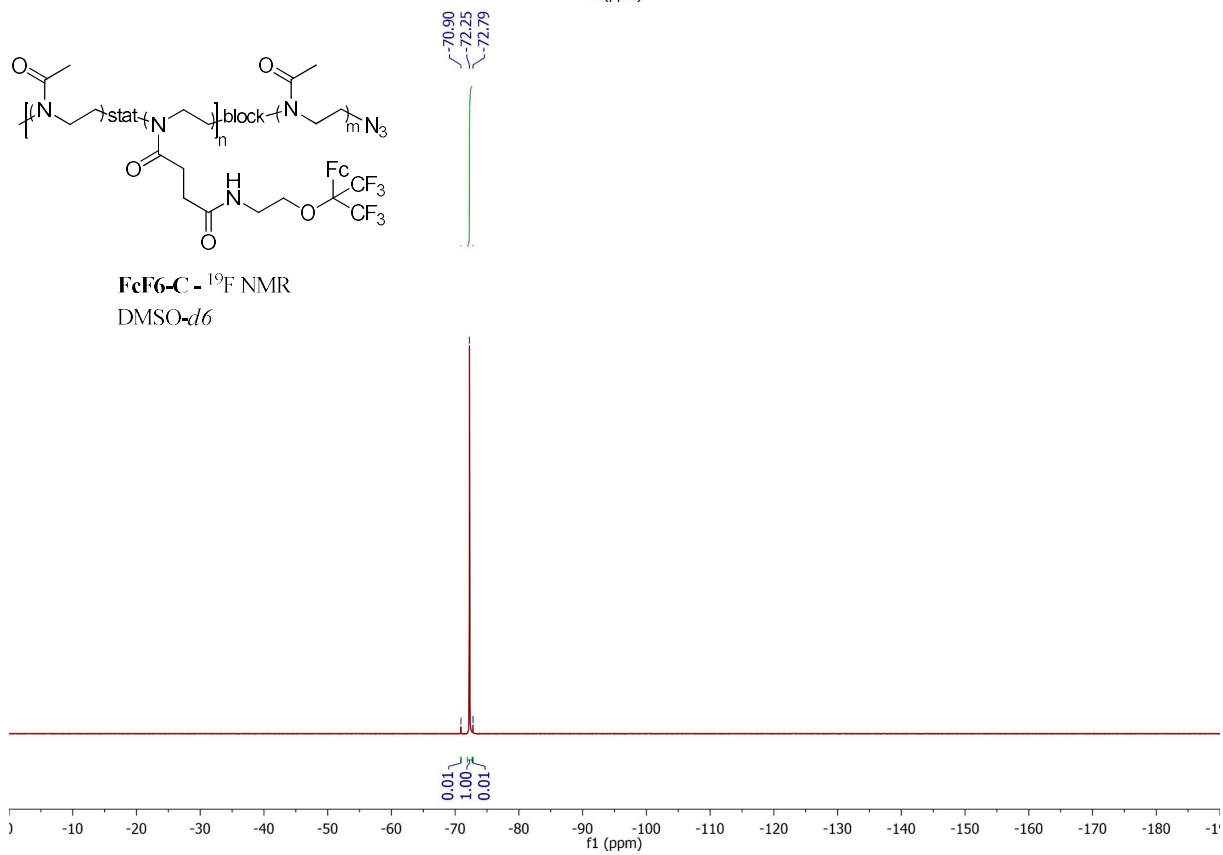
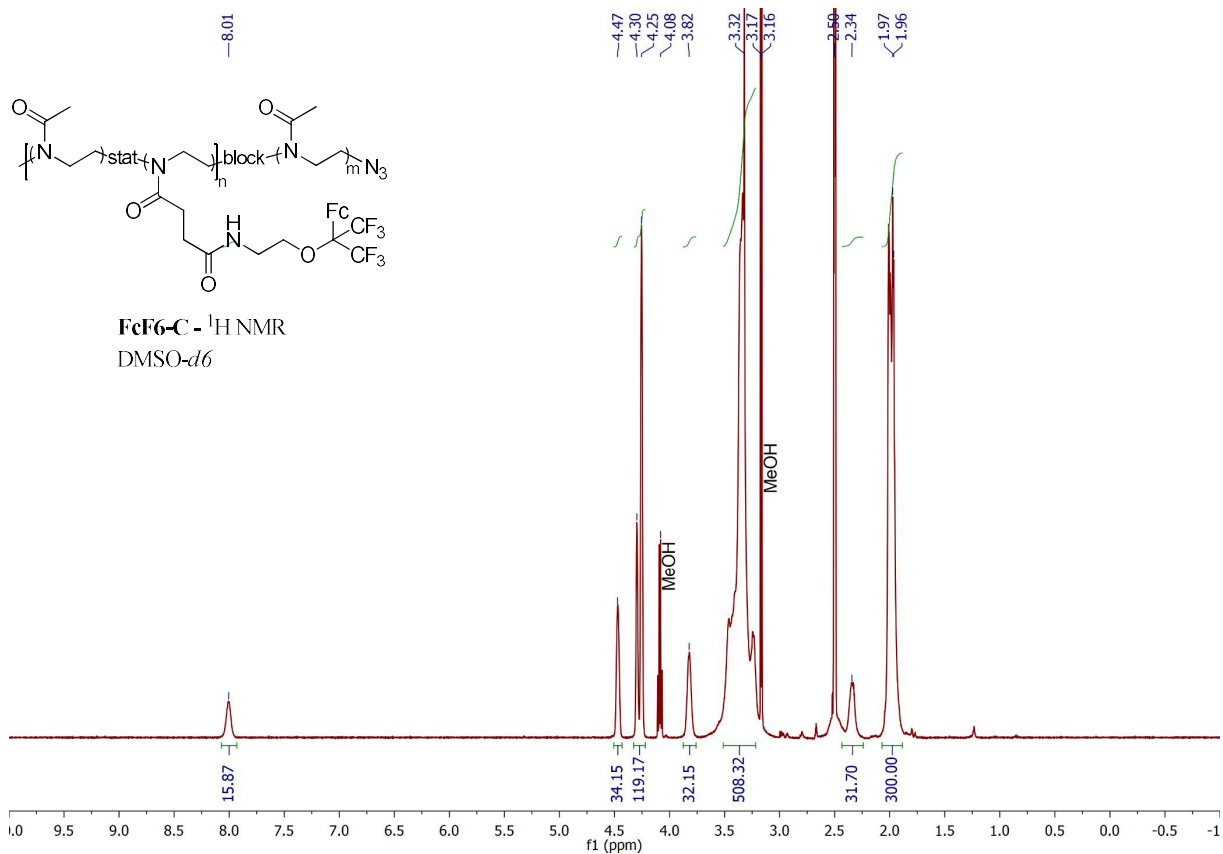


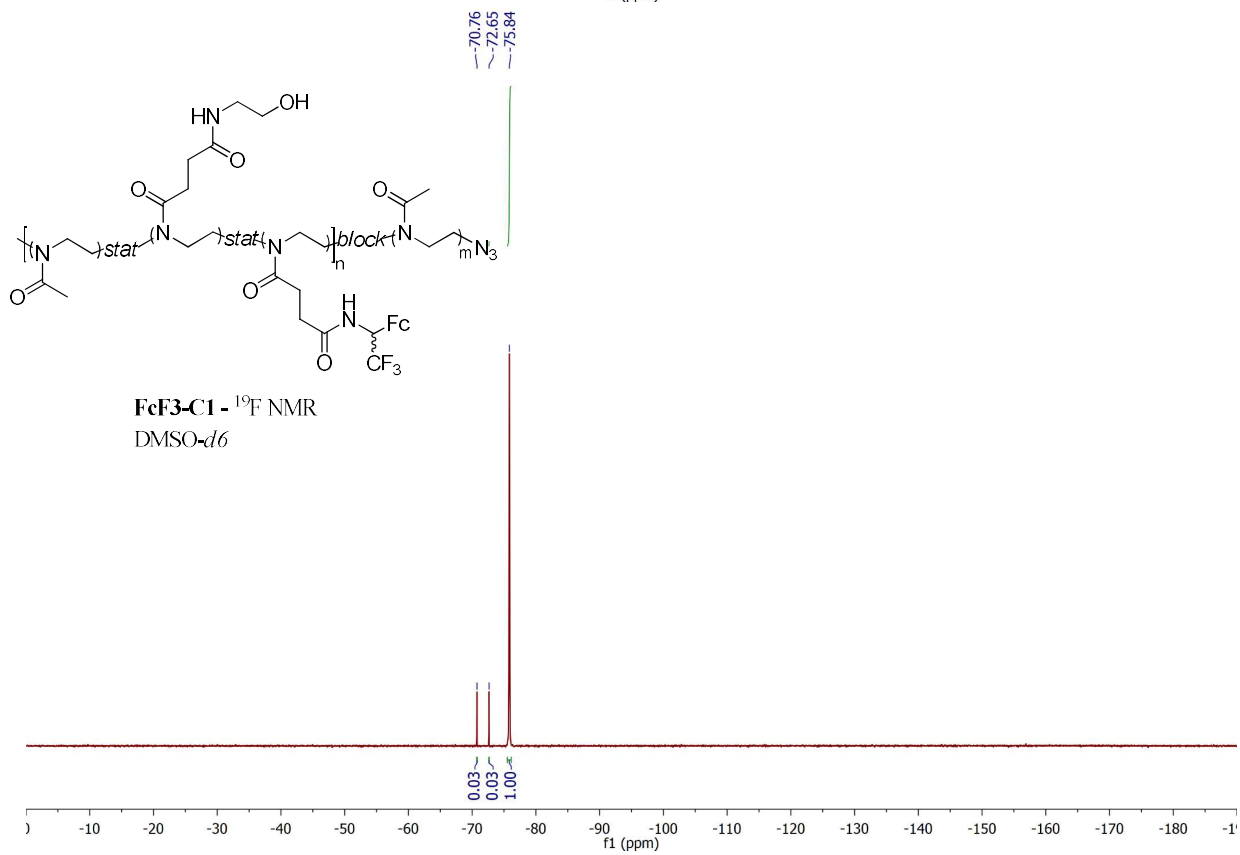
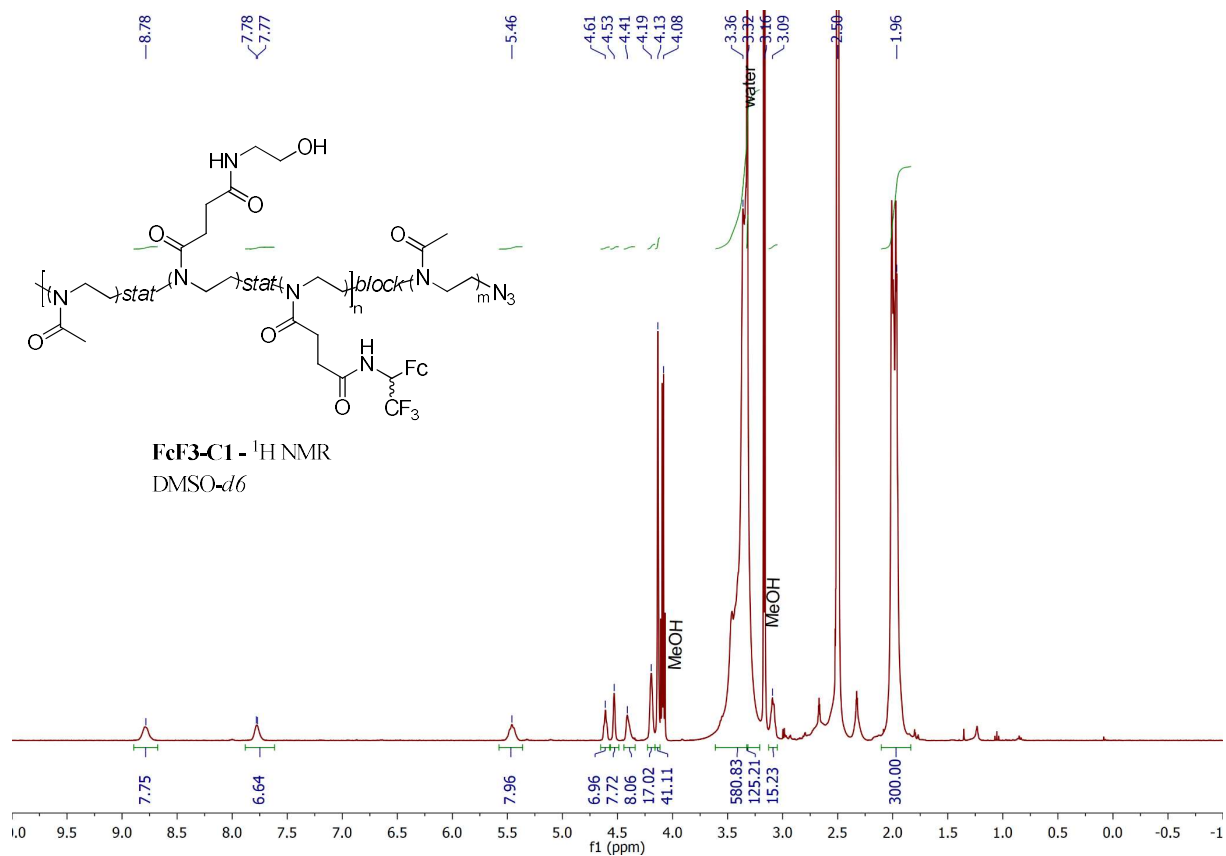


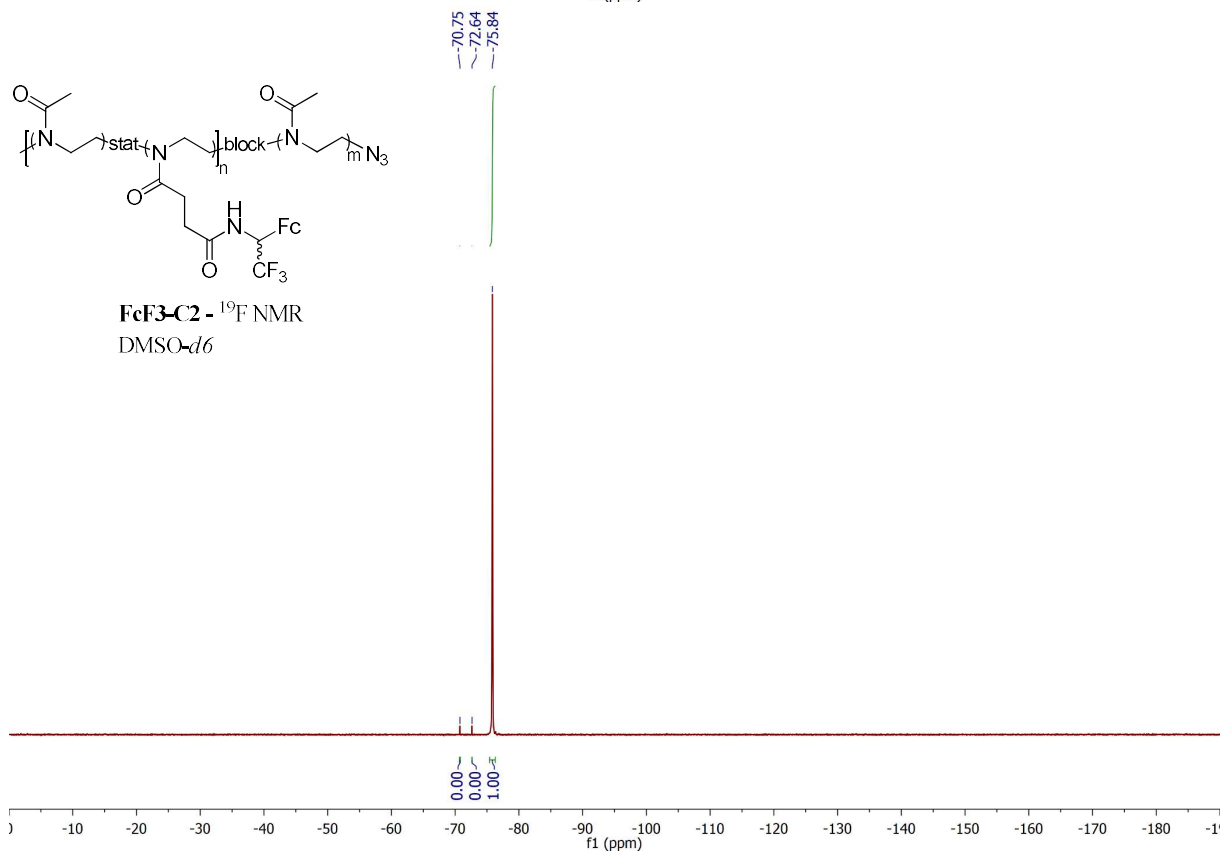
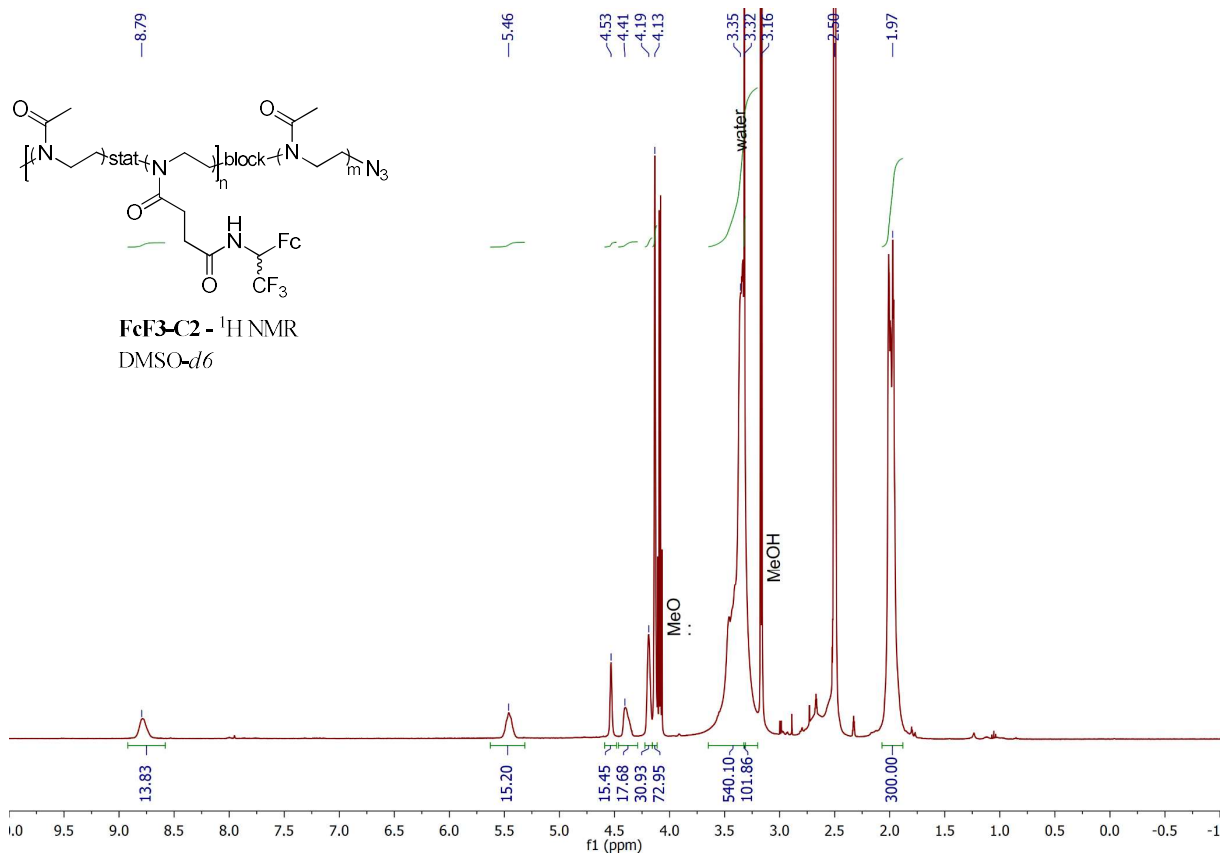












10 References

1. Bouten, P. J. M.; Hertsen, D.; Vergaelen, M.; Monnery, B. D.; Boerman, M. A.; Goossens, H.; Catak, S.; van Hest, J. C. M.; Van Speybroeck, V.; Hoogenboom, R., Accelerated Living Cationic Ring-Opening Polymerization of a Methyl Ester Functionalized 2-Oxazoline Monomer. *Polym. Chem.* **2015**, *6*, 514-518.
2. Barrière, F.; Geiger, W. E., Use of Weakly Coordinating Anions to Develop an Integrated Approach to the Tuning of $\Delta E_{1/2}$ Values by Medium Effects. *J. Am. Chem. Soc.* **2006**, *128*, 3980-3989.
3. Borgia, G. C.; Brown, R. J. S.; Fantazzini, P., Uniform-Penalty Inversion of Multiexponential Decay Data. *J. Magn. Reson.* **1998**, *132*, 65-77.
4. Yen, C. *read_2dseq: Quickly Reads Bruker's 2dseq MRI Images*, version 1.0.1; retrieved February 20, 2021. https://www.mathworks.com/matlabcentral/fileexchange/69177-read_2dseq-quickly-reads-bruker-s-2dseq-mri-images
5. Maschke, M.; Alborzina, H.; Lieb, M.; Wölfl, S.; Metzler-Nolte, N., Structure–Activity Relationship of Trifluoromethyl-Containing Metallocenes: Electrochemistry, Lipophilicity, Cytotoxicity, and ROS Production. *ChemMedChem* **2014**, *9*, 1188-1194.
6. Sanders, R.; Mueller-Westerhoff, U. T., The Lithiation of Ferrocene and Ruthenocene: A Retraction and an Improvement. *J. Organomet. Chem.* **1996**, *512*, 219-224.
7. Gosselin, F.; O'Shea, P. D.; Roy, S.; Reamer, R. A.; Chen, C.-y.; Volante, R. P., Unprecedented Catalytic Asymmetric Reduction of N–H Imines. *Org. Lett.* **2005**, *7*, 355-358.
8. Zhang, Y.; Hetherington, H. P.; Stokely, E. M.; Mason, G. F.; Twieg, D. B., A novel k-space trajectory measurement technique. *Magn. Reson. Med.* **1998**, *39*, 999-1004.
9. Neese, F., The ORCA Program System. *Wiley Interdiscip. Rev.: Comput. Mol. Sci.* **2012**, *2*, 73-78.
10. Neese, F., Software Update: The ORCA Program System, Version 4.0. *Wiley Interdiscip. Rev.: Comput. Mol. Sci.* **2018**, *8*, e1327.
11. *Avogadro: an open-source molecular builder and visualization tool.*, 1.2.0. <http://avogadro.cc/>
12. Hanwell, M. D.; Curtis, D. E.; Lonie, D. C.; Vandermeersch, T.; Zurek, E.; Hutchison, G. R., Avogadro: An Advanced Semantic Chemical Editor, Visualization, and Analysis Platform. *J. Cheminf.* **2012**, *4*, 17.
13. *Chemcraft - graphical software for visualization of quantum chemistry computations.*, b595. <https://www.chemcraftprog.com>
14. Humphrey, W.; Dalke, A.; Schulten, K., VMD: Visual Molecular Dynamics. *J. Mol. Graphics* **1996**, *14*, 33-38.

15. Becke, A. D., Density-Functional Thermochemistry. III. The Tole of Exact Exchange. *J. Chem. Phys.* **1993**, *98*, 5648-5652.
16. Weigend, F.; Ahlrichs, R., Balanced Basis Sets of Split Valence, Triple Zeta Valence and Quadruple Zeta Valence Quality for H to Rn: Design and Assessment of Accuracy. *Phys. Chem. Chem. Phys.* **2005**, *7*, 3297-3305.
17. Grimme, S.; Ehrlich, S.; Goerigk, L., Effect of the Damping Function in Dispersion Corrected Density Functional Theory. *J. Comput. Chem.* **2011**, *32*, 1456-1465.
18. Grimme, S.; Antony, J.; Ehrlich, S.; Krieg, H., A Consistent and Accurate Ab Initio Parametrization of Density Functional Dispersion Correction (DFT-D) for the 94 Elements H-Pu. *J. Chem. Phys.* **2010**, *132*, 154104.
19. Marenich, A. V.; Cramer, C. J.; Truhlar, D. G., Universal Solvation Model Based on Solute Electron Density and on a Continuum Model of the Solvent Defined by the Bulk Dielectric Constant and Atomic Surface Tensions. *J. Phys. Chem. B* **2009**, *113*, 6378-6396.
20. Neese, F.; Wennmohs, F.; Hansen, A.; Becker, U., Efficient, Approximate and Parallel Hartree–Fock and Hybrid DFT Calculations. A ‘Chain-of-Spheres’ Algorithm for the Hartree–Fock Exchange. *Chem. Phys.* **2009**, *356*, 98-109.
21. Izsák, R.; Neese, F., An Overlap Fitted Chain of Spheres Exchange Method. *J. Chem. Phys.* **2011**, *135*, 144105.
22. Weigend, F., Accurate Coulomb-Fitting Basis Sets for H to Rn. *Phys. Chem. Chem. Phys.* **2006**, *8*, 1057-1065.
23. Hellweg, A.; Hättig, C.; Höfener, S.; Klopper, W., Optimized Accurate Auxiliary Basis Sets for RI-MP2 and RI-CC2 Calculations for the Atoms Rb to Rn. *Theor. Chem. Acc.* **2007**, *117*, 587-597.
24. Chmela, J.; Harding, M. E., Optimized Auxiliary Basis Sets for Density Fitted Post-Hartree–Fock Calculations of Lanthanide Containing Molecules. *Mol. Phys.* **2018**, *116*, 1523-1538.
25. Bykov, D.; Petrenko, T.; Izsák, R.; Kossmann, S.; Becker, U.; Valeev, E.; Neese, F., Efficient Implementation of the Analytic Second Derivatives of Hartree–Fock and Hybrid DFT Energies: a Detailed Analysis of Different Approximations. *Mol. Phys.* **2015**, *113*, 1961-1977.
26. Garcia-Ratés, M.; Neese, F., Efficient Implementation of the Analytical Second Derivatives of Hartree–Fock and Hybrid DFT Energies within the Framework of the Conductor-Like Polarizable Continuum Model. *J. Comput. Chem.* **2019**, *40*, 1816-1828.
27. Riplinger, C.; Neese, F., An Efficient and Near Linear Scaling Pair Natural Orbital Based Local Coupled Cluster Method. *J. Chem. Phys.* **2013**, *138*, 034106.

28. Riplinger, C.; Sandhoefer, B.; Hansen, A.; Neese, F., Natural Triple Excitations in Local Coupled Cluster Calculations with Pair Natural Orbitals. *J. Chem. Phys.* **2013**, *139*, 134101.
29. Arumugam, K.; Becker, U., Computational Redox Potential Predictions: Applications to Inorganic and Organic Aqueous Complexes, and Complexes Adsorbed to Mineral Surfaces. *Minerals* **2014**, *4*, 345-387.
30. Dunlop, D.; Večeřa, M.; Gyepes, R.; Kubát, P.; Lang, K.; Horáček, M.; Pinkas, J.; Šimková, L.; Liška, A.; Lamač, M., Luminescent Cationic Group 4 Metallocene Complexes Stabilized by Pendant N-Donor Groups. *Inorg. Chem.* **2021**, *60*, 7315-7328.
31. Isegawa, M.; Neese, F.; Pantazis, D. A., Ionization Energies and Aqueous Redox Potentials of Organic Molecules: Comparison of DFT, Correlated *Ab Initio* Theory and Pair Natural Orbital Approaches. *J. Chem. Theory Comput.* 2016, *12*, 2272-2284.

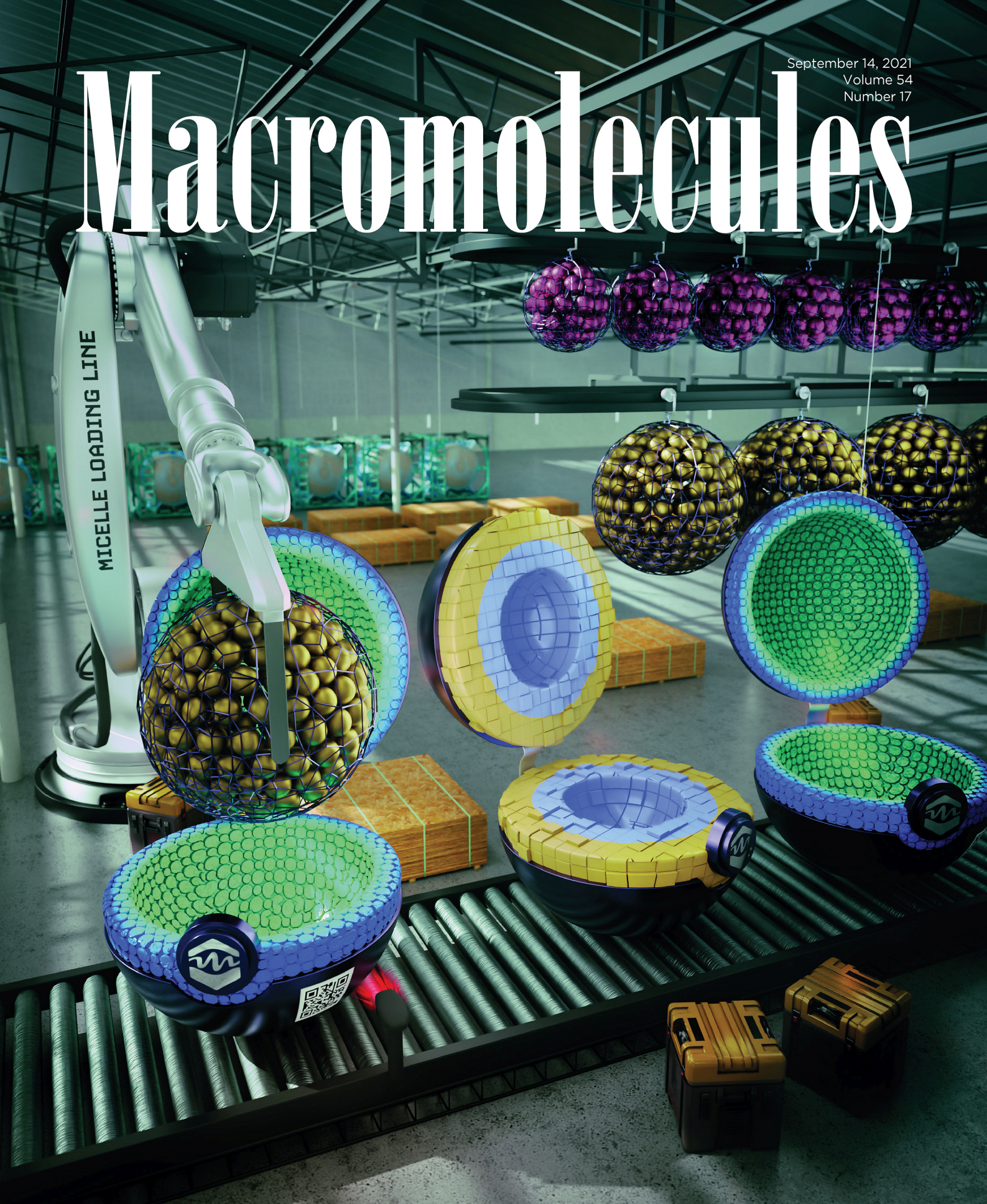
Appendix 6

Loukotová, L.; Švec, P.; Groborz, O.; Heizer, T.; Beneš, H.; Raabová, H.; Bělinová, T.; Herynek, V.; Hrubý, M., Direct Comparison of Analogous Amphiphilic Gradient and Block Polyoxazolines. *Macromolecules* **2021**, *54* (17), 8182-8194. **Times Cited: 15; IF = 6.06.**

P. Švec designed and performed the synthesis, purification and characterization of the novel 2-aryl(2-oxazoline) monomers, assisted with the experimental design, and co-wrote the manuscript.

September 14, 2021
Volume 54
Number 17

Macromolecules



ACS Publications
Most Trusted. Most Cited. Most Read.

www.acs.org

Direct Comparison of Analogous Amphiphilic Gradient and Block Polyoxazolines

Lenka Loukotová, Pavel Švec, Ondřej Groborz, Tomáš Heizer, Hynek Beneš, Helena Raabová, Tereza Bělinová, Vít Herynek, and Martin Hrubý*

Cite This: *Macromolecules* 2021, 54, 8182–8194

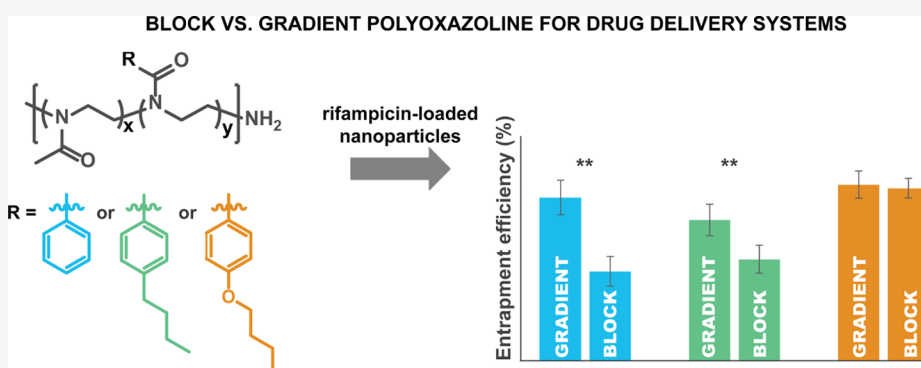
Read Online

ACCESS |

Metrics & More

Article Recommendations

Supporting Information



ABSTRACT: Both gradient and block copolymers can be used as drug delivery systems, but their relative (dis)advantages remain unknown. Thus, we directly compared analogous amphiphilic gradient and block polyoxazolines for their physicochemical properties and potential as building components of nanodrugs. For this purpose, we prepared a library of 18 polymers with varying ratios of monomeric units, using 2-methyl-2-oxazoline (MeOx) as a hydrophilic monomer and 2-phenyl-2-oxazoline (PhOx), 2-(4-butylphenyl)-2-oxazoline (BuPhOx), or 2-(4-butoxyphenyl)-2-oxazoline (BuOPhOx) as a hydrophobic monomer, and determined their homo/heteropolymerization kinetics. Our results showed that gradient copolymers had broader glass transition intervals and formed nanoparticles several times smaller and more compact than the corresponding block analogs. In particular, PMeOx₇₀-grad-PhOx₃₀ and PMeOx₇₀-grad-BuPhOx₃₀ exhibited a significantly higher drug loading capacity and entrapment efficiency than their corresponding block analogs. Notwithstanding these differences, all polymers were cyto- and hemocompatible *in vitro*. Therefore, analogous gradient and block copolymers may be alternatively used for specific biomedical applications.

1. INTRODUCTION

Amphiphilic polymers are among the most commonly used building components of nanodrugs because of their ability to spontaneously self-assemble into various nanoscale architectures. As such, they provide extremely variable pharmacokinetic properties¹ depending on their chemical composition, concentration, and molecular weight and on the solvent used for nanoparticle (NP) preparation.² Therefore, these NPs can be applied to a wide range of biomedical purposes as therapeutic or imaging agents to enhance active pharmaceutical ingredient (API) efficiency and solubility, protect API in biological environments, reduce API toxicity, and/or control API release and biodistribution.³

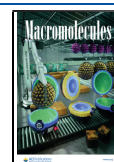
Amphiphilic polymer micelles can be tailored for controlled delivery systems of poorly water-soluble drugs. Moreover, block copolymer micelles are much more thermodynamically stable than classical micelle formulations derived from low-molecular-weight surfactants.^{4,5} The only micellar formulation approved by the Food and Drug Administration (FDA) thus

far is Estrasorb, a topical treatment for vasomotor symptoms of menopause, which stabilizes estrogen serum levels for 8–14 days.⁶ Nevertheless, many micelle systems are currently under clinical trials. For example, CriPec from Cristal Therapeutics is now under evaluation in a phase II trial as a potential treatment for ovarian cancer.⁷ The predecessor platform of CriPec, based on the block copolymer of monomethoxy poly(ethylene glycol) (mPEG) and *N*-2-hydroxypropyl methacrylamide monolactate/dilactate with conjugated docetaxel via a hydrolyzable ester linker, induced complete tumor remission after a single intravenous injection in a xenograft breast cancer model.⁸ Similarly, Genexol-PM (Samyang Biopharm), a

Received: December 2, 2020

Revised: July 15, 2021

Published: July 28, 2021



micellar formulation of paclitaxel based on mPEG-*block*-poly(lactic acid) (PLA), is currently under investigation in various clinical trials^{9–12} and has already been approved for the treatment of advanced lung cancer and metastatic breast cancer in South Korea.¹³

Unlike block copolymers, whose monomer composition changes abruptly, gradient copolymers exhibit a continuous gradual change in monomer composition along their macromolecular chains due to differences in the polymerization reactivity of the monomers.¹⁴ Because of their easier one-pot synthesis, they have been considered as inexpensive alternatives of block copolymers in applications such as emulsion/dispersion stabilization or compatibilization of immiscible polymer blends.¹⁵ Currently, research on gradient copolymers also focuses on their applications in drug delivery systems. For such purposes, one of the most convenient copolymers forming polymeric NPs in aqueous solutions are poly(2-alkyl-2-oxazoline)s (POXs), biocompatible pseudopeptides.^{16–19} Poly(2-methyl-2-oxazoline-*grad*-2-phenyl-2-oxazoline) (PMeOx-*grad*-PhOx) particles were successfully used for the delivery of DNA chains²⁰ and encapsulation of indomethacin.²¹ Moreover, in aqueous environment, PMeOx-*grad*-PhOx particles form a new type of micelles, “bitterball-core micelles”, with a denser outer layer than the core.²² Notwithstanding these advances in research on gradient and block copolymers, their relative advantages and disadvantages in terms of applications as drug delivery systems remain unknown.

Based on the above, in the present study, we directly compare the physicochemical properties of analogous gradient and block POXs and their potential applications as drug delivery systems. We hypothesize that bitterball-core micelles of PMeOx-*grad*-PhOx have higher drug loading (DL) than classical micelles of analogous block copolymers because gradient copolymers form micelles with a larger empty core structure. Accordingly, three series of gradient and analogous block POXs were prepared using 2-methyl-2-oxazoline (MeOx) as a hydrophilic monomer and 2-phenyl-2-oxazoline (PhOx), 2-(4-butylphenyl)-2-oxazoline (BuPhOx), or 2-(4-butoxyphenyl)-2-oxazoline (BuOPhOx) as a hydrophobic monomer, which also enabled us to assess the effect of substituents on the benzene ring on the polymer properties. In addition, we performed a copolymerization kinetic study of two novel monomers, BuPhOx and BuOPhOx.

2. EXPERIMENTAL SECTION

2.1. Materials and Instrumentation. Dichloromethane (CH₂Cl₂), diethyl ether, dimethylformamide (DMF), ethyl acetate (EtOAc), hexane, and methanol (MeOH) were purchased from Lach-Ner Ltd. (Neratovice, Czech Republic) and were of analytical grade. Chloroform-*d*, dimethyl sulfoxide-*d*₆, and deuterated water were purchased from Eurisotop (Cambridge, U.K.). Dyomics-560 *N*-hydroxysuccinimide (Dy560 NHS ester) was purchased from Dyomics GmbH (Jena, Germany). Alexa Fluor 488 and Mowiol were purchased from Thermo Fischer Scientific (Prague, Czech Republic). Normal human dermal fibroblast was purchased from Lonza (Prague, Czech Republic).

All other chemicals were purchased from Sigma Aldrich Ltd. (Prague, Czech Republic). The chemicals were used without further purification unless stated otherwise.

All polymerization mixtures were prepared under an argon atmosphere in a glovebox, and the polymerization reactions were performed using a Biotage Initiator⁺ microwave synthesizer (Biotage, Uppsala, Sweden).

All NMR spectra were recorded on a Bruker Avance III HD 400 MHz spectrometer (Bruker Co., Billerica, MA) operating at a frequency of 400.13 MHz equipped with a broadband probe. Chemical shifts are reported relative to the residual solvent signals. The following experiments were performed to determine interactions in the drug-loaded NPs: polymer (1.0 mg) and rifampicin (1.0 mg) were dissolved in acetonitrile (ACN, 0.20 mL), D₂O (1.00 mL) was added, ACN was evaporated, and nuclear Overhauser effect (NOESY) spectra were recorded²³ (16 scans, mixing time of 300 ms, relaxation delay $D_1 = 2.00$ s, size of fid 2048 by 256) using ¹H NMR (128 scans, relaxation delay $D_1 = 20.00$ s) as an external projection.

Elemental analysis was performed on a PerkinElmer 2400 Series II CHNS/O elemental analyzer (PerkinElmer Systems Ltd., Czech Republic).

The molecular weight of all polymers prepared in this study was determined with size exclusion chromatography (SEC) using a HPLC DeltaChrom P102 Pump SS system equipped with a SEC column (Deltagel Mixed-B, 300 × 8 mm), an autosampler AS250, and refractive index RI200 (all from Watrex, Prague, Czech Republic). The mixture of chloroform/triethylamine/isopropanol = 94:4:2 (volume ratio) was used as the mobile phase for all polymers, except for PMeOx₁₀₀, for which dimethylformamide was used as the mobile phase. The molecular weights were calculated using poly(methyl methacrylate) (PMMA) calibration (12 standards with M_n values ranging from 360 to 721 000 Da).

The remaining content of monomers in each kinetic sample was determined by high-performance liquid chromatography (HPLC), using a chromatograph with UV detection (Dionex Ultimate 3000, Dionex, California). MeOx was determined using a ZIC-HILIC column (100 × 2.1 mm) and an isocratic mobile phase A/B = 20/80 (phase A: 95% deionized water, 5% ACN + 0.1% trifluoroacetic acid (TFA); phase B: 5% deionized water, 95% ACN + 0.1% TFA) with a flow rate of 0.5 mL/min. BuPhOx and BuOPhOx were determined using a reverse-phase column Chromolith Performance RP-18e (100 × 4.6 mm) with a mobile phase composition of 0.00–0.25 min: 15% of phase B; 0.25–5.50 min: linear gradient 15–50% of phase B; 5.50–6.50 min: linear gradient 50–100% of phase B; 7.00 min: 100% of phase B; and a flow rate: 3.5 mL/min. The chromatograms were obtained at 225 nm.

The size of the NPs was determined using dynamic light scattering (DLS) on a Zetasizer Nano-ZS, Model ZEN3600 (Malvern Instruments, U.K.) at $\theta = 173^\circ$ scattering angle and 25 °C. The data were evaluated using the DTS software (version 6.20, Nano, Malvern, U.K.). All samples were filtered through 0.45 μm PVDF filters before the measurements.

The morphology of the NPs was visualized using transmission electron microscopy (TEM). Copper grids (400 mesh) with a 5 nm carbon film were freshly glow-discharged. The sample (4 μL) was placed on top of the grid for 30 s, washed twice with 7 μL of the staining solution (1% wt ammonium molybdate and 0.1% wt trehalose in Milli-Q water), stained with another 7 μL of the staining solution for 30 s, and dried with a piece of filter paper. Sample solutions were used as prepared, only PMeOx₈₀-*grad*-PhOx₂₀ was diluted twice with Milli-Q water. The images were acquired using a Jeol JEM-1400 FLASH transmission electron microscope with a bottom-mounted FLASH 2kx2k CMOS camera at 80 kV. The images of spherical particles were analyzed in ImageJ (Fiji Is Just) software, using the Trainable WEKA segmentation plugin for particle detection (at least 500 particles per sample), manual thresholding, and particle analysis of binary images where the particle area and circularity were evaluated. Equivalent circular area diameters were calculated from the respective particle areas and sorted in histograms showing number-weighted particle size distribution. Rodlike micelles were characterized by measuring their lengths in the longest direction.

Thermogravimetric analysis (TGA) of the homopolymers and copolymers was performed using a Pyris 1 TGA Thermogravimetric Analyzer (PerkinElmer, Czech Republic). Prior to TGA, the samples were purified by extensive drying under reduced pressure at an increased temperature. Approximately 5 mg of the sample was placed

in a ceramic crucible and heated from 30 to 500 °C at a heating rate of 10 °C/min under a nitrogen flow of 25 mL/min. The temperature of 5% weight loss ($T_{d,5\%}$) and the temperature of maximum decomposition ($T_{d,max}$) were evaluated for all samples. The standard deviation of the TGA measurement was under 5%.

The thermal behavior of the homopolymers and copolymers was evaluated by differential scanning calorimetry (DSC) using a Q 2000 calorimeter (TA Instruments), calibrated with an indium standard. The samples (2–5 mg) were encapsulated in aluminum hermetic Tzero pans with a pinhole. All DSC measurements were performed under a nitrogen atmosphere (at a flow rate of 50 mL/min) at a temperature ranging from 0 to 250 °C. Glass transition temperature (T_g) data were extracted from the second heat scan using a heat-cool-heat cycle with a heating rate of 50 °C/min and a cooling rate of 5 °C/min. The glass transition temperature T_g values were determined as the midpoint of heat flow change. The breadth of the glass transition region (ΔT_g) was determined from the derivatives of heat curves as the difference between T_e and T_0 ,²⁴ where T_e was the end point T_g corresponding to the local minimum of the derivatives of heat curves (as a consequence of the presence of a small enthalpy relaxation/endothemic peak on the original DSC heat curves) and T_0 was the onset point of the T_g peak on the derivate heat curve. Crystallization and melting of the selected samples were studied with a heating/cooling rate of 5 °C/min. All DSC measurements were repeated.

In all calculations performed in this article, the following statistical processing was applied: the mean value \bar{x} was calculated as the arithmetic mean, and the standard deviation s was calculated according to eq 1

$$s = \sqrt{\frac{\sum (x - \bar{x})^2}{n - 1}} \quad (1)$$

where n is the number of independent experiments. To study the variation among and between groups, analysis of variance (ANOVA) was applied using OriginPro 8.6 software.

2.2. Polymer Synthesis. **2.2.1. Kinetics.** **2.2.1.1. Homopolymerization.** A stock solution containing methyl 4-nitrobenzenesulfonate (MeONs) as the initiator and the monomer BuPhOx (or BuOPhOx) in the ratio $[\text{BuPhOx}/\text{BuOPhOx}]/[\text{MeONs}] = 100:1$ with a total monomer concentration of 2 M in anhydrous ACN was prepared under an argon atmosphere. The stock solution was then divided into six microwave vials, sealed, and polymerized in a microwave synthesizer at 140 °C for various periods. After cooling the polymerization mixture to room temperature, the reaction was quenched with a methanolic ammonia solution (3 mol equiv of MeONs). The sample concentration was measured using HPLC and compared to the concentration of a stock solution ($t = 0$ s). The sample molecular weight was determined using SEC.

The monomer polymerization constant (k_p) was determined using eqs 2 and 3 assuming that k_{eff} corresponds to the slope of the linear fit of $\ln([M]_0/[M]_t)$.²⁵

$$\ln M_0 - \ln M_t = k_{\text{eff}} \cdot t \quad (2)$$

$$k_{\text{eff}} = k_p [I]_0 \quad (3)$$

where M_0 is the initial monomer concentration and M_t is the monomer concentration at time t .

2.2.1.2. Copolymerization. Stock solutions containing methyl 4-nitrobenzenesulfonate (MeONs) as the initiator ($[M]/[I] = 100$) and the monomers MeOx and BuPhOx or BuOPhOx ($[\text{MeOx}]_0/[\text{BuPhOx}/\text{BuOPhOx}]_0 = 90:10, 80:20, 70:30, 50:50, 30:70, \text{ and } 15:85$), with a total monomer concentration of 4 M in anhydrous ACN, were prepared under an argon atmosphere. The stock solution was then divided into six microwave vials inside a glovebox, sealed, and polymerized in the microwave synthesizer at 140 °C for various periods (absorption level: high). After cooling the mixture to room temperature, polymerization was terminated by adding the methanolic ammonia solution (3 mol equiv of MeONs). The sample concentration was measured using HPLC and compared with the

concentration of a stock solution ($t = 0$ s). The sample molecular weight was determined using SEC.

The reaction time at 30% MeOx conversion ($\ln(M_0/M_t) = 0.357$) was determined. At this time, the PhOx conversion was calculated from the kinetic plots. In turn, the monomer reactivity ratios were determined by nonlinear least-squares fitting of the data plot F_1 versus f_1 (Figure 3E,F) (Equation 4, OriginPro 8.6 software).^{26,27}

$$F_1 = \frac{(r_1 - 1)f_1^2 + f_1}{(r_1 + r_2 - 2)f_1^2 + 2(1 - r_2)f_1 + r_2} \quad (4)$$

where F_1 is the instant mole fraction incorporated into the polymer chain, f_1 is the fraction of BuPhOx/BuOPhOx in the monomer feed, r_1 is the reactivity ratio of BuPhOx/BuOPhOx, and r_2 is the reactivity ratio of MeOx.

2.2.2. Synthesis of Copolymers. The gradient polymers were synthesized as follows: 2-methyl-2-oxazoline (MeOx), the hydrophobic 2-aryl-2-oxazoline (a total monomer concentration of 4 M; for more detailed information, see Table 1), and the initiator MeONs

Table 1. Detailed Polymerization Data^a

name	MeOx (μL)	mass of hydrophobic monomer (mg)	reaction time (min)
PMeOx ₉₀ -grad-PhOx ₁₀	404	79	120
PMeOx ₉₀ -block-PhOx ₁₀	404	79	20 + 100
PMeOx ₈₀ -grad-PhOx ₂₀	359	158	120
PMeOx ₈₀ -block-PhOx ₂₀	359	158	20 + 100
PMeOx ₇₀ -grad-PhOx ₃₀	314	316	120
PMeOx ₇₀ -block-PhOx ₃₀	314	316	15 + 105
PMeOx ₉₀ -grad-BuPhOx ₁₀	404	108	120
PMeOx ₉₀ -block-BuPhOx ₁₀	404	108	20 + 100
PMeOx ₈₀ -grad-BuPhOx ₂₀	359	218	120
PMeOx ₈₀ -block-BuPhOx ₂₀	359	218	20 + 100
PMeOx ₇₀ -grad-BuPhOx ₃₀	314	323	120
PMeOx ₇₀ -block-BuPhOx ₃₀	314	323	15 + 105
PMeOx ₉₀ -grad-BuOPhOx ₁₀	404	116	120
PMeOx ₉₀ -block-BuOPhOx ₁₀	404	116	20 + 100
PMeOx ₈₀ -grad-BuOPhOx ₂₀	359	235	120
PMeOx ₈₀ -block-BuOPhOx ₂₀	359	235	20 + 100
PMeOx ₇₀ -grad-BuOPhOx ₃₀	314	348	120
PMeOx ₇₀ -block-BuOPhOx ₃₀	314	348	15 + 105

^aMeOx, 2-methyl-2-oxazoline; PhOx, 2-phenyl-2-oxazoline; BuPhOx, 2-(4-butylphenyl)-2-oxazoline; and BuOPhOx, 2-(4-butoxyphenyl)-2-oxazoline.

(11.4 mg; 0.053 mmol) were mixed in anhydrous ACN (1.50 mL) under an argon atmosphere. Polymerization was performed in microwave vials under an argon atmosphere at 140 °C for 2 h. Then, the living polymerization chains were terminated by adding the methanolic ammonia solution (0.200 mL; 4 M in MeOH; stirred for the next 3 h). The resulting copolymers were precipitated in diethyl ether and purified on a Sephadex LH-20 column.

The analogous block copolymers were synthesized as described above, except that MeOx was first polymerized for a specific time and only then was the second monomer added (4 M total monomer concentration), thereby continuing the living polymerization.

To measure the thermal properties of the copolymers, the analogous homopolymers PMeOx, PPhOx, PBuPhOx, and PBuOPhOx were prepared, as described above, using only one monomer.

Polymers expected to be most and least hydrophobic were selected for conjugation with Dy560 NHS ester as follows: each polymer (20 mg) was dissolved in anhydrous DMF (2.000 mL) with *N,N*-diisopropylethylamine (DIPEA, 0.120 mL). Then, Dy560 NHS ester was added, stirring the reaction mixture overnight. The product was purified twice on a Sephadex LH-20 column using methanol as the mobile phase. The amount of Dy560 was determined spectrophotometrically (PMeOx₉₀-grad-PhOx₁₀-Dy560, 1.8 wt %; PMeOx₉₀-block-PhOx₁₀-Dy560, 2.5 wt %; PMeOx₇₀-block-BuPhOx₃₀-Dy560, 3.0 wt %; PMeOx₇₀-block-BuOPhOx₃₀-Dy560, 3.4 wt %).

2.3. Preparation of Drug-Loaded NPs. The NPs loaded with rifampicin were prepared by nanoprecipitation as follows. Each polymer (10.0 mg) and rifampicin (10.0 mg) were dissolved in ACN (1.5 mL). Milli-Q water (10 mL) was then quickly added to the solution under vigorous stirring via a syringe, and ACN was evaporated under reduced pressure at 45 °C. Then, the solution volume was adjusted to 10.00 mL by adding Milli-Q water.

The mass of the drug incorporated into the NPs was determined as the difference between the mass of the drug used to prepare the NPs and the mass of the free drug. The solution of the prepared NPs was ultracentrifuged through a 10 kDa membrane (Amicon Ultra-15 Centrifugal Filters with Ultracel 10 kDa membrane, Millipore, Ireland), and the filtrate (0.100 mL) was mixed with ACN (1.900 mL). The mass of the free drug (non-encapsulated in NPs) was calculated using this sample absorbance at $\lambda = 477$ nm measured using an UV-vis spectrometer, Thermo Scientific Evolution 220 (Waltham, Massachusetts).

The efficiency of drug incorporation was evaluated as the entrapment efficiency (EE) and drug loading (DL), which were calculated according to eqs 5 and 6, respectively.

$$EE = \frac{\text{mass of the drug incorporated into the NPs}}{\text{mass of the drug used to prepare the NPs}} \quad (5)$$

$$DL = \frac{\text{mass of the drug incorporated into the NPs}}{\text{total mass of the NPs}} \quad (6)$$

The EE and DL data were collected from three independent experiments ($n = 3$).

2.4. In Vitro Experiments. **2.4.1. Cytotoxicity.** Normal human dermal fibroblast (NHDF) cells were cultured in Dulbecco's modified Eagle medium (DMEM) supplemented with 10% fetal bovine serum and 1% penicillin streptomycin at 37 °C in a humidified incubator containing 5% CO₂.

NHDF cells were precultivated for 24 h in 96-well plates (clear, flat bottom plates; density of 10⁴ cells/cm²). The cells were incubated with varying concentrations of the polymer solution for 48 h, and the cell viability was determined using a 3-(4,5-dimethylthiazol-2-yl)-2,5-diphenyltetrazolium bromide (MTT) assay.²⁸ MTT is reduced to formazan in the mitochondria of living cells, and thus cell viability can be spectrophotometrically determined using absorbance at 570 nm after cell lysis (sodium dodecyl sulfate lysis buffer).²⁸ The cells were observed and photographed before lysis under phase-contrast light microscopy (Olympus IX71 with camera DP74). The MTT assay results were compared with the control samples (adding phosphate-buffered saline, PBS, instead of polymer solution), and the cell viability of these samples was set to 100%. The results are expressed as the average values of three independent experiments.

2.4.2. Hemolysis Test. The hemolysis test was performed according to the protocol reported by Anand et al.²⁹ The tail vein blood of Wistar rats (purchased from Velaz, Prague, Czech Republic) was collected via a cannula to ethylenediamine tetraacetic acid (EDTA)-

coated vacuum test tubes containing the polymers ($c = 0.5$ mg/mL). The blood was used within 1 h from collection.

The blood was diluted with saline (0.9% NaCl) in a 1:50 volume ratio and then mixed with the polymer solutions ($c_{\text{final}} = 0.5$ mg/mL). An equivalent volume of PBS or Triton X-100 ($c_{\text{final}} = 17$ mM) was used as a negative or positive control, respectively. The samples were incubated for 1 h and centrifuged for 5 min at 500g, subsequently recording absorption spectra (460–600 nm) of the supernatants on a Tecan Spark reader (Tecan Life Sciences, Männedorf, Switzerland).

Polymers had substantial absorbance in the selected range, which could alter the results. Therefore, the absorption spectra were decomposed using the method of least-squares (Matlab, Natick, Massachusetts) to separate the contribution to absorption of the polymers from that of the released hemoglobin.

The results are expressed as a relative hemolysis index (PBS control, 0%; Triton X-100 control, 100%). The tests were repeated four times (using blood samples from different animals), and the data are presented as average values \pm standard deviation.

2.4.3. Cellular Association Assay. NHDF cells were cultivated overnight in six-well plates (density, 3×10^4 cells/cm²). Then, they were incubated with a solution of each polymer conjugated with Dy560 ($c = 1$ mg/mL) for 48 h. The cells were collected after trypsinization and washed with the cultivation medium and PBS. Each cell suspension was measured on a BD Aria Iiu flow cytometer (FACS) equipped with a laser of 561 nm (yellow detector 586/15; 400 V). The results are expressed as the increase in the mean fluorescence intensity (MFI) (in arbitrary units) from at least 1.5×10^4 cells for each polymer and each time point. Fluorescence was correlated with the weight amount of Dy560 in the polymer samples.

2.4.4. Fluorescence Imaging. NHDF cells were cultivated overnight at a concentration of 5×10^3 cells/cm². The selected polymers labeled with Dy560 ($c = 1$ mg/mL) were mixed with cells and incubated for 48 h. After incubation, the supernatant was discarded, and the cells were washed three times with prewarmed PBS and fixed in 4% paraformaldehyde in PBS for 15 min. The cells were treated with 0.1% Triton X-100 in PBS for 20 min and then blocked in 1% fetal bovine serum and 0.05% Tween in PBS for 30 min. The actin cytoskeleton of the cells was stained with phalloidin conjugated with Alexa Fluor 488 (Phall/AF488, Invitrogen) for 30 min. Subsequently, the cell nuclei were stained with 4',6-diamidino-2-phenylindole dihydrochloride (DAPI) in the dark at 37 °C. Both dyes were diluted 1000 \times from the stock solution ($c = 1$ mg/mL). All staining steps were separated by two washing steps (PBS). After completing the staining procedure, the cells were washed three times with PBS, mounted in Mowiol, and covered with a coverslip. The samples were kept in the refrigerator for at least 48 h.

The samples were observed under a confocal laser scanning microscope (Leica TCS SP8X, Leica Microsystems). The polymers PMeOx₉₀-grad-PhOx₁₀-Dy560 and PMeOx₉₀-block-PhOx₁₀-Dy560 were excited using a light laser (40% laser intensity, 488 nm), and the emission was collected on a hybrid detector from 580 to 600 nm. Phall/AF488-stained actin filaments were also excited using a white light laser (40% laser intensity), and the emission was collected from 510 to 530 nm. DAPI-stained cell nuclei were excited using a diode laser (405 nm, 40% laser intensity), acquiring emission from 435 to 478 nm using a Leica DFC365 FX monochrome digital CCD camera and an HC PL APO CS2 63x/1.40 OIL objective (both Leica Microsystems). ImageJ software was used for contrast and smoothness correction purposes.

3. RESULTS AND DISCUSSION

In this study, the novel monomers 2-(4-butylphenyl)-2-oxazoline (BuPhOx) and 2-(4-butoxyphenyl)-2-oxazoline (BuOPhOx) were first synthesized, and the monomer synthesis is described in detail in the Supporting Information (SI) (Monomer Synthesis).

3.1. Kinetics and Polymer Synthesis. All copolymers were synthesized by cationic ring-opening polymerization (CROP) (Figure 1). The mechanism starts with a nucleophilic

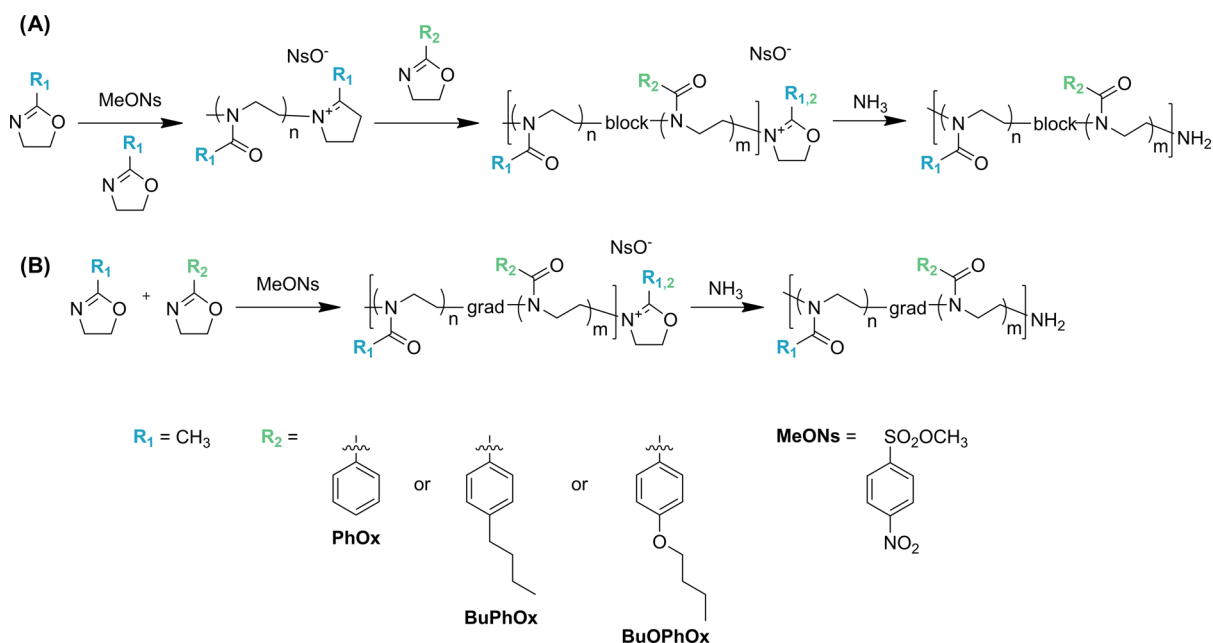


Figure 1. General scheme of cationic ring-opening polymerization (CROP) of 2-aryl-2-oxazolines to produce block (A) and gradient (B) POX.

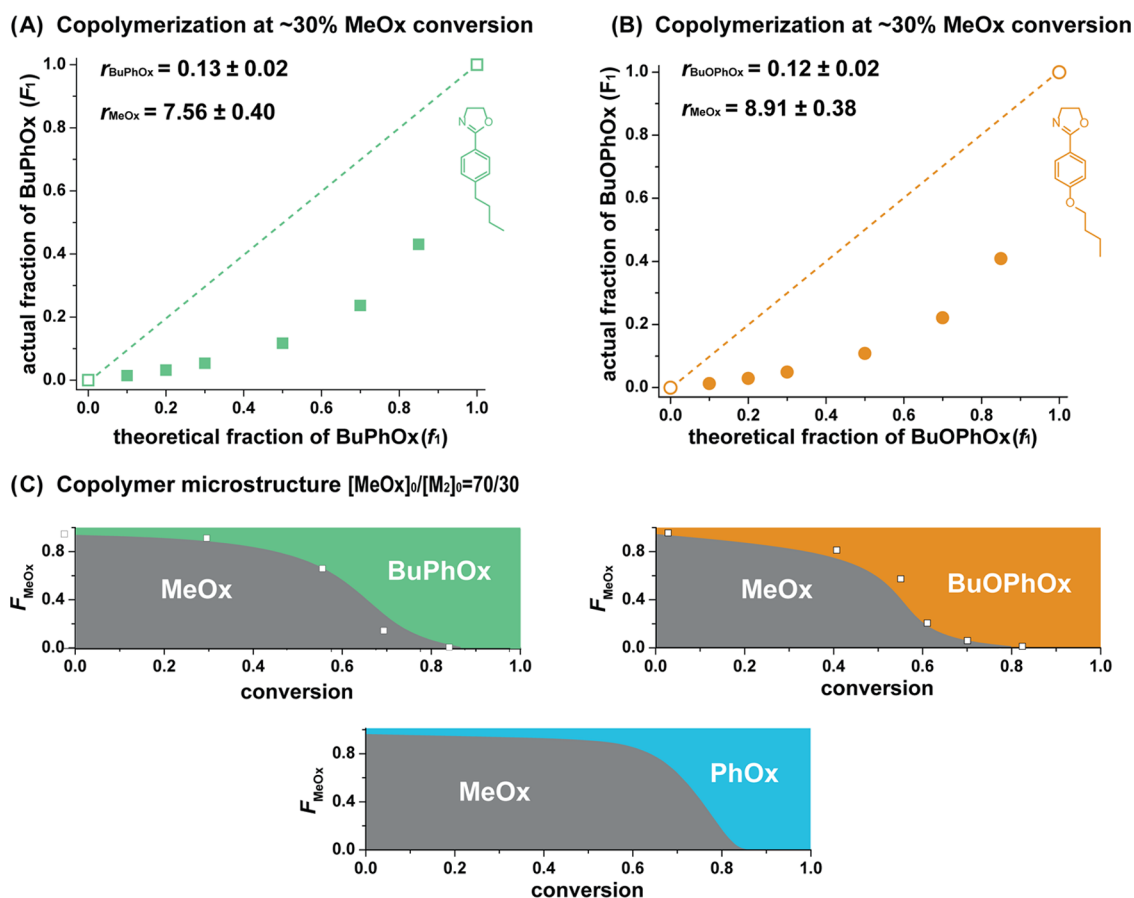


Figure 2. (A) and (B) relationship between the fraction of BuPhOx/BuOPhOx in the monomer feed (f_1) and the fraction of BuPhOx/BuOPhOx incorporated into the copolymer (F_1) at 30 mol % MeOx conversion. (C) Microstructure of the copolymers resulting from a feed containing monomers at a 70:30 ratio (based on the Skeist model). The white squares correspond to the real data. For the microstructure of the PhOx copolymer, the literature data were used ($r_{\text{MeOx}} = 10.02$, $r_{\text{BuPhOx}} = 0.02$).³²

attack of the lone electron pair of the nitrogen atom of 2-alkyl-2-oxazoline on an electrophilic initiator species (in this case, methyl nosylate). The carbon atom of the $\text{CH}_2\text{-O}$ bond

undergoes a nucleophilic attack by the nitrogen atom of the next monomer molecule and ring opening, thereby forming poly(2-alkyl-2-oxazoline). Under ideal polymerization con-

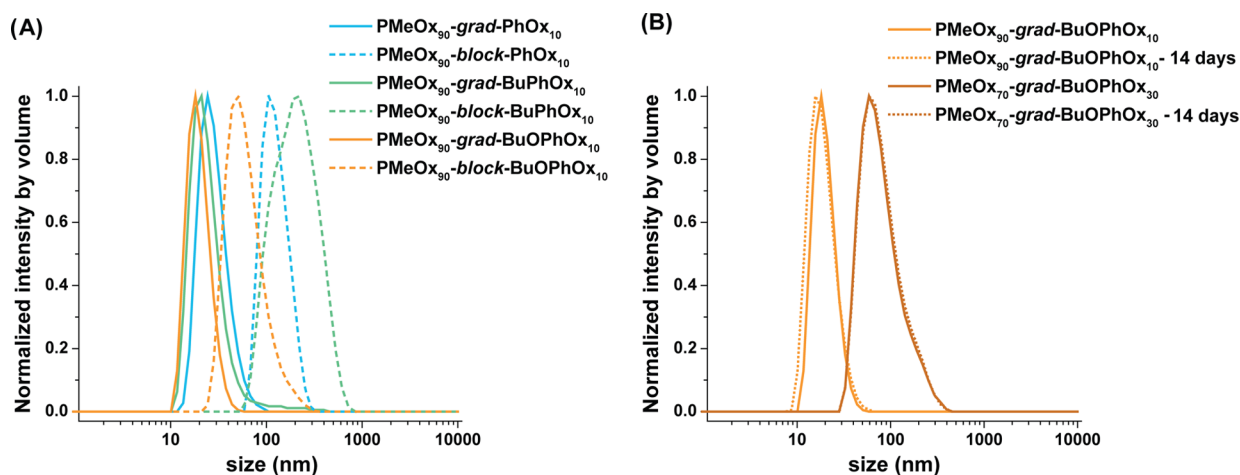


Figure 3. Size distributions by volume of the rifampicin-loaded NPs monitored by DLS.

ditions, the termination or chain-transfer reaction is almost missing (living polymerization); therefore, the polymerization reaction proceeds until a terminating agent is added or all monomers are consumed. Generally, a block copolymer is formed when only one type of monomer is present in the starting polymerization mixture, and the second monomer is added just after the first one is consumed (Figure 1A). Conversely, when two types of monomers are present at initiation (Figure 1B), both monomers participate in polymerization and produce statistical copolymers. If the reactivities of both monomers are extremely different, the resulting polymers will have a varying composition along the polymer chain and are hence known as gradient polymers.

To investigate the newly prepared monomers, their kinetics of homopolymerization and copolymerization with 2-methyl-2-oxazoline (MeOx) were studied. The first set of experiments was performed to investigate the homopolymerization kinetics of BuPhOx and BuOPhOx, and the results are clearly summarized in the SI (Homopolymerization Kinetics). The second set of kinetic experiments was performed to study the copolymerization of the novel monomers with MeOx ($[MeOx]_0/[BuPhOx/BuOPhOx]_0 = 90:10, 80:20, 70:30, 50:50, 30:70, \text{ and } 15:85$) using the typical conditions of polymerization, as described above. Here, all of the copolymerization reactions displayed pseudo-first-order kinetics (Figures S4–S15 in the SI), which confirms the living polymerization mechanism and also showed a linear increase in the measured M_n against the theoretical M_n . The fast consumption of MeOx and the slow incorporation of BuPhOx/BuOPhOx were monitored for both copolymerization reactions. The reactivity ratios of CROP are usually determined by measuring the incorporated monomer fractions (F_1) at low conversion ($\sim 30\%$), which are plotted against the theoretical monomer fractions (f_1). The r_1 and r_2 values are then calculated by nonlinear least-squares fitting.²⁶ When the reactivity ratios differ significantly, the composition can be difficult to determine because a negligible amount of one monomer is incorporated, as described for the copolymerization of MeOx and PhOx ($r_{MeOx} \gg 1$ and $r_{PhOx} \ll 1$).³⁰ Thus, the approach developed by Schubert et al.²⁷ was implemented using kinetic plots ($\ln([M]_0/[M]_t)$ versus time; see Figures S4–S15, SI) for the copolymerization at different monomer ratios, which were determined using HPLC. The reaction time was calculated at 30% MeOx conversion ($\ln(M_0/M_t) = 0.357$),

and the real PhOx conversion was detected at this time. The reactivity ratios were determined by nonlinear least-squares fitting of the data plot F_1 versus f_1 (Figure 2A,B). A slight delay in MeOx incorporation was observed in the copolymerization with BuPhOx ($r_{MeOx} = 7.56, r_{BuPhOx} = 0.13$) in comparison with BuOPhOx ($r_{MeOx} = 8.91, r_{BuOPhOx} = 0.12$), which denotes a steeper gradient for copolymers of MeOx and BuOPhOx. To visualize the distribution of the monomeric units (MUs) along the polymer chain, the microstructure composition was predicted for a monomer feed ratio of MeOx/BuPhOx or BuOPhOx = 70:30 using the Skeist model³¹ (Figure 3D), which revealed that the initial part of the copolymer is rich in MeOx, whereas the final 10–20% of the chain consists of a homopolymer of BuPhOx or BuOPhOx. Moreover, the gradient of MeOx/BuPhOx was slightly less steep than that of MeOx/BuOPhOx (the microstructure compositions of the other monomer feed ratios are plotted in Figures S4–S15 in the SI). The microstructure composition for a monomer feed ratio of MeOx/PhOx = 70:30 was simulated based on the reported data ($r_{MeOx} = 10.02, r_{BuPhOx} = 0.02$),³² showing a steeper gradient than in the case of substituted monomers.

To compare the properties of analogous block and gradient copolymers, the three series of copolymers were synthesized. In all cases, MeOx was used as the hydrophilic monomer, whereas the hydrophobic monomer differs in each series: (a) PhOx, (b) BuPhOx, and (c) BuOPhOx. Moreover, polymers with varying monomer ratios were prepared to assess the effect of different hydrophobic monomers on the polymer properties. The characterization of all copolymers prepared in this study is summarized in Table 2. All of them have monomer compositions and molecular weights ($M_w = 8260\text{--}12\,980$ Da) close to those of the desired copolymers, as well as acceptable dispersity. Furthermore, the dispersity of the final gradient polymers ($\mathcal{D}_n = 1.03\text{--}1.21$) was lower than that of the block copolymers ($\mathcal{D}_n = 1.09\text{--}1.28$), with only a few exceptions. This is most likely due to the addition of the second monomer after polymerizing the first block, which potentially introduces additional impurities to the living polymerization process during the synthesis of these block copolymers, thereby increasing the final dispersity.

3.2. Thermal Properties of the Copolymers. The thermal bulk properties of the gradient and block copolymers, as well as homopolymers (see Table S3 in the SI), were investigated using TGA and DSC. All gradient and block

Table 2. Characterization of the Block and Gradient Copolymers

name	real ratio of MUs ^a	M_w (g/mol) ^b	D_n ^b	T_g (°C) ^c	ΔT_g (°C) ^d
PMeOx ₉₀ -grad-PhOx ₁₀	90/10	8540	1.03	85	39
PMeOx ₉₀ -block-PhOx ₁₀	91/9	10 120	1.09	87	23
PMeOx ₈₀ -grad-PhOx ₂₀	80/20	10 820	1.09	88	29
PMeOx ₈₀ -block-PhOx ₂₀	80/20	8070	1.25	86	24
PMeOx ₇₀ -grad-PhOx ₃₀	70/30	11 580	1.14	89	32
PMeOx ₇₀ -block-PhOx ₃₀	67/33	7970	1.13	89	28
PMeOx ₉₀ -grad-BuPhOx ₁₀	89/11	9280	1.21	79	32
PMeOx ₉₀ -block-BuPhOx ₁₀	89/11	8520	1.28	80	19
PMeOx ₈₀ -grad-BuPhOx ₂₀	80/20	10 740	1.11	78	32
PMeOx ₈₀ -block-BuPhOx ₂₀	79/21	8170	1.19	79	26
PMeOx ₇₀ -grad-BuPhOx ₃₀	67/33	11 100	1.18	72	28
PMeOx ₇₀ -block-BuPhOx ₃₀	68/32	8260	1.21	78	29
PMeOx ₉₀ -grad-BuOPhOx ₁₀	87/13	11 050	1.05	79	25
PMeOx ₉₀ -block-BuOPhOx ₁₀	91/9	9680	1.21	81	20
PMeOx ₈₀ -grad-BuOPhOx ₂₀	76/24	12 800	1.13	80	23
PMeOx ₈₀ -block-BuOPhOx ₂₀	80/20	9690	1.20	86	29
PMeOx ₇₀ -grad-BuOPhOx ₃₀	69/31	12 980	1.11	79	30
PMeOx ₇₀ -block-BuOPhOx ₃₀	72/28	11 500	1.19	82	22

^aDetermined using ¹H NMR. ^bValues measured and calculated using SEC. ^cDetermined using DSC. MeOx, 2-methyl-2-oxazoline; PhOx, 2-phenyl-2-oxazoline; BuPhOx, 2-(4-butylphenyl)-2-oxazoline; BuOPhOx, 2-(4-butoxyphenyl)-2-oxazoline; and MU, monomeric unit. Glass transition temperature. ^dBreadth of the glass transition region.

copolymers were thermally stable up to 300 °C, exhibiting 5% weight loss in the temperature range of 301–375 °C (Table S3 in the SI). In general, the thermal stability of the gradient copolymers was slightly higher than that of the analogous block copolymers, which may be convenient for their potential applications in areas beyond biomedicine, for example, as compatibilizers for immiscible polymer blends.³³ With the increase in the content of hydrophobic (aromatic) units, the main degradation step (the DTG peak, Figures S17–S19 in the SI) began to either broaden (the case of gradient copolymers) or split into two steps, two DTG peaks (block copolymers), and shifted to higher temperatures because all aromatic POX homopolymers are more thermally stable than the aliphatic PMeOx homopolymer (Figure S16 in the SI).

The DSC analysis revealed only one T_g for all copolymers, with no significant differences in the T_g s between gradient and block copolymers (Figures S17–S19 in the SI), which is a typical feature of copolymers composed of monomers whose homopolymers have T_g s close to each other.³³ Moreover, the copolymer PMeOx₅₀-block-PhOx₅₀, which has a longer aromatic chain than our copolymers (10–30 aromatic MUs along the block chain), also showed only one T_g .³⁴ One glass

transition was also observed in the gradient copolymers, which generally show a single, albeit distinctly broad, glass transition.³⁵ Therefore, the breadth of the T_g transition (ΔT_g values, Table S3 in the SI) was evaluated from the derivative DSC curves. In contrast to the block copolymers, the breadth of the T_g transition (ΔT_g values, derivative DSC curves) was higher for the gradient copolymers than for the block copolymers. In contrast, the gradient copolymers exhibited significantly higher ΔT_g values of approximately 30 °C, further demonstrating the gradient microstructure.

3.3. Comparison of Gradient and Block Copolymers: Drug Loading Experiments. Because the samples of gradient and analogous block copolymers exhibited similar molecular weights and ratios of hydrophilic and hydrophobic monomeric units (MUs) incorporated into the chain, we were able to investigate how their properties depend on the structure of the hydrophobic monomer and the ratios of specific MUs in each macromolecule. In general, the advantage of gradient polymers is that their one-pot one-step synthesis is easier than the two-step preparation of block copolymers. Another known advantage of gradient polymers is their higher solubility,¹⁵ as observed in our study (Table S1 in the SI).

Nanoparticles of PMeOx-grad-PhOx form a specific type of micelles, bitterball-core micelles, with an outer layer denser than the core.²² Thus, we tested a possibility of incorporating a drug inside the looser core of such NPs in comparison with the incorporation of the same drug into traditional micelles of analogous block polymers. For such purposes, antibiotic drug rifampicin ($\log D = 1.3$)³⁶ was chosen as the model drug to compare the drug encapsulation into the micelles. The rifampicin-loaded polymeric micelles were prepared by nanoprecipitation ($m_{\text{polymer}}/m_{\text{rifampicin}} = 1:1$).

The size of the rifampicin-loaded NPs was measured by dynamic light scattering (DLS, Table 3). In general, the gradient polymers ($D_h = 27$ –225 nm) were much smaller than the block analogs ($D_h = 66$ –302 nm), and all polymers showed a relatively narrow size distribution (Figure 3 and Table 3). Moreover, we observed that the more hydrophobic MUs present in a polymer, the larger the nanoparticle. The BuPhOx copolymers were significantly larger ($D_h = 24$ –283 nm) than the analogous PhOx copolymers ($D_h = 32$ –163 nm), which denotes the higher level of hydrophobicity of BuPhOx caused by the butyl substituent on the phenyl ring. This effect was strongest on the gradient copolymers with the highest amount of the hydrophobic monomer: D_h (PMeOx₇₀-grad-PhOx₃₀) = 72 nm and D_h (PMeOx₇₀-grad-BuPhOx₃₀) = 225 nm. Interestingly, in polymers with a ratio of hydrophilic/hydrophobic MUs = 90/10, the structure of the hydrophobic monomer had almost no effect on the final nanoparticle size of the gradient polymers ($D_h = 20$ –32 nm) but strongly affected the size of the block analogs ($D_h = 66$ –187 nm, Figure 3A). Furthermore, all formulations displayed the same value of hydrodynamic diameter D_h after 14 days of storage at room temperature as that observed at day 0, which demonstrates that the formulations were colloidal stable (Figure 3B). In addition, the polymeric NPs without rifampicin were consistently up to 5 nm in size when prepared from polymers soluble in an aqueous environment (Table S1 in the SI), whereas the NPs prepared from insoluble polymers varied more in size and were consequently much less reproducible.

The morphology of NPs was visualized using transmission electron microscopy (TEM). The samples were negatively stained in the presence of trehalose to stabilize the structure of

Table 3. Characterization of the Rifampicin-Loaded NPs Prepared from Gradient and Analogous Block Copolymers

name	D_h (nm) ^{ab}	entrapment efficiency (%) ^b	drug loading (%) ^b
PMeOx ₉₀ -grad-PhOx ₁₀	32 ± 2	34.8 ± 1.0	25.8 ± 0.6
PMeOx ₉₀ -block-PhOx ₁₀	135 ± 10	39.3 ± 1.6	28.2 ± 0.8
PMeOx ₈₀ -grad-PhOx ₂₀	27 ± 2	39.9 ± 2.7	28.5 ± 1.4
PMeOx ₈₀ -block-PhOx ₂₀	126 ± 15	37.8 ± 3.2	27.4 ± 1.7
PMeOx ₇₀ -grad-PhOx ₃₀	72 ± 4	47.8 ± 3.5	32.3 ± 1.6
PMeOx ₇₀ -block-PhOx ₃₀	163 ± 20	33.0 ± 2.9	24.8 ± 1.7
PMeOx ₉₀ -grad-BuPhOx ₁₀	24 ± 1	37.1 ± 0.6	27.1 ± 0.3
PMeOx ₉₀ -block-BuPhOx ₁₀	187 ± 16	34.1 ± 1.6	25.4 ± 0.9
PMeOx ₈₀ -grad-BuPhOx ₂₀	132 ± 26	39.7 ± 2.4	28.4 ± 1.3
PMeOx ₈₀ -block-BuPhOx ₂₀	184 ± 29	35.7 ± 3.2	26.3 ± 1.7
PMeOx ₇₀ -grad-BuPhOx ₃₀	225 ± 20	43.3 ± 3.1	30.2 ± 1.5
PMeOx ₇₀ -block-BuPhOx ₃₀	283 ± 28	35.4 ± 2.8	26.1 ± 1.5
PMeOx ₉₀ -grad-BuOPhOx ₁₀	20 ± 1	50.9 ± 4.5	33.4 ± 2.5
PMeOx ₉₀ -block-BuOPhOx ₁₀	66 ± 2	43.2 ± 0.5	30.2 ± 0.4
PMeOx ₈₀ -grad-BuOPhOx ₂₀	79 ± 4	51.9 ± 0.6	34.2 ± 0.1
PMeOx ₈₀ -block-BuOPhOx ₂₀	152 ± 17	46.7 ± 3.1	31.8 ± 1.4
PMeOx ₇₀ -grad-BuOPhOx ₃₀	93 ± 7	50.4 ± 2.7	33.5 ± 1.2
PMeOx ₇₀ -block-BuOPhOx ₃₀	302 ± 40	49.7 ± 2.0	33.2 ± 0.9

^aHydrodynamic diameter determined by DLS (volume mean).

^bAverage value from three independent experiments. MeOx, 2-methyl-2-oxazoline; PhOx, 2-phenyl-2-oxazoline; BuPhOx, 2-(4-butylphenyl)-2-oxazoline; and BuOPhOx, 2-(4-butoxyphenyl)-2-oxazoline. All data are presented as a mean value ± standard deviation ($n = 3$).

NPs and mitigate material shrinkage caused by sample drying.³⁷ The PhOx copolymers formed spherical micelles with diameters similar to those obtained by DLS (Figures 4, S22, and S23 and Table S4 in the SI). However, the diameters detected using TEM were smaller than the diameters obtained by DLS, which is caused by polymer shrinkage in its dry state (trehalose does not completely prevent deformation of the NPs upon dehydration). Furthermore, DLS systematically overestimates the NP diameter because of the hydration layer. Despite having the same monomer ratios (MeOx/PhOx or BuPhOx or BuOPhOx = 80:20) and the same polymer architecture, the BuPhOx and BuOPhOx copolymers formed rodlike micelles with the lengths in line with the diameters detected by DLS (Figures 4, S22, and S23 and Table S5 in the SI). In the BuPhOx and BuOPhOx copolymers, the number of spherical particles ranged from minor to undetectable (except for the sub-10 nm fraction, which was present in all samples). The monomeric unit of BuPhOx and BuOPhOx has a 50% higher volume than the PhOx monomeric unit, and, thus, the hydrophobic parts of PMeOx₈₀-BuPhOx₂₀ and PMeOx₈₀-BuOPhOx₂₀ have a significantly higher volume compared to PMeOx₈₀-PhOx₂₀. This results in the formation of rodlike micelles because the shape of NPs containing a single

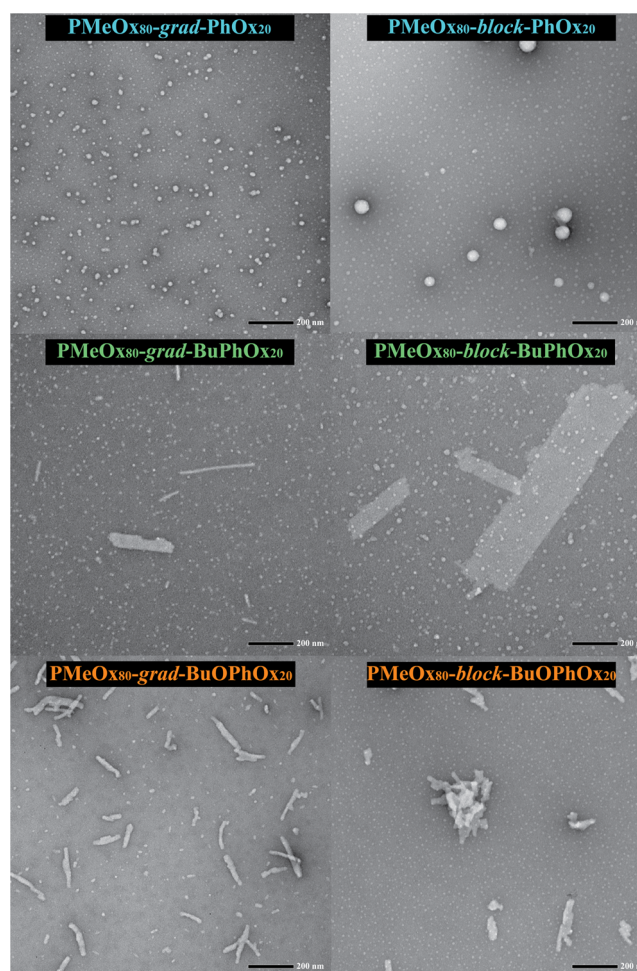


Figure 4. TEM images of rifampicin-loaded NPs. Scale bar represents 200 nm.

amphiphile is controlled by the packing factor p proportional to the volume of the hydrophobic part ($0 < p \leq 1/3 \rightarrow$ spherical micelles, $0.406 < p \leq 1/2 \rightarrow$ rodlike micelles^{38,39}).

We have also studied the entrapment efficiency (EE, %) of rifampicin and the drug loading capacity (DL, %) of the copolymers. We determined the micelle content of rifampicin using UV–vis spectroscopy, and we assessed the effect of various substituents on the phenyl ring of hydrophobic monomeric units and the effect of the ratio of hydrophilic/hydrophobic MUs on EE and DL (Table 3 and Figure 5).

EE increased with the content of hydrophobic MUs in PMeOx-grad-PhOx but remained relatively constant in PMeOx-block-PhOx. Consequently, PMeOx₇₀-grad-PhOx₃₀ showed a significantly higher EE (47.8%) than PMeOx₇₀-block-PhOx₃₀ (33.0%), most likely because gradient copolymers have a less dense core structure than block polymers, as mentioned above. The results were similar for copolymers of MeOx and BuPhOx, with PMeOx₇₀-grad-BuPhOx₃₀ also showing a significantly higher EE (43.3%) than PMeOx₇₀-block-BuPhOx₃₀ (35.4%). In contrast, both gradient and block copolymers of MeOx and BuOPhOx had similar EEs, albeit with slightly higher absolute values (43.2–51.9%) than PMeOx-PhOx and PMeOx-BuPhOx possibly due to rifampicin interactions with BuOPhOx monomeric units (Table 3).

In general, DL reproduces the trends of EE. DL increased with the content of hydrophobic MUs in the chains of the

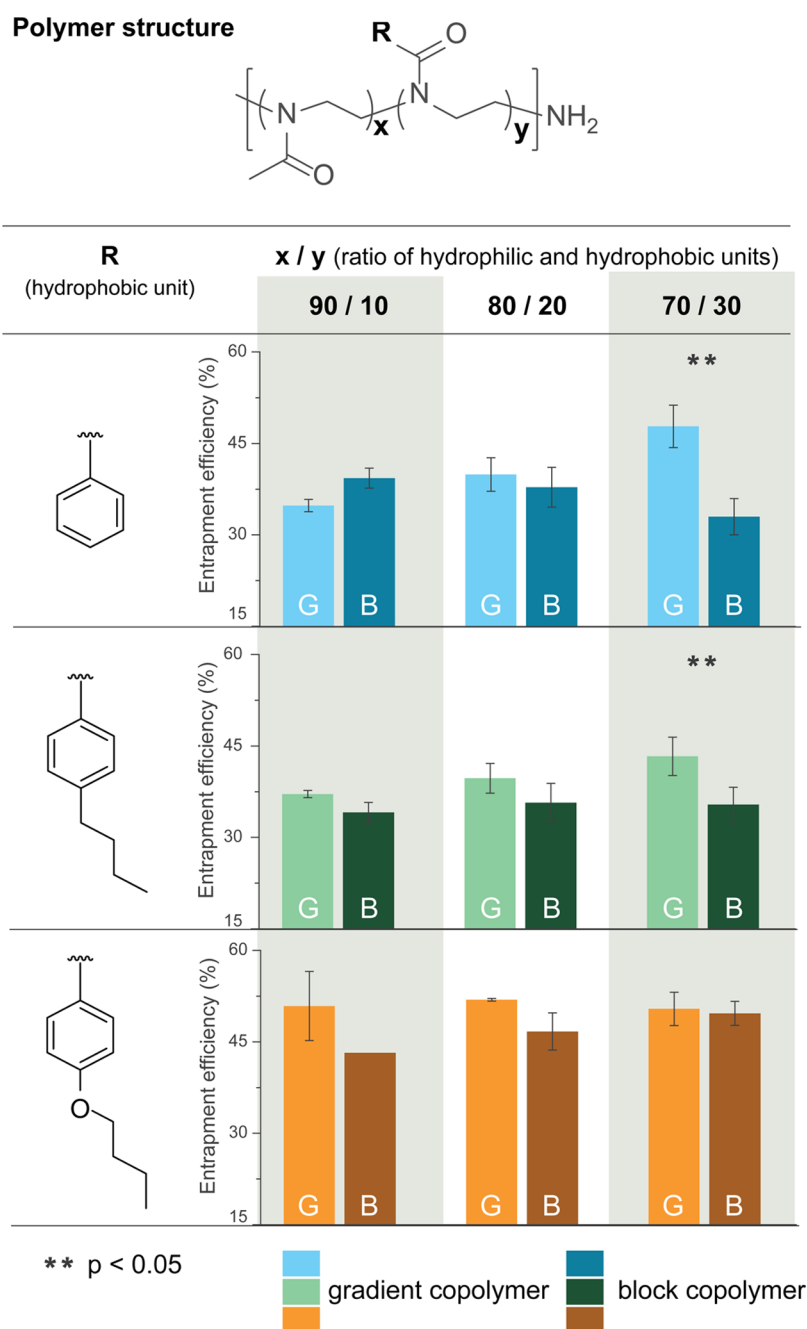


Figure 5. Comparison of the entrapment efficiency between gradient and analogous block copolymers: the effect of substituents and the ratios of monomeric units incorporated into the polymer chain. All data are presented as mean \pm standard deviation ($n = 3$).

gradient copolymers. The effect was stronger on $\text{PMeOx}_{70}\text{-grad-PhOx}_{30}$ (32.3%) and $\text{PMeOx}_{70}\text{-grad-BuPhOx}_{30}$ (30.2%) than on their block analogs (24.8 and 26.1%, respectively). Similarly, the BuOPhOx copolymers had the highest absolute values of DL (30.2–34.2%), most likely due to rifampicin interactions with BuOPhOx monomeric units. To provide further evidence, these interactions were analyzed using NMR (Figure 6).

NMR was used to investigate the behavior of rifampicin-loaded polymer nanoparticles in D_2O in comparison with their CDCl_3 solution as a control (no particles are formed in chloroform) (Figure 6B,C). The recorded spectra in D_2O showed weaker signals than those recorded in CDCl_3 . Such a decrease in signal intensity in an aqueous environment can be

explained by the nature of the polymeric nanoparticles, which consist of a lipophilic core of hydrophobic MUs with limited mobility (aggregation may decrease the T_2 relaxation below the NMR detection limit) surrounded by a much more mobile corona of hydrophilic MeOx MUs. To quantify the decrease in signal intensity, the x_x ratio was calculated for all polymer moieties according to eq 7

$$x_x = \frac{I_{x, \text{D}_2\text{O}}}{I_{x, \text{CDCl}_3}} \cdot \frac{I_{M, \text{CDCl}_3}}{I_{M, \text{D}_2\text{O}}} \times 100\% \quad (7)$$

where $I_{x, \text{D}_2\text{O}}$ and I_{x, CDCl_3} are the absolute integrals of a given signal in D_2O and CDCl_3 , respectively, and $I_{M, \text{D}_2\text{O}}$ and I_{M, CDCl_3} are the absolute integrals of signal M (methyl moieties of

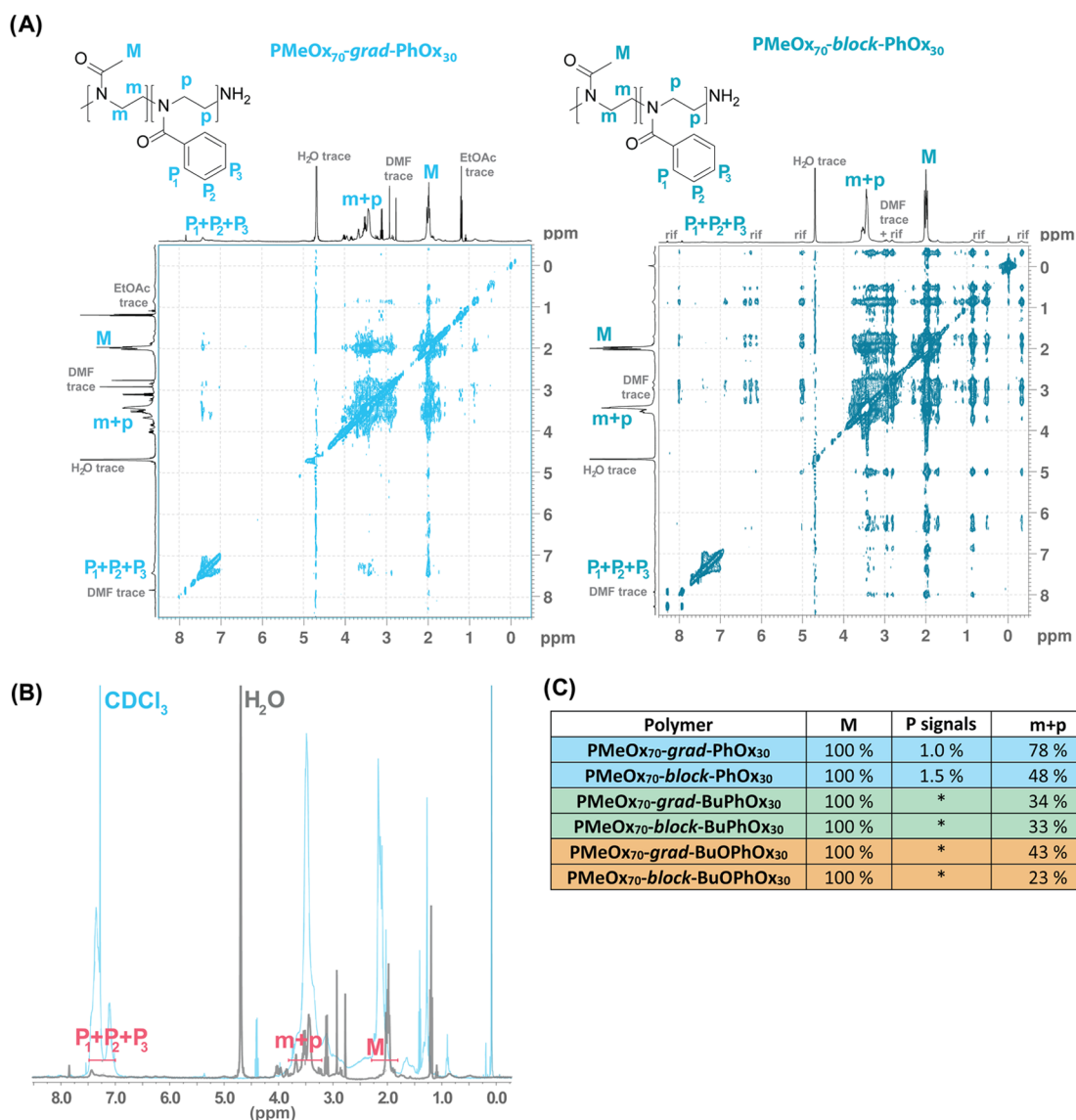


Figure 6. (A) NOESY spectra of PMeOx₇₀-grad-PhOx₃₀ (left) and PMeOx₇₀-block-PhOx₃₀ (right) loaded with rifampicin in D₂O and (B) ¹H NMR spectra of PMeOx₇₀-grad-PhOx₃₀ samples in CDCl₃ (blue) and rifampicin-loaded particles in D₂O (gray) (residual solvent peaks are not shown in their original amplitude). (C) x_M , $x_{P_1+P_2+P_3}$, and x_{m+p} correspond to ratios of the integral values measured in CDCl₃/D₂O (M was used as a reference, by definition set to 100%; * indicates a detectable signal below the limit of quantification).

MeOx) in D₂O and CDCl₃, respectively. The value of x_M was arbitrarily set to 100%, assuming that M groups were the least restricted in their mobility among all polymer moieties. Thus, the reduction in the signal intensity of the other groups can be compared with the decrease in the mobility of M groups (Figure 6C). The $x_{P_{\text{signals}}}$, corresponding to the phenyl rings of hydrophobic MUs, were lower than 2% in all nanoparticles. Therefore, the moieties of the hydrophobic MUs must be significantly restricted in their mobility in both gradient and block copolymers.

The NOESY spectra of PMeOx₇₀-grad-PhOx₃₀, PMeOx₇₀-block-PhOx₃₀ (Figure 6A), PMeOx₇₀-grad-BuPhOx₃₀, PMeOx₇₀-block-BuPhOx₃₀, PMeOx₇₀-grad-BuOPhOx₃₀, and PMeOx₇₀-block-BuOPhOx₃₀ (Figure S24 in the SI) loaded with rifampicin in D₂O showed that the main polymer backbone (signals $m+p$) strongly interacts with the methyl groups (signal M) contained in MeOx and the phenyl moiety (signal $P_1+P_2+P_3$) from PhOx, as expected, due to their

adjacency. Moreover, cross-interactions between hydrophilic MUs (MeOx, signal M) and hydrophobic MUs (PhOx, BuOPhOx, signals in the aromatic area) were detected in all gradient copolymers (except for PMeOx₇₀-grad-BuPhOx₃₀), thus indicating that these moieties are close to each other in agreement with the gradual change in monomer composition of the polymer chain. Conversely, less intense cross-peak interactions between these moieties were observed in block copolymers, as expected, because of the abrupt change in monomer composition of the polymer chain in block copolymers as well as due to a more strictly separated core area than in the case of analogous gradient copolymers.

As mentioned above, unlike all other copolymers, PMeOx₇₀-grad-BuPhOx₃₀ and PMeOx₇₀-block-BuPhOx₃₀ exhibited negligible cross-interaction NMR signals between their hydrophobic and hydrophilic MUs, which suggests that the high hydrophobicity of BuPhOx enabled the formation of a low-mobility core in both gradient and block copolymers.

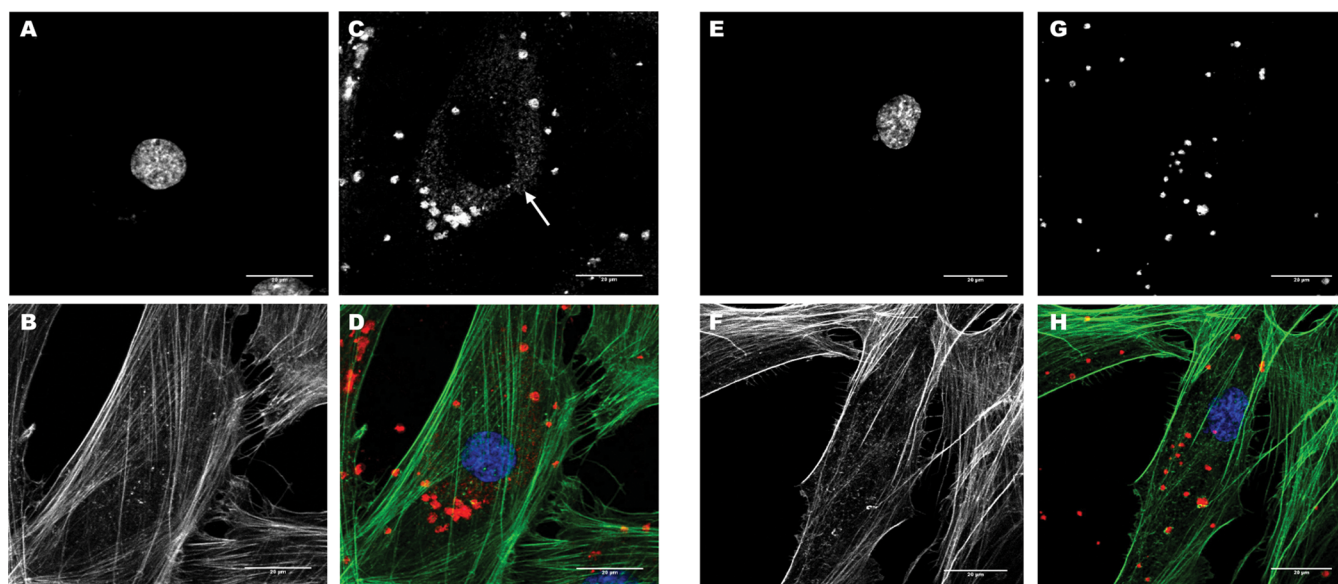


Figure 7. Representative fluorescence microscopy images of NHDF cells incubated with PMeOx₉₀-*block*-PhOx₁₀ (left) and PMeOx₉₀-*grad*-PhOx₁₀ (right). (A) Cell nucleus, (B) actin cytoskeleton, (C) PMeOx₉₀-*block*-PhOx₁₀; white arrows mark sandlike clusters of the polymer, (D) composite of A + B + C, (E) cell nucleus, (F) actin cytoskeleton, (G) PMeOx₉₀-*grad*-PhOx₁₀, and (H) composite of E + F + G. Scale bar represents 20 μ m.

Furthermore, all block copolymer samples (except for PMeOx₇₀-*block*-BuPhOx₃₀) showed intense rifampicin signals, but their cross-peak interactions with any part of the polymer were negligible, thus indicating that predominantly the “mobile” free aqueous rifampicin (with no interaction with the polymer) NMR signals were observed in these samples. The strongest signals of rifampicin were seen in the polymers with the lowest drug loading capacity, further supporting the assumption that the detected signal corresponds to the rifampicin molecules located outside the nanoparticles. Moreover, the lack of rifampicin signals in the polymers with high drug loading suggests that rifampicin may be primarily loaded into the hydrophobic low-mobility core of the particles, where the NMR signal of rifampicin decreases due to significantly shortened relaxation times. Accordingly, gradient polymers have a noticeably higher loading capacity and a larger, albeit less defined, core than their block counterparts.

Notwithstanding their similarity in the restricted mobility of their hydrophobic MUs, gradient and block copolymer micelles differ in their architecture. For example, the x_{m+p} values of the main chain moieties of the block copolymers are lower than those of their gradient analogs, which suggests further solidification of the main chain groups and their incorporation into the nanoparticle core in block copolymers. Moreover, all BuPhOx and OPhOx copolymers display low x_{m+p} values, most likely because they are more hydrophobic than their corresponding monomer (PhOx). In contrast, the main chain groups (signals $m + p$) of gradient copolymers are more mobile, forming a less compact core than those of their block analogs, in line with the enhanced solubility of gradient copolymers.

3.4. Comparison of Gradient and Block Copolymers: *In Vitro* Experiments. Polymer cytotoxicity was studied in normal human dermal fibroblast (NHDF) cells using the 3-(4,5-dimethylthiazol-2-yl)-2,5-diphenyltetrazolium bromide (MTT) assay. The cytotoxicity of all polymers was negligible up to a concentration of 1 mg/mL (which is equivalent to a concentration of 5 g of polymer dissolved in the blood of an

average human) for both gradient and block copolymers (see Figure S25 in the SI). Only PMeOx₇₀-*block*-BuPhOx₃₀ and BuOPhOx copolymers showed cell viability slightly lower than 75% at $c = 1$ mg/mL, which may be unsuitable for some biological applications.

The hemolytic potential of the polymers ($c = 0.5$ mg/mL) was determined in diluted blood after 1 h of incubation. The data revealed that neither the block nor the gradient polymers have significant hemolytic activity (Figure S26 in the SI).

Furthermore, the cellular association of polymers (labeled with Dy560) was confirmed by flow cytometry (Figure S27 in the SI). As the time of cell cultivation with the polymers increases, the normalized polymer signal of Dy560 becomes stronger, suggesting cumulative polymer internalization/binding into/to cells/cell membranes.

The cellular association of two polymers (PMeOx₉₀-*grad*-PhOx₁₀ and its block analog) tested in NHDF cell cultures was further studied using confocal microscopy. PMeOx₉₀-*grad*-PhOx₁₀ clusters with sizes of 1.71 ± 0.78 μ m were observed (Figures 7 and S26 in the SI) and likely did not enter the cells. On the other hand, PMeOx₉₀-*block*-PhOx₁₀ formed two types of clusters: big (2.45 ± 1.29 μ m) and small (0.58 ± 0.16 μ m) ones with sandlike structures (marked by gray arrows in Figures 7 and S27 in the SI). These structures followed well cell (and nuclei) contours, which might indicate intracellular localization.

The *in vitro* results confirmed the suitability of the prepared polymers for further biological and biomedical research.

4. CONCLUSIONS

We directly compared amphiphilic gradient and analogous block polyoxazolines based on their physicochemical behavior and potential as drug delivery systems. More specifically, we synthesized three series of gradient and block copolymers of 2-methyl-2-oxazoline (MeOx) with various hydrophobic monomers, 2-phenyl-2-oxazoline (PhOx), 2-(4-butylphenyl)-2-oxazoline (BuPhOx), or 2-(4-butoxyphenyl)-2-oxazoline (BuOPhOx), to assess the effect of the substituent on the benzene

ring of the hydrophobic monomer on the final polymer properties. In addition, BuPhOx and BuOPhOX were synthesized as novel monomers to investigate their homopolymerization and copolymerization kinetics with MeOx, displaying pseudo-first-order kinetics with a slightly steeper gradient microstructure in both monomers than in PhOx. Furthermore, the gradient copolymers revealed a slightly higher thermal stability and a broader glass transition region than the analogous blocks, which could also be useful for applications in areas other than biomedicine, for example, as compatibilizers for immiscible polymer blends. The diameter of all gradient nanoparticles loaded with rifampicin was significantly smaller than that of their block analogs. In addition, gradient copolymers PMeOx₇₀-grad-PhOx₃₀ and PMeOx₇₀-grad-BuPhOx₃₀ exhibited significantly higher entrapment efficiency and drug loading capacity than their block analogs, most likely because their core structure is less dense. This difference in core density was further confirmed by NMR experiments, which suggested that the gradient-polymer-derived nanoparticles form a less compact core than their block analogs. Lastly, all polymers showed negligible hemolytic activity, low toxicity, and cellular association in our *in vitro* experiments. Thus, gradient copolymers may be a valuable and easy-to-prepare alternative to the more commonly used block copolymers as drug delivery systems. Ultimately, our findings may help synthetic chemists select the most appropriate type of polymer for a target application considering the different properties and relative advantages of block and gradient copolymers.

■ ASSOCIATED CONTENT

Supporting Information

The Supporting Information is available free of charge at <https://pubs.acs.org/doi/10.1021/acs.macromol.0c02674>.

Monomer synthesis; additional polymerization data; additional *in vitro* data; NMR spectra; and SEC traces (PDF)

■ AUTHOR INFORMATION

Corresponding Author

Martin Hrubý – Institute of Macromolecular Chemistry CAS, Prague 162 00, Czech Republic; orcid.org/0000-0002-5075-261X; Email: mhruby@centrum.cz

Authors

Lenka Loukotová – Institute of Macromolecular Chemistry CAS, Prague 162 00, Czech Republic; orcid.org/0000-0002-8087-1425

Pavel Švec – Institute of Macromolecular Chemistry CAS, Prague 162 00, Czech Republic; Department of Physical and Macromolecular Chemistry, Faculty of Science, Charles University, Prague 128 43, Czech Republic; orcid.org/0000-0002-6604-2815

Ondřej Groborz – Institute of Macromolecular Chemistry CAS, Prague 162 00, Czech Republic; Department of Organic Chemistry, Faculty of Science, Charles University, Prague 128 43, Czech Republic; orcid.org/0000-0002-3164-6168

Tomáš Heizer – Center for Advanced Preclinical Imaging, First Faculty of Medicine, Charles University, Prague 120 00, Czech Republic

Hynek Beneš – Institute of Macromolecular Chemistry CAS, Prague 162 00, Czech Republic; orcid.org/0000-0002-6861-1997

Helena Raabová – Electron Microscopy Core Facility of the Microscopy Centre, Institute of Molecular Genetics of the Czech Academy of Sciences, Prague 142 20, Czech Republic

Tereza Bělinová – Biomedical Center, Faculty of Medicine in Pilsen, Charles University in Prague, Pilsen 323 00, Czech Republic

Vít Herynek – Center for Advanced Preclinical Imaging, First Faculty of Medicine, Charles University, Prague 120 00, Czech Republic; orcid.org/0000-0002-1775-2394

Complete contact information is available at: <https://pubs.acs.org/doi/10.1021/acs.macromol.0c02674>

Notes

The authors declare no competing financial interest.

■ ACKNOWLEDGMENTS

The study was financially supported by the Czech Science Foundation (grant #19-01602S), the Ministry of Education, Youth and Sports the Czech Republic (grant #LTC19032, the project “Fighting Infectious Diseases” financed from ERDF, grant #CZ.02.1.01/0.0/0.0/16_019/0000787) and the Academy of Sciences of the Czech Republic (grant #FWO-19-03). The CAPI, 1st FM CUNI, and EM CF IMG are supported by the Czech-BioImaging large RI project funded by MEYS CR (#LM2015062, LM2018129) and by the ERDF grant #CZ.02.1.01/0.0/0.0/16_013/0001775 “Modernization and support of research activities of the national infrastructure for biological and medical imaging Czech-BioImaging”. The authors thank Dr. Olga Trhlíková for the elemental analysis measurements, Dr. Peter Cernoch for the SEC measurement, and Dr. Carlos V. Melo for editing the manuscript.

■ REFERENCES

- (1) Sutton, D.; Nasongkla, N.; Blanco, E.; Gao, J. Functionalized Micellar Systems for Cancer Targeted Drug Delivery. *Pharm. Res.* **2007**, *24*, 1029–1046.
- (2) Zhang, L.; Eisenberg, A. Multiple Morphologies of “Crew-Cut” Aggregates of Polystyrene-*b*-Poly(Acrylic Acid) Block Copolymers. *Science* **1995**, *268*, 1728–1731.
- (3) Wang, R.; Billone, P. S.; Mullett, W. M. Nanomedicine in Action: An Overview of Cancer Nanomedicine on the Market and in Clinical Trials. *J. Nanomater.* **2013**, *2013*, No. 629681.
- (4) Adams, M. L.; Lavasanifar, A.; Kwon, G. S. Amphiphilic Block Copolymers for Drug Delivery. *J. Pharm. Sci.* **2003**, *92*, 1343–1355.
- (5) Oerlemans, C.; Bult, W.; Bos, M.; Storm, G.; Nijssen, J. F. W.; Hennink, W. E. Polymeric Micelles in Anticancer Therapy: Targeting, Imaging and Triggered Release. *Pharm. Res.* **2010**, *27*, 2569–2589.
- (6) Bobo, D.; Robinson, K. J.; Islam, J.; Thurecht, K. J.; Corrie, S. R. Nanoparticle-Based Medicines: A Review of FDA-Approved Materials and Clinical Trials to Date. *Pharm. Res.* **2016**, *33*, 2373–2387.
- (7) Cristal Therapeutics. Efficacy Study of CPC634 (CriPec Docetaxel) in Platinum Resistant Ovarian Cancer (CINOVA), 2018. <https://clinicaltrials.gov/ct2/show/NCT03742713>.
- (8) Hu, Q.; Rijcken, C. J.; Bansal, R.; Hennink, W. E.; Storm, G.; Prakash, J. Complete Regression of Breast Tumour with a Single Dose of Docetaxel-Entrapped Core-Cross-Linked Polymeric Micelles. *Biomaterials* **2015**, *53*, 370–378.
- (9) Samyang Biopharmaceuticals Corporation. Study to Evaluate the Efficacy and Safety of Genexol-PM Once a Week for Gynecologic Cancer, 2017. <https://clinicaltrials.gov/ct2/show/NCT02739529?cond=genexol&draw=2&rank=6>.

- (10) Samyang Biopharmaceuticals Corporation. Study of Weekly Genexol-PM Plus Gemcitabine in Subjects With Recurrent and Metastatic Adenocarcinoma of the Pancreas, 2018. <https://clinicaltrials.gov/ct2/show/NCT02739633?cond=genexol&draw=2&rank=3>.
- (11) Gachon University Gil Medical Center. A Phase II Study of Weekly Genexol-PM in Patients With Hepatocellular Carcinoma After Failure of Sorafenib, 2019. <https://clinicaltrials.gov/ct2/show/NCT03008512?cond=genexol&draw=2&rank=4>.
- (12) Park, I. H.; Sohn, J. H.; Kim, S. B.; Lee, K. S.; Chung, J. S.; Lee, S. H.; Kim, T. Y.; Jung, K. H.; Cho, E. K.; Kim, Y. S. An Open-Label, Randomized, Parallel, Phase III Trial Evaluating the Efficacy and Safety of Polymeric Micelle-Formulated Paclitaxel Compared to Conventional Cremophor EL-Based Paclitaxel for Recurrent or Metastatic HER2-Negative Breast Cancer. *Cancer Res. Treat.* **2017**, *49*, 569–577.
- (13) Ventola, C. L. Progress in Nanomedicine: Approved and Investigational Nanodrugs. *Pharmacol. Ther.* **2017**, *42*, 742–755.
- (14) Beginn, U. Gradient Copolymers. *Colloid Polym. Sci.* **2008**, *286*, 1465–1474.
- (15) Chen, Y.; Chen, H.; Feng, M.; Dong, Y. Amphiphilic Gradient Copolymers: Synthesis, Self-Assembly, and Applications. *Eur. Polym. J.* **2016**, *85*, 489–498.
- (16) Sedláček, O.; Černoč, P.; Kučka, J.; Konefal, R.; Štěpánek, P.; Vetrík, M.; Lodge, T. P.; Hrubý, M. Thermoresponsive Polymers for Nuclear Medicine: Which Polymer Is the Best? *Langmuir* **2016**, *32*, 6115–6122.
- (17) Glassner, M.; Vergaalen, M.; Hoogenboom, R. Poly(2-oxazoline)s: A Comprehensive Overview of Polymer Structures and Their Physical Properties. *Polym. Int.* **2018**, *67*, 32–45.
- (18) Lorson, T.; Lübtow, M. M.; Wegener, E.; Haider, M. S.; Borova, S.; Nahm, D.; Jordan, R.; Sokolski-Papkov, M.; Kabanov, A. V.; Luxenhofer, R. Poly(2-Oxazoline)s Based Biomaterials: A Comprehensive and Critical Update. *Biomaterials* **2018**, *178*, 204–280.
- (19) Vlassi, E.; Papagiannopoulos, A.; Pispas, S. Amphiphilic Poly(2-Oxazoline) Copolymers as Self-Assembled Carriers for Drug Delivery Applications. *Eur. Polym. J.* **2017**, *88*, 516–523.
- (20) Vlassi, E.; Pispas, S. Solution Behavior of Hydrolyzed Gradient Methyl/Phenyl Oxazoline Copolymers and Complexation with DNA. *Macromol. Chem. Phys.* **2015**, *216*, 873–883.
- (21) Milonaki, Y.; Kaditi, E.; Pispas, S.; Demetzos, C. Amphiphilic Gradient Copolymers of 2-methyl-and 2-phenyl-2-oxazoline: Self-organization in Aqueous Media and Drug Encapsulation. *J. Polym. Sci., Part A: Polym. Chem.* **2012**, *50*, 1226–1237.
- (22) Filippov, S. K.; Verbraeken, B.; Konarev, P. V.; Svergun, D. I.; Angelov, B.; Vishnevetskaya, N. S.; Papadakis, C. M.; Rogers, S.; Radulescu, A.; Courtin, T. Block and Gradient Copoly(2-Oxazoline) Micelles: Strikingly Different on the Inside. *J. Phys. Chem. Lett.* **2017**, *8*, 3800–3804.
- (23) Wagner, R.; Berger, S. *Gradient-Selected NOESY—A Fourfold Reduction of the Measurement Time for the NOESY Experiment*; Academic Press, 1996.
- (24) Kim, J.; Mok, M. M.; Sandoval, R. W.; Woo, D. J.; Torkelson, J. M. Uniquely Broad Glass Transition Temperatures of Gradient Copolymers Relative to Random and Block Copolymers Containing Repulsive Comonomers. *Macromolecules* **2006**, *39*, 6152–6160.
- (25) Hertz, D.; Leiske, M. N.; Wloka, T.; Traeger, A.; Hartlieb, M.; Kessels, M. M.; Schubert, S.; Qualmann, B.; Schubert, U. S. Comparison of Random and Gradient Amino Functionalized Poly(2-oxazoline)s: Can the Transfection Efficiency Be Tuned by the Macromolecular Structure? *J. Polym. Sci., Part A: Polym. Chem.* **2018**, *56*, 1210–1224.
- (26) Meyer, V. E.; Lowry, G. G. Integral and Differential Binary Copolymerization Equations. *J. Polym. Sci., Part A: Gen. Pap.* **1965**, *3*, 2843–2851.
- (27) Fijten, M. W. M.; Hoogenboom, R.; Schubert, U. S. Initiator Effect on the Cationic Ring-opening Copolymerization of 2-ethyl-2-oxazoline and 2-phenyl-2-oxazoline. *J. Polym. Sci., Part A: Polym. Chem.* **2008**, *46*, 4804–4816.
- (28) Mosmann, T. Rapid Colorimetric Assay for Cellular Growth and Survival: Application to Proliferation and Cytotoxicity Assays. *J. Immunol. Methods* **1983**, *65*, 55–63.
- (29) Anand, V. P.; Cogdill, C. P.; Klausner, K. A.; Lister, L.; Barbolt, T.; Page, B. F. J.; Urbanski, P.; Woss, C. J.; Boyce, J. Reevaluation of Ethylene Oxide Hemolysis and Irritation Potential. *J. Biomed. Mater. Res., Part A* **2003**, *64*, 648–654.
- (30) Hoogenboom, R.; Thijs, H. M. L.; Fijten, M. W. M.; Van Lankvelt, B. M.; Schubert, U. S. One-pot Synthesis of 2-phenyl-2-oxazoline-containing Quasi-diblock Copoly(2-oxazoline)s under Microwave Irradiation. *J. Polym. Sci., Part A: Polym. Chem.* **2007**, *45*, 416–422.
- (31) Blankenburg, J.; Wagner, M.; Frey, H. Well-Defined Multi-Amino-Functional and Stimuli-Responsive Poly(Propylene Oxide) by Crown Ether Assisted Anionic Ring-Opening Polymerization. *Macromolecules* **2017**, *50*, 8885–8893.
- (32) Kagiya, T.; Matsuda, T.; Nakato, M.; Hirata, R. Polymerization of 2-Oxazolines. IV. The Structure and the Reactivity of 2-Substituted-2-Oxazolines and Oxazolinium Perchlorates. *J. Macromol. Sci., Chem.* **1972**, *6*, 1631–1652.
- (33) Alam, M. M.; Jack, K. S.; Hill, D. J. T.; Whittaker, A. K.; Peng, H. Gradient Copolymers—Preparation, Properties and Practice. *Eur. Polym. J.* **2019**, *116*, 394–414.
- (34) Wiesbrock, F.; Hoogenboom, R.; Leenen, M.; van Nispen, S. F. G. M.; van der Loop, M.; Abeln, C. H.; van den Berg, A. M. J.; Schubert, U. S. Microwave-Assisted Synthesis of a 42-Membered Library of Diblock Copoly(2-Oxazoline)s and Chain-Extended Homo Poly(2-Oxazoline)s and Their Thermal Characterization. *Macromolecules* **2005**, *38*, 7957–7966.
- (35) Mok, M. M.; Kim, J.; Wong, C. L. H.; Marrou, S. R.; Woo, D. J.; Dettmer, C. M.; Nguyen, S. T.; Ellison, C. J.; Shull, K. R.; Torkelson, J. M. Glass Transition Breadths and Composition Profiles of Weakly, Moderately, and Strongly Segregating Gradient Copolymers: Experimental Results and Calculations from Self-Consistent Mean-Field Theory. *Macromolecules* **2009**, *42*, 7863–7876.
- (36) Rossi Sebastiano, M.; Doak, B. C.; Backlund, M.; Poongavanam, V.; Over, B.; Ermondi, G.; Caron, G.; Matsson, P.; Kihlberg, J. Impact of Dynamically Exposed Polarity on Permeability and Solubility of Chameleonic Drugs beyond the Rule of 5. *J. Med. Chem.* **2018**, *61*, 4189–4202.
- (37) Chiu, P.-L.; Kelly, D. F.; Walz, T. The Use of Trehalose in the Preparation of Specimens for Molecular Electron Microscopy. *Micron* **2011**, *42*, 762–772.
- (38) Tanford, C. *The Hydrophobic Effect: Formation of Micelles and Biological Membranes*, 2nd ed.; Wiley, 1980.
- (39) Manohar, C.; Narayanan, J. Average Packing Factor Approach for Designing Micelles, Vesicles and Gel Phases in Mixed Surfactant Systems. *Colloids Surf., A* **2012**, *403*, 129–132.

Supporting Information – Direct Comparison of Analogous Amphiphilic Gradient and Block Polyoxazolines

Lenka Loukotová^a, Pavel Švec^{a,b}, Ondřej Groborz^{a,c}, Tomáš Heizer^d, Hynek Beneš^a, Helena Raabová^e, Tereza Bělinová^f, Vít Herynek^d and Martin Hrubý^{a}*

^a Institute of Macromolecular Chemistry CAS, Heyrovsky sq. 2, Prague, 162 00, Czech Republic

^b Department of Physical and Macromolecular Chemistry, Faculty of Science, Charles University, Hlavova 8, Prague, 128 43, Czech Republic

^c Department of Organic Chemistry, Faculty of Science, Charles University, Hlavova 8, Prague, 128 43, Czech Republic

^d Center for Advanced Preclinical Imaging, First Faculty of Medicine, Charles University, Salmovska 3, Prague, 120 00, Czech Republic

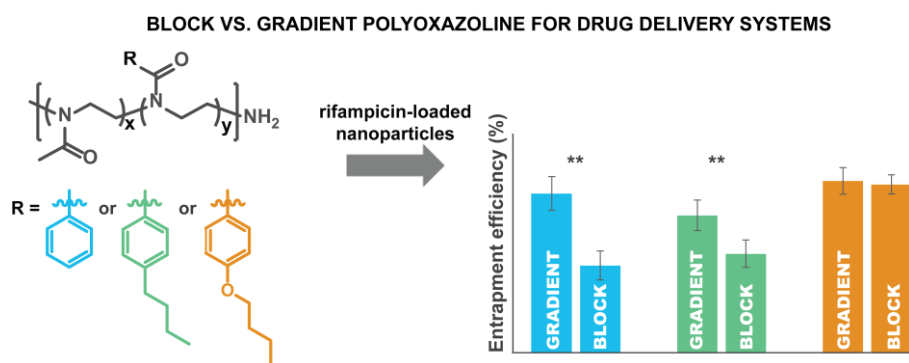
^e Electron Microscopy Core Facility of the Microscopy Centre, Institute of Molecular Genetics of the Czech Academy of Sciences, Videnska 1083, Prague, 142 20, Czech Republic

^f Biomedical Center, Faculty of Medicine in Pilsen, Charles University in Prague, alej Svobody 1655/76, Pilsen, 323 00, Czech Republic

*Corresponding author, e-mail: mhruby@centrum.cz

Keywords: poly-2-phenyl-2-oxazoline; gradient polymer; polymerization kinetics; drug loading; drug delivery

TABLE OF CONTENTS



Content

1. Monomer synthesis	3
1.1 Optimal synthesis of monomers	3
1.1.1 Synthesis of 4-butyl-N-(2-chloroethyl)benzamide (1).....	3
1.1.2 Synthesis of 2-(4-butylphenyl)-2-oxazoline – BuPhOx	4
1.1.3 Synthesis of 4-butoxy-N-(2-chloroethyl)benzamide (2).....	4
1.1.4 Synthesis of 2-(4-butoxyphenyl)-2-oxazoline – BuOPhOx.....	5
1.2 An alternative synthesis of monomers.....	5
1.2.1 Synthesis of 4-butylbenzotrile (3).....	6
1.2.2 Synthesis of 2-(4-butylphenyl)-2-oxazoline – BuPhOx	6
1.2.3 Synthesis of 4-butoxybenzotrile (4).....	6
1.2.4 Synthesis of 2-(4-butoxyphenyl)-2-oxazoline – BuOPhOx.....	7
1.3 Monomer synthesis – result and discussion part	7
2. Additional polymerization data	8
2.1 Homopolymerization kinetics.....	8
2.2 Copolymerization kinetics	10
2.2 Polymer characterization data	22
2.2.1 Additional results of thermal properties of the copolymers.....	22
2.2.2 Additional results of NPs morphology	28
2. In vitro data	32
3. NMR spectra	35
4. SEC traces	42

1. Monomer synthesis

1.1 Optimal synthesis of monomers

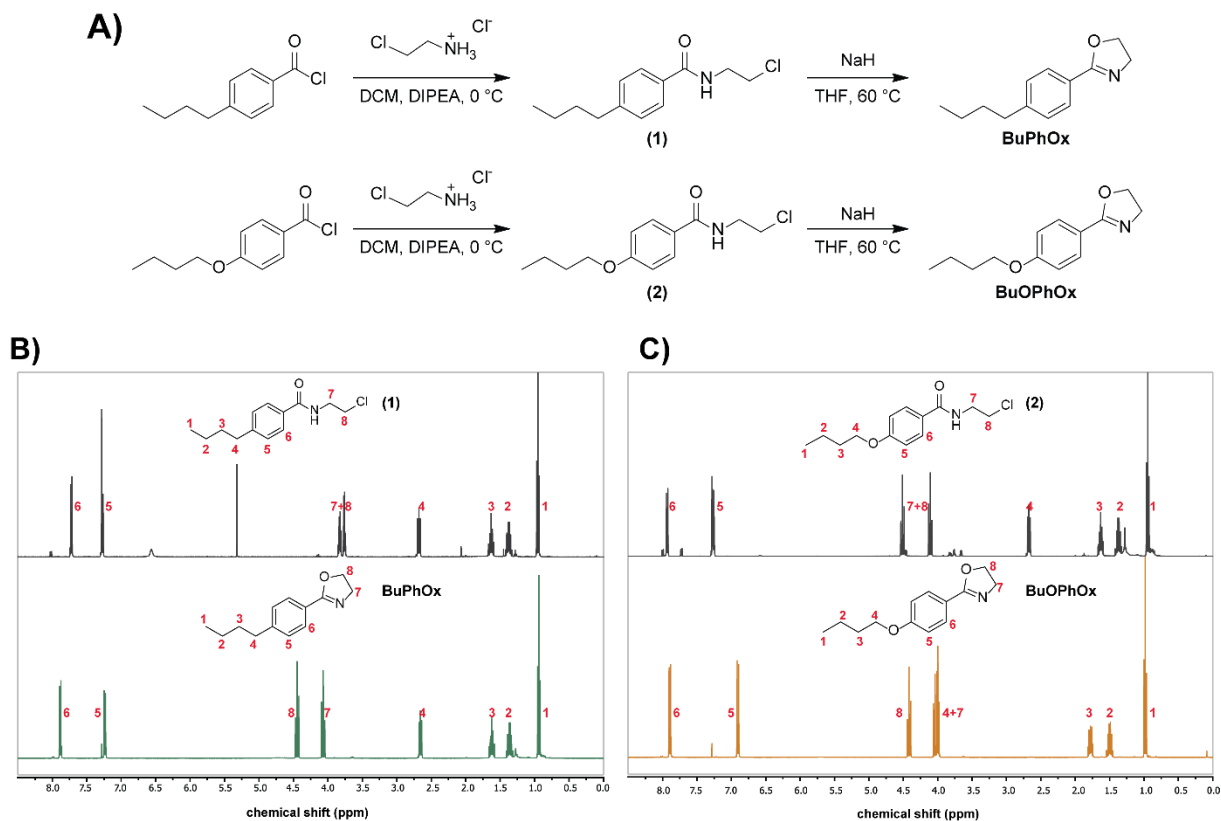


Figure S1. A) Scheme of synthesis of BuPhOx and BuOPhOx. B) and C) $^1\text{H-NMR}$ spectra of the intermediate products **(1)**, **(2)**, and BuPhOx and BuOPhOx. The spectra were recorded in CDCl_3 .

1.1.1 Synthesis of 4-butyl-N-(2-chloroethyl)benzamide (**1**)

4-Butylbenzoyl chloride (15.00 g, 0.076 mol) and 2-chloroethylamine hydrochloride (8.85 g, 0.076 mol) were suspended in dry dichloromethane (100 mL) under an argon atmosphere, and the reaction mixture was cooled to 0 °C. *N,N*-Diisopropylethylamine (DIPEA, 29.00 mL, 0.168 mol) was added dropwise under vigorous stirring over the course of 3 h. After the full addition of DIPEA, the reaction was allowed to warm to room temperature and left overnight. The mixture was washed with deionized water (2 x 50 mL) and with brine (1 x 50 mL). The organic layer was dried over anhydrous magnesium sulfate and evaporated. The crude product was purified by flash chromatography (linear gradient 20 \rightarrow 50% EtOAc in hexane, R_f in 20% EtOAc = 0.14, R_f in 50% EtOAc = 0.59) yielding the product **(1)** as a colorless oil (14.05 g, 0.059 mol, 78%).

¹H-NMR (400 MHz, CDCl₃), δ (ppm): 0.93 (t, 3H, $J = 7.3$ Hz, CH₃CH₂), 1.28-1.45 (m, 2H, CH₃CH₂CH₂), 1.55-1.67 (m, 2H, CH₃CH₂CH₂), 2.61-2.70 (m, 2H, CH₃CH₂CH₂CH₂), 3.70-3.77 (m, 2H, NHCH₂CH₂Cl), 3.77-3.85 (m, 2H, NHCH₂CH₂Cl), 6.54 (brs, 1H, NH), 7.21-7.29 (m, 2H, phenyl), 7.66-7.74 (m, 2H, phenyl).

1.1.2 Synthesis of 2-(4-butylphenyl)-2-oxazoline – BuPhOx

The product (**1**) (13.00 g, 0.055 mol) was treated with sodium hydride (1.87 g, 0.078 mol) in dry tetrahydrofuran (75 mL) at 60 °C for 1 h. The suspension was then filtered, and the filtrate was dried over anhydrous magnesium sulfate and evaporated to yield BuPhOx as a pale-yellow oil (8.13 g, 0.040 mol, 73%).

Prior to polymerization, the product was stirred overnight with calcium hydride and distilled at reduced pressure (145 °C, 1.0 mbar).

¹H-NMR (400 MHz, CDCl₃), δ (ppm): 0.91 (t, 3H, $J = 7.3$ Hz, CH₃CH₂), 1.29-1.39 (m, 2H, CH₃CH₂CH₂), 1.55-1.63 (m, 2H, CH₃CH₂CH₂), 2.60-2.67 (m, 2H, CH₃CH₂CH₂CH₂), 4.04 (t, 2H, $J = 9.5$ Hz, OCH₂CH₂N), 4.42 (t, 2H, $J = 9.4$ Hz, OCH₂CH₂N), 7.18-7.25 (m, 2H, phenyl), 7.83-7.89 (m, 2H, phenyl). ¹³C-NMR (101 MHz, CDCl₃), δ (ppm): 14.01, 22.38, 33.42, 35.63, 54.82, 67.66, 125.11, 128.28, 128.53, 146.81, 164.97. Elemental analysis: found C 76.48%, H 8.45%, N 6.88%; calculated C 76.81%, H 8.43%, N 6.89%.

1.1.3 Synthesis of 4-butoxy-N-(2-chloroethyl)benzamide (2)

4-Butoxybenzoyl chloride (15.00 g, 0.071 mol) and 2-chloroethylamine hydrochloride (8.18 g, 0.071 mol) were suspended in dry dichloromethane (100 mL) under an argon atmosphere, and the reaction mixture was cooled to 0 °C. *N,N*-Diisopropylethylamine (DIPEA, 30.00 mL, 0.175 mol) was added dropwise under vigorous stirring over the course of 3 h. After the full addition of DIPEA, the reaction was allowed to warm to room temperature and left overnight. The mixture was washed with deionized water (2 x 50 mL) and with brine (1 x 50 mL). The organic layer was dried over anhydrous magnesium sulfate and evaporated. The crude product was purified by flash chromatography (linear gradient 20 → 50% EtOAc in hexane, R_f in 20% EtOAc = 0.22, R_f in 50% EtOAc = 0.66) yielding the product (**2**) as a pale-yellow oil (12.94 g, 0.051 mol, 72%).

$^1\text{H-NMR}$ (400 MHz, CDCl_3), δ (ppm): 0.92 (t, 3H, $J = 7.3$ Hz, CH_3CH_2), 1.28-1.42 (m, 2H, $\text{CH}_3\text{CH}_2\text{CH}_2$), 1.55-1.67 (m, 2H, $\text{CH}_3\text{CH}_2\text{CH}_2$), 2.61-2.71 (m, 2H, $\text{CH}_3\text{CH}_2\text{CH}_2\text{CH}_2\text{O}$), 4.04-4.13 (m, 2H, $\text{NHCH}_2\text{CH}_2\text{Cl}$), 4.41-4.54 (m, 2H, $\text{NHCH}_2\text{CH}_2\text{Cl}$), 7.20-7.28 (m, 2H, phenyl), 7.89-7.93 (m, 2H, phenyl).

1.1.4 Synthesis of 2-(4-butoxyphenyl)-2-oxazoline – BuOPhOx

The product (2) (12.00 g, 0.047 mol) was treated with sodium hydride (1.80 g, 0.075 mol) in dry tetrahydrofuran (75 mL) at 60 °C for 1 h. At the end of this time, the suspension was filtered, and the filtrate was dried over anhydrous magnesium sulfate and evaporated. The crude product was further purified by sublimation (0.2 mbar, 120 °C) to give BuOPhOx as a white powder (8.92 g, 0.041 mol, 87%).

$^1\text{H-NMR}$ (400 MHz, CDCl_3), δ (ppm): 0.98 (t, 3H, $J = 7.4$ Hz, CH_3CH_2), 1.44-1.56 (m, 2H, $\text{CH}_3\text{CH}_2\text{CH}_2$), 1.73-1.82 (m, 2H, $\text{CH}_3\text{CH}_2\text{CH}_2$), 3.96-4.07 (m, 4H, $\text{CH}_3\text{CH}_2\text{CH}_2\text{CH}_2\text{O}$, $\text{OCH}_2\text{CH}_2\text{N}$), 4.38-4.45 (m, 2H, $\text{OCH}_2\text{CH}_2\text{N}$), 6.88-6.93 (m, 2H, phenyl), 7.86-7.92 (m, 2H, phenyl). $^{13}\text{C-NMR}$ (101 MHz, CDCl_3), δ (ppm): 13.91, 19.29, 31.29, 54.74, 67.63, 67.88, 114.28, 119.92, 129.99, 161.83, 164.69. Elemental analysis: found C 71.37%, H 7.84%, N 6.41%; calculated C 71.21%, H 7.81%, N 6.39%.

1.2 An alternative synthesis of monomers

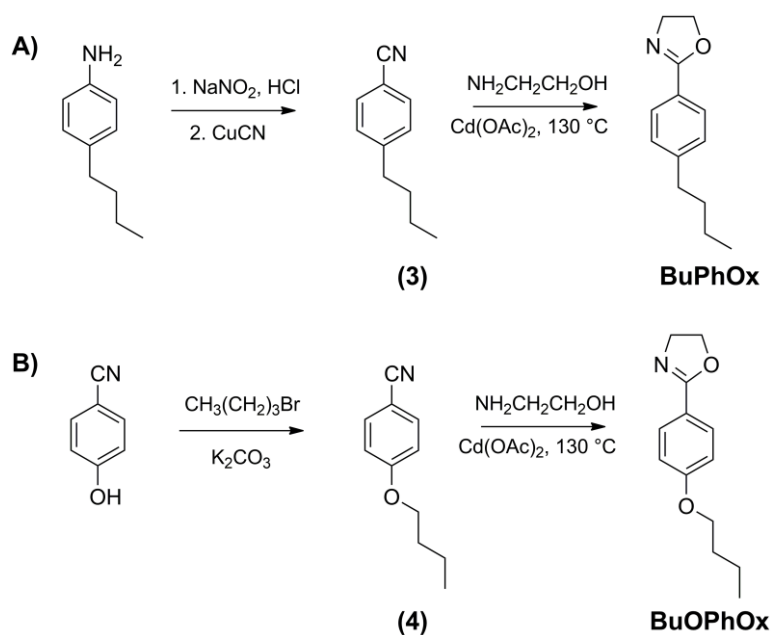


Figure S2. Scheme of the alternative syntheses of BuPhOx (A) and BuOPhOx (B).

1.2.1 Synthesis of 4-butylbenzotrile (3)

The mixture of 4-butylaniline (97.00 g; 0.65 mol), deionized water (600 mL) and 35% hydrochloric acid (143 mL, 1.62 mol) was cooled with ice-salt-bath $-1\text{ }^{\circ}\text{C}$ and stirred. The solution of sodium nitrite (44.37 g; 0.65 mol in 200 mL of deionized water) was added dropwise for 1 h. Meanwhile, an aqueous suspension of copper(I) cyanide was prepared by mixing copper(II) sulfate pentahydrate (154 g; 0.62 mol) with potassium cyanide (189 g; 2.90 mol) in deionized water (400 mL). The resulting diazonium salt solution was added dropwise to the freshly prepared aqueous suspension of copper(I) cyanide. After 30 min, the reaction mixture was extracted twice with diethyl ether, and the organic layer was further washed with deionized water. The organic layer was dried over anhydrous magnesium sulfate and evaporated. The crude product was purified by flash chromatography (EtOAc/CH₂Cl₂/hexane = 3/10/87) to give 4-butylbenzotrile as a colorless oil (25.84 g; 25%).

¹H-NMR (400 MHz, DMSO), δ (ppm): 0.87 (t, 3H, $J=7.3$ Hz, CH₃CH₂), 1.21-1.33 (m, 2H, CH₃CH₂CH₂), 1.49-1.59 (m, 2H, CH₃CH₂CH₂), 2.60-2.68 (m, 2H, CH₃CH₂CH₂CH₂), 7.36-7.42 (m, 2H, phenyl), 7.68-7.75 (m, 2H, phenyl). ¹³C-NMR (101 MHz, CDCl₃), δ (ppm): 12.19, 20.26, 31.16, 33.63, 107.28, 117.31, 127.72, 130.40, 146.79.

1.2.2 Synthesis of 2-(4-butylphenyl)-2-oxazoline – BuPhOx

4-Butylbenzotrile (22.92 g; 0.14 mol) was mixed with cadmium acetate dihydrate (1.91 g; 7.20 mmol), and 2-aminoethanol (8.80 g; 0.14 mol) was added dropwise. The reaction mixture was stirred for 48 h at 130 $^{\circ}\text{C}$. The crude product was purified by flash chromatography (EtOAc/hexane = 10/90) to give 2-(4-butylphenyl)-2-oxazoline (BuPhOx) as a pale-yellow oil (13.74 g, 47%).

Prior to polymerization, the product was stirred overnight with calcium hydride and distilled at reduced pressure (145 $^{\circ}\text{C}$, 1.0 mbar)

¹H-NMR (400 MHz, CDCl₃), δ (ppm): 0.89 (t, 3H, $J=7.3$ Hz, CH₃CH₂), 1.26-1.37 (m, 2H, CH₃CH₂CH₂), 1.52-1.63 (m, 2H, CH₃CH₂CH₂), 2.57-2.64 (m, 2H, CH₃CH₂CH₂CH₂), 4.01 (t, 2H, $J=9.4$ Hz, OCH₂CH₂N), 4.37 (t, 2H, $J=9.3$ Hz, OCH₂CH₂N), 7.16-7.22 (m, 2H, phenyl), 7.79-7.85 (m, 2H, phenyl). ¹³C-NMR (101 MHz, CDCl₃), δ (ppm): 14.09, 22.49, 33.51, 35.80, 55.08, 67.65, 125.33, 128.29, 128.57, 146.73, 164.88. Elemental analysis: found C 76.13%, H 8.44%, N 6.82%; calculated C 76.81%, H 8.43%, N 6.89%.

1.2.3 Synthesis of 4-butoxybenzotrile (4)

4-Cyanophenol (25.00 g; 0.21 mol) and potassium carbonate (66.80 g; 0.63 mol) were mixed in DMF (75 mL) and stirred at room temperature for 20 min. 1-Bromobutane (25.00 mL; 0.23 mol) was added dropwise, and the reaction mixture was stirred overnight. Subsequently, the reaction mixture was extracted twice with diethyl ether and deionized water. The organic layer was dried over anhydrous

magnesium sulfate and evaporated. The crude product was purified by flash chromatography (EtOAc/hexane = 10/90) to give 4-butoxybenzotrile (36.76 g, 99%).

¹H-NMR (400 MHz, CDCl₃), δ (ppm): 0.93 (t, 3H, J = 7.4 Hz, CH₃CH₂), 1.39-1.51 (m, 2H, CH₃CH₂CH₂), 1.69-1.78 (m, 2H, CH₃CH₂CH₂), 3.95 (t, 2H, J = 6.5 Hz, CH₃CH₂CH₂CH₂), 6.85-6.91 (m, 2H, phenyl), 7.48-7.54 (m, 2H, phenyl). ¹³C-NMR (101 MHz, CDCl₃), δ (ppm): 13.85, 19.92, 31.07, 68.18, 103.65, 115.27, 119.39, 133.98, 162.55.

1.2.4 Synthesis of 2-(4-butoxyphenyl)-2-oxazoline – BuOPhOx

4-Butoxybenzotrile (36.60 g; 0.21 mol) was mixed with cadmium acetate dihydrate (2.78 g; 10.50 mmol) and 2-aminoethanol (15.95 g; 0.26 mol) was added dropwise. The reaction mixture was stirred for 48 h at 130 °C. Then, deionized water was added, and the solution was washed twice with CH₂Cl₂. The organic layer was collected and purified by flash chromatography (CH₂Cl₂/MeOH = 98/2). The crude product was further purified by sublimation (0.2 mbar, 120 °C) to give 2-(4-butoxyphenyl)-2-oxazoline (BuOPhOx) as a white powder (17.95 g, 42%).

¹H-NMR (400 MHz, CDCl₃), δ (ppm): 0.95 (t, 3H, J = 7.4 Hz, CH₃CH₂), 1.42-1.52 (m, 2H, CH₃CH₂CH₂), 1.70-1.79 (m, 2H, CH₃CH₂CH₂), 3.93-4.04 (m, 4H, CH₃CH₂CH₂CH₂O, OCH₂CH₂N), 4.39 (t, 2H, J = 9.4 Hz, OCH₂CH₂N), 6.85-6.90 (m, 2H, phenyl), 7.82-7.87 (m, 2H, phenyl). ¹³C-NMR (101 MHz, CDCl₃), δ (ppm): 14.04, 19.42, 31.42, 55.07, 67.67, 67.98, 114.36, 120.27, 130.01, 161.83, 164.67. Elemental analysis: found C 71.58%, H 7.83%, N 6.63%; calculated C 71.21%, H 7.81%, N 6.39%.

1.3 Monomer synthesis – result and discussion part

The novel monomers 2-(4-butyphenyl)-2-oxazoline (BuPhOx) and 2-(4-butoxyphenyl)-2-oxazoline (BuOPhOx) were designed to increase the mobility of the alkyl chains of the relatively rigid poly(2-phenyl-2-oxazoline) (PPhOx). They were synthesized *via* 3 different approaches. In the first approach (Fig. S1 in ESI), 4-butyl/butoxybenzotrile was formed in a Sandmeyer reaction¹ albeit in low yields (25% for 4-butylbenzotrile and 4% for 4-butoxybenzotrile), starting from commercially available 4-butyl/butoxyaniline. The Sandmeyer reaction is an exothermic process, but cyanation of unstable diazonium salts must be performed at 0 °C to prevent side reactions through thermal decomposition.² In this case, insufficient reaction heat removal capacity for the 50 g-scale reaction mixture (~ 900 mL) under laboratory conditions probably caused the formation of side products and the aforementioned low yields. Thus, 4-butoxybenzotrile was synthesized by alkylation of commercially available 4-cyanophenol in very high yield (99%, Fig. S2). The resulting nitriles were mixed with ethanolamine in

the presence of a Lewis-acid catalyst (cadmium acetate) according to Witte and Seeliger³, producing BuPhOx and BuOPhOx in mediocre yields (47% and 42%, respectively). To overcome the insufficient overall monomer yields (11% for BuPhOx and 42% for BuOPhOx) and to further avoid the use of toxic cadmium acetate, the monomer synthesis was optimized (**Fig. S1**). For this purpose, acid chlorides were transformed with 2-chloroethylamine into the corresponding chloroethylamide derivatives, and the intramolecular ring-closure initiated with sodium hydride produced the desired 2-oxazoline by hydrogen chloride elimination.⁴ This method provided significantly higher overall yields (57% for BuPhOx and 63% for BuOPhOx). The intermediate amide structures were confirmed in ¹H-NMR spectra (**Fig. S1B,C**) by the presence of multiplet signals at 3.70-3.85 ppm for (**1**) and at 4.00-4.55 ppm for (**2**), corresponding to the ethylene protons of the chloroethyl group. The final oxazoline monomers displayed the characteristic triplet signals present at 4.0 and 4.4 ppm, which correspond to the two methylene protons in the oxazoline ring, next to the nitrogen and oxygen atoms, respectively.

2. Additional polymerization data

2.1 Homopolymerization kinetics

The kinetics of homopolymerization of BuPhOx and BuOPhOx was investigated to assess whether it followed the first-order kinetics of monomer consumption, as suggested by the living polymerization mechanism of CROP. For this purpose, the homopolymerization reactions were terminated in six different time points, and the conversion was assessed using HPLC and SEC (**Fig. S3**). Because of the lower solubility of P BuPhOx and P BuOPhOx in ACN, the homopolymerization was performed at an initial monomer concentration lower than that used typical polymerization conditions (2 M for BuPhOx and 1.25 M for BuOPhOx instead of 4 M). The polymerization rate constant k_p was calculated according to Equations 1 and 2 (see the main text). Both monomers showed first-order kinetics; however, the homopolymerization rate constants k_p ($k_{p, \text{BuPhOx}} = (1.47 \pm 0.02) \cdot 10^{-2} \text{ L/mol} \cdot \text{s}$, $k_{p, \text{BuOPhOx}} = (1.03 \pm 0.14) \cdot 10^{-2} \text{ L/mol} \cdot \text{s}$) were lower than the polymerization rate of PhOx⁵, which could be caused by the presence of the electron donating substituents (butyl and butoxy) in the *p*-position on the phenyl ring.

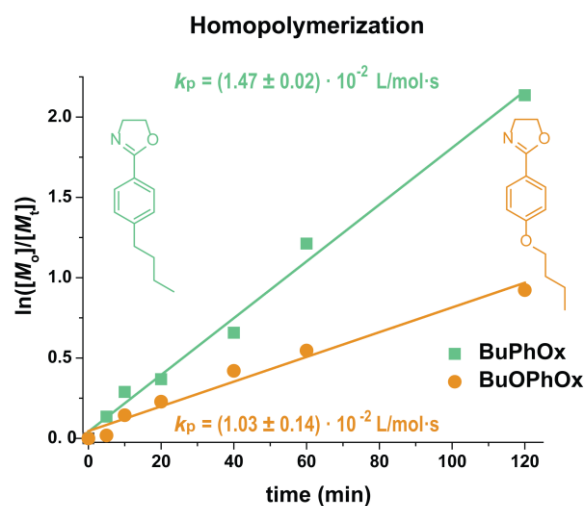


Figure S3. Homopolymerization kinetics of BuPhOx and BuOPhOx and polymerization constants.

2.2 Copolymerization kinetics

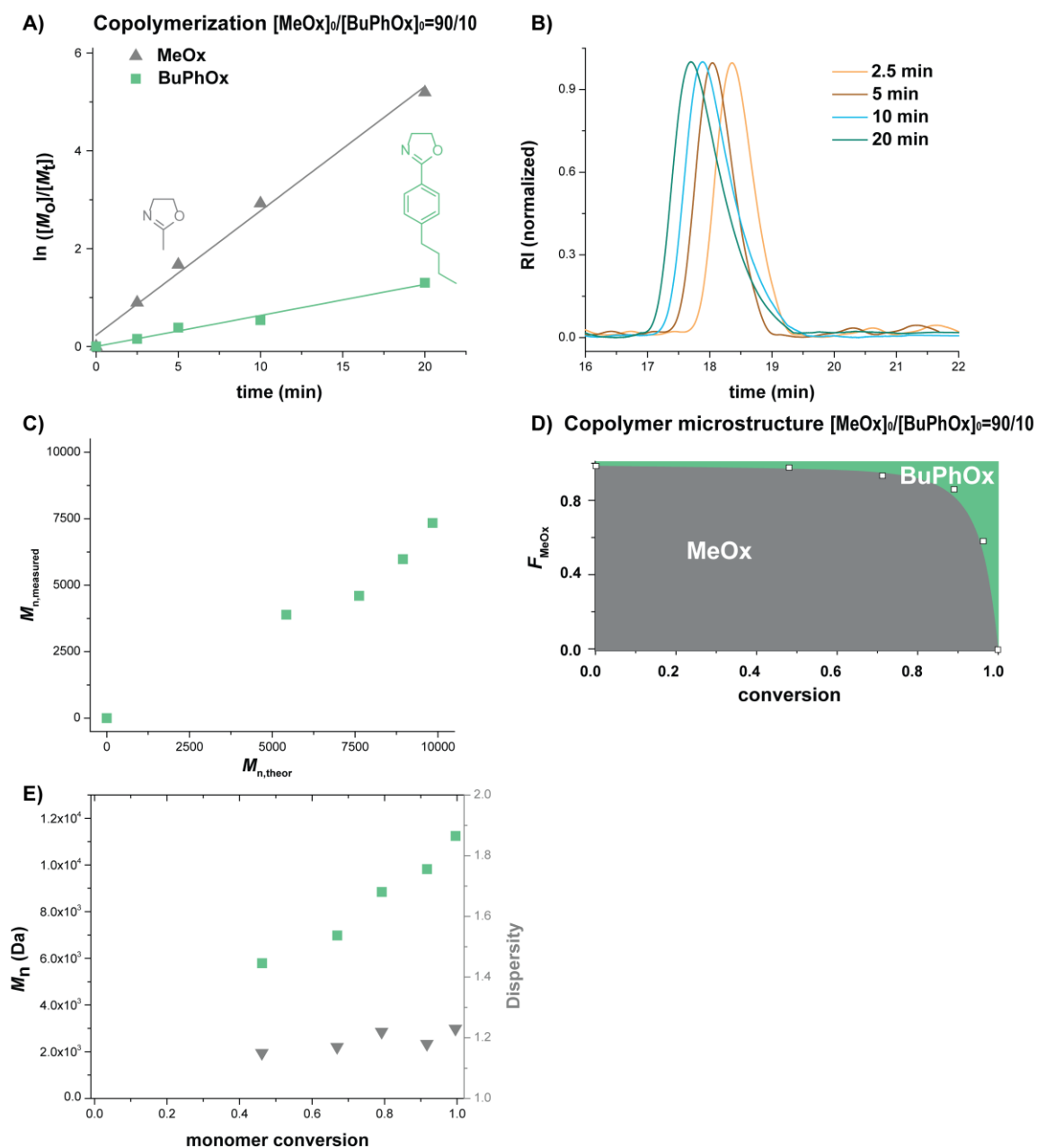


Figure S4. Copolymerization study of BuPhOx with MeOx – [MeOx]₀/[BuPhOx]₀ = 90/10. A) Time-dependent kinetics (monomer conversion obtained by HPLC); B) SEC traces; C) Measured M_n versus calculated M_n ; D) Copolymer microstructure (based on the Skeist model), the white squares correspond to the real data; E) increase in molar mass and the stability of D plotted versus monomer conversion. All polymerizations were performed in ACN at 140 °C initiated by MeONs, $[M_0] = 4$ M, $[M_0]/[MeONs_0] = 100$.

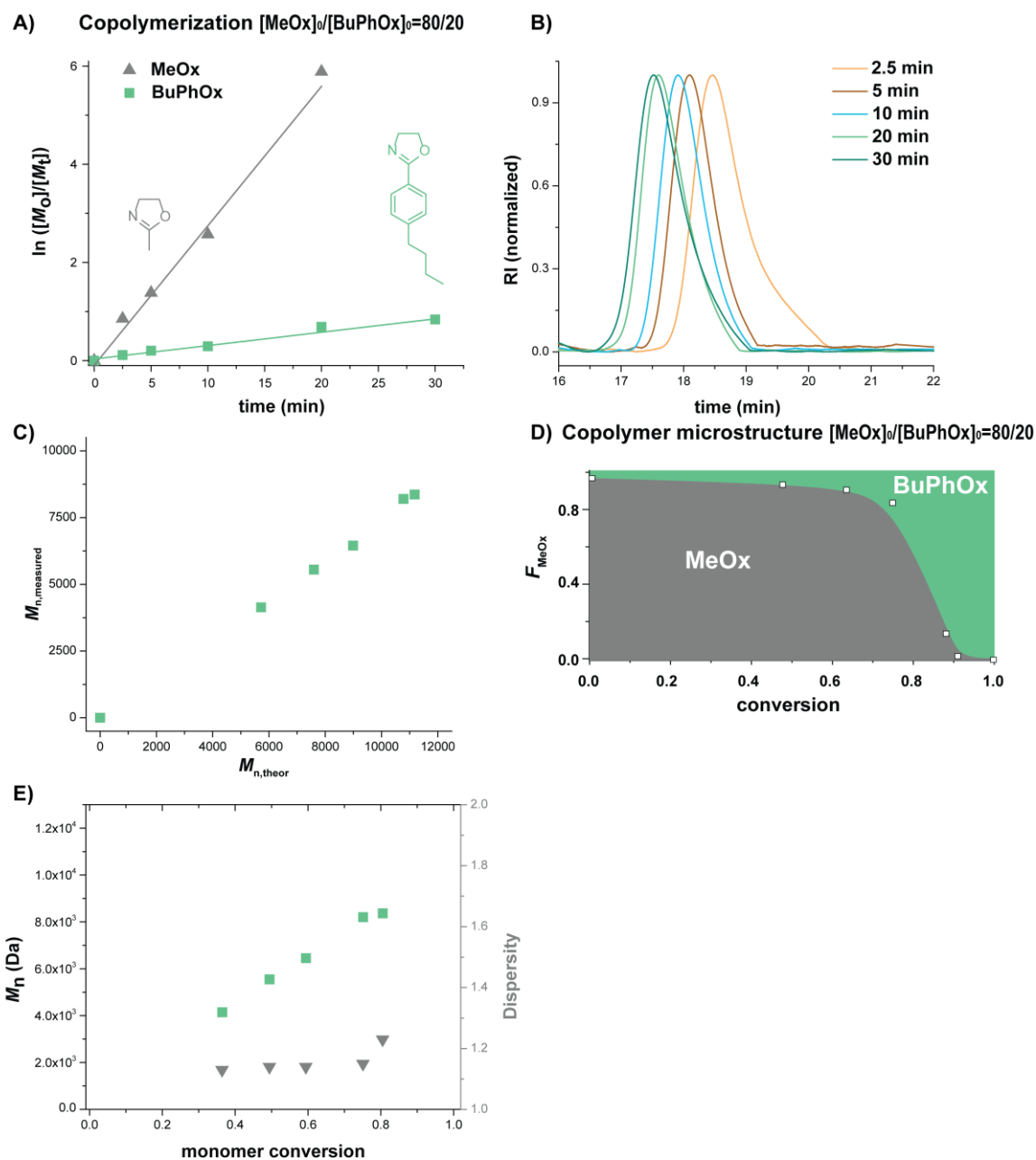


Figure S5. Copolymerization study of BuPhOx with MeOx – $[\text{MeOx}]_0/[\text{BuPhOx}]_0 = 80/20$. A) Time-dependent kinetics (monomer conversion obtained by HPLC); B) SEC traces; C) measured M_n versus calculated M_n ; D) copolymer microstructure (based on the Skeist model), the white squares correspond to the real data; E) increase in molar mass and the stability of D plotted versus monomer conversion. All polymerizations were performed in ACN at 140 °C initiated by MeONs, $[M_0] = 4 \text{ M}$, $[M_0]/[\text{MeONs}]_0 = 100$.

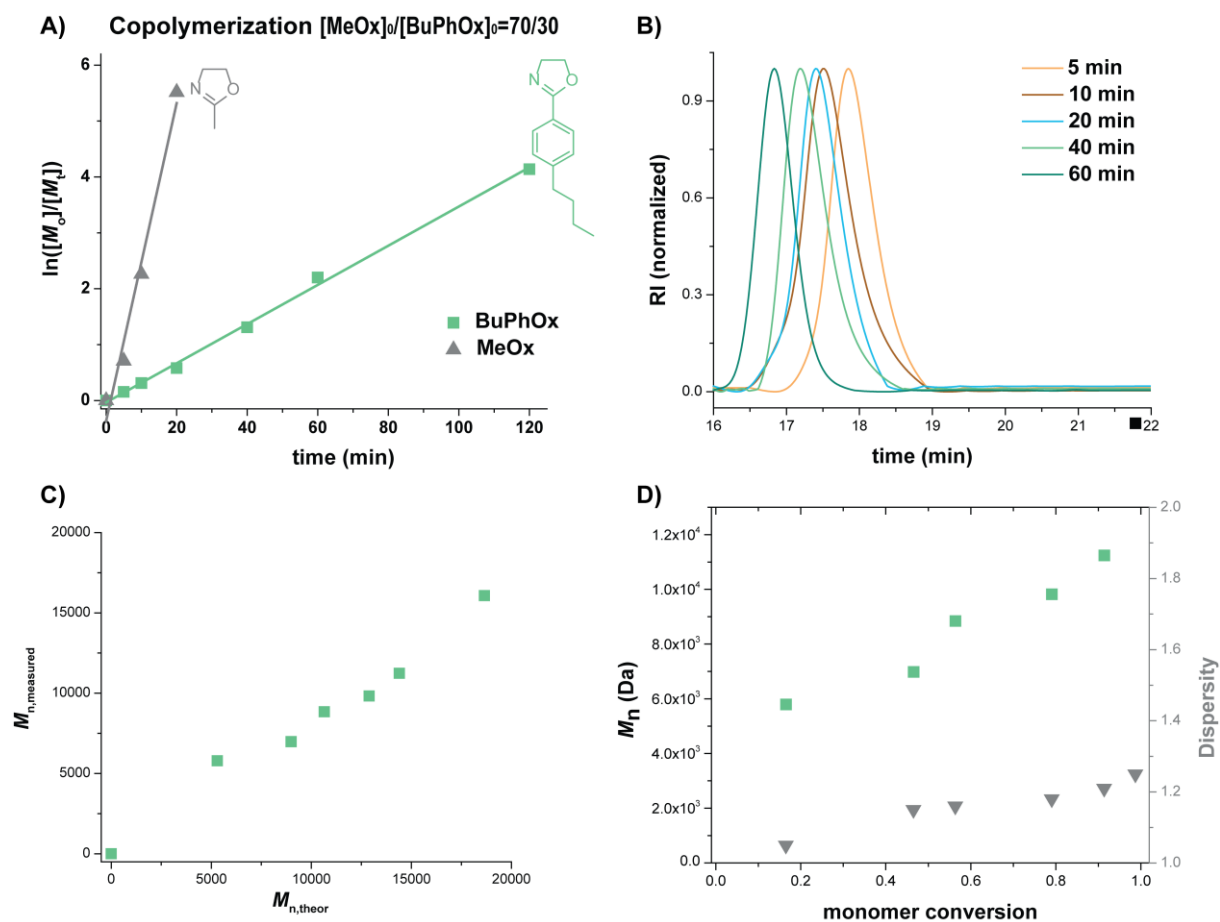


Figure S6. Copolymerization study of BuPhOx with MeOx – $[MeOx_0]/[BuPhOx_0] = 70/30$. A) Time-dependent kinetics (monomer conversion obtained by HPLC); B) SEC traces; C) measured M_n versus calculated M_n ; D) increase in molar mass and the stability of D plotted versus monomer conversion. All polymerizations were performed in ACN at 140 °C initiated by MeONs, $[M_0] = 4$ M, $[M_0]/[MeONs_0] = 100$.

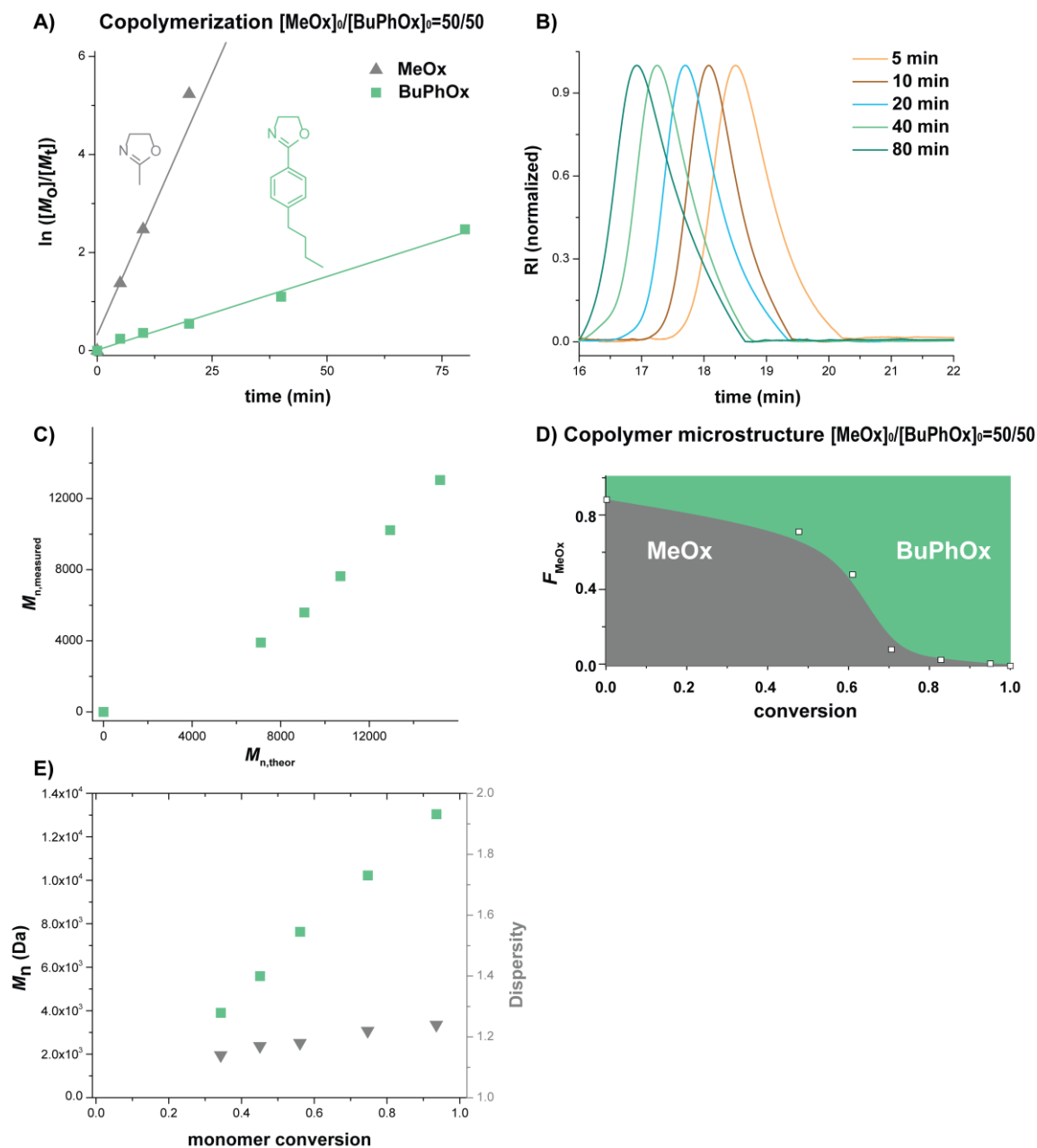


Figure S7. Copolymerization study of BuPhOx with MeOx – $[MeOx_0]/[BuPhOx_0] = 50/50$. A) Time-dependent kinetics (monomer conversion obtained by HPLC); B) SEC traces; C) measured M_n versus calculated M_n ; D) copolymer microstructure (based on the Skeist model), the white squares correspond to the real data; E) increase in molar mass and the stability of D plotted versus monomer conversion. All polymerizations were performed in ACN at 140 °C initiated by MeONs, $[M_0] = 4$ M, $[M_0]/[MeONs_0] = 100$.

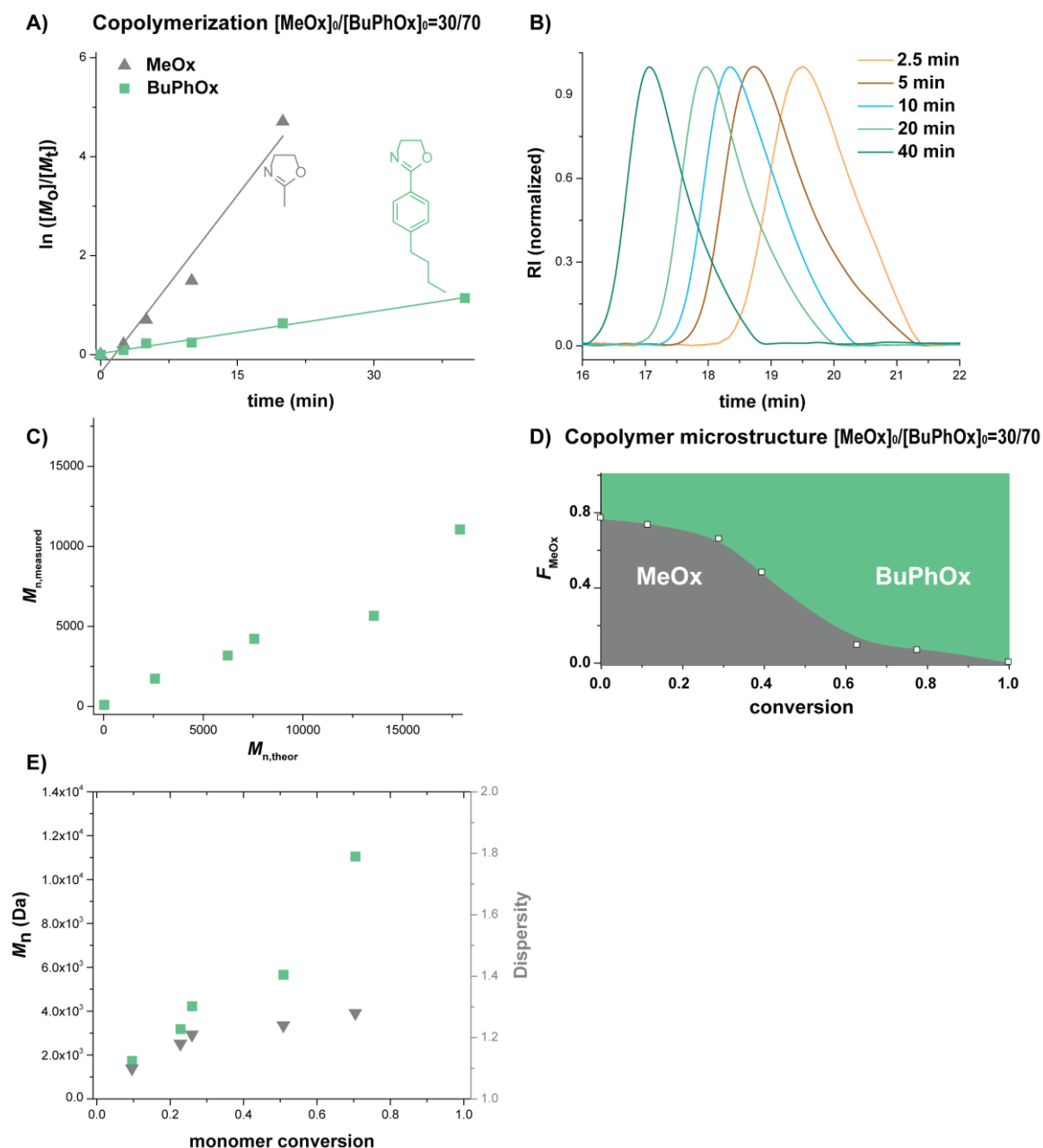


Figure S8. Copolymerization study of BuPhOx with MeOx – $[\text{MeOx}_0]/[\text{BuPhOx}_0] = 30/70$. A) Time-dependent kinetics (monomer conversion obtained by HPLC); B) SEC traces; C) measured M_n versus calculated M_n ; D) copolymer microstructure (based on the Skeist model), the white squares correspond to the real unfitted data; E) increase in molar mass and the stability of \mathcal{D} plotted versus monomer conversion. All polymerizations were performed in ACN at 140 °C initiated by MeONs, $[M_0] = 4 \text{ M}$, $[M_0]/[\text{MeONs}_0] = 100$.

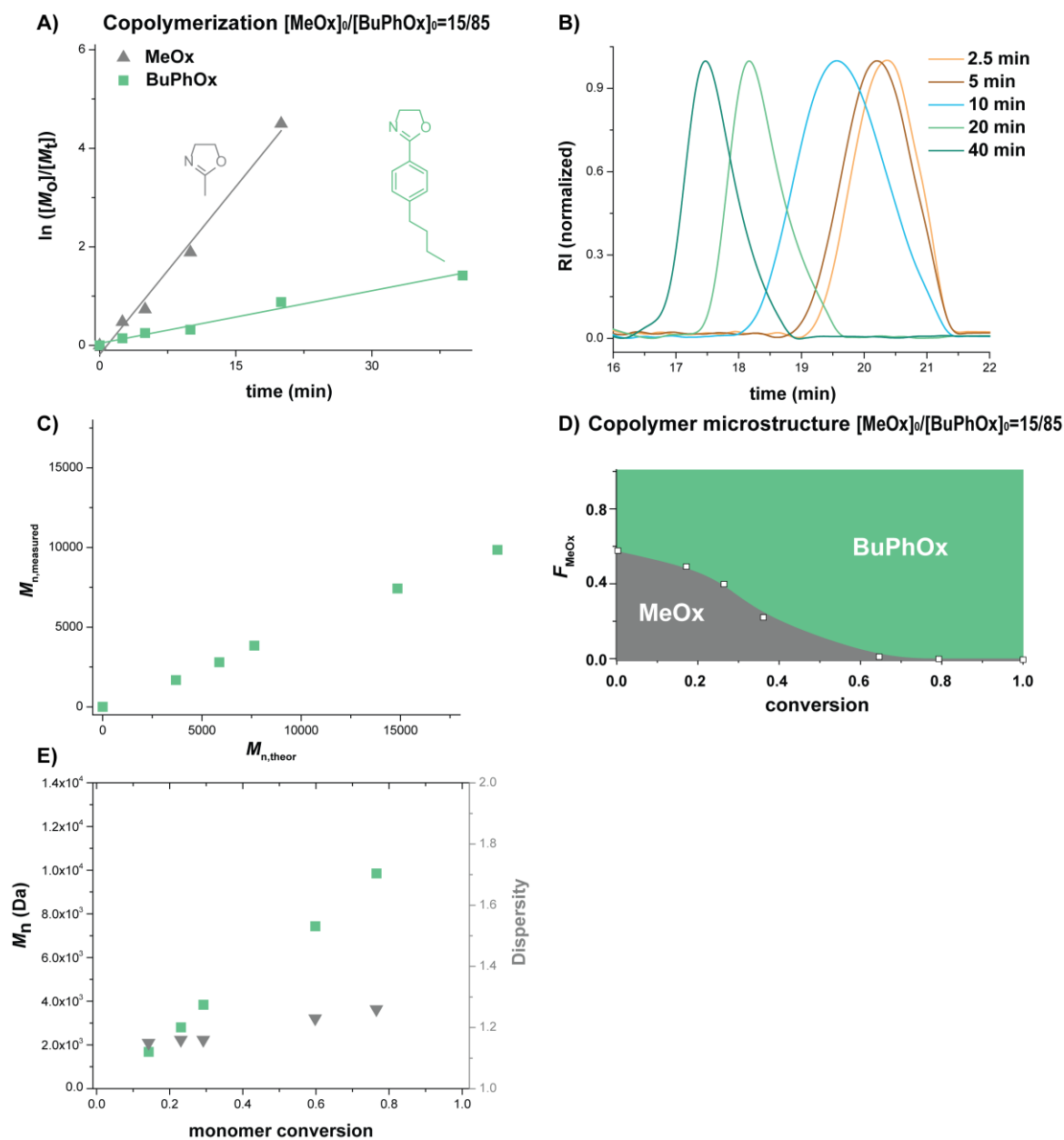


Figure S9. Copolymerization study of BuPhOx with MeOx – $[MeOx_0]/[BuPhOx_0] = 15/85$. A) Time-dependent kinetics (monomer conversion obtained by HPLC); B) SEC traces; C) measured M_n versus calculated M_n ; D) copolymer microstructure (based on the Skeist model), the white squares correspond to the real data; E) increase in molar mass and the stability of D plotted versus monomer conversion. All polymerizations were performed in ACN at 140 °C initiated by MeONs, $[M_0] = 4$ M, $[M_0]/[MeONs_0] = 100$.

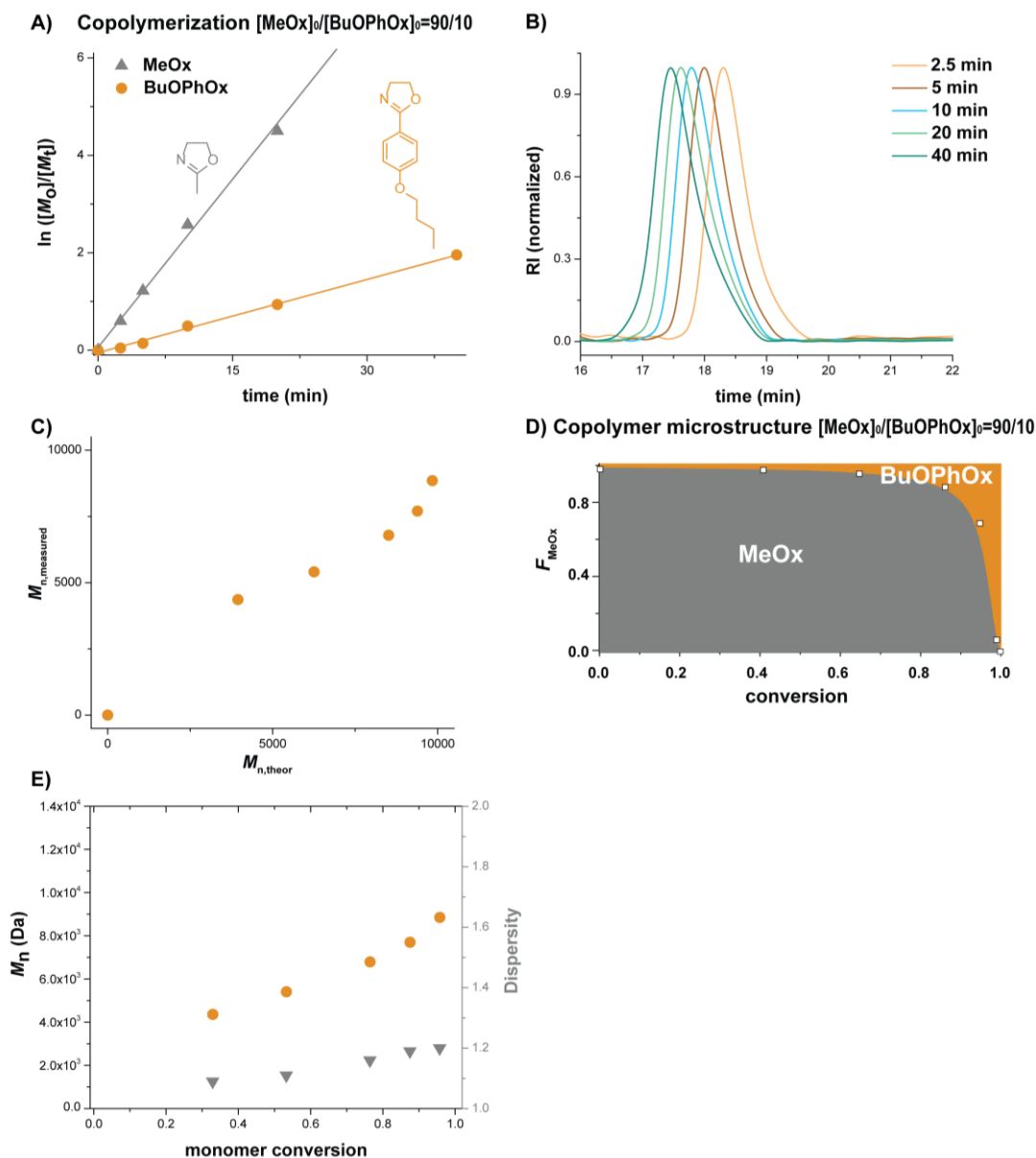


Figure S10. Copolymerization study of BuOPhOx with MeOx – $[MeOx_0]/[BuOPhOx_0] = 90/10$.

A) Time-dependent kinetics (monomer conversion obtained by HPLC); B) SEC traces; C) measured M_n versus calculated M_n ; D) copolymer microstructure (based on the Skeist model), the white squares correspond to the real data; E) increase in molar mass and the stability of \bar{D} plotted versus monomer conversion. All polymerizations were performed in ACN at 140 °C initiated by MeONs, $[M_0] = 4 M$, $[M_0]/[MeONs_0] = 100$.

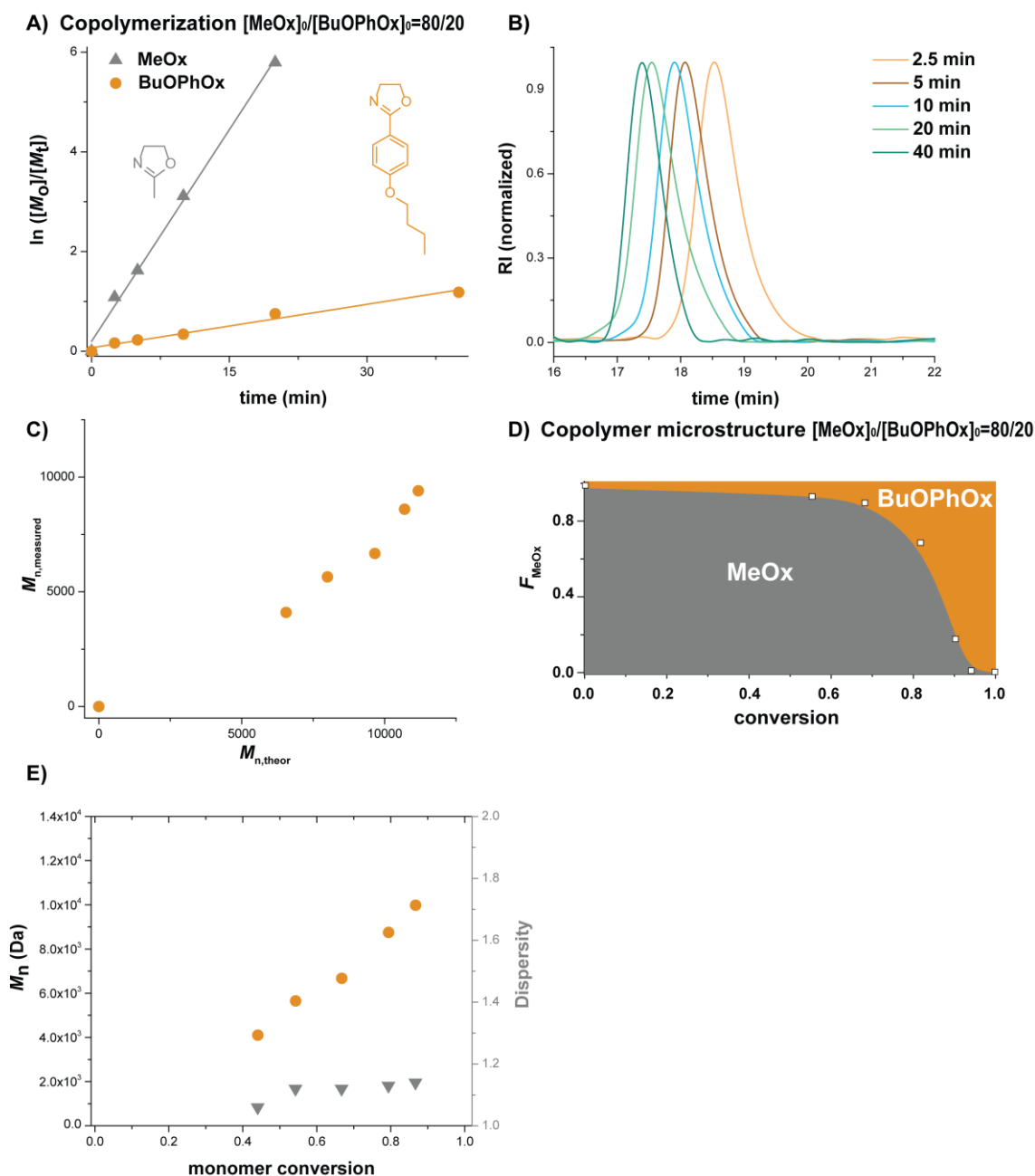


Figure S11. Copolymerization study of BuOPhOx with MeOx – $[\text{MeOx}]_0/[\text{BuOPhOx}]_0 = 80/20$. A) Time-dependent kinetics (monomer conversion obtained by HPLC); B) SEC traces; C) measured M_n versus calculated M_n ; D) copolymer microstructure (based on the Skeist model), the white squares correspond to the real data; E) increase in molar mass and the stability of D plotted versus monomer conversion. All polymerizations were performed in ACN at 140 °C initiated by MeONs, $[M_0] = 4 \text{ M}$, $[M_0]/[\text{MeONs}_0] = 100$.

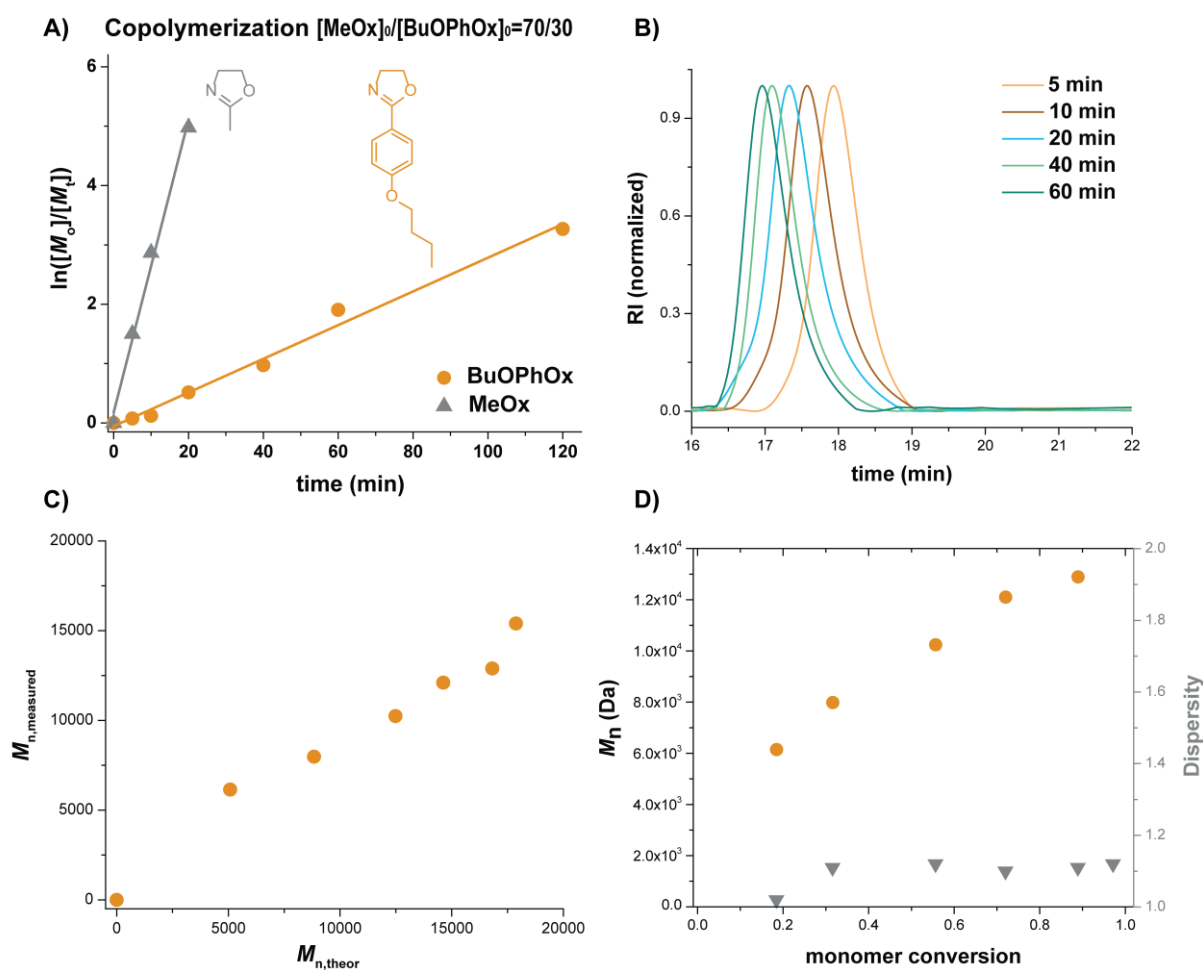


Figure S12. Copolymerization study of BuOPhOx with MeOx – $[MeOx_0]/[BuOPhOx_0] = 70/30$. A) Time-dependent kinetics (monomer conversion obtained by HPLC); B) SEC traces; C) measured M_n versus calculated M_n ; D) increase in molar mass and the stability of D plotted versus monomer conversion. All polymerizations were performed in ACN at 140 °C initiated by MeONs, $[M_0] = 4 M$, $[M_0]/[MeONs_0] = 100$.

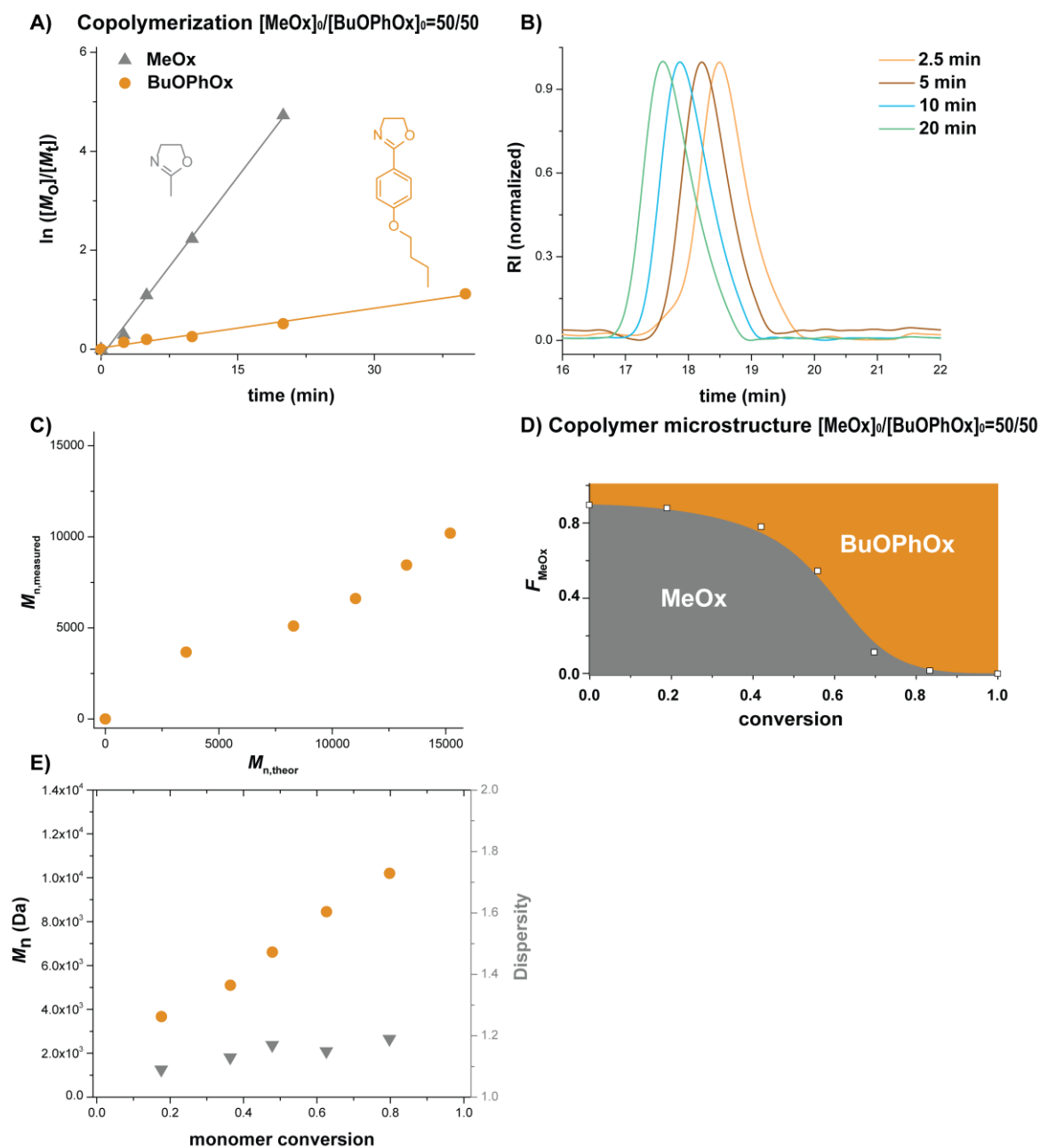


Figure S13. Copolymerization study of BuOPhOx with MeOx – $[\text{MeOx}_0]/[\text{BuOPhOx}_0] = 50/50$. A) Time-dependent kinetics (monomer conversion obtained by HPLC); B) SEC traces; C) measured M_n versus calculated M_n ; D) copolymer microstructure (based on the Skeist model), the white squares correspond to the real data; E) increase in molar mass and the stability of \bar{D} plotted versus monomer conversion. All polymerizations were performed in ACN at 140 °C initiated by MeONs, $[M_0] = 4 \text{ M}$, $[M_0]/[\text{MeONs}_0] = 100$.

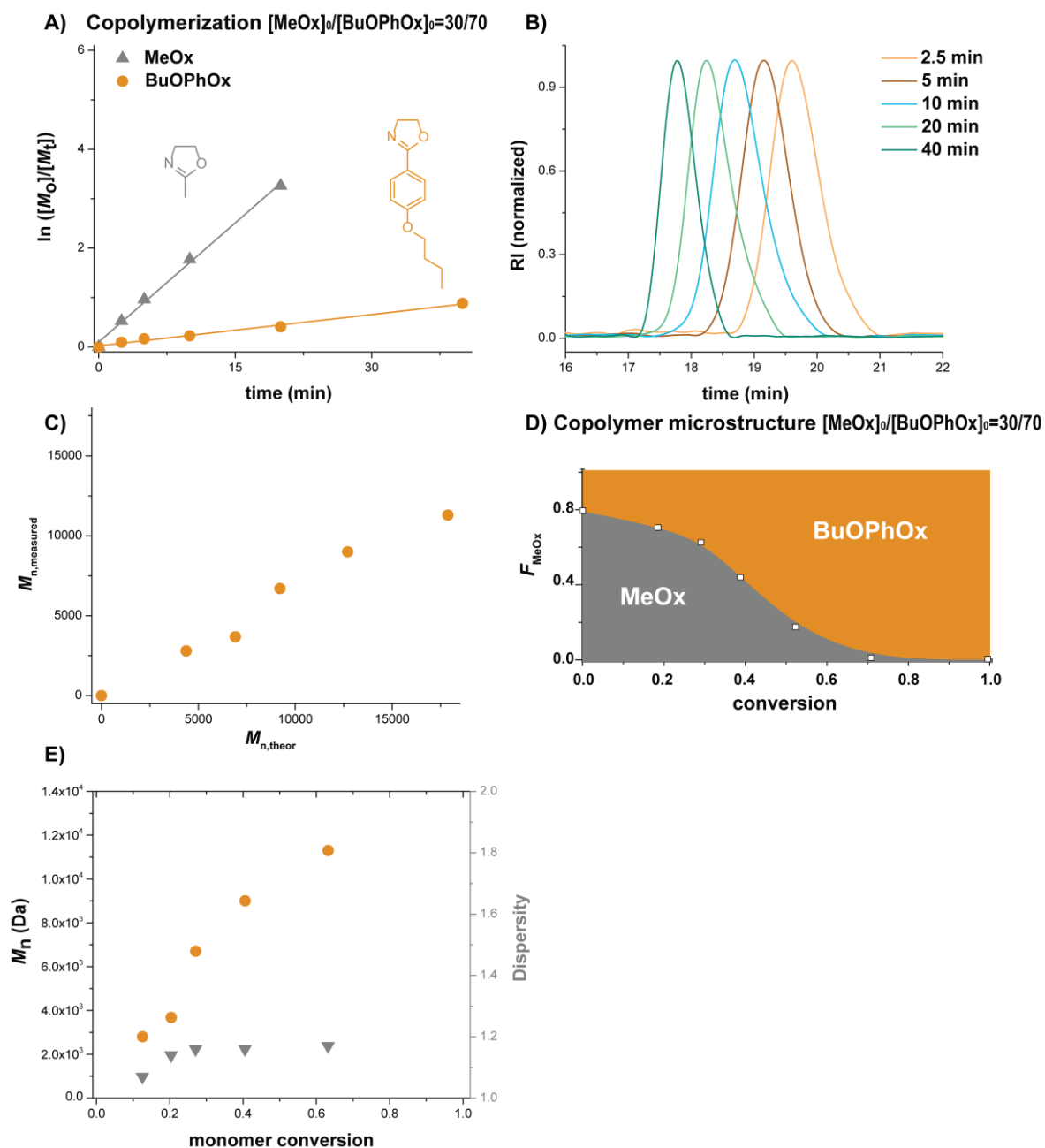


Figure S14. Copolymerization study of BuOPhOx with MeOx – $[MeOx_0]/[BuOPhOx_0] = 30/70$. A) Time-dependent kinetics (monomer conversion obtained by HPLC); B) SEC traces; C) measured M_n versus calculated M_n ; D) copolymer microstructure (based on the Skeist model), the white squares correspond to the real data; E) increase in molar mass and the stability of D plotted versus monomer conversion. All polymerizations were performed in ACN at 140 °C initiated by MeONs, $[M_0] = 4$ M, $[M_0]/[MeONs_0] = 100$.

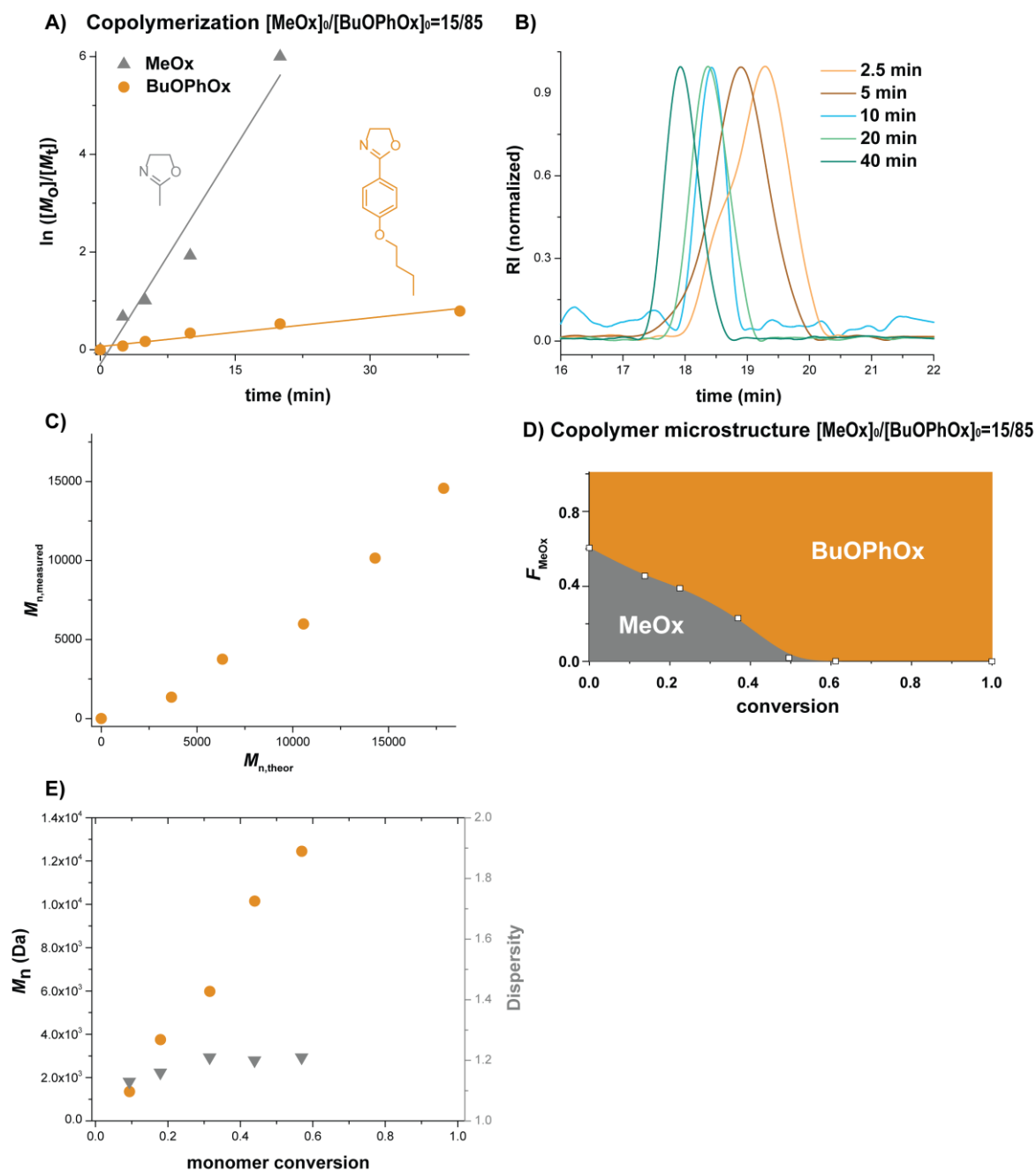


Figure S15. Copolymerization study of BuOPhOx with MeOx – $[\text{MeOx}_0]/[\text{BuOPhOx}_0] = 15/85$. A) Time-dependent kinetics (monomer conversion obtained by HPLC); B) SEC traces; C) measured M_n versus calculated M_n ; D) copolymer microstructure (based on the Skeist model), the white squares correspond to the real data; E) increase in molar mass and the stability of \bar{D} plotted versus monomer conversion. All polymerizations were performed in ACN at 140 °C initiated by MeONs, $[M_0] = 4 \text{ M}$, $[M_0]/[\text{MeONs}_0] = 100$.

2.2 Polymer characterization data

Table S1. Solubility chart of the prepared polymers (c = 5 mg /mL).

- soluble (transparent solution, no formation of nanoparticles by DLS at 20 °C)
- * partly soluble (transparent to cloudy solution, formation of nanoparticles by DLS at 20 °C)
- × insoluble

Name	Water	Methanol	Chloroform
PMeOx ₉₀ - <i>grad</i> -PhOx ₁₀	○	○	*
PMeOx ₉₀ - <i>block</i> -PhOx ₁₀	*	*	*
PMeOx ₈₀ - <i>grad</i> -PhOx ₂₀	*	*	○
PMeOx ₈₀ - <i>block</i> -PhOx ₂₀	*	*	*
PMeOx ₇₀ - <i>grad</i> -PhOx ₃₀	*	*	○
PMeOx ₇₀ - <i>block</i> -PhOx ₃₀	×	×	○
PMeOx ₉₀ - <i>grad</i> -BuPhOx ₁₀	○	○	*
PMeOx ₉₀ - <i>block</i> -BuPhOx ₁₀	*	*	*
PMeOx ₈₀ - <i>grad</i> -BuPhOx ₂₀	*	*	○
PMeOx ₈₀ - <i>block</i> -BuPhOx ₂₀	×	×	*
PMeOx ₇₀ - <i>grad</i> -BuPhOx ₃₀	*	*	○
PMeOx ₇₀ - <i>block</i> -BuPhOx ₃₀	×	×	○
PMeOx ₉₀ - <i>grad</i> -BuOPhOx ₁₀	*	○	*
PMeOx ₉₀ - <i>block</i> -BuOPhOx ₁₀	*	×	*
PMeOx ₈₀ - <i>grad</i> -BuOPhOx ₂₀	*	*	○
PMeOx ₈₀ - <i>block</i> -BuOPhOx ₂₀	×	×	○
PMeOx ₇₀ - <i>grad</i> -BuOPhOx ₃₀	*	*	○
PMeOx ₇₀ - <i>block</i> -BuOPhOx ₃₀	×	×	○

MeOx – 2-methyl-2-oxazoline, PhOx – 2-phenyl-2-oxazoline, BuPhOx – 2-(4-butylphenyl)-2-oxazoline, BuOPhOx – 2-(4-butoxyphenyl)-2-oxazoline

2.2.1 Additional results of thermal properties of the copolymers

The results from TGA revealed that PMeOx, PPhOx and PBUPhOx homopolymers were thermally stable up to 300 °C (Table S3) and that they degraded in one step (Fig. S16 in ESI, Table S3). The main degradation step of the fully aliphatic PMeOx shifted to a lower temperature ($T_{d\max1} = 384$ °C) than that of the aromatic PPhOx and PBUPhOx ($T_{d\max1} = 440$ °C). Conversely, PBUOPhOx was thermally stable up to ca 260 °C (Table S3) and exhibited a two-step degradation process (Fig. S16 in ESI); the first weight loss with $T_{d\max1} = 311$ °C was likely connected to thermal decomposition of the butoxy side group, whereas the polymer backbone degraded during the second (main) degradation step ($T_{d\max2} = 429$ °C).

The thermal transitions of the homopolymers and copolymers in bulk were further investigated by DSC. PMeOx and PPhOx homopolymers were fully amorphous exhibiting no melting point and only one glass transition temperature (T_g) of 83 °C and 105 °C, respectively (Table S3, Fig. S18), in line with the literature data.^{6,7} DSC analysis of the novel PBuPhOx and PBuOPhOx homopolymers showed no glass transition temperature (Table S3 and Fig. S18). The DSC runs performed at lower heating/cooling rates (5 °C/min) further revealed a melting endotherm of approximately 240 °C and a crystallization exotherm of approximately 160 °C for the PBuPhOx homopolymer (Table S2 and Fig. S21). The incorporation of the butyl side chain on the benzene ring thus changed the thermal behaviour from amorphous to semi-crystalline, and the PBuPhOx homopolymer exhibited butyl side-chain crystallization.⁸ In turn, the butoxy substitution in the benzene ring did not induce crystallization due to the increased side chain mobility of the flexible ether linkages.⁹ Consequently, the PBuOPhOx homopolymer remained amorphous.

Similar to the PBuPhOx homopolymerization, the formation of longer BuPhOx sequences in the block PMeOx-*block*-BuPhOx copolymers induced the crystallization of the butyl side chain. For this reason, the block copolymers containing 20% and 30% BuPhOx comonomer units exhibited a semi-crystalline behaviour, as shown by the DSC melting endotherm at slightly lower temperature than that of the PBuPhOx homopolymer (Table S2 and Fig. S18 in ESI). The melting enthalpy of these two copolymers correlated well with the content of BuPhOx comonomer units, showing a similar crystallization potential of the butyl side chain in the block copolymers and in the PBuPhOx homopolymer. In contrast to the block copolymers, the PMeOx-*grad*-BuPhOx copolymers were 100% amorphous in the whole range (10 to 30%) of BuPhOx comonomer units, thus proving their gradient microstructure, without the formation of longer BuPhOx sequences.

Table S2. Summary of crystallization characteristics of PBUPhOx homopolymer and PMeOx₈₀-*block*-BuPhOx₂₀ and PMeOx₇₀-*block*-BuPhOx₃₀ copolymers.

Name	T_c peak (°C)	T_c onset (°C)	ΔH_c (J/g)	T_m onset (°C)	T_m peak (°C)	ΔH_m (J/g)
PBUPhOx	187	198	26	234	247	31
PMeOx₈₀-<i>block</i>-BuPhOx₂₀	113	121	1	219	223	6
PMeOx₇₀-<i>block</i>-BuPhOx₃₀	160	170	13	229	236	10

Table S3. TGA and DSC results of the homopolymers and block and gradient copolymers.

Name	T_d 5% (°C) ^a	T_d max1 (°C) ^b	T_d max2 (°C) ^c	T_g (°C) ^d	T_0 (°C) ^e		T_e (°C) ^f	ΔT_g (°C) ^g
PMeOx	354	384	-	83	73		95	21
PPhOx	303	440	-	105	98		117	20
PBUPhOx	321	440	-	-	-		-	-
PBUOPhOx	294	311	429	-	-		-	-
PMeOx₉₀-<i>grad</i>-PhOx₁₀	370	422	-	85	59		99	39
PMeOx₉₀-<i>block</i>-PhOx₁₀	368	410	-	87	78		101	23
PMeOx₈₀-<i>grad</i>-PhOx₂₀	357	429	-	88	74		103	29
PMeOx₈₀-<i>block</i>-PhOx₂₀	358	413	-	86	77		101	24
PMeOx₇₀-<i>grad</i>-PhOx₃₀	374	410	441	89	73		105	32
PMeOx₇₀-<i>block</i>-PhOx₃₀	361	406	443	89	75		103	28
PMeOx₉₀-<i>grad</i>-BuPhOx₁₀	324	433	-	79	62		94	32
PMeOx₉₀-<i>block</i>-BuPhOx₁₀	366	424	-	80	74		93	19
PMeOx₈₀-<i>grad</i>-BuPhOx₂₀	364	439	-	78	60		91	32
PMeOx₈₀-<i>block</i>-BuPhOx₂₀	364	422	445	79	67		93	26
PMeOx₇₀-<i>grad</i>-BuPhOx₃₀	340	446	-	72	60		88	28
PMeOx₇₀-<i>block</i>-BuPhOx₃₀	368	411	448	78	65		94	29
PMeOx₉₀-<i>grad</i>-BuOPhOx₁₀	301	421	-	79	66		91	25
PMeOx₉₀-<i>block</i>-BuOPhOx₁₀	336	422	-	81	72		92	20
PMeOx₈₀-<i>grad</i>-BuOPhOx₂₀	348	429	-	80	70		92	23
PMeOx₈₀-<i>block</i>-BuOPhOx₂₀	360	413	-	86	74		103	29
PMeOx₇₀-<i>grad</i>-BuOPhOx₃₀	370	419	-	79	64		94	30
PMeOx₇₀-<i>block</i>-BuOPhOx₃₀	375	425	-	82	71		94	22

^a Temperature of 5% weight loss; ^{b,c} temperature of maximum decomposition; ^d glass transition temperature; ^e onset point of the T_g peak on the derivate heat curve; ^f end point of the T_g peak on the derivate heat curve; ^g breadth of the glass transition region

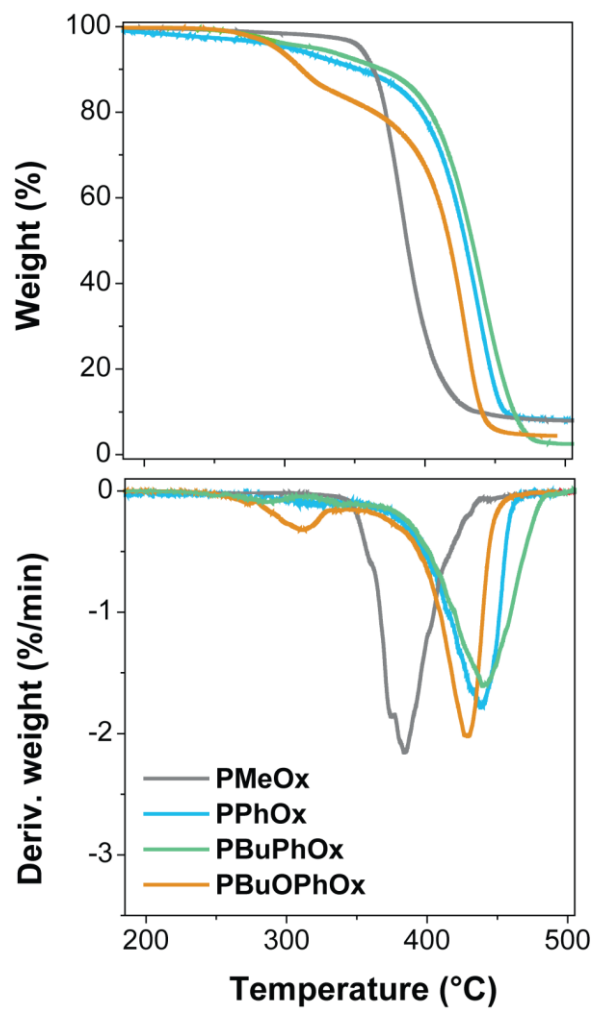


Figure S16. TGA and DTG curves of the prepared homopolymers.

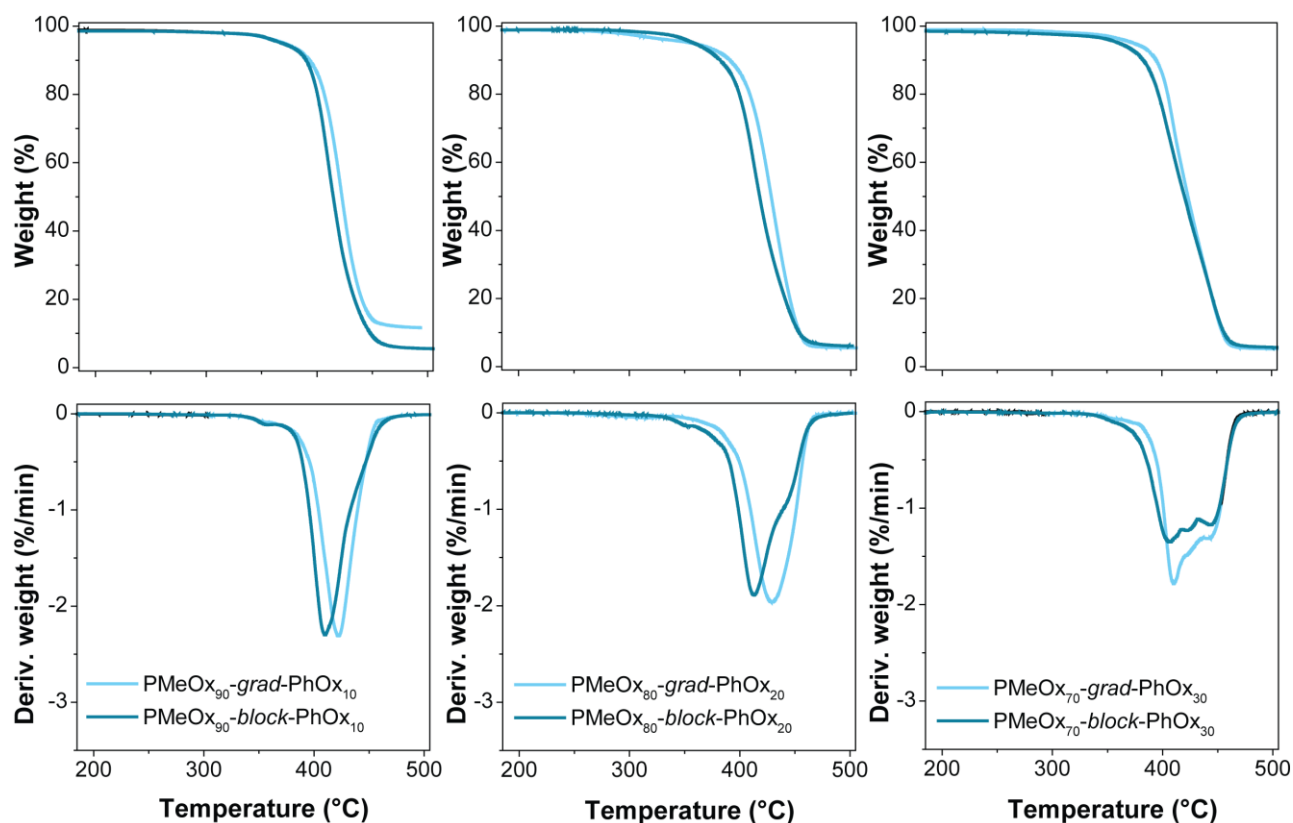


Figure S17. TGA and DTG curves of the PMeOx-PhOx copolymers.

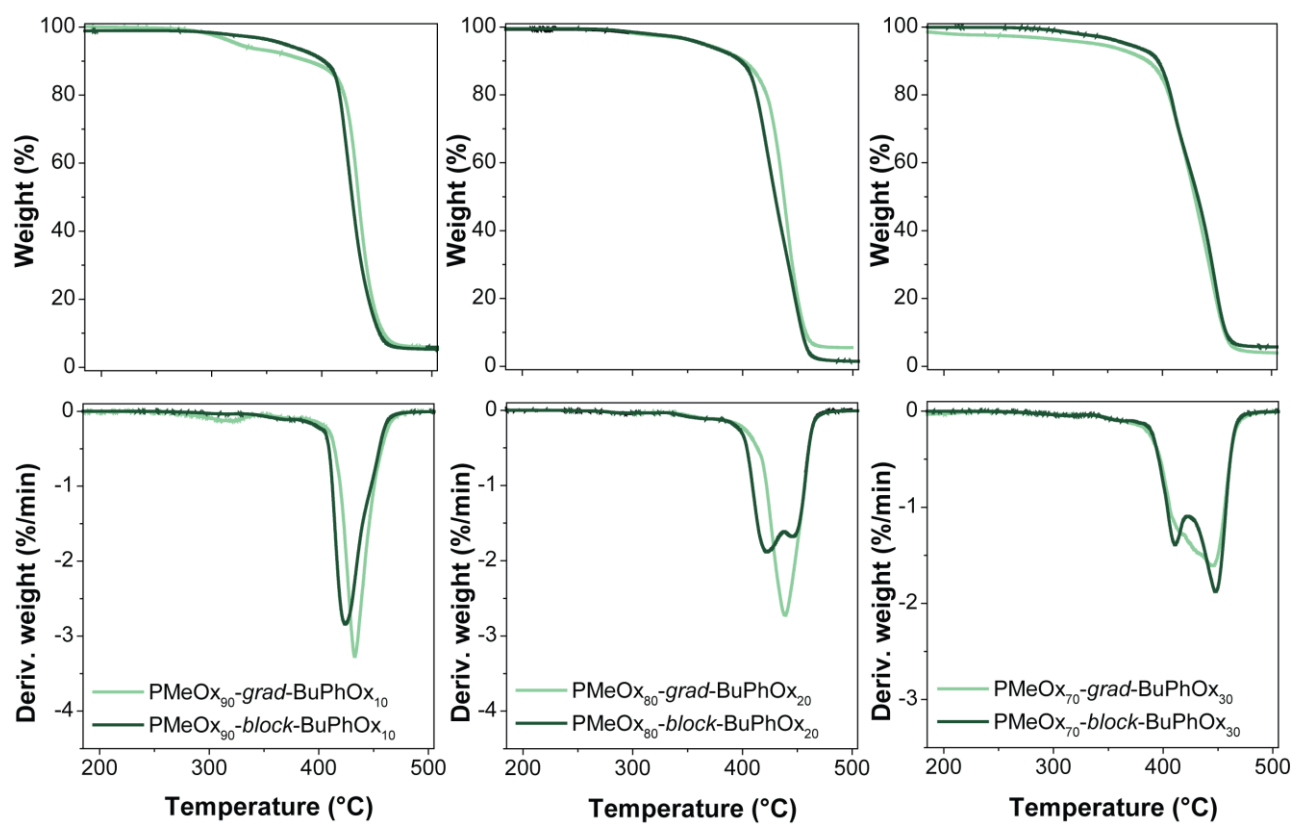


Figure S18. TGA and DTG curves of the PMeOx-BuPhOx copolymers.

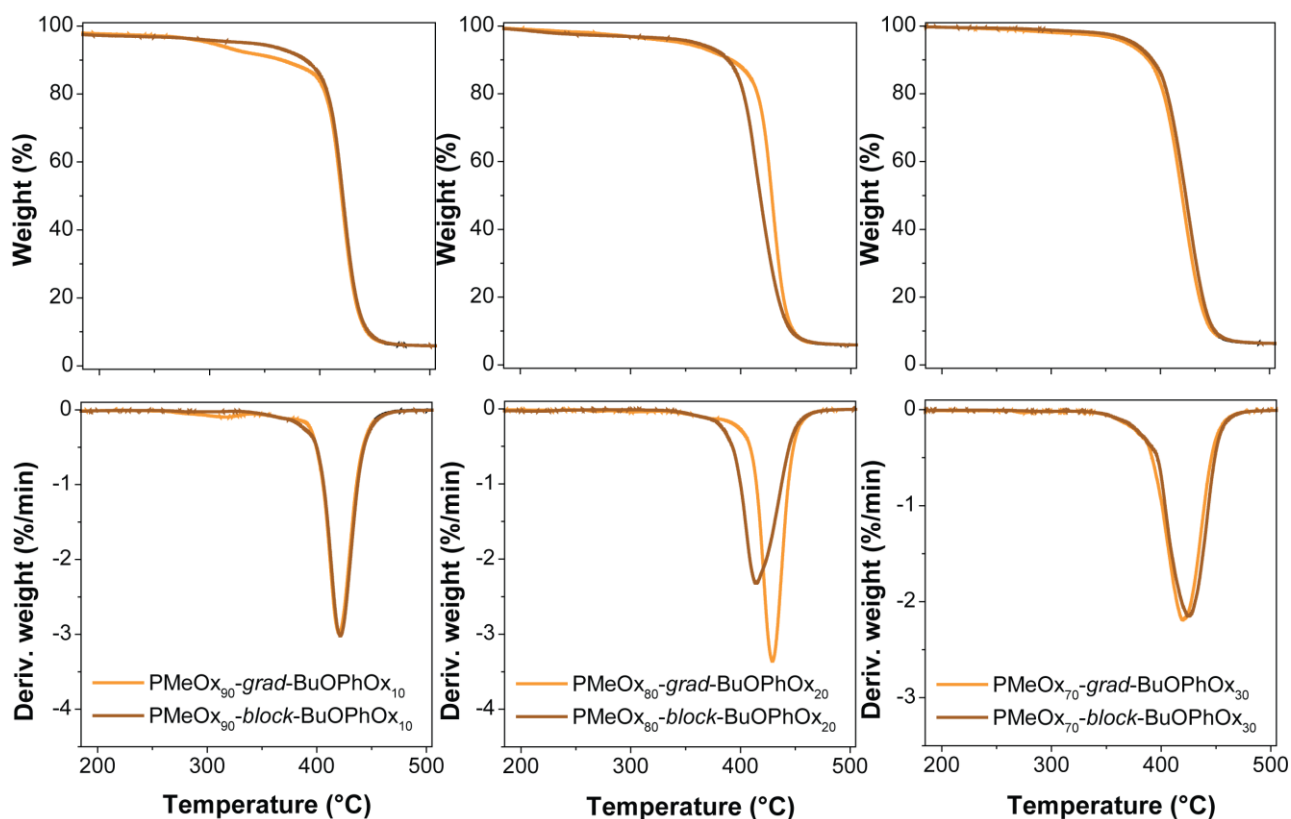


Figure S19. TGA and DTG curves of the PMeOx-BuOPhOx copolymers.

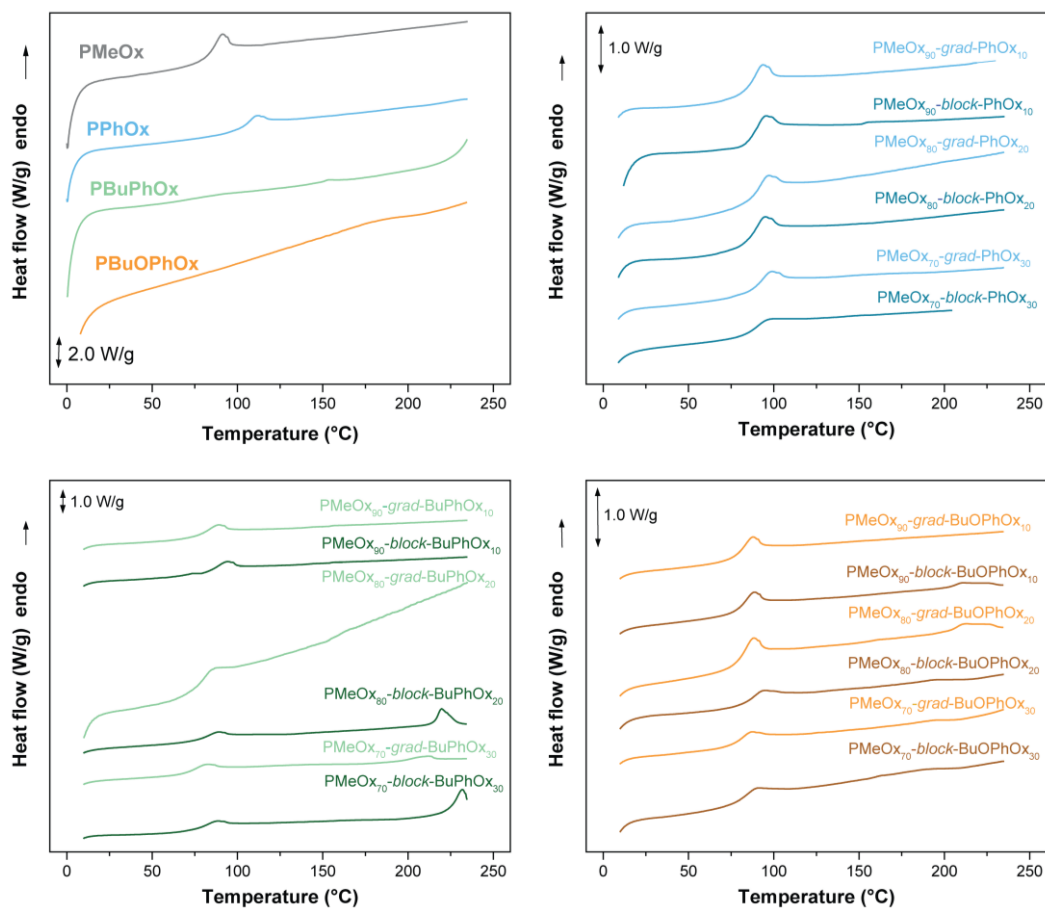


Figure S20. DSC traces (2nd heating run, 50 °C/min) of the homopolymers and of the block and gradient copolymers

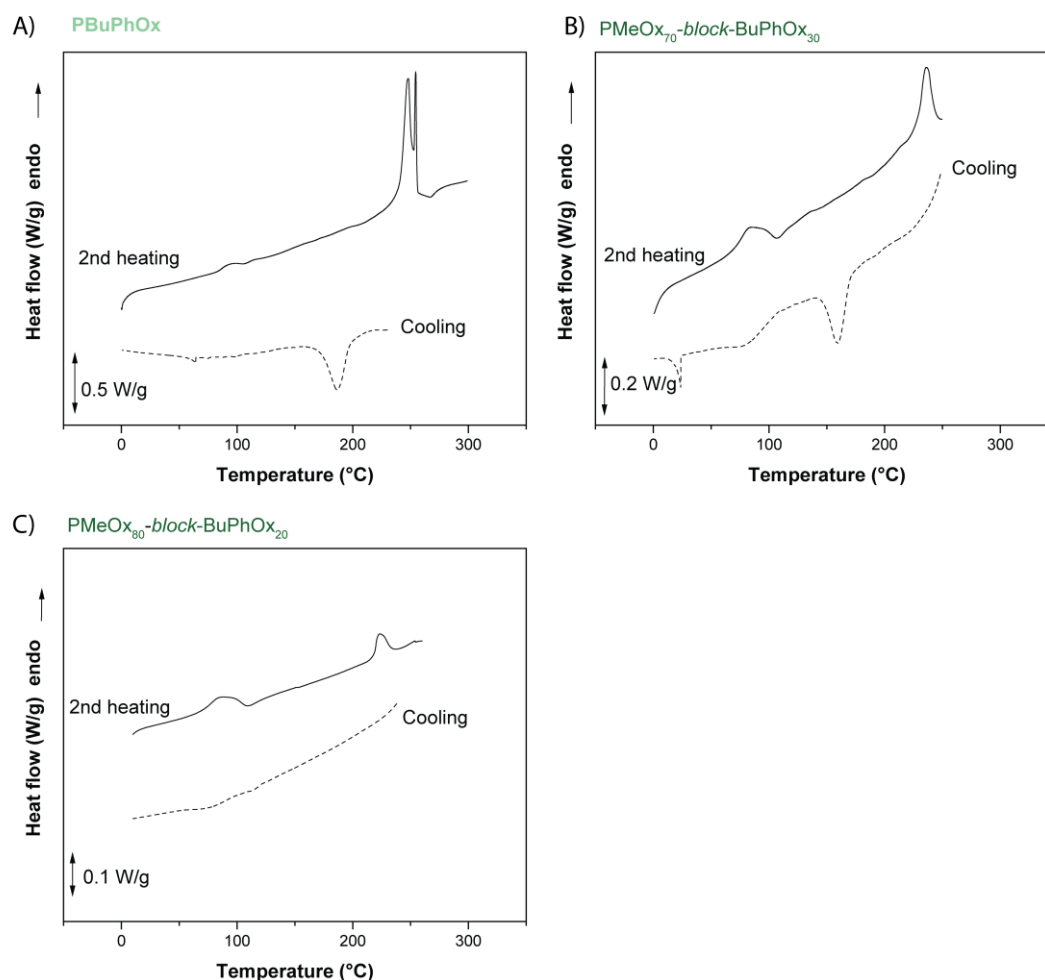


Figure S21. DSC traces (cooling and 2nd heating run, 5 °C/min) of: A) PBUPhOx; B) PMeOx₇₀-*block*-BuPhOx₃₀ and C) PMeOx₈₀-*block*-BuPhOx₂₀.

2.2.2 Additional results of NPs morphology

In order to visualize the nanoparticle morphology, TEM imaging technique was employed. This approach involved negative staining with the addition of trehalose, stabilizing the structure of NPs and mitigating a material shrinkage caused by sample drying. For spherical micelles, the size difference between TEM and DSL is caused by a polymer shrinkage in its dry state (which cannot be completely prevented by trehalose) and by overestimating the particle sizes by DLS due to their hydration layer. Further inaccuracy in particle size determination by image analysis can be brought in by improper thresholding. For this reason, instead of simple thresholding, which caused significant systematic error leading to further lowering of the measured particle diameters (data not showed), the trainable WEKA segmentation (TWS) plugin was used. Compared to simple thresholding, TWS detected the particles

with higher precision. The analyzed data are shown in the Table S4 and the number-weighted particle size distribution in Figure S22A.

The NPs of PMeOx-BuPhOx and PMeOx-BuOPhOx contained particles of irregular or even rod-like shape, often in aggregates. The proper image analysis of such heterogeneous samples would be significantly more challenging so within the scope of this paper we decided for only rough analysis by measuring the particle lengths in their longest direction, including particle aggregates as one particle/fiber (Table S5). In the histograms (200 particles per sample) can be seen a peak of shorter particles correlating with the DLS data and much larger particle aggregates located in the distribution right tail (Fig. S22B).

Table S4. TEM image analysis of the spherical nanoparticles.

Name	Number of the analyzed NPs	Average equivalent circular diameter (nm)	Average circularity (-)	D_h (nm) from DLS
PMeOx ₈₀ - <i>grad</i> -PhOx ₂₀	673	18.4 ± 3.2	0.82 ± 0.07	27 ± 2
PMeOx ₈₀ - <i>block</i> -PhOx ₂₀	500	50.3 ± 19.6	0.81 ± 0.11	126 ± 15

Table S5. TEM image analysis of the rod-like particles.

Name	Number of the analyzed NPs	Average particle/aggregate length (nm)	D_h (nm) from DLS
PMeOx ₈₀ - <i>grad</i> -BuPhOx ₂₀	201	248 ± 189	132 ± 26
PMeOx ₈₀ - <i>block</i> -BuPhOx ₂₀	198	355 ± 234	184 ± 29
PMeOx ₈₀ - <i>grad</i> -BuOPhOx ₂₀	237	89 ± 44	79 ± 4
PMeOx ₈₀ - <i>block</i> -BuOPhOx ₂₀	200	135 ± 73	152 ± 17

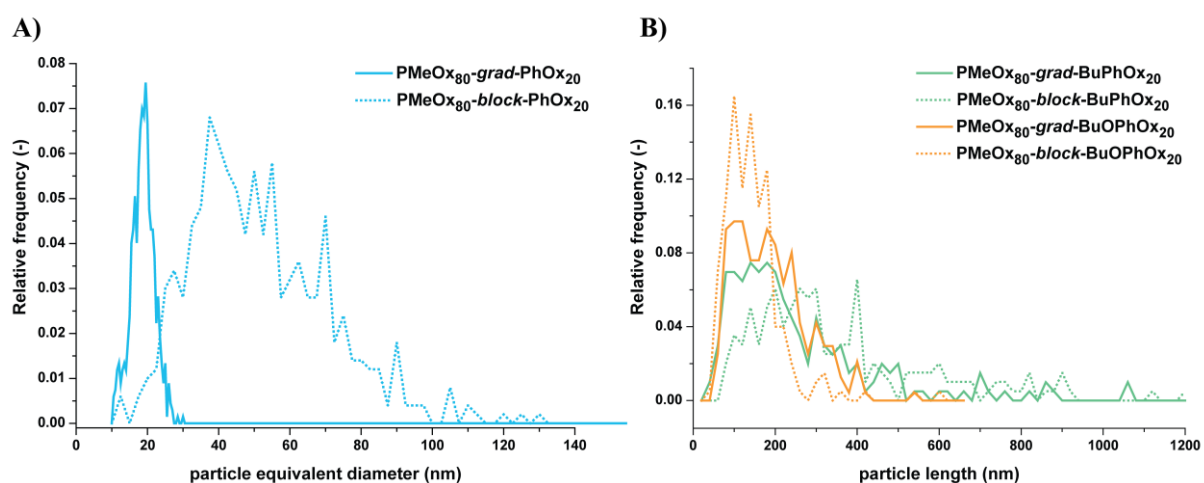


Figure S22. Particle size distributions from TEM image analysis. A) number-weighted particle size distribution of PMeOx₈₀-*grad*-PhOx₂₀ and PMeOx₈₀-*block*-PhOx₂₀; B) particle length distribution of PMeOx₈₀-*grad*-BuPhOx₂₀, PMeOx₈₀-*block*-BuPhOx₂₀, PMeOx₈₀-*grad*-BuOPhOx₂₀ and PMeOx₈₀-*block*-BuOPhOx₂₀.

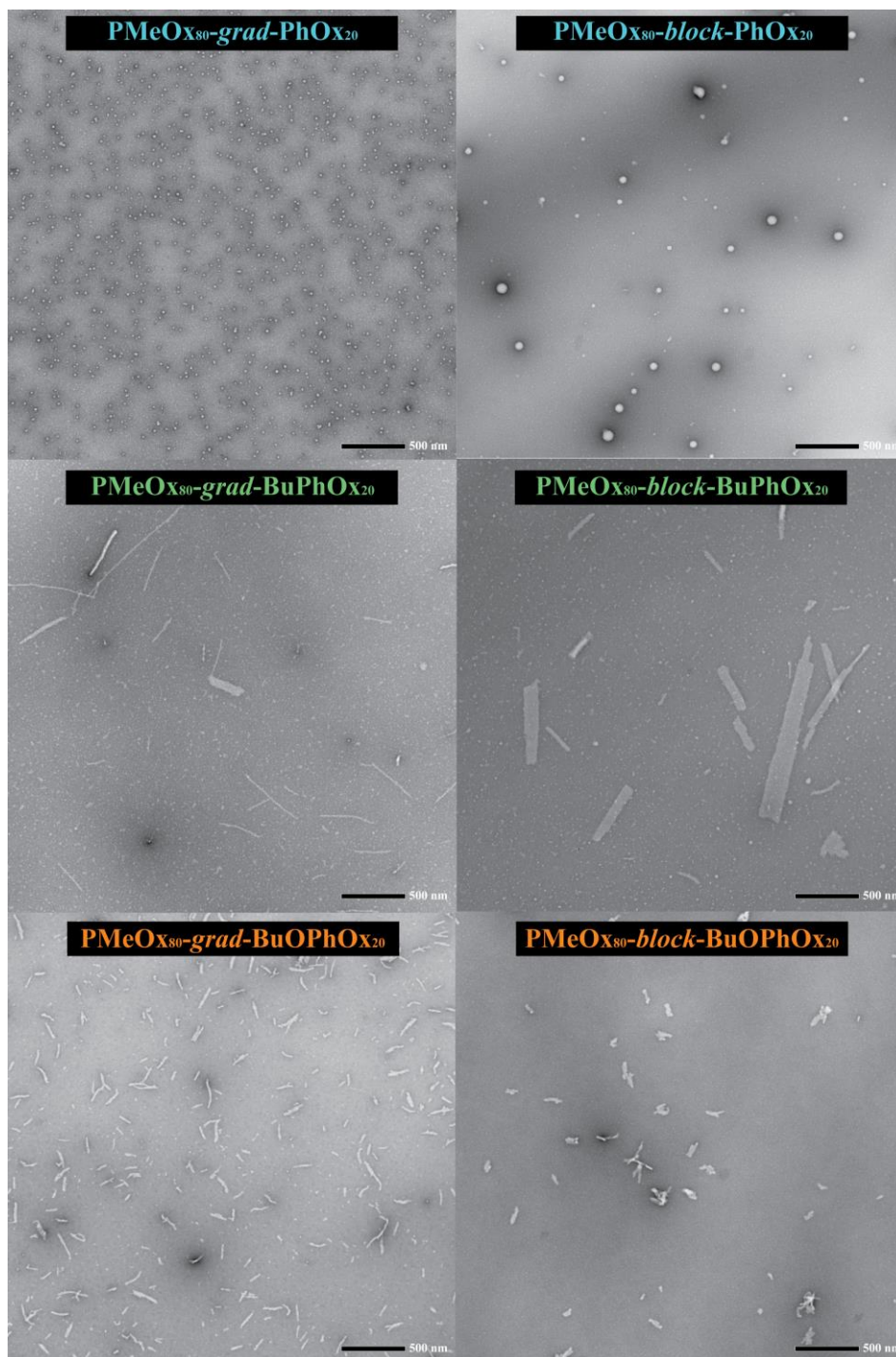


Figure S23. TEM images of rifampicin-loaded NPs. Scale bar represents 500 nm.

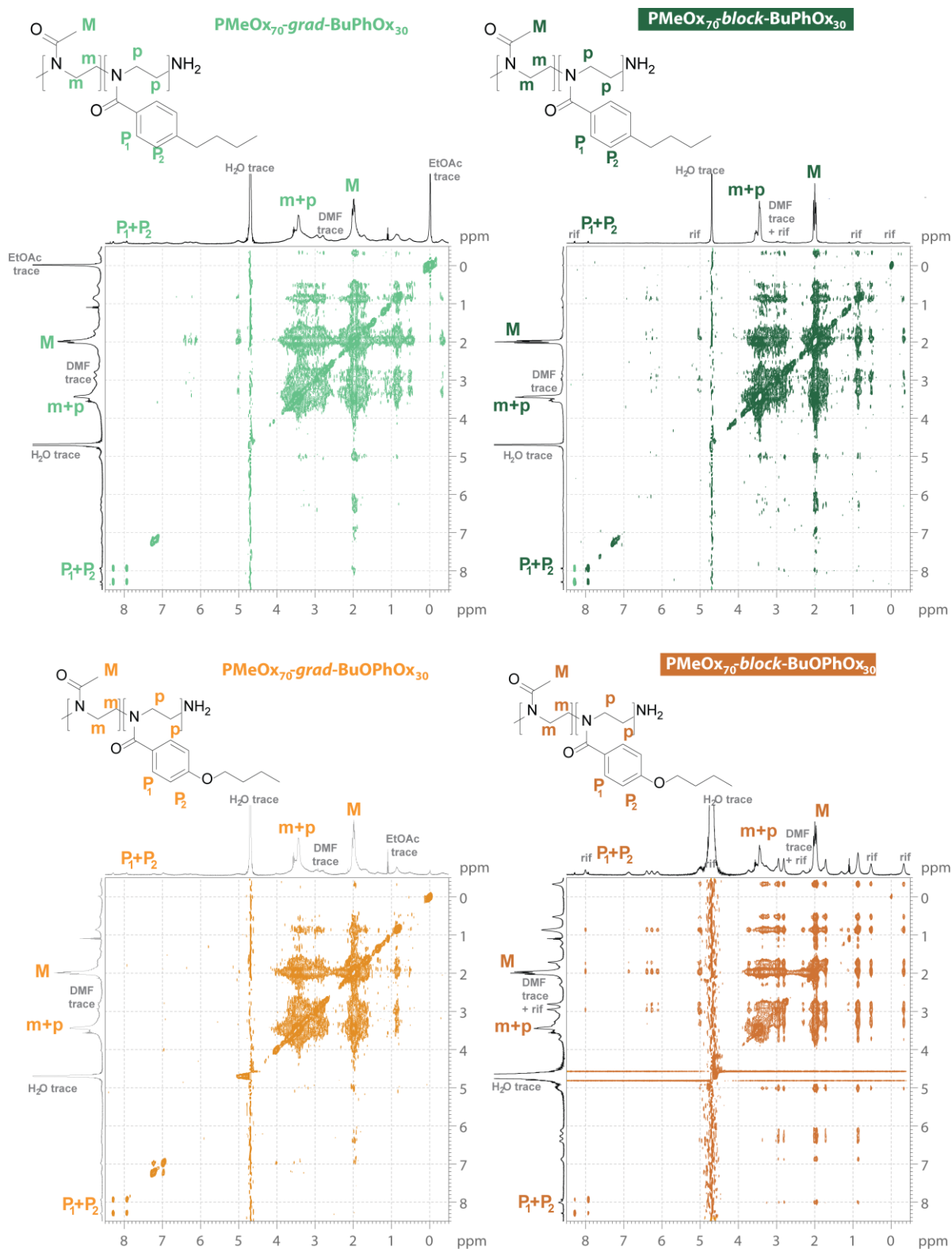


Figure S24. NOESY spectra of PMeOx₇₀-*grad*-BuPhOx₃₀ (left top), PMeOx₇₀-*block*-BuPhOx₃₀ (right top), PMeOx₇₀-*grad*-BuOPhOx₃₀ (left bottom) and PMeOx₇₀-*block*-BuOPhOx₃₀ (right bottom).

2. *In vitro* data

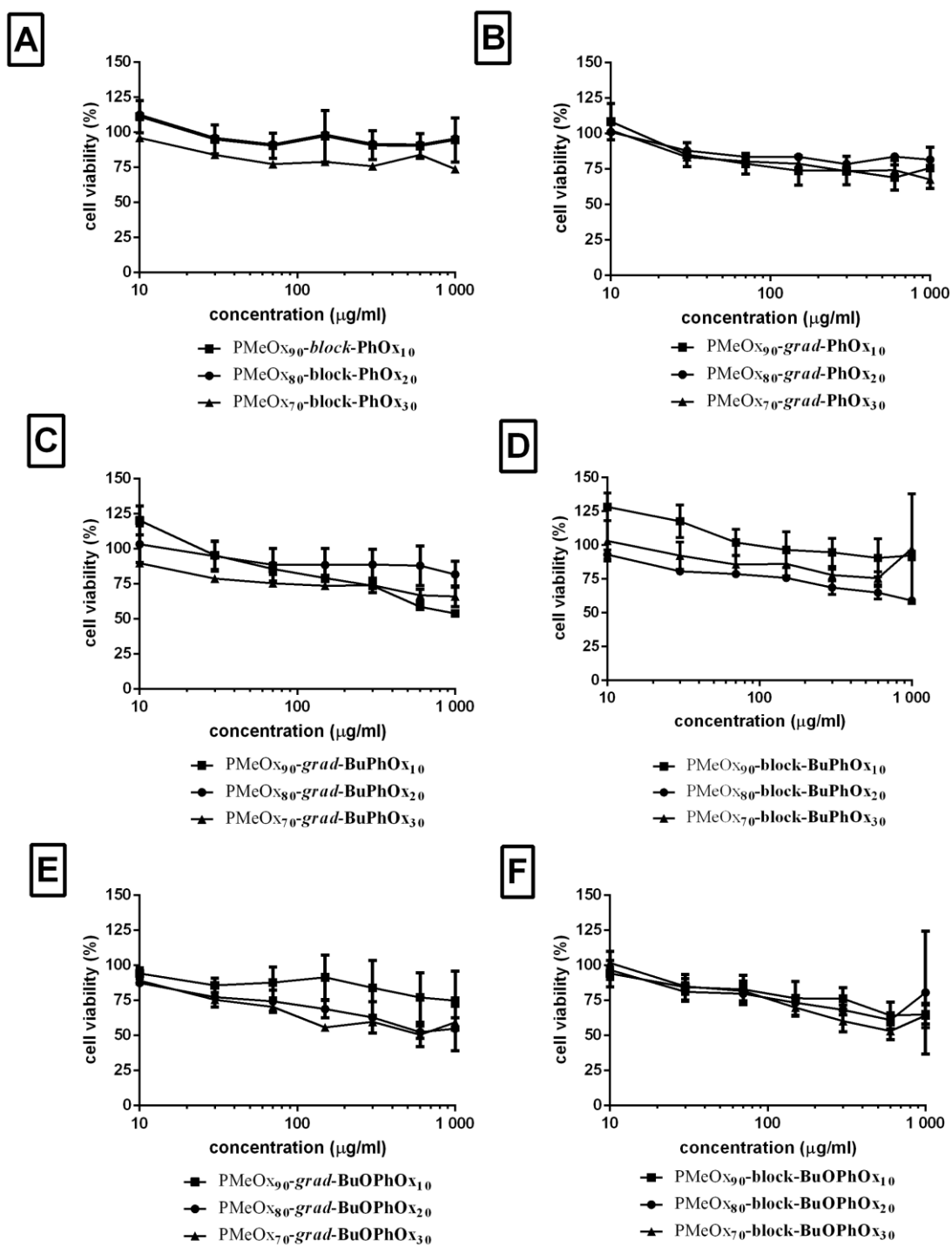


Figure S25. Polymer cytotoxicity on NHDF cells.

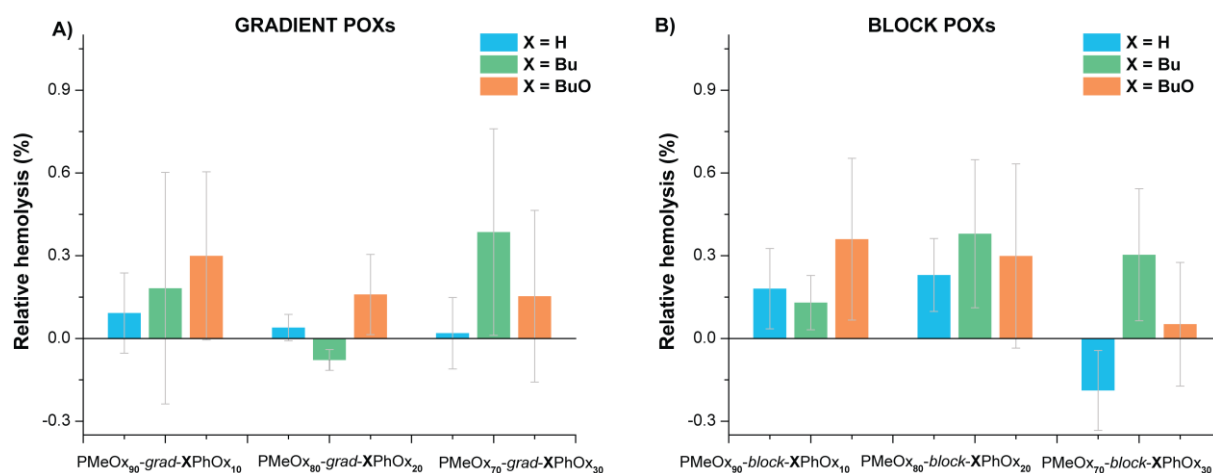


Figure S26. Hemolysis potential of the gradient (A) and block (B) polymers.

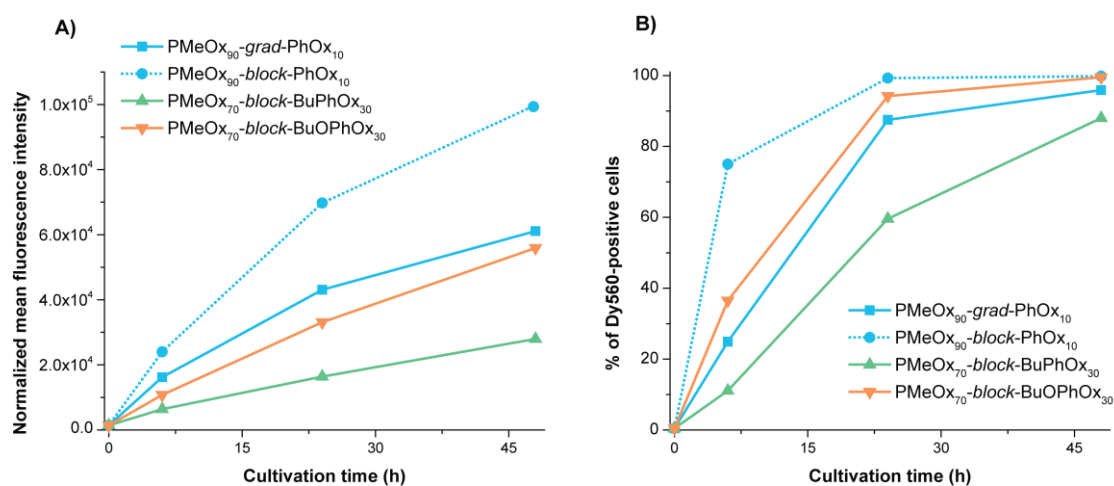


Figure S27. Cellular association assay of the polymers labeled with Dy560 ($c = 1 \text{ mg/mL}$). A) Normalized signal correlated with the weight amount of Dy560 in the polymers, B) content of Dy560-positive cells

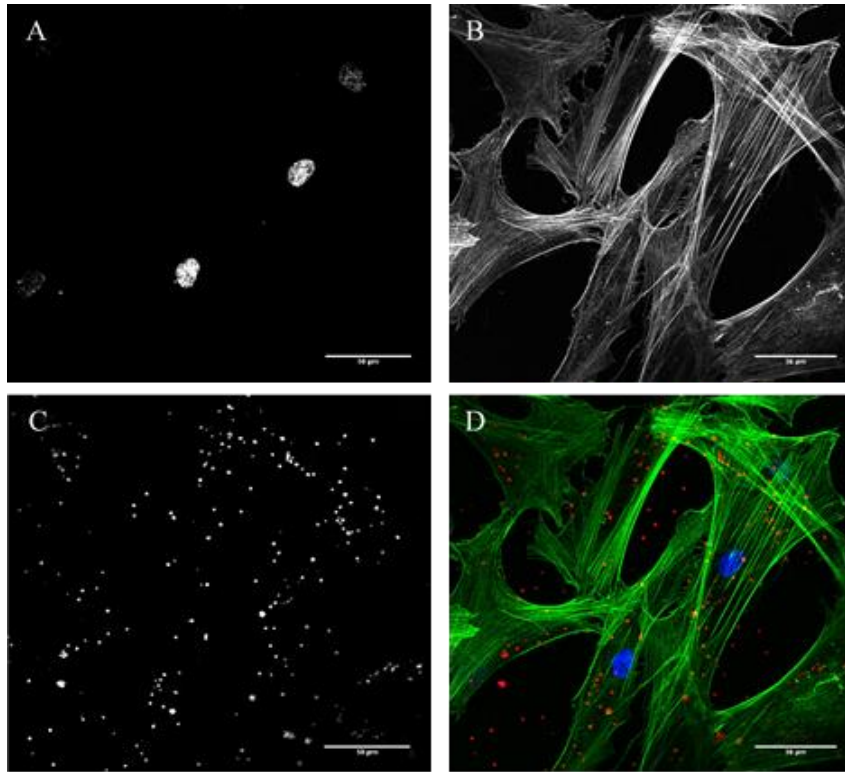


Figure S28. Representative fluorescent image of NHDF cells incubated with PMeOx₉₀-*grad*-PhOx₁₀ (A – cell nuclei; B – actin cytoskeleton; C – derivate; D – composite. Scale bar represents 50 μ m).

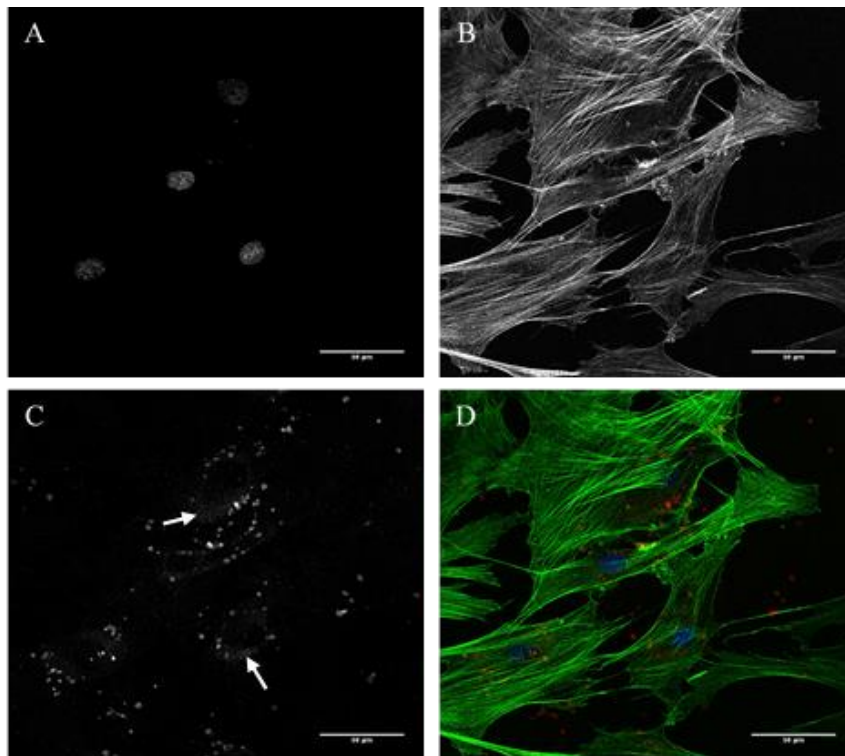


Figure S29. Representative fluorescent image of NHDF cells incubated with PMeOx₉₀-*block*-PhOx₁₀ (A – cell nuclei; B – actin cytoskeleton; C – derivate; D – composite. Scale bar represents 50 μ m).

3. NMR spectra

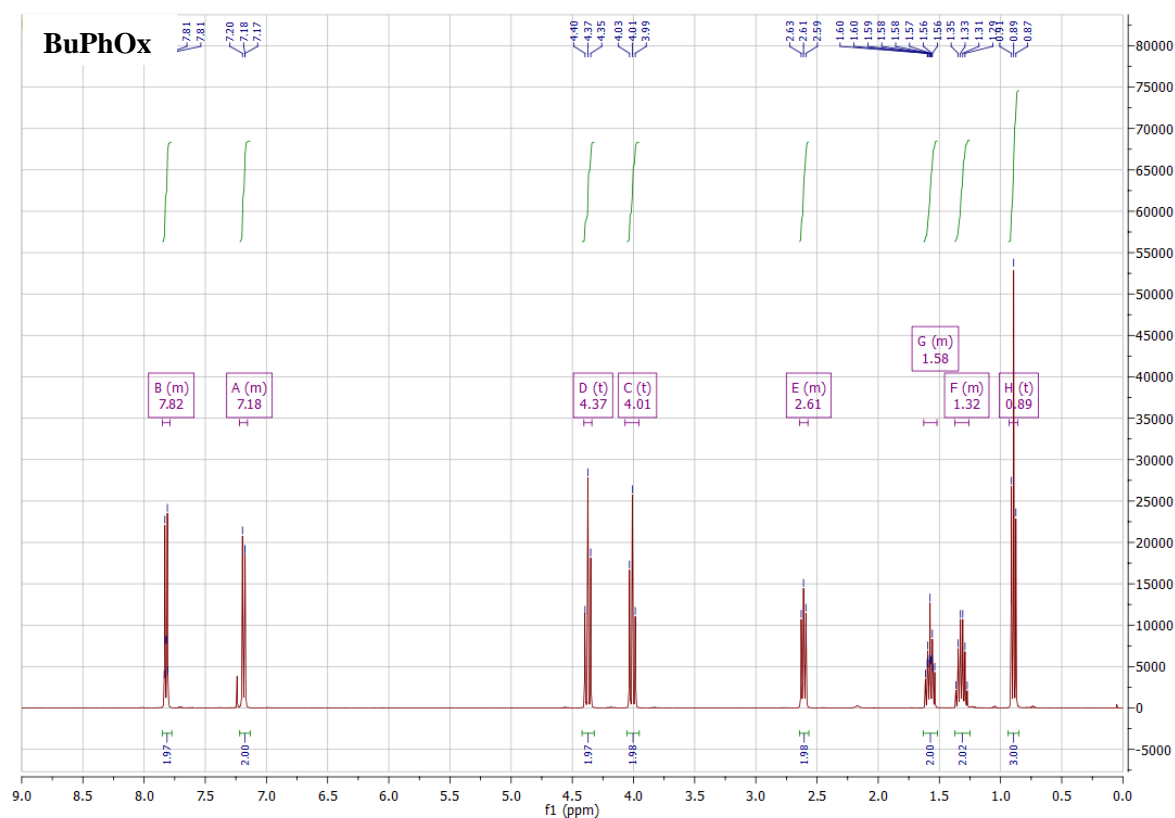


Figure S30. ¹H-NMR spectrum of BuPhOx.

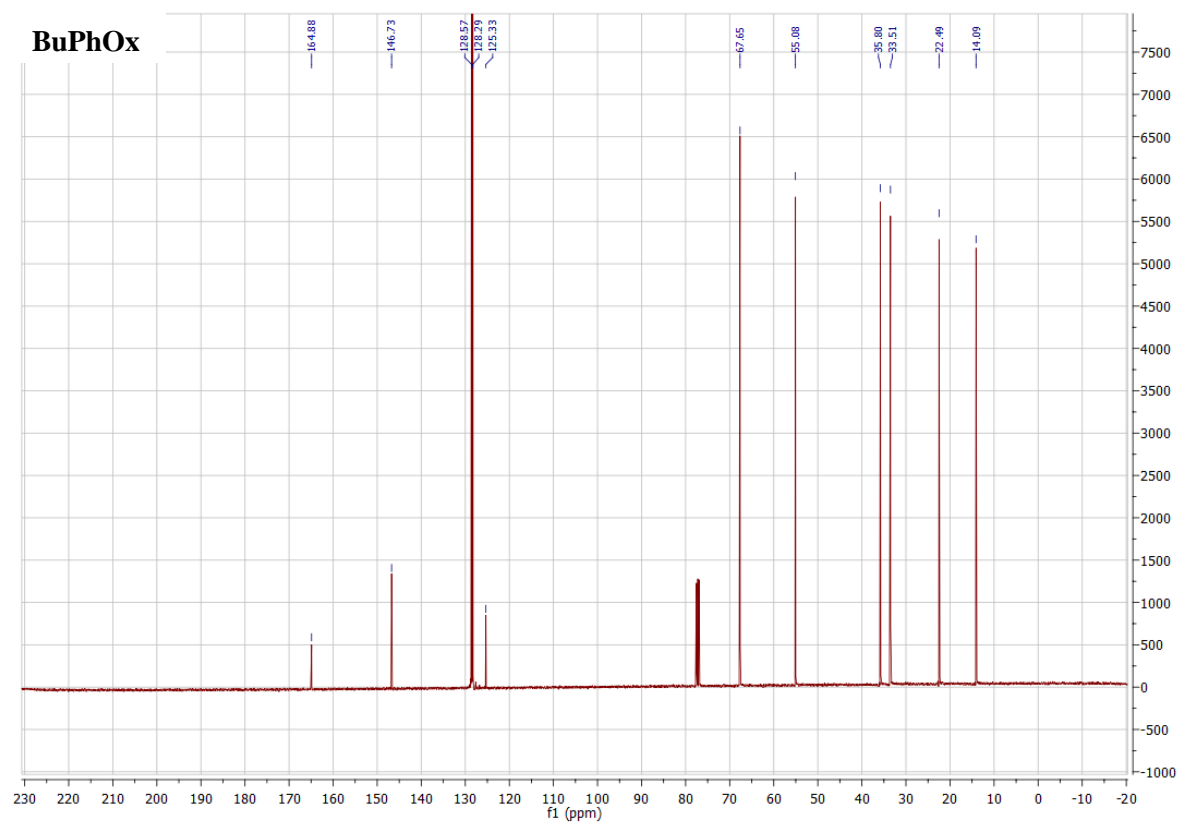


Figure S31. ¹³C-NMR spectrum of BuPhOx.

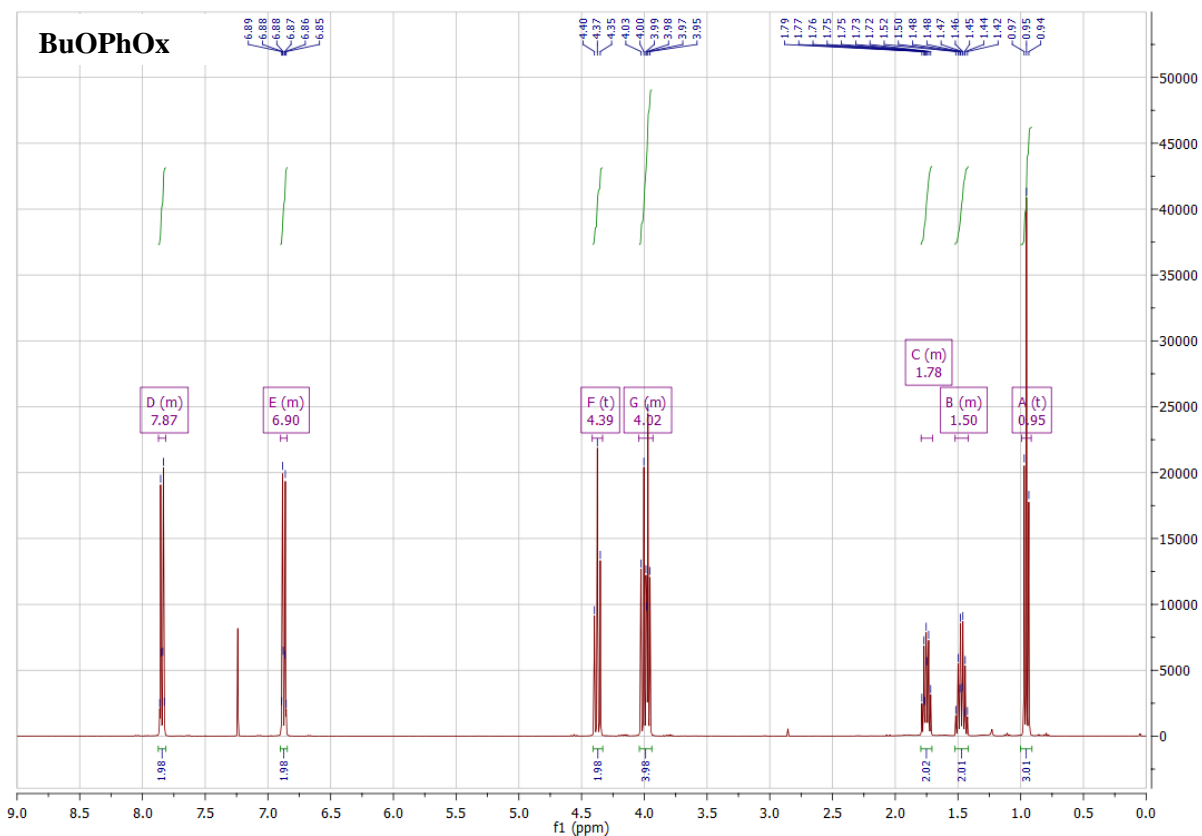


Figure S32. ^1H -NMR spectrum of BuOPhOx.

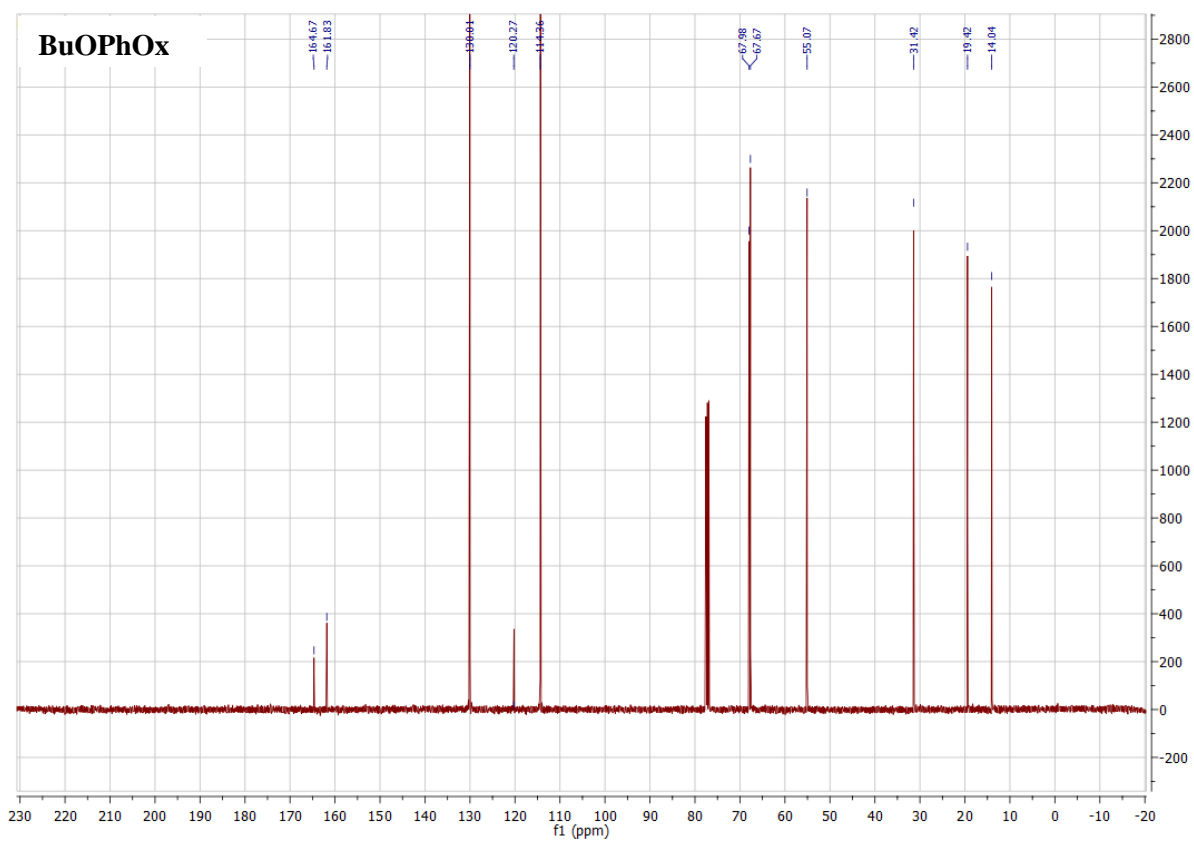


Figure S33. ^{13}C -NMR spectrum of BuOPhOx.

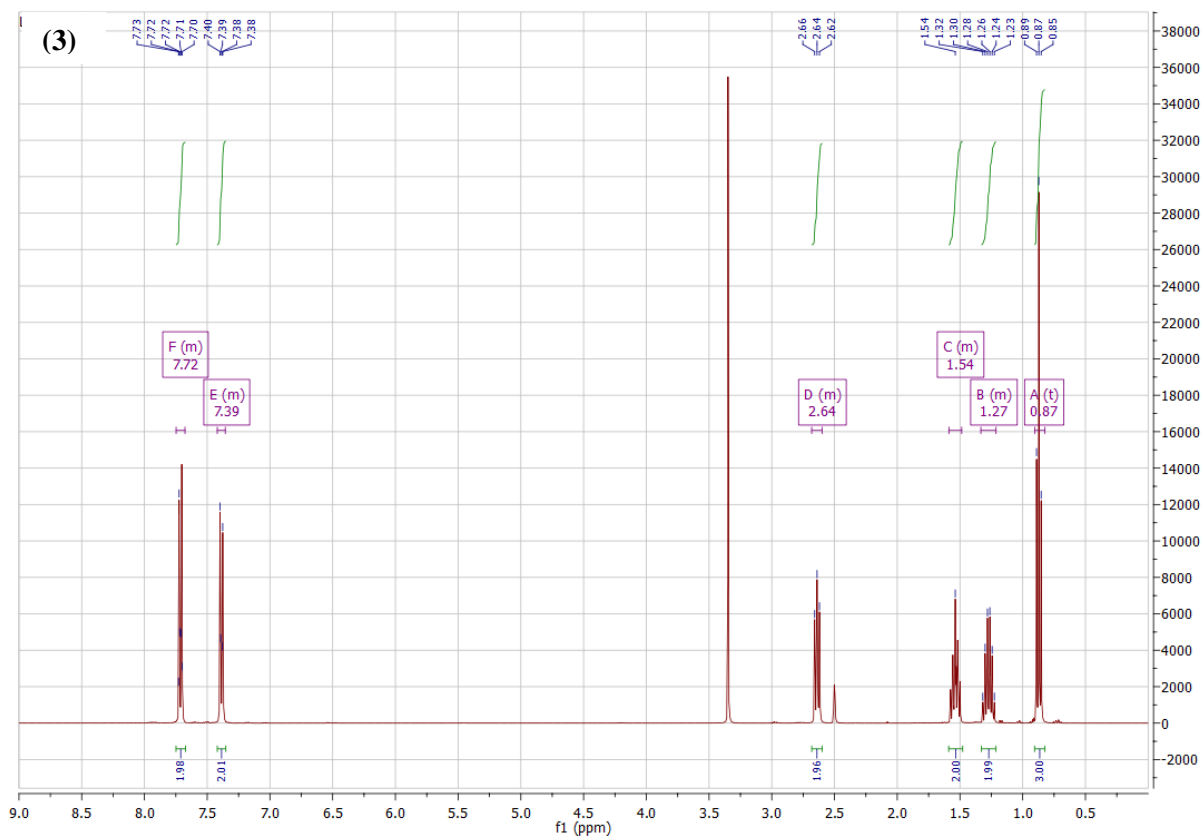


Figure S34. ^1H -NMR spectrum of 4-butylbenzotrile (3).

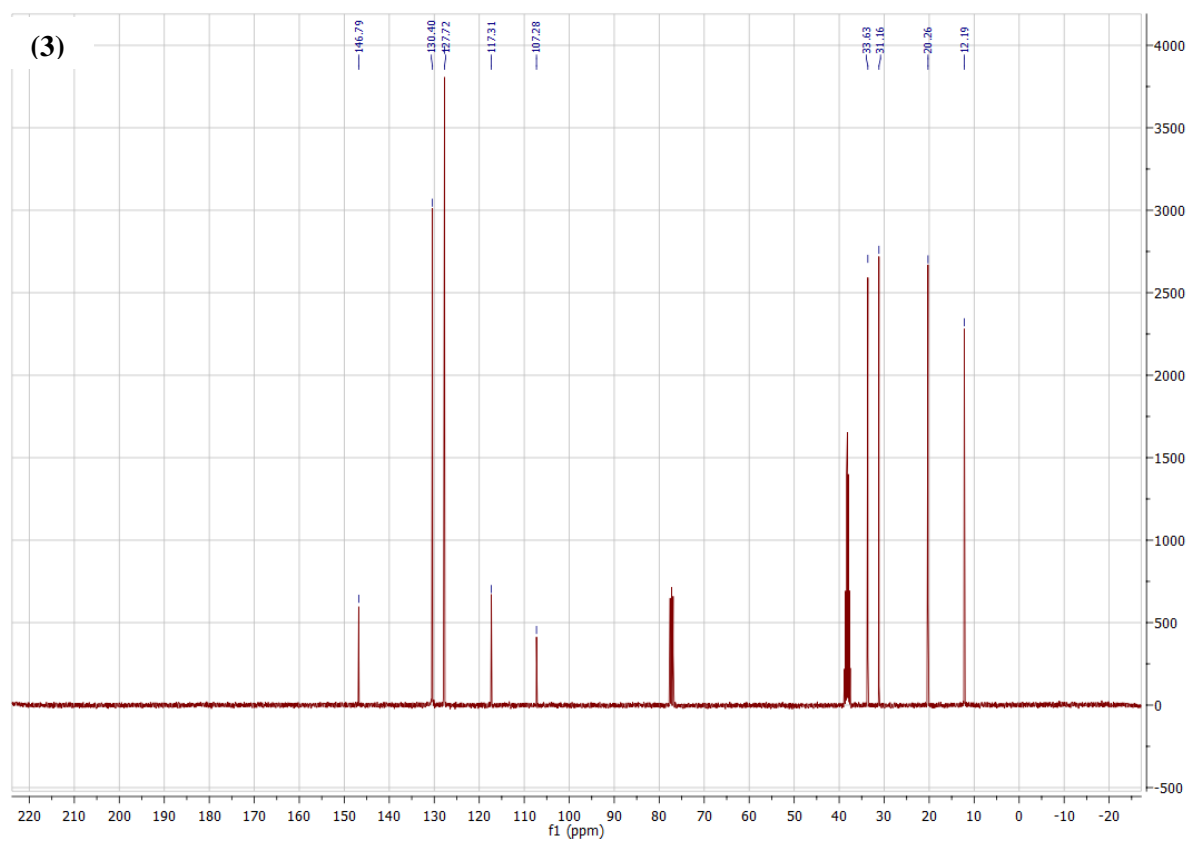


Figure S35. ^{13}C -NMR spectrum of 4-butylbenzotrile (3).

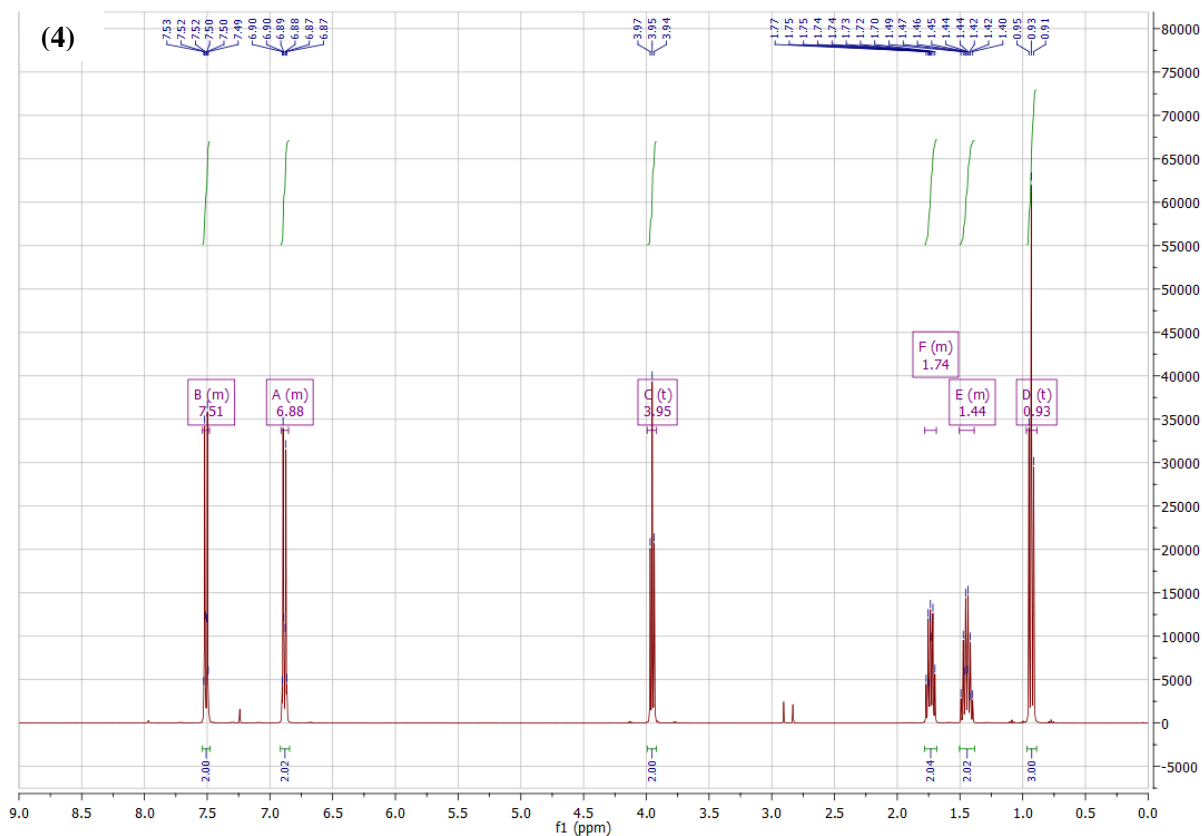


Figure S36. ^1H -NMR spectrum of 4-butoxybenzotrile (4).

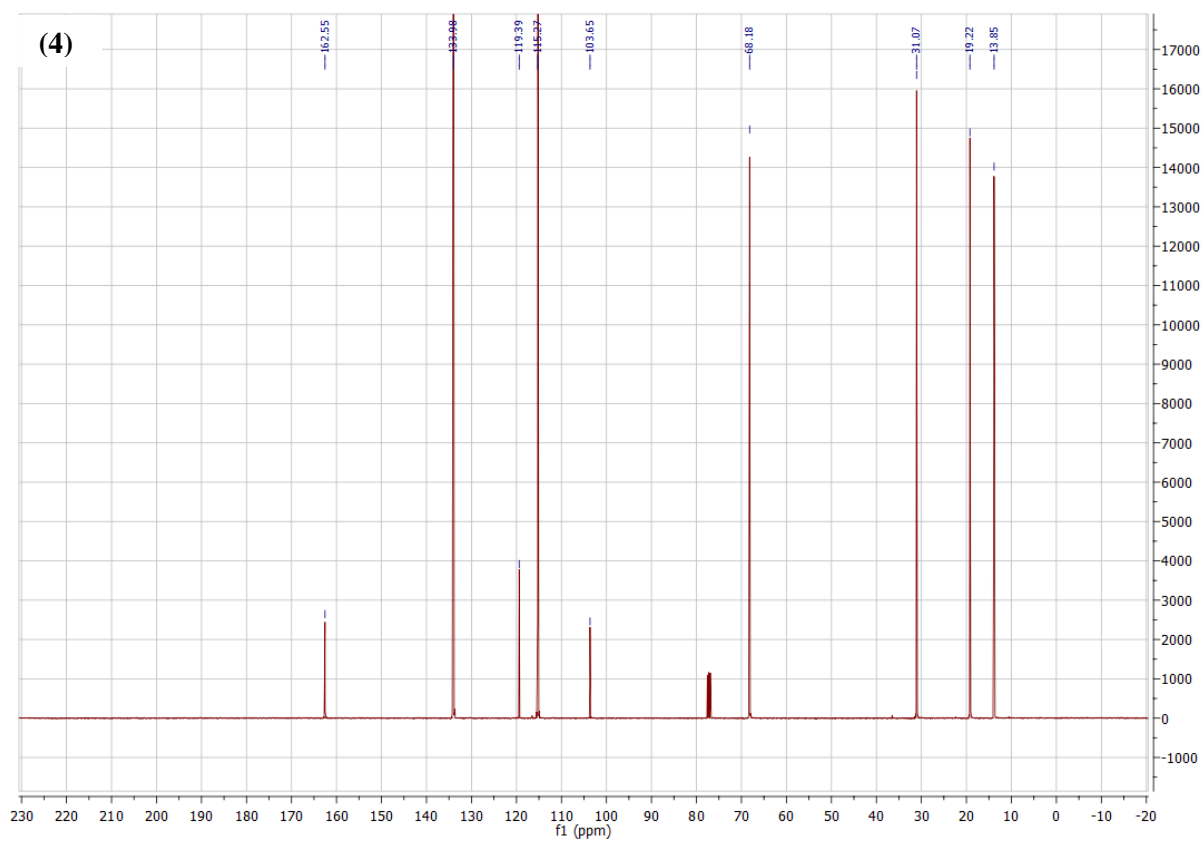


Figure S37. ^{13}C -NMR spectrum of 4-butoxybenzotrile (4).

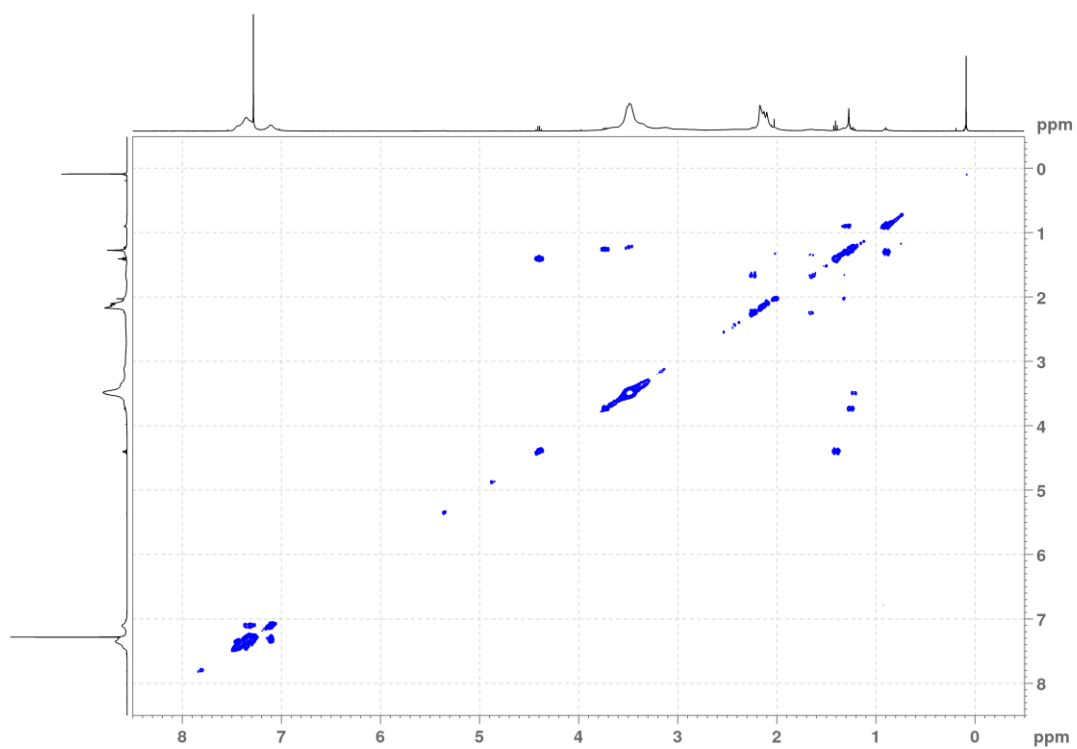


Figure S38. ^1H - ^1H COSY spectrum of PMeOx_{70} -*grad*- PhOx_{30} .

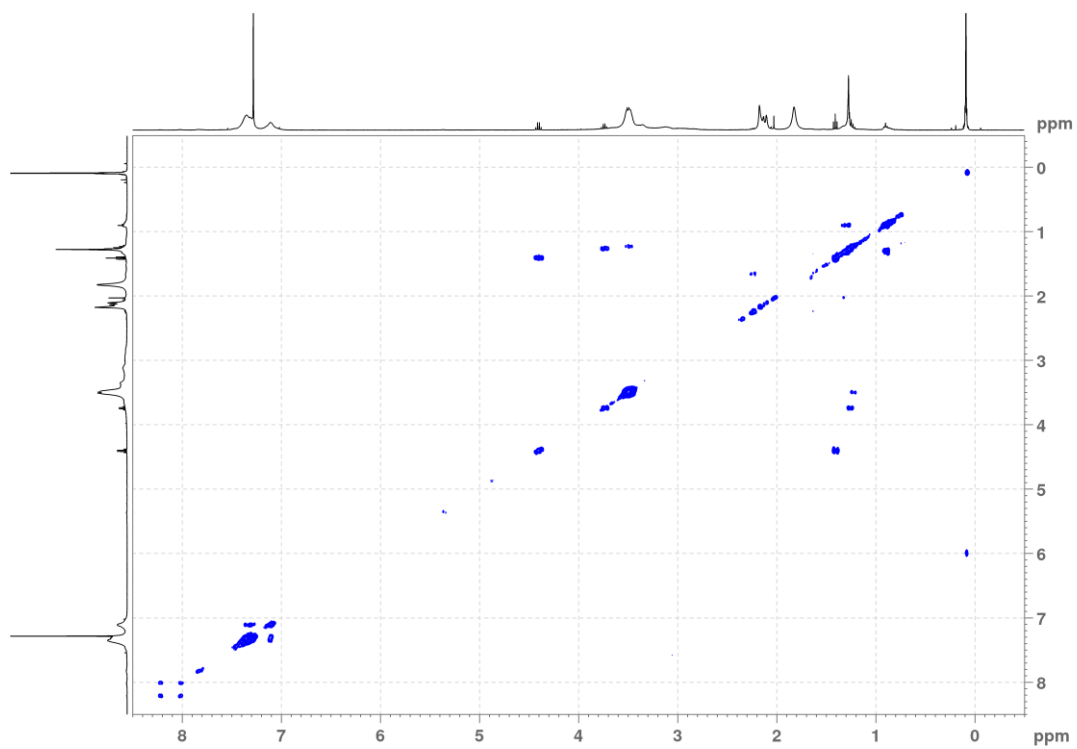


Figure S39. ^1H - ^1H COSY spectrum of PMeOx_{70} -*block*- PhOx_{30} .

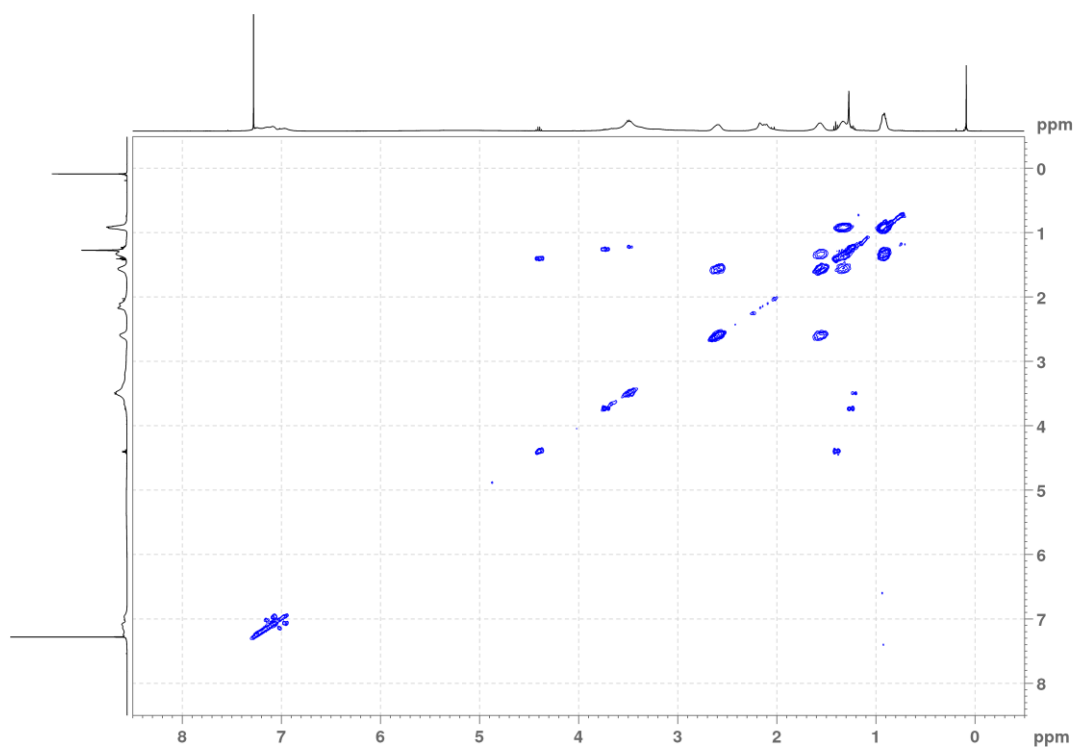


Figure S40. ^1H - ^1H COSY spectrum of PMeOx_{70} -*grad*- BuPhOx_{30} .

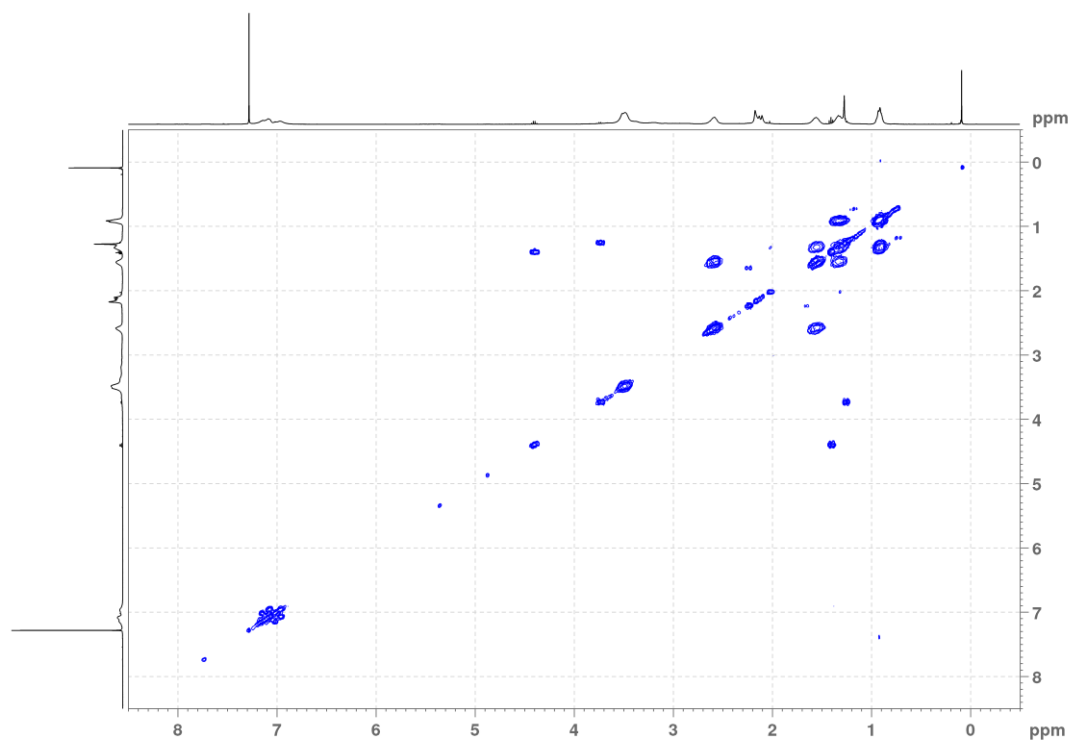


Figure S41. ^1H - ^1H COSY spectrum of PMeOx_{70} -*block*- BuPhOx_{30} .

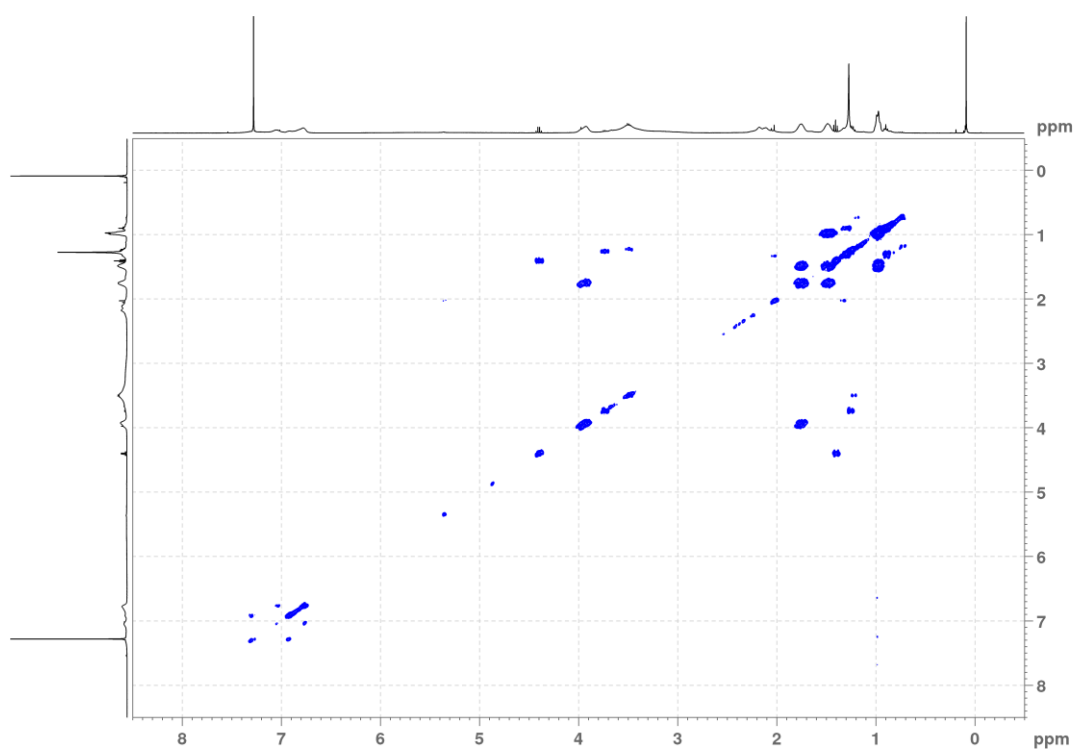


Figure S42. ^1H - ^1H COSY spectrum of PMeOx_{70} -*grad*- BuOPhOx_{30} .

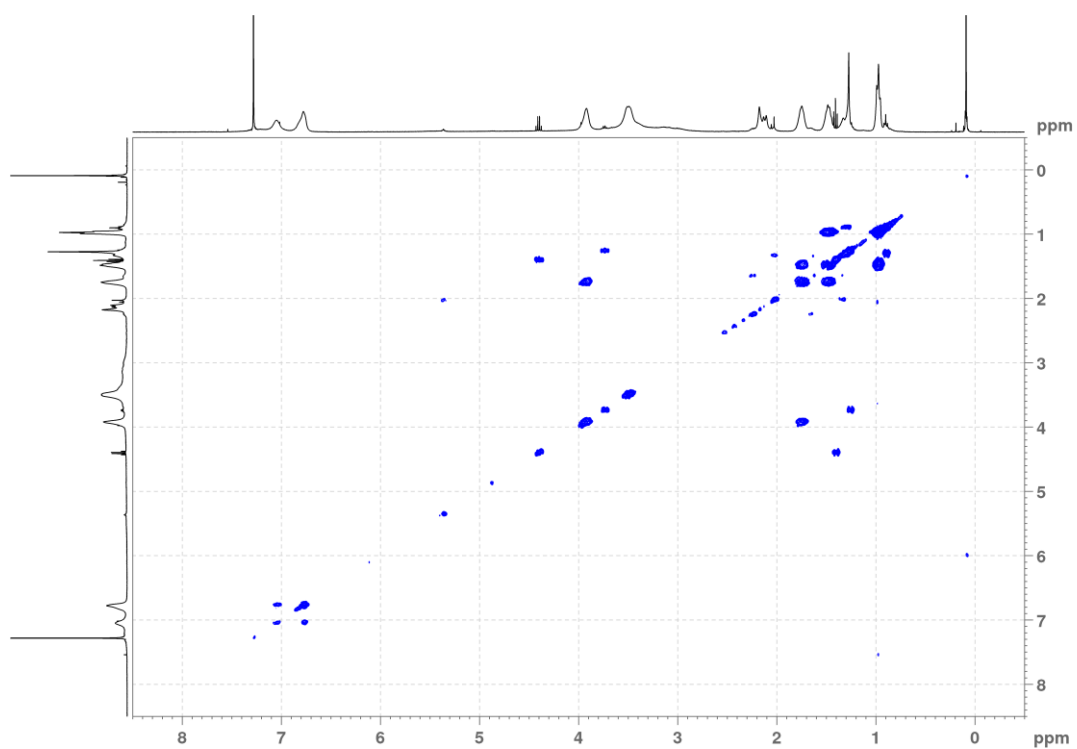


Figure S43. ^1H - ^1H COSY spectrum of PMeOx_{70} -*block*- BuOPhOx_{30} .

4. SEC traces

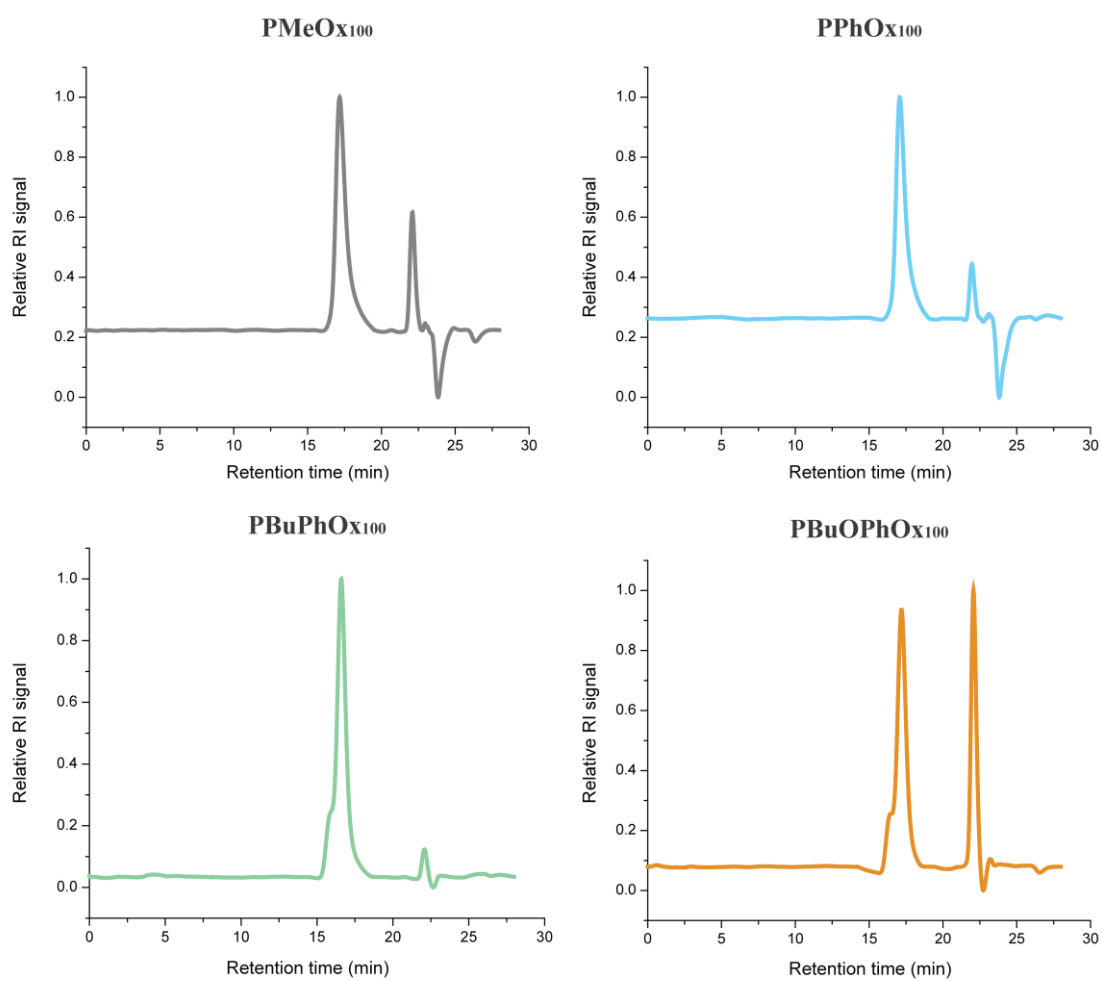


Figure S44. SEC traces of the homopolymers PMeOx₁₀₀, PPhOx₁₀₀, PBuPhOx₁₀₀, and PBuOPhOx₁₀₀.

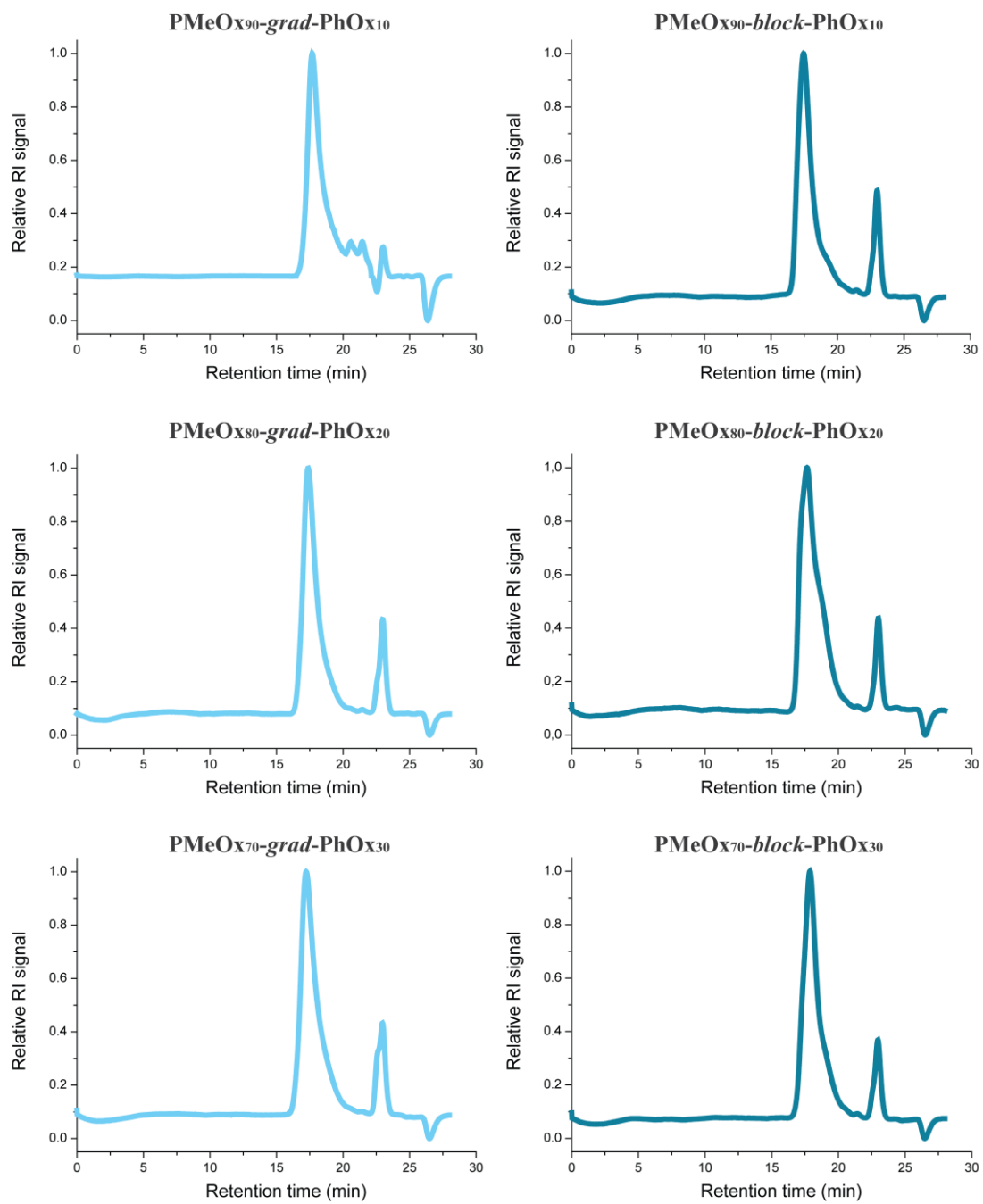


Figure S45. SEC traces of the copolymers PMeOx-PhOx.

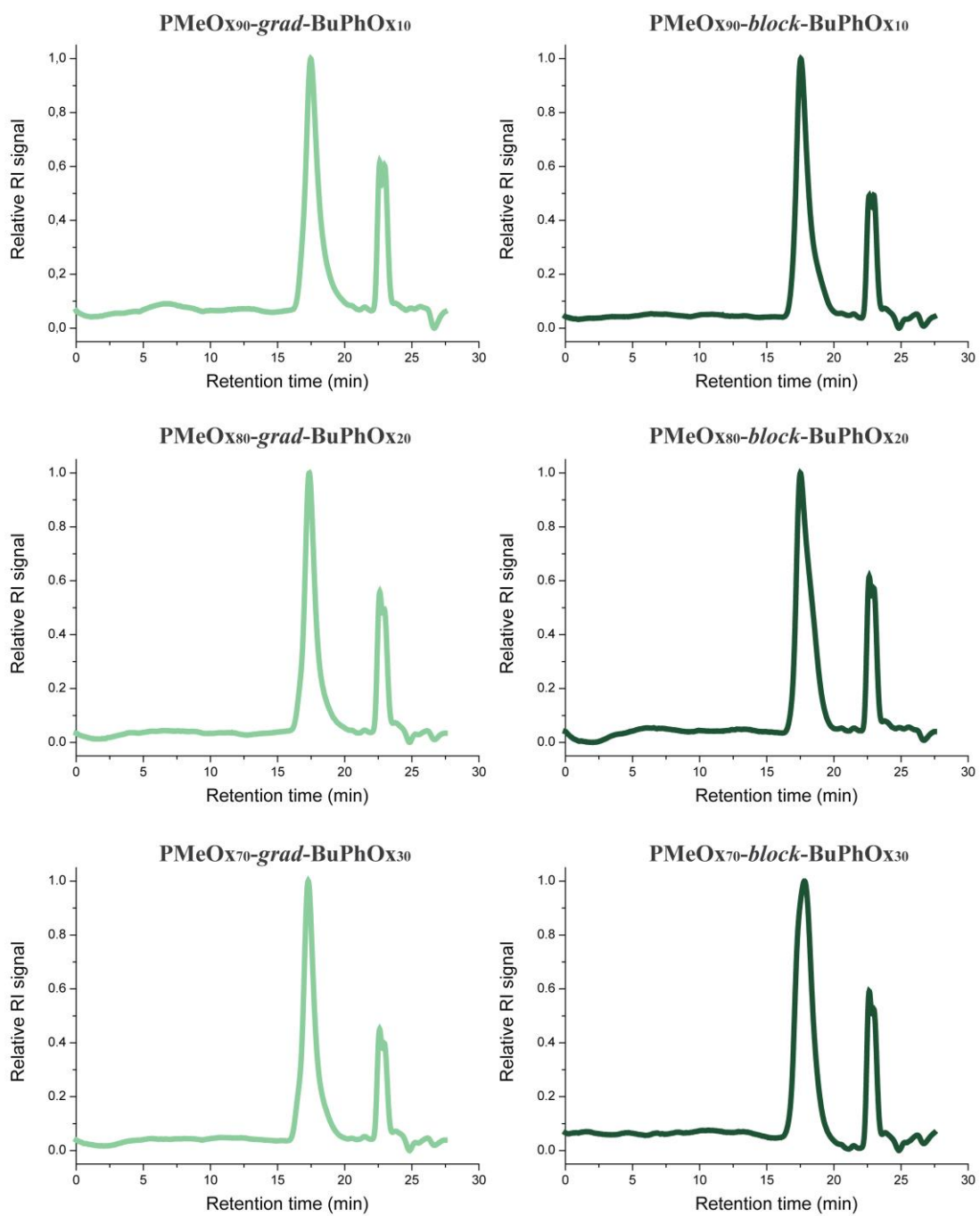


Figure S46. SEC traces of the copolymers PMeOx-BuPhOx.

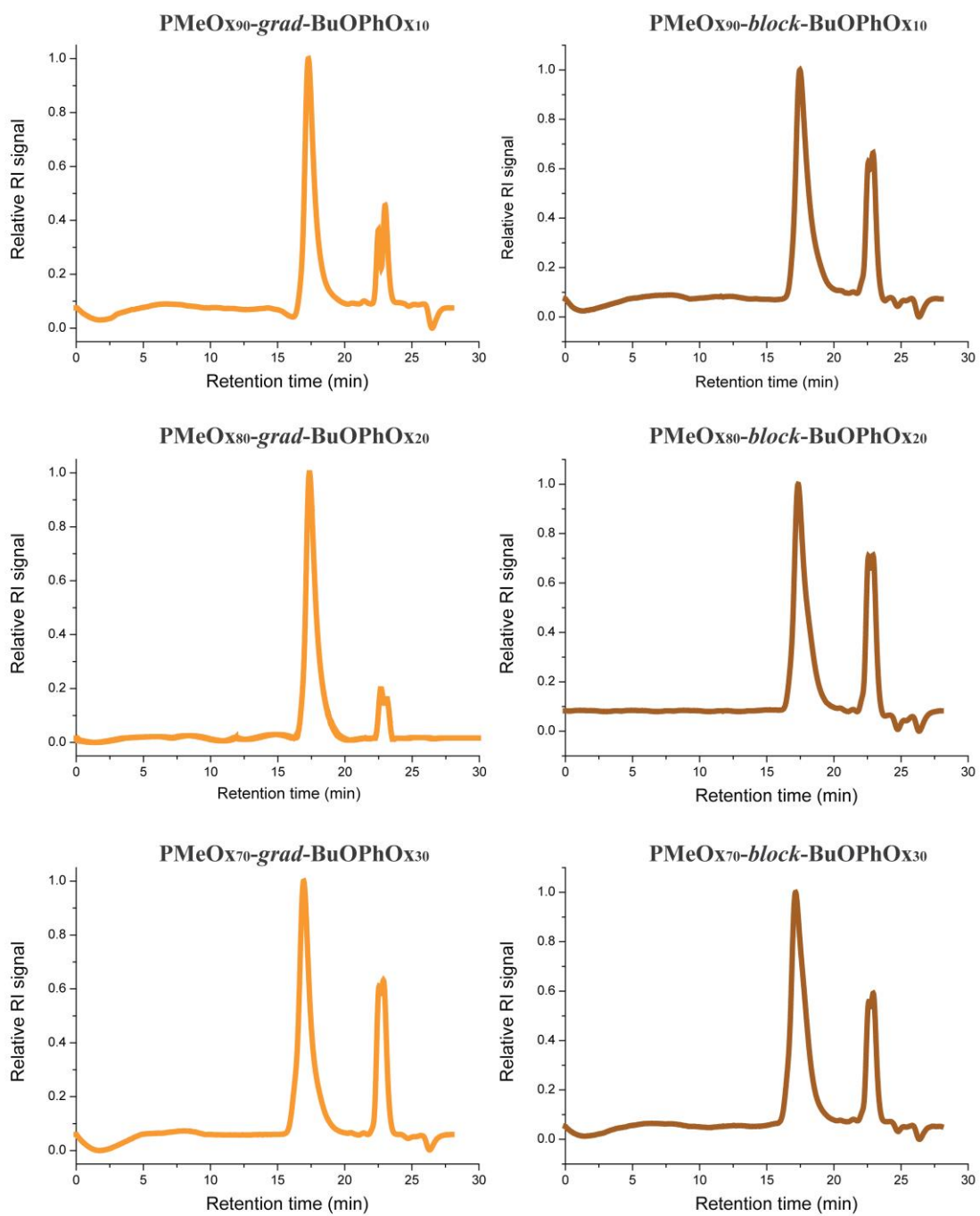


Figure S47. SEC traces of the copolymers PMeOx-BuOPhOx.